Friedrich-Schiller-Universität Jena

Chemisch-Geowissenschaftliche Fakultät

Ruthenium(II) Terpyridyl Complexes Featuring Donor and Acceptor Moieties

Dissertation

(kumulativ)

zur Erlangung des akademischen Grades

doctor rerum naturalium (Dr. rer. nat.)

vorgelegt dem Rat der Chemisch-Geowissenschaftlichen Fakultät

der Friedrich-Schiller-Universität Jena

von Dipl.-Chem. Kevin Barthelmes

geboren am 24.04.1988 in Meiningen

Gutachter:

1. Prof. Dr. Ulrich S. Schubert (Friedrich-Schiller-Universität Jena)
2. Prof. Dr. Benjamin Dietzek (Friedrich-Schiller-Universität Jena)

Tag der öffentlichen Verteidigung: 20.09.2017

Table of content

Documentation of authorship

This section contains a list of individual authors' contributions to the publications reprinted in this thesis.

P1) K. Barthelmes,[1] A. Winter,[2] U. S. Schubert,[3] "Hybrid Materials based on Ruthenium and Fullerene Assemblies", *Dalton Trans.* **2016**, *45*, 14855-14882.			
Author	1	2	3
Development of concept	×		
Preparation of the manuscript	×		
Correction of the manuscript		×	×
Supervision of K. Barthelmes		×	×
Proposed publication equivalent	0.5		

P2) K. Barthelmes,[1,‡] J. Kübel,[2,‡] A. Winter,[3] M. Wächtler,[4] C. Friebe,[5] B. Dietzek,[6] U. S. Schubert,[7] "New Ruthenium Bis(terpyridine) Methanofullerene and Pyrrolidinofullerene Complexes: Synthesis and Electrochemical and Photophysical Properties", *Inorg. Chem.* **2015**, *54*, 3159-3171. ‡ Authors contributed equally.							
Author	1	2	3	4	5	6	7
Synthesis	×						
Characterization	×	×		×	×		
Time-resolved spectroscopy		×		×			
Development of concept	×	×	×	×		×	
Preparation of the manuscript	×	×					
Correction of the manuscript		×	×	×	×	×	×
Supervision of K. Barthelmes			×				×
Proposed publication equivalent	1.0						

P3) K. Barthelmes,[1] A. Winter,[2] U. S. Schubert,[3] "Dyads and Triads based on Phenothiazine, Bisterpyridine Ruthenium(II) Complexes and Fullerene", *Eur. J. Inorg. Chem.* **2016**, 5132-5142.			
Author	1	2	3
Synthesis	×		
Characterization	×		
Development of concept	×	×	
Preparation of the manuscript	×		
Correction of the manuscript		×	×
Supervision of K. Barthelmes		×	×
Proposed publication equivalent	1.0		

P4) K. Barthelmes,[1] M. Sittig,[2] A. Winter,[3] U. S. Schubert,[4] "Molecular Dyads and Triads Based on Phenothiazine and π-extended Tetrathiafulvalene Donors, Ruthenium(II) Bisterpyridine Complexes and Polyoxometalates", *submitted*.				
Author	1	2	3	4
Synthesis	×	×		
Characterization	×	×		
Development of concept	×		×	
Preparation of the manuscript	×			
Correction of the manuscript		×	×	×
Supervision of K. Barthelmes			×	×
Proposed publication equivalent	1.0			

P5) K. Barthelmes,[1] M. Jäger,[2] J. Kübel,[3] C. Friebe,[4] A. Winter,[5] M. Wächtler,[6] B. Dietzek,[7] U. S. Schubert,[8] "Efficient Energy Transfer and Metal Coupling in Cyanide-Bridged Heterodinuclear Complexes Based on (Bipyridine)(terpyridine)ruthenium(II) and (Phenylpyridine)iridium(III) Complexes", *Inorg. Chem.* **2016**, *55*, 5152-5167.								
Author	1	2	3	4	5	6	7	8
Synthesis	×							
Characterization	×		×	×				
Time-resolved spectroscopy			×					
Computational study		×						
Development of concept	×							
Preparation of the manuscript	×	×	×					
Correction of the manuscript		×	×	×	×	×	×	×
Supervision of K. Barthelmes					×			×
Proposed publication equivalent	1.0							

Erklärung zu den Eigenanteilen des Promovenden/der Promovendin sowie der weiteren Doktoranden/Doktorandinnen als Koautoren an den Publikationen und Zweitpublikationsrechten bei einer kumulativen Dissertation

Für alle in dieser kumulativen Dissertation verwendeten Manuskripte liegen die notwendigen Genehmigungen der Verlage („Reprint permissions“) für die Zweitpublikation vor.

Die Co-Autoren der in dieser kumulativen Dissertation verwendeten Manuskripte sind sowohl über die Nutzung, als auch über die oben angegebenen Eigenanteile informiert und stimmen dem zu (es wird empfohlen, diese grundsätzliche Zustimmung bereits mit Einreichung der Veröffentlichung einzuholen bzw. die Gewichtung der Anteile parallel zur Einreichung zu klären).

Die Anteile des Doktoranden/der Doktorandin sowie der weiteren Doktoranden/Doktorandinnen als Co-Autoren an den Publikationen sind in der Anlage aufgeführt.

Ich bin mit der Abfassung der Dissertation als publikationsbasiert, d.h. kumulativ, einverstanden und bestätige die vorstehenden Angaben. Eine entsprechend begründete Befürwortung mit Angabe des wissenschaftlichen Anteils des Doktoranden/der Doktorandin an den verwendeten Publikationen werde ich parallel an den Rat der Fakultät der Chemisch-Geowissenschaftlichen Fakultät richten.

Name Doktorand(in)	Datum	Ort	Unterschrift
Name Erstbetreuer(in)	Datum	Ort	Unterschrift

1. Introduction

With a rapidly increasing world energy consumption it becomes more and more problematic to cover the demand with the dwindling resources of fossil fuels, which still contribute by around 80% to the total energy supply. In addition to the limited availability, the continued emission of greenhouse gases has been deemed as significant effect on the global warming. In order to build a sustainable economy and to retard the climate change, it is necessary to reduce the dependency on fossil fuels and to search for clean and renewable energy sources. Hence, the globally accessible, inexhaustible sunlight is one of the few alternatives that could serve as source for energy supply in the future.[1-3] In the last decades, tremendous research has been focused on the conversion of solar energy into electricity (*i.e.*, photovoltaics)[4-6] or chemical energy (*i.e.*, photocatalysis).[7-8] In the latter case, two important photocatalytic processes have been investigated to produce the so-called "solar fuels": The oxidative water splitting into oxygen[9-12] and the reduction of protons into hydrogen.[11, 13-14] Those redox reactions require sophisticated photocatalysts that undergo multiple electron transport reactions, whereby the charge accumulation currently represents a significant challenge. The molecular design of some catalysts has been inspired by the efficient processes in the natural photosynthesis. Hereby, scientists tried to mimic the fundamental processes of light-harvesting and photoinduced charge separation, in order to prepare artificial photosynthetic devices (Figure 1.1).[15]

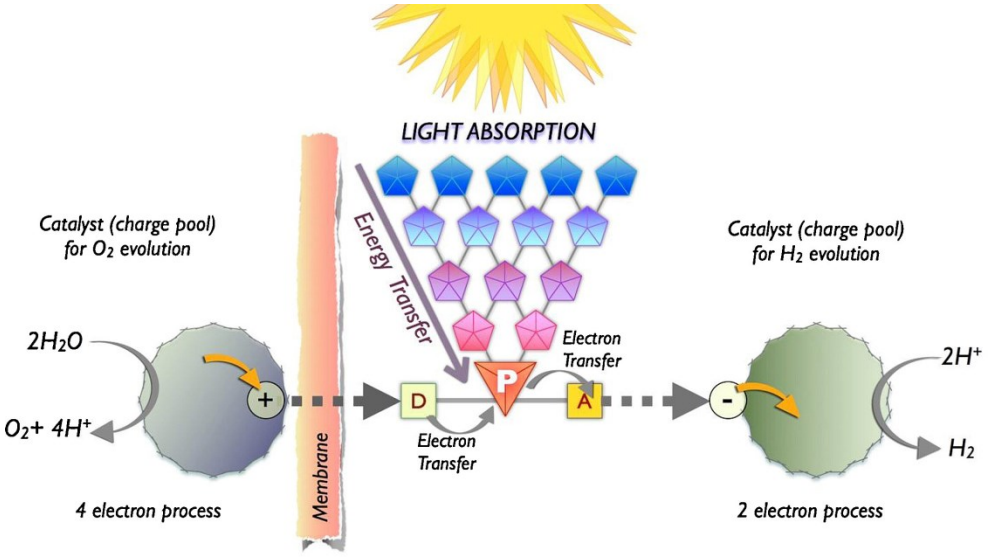

Figure 1.1. Schematic representation of an artificial photosynthetic device. Figure reprinted with permission from ref. [10], copyright 2011 Elsevier B.V..

Such a molecular device can consist of an electron donor (D), a photosensitizer (P) and an electron acceptor (A), whereby the photosensitizer gets excited by light and two consecutive electron transfer processes result in a charge separated state between the donor and the acceptor moieties. Additional light-harvesting chromophores can be attached on the photosensitizer to enhance the spectral absorption, which transfer the solar energy to the photosensitizer by energy transfer processes. In this respect, ruthenium(II) complexes with polypyridyl ligands (*e.g.*, bpy = 2,2'-bipyridine and tpy = 2,2':6',2''-terpyridine) have been studied as photosensitizer, since they are redox stable, exhibit broad absorption in the visible region, can serve as electron donor and acceptor and perform a charge separation between the Ru(II) center and the ligand upon light irradiation. In particular, Ru(II) bisterpyridine complexes are well-suited buildings block for the preparation of D–P–A systems, because they can be formed free of isomers and the functionalization of the two tpy ligands in 4'-position with acceptor and donor units result in a linear and rigid separation between the components compared to similar bpy-based complex (Figure 1.2).[16-18]

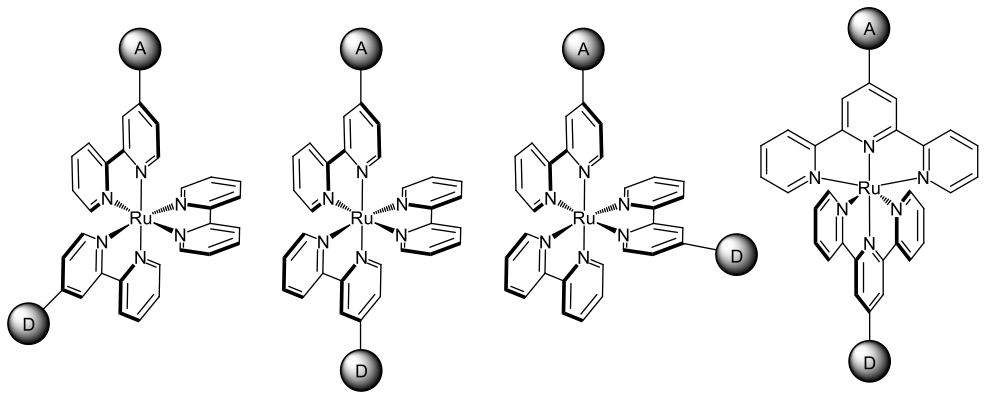

Figure 1.2. Schematic representation of some isomers obtained with a Ru(II) complex based on 4-substituted bpy's and the only geometric isomer obtained with a complex based on 4'-substituted tpy's.[16]

The goal of this thesis is to synthesize molecular dyads and triads based on ruthenium(II) terpyridyl complexes featuring electron and energy donors (*i.e.*, phenothiazines, π-extended tetrathiafulvalenes and Ir(III) complexes) and acceptors (*i.e.*, fullerenes and polyoxometalates). The compounds were investigated in cooperation with the group of Prof. Dietzek according to their structure-property relationship, in particular, their photophysical interaction between the active moieties, such as photoinduced energy and electron transfer processes.

The thesis is structured as follows: **Chapter 2** provides a short literature survey over the different types of ruthenium-fullerene assemblies. This is followed by a more detailed insight into the molecular dyads with Ru(II) complexes, which are covalently attached to the fullerene by surface modification reactions. Different synthetic approaches are shown for the preparation of such Ru(II) complex-fullerene (Ru-C_{60}) systems at the example of C_{60} and bpy as metal binding unit. Subsequently, the possible photodynamic pathways of Ru-C_{60} systems, which can occur after excitation of the Ru(II) complex, are explained. **Chapter 3** deals with the preparation of Ru-C_{60} systems based on Ru(II) bisterpyridine complexes ($[Ru(tpy)_2]^{2+}$) with several aromatic spacer units in between the Ru(II) complex and the C_{60} to tune the donor-acceptor distance. Moreover, the functionalization pattern on the fullerene surface is varied to adjust the angle between the donor and acceptor. The modular design of $[Ru(tpy)_2]^{2+}$ is utilized to establish a synthetic route for the preparation of molecular triads with an additional, easier to oxidize, organic donor (*i.e.*, phenothiazine). In this case, the new donor and acceptor is additionally separated by the Ru(II) complex, which should enhance the photoinduced electron transfer to form long-range charge separation. **Chapter 4** describes the preparation of similar molecular dyads and triads, however the organic C_{60} unit is replaced by an inorganic polyoxometalate framework and an additional, stronger organic donor (*i.e.*, π-extended tetrathiafulvalene) is incorporated. In the last chapter (**Chapter 5**), a different approach is used to attach Ru(II) complexes with Ir(III) complexes. The preparation of Ru(II) complexes with a bpy and a tpy ligand enabled the coordination of a mono-, and ambidentate cyanide ligand of an Ir(III) complex *via* the last open coordination site. By this approach, close-coupled heterodinuclear complexes are formed with a metal-metal distance of only 5 Å. Consequently, strong interactions between the metal centers are observed in the ground, the oxidized and the excited state.

2. Hybrid materials based on ruthenium-fullerene assemblies

Parts of this chapter have been published in **P1**) K. Barthelmes, A. Winter, U. S. Schubert, *Dalton Trans.* **2016**, *45*, 14855-14882.

Molecular systems based on Ru(II) complexes and fullerenes were frequently described in the literature. The following chapter gives a brief overview about the synthesis and photophysical properties of covalently connected Ru(II) complex-C_{60} assemblies.

An enormous amount of research has focused on the chemistry of fullerenes after the discovery of the spherically shaped C_{60} in 1985.[19] The discovery of new carbon allotropes did not tarnish the status of C_{60} as the flagship in the ongoing research of carbon surface modification. The unique spherical shape makes C_{60} to the favored structure in the context of product selectivity, functionalization, characterization or network formation, if compared to the spheroidal C_{70} or the family of higher fullerenes, the tube-shaped nanotubes, and the flat graphene. One of the most remarkable properties of fullerenes and their derivatives is their pronounced electron accepting character and low reorganization energy, which makes them to a favored unit in donor-acceptor systems, such as organic solar cells.[20] C_{60} features a strong absorption in the UV region with weaker spin-forbidden transitions in the visible region[21] and photoexcitation results in the formation of the singlet state ($^1C_{60}$*), which decays quantitatively (with a triplet quantum yield of >99%) *via* intersystem crossing (ISC) to the triplet state ($^3C_{60}$*). The latter one is highly sensitive to oxygen and results in the formation of singlet oxygen that has, for example, been applied in photodynamic therapy.[22]

Within the last 25 years, the interaction of various transition metal ions with fullerenes has thoroughly been examined regarding catalytic activity, photoinduced formation of charge separated states, self-assembly in solution or surface modification.[23-30] In this context, ruthenium(II) as transition metal ion features interesting and unique properties: Most of its complexes (*i.e.*, Ru(II) polypyridyl complexes) are very stable, exhibit an electron donating and redox-active metal center,[31] show intense absorption of visible light and have rather long-lived excited states;[31-32] moreover, their catalytic activity is well-documented in literature.[12] All these characteristics make Ru(II) complexes to attractive candidates for the incorporation into fullerene-based architectures. By this approach new hybrid materials can be generated that feature the individual properties of the active units as well as combined properties mediated by intramolecular interactions between them.

Hybrid materials based on ruthenium complexes and fullerene assemblies can be classified in three groups. The first group contains organometallic ruthenium complexes in which the ruthenium is directly connected to the surface of the fullerene sphere by exohedral coordination. Ruthenium complexes that are not directly coordinated onto the fullerene surface can be summarized in the second group. Most of these compounds were prepared by ruthenium complexation of ligand-functionalized fullerenes. In the last group, a variety of non-covalently bonded ruthenium-fullerene architectures can be found – including supramolecular structures (*i.e.*, encapsulated fullerenes), ruthenium-impregnated fullerenes, ruthenium fulleride salts and ruthenium-fullerene blends.

In particular for the second group, the following Ru(II) complexes are discussed: Ru(II) trisbipyridines $[Ru(bpy)_3]^{2+}$, Ru(II) bisterpyridines $[Ru(tpy)_2]^{2+}$, Ru(II) porphyrins with axial coordinated pyridine and carbon monoxide [Ru(por)(py)(CO)], and ruthenocenes $[Ru(cp)_2]$ (cp = cyclopentadienyl anion) (Figure 2.1). The complexes are attached covalently by certain connections, *e.g.*, C–C bonds, ester or amide groups to a functionalized C_{60} ($F\text{-}C_{60}$) moiety. To the best of my knowledge, there are no examples reported so far utilizing C_{70} or higher fullerenes for the same purpose. Some of the compounds exhibit a bridging unit between the Ru(II) complex and the C_{60} to enlarge the distance between the moieties. These bridges (B) can consist of either aliphatic or aromatic spacer units. In such $Ru–B–C_{60}$ assemblies, the most common fullerene functionalization is by far the group of pyrrolidino[60]fullerenes (Figure 2.1). These surface modified C_{60} derivatives can be obtained by the reaction of an aldehyde group with an α-amino acid (*e.g.*, *N*-methylglycine) to *in situ* generate an azomethine ylide. The subsequent 1,3-dipolar cycloaddition reaction with a [6,6]-bond of C_{60} yields a functionalized pyrrolidine ring in 2-position.[33-35] Commonly, this type of fullerene functionalization is referred to as the Prato reaction. By inverting the substituents on the reagents, *i.e.*, employing formaldehyde and a *N*-substituted α-amino acid, the synthesis leads to analogous *N*-substituted pyrrolidines.[36] Another prominent example for functionalized C_{60} is the methano[60]fullerene (Figure 2.1). Such compounds feature a 1,1-disubstituted cyclopropane ring attached on the fullerene surface. The synthesis is often accomplished by the reaction of the α-carbon of malonic acid derivatives or diazo compounds with a [6,6]-double bond of C_{60} under basic conditions.[37-38] Rarely used are the group of pyrazolino[60]fullerenes (Figure 2.1), however, they feature enhanced electron delocalization compared to the non-conjugated pyrrolidino[60]fullerenes and methano[60]fullerenes.[39]

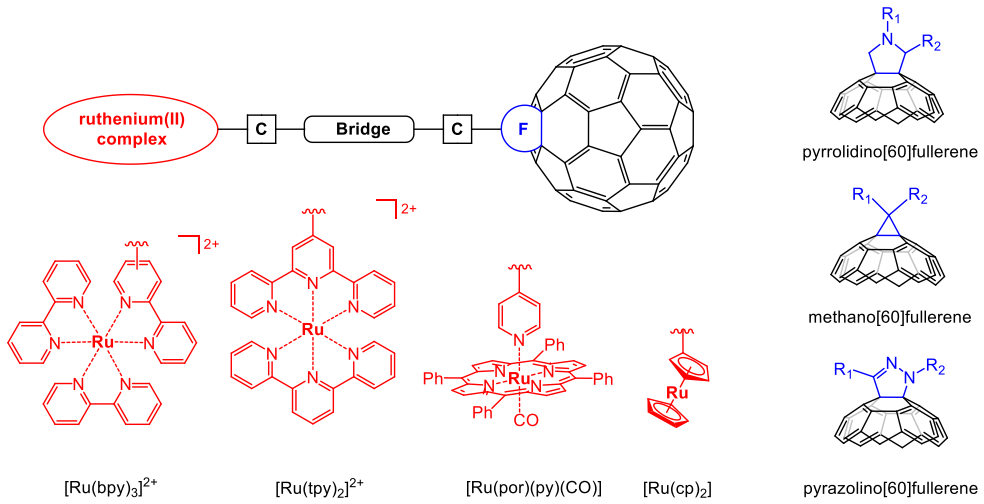

Figure 2.1. Schematic representation of the Ru–B–C_{60} assemblies with the most common ruthenium(II) complexes and fullerene functionalities.

The bidentate binding of bpy to Ru(II) centers is, by far, the most common motive to be found in Ru–B–C_{60} assemblies. Basically, there are three synthetic approaches used for the preparation of such complexes: The first approach starts from a bpy derivative bearing a bridging unit in 3 or 4 position (***1A***) (Route 1 in Scheme 2.1). The bridge itself contains a reactive group suited for the functionalization of fullerenes. The reaction with one double bond of the C_{60} yields a bpy–B–C_{60} conjugate (***1/2B***) with various functionalities on the fullerene surface. The subsequent metal coordination of these "bucky ligands" to the Ru(II) center is accomplished by the reaction of ***1/2B*** with the *cis*-[Ru(bpy)$_2$Cl$_2$] precursor complex in refluxing ethanol,[40] 1,2-dichloroethane,[34-35, 41] DMF[37, 42] or solvent mixtures with toluene[33] or *ortho*-dichlorobenzene (*o*DCB)[36] to increase the solubility of the bpy–B–C_{60} ligand. Coordination under significantly milder conditions can be achieved by activation of the precursor complex with Ag(I) salts in acetone to substitute the chlorides by weakly bound acetone molecules.[39] For Route 1 an alternative approach is also possible: Switching the order of the reaction steps, *i.e.*, performing at first the ruthenium coordination and subsequently the C_{60}-functionalization. However, this protocol has not yet been reported as an efficient method, due to the poor solubility of Ru(II) complexes in non-polar solvents used for the C_{60}-functionalization, *i.e.* toluene, chlorobenzene or *o*DCB.[39] The second route appears to be similar to the first one, but starts from C_{60} that has been pre-functionalized with a reactive group (Route 2 in Scheme 2.1). The following reaction with an appropriate bpy derivative that contains the bridging unit (***2A***) establishes a connection between the bpy-B unit and the F-C_{60} to yield the bpy–B–C_{60} ligand (***1/2B***). This approach has, for example, been used by Armaroli *et al.*[42] in an esterification reaction

of a carboxylic acid containing methano[60]fullerene with a hydroxy functionalized bpy. The final step in this sequence is the above-mentioned ruthenium coordination. Finally, for the third approach, the synthetic route starts with the functionalization of C_{60}, as already shown in Route 1. Subsequently, the formed F-C_{60} (***3A***) is reacted with an appropriate $[Ru(bpy)_2(X\text{-}bpy)]^{2+}$ complex to afford directly the Ru–B–C_{60} assembly. For example, Chaignon *et al.*[43] used the 3-bromo-bpy containing complex $[Ru(bpy)_2(3\text{-}Br\text{-}bpy)]^{2+}$ and various terminal alkyne-functionalized pyrrolidino[60]fullerenes in a Pd(0)-catalyzed cross-coupling reaction. In general, the three routes outlined in Scheme 2.1 can similarly be applied for attaching Ru(II) bisterpyridine complexes to C_{60}. Here, the reported complexes are exclusively connected to the bridge in the 4'-position of the central pyridine ring in the terpyridine scaffold. The reason for this particular pattern is rationalized by the facile synthetic accessibility of the 4'-substituted tpy.

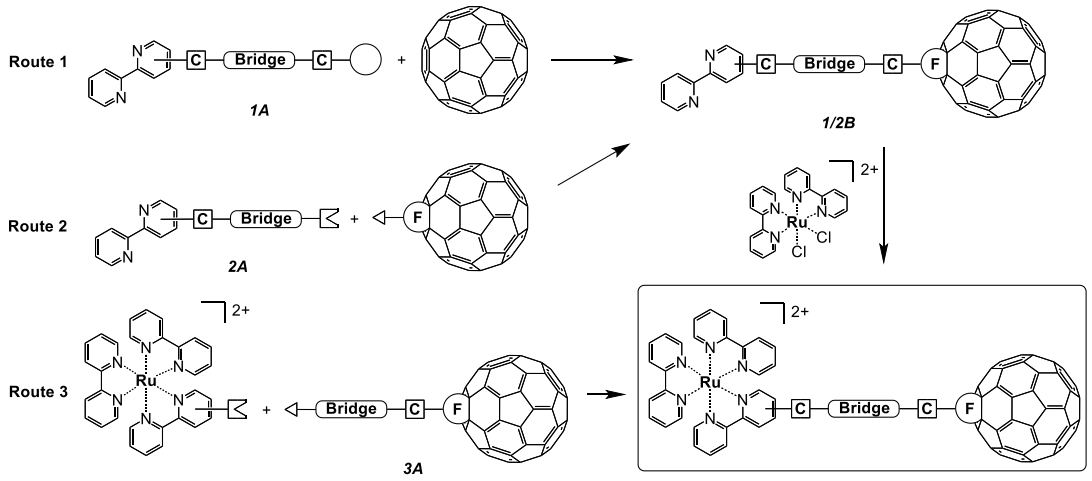

Scheme 2.1. Schematic representation of reported synthetic routes towards Ru–B–C_{60} assemblies with bpy as metal-binding unit.

The photophysical and electrochemical properties of $[Ru(bpy)_3]^{2+}$ and $[Ru(tpy)_2]^{2+}$ complexes have thoroughly been analyzed in literature.[31-32] Such complexes exhibit a broad absorption in the visible region arising from intense metal-to-ligand charge transfer (^{1}MLCT) transitions and are weakly emitting. After excitation in their ^{1}MLCT transitions the Ru(II) complexes undergo a very fast ISC towards the lower lying triplet state (^{3}MLCT), due to the heavy ruthenium atom.[31] The most striking photophysical difference between $[Ru(bpy)_3]^{2+}$ and $[Ru(tpy)_2]^{2+}$ can be observed in their excited state properties: At room temperature, $[Ru(tpy)_2]^{2+}$ complexes exhibit a significantly shorter excited state ^{3}MLCT lifetime (τ = 0.21 ns for $[Ru(tpy)_2](PF_6)_2$ in butyronitrile at 290 K)[44] by around three orders of magnitude compared to similar $[Ru(bpy)_3]^{2+}$

complexes.[17, 45] This behavior also impacts on the emission quantum yields and results in even weaker emitting complexes. The reason for the reduced lifetime of $[Ru(tpy)_2]^{2+}$ is caused by the low-lying metal-centered triplet states (^{3}MC). A population of these states becomes thermal accessible and, thereby, increases the fast non-radiative decay back to the ground state. However, a long-lived excited state is often required to guarantee subsequent photodynamic processes in the excited state. Therefore, $[Ru(bpy)_3]^{2+}$ is basically the more promising candidate to gain efficient charge transfer towards fullerene. Disadvantageously, these complexes suffer from the formation of Λ-/Δ-isomers upon further substitution of the bpy ligands. On the other hand, $[Ru(tpy)_2]^{2+}$ complexes will be formed free of isomers and, if the competing energy and electron transfer processes are fast enough, the limitation by the intrinsic low excited state lifetime can be circumvented.

In general, Ru–B–C_{60} assemblies can be considered as molecular dyad, whereby the Ru(II) complex is the photosensitizer and the electron donor, and the fullerene represents the electron acceptor. There are several photodynamic processes plausible following the photoexcitation of the ruthenium center and population of the lowest excited Ru-based ^{3}MLCT transitions (^{3}Ru*).

$$^3Ru^*–B–C_{60} \rightarrow {}^+Ru–B–C_{60}^{\bullet-} \rightarrow Ru–B–C_{60} \quad (1)$$

$$^3Ru^*–B–C_{60} \rightarrow {}^+Ru–B–C_{60}^{\bullet-} \rightarrow Ru–B–{}^3C_{60}^* \quad (2)$$

$$^3Ru^*–B–C_{60} \rightarrow Ru–B–{}^3C_{60}^* \quad (3)$$

$$^3Ru^*–B–C_{60} \rightarrow Ru–{}^3B^*–C_{60} \rightarrow Ru–B–{}^3C_{60}^* \quad (4)$$

In the first case (Eqn 1), the formation of a charge separated state (CSS) by an electron transfer process is proposed. The nature of this state consists of the oxidized Ru(III) center ($^+$Ru) and the reduced C_{60} radical anion ($C_{60}^{\bullet-}$). A subsequent back-electron transfer (*i.e.*, charge recombination) results in the reformation of the ground state. However, if the energy of the CSS (E_{CSS}) is higher than the $^3C_{60}$* energy, an exergonic process towards this state is possible (Eqn 2). An estimation of E_{CSS} energy and the driving force (ΔG_{CSS}) towards the CSS can be made by the simplified Rehm-Weller equation (Eqn 5 and 6).[46]

$$E_{CSS} = E_{ox,1} - E_{red,1} \quad (5)$$

$$\Delta G_{CSS} = E_{CSS} - E_{Ru*} \quad (6)$$

Here, $E_{ox,1}$ and $E_{red,1}$ are the first oxidation and reduction potentials of the electron donor and the electron acceptor, respectively. In the case of Ru(II) complexes, E_{Ru*} is the energy of the lowest excited ^{3}MLCT state, which can be estimated from the energy of the Ru-based emission maxima.

Another possible mechanism describes the direct triplet-triplet energy transfer from the Ru(II) center towards the C_{60} (Eqn 3). For rigid, conjugated bridges, often a Dexter-type energy transfer is discussed to describe the rate constants. This electron exchange process requires an orbital overlap and the rate constants exponentially decrease with increasing donor-acceptor distance. This is the case for "innocent" bridges that do not interfere with the excited states of the Ru(II) complex or the C_{60}. For π-conjugated bridges with an increasing number of conjugated units, this does often not hold true. These bridges exhibit low-lying $^3\pi$-π* transitions that can also be populated from the ^{3}MLCT state; subsequent energy transfer towards the $^3C_{60}$* state concludes this step-wise, so called "hopping" mechanism (Eqn. 4).

The competing intramolecular energy and electron transfer processes have been studied intensively and solvent, temperature and concentration dependencies were found. It can be concluded that short and aromatic bridges between $[Ru(bpy)_3]^{2+}$/$[Ru(tpy)_2]^{2+}$ complexes and C_{60} result mainly in a very fast triplet-triplet energy transfer within picoseconds,[36, 39, 43] while for systems with longer non-aromatic bridges both energy and electron transfer processes can be observed on a nanosecond timescale.[34, 41-42] In the case of electron transfer, the subsequently formed charge separated state usually features a lifetime of several 100 ns. For [Ru(por)(py)(CO)]-containing systems mainly electron transfer is observed in the picosecond range. A long-lived CSS is formed and decays with a lifetime of around 50 µs, which is ascribed to dissociation of the donor and acceptor, thereby hampering the charge recombination process.[47] Ru–B–C_{60} assemblies were also studied regarding their amphiphilic character and have shown self-assembly in solution, leading to vesicles[48] and monolayers.[49] The latter once could, for example, be deposited on indium tin oxide (ITO) substrates to fabricate photocurrent-generating devices.[50]

3. Ruthenium(II) bisterpyridine complexes attached to fullerenes

Parts of this chapter have been published in **P2**) K. Barthelmes, J. Kübel, A. Winter, M. Wächtler, C. Friebe, B. Dietzek, U. S. Schubert, *Inorg. Chem.* **2015**, *54*, 3159-3171. **P3**) K. Barthelmes, A. Winter, U. S. Schubert, *Eur. J. Inorg. Chem.* **2016**, 5132-5142.

The following Chapter gives a detailed investigation of several Ru–B–C_{60} assemblies, which have previously been mentioned in **Chapter 2**. The systems contain $[Ru(tpy)_2]^{2+}$ complexes, π-conjugated, aromatic bridges and methano- and pyrrolidino[60]fullerene moieties. In the series, the donor-acceptor distance was adjusted by increasing the bridge length with several *para*-phenylene or *para*-phenyleneethynylene (PPE) spacer units. Moreover, the modular design of $[Ru(tpy)_2]^{2+}$ complexes was used to extend the concept further to molecular triads. By this approach D–Ru–B–C_{60} assemblies could be prepared, whereby the Ru(II) complex is covalently attached to an additional electron donor (D), *i.e. N*-methylphenothiazine.

3.1. Molecular dyads based on Ru(II) bisterpyridine complexes and fullerene.

The following Ru–B–C_{60} assemblies were synthesized by the Route 1 (Scheme 2.1), which has been introduced in **Chapter 2**. For this approach, first the preparation of tpy-functionalized fullerenes and second the ruthenium coordination was necessary. The tpy-functionalized fullerenes could be synthesized by two different fullerene functionalization reactions. The first reaction represents the synthesis of methano[60]fullerenes, which was briefly discussed in **Chapter 2**. The synthetic route started from 4-methyl benzophenone, which was oxidized with chromium(VI) oxide to 4-formyl benzophenone (**1**) and subsequently rendered into a tpy-functionalized benzophenone **2** according to a modified Kröhnke-type procedure (Scheme 3.1). The tpy-functionalized benzophenone **2** was then reacted with tosylhydrazine and catalytic amounts of tosylic acid to yield the tosylhydrazone derivative **3**, which served as stable precursor for diazo compounds. The elimination of the tosyl group (Tos) with sodium methoxide in pyridine at room temperature by a mechanism analog to the Bamford-Stevens reaction[51] yielded *in situ* the desired diazo compounds. Subsequently, the addition of an *o*DCB solution of C_{60} and heating to 180 °C resulted in the formation of pyrazolino[60]fullerene intermediates, which directly underwent an elimination of molecular nitrogen to generate the desired tpy-functionalized methano[60]fullerene **4** in 28% yield.

The analogue tpy-functionalized pyrrolidino[60]fullerene **8** (Scheme 3.1) was synthesized by the previously mentioned Prato reaction. For this purpose, 4-methylbenzaldhehyde was reacted with 2-acetylpyridine in a Kröhnke-type reaction to yield the 4'-(4-tolyl)-tpy (**5**), rendered into 4'-(4-(bromomethyl)phenyl)-tpy (**6**) by a bromination reaction with NBS and subsequently oxidized by DMSO in a Kornblum reaction to the corresponding aldehyde (**7**) (Scheme 3.1).[52] Pyrrolidino[60]fullerene **8** was synthesized by the 1,3-dipolar cycloaddition of the azomethine ylide, derived from **7**, and *N*-methylglycine to C_{60} in an optimized 1:10:4 ratio.[53] The tpy-C_{60} compounds **4** and **8** were purified by column chromatography using neutral alumina to remove and to recover the unreacted C_{60} as well as to separate them from higher addition products. Both compounds exhibit a rigid *para*-phenylene spacer unit in between the tpy and the C_{60}, which result in an edge-to-center distance of 11 Å.[54]

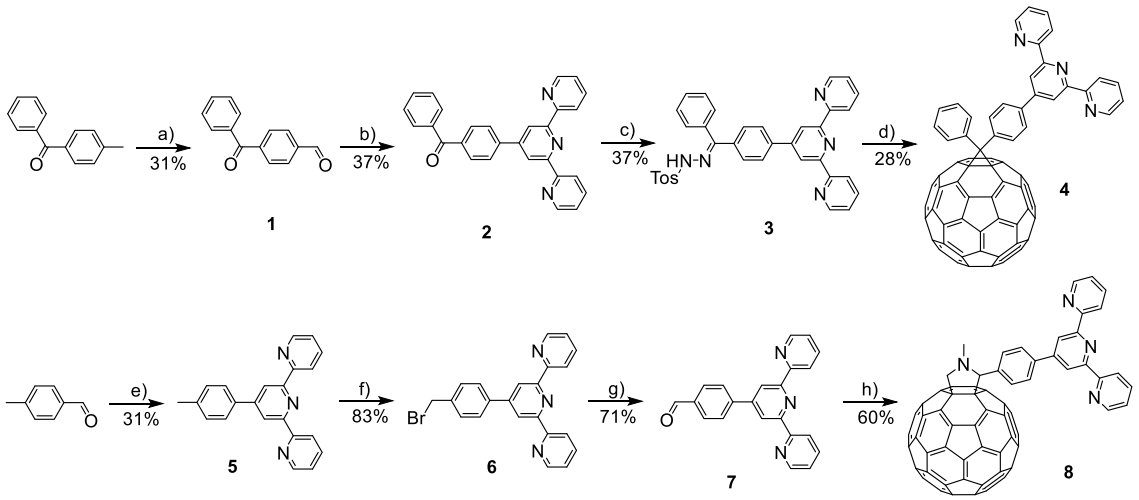

Scheme 3.1. Schematic representation of the syntheses of methano[60]fullerene and pyrrolidino[60]fullerene tpy's **4** and **8**, respectively: a) CrO_3, H_2SO_4, acetic anhydride, r.t., 16 h; b) (i) 2-acetylpyridine, NaOH, grinding, r.t., 30 min, (ii) $NH_{3\ (aq.)}$, EtOH, r.t., 48 h; c) tosylhydrazine, tosylic acid, THF, 80 °C, 2 d; d) (i) $NaOCH_3$, pyridine, r.t., 20 min, (ii) C_{60}, *o*DCB, 180 °C, 24 h; e) 2-acetylpyridine, $NH_{3\ (aq.)}$, NaOH, EtOH, r.t., 48 h; f) NBS, CCl_4, 85 °C, 3 h; g) $NaHCO_3$, DMSO, 120 °C, 15 h; h) C_{60}, *N*-methylglycine, toluene, 120 °C, 24 h.

Several other tpy-functionalized fullerenes (Figure 3.1) with differently long π-conjugated units were synthesized by similar approaches. In detail, for the methano[60]fullerenes at least the last two steps and for the pyrrolidino[60]fullerenes the last step were the same as shown in Scheme 3.1. The compounds **9**, **10** and **12** were synthesized from hydroquinone as starting material, involving several Sonogashira cross-coupling reactions and exhibit rigid PPE-type units in between the tpy to C_{60} moiety, which resulted in edge-to-center distances of 17 and 23 Å, respectively.[54] Additionally, the phenyl rings are substituted with octyl chains, which increase the solubility significantly. Compound **11** (Figure 3.1) exhibits no spacer unit and,

consequently, represents the shortest tpy-C_{60} ligand (*i.e.*, 9 Å); it was prepared by the Prato reaction of 4'-formyl-2,2':6',2''-terpyridine with C_{60}. Compound **13** (Figure 3.1) is a methano[60]fullerene with two terpyridine units attached and was synthesized from 4,4'-dimethyl benzophenone as starting material with identical steps as shown for compound **4**.

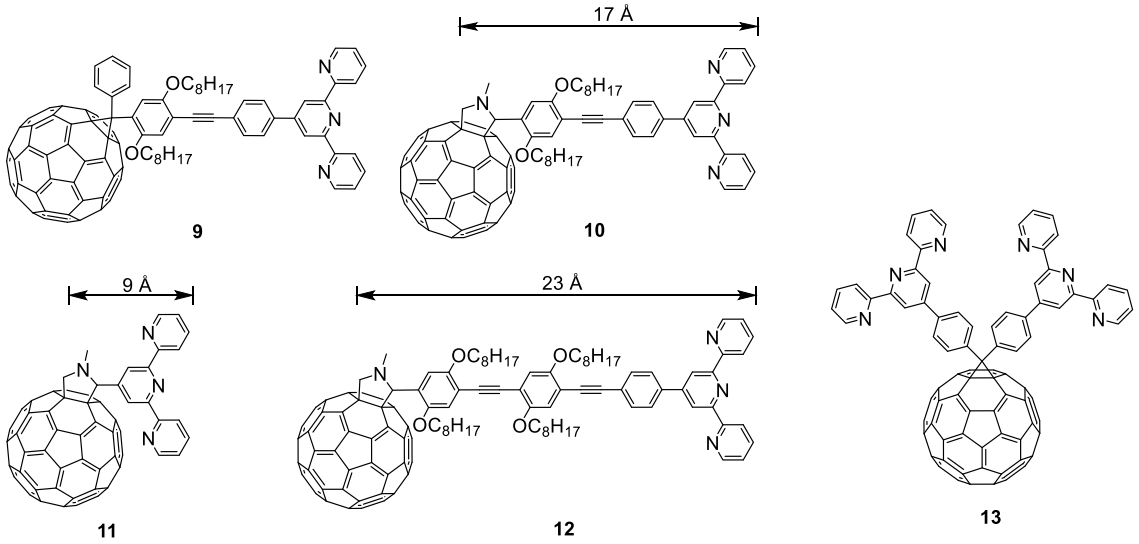

Figure 3.1. Schematic representation of the tpy-functionalized methano- and pyrrolidino[60]fullerene with various spacer units. The arrows mark the edge-to-center distance between the tpy and the C_{60}.

Heteroleptic Ru(II) complexes of the tpy-C_{60} ligands **4**, **8**, **9** and **10** were prepared by the reaction with the Ru(II) precursor $[Ru(tpy)(MeCN)_3](PF_6)_2$ (Scheme 3.2). The precursor was synthesized in two steps according to procedures developed by Meyer *et al.*[55] and Jäger *et al.*[56] and already proved its potential for a facile ruthenium coordination of tridentate ligands.[56-58] A more detailed explanation on the synthesis will be given for a similar Ru(II) precursor in **Chapter 3.2** (*vide infra*). The reaction of $[Ru(tpy)(MeCN)_3](PF_6)_2$ with the tpy-C_{60} ligands was performed under microwave (MW) irradiation for 30 min at 140 °C in DMF and afforded the dark red colored complexes **14**-**17** in moderate yields. Since column chromatography on silica was not applicable for these C_{60}-containing complexes, the complexes were purified by treatment of a concentrated acetonitrile (MeCN) solution with diethyl ether vapor to force slow precipitation. The Ru(II) complexes **18** and **19** that misses the C_{60} unit were prepared as references in a similar synthetic approach (Scheme 3.2).

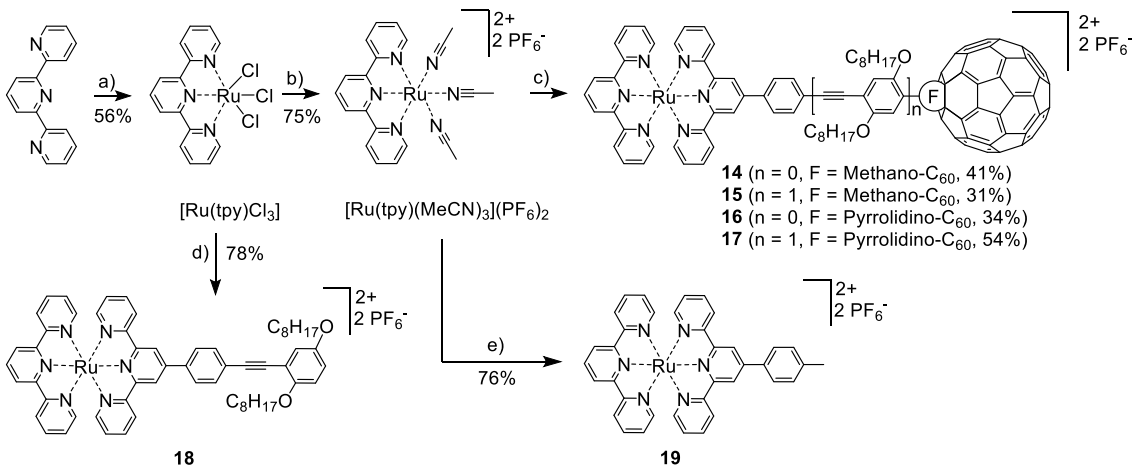

Scheme 3.2. Schematic representation of the syntheses of the heteroleptic Ru(II) complexes: a) $RuCl_3{\cdot}xH_2O$, EtOH, 96 °C, 4h; b) (i) $AgNO_3$, MeCN/EtOH/H_2O, 80 °C, 24 h, (ii) excess NH_4PF_6; c) **4**, **8**, **9** or **10**, DMF, 140 °C MW irradiation, 30 min; d) (i) $AgBF_4$, acetone, 70 °C, 2h, (ii) 4'-(4-((2,5-bis(octyloxy)phenyl)ethynyl)phenyl)-2,2':6',2''-terpyridine, DMF, 160 °C, 3h, (iii) excess NH_4PF_6; e) **5**, EtOH, 130 °C MW irradiation, 30 min.

The redox behavior of the tpy-C_{60} ligands and Ru(II) complexes was studied by cyclic voltammetry (CV) and representative voltammograms of the phenyl-bridged compounds (*i.e.*, **4**, **8**, **14**, **16** and **19**) are depicted in Figure 3.2. The electrochemical measurements were performed in dichloromethane with Bu_4NPF_6 as conducting salt and referenced against ferrocene (Fc). Within the accessible potential window, all tpy-C_{60} ligands (*i.e.*, **4**, **8**-**13**) featured three reversible C_{60}-based reduction waves of similar half-wave potentials at around −1.1, −1.5, and −2.0 V. In general, the potentials are shifted cathodically compared to pristine C_{60}. This can be attributed to the attached pyrrolidine and cyclopropane units, causing a disruption of π-conjugation and a decreased electron affinity of C_{60}.[59] As reported elsewhere,[60] the values for the C_{60} reductions are slightly cathodically shifted (*i.e.*, 20 to 50 mV) when comparing pyrrolidine to cyclopropane rings attached to C_{60}. Accordingly, the electron affinity is slightly higher in the methano[60]fullerene compounds. Noteworthy, an irreversible oxidation at around 1.0 V was observed for the pyrrolidino[60]fullerene ligand **8**. This process is attributed to the electrochemical retro-cycloaddition of the pyrrolidine fragment.[61] The reference Ru(II) complexes **18** and **19** exhibit two reversible tpy reductions at −1.6 and −1.95 V. Moreover, a reversible Ru(III)/Ru(II) redox couple with a half-wave potential at around 0.9 V is observed. There is no significant shift of the tpy reductions and ruthenium oxidation observed, when analyzing the Ru(II) complexes **14**-**17** with the C_{60} moiety attached, indicating negligible electrostatic influence of the fullerene moiety on the Ru(II) complex. However, a slight anodic shift of around 25 mV is observed for the first and second C_{60}-based reduction, indicating small electrostatic

interactions of the positive charged complex, which results in stabilization of the lowest unoccupied molecular orbital (LUMO) of C_{60}. Another trend that holds true – at least for the first C_{60}-based reduction – is a cathodic shift of around 30 mV when changing to larger bridge lengths, indicating the separation of the positive charged Ru(II) complex away from the C_{60} unit.

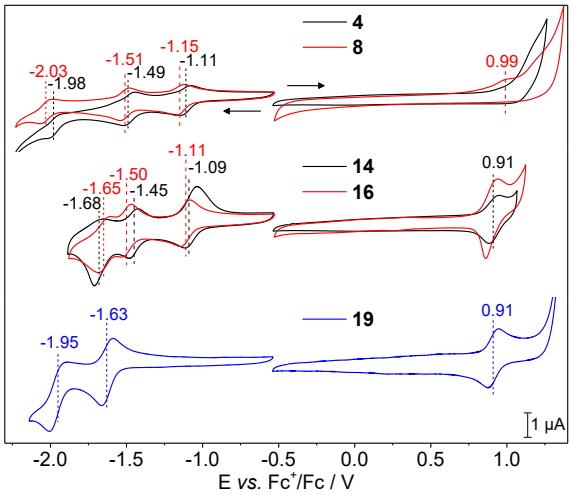

Figure 3.2. Cyclic voltammograms (5th cycle shown) of the phenyl-bridged methano- and pyrrolidino[60]fullerene tpy ligands **4** and **8** and the corresponding Ru(II) complexes **14** and **16,** and the reference Ru(II) complex **19** in dichloromethane/0.1 M Bu_4NPF_6. The half-wave potentials from the CV are shown as vertical dashed lines. The arrows show the scan direction.

A comparison of the UV-vis absorption spectra of C_{60}, and the PPE-bridged compounds **15**, **17** and **18** in dichloromethane is shown in Figure 3.3, Panel A. The spectra reveal that **15** and **17** can be regarded virtually as a superposition of the spectra of the references **18** and C_{60}. In detail, intense absorption bands between 250 and 350 nm are based on $^1\pi$-π* transitions within the fullerene moiety, PPE unit, and terpyridine groups, absorption bands in the region around 485 nm are related to Ru-based ^{1}MLCT transitions.[62] In agreement with the electrochemical measurements, there is no evidence for an interaction between the Ru(II) center and the fullerene unit in the ground state. The contribution of the extended π-conjugated PPE bridge *vs.* the phenyl-bridge on the ^{1}MLCT absorption maxima is clearly indicated by bathochromic shifts and increased extinction coefficients (*e.g.*, λ_{MLCT} = 484 nm, $\varepsilon_{MLCT} \approx 25{,}000$ M^{-1} cm^{-1} for **14**, **16** and **19**; λ_{MLCT} = 487 nm, $\varepsilon_{MLCT} \approx 35{,}000$ M^{-1} cm^{-1} for **15**, **17** and **18**).[17]

Emission spectroscopy was applied to investigate the influence of the C_{60} moiety on the excited states of the Ru(II) complex. The room temperature emission spectra of complexes **17** and **18** upon excitation in their ^{1}MLCT transition (*i.e.*, λ_{exc} = 470 nm) are depicted in Figure 3.3, Panel B. The weak ^{3}MLCT emission band of $[Ru(tpy)_2]^{2+}$

complexes (*i.e.*, for **18**: $\lambda_{em,\ max}$ = 645 nm) in general, is partially quenched in complex **17**. Furthermore, a weak C_{60}-based fluorescence at around 710 nm is observed, which occurred by direct excitation of weak C_{60}-based transitions in the visible region.[21]

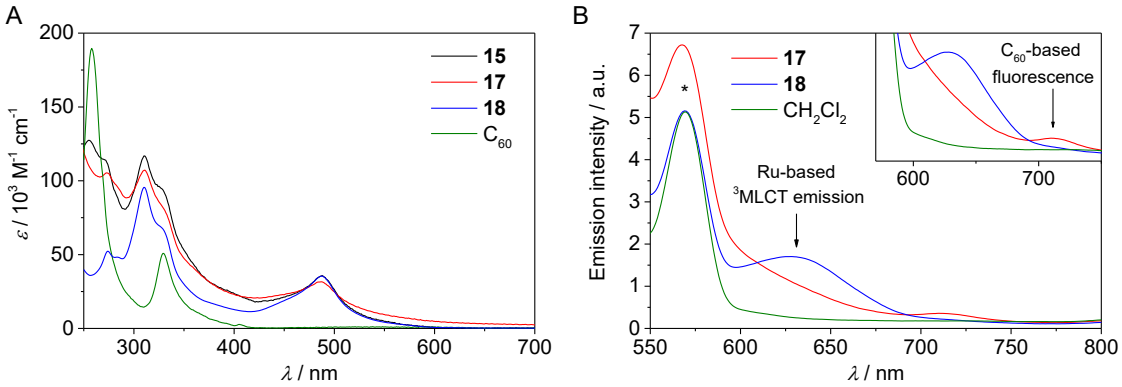

Figure 3.3. Panel A: UV-vis absorption spectra of the PPE-bridged dyads **15** and **17**, the reference Ru(II) complex **18** and C_{60} in dichloromethane. Panel B: Emission spectra (λ_{exc} = 470 nm) of isoabsorbing solutions of **17** and **18** in dichloromethane together with the spectra the emission spectra of the solvent. The asterisk marks spectrometer artifacts.

The photoinduced dynamics occurring after excitation of the ^{1}MLCT transition (λ_{exc} = 520 nm) were investigated using transient absorption (TA) spectroscopy in order to clarify the quenching mechanism in dichloromethane. The interpretation of the TA data is based on global multiexponential fits corresponding to a kinetic scheme involving consecutive first-order reactions. Molecular dyad **17** shows femtosecond (fs) TA features similar to those observed for the reference **18** at early delay times. Both the spectra and the kinetic traces are similar up to 30 ps. Later processes, like the decay of the excited ^{3}MLCT state are significantly accelerated in **17** (*i.e.*, τ = 245 ps) *vs.* **18** (*i.e.*, τ = 1553 ps) and clearly show the influence of the C_{60} moiety. A more pronounced decay is observed later only in **17**, which is not complete and the TA spectra stay positive over the entire spectral range, including a rise toward 700 nm with an offset lifetime > 1.5 ns (Figure 3.4), indicating the formation of a long-lived species.

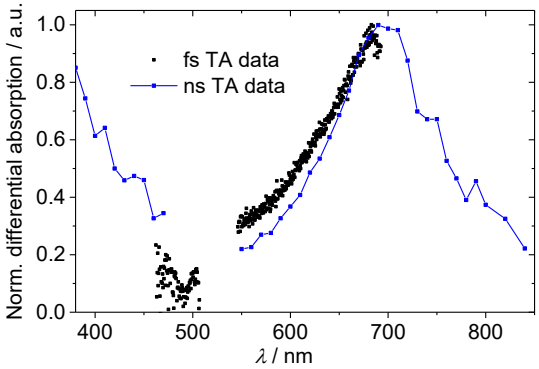

Figure 3.4. Fs TA data (black squares, offset process) and ns TA data (blue squares, constructed from integrated intervals of ns TA kinetics) of **17** in dichloromethane (λ_{exc} = 520 nm) that contains the absorption spectra of the long-lived species.

Thus, the nanosecond (ns) dynamics of **17** are clearly different from those of **18**, and for this purpose, ns TA experiments were conducted to investigate the nature of this long-lived state. A broad absorption peak is found with a maximum at ca. 700 nm and steep flanks on both the high- and low energy sides (Figure 3.4). Moreover, the offset process determined from the fs TA data is in good agreement with the ns TA spectrum. The observed excited state absorption coincides with the known spectral features of the $^3C_{60}$* state,[63] in particular the maximum at around 700 nm. Additional support for the assignment of the long-lived state as $^3C_{60}$* is based on oxygen-quenching experiments: Triplet states of organic molecules prone to undergo quenching reactions with triplet oxygen, strongly reducing the excited state lifetime.[64] From a comparison of kinetic traces at 700 nm recorded in the presence and absence of oxygen, it is taken that the lifetime significantly increases in the absence of oxygen, indicative of a triplet state. The lifetimes of 800 ns and 13 µs with and without oxygen, respectively, are consistent with literature reports on $^3C_{60}$*.[63]

Solvent-polarity-dependent TA spectroscopy was performed to yield additional insight into the photoinduced processes and to validate the absence of an electron transfer reaction. Despite the higher polarity of acetonitrile in comparison to dichloromethane, the data reveal almost identical spectral and temporal characteristics. In particular, no significantly different time constants (*e.g.*, ^{3}MLCT lifetime in **17**: 245 ps in dichloromethane and 318 ps in acetonitrile) were found, ruling out the possibility that charge separation is contributing to the photophysics of **17**. Similar observations are made for **16**, *i.e.* the phenyl-bridged analogue, as well as the methano[60]fullerene dyads **14** and **15**, as the photoinduced dynamics probed in TA experiments are rather similar for all of these compounds.

Nevertheless, the ^{3}MLCT lifetimes are not identical for the compounds at hand. In fact, the rate constant measured in acetonitrile depends on both the C_{60}-functionalization and the length of the bridge. The fastest ^{3}MLCT decay (*i.e.*, 73 ps) is observed for the phenyl-bridged pyrrolidino[60]fullerene dyad **16** (Figure 3.5). In the analog methano[60]fullerene dyad **14**, the decay is somewhat slower (*i.e.*, 93 ps), possibly due to the different angle of the Ru(II) complex with respect to the fullerene surface. The larger PPE-based bridge increases the donor-acceptor distance in the dyads **15** and **17** and causes a significant prolongation of the lifetime of 406 and 318 ps, respectively (Figure 3.5).

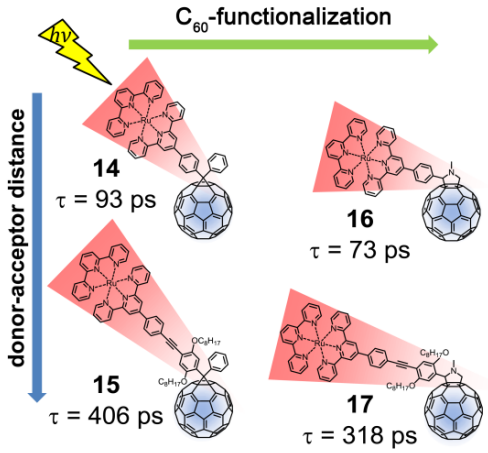

Figure 3.5. Schematic representation of the distance and linker dependence of the energy transfer (*i.e.*, decay of the ^{3}MLCT state) rate.

There are several possible quenching mechanisms leading to the $^3C_{60}$* state (see **Chapter 2**). The most likely route is by triplet-triplet Dexter-type energy transfer from the excited ^{3}MLCT state (*e.g.*, E_{Ru*} = 1.92 eV for **17**) towards the lower lying $^3C_{60}$* state (E_{C60*} = 1.5 eV[21]). A short-lived CSS between the Ru(II) center and C_{60} unit ($^+$Ru–B–C_{60}^-) as intermediate state is not plausible, since the energy of this state (*e.g.*, E_{CSS} = 2.04 eV for **17** according to Eqn 5 in **Chapter 2**) is higher than E_{Ru*} energy and, consequently, the electron transfer is a less-favored endergonic process.

3.2. Molecular triads based on phenothiazine, Ru(II) bisterpyridine complexes and fullerene

The initial idea of the formation of photoinduced charge separated states in Ru–B–C_{60} assemblies was mainly hampered by the high E_{CSS} energy. One approach to lower the E_{CSS} is the introduction of an additional organic electron donor moiety, which is easier to oxidize than the Ru(II) bisterpyridine complex ($E_{1/2}$ ≈ 0.9 V *vs.* Fc^+/Fc for

$[Ru(tpy)_2]^{2+}$ complexes). By this approach, a redox gradient can be introduced whereby the spectral properties of the photosensitizer remain almost unchanged and a sequential electron transfer process should facilitate the population of the CSS and enhance its lifetime. Phenothiazine ($E_{1/2} \approx 0.3$ V *vs.* Fc^+/Fc) is commonly used as organic electron donor and its potential to form CSSs has been documented for several photoactive assemblies.[65-69] On this basis, the modular design of $[Ru(tpy\text{-}R_1)(tpy\text{-}R_2)]^{2+}$ has been used to substitute the second non-functionalized tpy ligand with a new *N*-methylphenothiazine (PTZ) functionalized one. By this approach, molecular triads could be prepared, whereby the Ru(II) center additionally separates the electron donor from the electron acceptor with a fixed PTZ-to-Ru distance and a variable Ru-to-C_{60} distance. The synthesis route towards the PTZ-tpy ligand **21** is shown in Scheme 3.3 and was accomplished in two steps starting from *N*-methylphenothiazine, which was formylated in 3-position (**20**) by a Vilsmeier reaction[70] and subsequently rendered into the 4'-functionalized tpy (**21**). The PTZ-tpy ligand **21** was than reacted with the more facile coordinating Ru(III) source $[Ru(i\text{PrSPh})_2(MeOH)Cl_3]$ *vs.* Ru(III) trichloride hydrate in acetonitrile to afford the precursor complex $[Ru(PTZ\text{-}tpy)Cl_3]$ (**22**). Importantly, the PTZ-tpy ligand **21** is more appropriate for the preparation of a $[Ru(tpy\text{-}R)Cl_3]$ precursor complex compared to the C_{60}-tpy ligands, because the C_{60} unit itself can act as a ligand for the Ru(III) center and a purification is more difficult. Subsequently, the chlorido ligands in **22** were substituted by neutral acetonitrile ones according to an Ag(I)-assisted procedure in an acetonitrile/ethanol/water mixture to obtain $[Ru(oxPTZ\text{-}tpy)(MeCN)_3](PF_6)_2$ (**23**). During this reaction, the Ru(III) center is usually reduced by the solvent to Ru(II). However, electrospray ionization mass spectrometry (ESI MS) analysis indicated that additionally the sulfide in the PTZ is oxidized to the sulfoxide (oxPTZ). This drawback has been overcome by a selective sulfoxide reduction, as final step in the triad preparation.[71] The oxPTZ Ru(II) precursor **23** were subsequently reacted with equimolar amount of the C_{60}-tpy ligands **8**, **10**, **11** or **12** in DMF at 130 °C for 1 h to obtain the sulfoxide containing Ru(II) bisterpyridine complexes as intermediate in 53 to 84% yield. Subsequently, triflic anhydride (Tf_2O) and potassium iodide were added to the complexes dissolved in acetonitrile, which quantitatively reduced the sulfoxide at room temperature within 30 min to yield **24a-d**. The same procedure was applied for the preparation of a reference dyad (**26**) missing the bridge and C_{60} unit. In this case the sulfoxide intermediate (**25**) was isolated and also used as reference for the characterization of the triads. The

pyrrolidino[60]fullerene-tpy ligands were chosen for the ruthenium coordination, due to their more facile synthesis and faster energy transfer rates compared to methano[60]fullerene-tpy ligands, as shown previously (see **Chapter 2**). Triad **24a**, which basically is the complex without any bridge, consequently exhibits the shortest donor-acceptor distance (*i.e.*, the distance between the sulphur atom and the center of the C_{60}) of 18 Å.[54] The increasing bridge length in **24b**, **24c** and **24d** results in donor-acceptor distances of 23, 30, and 37 Å, respectively.[54]

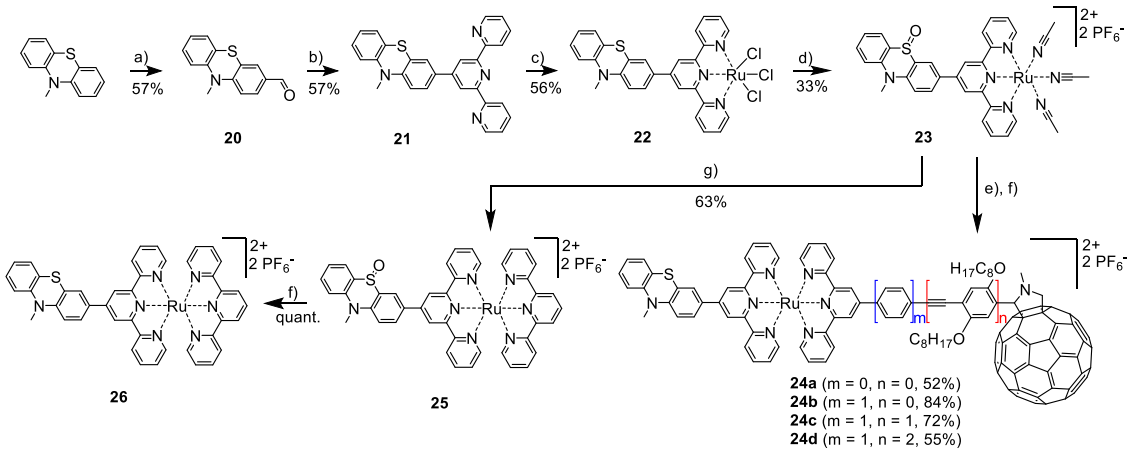

Scheme 3.3. Schematic representation of the syntheses of PTZ-tpy ligand **21**, triads **24a-d** and dyad **26**: a) DMF, $POCl_3$ $CHCl_3$, 0 to 70 °C, 12 h; b) 2-acetylpyridine, $NH_{3\ (aq.)}$, KOH, EtOH, r.t., 24 h; c) [Ru(*i*PrSPh)$_2$(MeOH)Cl_3], MeCN, 90 °C, 21 h; d) (i) $AgNO_3$, MeCN/EtOH/H_2O, 90 °C, 2 h, (ii) excess NH_4PF_6; e) **8**, **10**, **11** or **12**, DMF, 130 °C, 1 h; f) Tf_2O, KI, MeCN, r.t., 30 min; (ii) excess NH_4PF_6; g) (i) 2,2':6',2"-tpy, DMF, 130 °C, 1 h; (ii) excess NH_4PF_6.

CV and differential pulse voltammetry (DPV) measurements were performed in dichloromethane solution containing 0.1 M Bu_4NPF_6 and representative spectra of **25**, **26** and **24c** are depicted in Figure 3.6. In the anodic region, the oxPTZ dyad **25** revealed the reversible Ru(III)/Ru(II) couple at 0.9 V and an irreversible process at 1.1 V (only observed in the CV). The latter process appeared to be correlated with the presence of the oxPTZ unit, since it is absent in [Ru(tpy)$_2$](PF$_6$)$_2$.[72] In the cathodic region, the two reversible tpy-based reductions occurred at −1.6 and −1.9 V. PTZ dyad **26** exhibits in principle the same redox processes as found for **25** without any significant shifts. However, an additional reversible oxidation process occurred at 0.35 V (0.39 V in MeCN), which is assigned to an one-electron oxidation of the PTZ unit to the radical cation ($PTZ^{\bullet+}$).[68] In triad **24c**, the aforementioned redox processes as well as the additional reversible C_{60}-based processes at −1.1 and −1.5 V were present. The signal of the second C_{60}-based reduction is overlapping with that of the first tpy-based reduction in the CV, while two separated peaks occurred in the DPV spectrum. When measuring in acetonitrile, both C_{60}-based redox processes became anodically shifted by ca. 200

mV, caused by the stabilization of the negatively charged C_{60} anions in the more polar solvent. The observed values for the PTZ redox couple were the same as those in **26**, indicating no electronic interaction of the spacer unit or the C_{60} with the lateral PTZ moiety. The same holds true when comparing the Ru(III)/Ru(II) couple of triad **24c** with that of dyad **26**. A slight cathodic shift of 50 mV was observed for the first tpy-based reduction process *vs.* **26**. A similar behavior was also observed in the previously mentioned dyad **17** (see **Chapter 3.1**). Interestingly, the shortest triad **24a** shows an anodically shifted first C_{60}-based redox wave by ca. 100 mV *vs.* the rest of the series (*i.e.*, **24b-d**). Moreover, **24a** revealed its individual role when compared to the other triads by deviations in the Ru(III)/Ru(II) couple. Apparently, a cathodic shift of ca. 100 mV of this latter process was observed for **24a** *vs.* **24b-d** and **26** in dichloromethane. This behavior clearly indicates a certain degree of electronic interaction due to the rather close distance between the ruthenium center and the C_{60} cage in **24a**.

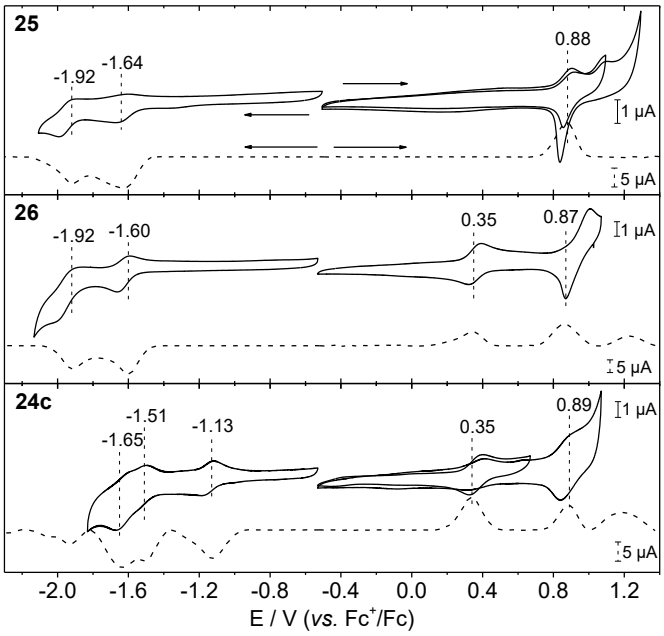

Figure 3.6. Cyclic (solid line, 5th cycle is shown, 0.2 V/s scan rate) and differential pulse voltammograms (dashed line) of oxPTZ dyad **25**, PTZ dyad **26**, and triad **24c** in dichloromethane/0.1 M Bu_4NPF_6. The arrows show the scan direction. The potentials from the DPV spectra are shown by vertical dashed lines.

UV-vis absorption spectra were recorded in dichloromethane and representative spectra are depicted in Figure 3.7. The oxPTZ dyad **25** exhibits the characteristic spectral features known for Ru(II) polypyridyl complexes (Figure 3.7, Panel A), as described previously (see **Chapter 3.1**). However, a bathochromic shift and higher intensity of the ^{1}MLCT transition (*i.e.*, λ_{MLCT} = 489 nm, $\varepsilon_{MLCT} \approx$ 40,000 M^{-1} cm^{-1}) is observed compared to the 4'-tolyl functionalized Ru(II) complex **19** (*i.e.*, λ_{MLCT} = 484 nm, $\varepsilon_{MLCT} \approx$

25,000 M^{-1} cm^{-1}), resulted by a significant contribution of oxPTZ moiety to the π^* orbitals of the tpy unit. Interestingly, the oxPTZ moiety shows a distinct absorption band at 379 nm in dichloromethane. When changing the solvent to acetonitrile, a significant increase (*i.e.*, 1.5 times) and hypsochromic shift to 357 nm of this latter band was observed, indicating a certain degree of solvatochromism. The PTZ dyad **26** exhibits similar spectral features as **25**, though missing the absorption peak exclusively assigned to the oxPTZ unit (Figure 3.7, Panel A), and a weaker intense and bathochromically shifted ^{1}MLCT transition was observed (*i.e.*, λ_{MLCT} = 496 nm, $\varepsilon_{MLCT} \approx$ 30,000 M^{-1} cm^{-1}). As shown previously in dyad **17** (see **Chapter 3.1**), triad **24c** also shows a stronger absorption in the UV region compared to those of **26** and **25**, which is caused by an additional absorption of $^1\pi$-π^* transitions in the C_{60} and the spacer unit. Furthermore, the ^{1}MLCT transition was bathochromically shifted to 505 nm compared to those of **26** and **25**, due to the extended π-conjugated system connected to the tpy ligand. When comparing triads **24a-d**, an increase in the bridge length, along with an enhanced π-conjugation, causes a bathochromic shift of the spacer unit-based $^1\pi$-π^* transitions in the UV region (Figure 3.7, Panel B). In fact, a shoulder at 375 nm was observed for **24d** with the longest bridge length. In the visible region, a bathochromic shift and increased extinction coefficients were observed for the ^{1}MLCT absorption maxima in the series of **24a-d**, which is excellent agreement with the similar series of **14-17** (see **Chapter 3.1**).

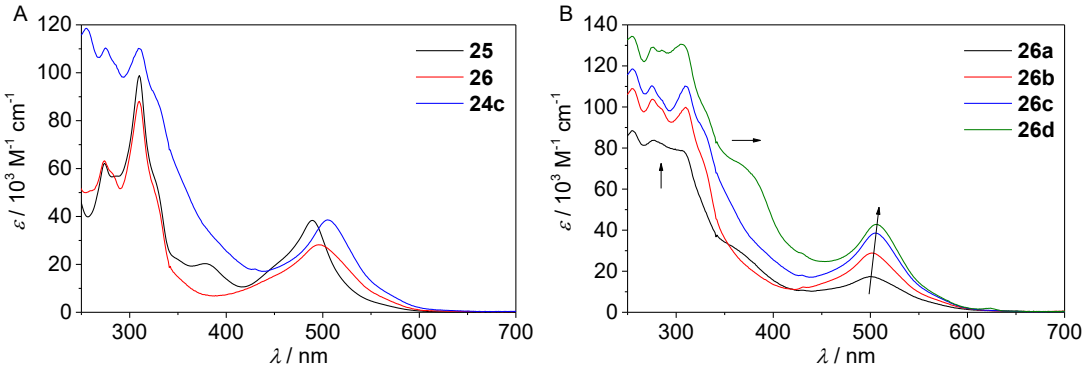

Figure 3.7. UV-vis absorption spectra in dichloromethane. Panel A: oxPTZ dyad **25**, PTZ dyad **26** and triad **24c**. Panel B: triads **24a-d**. The arrows show the spectral changes in the series.

The emission spectra of the dyads **25** and **26** as well as those of the triads **24a-d** in isoabsorbing acetonitrile solutions are shown in Figure 3.8. Upon light irradiation (*i.e.*, λ_{exc} = 495 nm) of **25** and **26**, a weak ^{3}MLCT emission at 646 and 658 nm was observed, respectively. Interestingly, the emission intensity of **26** was reduced in comparison to that of **25**, which indicated quenching by electron transfer from the PTZ unit. This effect

was previously been previously ascribed in related PTZ-containing Ru(II) complexes as a reductive emission quenching by the PTZ unit, which resulted in a charge separated species with a oxidized donor and reduced Ru(II) complex.[73-74] For triads **24a-d**, the ^{3}MLCT-based emission was generally reduced relative to that of the dyads and is explained by the occurrence of an additional quenching process induced by the C_{60} moiety. The strongest quenching was observed for **24a**, while higher residual emissions were recorded for triads **24b** and **24d** (Figure 3.8). This behavior can be explained by the increasing bridge length along with a longer distance between the Ru(II) complex and the C_{60} moiety. Surprisingly, for triad **24c** the residual emission intensity was higher than in the longer triad **24d** (Figure 3.8). A possible explanation could be the participation of a low-lying $^3\pi$-π^* transition of the bridge in the quenching process, which could act as a reservoir for the ^{3}MLCT emission.[32, 75-76] In all triads a second emission was observed at ca. 715 nm and is assigned to residual C_{60}-based fluorescence, like it was observed in dyad **17** (see **Chapter 3.1**).

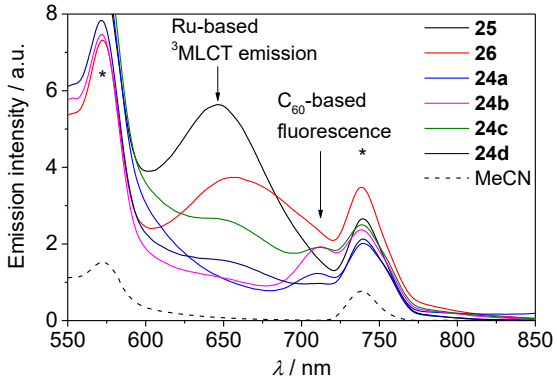

Figure 3.8. Emission spectra (λ_{exc} = 495 nm) of dyads **25** and **26**, and triads **24a-d** in isoabsorbing acetonitrile solution at room temperature. Blank measurements of the solvents are marked with black, dashed lines (*i.e.*, MeCN). Spectrometer artifacts are marked with an asterisk.

The photoinduced dynamics occurring after excitation of the ^{1}MLCT transition (λ_{exc} = 520 nm) were investigated using TA spectroscopy in order to clarify the quenching mechanism. The TA data indicate that long-range charge separation occurs as a result of two consecutive electron transfer processes.[77] First, a reductive electron transfer from the PTZ unit to the excited Ru(II) complex forms a CSS of $^+$PTZ–Ru$^-$–B–C_{60} character. This process already occurs in the dyad **26** and is in excellent agreement with the observed emission quenching *vs.* **25**. The following process describes an oxidative electron transfer from the $^+$PTZ–Ru$^-$–B–C_{60} species towards the long-range charge separated species $^+$PTZ–Ru–B–C_{60}^-. It could be shown that in triads, the final CSS decays with a distance-dependent lifetime of up to 180 ns, which is remarkable value

for D–P–A systems with $[Ru(tpy)_2]^{2+}$ photosensitizers. However, the formation of the CSS is not quantitative and, energy transfer towards the $^3C_{60}$* state is another decay channel of the excited ^{3}MLCT state, whereby the ratio between electron and energy transfer can be controlled by the excitation wavelength.[77]

Finally, it can be concluded that the introduction of the PTZ unit as additional electron donating moiety successfully reduces the E_{CSS} (*i.e.*, 1.46 eV according to Eqn 5 in **Chapter 2**) and thereby renders the electron transfer reactions into favored exergonic processes. Moreover, the intrinsic short excited state lifetime of $[Ru(tpy)_2]^{2+}$ photosensitizers did not circumvent the formation of long-lived charge separated species in the molecular triads.

4. Ruthenium(II) bisterpyridine complexes attached to polyoxometalates

Parts of this chapter will be published. **P4**) K. Barthelmes, M. Sittig, A. Winter, U. S. Schubert, *submitted*.

In the following Chapter, similar molecular dyads and triads are discussed as shown in **Chapter 3**; however, the C_{60} moiety is replaced by a polyoxometalate (POM) framework. These cluster-type metal oxides have attracted considerable interest for use as alternative electron acceptor material.[78-79] As a main characteristic, the redox-active POMs are able to store several electrons like C_{60}, however the reduction potentials are more tunable, because of a variety of differently structured POMs.[80] Another advantage compared to C_{60} is the absence of low-lying triplet states and, thus, no competition between photoinduced energy and electron transfer processes can occur.

The ability to functionalize POMs by surface attachment of organic fragments opens the field of organic-inorganic hybrid materials – a fundamental basis for the preparation of molecular dyads and triads.[78, 81-83] It has already been shown that molecular dyads of POMs that were covalently connected to metal-based photosensitizers, like Ru(II)[84] and Ir(III)[85-88] polypyridyl complexes or metalloporphyrins with Zn(II)[89-90] and Ru(II) ions,[91] could form a CSS by a photoinduced intramolecular electron transfer process. As shown in **Chapter 3.2**, the functionalization of the organometallic photosensitizer with an organic electron donor with a lower oxidation potential than the Ru(II) complex would introduce a redox gradient and should facilitate the population of the CSS and enhance its lifetime. Besides the PTZ donor unit, additionally an even stronger π-extended tetrathiafulvalene (exTTF) donor unit was introduced.

The initial idea of the synthesis of POM-tpy ligands, which were subsequently coordinated to ruthenium centers was not successful. At first the harsh conditions required for the ruthenium coordination were not capable for the POM system and second, the purification of these Ru(II) complex/POM conjugates turned out to be challenging. Hence, a grafting approach developed by the group of Izzet and Proust was used to covalently connect Ru(II) complexes to a POM framework by a Sonogashira cross-coupling reaction.[83]

For this purpose, the preparation of an alkyne-functionalized Ru(II) bisterpyridine complexes was required and a synthetic route was developed (Scheme 4.1) following a method introduced by the group of Stahl.[92] Here, the Sonogashira cross-coupling reaction of 4'-(4-bromophenyl)-2,2':6',2''-terpyridine with (triisopropylsilyl)acetylene gave the triisopropylsilyl-protected (TIPS) alkyne-functionalized tpy **27**. The protection group is necessary for the subsequent ruthenium coordination with Ru(III) trichloride hydrate, since it has been reported that unprotected alkynes decompose during the reaction.[93] The resulting Ru(III) trichloro precursor **28** was subsequently rendered to the Ru(II) trisacetonitrile precursor **29** by the Ag(I)-assisted dehalogenation method shown in **Chapter 3**. The reaction of **29** with 2,2':6',2''-terpyridine, the PTZ-tpy ligand (**21**) and an new exTTF-containing tpy ligand at 130 °C in DMF resulted in the Ru(II) complexes **30a-c**. The synthesis of the exTTF-tpy ligand was performed in analogy to **21**. Finally, the TIPS groups were cleaved of with a Bu_4NF/KF salt mixture at 40 °C in CH_2Cl_2/MeOH and the alkyne-functionalized Ru(II) complexes **31a-c** were obtained in good yields (Scheme 4.1). Worth a note, the reaction proceeded very slow and required five days at elevated temperatures to reach a full conversion; an alternative protocol employing AgF in MeCN, followed by a protonation with perchloric acid was also successfully applied on **30b**.

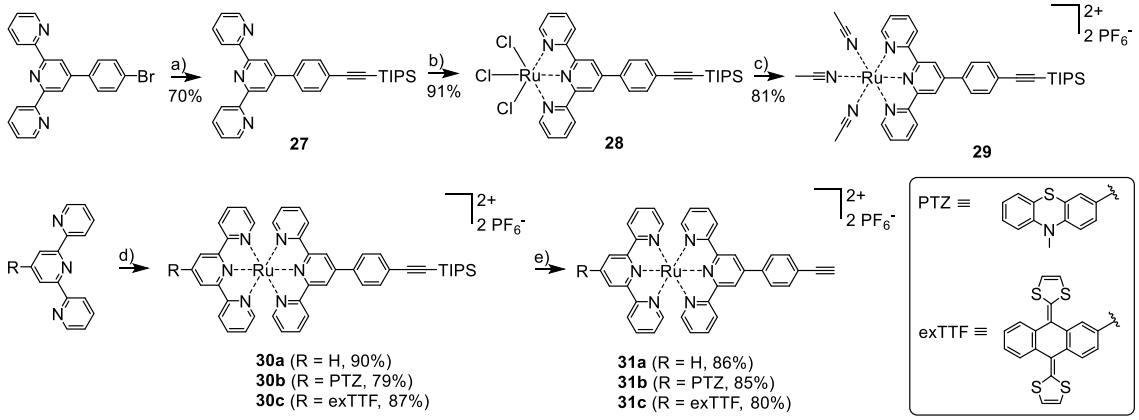

Scheme 4.1. Schematic representation of the synthesis of the alkyne-functionalized Ru(II) complexes **31a-c**: a) (triisopropylsilyl)acetylene, $Pd(PPh_3)_2Cl_2$, CuI, NEt_3, THF, 60 °C, 24 h; b) $RuCl_3{\cdot}xH_2O$, EtOH, 96 °C, 4 h; c) (i) $AgNO_3$, MeCN/EtOH/H_2O, 80 °C, 4 h, (ii) excess NH_4PF_6; d) **29**, DMF, 130 °C, 1 h; e) Bu_4NF/KF, CH_2Cl_2/MeOH, 40 °C, 5 days

The positively charged Ru(II) complexes **31a-c** were then coupled in a Sonogashira cross-coupling reaction *via* their terminal alkyne groups to a negatively charged organo-functionalized Keggin-type polyoxotungstate $[PW_{11}O_{39}\{GeC_6H_4I\}]^{4-}$ (**32**), which was prepared in two steps starting from sodium tungstate.[94] The coupling reaction was performed under microwave irradiation and gave the molecular dyad (**33a**) and the two

triads (**33b** and **33c**) in high yields within 1 h (Scheme 4.2). The cation was subsequently exchanged to 1-butyl-3-methyl-1*H*-imidazol-3-ium ($BMIm^+$); as reported in literature,[84] isolation problems might occur when retaining the tetrabutylammonium cations. In contrast to the starting Ru(II) complexes and the starting POM, the Ru(II) complex/POM conjugates were virtually insoluble in acetonitrile and only moderately soluble in DMF or DMSO, which is presumably caused by strong intermolecular electrostatic interactions.

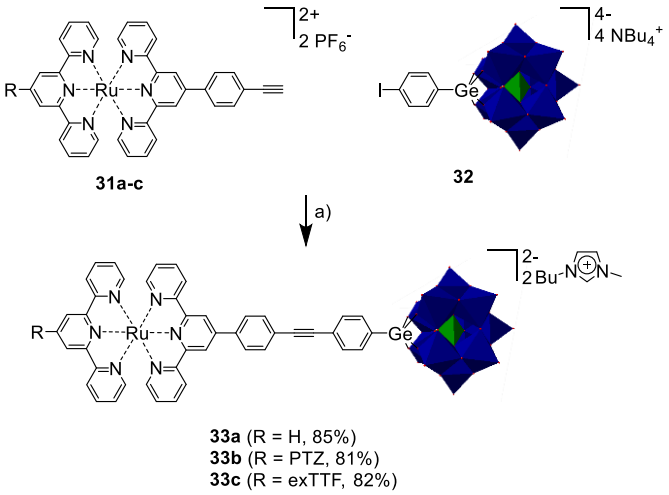

Scheme 4.2. Schematic representation of the syntheses of the Ru(II) complex/POM conjugates **33a-c**: a) (i) $Pd(PPh_3)_2Cl_2$, CuI, NEt_3, DMF, 70 °C MW irradiation, 1 h, (ii) excess BMImCl, DMSO, r.t., 1 h.

The electrochemical properties of the compounds were investigated by CV and DPV measurements in 0.1 M Bu_4NPF_6/DMF solution. The Ru(II) complex **31a** exhibits two reversible tpy reduction processes at −1.56 and −1.81 V (*i.e.*, DPV potentials), and the reversible Ru(III)/Ru(II) redox couple at 0.82 V. In the case of PTZ-containing dyad **31b**, the same redox processes were observed with the Ru(III)/Ru(II) couple being slightly cathodically shifted to 0.78 V (Figure 4.1) and the $PTZ^{\bullet+}$/PTZ redox couple at 0.37 V. An irreversible oxidation was observed at 0.73 V close to the Ru(III)/Ru(II) redox couple and might be the reason for the irreversibility of the $PTZ^{\bullet+}$/PTZ redox couple when the ruthenium center was oxidized in the same cycle (Figure 4.1). For the dyad **31c**, the Ru(III)/Ru(II) redox wave was centered at +0.84 V and similar potentials were observed for the tpy reductions (Figure 4.1). Furthermore, the exTTF unit could be oxidized at −0.03 V (*i.e.*, anodic peak potential) quasi-reversibly in one two-electron oxidation step to the dicationic $exTTF^{2+}$ species and got re-reduced at −0.30 V (*i.e.,* cathodic peak potential) in one two-electron reduction step (Figure 4.2).[95-96] Consequently, the exTTF unit represented the stronger donor when compared to PTZ by roughly 0.4 V. The large peak split (*i.e.*, 270 mV) of the $exTTF^{2+}$/exTTF redox couple

is known from literature and is caused by the tremendous geometrical changes of the exTTF fragment during its oxidation/re-reduction.[95-97] It is supposed that this behavior caused the difference between the DPV potential and the half-wave potential of the CV.

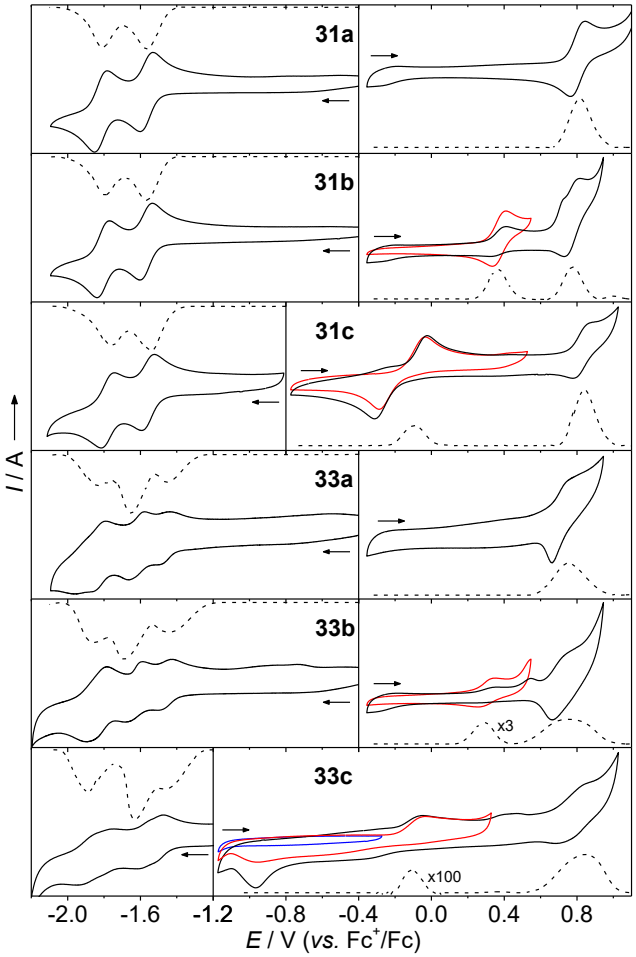

Figure 4.1. Cyclic (solid lines, different colors illustrate different potential ranges, scan rate = 0.2 V s^{-1}, 5th cycle is shown) and differential pulse (dashed lines) voltammograms of the Ru(II) complexes **31a-c** and the Ru(II)complex/POM conjugates **33a-c** in DMF/0.1 M Bu_4NPF_6. Left: Cathodic region. Right: Anodic region. The arrows show the scan direction.

As reported,[94] the starting POM (**32**) exhibited no oxidation process and two reversible redox waves at −1.50 and −2.00 V arising from two one-electron reductions of the polyoxotungstate unit (voltammogram not shown). In the Ru(II) complex/POM conjugate **33a**, the Ru(III)/Ru(II) couple was shifted to +0.75 V and, thus, the ruthenium center became easier to be oxidized – probably due to the anionic effect of the POM (Figure 4.1). The first reductive process in this system occurred at −1.46 V and was tentatively assigned to the first one-electron reduction of the POM. The potential appeared slightly anodically shifted (*i.e.*, 40 mV) *vs.* **32**, indicating a certain electrostatic interaction to the Ru(II) complex. The following redox processes appear at −1.65 and −1.84 V; however, a precise assignment of each process to a certain fragment

in the molecule by comparing it to the reference spectra was not possible. According to the spectra of **31a** and **32** four reductive processes should appear in cathodic region, however, only three processes could be observed and presumably two processes were overlapping. An indication for this could be the increased peak current in the CV for the third reductive process at −1.84 V. The PTZ-containing triad **33b** exhibited similar potentials as **33a** with the additional $PTZ^{\bullet+}$/PTZ redox couple at +0.29 V. The process was anodically shifted *vs.* the dyad **31b**, and indicated that the anionic POM still had an effect on the PTZ redox potential although they were separated by the Ru(II) complex. The exTTF-containing triad **33c** revealed a worse resolved cathodic region in the CV voltammogram; nevertheless, the DPV potentials were similar to the other Ru(II) complex/POM conjugates (Figure 4.1). The anodic peak potential of the exTTF oxidation in **33c** was identical to that of **31c**, however the re-reduction occurred in two one-electron steps with cathodic peak potentials at −0.57 and −0.97 V and, consequently, resulted in an even larger peak split, respectively (Figure 4.2). To proof that the two re-reduction steps were the result of the oxidation step, a narrower potential range (*i.e.*, excluding the oxidation step) was applied, which did not show any reduction processes (Figure 4.1, blue line). The larger peak split, as well as the two one-electron re-reductions clearly showed the influence of the POM on the $exTTF^{2+}$/exTTF redox couple, in particular during the re-reductions of the $exTTF^{2+}$ species, which was more hindered. In both triads (**33b** and **33c**) the peak current in the DPV voltammogram of the donor oxidation was low compared to the peak current of the ruthenium oxidation (Figure 4.1). A possible explanation for this could be an adsorption processes during the ruthenium oxidation on the electrode.

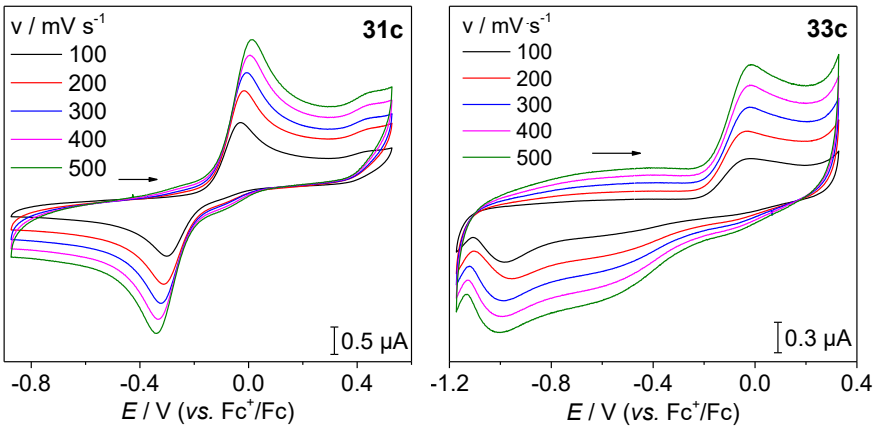

Figure 4.2. Cyclic (5th cycle is shown) voltammograms of **31c** and **33c** in DMF/0.1 M Bu_4NPF_6 with different scan rates showing the $exTTF^{2+}$/exTTF redox couple with a two-electron oxidation step and the re-reduction in either a two-electron re-reduction (left) or two one-electron re-reduction steps (right). The arrow shows the scan direction.

The normalized UV-vis absorption spectra of the Ru(II) complexes and their POM conjugates in DMSO are depicted in Figure 4.3. The Ru(II) complexes **31a-c** showed the typical spectral shape of Ru(II) polypyridyl complexes:[31] The UV region was dominated by an absorption band with a maximum at around 314 nm and a weakly pronounced lower energetic shoulder. The absorption was ascribed mainly to $^1\pi$-π^* transitions of the tpy ligands and their 4'-functionalities, *i.e.*, the PTZ unit, the exTTF unit and the 4-ethynylphenyl group. The visible region of the Ru(II) complexes was dominated by absorption bands of ^{1}MLCT transitions with maxima at 490 nm ($\varepsilon_{MLCT} \approx 22{,}000$ M^{-1} cm^{-1}), 506 nm ($\varepsilon_{MLCT} \approx 34{,}000$ M^{-1} cm^{-1}) and 505 nm ($\varepsilon_{MLCT} \approx 35{,}000$ M^{-1} cm^{-1}) for **31a**, **31b** and **31c**, respectively. The bathochromic shift and increased extinction coefficient clearly revealed the influence of the PTZ unit and the exTTF unit on the ^{1}MLCT absorption band. Moreover, the complex **31c** exhibited a distinct absorption band at 436 nm, which was assigned to lower energetic $^1\pi$-π^* transitions within the exTTF unit (Figure 4.3).[98] The spectra of the Ru(II) complex/POM conjugates **33a-c** were similar regarding their spectral shape to the corresponding Ru(II) complexes without the POM unit (Figure 4.3). Additional absorbance appeared at around 280 nm, which was presumably associated with the spectral characteristics of the starting POM (**32**).

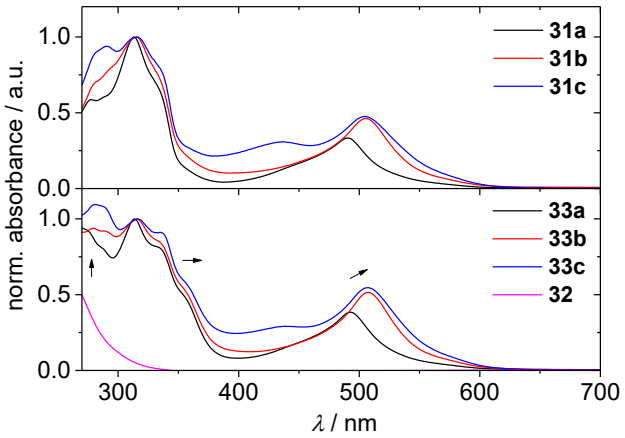

Figure 4.3. Normalized UV-vis absorption spectra of the Ru(II) complexes (**31a-c**), the starting POM (**32**) and the Ru(II) complex/POM conjugates (**33a-c**) in DMSO. The black arrows indicate the spectral changes compared to their reference Ru(II) complexes and the starting POM.

Moreover, next to the UV absorption band at 314 nm, a second shoulder at 358 nm on the low-energetic flank could be related to $^1\pi$-π^* transitions in the increased π-conjugated system of the 4-phenylethynyl-4'-phenyl subunit. The effect of increased π-conjugation was also visible in a slight bathochromic shift and higher extinction coefficients of the ^{1}MLCT absorption maxima.[17]

The emission spectra of the Ru(II) complexes and their POM conjugates were recorded in isoabsorbing DMSO solutions at the excitation wavelength. The compounds were excited with 500 nm, which is the lower energetic flank of ^{1}MLCT absorption band in **31a** and **33a**, while it is the higher energetic flank in the donor-functionalized compounds. A weak emission with a maximum at 660 nm was observed for the complex **31a** (Figure 4.4). The PTZ-containing complex **31b** showed a similar emission band at 662 nm; however, the emission intensity (*i.e.*, the area of the emission band) was reduced to ca. 50% compared to **31a** (Figure 4.4). The partial quenching is in excellent agreement with the reductive quenching seen in the PTZ-Ru-C_{60} systems (see **Chapter 3.2**). The fact that the exTTF unit represents the stronger electron donor was in full agreement with the observed further reduced emission in **31c** (Figure 4.4). Here, the emission intensity is decreased down to ca. 10% compared to **31a** and ca. 20% compared to **31b**, respectively. Also in this case reductive quenching by the exTTF moiety results in the formation of the charge-separated species with a formal $exTTF^{+}$–P^{-} character and was already described in several TTF-P systems.[99-102]

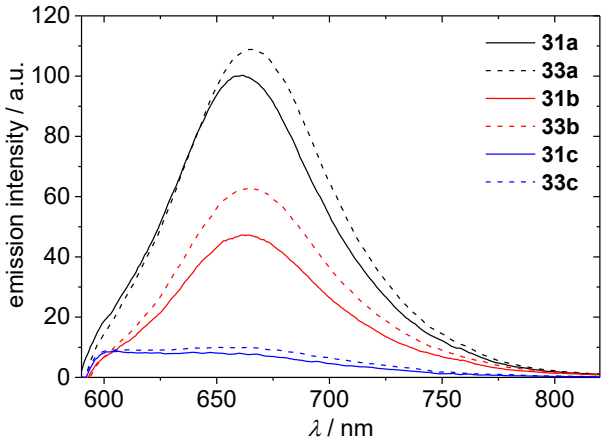

Figure 4.4. Room temperature emission spectra in isoabsorbing (λ_{exc} = 500 nm) DMSO solutions of the Ru(II) complexes (**31a-c**) and the Ru(II) complex/POM conjugates (**33a-c**).

It was expected that the emission was reduced further in the Ru(II) complex/POM conjugates, due to an oxidative quenching by POM framework; however, no additional emission quenching was observed. In contrast, higher emission intensities and slightly bathochromically shifted emission maxima were observed compared to the corresponding Ru(II) complexes (Figure 4.4). In the case of the dyad **33a**, the emission was increased by around 10%, while for the triads an increase of 30% (**33b**) and 25% (**33c**) could be observed. The reason for the increased emission intensity is tentatively ascribed to the presence of an increased π-conjugated system, resulting in stabilization of the excited ^{3}MLCT state.[17]

According to the simplified Rehm-Weller equation (see Eqn 6 in **Chapter 2**), the estimated driving forces to the full charge separated species in the Ru(II) complex/POM conjugates would occur by an endergonic process in **33a** (ΔG_{CSS} = 0.35 eV to the Ru^{+}–POM^{-} species) and by an exergonic processes in **33b** (ΔG_{CSS} = −0.12 eV to the PTZ^{+}–Ru–POM^{-} species) and **33c** (ΔG_{CSS} = −0.43 eV to the $exTTF^{+}$–Ru–POM^{-} species). If one would argue with the driving forces, a CS involving the POM should be plausible at least for **33c**. However, based on the emission spectra alone, a population of a long-range CS state between the donor and the POM cannot be evaluated.

Finally, it can be concluded that a donor strength depending emission quenching behavior of the Ru-based emission was found, which tentatively resulted in a charge separation between the donor and the Ru(II) complex. The substitution of C_{60} with POM as electron acceptor unit does not *per se* guarantee oxidative emission quenching. However, to elucidate the photodynamic processes in detail, time-resolved spectroscopy measurements are required and are part of ongoing research. For future works, a different, easier to reduce POM should be incorporated, since the currently used POM has similar redox potentials like the first tpy reduction in the Ru(II) complex and, thereby, hinders the electron transfer from the reduced tpy to the POM.

5. Ruthenium(II) polypyridine complexes attached to Ir(III) complexes

Parts of this chapter have been published in **P5**) K. Barthelmes, M. Jäger, J. Kübel, C. Friebe, A. Winter, M. Wächtler, B. Dietzek, U. S. Schubert, *Inorg. Chem.* **2016**, *55*, 5152-5167.

Besides the attachment of PTZ and exTTF as organic electron donors, and C_{60} or POM as electron acceptors on Ru(II) complexes, also other transition metal complexes could be introduced as energy donor or acceptor to mediate energy transfer processes. For instance, Ir(III) polypyridyl complexes feature higher ^{3}MLCT state energies compared to similar Ru-based complexes and act in this case as energy donor,[103-104] while similar Fe(II) and Os(II) polypyridyl complexes are energy acceptors, because of lower ^{3}MLCT state energies.[105] Taking this into account, in a linked heterometallic system, the excitation of the highest M_1LCT transition (M_1 = first metal center) should undergo by an exergonic triplet-triplet energy transfer process towards the lower lying M_2LCT state (M_2 = second metal center). The following chapter discusses the preparation and characterization of several heterodinuclear systems, whereby Ru(II) and Ir(III) complexes are bridged by a coordinating cyanide ligand.

In the last three decades, the research on the very short ambidentate cyanide ligand focused on its use as bridging unit, since it is able to simultaneously bind two metal ions and to promote strong electronic as well as magnetic coupling between them.[106-111] For this purpose, a synthetic route was developed which links Ir(III) bis(2-phenylpyridine) complexes with Ru(II) (tpy)(bpy) complexes by a cyanide (CN) ligand (Scheme 5.1). The Ir(III) building blocks $Bu_4N[Ir(ppy\text{-}(R_2)_2)_2(CN)_2]$ (**34**, R_2 = H and **35**, R_2 = F) were synthesized in two steps, starting from 2-phenylpyridine (ppy) or 2-(2,4-difluoro-phenyl)pyridine.[112] In fact, the bidentate ligands were coordinated to an Ir(III) center by heating with Ir(III) trichloride hydrate in an 2-ethoxyethanol/water mixture to afford the dimeric Ir(III) precursors $[Ir_2(ppy\text{-}(R_2)_2)_4(\mu\text{-}Cl)_2]$. Subsequently, the two chloro bridging ligands were cleaved by tetrabutylammonium cyanide, which yielded the mononuclear, anionic complexes (**34** and **35**) with two *C*-coordinated cyanide ligands. The different substituents (*i.e.*, R_2) were introduced to investigate the influence of peripheral ligand functionalization of the Ir(III) complex on the properties of the Ru(II) fragment.

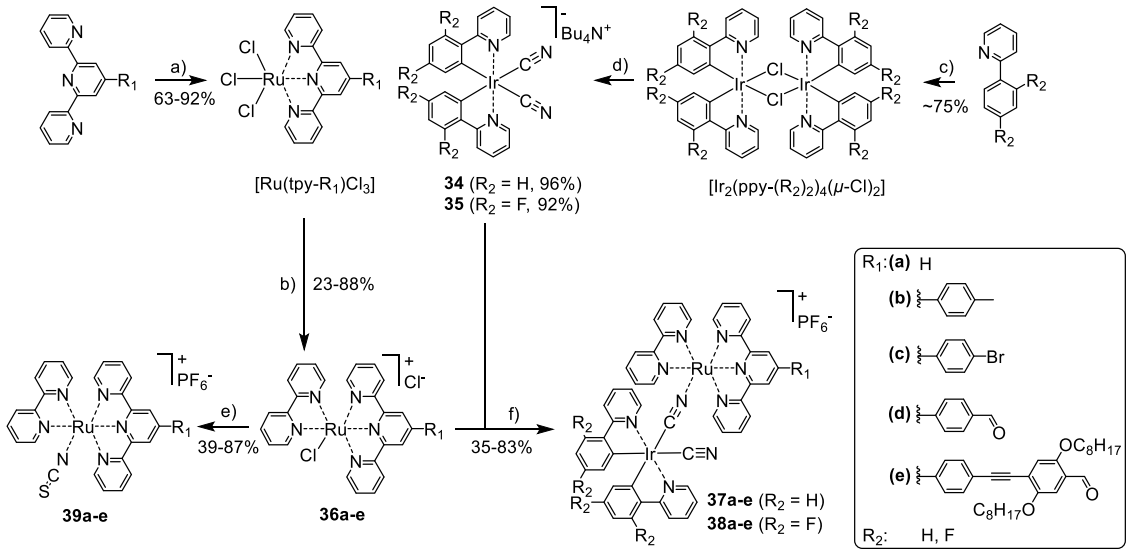

Scheme 5.1. Schematic representation of the syntheses of the Ir(III)-Ru(II) complexes **37a-e** and **38a-e**: a) $RuCl_3 \cdot xH_2O$, EtOH, 96 °C, 4 h; b) 2,2'-bipyridine, LiCl, *N*-ethylmorpholine, MeOH/H_2O, 75 °C, 3 h; c) $IrCl_3 \cdot H_2O$, 2-ethoxyethanol/H_2O, 120 °C, 24 h; d) NBu_4CN, MeOH/$CHCl_3$, 70 °C, 24 h; e) (i) KSCN, MeOH/H_2O, 120 °C MW irradiation, 30 min, (ii) excess NH_4PF_6, (iii) DMSO, 80 °C, 3 h; f) (i) MeOH/H_2O, 120 °C MW irradiation, 30 min, (ii) excess NH_4PF_6.

On the other hand, the Ru(II) building blocks [Ru(bpy)(tpy-R_1)Cl]Cl (**36a-e**) were prepared starting from 2,2′:6′,2″-terpyridine and four other 4'-functionalized tpy derivates. As shown in Scheme 5.1, the ligands were coordinated to a Ru(III) center by heating with Ru(III) trichloride hydrate in ethanol. The formed precursors [Ru(tpy-R_1)Cl_3] were subsequently reacted with stoichiometric amounts of 2,2'-bipyridine in a methanol/water mixture under reflux, which resulted in the monochloro containing complexes **36a-e**.[113] The functionalization pattern on the tpy ligand is additionally labeled by **a-e**, *i.e.*, **a** for pristine tpy, **b**, **c**, and **d** for 4'-phenyl-functionalized tpy's, and **e** for 4'-functionalized tpy with an extended π-conjugated group. The reaction of the anionic Ir(III) building blocks (**34** and **35**) with the cationic Ru(II) building blocks (**36a-e**) gave the dinuclear, cyanide-bridged complexes **37a-e** (R_2 = H) and **38a-e** (R_2 = F), whereby the chloro ligand in **36a-e** was substituted by *N*-coordination of one cyanide ligand in **34** or **35**. The synthesis was performed in a methanol/water mixture at 120 °C under microwave irradiation for 30 min with a 1.5 times excess of the **34** or **35** to retard the formation of the trinuclear complexes as side product. The complexes were purified by preparative size-exclusion chromatography to remove the excess of **34** or **35**. Related mononuclear Ru(II) reference complexes based on [Ru(bpy)(tpy-R_1)(SCN)]PF_6 (**39a-e**) were prepared in an analogous manner, using an excess of potassium thiocyanate. The isothiocyanate ligand was chosen to mimic the cyanide fragment on the Ru(II) complex and the sulphur atom can act like the Ir(III) center as electron withdrawing group. On

the other hand, the mononuclear Ir(III) complexes **34** and **35** were used as reference system for the Ir(III) fragment in dinuclear complexes, because the nitrogen in the cyanide ligands can be protonated and, thereby, simulate a Coulombic contribution by the Ru(II) center.

CV measurements for all dinuclear and reference complexes were performed in dichloromethane using a potential window between −2.5 and +1.5 V against ferrocene as the reference, representative spectra are depicted in Figure 5.1. The reference compound **34** revealed an irreversible process in the anodic region at 0.53 V (*i.e.*, anodic peak potential) assigned to an oxidation to Ir(IV).[114-115] For the fluorinated compound **35**, this process is anodically shifted by 0.3 V because of the electron withdrawing substituents (Figure 5.1). The Ru(II) reference complex **39a** shows a reversible signal in the anodic region with a peak potential at 0.56 V, assigned to a Ru(III)/Ru(II) couple (Figure 5.1).[116] In the cathodic region, two redox processes at around −1.7 and −2.2 V are present, ascribed to the tpy and bpy reduction (spectra not shown). Here, the functionalization on the tpy moiety has a negligible influence on the latter three redox potentials. In the case of the non-fluorinated dinuclear complex **37a**, the first oxidation is observed at 0.7 V. Because of its irreversible nature, this process is assigned to the oxidation to Ir(IV) (Figure 5.1). The process is shifted anodically by 0.17 V *vs.* **34** because of electrostatic interactions by the Ru(III) center to the iridium oxidation. Consequently, the second process at 0.92 V is assigned to the Ru(III)/Ru(II) redox couple. In contrast, the order of metal center oxidation is inverted for the fluorinated compound **38a**, because the fluorine substituents have a strong influence on the iridium oxidation potential, as it was already seen for the reference compounds (Figure 5.1). Here, the first process at 0.77 V is related to the reversible Ru(III)/Ru(II) redox couple and is shifted anodically by 0.2 V *vs.* **32a** because of the higher electron withdrawing effect by the iridium metal. The second process at around 1.13 V is the irreversible oxidation to Ir(IV). The functionalization pattern on the tpy fragment in **37a-e** and **38a-e** results in minor shifts of the Ru(III)/Ru(II) redox couple, as for the reference complexes **39a-e**.

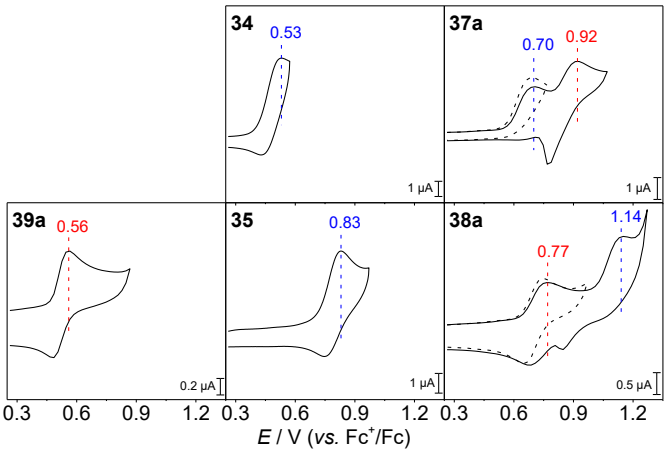

Figure 5.1. Cyclic voltammograms (*i.e.*, anodic region) of Ru(II) complex **39a,** Ir(III) complexes **34** and **35**, and Ru(II)-Ir(III) complexes **37a** and **38a** in dichloromethane/0.1 M Bu_4NPF_6 (0.2 V/s scan rate, 5th cycle is shown; the black dashed lines illustrate a different potential range). The anodic peak potentials from the CV are shown as colored, vertical dashed lines (*i.e.*, blue = oxidation to Ir(IV), red = oxidation to Ru(III)).

Representative UV-vis absorption spectra of the dinuclear complex **38a** and the corresponding reference complexes **35** and **39a** are exemplarily shown in Figure 5.2. The Ir(III) reference complex **35** exhibits a distinct absorption band in the UV region (*i.e.*, λ_{max} = 253 nm), which mainly arises from ligand-centered (LC) $^1\pi$-π* transitions in the ppy moiety. Weaker absorption bands up to 400 nm correspond to Ir-based metal-ligand-to-ligand charge transfer (^{1}MLLCT) transitions, with the longest wavelength absorption maximum at 365 nm. Ru(II) reference complex **39a** features in the UV region a sharp absorption band (*i.e.*, λ_{max} = 293 nm) arises from LC $^1\pi$-π* transitions in the bpy and the tpy moieties. The visible region consists of a broad absorption band up to 600 nm (*i.e.*, λ_{MLCT} = 492 nm, $\varepsilon_{MLCT} \approx$ 11,000 M^{-1} cm^{-1}), which is assigned to Ru-based ^{1}MLCT transitions. When the absorption spectra of complexes **39a-e** are compared with each other, a shift of the ^{1}MLCT maximum is observed. In fact, upon functionalization on the tpy fragment, a bathochromic shift of the ^{1}MLCT maximum is observed in the following order: **39b**/**39c**, **39d**, and **39e**.

The absorption spectrum of the dinuclear complex **38a** corresponds, in principle, to the spectra of the respective reference complexes **35** and **39a**, *i.e.*, intensive absorption in the UV region and broad absorption in the visible region. A superposition of the spectra of the reference complexes (*i.e.*, **35** + **39a**) matches very well with that of **38a**, in particular for the UV region, while deviations are found for the broad absorption band between 400 and 700 nm, *i.e.*, the maximum in **39a** is slightly bathochromically shifted *vs.* **38a** (Figure 5.2). This spectral region is tentatively governed by the Ru-based

^{1}MLCT transitions because the Ir(III) reference complex shows no contribution. In the analogous series of non-fluorinated complexes **37a-e**, the ^{1}MLCT maximum is hypsochromically shifted compared to the fluorinated series. This obvious influence of fluorination on the absorption maximum in the visible indicates a contribution of the Ir(III) d orbitals to the Ru(II) ^{1}MLCT-dominated transitions. This behavior was further investigated for selected complexes by density functional theory (DFT) calculations and its time-dependent formalism (TD-DFT) employing the B3LYP functional. For each complex, the geometry was first optimized for its singlet ground state (S_0), which served as the basis for the TD-DFT calculation. TD-DFT calculations were performed to detail the absorption properties in terms of calculated singlet-singlet (s-s) transitions (S_n). The calculated s-s transitions fit qualitatively very well with the experimental absorption spectrum, as exemplified for the dinuclear complex **38a** (Figure 5.2, left, bottom inset). Characteristic electronic transitions are visualized by their electron density difference maps (EDDMs), which share similarities with natural transition orbitals but compact all contributing molecular orbital pairs into a single plot of redistributed electron density. The longest-wavelength transition (S_1) reveals the depletion of the electron density at the Ru–N≡C–Ir fragment and the increase of the electron density at the tpy fragment, which is best described as ^{1}MLCT with tpy π^* ← Ru d character, with admixing of donating Ir d orbitals and CN p orbitals (Figure 5.2, right panel). All further transitions >400 nm (*e.g.*, S_6) are of similar ^{1}MLCT character showing the contribution of the Ir d orbitals to the visible absorption. This behavior is in agreement with the deviation found in the superposition of **35** and **39a** *vs.* **38a**, and clearly revealed ground state interactions between the two metal centers. The remaining dinuclear complexes in the series exhibit qualitatively similar transitions in the visible region and the effect of delocalization by the tpy substituent (R_1) is observed, *i.e.*, a similar absorption profile for **38e** (R_1 = extended π-conjugated group with one PPE unit) but a hypsochromic shift for **37a** (R_1 = H). In addition, a blue-shifted absorption upon fluorination of the ppy fragment (**37a** *vs.* **38a**) was found and is in excellent agreement with the experimental absorption.

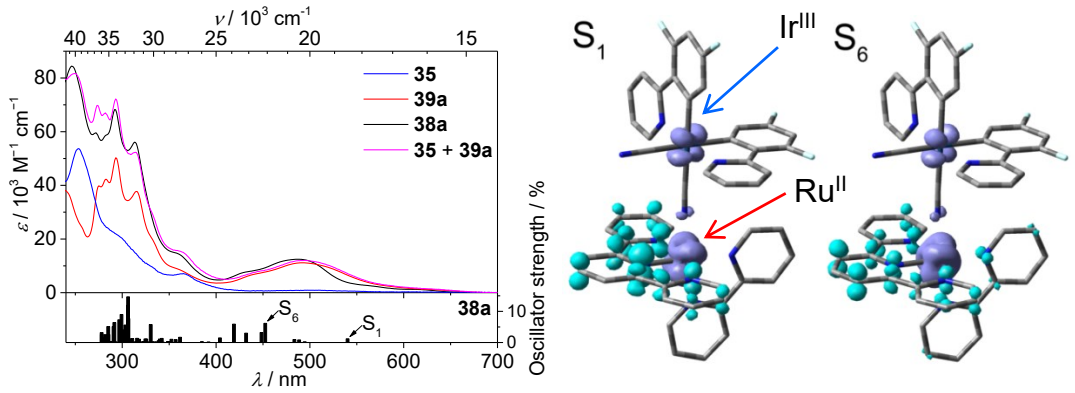

Figure 5.2. UV-vis absorption spectra of Ir(III) complex **35**, Ru(II) complex **39a** and Ir(III)-Ru(II) complex **38a** and superposition of **35** and **39a** in dichloromethane. Bottom inset: s-s transitions energies with selected EDDM plots (right, plum-blue = depletion of electron density; cyan = accumulation of electron density) of **38a**.

The dinuclear complexes were analyzed by vis-NIR spectroelectrochemistry in acetonitrile with 0.1 M Bu_4NPF_6 salt, whereby stepwise oxidations were performed and the related spectral changes were recorded. Since the first oxidation process in **37a-e** is irreversible and changes the chemical structure, the experiments were focused on the fluorinated complexes **38a-e**. Representative absorption spectra for the first, one-electron oxidation of **38a** are depicted in Figure 5.3. As discussed before, the order of metal oxidation for **38a** is inversed, rendering the first Ru-based oxidation process reversible, with a formal Ir(III)-Ru(III) mixed-valence character of the formed species (**38a**$^+$). As a result, the long-wavelength ^{1}MLCT band is fully depleted and weak absorptions with flat maxima at around 680 and 1220 nm (*i.e.*, $\varepsilon \approx 2{,}300$ M^{-1} cm^{-1}) arise. The second irreversible oxidation process changes the chemical structure and results in spectral changes that cannot be associated just by the oxidation to Ir(IV). Therefor the double-oxidized species is tentatively assigned as **38a**$^{2+}$ with a formal Ir(IV)/Ru(III) character. In this case the spectrum undergoes a depletion of the newly formed absorption at 1220 nm and partial decrease at 680 nm. The re-reduction shows qualitatively the reappearance of the ^{1}MLCT band, which is hypsochromically shifted and less intense, with respect to the initial state, caused by the irreversibility of the iridium oxidation. TD-DFT was applied on the single-oxidized species (**38a**$^+$) to investigate the nature of the low energy transitions. Figure 5.3 (*i.e.*, bottom inset) depicts the calculated doublet-doublet (d-d) transitions with characteristic EDDM plots (Figure 5.3, right panel) for the visualization. The most intense transition energies (S_3 and S_8) are shifted to lower wavenumbers by approximately 2000 cm^{-1} and the nature of most of the low energy transitions (<12,000 cm^{-1}) is best described as mixing of several transition types. The main contribution is dedicated to intervalence charge transfer

(IVCT) transitions, whereby electron density is transferred from Ir d orbitals to Ru d orbitals. In all cases, admixing of interconfigurational contributions is observed, whereby electron density is transferred in different d orbitals of the Ru(III) center. Moreover, the p orbitals of ppy and CN unit show contributions by electron donation and electron acceptance, respectively. Weak transition with higher energy (between 12,000 and 20,000 cm^{-1}) are attributed to ligand-to-metal charge transfer (LMCT) transition, whereby electron density is transferred from the tpy/bpy p orbitals to the Ru d orbitals. The former assignments by the computational methods are in excellent agreement with the observed spectral changes, *i.e.*, the disappearance of the IVCT absorption bands at 1220 and 680 nm, and the stay of the weak LMCT absorption at 680 nm upon double oxidation. In the case of the non-fluorinated complexes **37a-e**, single oxidation did not result in the appearance of any IVCT transitions, which is ascribed to the irreversible nature of the Ir(III) oxidation.

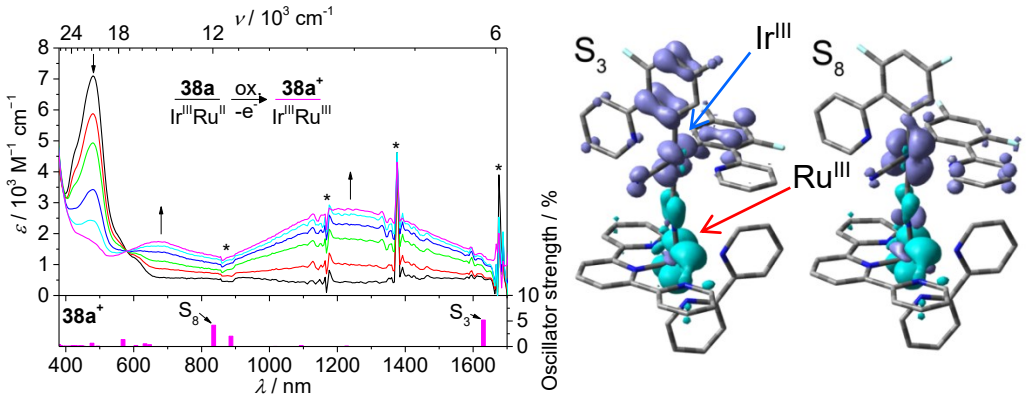

Figure 5.3. Vis-NIR spectroelectrochemistry spectra of **38a**, during the first Ru-based oxidation in acetonitrile/0.1 M Bu_4NPF_6. Spectrometer artifacts are marked with an asterisk. Bottom inset: d-d transitions energies with selected EDDM plots (right, plum-blue = depletion of electron density; cyan = accumulation of electron density) of **38a**$^+$.

The room temperature emission spectra of the Ir(III) complexes **34** and **35**, and the Ru(II)-Ir(III) complexes **37a-e** and **38a-e**, as measured in dichloromethane, are depicted in Figure 5.4. The excitation wavelengths were chosen according to the longest-wavelength maxima of the reference complexes. The Ir(III) reference complex **34** exhibits a vibronically structured emission band (λ_{exc} = 380 nm) with a maximum at 474 nm and shoulders at 503 and 540 nm, which indicates the emission from ^{3}LC states (Figure 5.4, Panel A).[117] However, the emission should also be associated with the ^{3}MLLCT states, according to TD-DFT calculations. In comparison, the fluorinated complex **35** (λ_{exc} = 360 nm) reveals a similar emission structure, although hypsochromically shifted by 20 nm. The Ru(II) reference complexes **39a-e** exhibit a

^{3}MLCT emission at around 704 nm (spectra not shown), and the tpy substituent likewise has a distinct influence on the energy of the emission. When the dinuclear complexes **37a-e** are excited at 380 nm (λ_{exc} = 360 nm for **38a-e**), virtually no Ir-based emission is observed (Figure 5.4, Panel A), indicating some kind of quenching by the Ru(II) complex. However, for some of the dinuclear complexes, a weak residual emission is visible, which is ascribed as inefficient quenching. To mimic a Coulombic contribution by the Ru(II) center on the emission spectra of the reference compounds **34** and **35**, a protonation of the cyanide ligands with a hexafluorophosphoric acid solution was performed. No quenching of the emission was observed, however a hypsochromic shift of the emission maxima occurred as it was observed for related Ir(III) isocyanoborato complexes.[118] In contrast, the residual Ir-based emission in **37a-e** and **38a-e** is only slightly hypsochromically shifted compared to the protonated reference complexes. This indicates that an additional contribution by the Ru(II) center leads to a compensation and, thus, to the less pronounced hypsochromic shift. The excitation of **37a-e** and **38a-e** in the absorption maxima of the visible region (λ_{exc} = 500 nm) leads to the occurrence of an emission (Figure 5.4, Panel B) similar to the Ru(II) reference complexes **39a-e**. The emission of **37a-e** (on average, $\lambda_{max,em}$ = 686 nm) is generally shifted hypsochromically *vs.* **39a-e**, while the trend on the emission energy upon tpy functionalization is the same. It is also worth noting that the fluoro substitution on the ppy moiety in **38a-e** leads to an emission (on average, $\lambda_{max,em}$ = 677 nm) which is hypsochromic shifted *vs.* the non-fluorinated analogues **37a-e**, confirming the influence of the peripheral substitution of the Ir(III) fragment (R_2) on the Ru-based ^{3}MLCT emission.

A rough estimate based on the extinction coefficients at 365 and 380 nm of the reference and the dinuclear complexes reveals that there is significant absorption of the Ru(II) reference complexes present over the whole range of Ir-based absorption. Hence, selective excitation of the Ir(III) center is not possible for these complexes. As a consequence, considering the emission spectra alone, it is not possible to conclude about the presence of intramolecular energy transfer between the Ir(III) and Ru(II) centers. However, the fact that the Ir-based absorption bands contribute to the Ru-based emission can serve as an indication for the presence of energy transfer. To investigate this matter, the origin of the Ru-based emission was analyzed by the corresponding excitation spectra and compared to the respective absorption profiles.

The excitation spectra match very well in the visible region of the absorption spectra (spectra not shown). More importantly, the excitation spectra of the dinuclear complexes below 400 nm also fit to the absorption profiles and clearly show the additive contribution of the iridium fragment to the Ru-based emission.

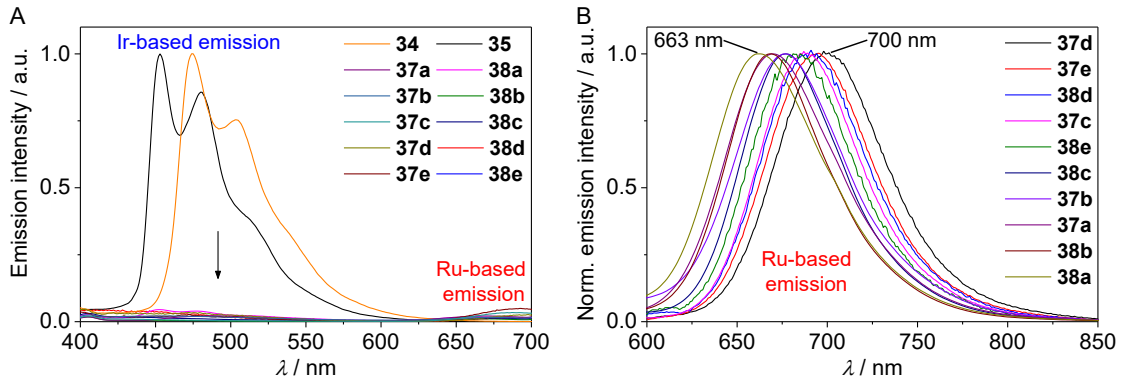

Figure 5.4. Panel A: Room-temperature emission spectra of Ir(III) complexes **34** and **35**, and Ir(III)-Ru(II) complexes **37a-e** and **38a-e** (λ_{exc} = 380 or 360 nm) in isoabsorbing dichloromethane solution. Panel B: Normalized room-temperature emission spectra of **37a-e** and **38a-e** (λ_{exc} = 500 nm) in dichloromethane solution. The arrow indicates the quenching of the Ir-based emission in the dinuclear complexes.

The quenching of the Ir-based emission in the dinuclear complexes is apparent from the steady state emission data presented above. Along with a reduced emission quantum yield, quenching, in general, is governed by a decrease of the donor emission lifetime. As a consequence, the respective lifetime measurements were carried out in aerated acetonitrile for selected complexes. The lifetime of the Ir-based emission is reduced in the dinuclear complexes compared to the respective reference complexes: For the non-fluorinated complex **37d** *vs.* **34**, lifetimes of 39 *vs.* 90 ns were determined, respectively, and for the fluorinated complexes **38d** *vs.* **35**, lifetimes of 60 *vs.* 183 ns were obtained, respectively. It should be noted that the apparent lifetime differences in the dinuclear complexes compared to the reference complexes contradict an assignment of the residual Ir-based emission to impurities of **34** or **35**. Thermal deactivation of the Ir-based ^{3}MLLCT/^{3}LC state is energetically favorable along with a population of the lower lying Ru-based ^{3}MLCT states, but time-resolved emission spectroscopy with ca. 120 ps time resolution enables no clear indication of emission quenching *via* this pathway. Hence, a closer look into the early events occurring after photoexcitation was investigated by fs TA spectroscopy. Excitation was carried out at 355 nm, because of the longest-wavelength absorption maxima in **34** and **35**. Already at early delay times (*i.e.*, 0.35 ps), the TA spectra of the dinuclear complexes **37d** and **38d** are nearly identical with the spectra of the Ru(II) reference complex **39d** showing the typical

characteristics of a Ru-based ^{3}MLCT state (spectra not shown). Within the first 10 ps, *i.e.*, a typical time scale for cooling and solvent relaxation processes, the spectra undergo only very minor changes indicating that no significant changes regarding the nature of the excited state or the molecular structure are occurring on this time scale. However, it has to be considered that the oscillator strength of the Ir-based ^{1}MLLCT transitions is much lower than that for the Ru-based ^{1}MLCT transitions. This trend might be the same in the excited state (also for triplet transitions), and the Ir-based population will lead to lower TA signals compared to the Ru-based population. On the other hand, in emission spectroscopy, even small populations of Ir-based ^{3}LC/^{3}MLLCT states can be identified, because of the absence of low-lying ^{3}MC states, and, thus, Ir(III) complexes typically possess significantly higher emission quantum yields than the ruthenium analogues.[45]

Finally, when the observations from emission spectroscopy are related with the TA data, it is intriguing to note that while an residual Ir-based emission is observed, no Ir-specific signatures are observed in the TA data, which suggests that there is a fast (within 0.35 ps), yet incomplete, energy transfer from higher Ir-based ^{3}MLLCT/^{3}LC states (*e.g.*, $E_{Ir*} \approx 2.62$ eV for **37a**) states toward lower lying Ru-based ^{3}MLCT states (*e.g.*, $E_{Ru*} = 1.85$ eV for **37a**).

6. Summary

The aim of the thesis was to build photoactive assemblies based on Ru(II) 2,2':6',2''-terpyridyl (tpy) complexes with donor and acceptor moieties that show photoinduced energy or electron transfer processes. These two processes are crucial factors for the efficiency of artificial photosynthesis devices. In particular, in light-harvesting antennae systems, energy transfer is the desired process to collect sunlight over a broad spectral range and to store in one chromophore. Aiming for photoinduced charge separation and, thereby, application in photocatalysis and photovoltaics, electron transfer represents the favored process. In this respect, various molecular dyads and triads were produced that revealed one of the two processes.

One approach to achieve photoinduced charge separation was the incorporation of Ru(II) bisterpyridine complexes into fullerene architectures. The well-known surface-modification chemistry of fullerenes was applied to prepare several tpy-functionalized C_{60} derivates. Hereby, two different fullerene functionalizations and four different long aromatic spacer units were introduced to vary the angle and the distance between the tpy unit and the C_{60} moiety. Subsequent coordination of the tpy-C_{60} ligands to a Ru(II) center with a second non-functionalized tpy ligand yielded molecular dyads, whereby the Ru(II) bisterpyridine complex should serve as photosensitizer, as well as electron donor, and the C_{60} as electron acceptor. Photoexcitation of the Ru(II) complex with visible light ($\lambda_{exc} \approx 500$ nm) revealed that the intrinsic weak Ru-based emission (Figure 6.1, A) from the lowest lying triplet metal-to-ligand charge transfer transition state (^{3}Ru*) is additionally reduced when the C_{60} is attached. Time-resolved spectroscopy could show that also the lifetime of this state is significantly reduced, which is caused by a fast triplet-triplet energy transfer process towards a lower lying triplet state of the C_{60} ($^3C_{60}$*). The desired electron transfer process, resulting in a charge separation between the Ru(II) complex and the C_{60} moiety ($^+$Ru-C_{60}^-), was not observed, since the energy of this state (Figure 6.1, A) is higher than ^{3}Ru* energy and, consequently, the electron transfer is a less-favored endergonic process. The molecular design of the Ru(II) complex/C_{60} assemblies was advanced by the incorporation of *N*-methylphenothiazine (PTZ) as additional organic electron donor. By this approach, molecular triads were prepared that lowered the energy of the charge separated states and, thus, renders the driving force for an electron transfer in to a favored exergonic process (Figure 6.1, B). Consequently, two consecutive electron transfer processes are

observed by TA spectroscopy resulting at first in a charge separation state (CSS) between the PTZ unit and the Ru(II) complex ($^{+}$PTZ-Ru^{-}-C$_{60}$), and subsequently in a long-ranged CSS between the PTZ unit and the C$_{60}$ moiety ($^{+}$PTZ-Ru-C$_{60}^{-}$) with a lifetime of up to 180 ns. Also in this case the triplet-triplet energy transfer to the ^{3}C$_{60}$* state occurs as side process, however the ratio between electron and energy transfer can be controlled by the excitation wavelength.

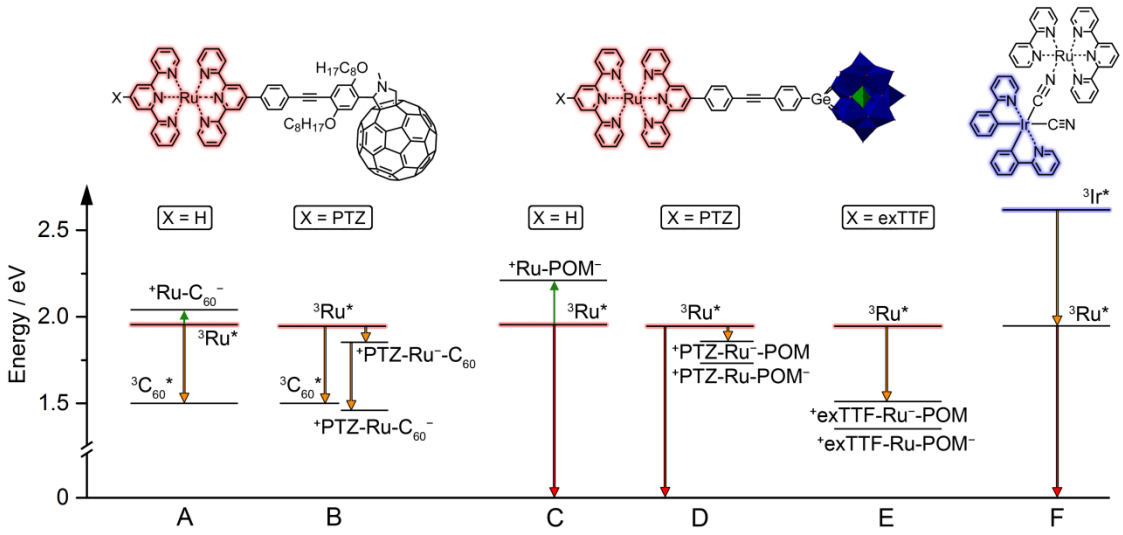

Figure 6.1. Qualitative energy level scheme of some of the investigated compounds with estimated energy levels for certain states. Key: The glowing marks the initial excited molecule fragment. Black framed arrows = observed processes. Green arrows = endergonic processes. Orange arrows = exergonic processes. Red arrows = Ru-based ^{3}MLCT emission.

Polyoxometalates (POMs) represent promising alternatives as electron acceptor materials and show some advantages compared to fullerenes. The variety of different structured POMs increases the window for tuning the redox potentials. Moreover, no competition between energy and electron transfer processes can occur due to the absence of low-lying triplet states. For this purpose, similar molecular dyads and triads with a POM framework instead of C$_{60}$ was prepared. Hereby, the systems were synthesized by the Pd(0)-catalyzed cross-coupling reaction of an alkyne functionalized Ru(II) complex and an iodophenyl functionalized Keggin-type polyoxotungstate. The electrochemical experiments show that the used POM is harder to reduce (*i.e.*, by around 0.3 V) than the C$_{60}$-unit in the similar system. This had an influence on the CSS energy and result in a high endergonic driving force for the charge separation process in the dyad without an additional donor (Figure 6.1, C). Consequently, the absence of a reduced Ru-based emission led tentatively to the conclusion that no charge separation occurs between the Ru(II) complex and the POM framework ($^{+}$Ru-POM^{-}). The introduction of the PTZ unit as an additional donor lowers the CSS energy and should

thereby render the electron transfer into an exergonic process. Steady-state emission spectroscopy revealed partial quenching of the Ru-based emission by the organic donor, which indicated the formation of a CSS between the PTZ unit and the Ru(II) complex ($^{+}$PTZ-Ru^{-}-POM) like it has been shown in PTZ-Ru-C_{60} systems. However, no further emission quenching was observed, when the POM framework was incorporated in the system (Figure 6.1, D). For this reason, the driving force to a CSS involving the POM-framework was further increased by the introduction of a stronger π-extended tetrathiafulvalene (exTTF) donor. Consequently, a nearly completely quenched Ru-based emission was observed (Figure 6.1, E), which indicates the formation of a CSS between the exTTF unit and the Ru(II) complex ($^{+}$exTTF-Ru^{-}-POM). Unfortunately, also in this system no further quenching was observed when the POM framework is connected. A possible reason could be the similar redox potentials for the tpy reduction and the POM reduction, which prevent the electron transfer from the reduced tpy (Ru^{-}) to the POM. However, the elucidation of the photodynamic processes in the excited state cannot be concluded alone by the steady-state emission spectroscopy results. Detailed time-resolved spectroscopy measurements are required to conclude about a long-ranged CSS and will be part of ongoing research.

Aiming for light-harvesting antennae systems, dinuclear Ru(II)-Ir(III) complexes were prepared by the linkage of Ru(II) (bpy)(tpy) complexes (bpy = 2,2'-bipyridine) *via* one coordinating cyanide ligand of Ir(III) $(ppy)_2$ complexes (ppy = 2-phenylpyridine). The distance between the two metal centers is only 5 Å and, thus, metal-metal interactions are observed in the ground, the oxidized and the excited state, respectively. In particular, the efficiently quenched Ir-based emission and an observable Ru-based emission represent the depopulation of high energetic Ir-based triplet states (^{3}Ir*) by a very fast triplet-triplet energy transfer to lower energetic Ru-based triplet states (^{3}Ru*) (Figure 6.1, F). It was shown that the concept of light-harvesting and storage in one chromophore also works for transition metal complexes.

In summary, it could be shown that the remarkable customizability of terpyridine ligands in 4'-position and readily coordination to ruthenium centers enables a rapid access to highly functionalized complexes. As a consequence, it was possible to employee conventional Ru(II) terpyridyl complexes in molecular devices as an effective photosensitizer to mediate energy and electron transfer processes, despite their short excited state lifetime.

7. Zusammenfassung

Ziel der vorliegenden Arbeit war es, photoaktive Systeme auf der Basis von Ruthenium(II)-2,2':6',2"-Terpyridyl (tpy) Komplexen mit Donor- und Akzeptor-Einheiten aufzubauen, die photoinduzierte Energie- oder Elektronentransferprozesse aufzeigen. Diese zwei Prozesse sind entscheidende Faktoren für die Effizienz von künstlichen Photosynthesebauteilen. Insbesondere bei lichtsammelnden Antennensystemen ist ein gerichteter Energietransfer wünschenswert, um Sonnenlicht über einen breiten Spektralbereich zu sammeln und in einem Chromophor zu speichern. Für die photoinduzierte Ladungstrennung und deren Anwendung in der Photokatalyse und der Photovoltaik stellt der Elektronentransfer den gewünschten Prozess dar. In dieser Hinsicht wurden verschiedene molekulare Dyaden und Triaden hergestellt, die einen der beiden Prozesse zeigen sollten.

Ein Ansatz zur Realisierung einer photoinduzierten Ladungstrennung war der Einbau von Ru(II)-Komplexen in Fulleren-Architekturen. Dabei wurde die bekannte Oberflächenmodifizierungschemie von Fullerenen angewendet, um mehrere tpy-funktionalisierte C_{60}-Derivate herzustellen. Hierbei wurden zwei verschiedenen Fulleren-Funktionalisierungen und vier verschieden lange aromatische Brückeneinheiten eingeführt, um den Winkel und den Abstand zwischen dem tpy-Fragment und der C_{60}-Einheit zu variieren. Die anschließende Koordination der tpy-C_{60} Liganden an ein Ru(II)-Zentrum zusammen mit einem zweiten nicht-funktionalisierten tpy-Liganden lieferte molekulare Dyaden, in denen der Ru(II)-Komplex als Photosensibilisator sowie Elektronendonor und die C_{60}-Einheit als Elektronenakzeptor dienen sollten. Die Anregung des Ru(II)-Komplexes mit sichtbarem Licht ($\lambda_{exc} \approx 500$ nm) zeigte, dass die intrinsisch schwache Ruthenium-basierte Emission (Abbildung 7.1, A) aus dem niedrigstem Triplett Metall-zu-Ligand-Ladungstransfer Zustand (^{3}Ru*), zusätzlich reduziert ist, wenn die C_{60}-Einheit befestigt ist.

Zeitaufgelöste spektroskopische Untersuchungen konnten zeigen, dass auch die Lebensdauer dieses Zustands signifikant reduziert ist und durch einen schnellen Triplett-Triplett-Energietransfer hin zu einem tiefer liegenden Triplett-Zustand des C_{60} ($^3C_{60}$*) verursacht wird. Der gewünschte Elektronentransferprozess, welcher zu einer Ladungstrennung zwischen dem Ru(II)-Komplex und der C_{60}-Einheit führen sollte ($^+$Ru-C_{60}^-), wurde nicht beobachtet, da die Energie dieses Zustandes (Abbildung 7.1, A)

höher ist als die ^{3}Ru*-Energie und folglich einen wenig begünstigten endergonischer Elektronentransferprozess darstellt.

Die molekulare Struktur der Ru(II)-Komplex/C_{60} Systeme wurde durch den Einbau von *N*-Methylphenothiazin (PTZ) als zusätzlichen organischen Elektronendonor erweitert. Auf diese Weise wurden molekulare Triaden hergestellt, die die Energie des ladungsgetrennten Zustandes senken und somit den Elektronentransfer in einen begünstigten exergonischen Prozess umwandeln sollten (Abbildung 7.1, B). Folglich wurden zwei aufeinanderfolgende Elektronentransferprozesse durch zeitaufgelöste Spektroskopie beobachtet, was zuerst zu einem ladungsgetrennten Zustand (CSS) zwischen dem PTZ-Fragment und dem Ru(II)-Komplex führte ($^+$PTZ-Ru$^-$-C_{60}), und anschließend zu einen weiter räumlich getrennten CSS zwischen dem PTZ-Fragment und der C_{60}-Einheit ($^+$PTZ-Ru-C_{60}^-) mit einer Lebenszeit von bis zu 180 ns führte. Auch in diesem Fall tritt Triplett-Triplett-Energietransfer in den $^3C_{60}$*-Zustand als Nebenprozess auf, wobei jedoch das Verhältnis zwischen Elektronen- und Energietransferprozessen durch die Anregungswellenlänge kontrolliert werden kann.

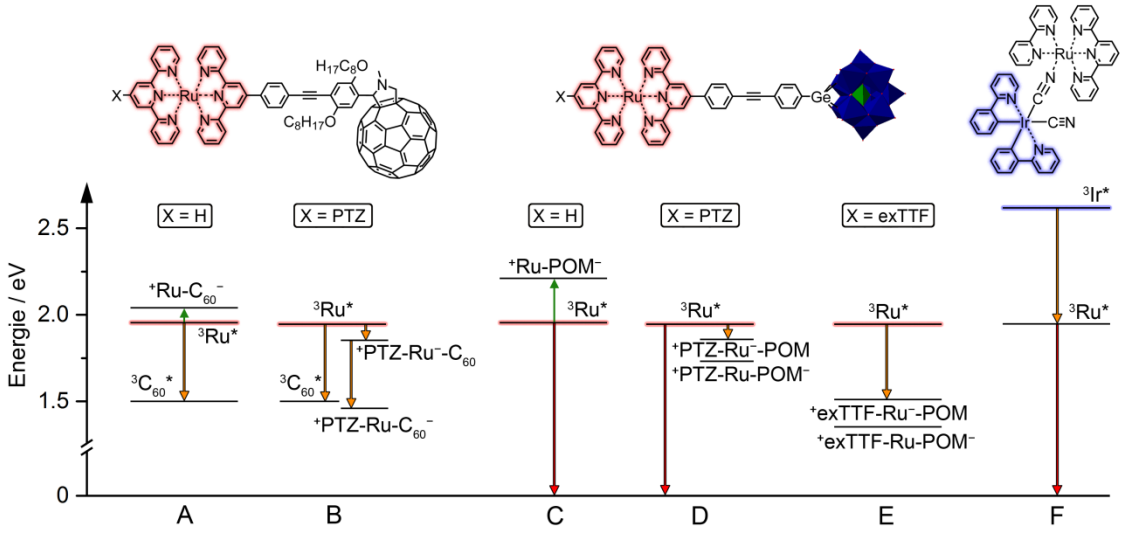

Abbildung 7.1. Qualitatives Energielevelschema einiger untersuchter Verbindungen mit geschätzten Energieniveaus für bestimmte Zustände. Legende: Das Leuchten markiert das initial angeregte Molekülfragment. Schwarz umrahmte Pfeile = beobachtete Prozesse. Grüne Pfeile = endergonische Prozesse. Orange Pfeile = exergonische Prozesse. Rote Pfeile = Ru-basierte ^{3}MLCT-Emission.

Polyoxometallate (POMs) stellen vielversprechende Alternativen als Elektronenakzeptor-Materialien dar und zeigen einige Vorteile gegenüber Fullerenen. Die Vielfalt der verschieden strukturierten POMs erhöht das Fenster zur Einstellung der Redoxpotentiale. Darüber hinaus schließt das Fehlen von niedrig liegenden Triplett-Zuständen eine Konkurrenz zwischen photoinduzierten Energie- und Elektronentransferprozessen aus.

Zu diesem Zweck wurden strukturanaloge molekulare Dyaden und Triaden mit einem POM-Baustein anstelle des C_{60} hergestellt. Die Systeme wurden durch die Pd(0)-katalysierte Kreuzkupplungsreaktion eines alkin-funktionalisierten Ru(II)-Komplexes und einem iodophenyl-funktionalisierten Polyoxowolframates vom Keggin-Typ synthetisiert. Die elektrochemischen Experimente zeigten, dass der verwendete POM-Baustein schwerer zu reduzieren ist (d. h. um etwa 0,3 V) als die C_{60}-Einheit in dem ähnlichen System. Dies hat einen Einfluss auf die CSS-Energie und führt zu einer hohen endergonischen Barriere für den Ladungstrennungsprozess in der Dyade ohne zusätzlichen Donor (Abbildung 7.1, C). Folglich wurde durch das Ausbleiben einer verminderten Ru-basierten Emission vorläufig geschlussfolgert, dass keine Ladungstrennung zwischen dem Ru(II)-Komplex und dem POM-Baustein ($^{+}$Ru-POM^{-}) auftritt. Die Einführung der PTZ-Einheit als zusätzlicher Donor erniedrigt die CSS-Energie und sollte dadurch den Elektronentransfer in einem exergonischen Prozess umwandeln. Durch Steady-State-Emissionsspektroskopie konnte gezeigt werden, dass die Ru-basierte Emission teilweise durch den organischen Donor ausgelöscht wird, und es wie in den PTZ-Ru-C_{60} Systemen, zu der Bildung eines ladungsgetrennten Zustandes zwischen der PTZ-Einheit und dem Ru(II)-Komplex ($^{+}$PTZ-Ru^{-}-POM) kommt. Es wurde jedoch keine weitere Emissionsintensitätsabnahme beobachtet, als der POM-Baustein in das System eingeführt wurde (Abbildung 6.1, D). Aus diesem Grund wurde die Triebkraft zu dem ladungsgetrennten Zustand, mit einer Beteiligung des POM-Bausteins weiter erhöht, indem ein noch stärkerer, π-ausgedehnter Tetrathiafulvalen (exTTF) Donor eingebaut wurde. Folglich wurde eine nahezu vollständige Abnahme der Ru-basierten Emission beobachtet (Abbildung 6.1, E), was zu der Bildung eines ladungsgetrennten Zustandes zwischen der exTTF-Einheit und dem Ru(II)-Komplex ($^{+}$exTTF-Ru^{-}-POM) führte. Jedoch wurde auch in diesem System keine weitere Abnahme der Emission beobachtet, sobald der POM-Baustein eingeführt wurde. Die zu ähnlichen Redoxpotentiale von der tpy- und der POM-Reduktion könnten Grund sein, warum ein Elektronentransfer von dem reduzierten tpy (Ru^{-}) zu dem POM erschwert ist. Es kann jedoch nicht allein durch Steady-State-Emissionsspektroskopie auf die photodynamischen Prozesse im angeregten Zustand geschlussfolgert werden. Detaillierte zeitaufgelöste spektroskopische Messungen sind erforderlich, um über eine Ladungstrennung, mit einer Beteiligung des POM-Bausteins zu urteilen, und werden Teil der laufenden Forschung sein.

Um lichtsammelnde Antennensysteme aufzubauen, wurden eine Reihe zweikerniger Ru(II)-Ir(III)-Komplexe synthetisiert. Diese Systeme konnten durch die Bindung eines Ru(II) (bpy)(tpy) Komplexes (bpy = 2,2'-Bipyridin) über einen koordinierenden Cyanoliganden von einem Ir(III) $(ppy)_2$ (ppy = 2-Phenylpyridin) Komplex hergestellt werden. Der Abstand zwischen den beiden Metallzentren beträgt nur 5 Å und folglich wurden Metall-Metall-Wechselwirkungen in dem Grund-, dem oxidierten und dem angeregten Zustand beobachtet. Insbesondere die reduzierte Iridium-basierte Emission und eine beobachtbare Ruthenium-basierte Emission repräsentieren den Zerfall von den energetisch höheren Iridium-Triplett-Zuständen (^{3}Ir*) durch einen sehr schnellen Triplett-Triplett-Energietransfer zu den energetisch niedrigeren Ruthenium-Triplett-Zuständen (^{3}Ru*) (Abbildung 7.1, F). Hierbei konnte gezeigt werden, dass das Konzept des Lichtsammelns und der Speicherung in einen Chromophor grundsätzlich auch für Übergangsmetall-Komplexe funktioniert.

Zusammenfassend wurde demonstriert, dass die bemerkenswerte Anpassbarkeit von Terpyridin-Liganden in 4'-Position und die leichte Koordination an Ruthenium(II)-Zentren einen schnellen Zugang zu hochfunktionalisierten Komplexen eröffnet. Dadurch war es möglich, konventionelle Ru(II)-Terpyridyl-Komplexe – trotz ihrer kurzlebigen, angeregten Zustände – in molekularen Anordnungen als effektiven Photosensibilisator einzusetzen, um Energie- und Elektronentransferprozesse zu vermitteln.

8. References

[1] N. Armaroli, V. Balzani, *Angew. Chem. Int. Ed.* **2006**, *46*, 52-66.
[2] L. Hammarström, S. Hammes-Schiffer, *Acc. Chem. Res.* **2009**, *42*, 1859-1860.
[3] Q. Schiermeier, J. Tollefson, T. Scully, A. Witze, O. Morton, *Nature* **2008**, *454*, 816-823.
[4] M. Gratzel, *Nature* **2001**, *414*, 338-344.
[5] C. J. Brabec, S. Gowrisanker, J. J. M. Halls, D. Laird, S. Jia, S. P. Williams, *Adv. Mater.* **2010**, *22*, 3839-3856.
[6] A. W. Hains, Z. Liang, M. A. Woodhouse, B. A. Gregg, *Chem. Rev.* **2010**, *110*, 6689-6735.
[7] C. K. Prier, D. A. Rankic, D. W. C. MacMillan, *Chem. Rev.* **2013**, *113*, 5322-5363.
[8] K. L. Skubi, T. R. Blum, T. P. Yoon, *Chem. Rev.* **2016**, *116*, 10035-10074.
[9] M. D. Kärkäs, O. Verho, E. V. Johnston, B. Åkermark, *Chem. Rev.* **2014**, *114*, 11863–12001.
[10] F. Puntoriero, A. Sartorel, M. Orlandi, G. La Ganga, S. Serroni, M. Bonchio, F. Scandola, S. Campagna, *Coord. Chem. Rev.* **2011**, *255*, 2594-2601.
[11] P. D. Tran, L. H. Wong, J. Barber, J. S. C. Loo, *Energy Environ. Sci.* **2012**, *5*, 5902-5918.
[12] Q. Zeng, F. W. Lewis, L. M. Harwood, F. Hartl, *Coord. Chem. Rev.* **2015**, *304-305*, 88-101.
[13] T. Stoll, C. E. Castillo, M. Kayanuma, M. Sandroni, C. Daniel, F. Odobel, J. Fortage, M.-N. Collomb, *Coord. Chem. Rev.* **2015**, *304-305*, 20-37.
[14] Z. Yu, F. Li, L. Sun, *Energy Environ. Sci.* **2015**, *8*, 760-775.
[15] D. Gust, T. A. Moore, A. L. Moore, *Acc. Chem. Res.* **2001**, *34*, 40-48.
[16] E. Baranoff, J.-P. Collin, L. Flamigni, J.-P. Sauvage, *Chem. Soc. Rev.* **2004**, *33*, 147-155.
[17] E. A. Medlycott, G. S. Hanan, *Coord. Chem. Rev.* **2006**, *250*, 1763-1782.
[18] J. P. Collin, P. Gaviña, V. Heitz, J. P. Sauvage, *Eur. J. Inorg. Chem.* **1998**, *1998*, 1-14.
[19] H. W. Kroto, J. R. Heath, S. C. O'Brien, R. F. Curl, R. E. Smalley, *Nature* **1985**, *318*, 162-163.
[20] C.-Z. Li, H.-L. Yip, A. K.-Y. Jen, *J. Mater. Chem.* **2012**, *22*, 4161-4177.
[21] G. Accorsi, N. Armaroli, *J. Phys. Chem. C* **2010**, *114*, 1385-1403.
[22] P. Mroz, G. P. Tegos, H. Gali, T. Wharton, T. Sarna, M. R. Hamblin, *Photochem. Photobiol. Sci.* **2007**, *6*, 1139-1149.
[23] A. L. Balch, M. M. Olmstead, *Chem. Rev.* **1998**, *98*, 2123-2166.
[24] M. D. Meijer, G. P. M. van Klink, G. van Koten, *Coord. Chem. Rev.* **2002**, *230*, 141-163.
[25] L. I. Denisovich, S. M. Peregudova, Y. N. Novikov, *Russ. J. Electrochem.* **2010**, *46*, 1-17.
[26] D. Soto, R. Salcedo, *Molecules* **2012**, *17*, 7151-7168.
[27] C. García-Simón, M. Costas, X. Ribas, *Chem. Soc. Rev.* **2016**, *45*, 40-62.
[28] M. A. Lebedeva, T. W. Chamberlain, A. N. Khlobystov, *Chem. Rev.* **2015**, *115*, 11301-11351.
[29] M. R. Axet, O. Dechy-Cabaret, J. Durand, M. Gouygou, P. Serp, *Coord. Chem. Rev.* **2016**, *308*, 236-345.
[30] A. L. Balch, K. Winkler, *Chem. Rev.* **2016**, *116*, 3812-3882.

[31] A. Juris, V. Balzani, F. Barigelletti, S. Campagna, P. Belser, A. von Zelewsky, *Coord. Chem. Rev.* **1988**, *84*, 85–277.
[32] E. A. Medlycott, G. S. Hanan, *Chem. Soc. Rev.* **2005**, *34*, 133-142.
[33] J. Modin, H. Johansson, H. Grennberg, *Org. Lett.* **2005**, *7*, 3977-3979.
[34] M. Maggini, A. Donò, G. Scorrano, M. Prato, *J. Chem. Soc., Chem. Commun.* **1995**, 845-846.
[35] M. Maggini, D. M. Guldi, S. Mondini, G. Scorrano, F. Paolucci, P. Ceroni, S. Roffia, *Chem. Eur. J.* **1998**, *4*, 1992-2000.
[36] Z. Zhou, G. H. Sarova, S. Zhang, Z. Ou, F. T. Tat, K. M. Kadish, L. Echegoyen, D. M. Guldi, D. I. Schuster, S. R. Wilson, *Chem. Eur. J.* **2006**, *12*, 4241-4248.
[37] F. Cardinali, J.-L. Gallani, S. Schergna, M. Maggini, J.-F. Nierengarten, *Tetrahedron Lett.* **2005**, *46*, 2969-2972.
[38] G. Possamai, E. Menna, M. Maggini, M. Carano, M. Marcaccio, F. Paolucci, D. M. Guldi, A. Swartz, *Photochem. Photobiol. Sci.* **2006**, *5*, 1154-1164.
[39] S. Karlsson, J. Modin, H.-C. Becker, L. Hammarström, H. Grennberg, *Inorg. Chem.* **2008**, *47*, 7286-7294.
[40] E. Brunet, M. Alonso, M. C. Quintana, O. Juanes, J.-C. Rodríguez-Ubis, *Tetrahedron Lett.* **2007**, *48*, 3739-3743.
[41] A. Polese, S. Mondini, A. Bianco, C. Toniolo, G. Scorrano, D. M. Guldi, M. Maggini, *J. Am. Chem. Soc.* **1999**, *121*, 3446-3452.
[42] N. Armaroli, G. Accorsi, D. Felder, J.-F. Nierengarten, *Chem. Eur. J.* **2002**, *8*, 2314-2323.
[43] F. Chaignon, J. Torroba, E. Blart, M. Borgström, L. Hammarström, F. Odobel, *New J. Chem.* **2005**, *29*, 1272-1284.
[44] A. Amini, A. Harriman, A. Mayeux, *Phys. Chem. Chem. Phys.* **2004**, *6*, 1157-1164.
[45] F. Puntoriero, F. Nastasi, M. Galletta, S. Campagna, in *Comprehensive Inorganic Chemistry II (Second Edition)* (Ed.: J. R. Poeppelmeier), Elsevier, Amsterdam, **2013**, pp. 255-337.
[46] D. Rehm, A. Weller, *Isr. J. Chem.* **1970**, *8*, 259-271.
[47] T. Da Ros, M. Prato, D. M. Guldi, M. Ruzzi, L. Pasimeni, *Chem. Eur. J.* **2001**, *7*, 816-827.
[48] G. Zhou, J. He, I. I. Harruna, K. E. Geckeler, *J. Mater. Chem.* **2008**, *18*, 5492-5501.
[49] D. M. Guldi, M. Maggini, S. Mondini, F. Guérin, J. H. Fendler, *Langmuir* **2000**, *16*, 1311-1318.
[50] C. Luo, D. M. Guldi, M. Maggini, E. Menna, S. Mondini, N. A. Kotov, M. Prato, *Angew. Chem. Int. Ed.* **2000**, *39*, 3905-3909.
[51] M. Yamada, T. Akasaka, S. Nagase, *Chem. Rev.* **2013**, *113*, 7209-7264.
[52] A. Winter, D. A. M. Egbe, U. S. Schubert, *Org. Lett.* **2007**, *9*, 2345-2348.
[53] M. Maggini, A. Donò, G. Scorrano, M. Prato, *J. Chem. Soc., Chem. Commun.* **1995**, 845-846.
[54] The distance is estimated by geometry optimized structures. Force field molecular modelling was performed with Accelrys Software Material Studio v7.0 using the Forcite module.
[55] B. P. Sullivan, J. M. Calvert, T. J. Meyer, *Inorg. Chem.* **1980**, *19*, 1404-1407.
[56] M. Jäger, R. J. Kumar, H. Görls, J. Bergquist, O. Johansson, *Inorg. Chem.* **2009**, *48*, 3228-3238.
[57] B. Schulze, D. Escudero, C. Friebe, R. Siebert, H. Görls, U. Köhn, E. Altuntas, A. Baumgaertel, M. D. Hager, A. Winter, B. Dietzek, J. Popp, L. González, U. S. Schubert, *Chem. Eur. J.* **2011**, *17*, 5494-5498.

[58] S. Sinn, B. Schulze, C. Friebe, D. G. Brown, M. Jäger, J. Kübel, B. Dietzek, C. P. Berlinguette, U. S. Schubert, *Inorg. Chem.* **2014**, *53*, 1637-1645.
[59] A. Hirsch, M. Brettreich, *Fullerenes*, WILEY-VCH, Weinheim, **2005**.
[60] A. La Rosa, K. Gillemot, E. Leary, C. Evangeli, M. T. González, S. Filippone, G. Rubio-Bollinger, N. Agraït, C. J. Lambert, N. Martín, *J. Org. Chem.* **2014**, *79*, 4871-4877.
[61] O. Lukoyanova, C. M. Cardona, M. Altable, S. Filippone, Á. Martín Domenech, N. Martín, L. Echegoyen, *Angew. Chem. Int. Ed.* **2006**, *45*, 7430-7433.
[62] U. S. Schubert, A. Winter, G. R. Newkome, *Terpyridine-based Materials*, WILEY-VCH, Weinheim, **2011**.
[63] N. Armaroli, F. Barigelletti, P. Ceroni, J. F. Eckert, J. F. Nicoud, J. F. Nierengarten, *Chem. Commun.* **2000**, 599-600.
[64] C. Grewer, H.-D. Brauer, *J. Phys. Chem.* **1994**, *98*, 4230-4235.
[65] N. Bucci, T. J. J. Müller, *Tetrahedron Lett.* **2006**, *47*, 8323-8327.
[66] P. K. Poddutoori, A. S. D. Sandanayaka, N. Zarrabi, T. Hasobe, O. Ito, A. van der Est, *J. Phys. Chem. A* **2011**, *115*, 709-717.
[67] C. B. KC, G. N. Lim, M. E. Zandler, F. D'Souza, *Org. Lett.* **2013**, *15*, 4612-4615.
[68] S.-H. Lee, C. T.-L. Chan, K. M.-C. Wong, W. H. Lam, W.-M. Kwok, V. W.-W. Yam, *J. Am. Chem. Soc.* **2014**, *136*, 10041-10052.
[69] T. Kamimura, K. Ohkubo, Y. Kawashima, S. Ozako, K.-i. Sakaguchi, S. Fukuzumi, F. Tani, *J. Phys. Chem. C* **2015**, *119*, 25634-25650.
[70] T. Miyazaki, M. Shibahara, J.-i. Fujishige, M. Watanabe, K. Goto, T. Shinmyozu, *J. Org. Chem.* **2014**, *79*, 11440-11453.
[71] K. Bahrami, M. M. Khodaei, A. Karimi, *Synthesis* **2008**, 2543-2546.
[72] B. Schulze, C. Friebe, M. D. Hager, A. Winter, R. Hoogenboom, H. Görls, U. S. Schubert, *Dalton Trans.* **2009**, 787-794.
[73] S. L. Larson, C. M. Elliott, D. F. Kelley, *Inorg. Chem.* **1996**, *35*, 2070-2076.
[74] G. Ajayakumar, K. Sreenath, K. R. Gopidas, *Dalton Trans.* **2009**, 1180-1186.
[75] P. P. Lainé, S. Campagna, F. Loiseau, *Coord. Chem. Rev.* **2008**, *252*, 2552-2571.
[76] R. Siebert, A. Winter, U. S. Schubert, B. Dietzek, J. Popp, *Phys. Chem. Chem. Phys.* **2011**, *13*, 1606-1617.
[77] Y. Luo, K. Barthelmes, M. Wächtler, A. Winter, U. S. Schubert, B. Dietzek, *Chem. Eur. J.* **2017**, DOI: 10.1002/chem.201700413.
[78] M.-P. Santoni, G. S. Hanan, B. Hasenknopf, *Coord. Chem. Rev.* **2014**, *281*, 64-85.
[79] J. J. Walsh, A. M. Bond, R. J. Forster, T. E. Keyes, *Coord. Chem. Rev.* **2016**, *306, Part 1*, 217-234.
[80] M. T. Pope, *Heteropoly and Isopoly Oxometalates*, Springer-Verlag, New-York, **1983**.
[81] A. Dolbecq, E. Dumas, C. R. Mayer, P. Mialane, *Chem. Rev.* **2010**, *110*, 6009-6048.
[82] A. Proust, B. Matt, R. Villanneau, G. Guillemot, P. Gouzerh, G. Izzet, *Chem. Soc. Rev.* **2012**, *41*, 7605-7622.
[83] G. Izzet, F. Volatron, A. Proust, *Chem. Rec.* **2017**, *17* 250-266.
[84] B. Matt, C. Coudret, C. Viala, D. Jouvenot, F. Loiseau, G. Izzet, A. Proust, *Inorg. Chem.* **2011**, *50*, 7761-7768.
[85] B. Matt, J. Moussa, L.-M. Chamoreau, C. Afonso, A. Proust, H. Amouri, G. Izzet, *Organometallics* **2012**, *31*, 35-38.
[86] B. Matt, X. Xiang, A. L. Kaledin, N. Han, J. Moussa, H. Amouri, S. Alves, C. L. Hill, T. Lian, D. G. Musaev, G. Izzet, A. Proust, *Chem. Sci.* **2013**, *4*, 1737-1745.

[87] B. Matt, J. Fize, J. Moussa, H. Amouri, A. Pereira, V. Artero, G. Izzet, A. Proust, *Energy Environ. Sci.* **2013**, *6*, 1504-1508.
[88] S. Schönweiz, S. A. Rommel, J. Kübel, M. Micheel, B. Dietzek, S. Rau, C. Streb, *Chem. Eur. J.* **2016**, *22*, 12002-12005.
[89] C. Allain, D. Schaming, N. Karakostas, M. Erard, J.-P. Gisselbrecht, S. Sorgues, I. Lampre, L. Ruhlmann, B. Hasenknopf, *Dalton Trans.* **2013**, *42*, 2745-2754.
[90] A. Harriman, K. J. Elliott, M. A. H. Alamiry, L. L. Pleux, M. Séverac, Y. Pellegrin, E. Blart, C. Fosse, C. Cannizzo, C. R. Mayer, F. Odobel, *J. Phys. Chem. C* **2009**, *113*, 5834-5842.
[91] C. Allain, S. Favette, L.-M. Chamoreau, J. Vaissermann, L. Ruhlmann, B. Hasenknopf, *Eur. J. Inorg. Chem.* **2008**, *2008*, 3433-3441.
[92] J. B. Gerken, M. L. Rigsby, R. E. Ruther, R. J. Pérez-Rodríguez, I. A. Guzei, R. J. Hamers, S. S. Stahl, *Inorg. Chem.* **2013**, *52*, 2796-2798.
[93] N. Zabarska, D. Sorsche, F. W. Heinemann, S. Glump, S. Rau, *Eur. J. Inorg. Chem.* **2015**, *2015*, 4869-4877.
[94] C. Rinfray, G. Izzet, J. Pinson, S. Gam Derouich , J.-J. Ganem, C. Combellas, F. Kanoufi, A. Proust, *Chem. Eur. J.* **2013**, *19*, 13838-13846.
[95] M. R. Bryce, A. J. Moore, *Synth. Met.* **1988**, *27*, 557-561.
[96] N. Martín, I. Pérez, L. Sánchez, C. Seoane, *J. Org. Chem.* **1997**, *62*, 870-877.
[97] N. E. Gruhn, N. A. Macías-Ruvalcaba, D. H. Evans, *Langmuir* **2006**, *22*, 10683-10688.
[98] N. Martín, L. Sánchez, C. Seoane, E. Ortí, P. M. Viruela, R. Viruela, *J. Org. Chem.* **1998**, *63*, 1268-1279.
[99] S. Campagna, S. Serroni, F. Puntoriero, F. Loiseau, L. D. Cola, C. J. Kleverlaan, J. Becher, A. P. Sørensen, P. Hascoat, N. Thorup, *Chem. Eur. J.* **2002**, *8*, 4461-4469.
[100] C. Goze, C. Leiggener, S.-X. Liu, L. Sanguinet, E. Levillain, A. Hauser, S. Decurtins, *ChemPhysChem* **2007**, *8*, 1504-1512.
[101] M. Abrahamsson, M. Jäger, R. J. Kumar, T. Österman, P. Persson, H.-C. Becker, O. Johansson, L. Hammarström, *J. Am. Chem. Soc.* **2008**, *130*, 15533-15542.
[102] N. Dupont, Y.-F. Ran, H.-P. Jia, J. Grilj, J. Ding, S.-X. Liu, S. Decurtins, A. Hauser, *Inorg. Chem.* **2011**, *50*, 3295-3303.
[103] C. Sabatini, A. Barbieri, F. Barigelletti, K. J. Arm, J. A. G. Williams, *Photochem. Photobiol. Sci.* **2007**, *6*, 397-405.
[104] J. O. Barcina, N. Herrero-García, F. Cucinotta, L. De Cola, P. Contreras-Carballada, R. M. Williams, A. Guerrero-Martínez, *Chem. Eur. J.* **2010**, *16*, 6033-6040.
[105] M. Wächtler, J. Kübel, K. Barthelmes, A. Winter, A. Schmiedel, T. Pascher, C. Lambert, U. S. Schubert, B. Dietzek, *Phys. Chem. Chem. Phys.* **2016**, *18*, 2350-2360.
[106] H. Vahrenkamp, A. Geiß, G. N. Richardson, *J. Chem. Soc., Dalton Trans.* **1997**, 3643-3651.
[107] S. Tanase, J. Reedijk, *Coord. Chem. Rev.* **2006**, *250*, 2501-2510.
[108] L. M. Baraldo, P. Forlano, A. R. Parise, L. D. Slep, J. A. Olabe, *Coord. Chem. Rev.* **2001**, *219*, 881-921.
[109] A. V. Macatangay, J. F. Endicott, *Inorg. Chem.* **2000**, *39*, 437-446.
[110] M. A. Watzky, A. V. Macatangay, R. A. Van Camp, S. E. Mazzetto, X. Q. Song, J. F. Endicott, T. Buranda, *J. Phys. Chem. A* **1997**, *101*, 8441-8459.
[111] M. D. Ward, *Dalton Trans.* **2010**, *39*, 8851-8867.

[112] M. K. Nazeeruddin, R. Humphry-Baker, D. Berner, S. Rivier, L. Zuppiroli, M. Graetzel, *J. Am. Chem. Soc.* **2003**, *125*, 8790-8797.
[113] D. J. Wasylenko, C. Ganesamoorthy, B. D. Koivisto, M. A. Henderson, C. P. Berlinguette, *Inorg. Chem.* **2010**, *49*, 2202-2209.
[114] J. Li, P. I. Djurovich, B. D. Alleyne, M. Yousufuddin, N. N. Ho, J. C. Thomas, J. C. Peters, R. Bau, M. E. Thompson, *Inorg. Chem.* **2005**, *44*, 1713-1727.
[115] D. Di Censo, S. Fantacci, F. De Angelis, C. Klein, N. Evans, K. Kalyanasundaram, H. J. Bolink, M. Grätzel, M. K. Nazeeruddin, *Inorg. Chem.* **2008**, *47*, 980-989.
[116] A. Cadranel, P. Albores, S. Yamazaki, V. D. Kleiman, L. M. Baraldo, *Dalton Trans.* **2012**, *41*, 5343-5350.
[117] Y. Chi, P. T. Chou, *Chem. Soc. Rev.* **2010**, *39*, 638-655.
[118] K.-C. Chan, W.-K. Chu, S.-M. Yiu, C.-C. Ko, *Dalton Trans.* **2015**, *44*, 15135-15144.

List of abbreviations

^{1}	singlet state
^{3}	triplet state
A	electron acceptor
a.u.	arbitrary units
bpy	2,2'-bipyridine
B	bridge
BMImCl	1-butyl-3-methyl-1*H*-imidazol-3-ium chloride
$^3C_{60}$*	lowest excited triplet state of C_{60}
CN	cyanide
cp	cyclopentadienyl anion
CSS	charge separated state
CV	cyclic voltammetry
ΔG_{CSS}	driving force towards the charge separated state
D	electron donor
d-d	calculated doublet-doublet transitions
DMF	*N,N*-dimethylformamide
DMSO	dimethyl sulfoxide
DPV	differential pulse voltammetry
E_{CSS}	energy of the lowest charge separated state
ε	extinction coefficient
EDDM	electron density difference maps

ESI MS	electrospray ionization mass spectrometry
exTTF	π-extended tetrathiafulvalene
F-C_{60}	functionalized C_{60}
Fc	ferrocene
fs TA	femtosecond transient absorption
*i*PrSPh	isopropyl phenyl sulfide
Ir	Ir(III) complex
^{3}Ir*	lowest excited triplet state of the Ir(III) complex
ITO	indium tin oxide
IVCT	intervalence charge transfer
λ_{exc}	excitation wavelength
λ_{MLCT}	MLCT-based absorption maximum
LC	ligand-centered
LMCT	ligand-to-metal charge transfer
LUMO	lowest unoccupied molecular orbital
MeCN	acetonitrile
MC	metal-centered
MLLCT	metal-ligand-to-ligand charge transfer
MLCT	metal-to-ligand charge transfer
MW	microwave
NBS	*N*-bromosuccinimide
NIR	near infrared
ns TA	nanosecond transient absorption

*o*DCB	*ortho*-dichlorobenzene
oxPTZ	oxidized *N*-methylphenothiazine to the sulfoxide
ISC	intersystem crossing
P	photosensitizer
PPE	*para*-phenyleneethynylene
POM	polyoxometalate
por	porphyrin
py	pyridine
ppy	2-phenylpyridine
PTZ	*N*-methylphenothiazine
r.t.	room temperature
Ru	Ru(II) complex
^{3}Ru*	lowest excited triplet state of the Ru(II) complex
s-s	calculated singlet-singlet transitions
SCN	thiocyanate
UV	ultraviolet
vis	visible
TD-DFT	time-dependent density functional theory
Tf_2O	triflic anhydride
THF	tetrahydrofuran
tpy	2,2':6',2''-terpyridine

Curriculum vitae

Personal Data

Date of birth:	April, 24th 1988
Place of birth:	Meiningen, Germany

University Education

03/2013–present:	PhD student in the group of Prof. Dr. U. S. Schubert at the *Institute of Organic Chemistry and Macromolecular Chemistry* of the *Friedrich Schiller University Jena*, Germany
12/2012:	Diploma (equivalent to M.Sc.)
01/2012–12/2012:	Diploma thesis in the group of Prof. Dr. U. S. Schubert at the *Institute of Organic Chemistry and Macromolecular Chemistry* of the *Friedrich Schiller University Jena*, Germany, thesis title: "Hierarchically Structured Coordination Oligomers – Synthesis and Characterization"
10/2007–12/2012:	Studies of Chemistry at the *Friedrich Schiller University Jena*, Germany

National Service

09/2006–06/2007:	Civilian service

Schooling

06/2006:	Abitur (university entrance certification) at the *Henfling-Gymnasium*, Meiningen, Germany

Jena,

_____

Kevin Barthelmes

Publication list

Peer-reviewed publications

[1] **K. Barthelmes**, J. Kübel, A. Winter, M. Wächtler, C. Friebe, B. Dietzek, U. S. Schubert, "New Ruthenium Bis(terpyridine) Methanofullerene and Pyrrolidinofullerene Complexes: Synthesis and Electrochemical and Photophysical Properties", *Inorg. Chem.* **2015**, *54*, 3159-3171.

[2] **K. Barthelmes**, M. Jäger, J. Kübel, C. Friebe, A. Winter, M. Wächtler, B. Dietzek, U. S. Schubert, "Efficient Energy Transfer and Metal Coupling in Cyanide-Bridged Heterodinuclear Complexes Based on (Bipyridine)(terpyridine)ruthenium(II) and (Phenylpyridine)iridium(III) Complexes", *Inorg. Chem.* **2016**, *55*, 5152-5167.

[3] M. Wächtler, J. Kübel, **K. Barthelmes**, A. Winter, A. Schmiedel, T. Pascher, C. Lambert, U. S. Schubert, B. Dietzek, "Energy transfer and formation of long-lived ^{3}MLCT states in multimetallic complexes with extended highly conjugated bis-terpyridyl ligands" *Phys. Chem. Chem. Phys.* **2016**, *18*, 2350-2360.

[4] **K. Barthelmes**, A. Winter, U. S. Schubert, "Hybrid Materials based on Ruthenium and Fullerene Assemblies", *Dalton Trans.* **2016**, *45*, 14855-14882.

[5] **K. Barthelmes**, A. Winter, U. S. Schubert, "Dyads and Triads based on Phenothiazine, Bisterpyridine Ruthenium(II) Complexes and Fullerene", *Eur. J. Inorg. Chem.* **2016**, 5132-5142.

[6] Y. Luo, **K. Barthelmes**, M. Wächtler, A. Winter, U. S. Schubert, B. Dietzek, "Energy vs. Electron Transfer – Controlling the Excitation Transfer in Molecular Triads", *Chem. Eur. J.*, DOI: 10.1002/chem.201700413.

Manuscripts submitted

[1] **K. Barthelmes**, M. Sittig, A. Winter, U. S. Schubert, "Molecular Dyads and Triads Based on Phenothiazine and π-extended Tetrathiafulvalene Donors, Ruthenium(II) Bisterpyridine Complexes and Polyoxometalates", *submitted*.

[2] Y. Luo, **K. Barthelmes**, M. Wächtler, A. Winter, U. S. Schubert, B. Dietzek, "Increased Charge Separation Rates with Increasing Donor-Acceptor Distance in Molecular Triads: the Effect of Solvent Polarity", *submitted*.

Oral presentations

[1] **K. Barthelmes**, C. Friebe, A. Winter, M. Wächtler, J. Kübel, B. Dietzek, U. S. Schubert, "Ruthenium Bisterpyridine-Fullerene Assemblies: Synthesis, Electrochemical and Photophysical Properties", Young-Researcher-Meeting (COST Action): Current Challenges in Supramolecular Artificial Photosynthesis, Jena, Germany, 03/09/14−03/11/14.

Poster presentations

[1] **K. Barthelmes**, C. Friebe, A. Winter, M. Wächtler, J. Kübel, B. Dietzek, U. S. Schubert, "Ruthenium Bisterpyridine-Fullerene Assemblies: Synthesis, Electrochemical and Photophysical Properties", European Symposium (COST Action): Current Challenges in Supramolecular Artificial Photosynthesis, Jena, Germany, 03/12/14−03/13/14.

[2] **K. Barthelmes**, C. Friebe, A. Winter, M. Wächtler, J. Kübel, B. Dietzek, U. S. Schubert, "Ruthenium Bisterpyridine-Fullerene Assemblies: Synthesis, Electrochemical and Photophysical Properties", 16. JCF spring symposium, Jena, Germany, 03/26/14−03/29/14.

[3] **K. Barthelmes**, M. Jäger, J. Kübel, C. Friebe, A. Winter, M. Wächtler, B. Dietzek, U. S. Schubert, "Efficient Energy Transfer and Metal Coupling in Cyanide-Bridged Heterodinuclear Complexes Based on (Bipyridine)(terpyridine)ruthenium(II) and (Phenylpyridine)iridium(III) Complexes", 25. Lecture Conference on Photochemistry (GDCh meeting), Jena, Germany, 09/26/16−09/28/16.

Acknowledgements

This thesis would not be possible without the assistance and advice of a lot of persons.

First of all, I would like to thank Prof. Dr. Ulrich S. Schubert for the opportunity to perform this work in his research group. He entrusted me with an exciting and very interesting topic, and gave me scientific freedom to pursue my own ideas.

Furthermore, I want to thank Dr. Andreas Winter for introducing me to the topic. Thank you very much for always having an open ear for me. Your continuous support and supervision during the years was crucial for the success of the thesis.

I want to thank Dr. Benjamin Schulze, Dr. Michael Jäger and Dr. Christian Friebe, for sharing your synthetic, computational, photophysical and electrochemical knowledge with me.

I am very grateful for the excellent cooperation with the group of Prof. Dr. Benjamin Dietzek. In particular, I want to thank Joachim Kübel, Yusen Luo, Dr. Maria Wächtler and Prof. Dr. Benjamin Dietzek for the time-resolved spectroscopy analysis as well as helpful comment and discussions.

Furthermore, I want to thank several staff members of the Institute of Organic Chemistry and Macromolecular Chemistry (IOMC) and (former) members of the Schubert group for their help with measurements and organizational issues, in particular Tina Schlotthauer, Dr. Esra Altuntaş, Nicole Fritz, and Sarah Crotty for the ESI MS as well as the MALDI MS measurements, Beate Lentvogt for the elemental analyses, Sandra Köhn for keeping the consumable cupboards full, Dr. Uwe Köhn for the ordering of chemicals, Dr. Wolfgang Günther, Gabrielle Sentis and Dr. Peter Bellstedt for the NMR experiments, and Simone Burchardt, Sylvia Braunsdorf, Tanja Wagner and Franca Frister for the administrational issues.

I want to thank my former lab colleagues Dr. Pier Caponi, Kristin Schreyer, Maria Sittig, Anette Kuse, Frieder Bayerköhler and Dr. Julia Kötteritzsch for a pleasant working atmosphere.

Furthermore, I want to thank Tino Hagemann, Robert Schroot, Ronny Tepper, Tina Schlotthauer, Dr. Christian Friebe and Dr. Daniel Schmidt. It was a pleasure to share lunch and coffee breaks with you.

Last but not least, I sincerely want to thank my family and my friends. I am very grateful for your amazing and continuous support in private life.

Declaration of authorship / Selbstständigkeitserklärung

I certify that the work presented here is, to the best of my knowledge and belief, original and the result of my own investigations, except as acknowledged, and has not been submitted, either in part or whole, for a degree at this or any other university.

Ich erkläre, dass ich die vorliegende Arbeit selbständig und unter Verwendung der angegebenen Hilfsmittel, persönlichen Mitteilungen und Quellen angefertigt habe.

Jena,

_____

Kevin Barthelmes

Publications P1 to P5

P1) Reprinted with permission from: The Royal Society of Chemistry, Copyright 2016.

P2) Reprinted with permission from: American Chemical Society, Copyright 2015.

P3) Reprinted with permission from: Wiley-VCH, Copyright 2016.

P4) Reprinted with permission from: K. Barthelmes, M. Sittig, A. Winter and U. S. Schubert.

P5) Reprinted with permission from: American Chemical Society, Copyright 2016.

Publication P1

"Hybrid Materials based on Ruthenium and Fullerene Assemblies"

K. Barthelmes, A. Winter, U. S. Schubert,

Dalton Trans. **2016**, *45*, 14855-14882.

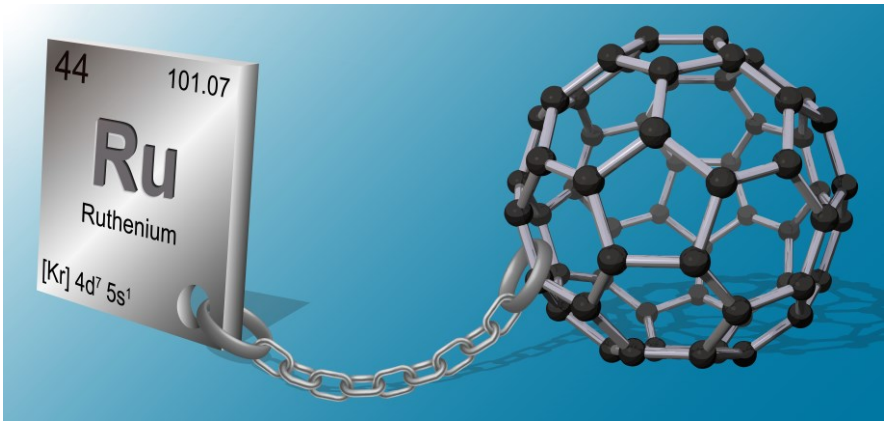

Dalton Transactions

PERSPECTIVE

View Article Online
View Journal | View Issue

CrossMark click for updates

Cite this: *Dalton Trans.*, 2016, **45**, 14855

Hybrid materials based on ruthenium and fullerene assemblies

Kevin Barthelmes,[a,b] Andreas Winter[a,b] and Ulrich S. Schubert*[a,b]

Received 30th June 2016,
Accepted 16th August 2016

DOI: 10.1039/c6dt02613c

www.rsc.org/dalton

This review provides a detailed overview about the synthesis, properties and applications of all ruthenium-fullerene compounds reported within the last 25 years. The incorporation of ruthenium centers into fullerene compounds by organometallic, covalent or non-covalent bonds has led to a broad range of useful hybrid materials. By this approach novel compounds could be generated that feature the electron-donating and electron-accepting character of ruthenium complexes and fullerenes, respectively. Intramolecular interactions between both units could result in new, combined properties that were studied in the spotlight of emerging applications, such as photovoltaics or catalysis.

1. Introduction

An enormous amount of research has been focused on the chemistry of fullerenes after the discovery of the spherically shaped C_{60} in 1985.[1] The discovery of new carbon allotropes did not tarnish the status of C_{60} as the flagship in the ongoing research of carbon surface modification. The unique spherical shape makes C_{60} to the favored structure in the context of product selectivity, functionalization, characterization or network formation, if compared to the spheroidal C_{70} or the family of higher fullerenes, the tube-shaped nanotubes or nanohorns, and the flat graphene. One of the most remarkable properties of fullerenes and their derivatives is their pronounced electron-accepting character and low reorganization energy, which makes them to a favored unit in donor/acceptor systems, such as organic solar cells.[2] C_{60} features a strong absorption in the UV-region with weaker spin-forbidden transitions in the visible region.[3] Photo-excitation results in the formation of the singlet state ($^1C_{60}$*), which decays quantitatively (with a triplet quantum yield of >99%) *via* intersystem crossing (ISC) to the triplet state ($^3C_{60}$*). The latter one is

[a]*Laboratory of Organic and Macromolecular Chemistry (IOMC), Friedrich Schiller University Jena, Humboldtstr. 10, 07743 Jena, Germany. E-mail: ulrich.schubert@uni-jena.de; http://www.schubert-group.de; Fax: +49 3641 948202*
[b]*Center for Energy and Environmental Chemistry Jena (CEEC Jena), Friedrich Schiller University Jena, Philosophenweg 7a, 07743 Jena, Germany*

Kevin Barthelmes

Kevin Barthelmes was born in Meiningen (Germany) in 1988. He studied chemistry at the Friedrich Schiller University Jena (Germany). Since 2013 he is PhD student in the group of Prof. Schubert at the Friedrich Schiller University Jena. His research interests cover metallo-supramolecular chemistry and fullerene chemistry.

Andreas Winter

Andreas Winter was born in Herne (Germany) and studied chemistry at the University of Dortmund (Germany) where he graduated in organic chemistry in 1999. In 2003 he received his PhD in chemistry (University of Paderborn, Germany) for work on applications of the Mannich reaction in the synthesis of pyridine derivatives under supervision of Prof. Risch, and stayed on as a postdoc. Subsequently, in 2005 he joined the group of Prof. Schubert at the TU Eindhoven, the Netherlands. In 2010, he moved with group from there to the Friedrich Schiller University Jena, Germany. His research is focused on the synthesis of redox-active metallo-supramolecular assemblies.

highly sensitive to oxygen and results in the formation of singlet oxygen that has, for example, been applied in photodynamic therapy (PDT).[4]

Within the last 25 years, the interaction of various transition metal ions with fullerenes has thoroughly been examined regarding catalytic activity, photo-induced formation of charge-separated states, self-assembly in solution or surface modification.[5–12] In this context, ruthenium as transition metal ion features interesting and unique properties. Most of its complexes (*i.e.*, ruthenium(II) polypyridyl complexes) are very stable, exhibit an electron-donating and redox-active metal center,[13] show intense absorption of visible light and have rather long-lived excited states;[13,14] moreover, their catalytic activity is well-documented in literature.[15] All these characteristics make ruthenium complexes to attractive candidates for the incorporation into fullerene-based architectures. By this approach new hybrid materials can be generated that feature the individual properties of the active units as well as combined properties mediated by intramolecular interactions between them. Hybrid materials based on ruthenium complexes and fullerene assemblies can be classified in three groups. The first group contains organometallic ruthenium complexes in which the ruthenium is directly connected to the surface of the fullerene sphere by exohedral coordination. Ruthenium complexes that are not directly coordinated onto the fullerene surface can be summarized in the second group. Most of these compounds were prepared by ruthenium complexation of ligand-functionalized fullerenes. In the last group, a variety of non-covalently bonded ruthenium-fullerene architectures can be found – including supramolecular structures (*i.e.*, encapsulated fullerenes), ruthenium-impregnated fullerenes, ruthenium fulleride salts and ruthenium-fullerene blends. There are a number of recent reviews available dealing with surface modification of fullerenes or nanotubes by transition metal ions in general.[9–12] However, they mainly focus on the properties, computational studies and potential application of these transition metal-fullerene architectures. The major aim of this review is to give a detailed overview about the synthesis, properties and applications of all reported ruthenium-fullerene compounds in the last 25 years.

Ulrich S. Schubert

Ulrich S. Schubert was born in Tübingen (Germany) in 1969. He studied chemistry in Frankfurt and Bayreuth (both Germany) and at the Virginia Commonwealth University, Richmond (USA). His PhD studies were performed at the Universities of Bayreuth and South Florida. After a post-doctoral training with J.-M. Lehn at the University of Strasbourg (France), he moved to the TU Munich (Germany) and obtained his Habilitation in 1999. During 1999–2000 he was Professor at the University of Munich, and during 2000–2007 Full-Professor at the TU Eindhoven (the Netherlands). Since 2007, he is a Full-Professor at the Friedrich Schiller University Jena, Germany.

2. Organometallic ruthenium complexes attached on the fullerene surface

A broad range of examples for organometallic transition metal complexes featuring an exohedral coordination of a fullerene moiety to the metal center have been reported in literature over the last two decades.[5,7,8,10–12] A selection of the possible metal-binding modes is shown in Fig. 1. From these, dihapto- (η^2) and pentahapto-type (η^5) coordination of the fullerene have been found to predominate when dealing with ruthenium-fullerene complexation. In the following, reported structures will be discussed in the order of increasing hapticity.

2.1. Fullerene as monohapto (η^1) ligand

Recently, Bowles *et al.*[16] reported a rare Ru(η^1-C_{60}) σ-complex. The authors intended to cocrystallize [Ru(η^5-Cp)$(CO)_2$]$_2$ in hexane with C_{60} in dichloromethane, 1,2-dichlorobenzene (*o*DCB) or benzene. After four months, single crystals suitable for X-ray structure analysis were obtained in 10 to 18% yield. According to this analysis, the dinuclear complex **1** was formed comprising two [Ru(η^5-Cp)$(CO)_2$] units, from which

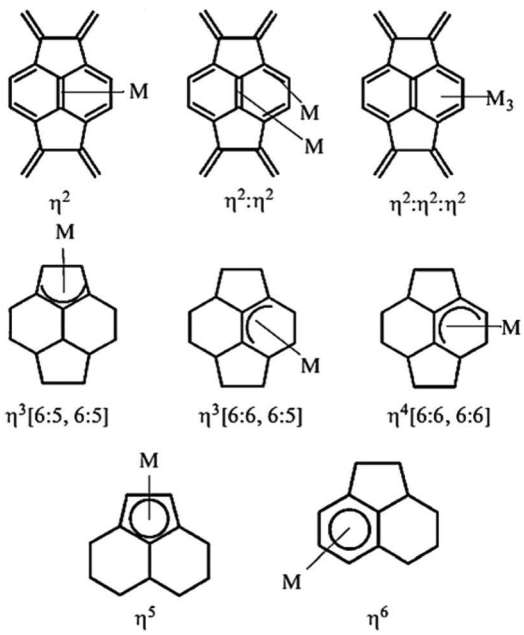

Fig. 1 Schematic representation of possible organometallic binding modes with C_{60}. The substructure of C_{60} is represented by the two 5- and 6-membered rings. Figure reprinted with permission from ref. 7, copyright 2010 Springer.

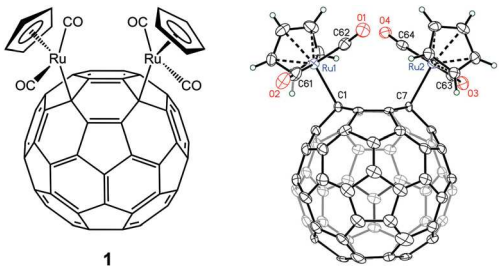

1

Fig. 2 Schematic representation of the dinuclear complex **1**. A representation of the X-ray single-crystal structure of **1** is also shown. Figure reprinted with permission from ref. 16, copyright 2014 American Chemical Society.

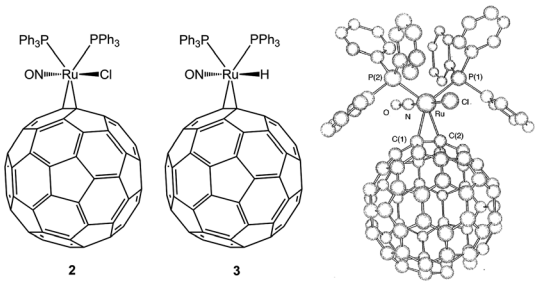

2 3

Fig. 3 Schematic representation of the mononuclear complexes **2** (left) and **3** (middle). A representation of the X-ray single-crystal structure of **2** is also shown (right). Figure reprinted with permission from ref. 22, copyright 1998 The Royal Chemical Society.

each ruthenium center coordinated one hexagoncarbon of the C_{60} in a η^1-fashion (Fig. 2). Remarkably, the two [Ru(η^5-Cp)$(CO)_2$] units were bonded to the hexagon in a 1,4-addition reaction. Consequently, the *para*-functionalization pattern forced one double bond between a [5,6]-bond, leading to an energetically unfavorable structure. However, the more common 1,2-addition product was not observed which was ascribed to steric hindrance of the two [Ru(η^5-Cp)$(CO)_2$] units. The reaction could be accelerated by irradiation with light to a high conversion within 70 min.

2.2. Fullerene as dihapto (η^2) ligand

The ability of electron-rich ruthenium precursor complexes, such as $Ru(CO)_5$ [17] or $[RuH(NO)(PPh_3)_3]$,[18] to react with appropriate electron-deficient alkenes allows the formation of stable η^2-complexes. This approach was extended to fullerene derivates in order to construct Ru(η^2-C_{60}) complexes. Already six years after the discovery of C_{60}, the first preliminary data on a ruthenium-containing C_{60} were given by Fagan *et al.* in 1991.[19] The reaction of C_{60} with a tenfold excess of [Ru(η^5-Cp)$(MeCN)_3$](O_3SCF_3) (Cp = cyclopentadienyl anion) in dichloromethane at room temperature for five days resulted in a brown precipitate. ^{1}H NMR spectroscopy and elemental analysis (EA) suggested the formation of a compound with the chemical formula $[Ru(\eta^5\text{-Cp})(MeCN)_2]_x(C_{60})(O_3SCF_3)_x$ with x values between 3 and 4. It was believed that the six-membered rings of C_{60} could be coordinated to ruthenium in a hexahapto fashion, as it has been shown for electron-rich aromatic hydrocarbons.[20] However, the remaining acetonitrile (MeCN) ligands indicated the coordination only in a η^2-fashion. Another early study giving preliminary data was carried out by Rasinkangas *et al.* in 1994:[21] Stoichiometric amounts of $Ru(CO)_5$ and C_{60} were dissolved in toluene. A red solution was obtained after stirring the solution overnight, and subsequent analysis by IR and ^{13}C NMR spectroscopy suggested the formation of $Ru(CO)_4(\eta^2\text{-}C_{60})$. However, the first X-ray single crystal structure of a mononuclear Ru(η^2-C_{60}) complex was reported by Chernega *et al.*[22] in 1998 (Fig. 3) providing an unambiguous proof of the η^2-nature in the Ru–C bond between a 6-membered ring-junction (*i.e.*, a [6,6]-bond). The green-colored complexes **2** and **3** of the general formula $[RuX(NO)(PPh_3)_2(\eta^2\text{-}C_{60})]$ (**2**: X = Cl; **3**: X = H) were synthesized in high yields (80% average yield) by the reaction of equimolar amounts of C_{60} and $[RuX(NO)(PPh_3)_3]$ in benzene at room temperature. The C–C bond length between the carbon atoms involved in the metal-binding were much longer (**2**: 1.489 Å) than in pristine C_{60} (1.392 Å). This elongation is caused by a proper Ru-to-C_{60} π-back-donation and can be considered more as a metallacyclopropane unit rather than a metal–alkene coordinative bond. However, the ruthenium centers in **2** and **3** were only weakly bound to the fullerene moiety and could be cleaved of by the addition of donor and/or π-acidic ligands (*e.g.*, triorganophosphines or I_2) to release pristine C_{60}.

It was found that the incorporation of more than one ruthenium center significantly increases the stability of such complexes. The first dinuclear Ru(η^2-C_{60}) complexes with the formula $[Ru_2(\eta^5\text{-Cp})_2(\mu\text{-Cl})(\mu\text{-X})(\mu\text{–}\eta^2, \eta^2\text{-}C_{60})]$ (**4**: X = H, **5**: X = Cl) were reported by Mavunkal *et al.* (Fig. 4):[23] **4** and **5** both consisted of two ruthenium centers, which were each coordinated to a Cp unit and the [6,6]-bonds of the same 6-membered ring. Furthermore, the metal centers were bridged by either one chloride and one hydride (**4**) or two chloride ligands (**5**). The compounds were synthesized in a straightforward fashion by heating of C_{60} and $[Ru(\eta^5\text{-Cp})(\mu\text{-H})_2]_2$ with $[Ru(\eta^5\text{-Cp})(\mu\text{-Cl})_2]_2$ (1 eq. for **4**; 2 eq. for **5**) in toluene.

Apparently, a maximum in stability for Ru(η^2-C_{60}) complexes is reached when three ruthenium centers occupy all three [6,6]-bonds of a single 6-membered ring. Such a tri-

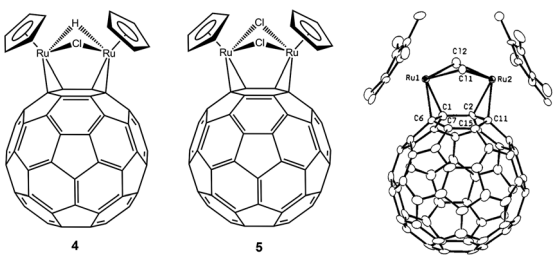

4 5

Fig. 4 Schematic representation of the dinuclear complexes **4** and **5**. A representation of the X-ray single-crystal structure of **5** is also shown. Figure reprinted with permission from ref. 23, copyright 1995 American Chemical Society.

nuclear Ru(η^2-C_{60}) compound with the formula [$Ru_3(CO)_9(\mu_3$–η^2, η^2, η^2-C_{60})] (**6**) was first synthesized by Hsu *et al.* (Fig. 5).[24] The synthesis was performed with C_{60} and 2 eq. of a zerovalent $Ru_3(CO)_{12}$ cluster in refluxing *n*-hexane for two days and afforded **6** in only 4% yield. The structure was proven by X-ray single crystal analysis (Fig. 5) and revealed that the triangular face of the ruthenium cluster is positioned centrally over a 6-membered ring. Thereby, each Ru center is coordinated onto a [6,6]-bond of the C_{60}. The same protocol was also applied to prepare the analogous C_{70}-based complex [$Ru_3(CO)_9(\mu_3$–η^2, η^2, η^2-C_{70})] **7** (Fig. 5).[25] The increased stability of these complexes was shown by CO-exchange experiments with PPh_3 where no fragmentation of the [Ru_3C_{60}] framework was observed.[26]

By the same time Wohlers *et al.* reported a similar reaction using equimolar amounts of $Ru_3(CO)_{12}$ with C_{60} in refluxing toluene for seven days.[27] Here, an insoluble black solid was obtained that was analyzed by transmission electron microscopy (TEM). The application thereof is discussed later in the context of ruthenium-coated fullerenes.

Lee *et al.* synthesized the penta- and hexanuclear carbido Ru(η^2-C_{60}) clusters [$Ru_5C(CO)_{11}(PPh_3)(\mu_3$–$\eta^2$, η^2, η^2-C_{60})] (**8**, Fig. 6) and [$Ru_6C(CO)_{12}$(dppm)(μ_3–η^2, η^2, η^2-C_{60})] (**9**, dppm = 1,2-bis(diphenylphosphino)methane, Fig. 7).[28,29] The compounds were prepared by refluxing equimolar amounts of the carbido clusters $Ru_5C(CO)_{15}$ or $Ru_6C(CO)_{17}$ with C_{60} in chlorobenzene. Subsequently, treatment with PPh_3 or dppm at room temperature yielded the final structures. In both cases, X-ray single crystal structure analysis revealed the same triangular face coordinated substructure as already observed in **6**. Moreover, a square pyramidal and octahedral metal framework is found in **8** and **9**, respectively.

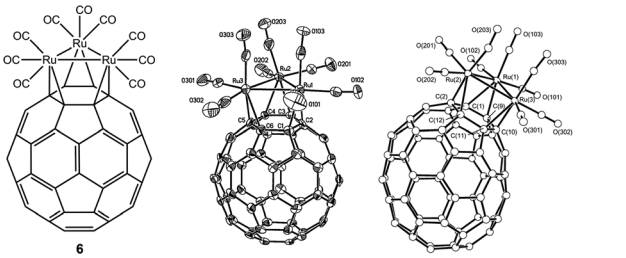

Fig. 5 Schematic representation of the trinuclear complex **6** (left). A representation of the X-ray single-crystal structures of **6** (middle, C_{60}-based) and **7** (right, C_{70}-based) is also shown. Figure reprinted with permission from ref. 24 and 25, copyright 1996 American Chemical Society and 1997 The Royal Chemical Society, respectively.

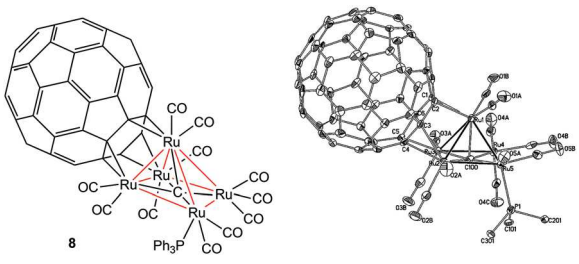

Fig. 6 Schematic representation of the pentanuclear complex **8**. The red bonds show the square pyramidal Ru_5 framework. A representation of the X-ray single-crystal structure of **8** is also shown (PPh_3 unit is shown in simplified form). Figure reprinted with permission from ref. 28, copyright 1997 American Chemical Society.

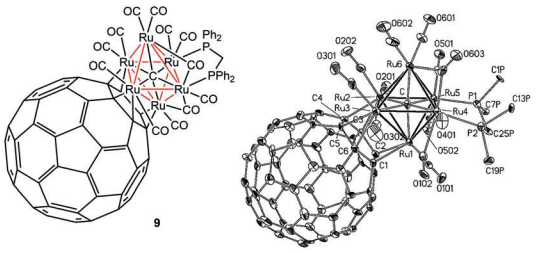

Fig. 7 Schematic representation of the hexanuclear complex **9**. The red bonds show the octahedral Ru_6 framework. A representation of the X-ray single-crystal structure of **9** is also shown (PPh_2 unit is shown in simplified form). Figure reprinted with permission from ref. 28, copyright 1997 American Chemical Society.

A different type of binding, *i.e.*, the Ru being indirectly attached to C_{60}, was reported by Song *et al.*:[30] The dihapto, zerovalent palladium (**10**) or platinum (**11**) complexes with a chelating ruthenocene moiety were prepared in a stepwise one-pot reaction – first equimolar amounts of M(dba) or $M(PPh_3)_4$ (M = Pd or Pt, dba = dibenzylideneacetone) were treated with C_{60} in toluene at room temperature, affording [M(η^2-C_{60})] or [$M(PPh_3)_2(\eta^2$-C_{60})], respectively (Scheme 1). Subsequently, an equimolar amount of 1,1′-bis(diphenylphosphino)ruthenocene (dppr) was added to the black suspension and the color of the reaction mixture turned to green. The diheteronuclear [M(dppr)$(PPh_3)_2(\eta^2$-C_{60})] assemblies were obtained in 60% and 90% yields, depending on the metal precursor used. X-ray diffraction analysis confirmed the structures and showed a η^2-type, square planar coordination mode (Scheme 1). Moreover, the dihedral angles between the two Cp ligands of 4.7° and 5.7° for **10** and **11**, respectively, indicated only a slight distortion of the ruthenocene unit. The latter value is lower than in the related complex Pt(dppr)Cl_2 (*i.e.*, 8.8°)[31] due to a larger

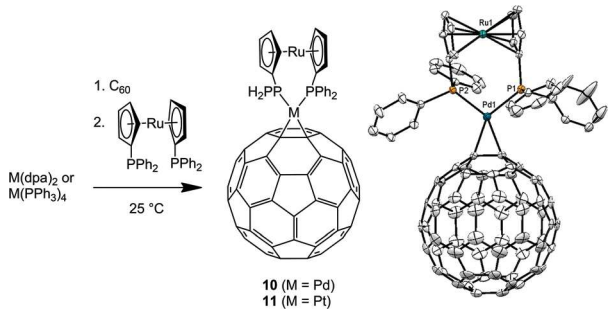

Scheme 1 Schematic representation of the synthesis of the ruthenocene-fullerene systems **10** and **11**. A representation of the X-ray single-crystal structures of **10** is also shown. Figure reproduced with permission from ref. 30, copyright 2004 American Chemical Society.

P–Pt–P angle and a smaller C–Pt–C angle. Electrochemical analysis revealed a slightly higher electron-acceptability of the C_{60} moiety in the case of the Pd-containing compound **10**. Independent from the coordinated metal center (Pd in **10** *vs.* Pt in **11**), the oxidation of the lateral ruthenocene entity remained irreversible.[32]

2.3. Fullerene as pentahapto (η^5) ligand

Early considerations on the stability of $[M(\eta^5\text{-}C_{60})(\eta^5\text{-}Cp)]^+$ and $[M(\eta^6\text{-}C_{60})(\eta^6\text{-}C_6H_6)]^{2+}$ complexes (M = Fe^{2+}, Ru^{2+} and Os^{2+}) suggested that the coordination by the five-membered rings in C_{60} should be energetically more favorable.[33] The failures to obtain stable $M(\eta^6\text{-}C_{60})$ compounds was mainly attributed to the curvature of the C_{60}, which orients each exohedral p-orbital by an angle of *ca.* 10° away from the perpendicular face of the six-membered ring and result is an unsufficient overlap to form a stable $M(\eta^6\text{-}C_{60})$ complex.[34,35]

Despite the predicted stability of $Ru(\eta^5\text{-}C_{60})$, their synthesis turned out to be challenging since the intrinsic 5-π-electron nature of the C_{60}'s 5-membered rings is different from Cp as the formal analog.[36] This restriction could be overcome by Nakamura *et al.* who discovered that organocopper reagents (*in situ* generated from RMgBr/CuBr·SMe_2) selectively add five times to the [6,6]-bond of the five 6-membered rings that surround a 5-membered ring (Scheme 2).[37]

On this basis, the authors were able to synthesize a variety of pentaalkyl- and pentaaryl-monohydro-[60]fullerenes with the formula $C_{60}R_5H$.[38–40] In these derivatives, the 5-membered ring could be deprotonated and act as a Cp-type ligand to build pentahapto-coordinated fullerene complexes. The first defined example for a $Ru(\eta^5\text{-}C_{60})$ compound was reported in 2003 by Matsuo *et al.* and started from $C_{60}Me_5K$, which was obtained by deprotonation of $C_{60}Me_5H$ with potassium *tert*-butoxide (Scheme 2).[41] The reaction of $C_{60}Me_5K$ with 0.5 eq. of $[RuCl_2(CO)_3]_2$ in THF at room temperature afforded $[Ru(CO)_2Cl(\eta^5\text{-}C_{60}Me_5)]$ (**12**) in high yields. The X-ray single crystal structure of **12** confirmed the pentahapticity of the C_{60} ligand (Fig. 8, left). Matsuo *et al.* later used different $\eta^5\text{-}C_{60}(CH_2SiMe_2R)_5$ ligands (R = Me, Et, *n*-Bu, *n*-hex) to produce $[Ru(CO)_2Cl(\eta^5\text{-}C_{60}(CH_2SiMe_2R)_5)]$ complexes with improved solubility.[42] Noteworthy, the reaction of $C_{60}Me_5H$ with the $Ru_3(CO)_{12}$ cluster did not afford any $Ru(\eta^5\text{-}C_{60})$ complexes, instead the dihapto complex $[Ru_3(CO)_9(\mu_3\text{–}\eta^2, \eta^2, \eta^2\text{-}C_{60}Me_5H)]$ (**13**) was formed (Fig. 8, right).[43] The structure of **13** is similar to that of **6** with the face-capped $[Ru_3(CO)_9]$ cluster being positioned in *trans*-position to the methyl groups.

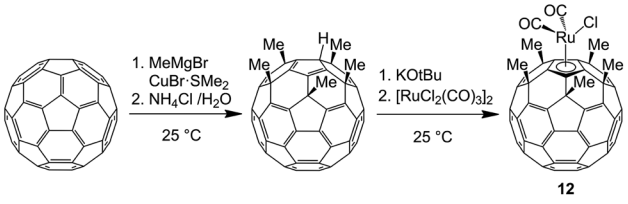

Scheme 2 Schematic representation of the synthesis of **12**.

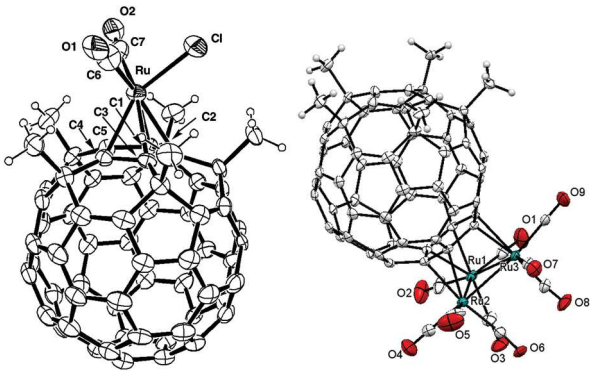

Fig. 8 Representation of the X-ray single crystal structures of **12** (left) and **13** (right). Figure reprinted and reproduced with permission from ref. 41 and 43, copyright 2003 American Chemical Society and 2014 Elsevier B.V., respectively.

In general, the η^5-complexes exhibit an enhanced stability compared to their mononuclear $Ru(\eta^2\text{-}C_{60})$ analogs. A variety of chemical transformations can be carried out on the complex that involve CO or Cl^- subtraction without losing the fullerene moiety (Scheme 3). In detail, the thermal treatment of **12** with organophosphines (*i.e.*, PEt_3 (**14**) or PPh_3 (**15**)) or organoisocyanides (*i.e.*, methyl isocyanide (MeNC) (**16**), *tert*-butyl isocyanide (^{t}BuNC) (**17**) or 2,6-xylyl isocyanide (XylNC) (**18**)) resulted in a mono-CO-exchange reaction.[41] Utilizing an excess of ^{t}BuNC (**22**) or XylNC (**23**) allowed a second CO-exchange reaction, while the more bulky PPh_3 did not show any subsequent exchange of CO. This behavior is due to the pronounced σ-donating character in combination with the small steric hindrance of the linear isocyanides. Moreover, the reaction of dppm, 1,1′-bis(diphenylphosphino)ferrocene (dppf) or bis(diphenylphosphino)butane (dppb) with **12** afforded only products with a monodentate binding of the in principle bidentate ligands (Scheme 3).[44] The monodentate coordination of dppm (**19**) and dppf (**20**) can be rationalized by their rigidity that causes congestion by the bidentate coordination with the bulky $RuCl(\eta^5\text{-}C_{60}Me_5)$ moiety. Also in the case of the more flexible dppb ligand (**21**), the large bite angle for a bidentate coordination requires a lot of space and is, thus, incompatibility with the sterically demanding pentamethyl[60]fullerene ligand. Bidentate coordination of phosphine ligands was achieved only with 1,2-bis(diphenylphosphino)ethane (dppe) (**24**) and its chiral congener (*R*)-1,2-bis(diphenylphosphino)propane ((*R*)-prophos) (**25**) in 47 and 41% yield, respectively (Scheme 3).[45,46] These particular ligands have an appropriate size and fit into the cavity of the $RuCl(\eta^5\text{-}C_{60}Me_5)$ moiety (Fig. 9).

The chiral (*R*)-prophos ligand afford the 1,3-chiral product **25** in almost diastereomeric purity (de ≈ 100%), because of the sterically demanding pentamethyl[60]fullerene ligand. The stereochemistry of **25** was retained upon subtraction of the chloride by $AgSbF_6$ that *in situ* formed the cationic complex **26**. Subsequent reaction of **26** with neutral ligands (*e.g.*, cyanides (**27**), methacrolein (**28**), acetone (**29**), isocyanides (**30**) or

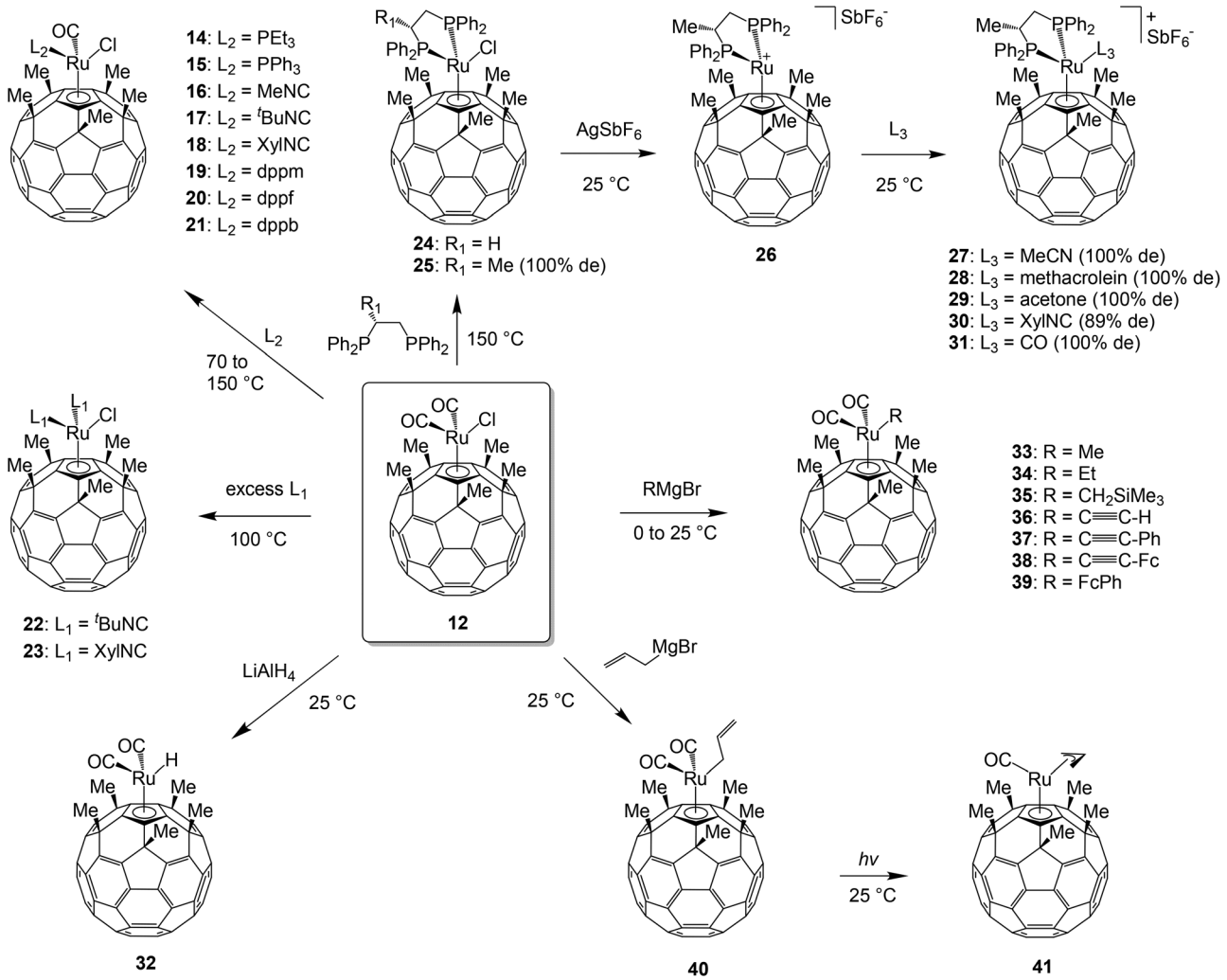

Scheme 3 Schematic representation of the Ru(η^5-C_{60}) complex **12** and the transformation into derivatives **14**–**41**.

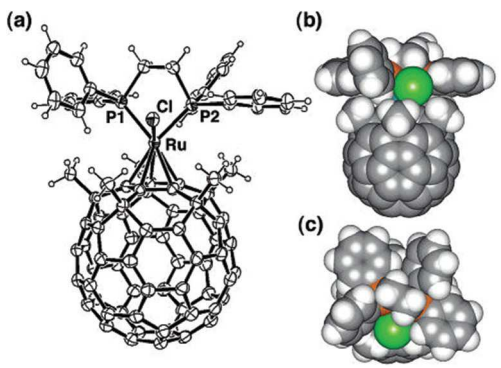

Fig. 9 Representation of the X-ray single crystal structure of **24** (a) and of the corresponding space-filling model with side (b) and top view (c). Figure reprinted with permission from ref. 45, copyright 2006 American Chemical Society.

CO (**31**)) yielded an excess of one diastereomer with de-values ranging from 84 to 100% (Scheme 3).[45] From these, complex **28** was used as catalyst in the Diels–Alder reaction of methacrolein with cyclopentadiene: the *exo* : *endo* ratio could be increased from 5.5 : 1 to 23 : 1 using 5 mol% of **28**, the enantioselectivity of the reaction was slightly improved from 0% to 20%. The enhanced *exo* : *endo* selectivity was attributed to the bulky pentamethyl[60]fullerene ligand, while the still poor enantioselectivity might be due to the rather improper chiral environment.

The chloride ligand of **12** can be removed selectively by lithium aluminum hydride ($LiAlH_4$) at room temperature to afford the corresponding hydrido complex **32** (Scheme 3).[47] Its catalytic activity in the isomerization reaction of alkenes was tested: with 0.01 mol% of **32** at 140 °C, a high conversion (95%) of 1-decene was observed yielding a mixture of 2-decene (49%) and other internal alkenes (46%). However, a high temperature was required to generate the catalytically active monocarbonyl species of **32**.

Exchange of the chloride ligand could also be achieved by a nucleophilic attack of Grignard reagents. The reaction of equimolar amounts of RMgBr with **12** at 0 °C in THF or toluene afforded alkyl substituted [Ru(R)(CO)$_2$(η^5-C$_{60}$Me$_5$)] (**33**: R = Me, **34**: R = Et, **35**: R = CH$_2$SiMe$_3$) as orange solids (Scheme 3).[41,47] A similar approach with alkynyl Grignard reagents at 25 °C in THF generated [Ru(CO)$_2$(C≡C–R)(η^5-C$_{60}$Me$_5$)] (**36**: R = H, **37**: R = Ph, **38**: R = Fc) (Fc = ferrocene) in high yields (*i.e.*, 87 to 93%).[41,48] So far, there is only one example reported for an analogous arylation reaction: the Grignard reaction of FcPhMgBr (FcPh = 4-ferrocenylphenyl) with **12** at 25 °C in THF yielded compound **39** (Scheme 3). Photoirradiation of the Fc-containing complexes **38** and **39** led to a light-induced charge separation, as evidenced by the formation of the Fc radical cation and the C$_{60}$ radical anion; charge-separation lifetimes of 152 ps and 355 ps were observed in THF for **38** and **39**, respectively.[48] These rather short lifetimes were attributed to a fast subsequent recombination reaction along with the population of the triplet excited state of C$_{60}$ (^{3}C$_{60}$*). This spin-forbidden intersystem crossing (ISC) process was accelerated by spin–orbit coupling induced by the heavy ruthenium atom. The reaction of allylmagnesium bromide with **12** at room temperature gave the η^1-allyl substituted complex [Ru(η^1-allyl)(CO)$_2$(η^5-C$_{60}$Me$_5$)] (**40**) in 99% yield (Scheme 3).[47] Irradiation with visible light at room temperature converted **40** under mono-decarbonylation within 14 h into the η^3-allyl complex [Ru(η^3-allyl)(CO)(η^5-C$_{60}$Me$_5$)] (**41**). The light irradiation was necessary to reach a high conversion; in comparison, thermal treatment of **40** at 110 °C proceeded slowly with only 10% conversion after 24 h. Noteworthy, the reaction exclusively yielded the *exo*-isomer, which was again attributed to the steric demanding pentamethyl[60]fullerene ligand.

2.4. Bucky ruthenocenes

Over 50 years after the discovery of ruthenocene by Wilkinson,[49] the first fullerene containing ruthenocene was accomplished in 2004 by Matsuo *et al.*[36,50] These so-called "bucky ruthenocenes" are organometallic sandwich complexes of ruthenium(II) with a η^5-Cp ligand and a η^5-C$_{60}$R$_5$ ligand coordinated to the metal center. The first approach to form such a system utilized complex **12** that was reacted with sodium cyclopentadienide (NaCp) at room temperature in THF to yield the unstable σ-complex [Ru(η^1-Cp)(CO)$_2$(η^5-C$_{60}$Me$_5$)] in 90% yield (**42**, Scheme 4). Heating to 90 °C led to decarbonylation of **42** along with a conversion of the η^1-coordinated Cp ligand to the final η^5-complex [Ru(η^5-Cp)(η^5-C$_{60}$Me$_5$)] (**43**) in 12% yield.

The electrochemistry of the sandwich complex **43** was studied and revealed the fullerene based reductions with half-wave potentials at −1.43 V and −2.01 V *vs.* ferrocenium/ferrocene (Fc$^+$/Fc) in THF.[51] However, it remained unclear if the ruthenocene oxidation is irreversible. A chemical reduction of **43** was carried out and the vis-NIR spectral changes were monitored: treatment of **43** with 9 eq. of potassium metal in THF resulted after 3 h in a color change from orange to a dark red; the absorption spectra indicated a broadening of the

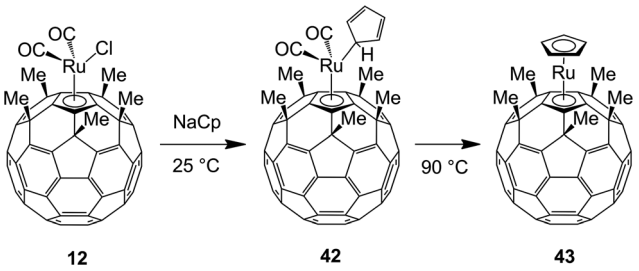

Scheme 4 Schematic representation of the synthesis of the bucky ruthenocene **43**.

spectra along with maxima at 592, 792, 1010 and 1174 nm, being assigned to the radical anion **43**$^{\bullet-}$ (Fig. 10).[52] Stirring for further 3 h resulted in another color change to green with more defined absorption maxima at 544 and 684 nm – the thusly formed species was identified as the **43**$^{2-}$ dianion.

The reactivity of bucky ruthenocene **43** was tested at the example of Friedel–Crafts acylation reactions.[53] Acetyl (**44**) and benzoyl (**45**) groups were introduced on the Cp ligand in 82% and 65% yield, respectively (Scheme 5). The acylation reaction was performed at room temperature in carbon disulfide with the corresponding acid chloride and AlCl$_3$. Acetylation caused a small distortion between the C$_{60}$Me$_5$ and Cp ligand planes in

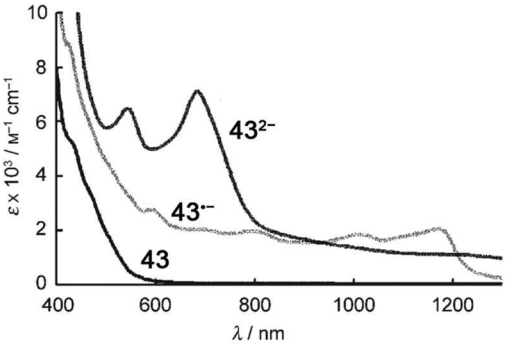

Fig. 10 Vis-NIR absorption spectra of **43** and of the singly (**43**$^{\bullet-}$) and doubly reduced species (**43**$^{2-}$) in THF. Figure adapted with permission from ref. 51, copyright 2007 Wiley-VCH.

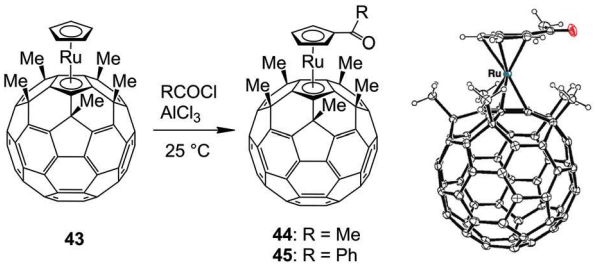

Scheme 5 Schematic representation of the Friedel–Crafts acylation of bucky ruthenocene **43**. A representation of the X-ray single-crystal structures of **44** is also shown. Figure reprinted with permission from ref. 53, copyright 2014 The Royal Chemical Society.

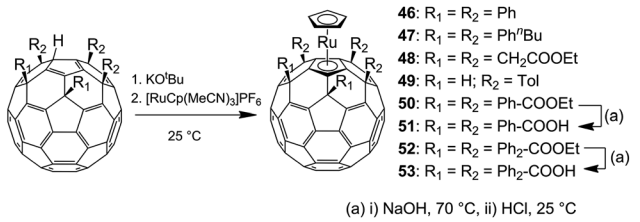

Scheme 6 Schematic representation of the synthesis of bucky ruthenocene **46–53**.

44 (Scheme 5, right) and was owed by the sterical hindrance of the methyl groups (distortion is not observed in the related, less hindered [Ru(η^5-Cp-Ac)(η^5-Cp)] complex). In subsequent reactions, compound **44** was reduced with $BH_3{\cdot}SMe_2$ to the corresponding alcohol [Ru(η^5-Cp-CH(OH)Me)(η^5-$C_{60}Me_5$)] and further modified with acetic anhydride to obtain the acetate [Ru(η^5-Cp-CH(OAc)Me)(η^5-$C_{60}Me_5$)].[53]

In 2006 an alternative route for the synthesis of bucky ruthenocenes was reported by Matsuo and Nakamura *et al.*[54] Here, $C_{60}Ph_5H$ was deprotonated with potassium *tert*-butoxide and subsequently reacted with a slight excess of [Ru(η^5-Cp)(MeCN)$_3$](PF_6) at room temperature (Scheme 6). Under these conditions, [Ru(η^5-Cp)(η^5-$C_{60}Ph_5$)] (**46**) was obtained in 60% yield, thus representing a vast increase compared to the first approach. The X-ray single crystal structure of **46** is depicted in Fig. 11 and proofs the formation of the sandwich complex. The ruthenium(II) center and the Cp ligand are shielded by the surrounding phenyl moieties of the pentaphenyl[60]fullerene ligand; an increased stability compared to **43** was proposed. It was reported that the analogous bucky ferrocene compound [Fe(η^5-Cp)(η^5-$C_{60}Ph_5$)] did not react under the above-mentioned Friedel–Crafts acylation conditions.[53]

The bucky ruthenocenes **43** and **46**, as well as the metal-free ligands $C_{60}Me_5H$ and $C_{60}Ph_5H$ were analyzed by steady-state and time-resolved spectroscopy. The ruthenocenes exhibit a reduced C_{60}-based fluorescence quantum yield ($\varphi_{F,C60}$) and a decreased lifetime ($\tau_{F,C60}$) compared to the free ligands in toluene. In fact, compound **43** has an eight times lower, and **46** a five-time lower $\varphi_{F,C60}$ value, compared to the corresponding values of the ligands. The $\tau_{F,C60}$ values in **43** and **46** are roughly decreased by 330 ps to 275 and 220 ps, respectively. Transient absorption (TA) spectroscopy confirmed the fast decay of the singlet state along with an efficient population (>92%) of the lower-lying $^3C_{60}$* states.

Thermal treatment of **43** and **46** up to 900 °C resulted first in the degradation of the bucky ruthenocenes into smaller hydrocarbons and, finally, in the formation of ruthenium nanoparticles deposited in a carbonaceous material.[55] Furthermore, the bucky ruthenocenes absorbed on silica and heated to 500 °C featured a catalytic activity in the hydrogenation of cyclohexene.[55] This catalytic ability of the ruthenium center has also been shown by TEM imaging for the transformation of the C_{60}-based compound **43** into free C_{70} under a certain electron dose.[56] There are a few other bucky ruthenocenes reported by the Nakamura group; they were all synthesized by the second approach (Scheme 6). Compound **47** was obtained in 49% yield and comprised a penta(1-phenylbutane)-C_{60} unit. The complex has been used as acceptor material with poly(3-hexylthiophene) (P3HT) as donor material in bulk-heterojunction organic solar cells (BHJ).[57] A short-circuit current density (J_{SC}) of 2.1 mA cm^{-2} and a photocurrent conversion efficiency of 0.4% was achieved. The modest values were attributed to the crystallinity of **47** and a homogenous morphology of the active layer – contrary to the typical phase separation in PCBM:P3HT BHJ solar cells (PCBM = phenyl-C61-butyric acid methyl ester) (Fig. 12).

Several other methods for the addition of nucleophilic reagents on the C_{60} surface were applied to prepare pentafunctionalized C_{60} ligands. The bucky ruthenocene **48** was synthesized by the second approach in 22% yield and contains a penta(ethylacetate)-C_{60} unit.[58] The synthesis of the corresponding C_{60}(ethylacetate)$_5$H ligand was achieved by a regioselective reaction with Reformatsky-type reagents in very high yields. Complex **49** was prepared in 11% yield and featured a less symmetric hydroarylated C_{60} moiety (*i.e.*, C_{60}(tolyl)$_3H_2$). The free ligand, *i.e.*, C_{60}(tolyl)$_3H_3$, was synthesized in toluene by an $AlCl_3$-catalyzed electrophilic fullerenation of three toluene molecules.[59] This reaction was already reported by Olah *et al.* but did not offer sufficiently high product selectivity.[60,61] The bucky ruthenocenes **50** and **52** represent molecular pentapods that consists of a penta(ethylbenzoat)-C_{60} or penta(ethyl [1,1′-biphenyl]-4-carboxylate)-C_{60} unit, respectively (Scheme 6).[62] These complexes were saponified with NaOH

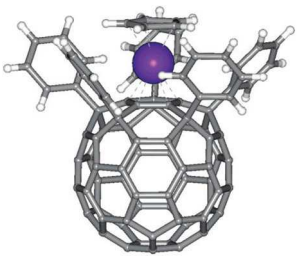

Fig. 11 Representation of the X-ray single-crystal structures of **46**. Figure reprinted with permission from ref. 54, copyright 2006 American Chemical Society.

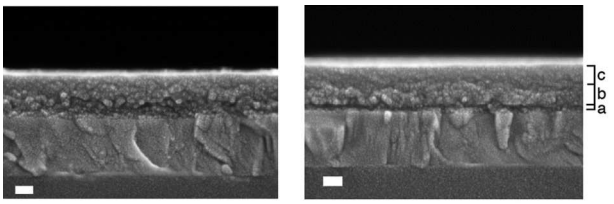

Fig. 12 SEM cross-section images of the active layers (scale bar: 40 nm): P3HT:**47** BHJ (left) and P3HT:PCBM BHJ (right). Layers a, b, and c represent PEDOT:PSS, aggregates ascribed to P3HT, and a rather homogenous substance ascribed to PCBM, respectively. Figure adapted with permission from ref. 57, copyright 2009 The Royal Chemical Society.

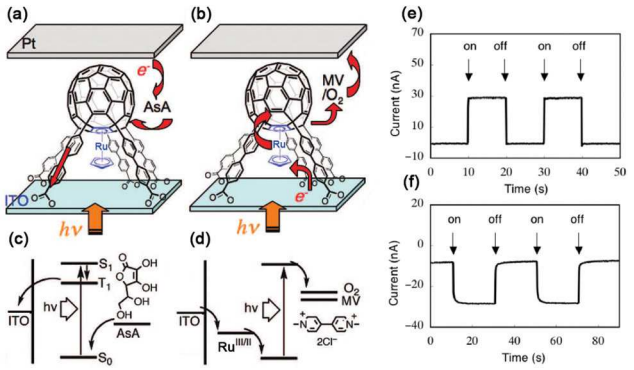

Fig. 13 Schematic representation of the plausible geometric configurations and photocurrent generation for ITO/**53**/AsA/Pt (a) and ITO/**53**/MV/Pt system (b). (c) Representation of the orbital diagrams for anodic and cationic photocurrent generation (c and , respectively). (e) Anodic photocurrent response of ITO/**53**/AsA/Pt. (f) Cathodic photocurrent response of ITO/**53**/MV/Pt after 400 nm irradiation. Figure adapted with permission from ref. 62, copyright 2008 American Chemical Society.

and protonated by HCl to yield the desired complexes **51** and **53** with free carboxylic acid groups. The five carboxylic acid-based legs of the pentapod were anchored onto an indium–tin oxide (ITO) surface to form a self-assembled monolayer (SAM) (Fig. 13).[62] The SAMs were then used as photoactive materials for the preparation of photocurrent-generating devices. The devices were analyzed under two different conditions: the first device contained ascorbic acid (AsA) as sacrificial electron-donor material to generate an anodic photocurrent. In the second approach oxygen/methyl viologen (MV) was utilized as electron acceptor to generate a cathodic photocurrent. In both cases, a photocurrent could be generated with compound **53** by 400 nm light irradiation. This behavior was ascribed to the ability of bucky ruthenocenes to populate excited triplet and charge-separated states. The devices with compound **53** could generate an anodic (with 0.1 V bias) and cathodic (with −0.1 V bias) current with 15% and 10% quantum yield, respectively. Compound **51** gave a higher quantum yield for the anodic current generation, but yielded almost no cathodic current. This behavior was ascribed to a worse stand of the shorter pentapods on the ITO surface. A similar C_{70}-based bucky ruthenocene with the formula $[Ru(\eta^5\text{-Cp})(\eta^5\text{-}C_{70}(Ph_2\text{-COOH})_3)]$ was applied for the same purpose. In this case, the compound had only three legs, thus acting as molecular tripod in the formation of SAMs. The device could also generate an anodic (with 0.1 V bias) and cathodic (with −0.1 V bias) current, but with lower quantum yields of 2.1% and 1.3%, respectively, when compared to **53**.[63]

2.5. Multiple exohedral ruthenium coordination

Multiple addition reactions on non-functionalized fullerene surfaces by ruthenium complexes or, in general, by any group could result in the formation of regioisomers.[64] Hsu *et al.* reported on the multiple addition reaction of the trinuclear $Ru_3(CO)_{12}$ cluster to pristine C_{70}.[25] Under the same reaction conditions applied for the preparation of the mono-adduct **7** (*vide supra*), the excess of $Ru_3(CO)_{12}$ yielded three different bis-adducts.[25] The three isomeric complexes **54a**, **54b** and **54c** could be separated by preparative thin-layer chromatography in an isolated ratio of 2 : 3 : 1. According to IR spectroscopy, no differences in the two CO vibration bands and only a slight difference for a third band at around 2010 cm^{-1} were observed, which indicated similar molecular structures. Single crystals suited for X-ray structure analysis were obtained for **54b** (Fig. 14) and confirmed the nature of the bis-adduct with two triangular face-coordinated $Ru_3(CO)_9$ units.

In order to achieve high product selectivity upon exohedral coordination of multiple ruthenium centers to more than one binding site of the fullerenes, functionalized fullerenes have been used to block certain positions for the coordination or to form cavities in which the ruthenium can smoothly coordinate. Following this strategy, Chen *et al.* recently reported the synthesis of a C_{60}-triruthenium cluster bis-adduct of the formula $[Ru_3(CO)_9]_2\{\mu_3\text{–}\eta^2, \eta^2, \eta^2\text{-}C_{60}[C(COOEt)_2]_4\}$ (**55**).[65] The number of possible bis-adducts was limited by introducing four ethyl malonate groups on the equatorial rings of the C_{60}. Compound **55** featured two sets of three ruthenium centers with the $\mu_3\text{–}\eta^2$, η^2, η^2 binding mode coordinated on the top and bottom pole hexagons of C_{60} (Fig. 15b). Each set of $Ru_3(CO)_9$ cluster is similar to that in compound **6**. The synthesis was performed with the $C_{60}[C(COOC_2H_5)_2]_4$ ligand and 2 eq. of $Ru_3(CO)_{12}$ in refluxing chlorobenzene affording **55** in 21% yield (Fig. 15a) along with 12% of the monoadduct. Compound **55** was obtained as a mixture of two regioisomers that are denoted as the *tilted* (**55a**) and the *parallel* (**55b**) form. It was shown by NMR spectroscopy and HPLC analysis that the isomers slowly interconvert at room temperature, indicating only small energy difference between them.

The bucky ruthenocenes **56**[66] and **57**[67] are regioisomers of a tenfold aryl-functionalized C_{60} (Fig. 16). The structures exhibit two $Ru(\eta^5\text{-Cp})$ units which are coordinated on either the top and bottom pentagons or the top and one of the five side pentagons. These structures were synthesized in a similar approach as shown in Scheme 6 by double coordination of the $Ru(\eta^5\text{-Cp})$ unit on two different pentagons. The different C_{60} ligands are deca-adducts of phenyl or *n*-butyl phenyl groups,

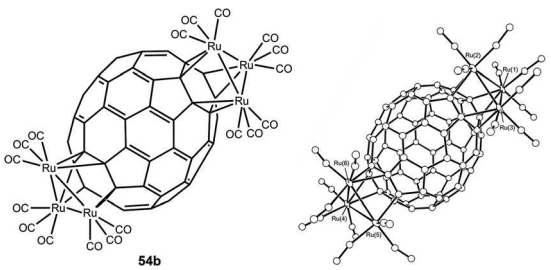

Fig. 14 Schematic representation of the hexanuclear complex **54b**. Representation of the X-ray single-crystal structures of **54b**. Figure reprinted with permission from ref. 25, copyright 1997 The Royal Chemical Society.

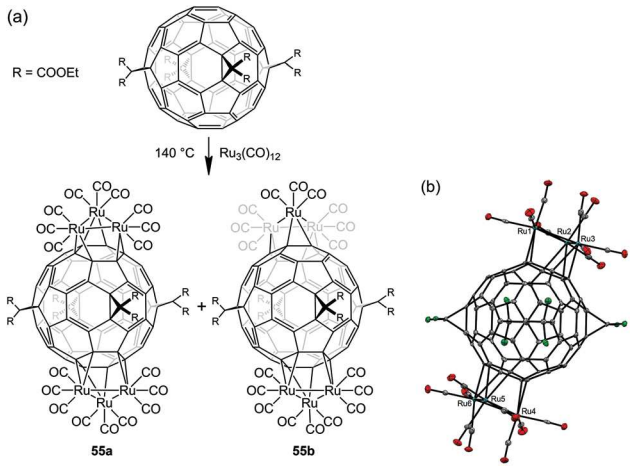

Fig. 15 Schematic representation of the synthesis of **55a** and **55b**. (b) Representation of the X-ray single-crystal structures of **55b** (side view; for clarity, the ethyl formate groups are depicted as green balls). Figure reproduced with permission from ref. 65, copyright 2015 The Royal Chemical Society.

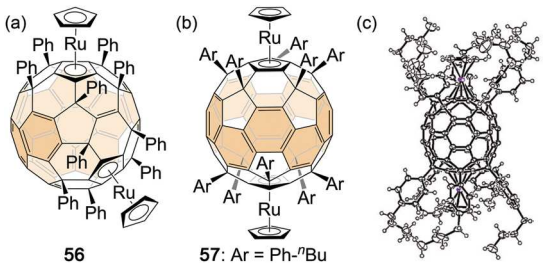

Fig. 16 (a) Schematic representation of **56** (a) and **57** (b); the orange color indicates the remaining conjugated system. (c) Representation of the X-ray single-crystal structures of **57**. Figure reprinted with permission from ref. 67, copyright 2007 Wiley-VCH.

respectively, and could be prepared in a one-pot approach similar to that depicted in Scheme 2. However, simply increasing the amount of CuBr·SMe2 and of the aryl-Grignard reagent up to 30 eq. relative to C_{60} did not yield the desired deca-adducts – only penta-addition was realized in 99% yield. In order to achieve higher degrees of addition, Matsuo *et al.* disclosed that a certain amount of pyridine (*i.e.*, 300 equivalents), as additive, facilitates deca-adducts in high yields.[67] Following this multi-arylation procedure, the two regioisomeric deca-adducts were obtained typically in a 1 : 2 ratio. The ruthenocene **56** featured a reduced conjugated system with 38 π-electrons, representing a dibenzo-fused corannulene motive (colored orange, Fig. 16a). On the other hand, compound **57**, had a total of 40 π-electrons in a hoop-shaped [10]cyclophenacene-type structure (colored orange, Fig. 16b). The different conjugation patterns in the C_{60}-based ligands of **56** and **57** exhibited blue and yellow luminescence, respectively, with moderate quantum yields (φ) up 0.18. However, the emission was fully quenched if the ruthenium is coordinated. Compound **56** could be further functionalized by nucleophilic Grignard reaction under reductive conditions. By this approach two further benzyl groups could be introduced on a central hexagon that yielded two regioisomers by either a 1,2- or 1,4-addition.[66]

The C_{70}-based bucky ruthenocenes were already briefly mentioned above in the preparation of SAMs, but their synthesis will be discussed in the following. There are a few examples known for dinuclear and trinuclear bucky ruthenocene complexes with a C_{70}-based ligand.[68] As shown in the multi-arylation of C_{60}, the copper-mediated nucleophilic addition is retarded after a certain number of additions, if no pyridine is used. In the case of C_{70}, threefold addition of aryl-Grignard reagents could be observed. However, the tris-adduct of C_{70} did not allow any further additions like in C_{60}, due to the inert equator area and formation of a stable π-indenyl substructure.[69] As in C_{60}, a higher degree of arylation of C_{70} could be reached by the usage of a certain amount of pyridine. Matsuo *et al.* followed this route and regioselectively synthesized hexakis-adducts with two sets of three aryl substitutents on the top and bottom area of C_{70} (Scheme 7).[68] Subsequent deprotonation with potassium *tert*-butoxide and ruthenium coordination with $[Ru(\eta^5\text{-Cp})(MeCN)_3](PF_6)$ afforded the dinuclear complex **58** in 95% yield.[68] Thereby, coordination occurred in a η^5-fashion on the pentagon ring, which is surrounded by the three aryl substituents. Moreover, a trinuclear complex was synthesized by first introducing an additional aryl substituent on **58** applying the same multi-arylation procedure used before. The reaction was carried out at elevated temperatures with an excess of the organocopper reagent, but stops after mono-addition of the aryl unit; the hepta-arylated, dinuclear complex **59** was obtained in 86% yield. Subsequently, the known ruthenium coordination procedure was applied to introduce a third $Ru(\eta^5\text{-Cp})$ unit: the coordination occurred selectively on the pentagon ring neighboring the newly attached aryl substituent; the trinuclear

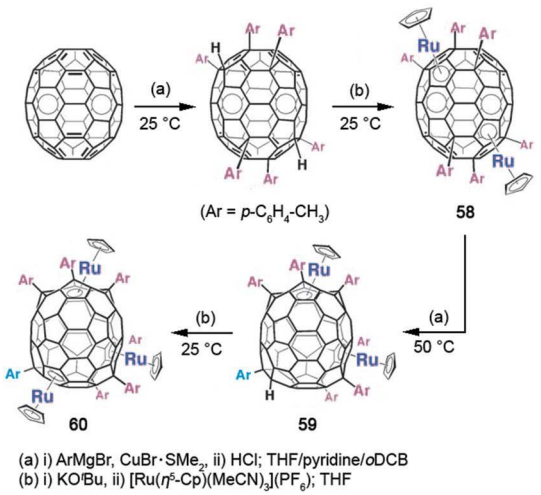

Scheme 7 Schematic representation of the synthesis of the C_{70}-based bucky ruthenocenes **58–60**. Figure adapted with permission from ref. 68, copyright 2009 Wiley-VCH.

ruthenocene complex **60** was obtained in 53% yield. The dinuclear complex **58** was electrochemically analyzed and features two well-separated one-electron processes ($E_{1/2}$ = 0.54 V and $E_{1/2}$ = 0.88 V *vs.* Fc^+/Fc in CH_2Cl_2). These processes were assigned to as oxidations of the two ruthenocenes units and were of quasi-reversibility nature. In contrast, this oxidation is irreversible for pristine ruthenocene [$Ru(\eta^5\text{-}Cp)_2$] clearly showing the influence of the fullerene moiety.[32] Moreover, the large potential difference of 340 mV indicated a metal–metal interaction, which was ascribed to as a direct HOMO conjugation of the two metal centers. Two reversible one-electron reduction processes were observed at $E_{1/2}$ = −1.5 V and $E_{1/2}$ = −2.06 V. These C_{70}-based reduction waves were cathodically shifted by *ca.* 0.6 V compared to the non-functionalized C_{70}. The reason for this can be found in the lower degree of conjugation, making **58** a weaker electron-accepting system than C_{70}.

2.6. Open-cage fullerenes

The modification of the fullerene σ framework by ring opening reactions results in open-cage fullerenes, in which one or more C–C bonds are chemically cleaved, and orifices in the spherical shell are formed. These compounds are often used as a starting material for the encapsulation of small molecules and have become an alternative for the preparation of endohedral fullerenes.[70,71] In this section, the reactivity of an open-cage fullerene with $Ru_3(CO)_{12}$ will be discussed. Murata *et al.* synthesized the aza-open-cage fullerene **61** by the reaction of a 1,2,4-triazine derivate with C_{60} in *o*DCB at 180 °C.[72] The oxidative cleavage of one double bond in **61** with singlet oxygen afforded two regioisomers (**62a** and **62b**, Scheme 8).[72] By this approach a ring-enlargement from an 8-membered-ring to a 12-membered-ring orifice in the fullerene-derivate takes place.

Chen *et al.* analysed the reactivity of the two azadioxo-open-cage fullerenes **62a** and **62b** with equimolar amounts of $Ru_3(CO)_{12}$ in refluxing chlorobenzene for 30 to 60 min, respectively.[73] First, the treatment with **62a** afforded the trinuclear complex **63** in 24% yield (Fig. 17). Here, the C–C bond between the two ketones is re-established and yields a vicinal diol along with ring-decrease to an 8-membered-ring orifice, like in **61**. Two of the three ruthenium-centers are directly coordinated to the open-cage fullerene *via* the hydroxyl groups, the imine group and one [6,6]-bond in a η^2-fashion. Each ruthenium

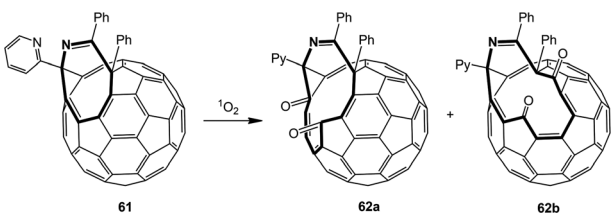

Scheme 8 Schematic representation of the synthesis of the open-cage fullerenes **61**, **62a** and **62b**. The bold lines represent the orifice size of the fullerene-derivatives.

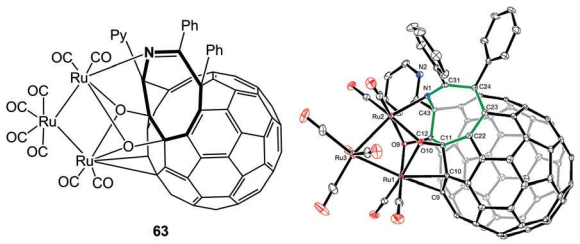

Fig. 17 Schematic representation of the trinuclear complex **63**. The bold line represents the 8-membered-ring orifice. A representation of the X-ray single-crystal structure of **63** is also shown. Figure reprinted with permission from ref. 73, copyright 2014 Wiley-VCH.

center features distorted octahedral geometries with two or four terminal carbonyl ligands, respectively.

Compound **63** is stable for several hours when heating in chlorobenzene at reflux. However, a defined thermal transformation of **63** was observed by heating the neat material at 350 °C in vacuum; this pyrolysis results in the formation of **64** (40% isolated yield, Fig. 18).[73] During this reaction a cleavage of one ruthenium atom, five terminal carbonyl ligands and the diooxyl group was observed, which resulted in a larger 11-membered-ring orifice. The remaining two ruthenium atoms rearrange and adopt several new ligands. One ruthenium atom features a distorted octahedral geometry, with a Ru–Ru-bond, an *ortho*-metalated phenyl substituent, an amine group, a pyridine substituent and two terminal carbonyls as ligands. The other ruthenium atom adopts a four-legged piano-stool-type geometry, with a ruthenium-azacyclopentadienyl ring as seat that binds in a η^5-fashion. The four legs are comprised of a terminal hydrid atom, a terminal carbonyl ligand, and two η^1-coordinated carbon centers of the fullerene.

A different coordination behavior is observed for the reaction of $Ru_3(CO)_{12}$ with the second regioisomer **62b**. Here, the mononuclear complex **65** is generated in 46% isolated yield after refluxing in chlorobenzene, followed by an extraction of the crude solid with pyridine (Fig. 19).[73] The $Ru_3(CO)_{12}$ cluster fragmented into a single ruthenium center and adopts a distorted octahedron with bindings to a ketone, two pyridines, a terminal carbonyl and two η^1-coordinated carbons of the full-

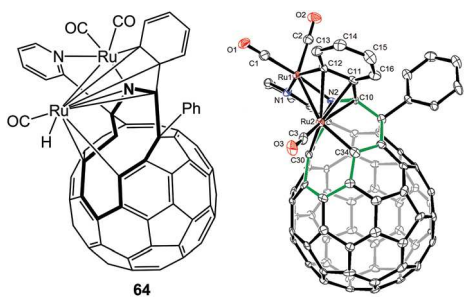

Fig. 18 Schematic representation of the dinuclear complex **64**. The bold line represents the 11-membered-ring orifice. A representation of the X-ray single-crystal structure of **64** is also shown. Figure reprinted with permission from ref. 73, copyright 2014 Wiley-VCH.

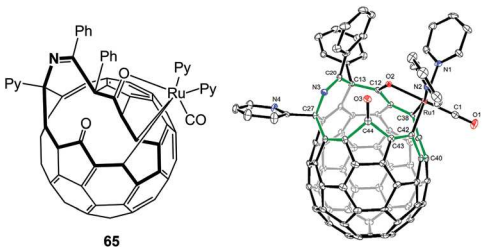

Fig. 19 Schematic representation of the mononuclear complex **65**. The bold line represents the 15-membered-ring orifice. A representation of the X-ray single-crystal structure of **65** is also shown. Figure reprinted with permission from ref. 73, copyright 2014 Wiley-VCH.

erene. During the reaction a ring-enlargement to a 15-membered-ring occurs. Consequently, the open-cage fullerene exhibits an expanded orifice which is close to the diameter of C_{60} (*i.e.*, the largest distance between two carbons of the orifice is 6.6 Å).

3. Covalently attached ruthenium complexes

This section provides an overview about ruthenium complexes with N-donor-type ligands that are attached covalently to the C_{60} moiety. To the best of our knowledge, there are no examples reported so far utilizing C_{70} or higher fullerenes for the same purpose. Some of the compounds exhibit a bridging unit between the Ru complex and the C_{60} to enlarge the distance between the moieties. These bridges can consist of either aliphatic or aromatic spacer units (Sp). The Ru–Sp–C_{60} systems are categorized on the basis of two criteria: nature of the spacer unit and denticity of the ligands. In particular, ruthenium-polypyridyl complexes, such as tris(bipyridine)s, bis(terpyridine)s, or ruthenium-mono(phorpyrine)s, are discussed in literature.

3.1. Bidentate and tridentate coordination in Ru–Sp–C_{60} systems

The bidentate binding of 2,2′-bipyridine (bpy) to transition metal ions is, by far, the most common motive to be found in Ru–Sp–C_{60} assemblies. Basically, there are three synthetic approaches used for the preparation of such complexes (Scheme 9): the first approach starts from a bpy derivative bearing a bridging unit in 3 or 4 position (**1A**) (route 1). The bridge itself contains a reactive group (R) suited for the functionalization of fullerenes. The reaction with one double bond of the C_{60} yields a bpy–Sp–C_{60} conjugate (**1/2B**) with various functionalities (F) on the fullerene surface. In this respect, the aldehyde group represents one of the most commonly utilized functionality that is reacted with an α-amino acid (*e.g.*, *N*-methyl glycine) to *in situ* generate an azomethine ylide. The subsequent cycloaddition reaction with a [6,6]-bond of C_{60} gives a pyrrolidino[60]fullerene with the bpy–Sp unit in 2-position of the pyrrolidine ring.[74–76] Commonly, this type of fullerene functionalization is referred to as the Prato reaction. By inverting the substituents on the reagents, *i.e.*, employing formaldehyde and a *N*-substituted α-amino acid, the synthesis leads to analogous *N*-substituted pyrrolidines.[77] Another prominent example for functionalized C_{60} (F-C_{60}) is the methano [60]fullerene. Such compounds feature a 1,1-disubstituted cyclopropane ring attached on the fullerene surface. The synthesis is often accomplished by the reaction of the α-carbon of malonic acid derivatives or diazo compounds with a [6,6]-double bond of C_{60} under basic conditions.[78,79] The subsequent metal coordination of these "bucky ligands" to the Ru(II) center is accomplished by the reaction of **1/2B** with the *cis*-$[Ru(bpy)_2Cl_2]$ precursor complex in refluxing ethanol,[80] 1,2-dichloroethane (DCE),[75,76,81] DMF[78,82] or solvents mixtures with toluene[74] or *o*DCB[77] to increase the solubility of the bpy–Sp–C_{60} ligand. Coordination under significantly milder conditions can be achieved by activation of the precursor complex with silver salts in acetone to substitute the chlorides by weakly bound acetone molecules.[83] For route 1 an alternative approach is also possible: switching the order of the reaction steps, *i.e.*, performing at first the ruthenium coordination and

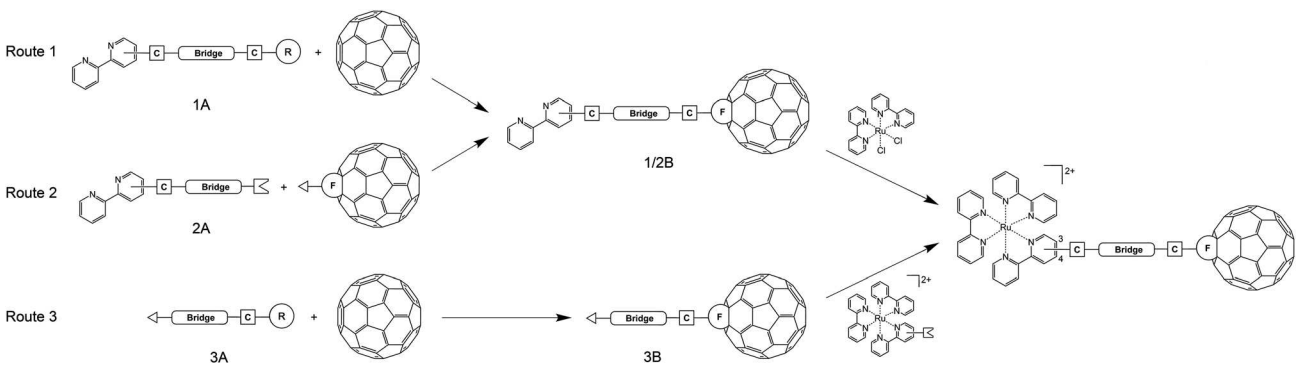

Scheme 9 Schematic representation of three synthetic routes towards Ru–Sp–C_{60} systems with bipyridine as metal-binding unit. The counterions are omitted.

subsequently the C_{60}-functionalization. However, this protocol has not yet been reported as an efficient method, due to the poor solubility of ruthenium complexes in nonpolar solvents used for the C_{60}-functionalization, *i.e.* toluene, chlorobenzene or *o*DCB.[83]

The second route appears to be similar to the first one, but starts from C_{60} that has been pre-functionalized with a reactive group (route 2). The following reaction with an appropriate bpy derivative that contains the bridging unit (**2A**) establishes a connection (C) between the bpy–Sp unit and the F-C_{60} to afford the bpy–Sp–C_{60} ligand (**1/2B**). This approach has, for example, been used by Armaroli *et al.*[82] in an esterification reaction of a carboxylic acid containing methano[60]fullerene with a hydroxy functionalized bpy. The final step in this sequence is the above-mentioned ruthenium coordination.

Finally, for the third approach, the synthetic route starts with the functionalization of C_{60}, as already in route 1. The corresponding reagent (**3A**) comprises the bridge, bearing a reactive group for fullerene functionalization and another reactive group used for the coupling with a ruthenium complex in the second step (route 3). Subsequently, the formed F-C_{60} (**3B**) is reacted with an appropriate $[Ru(bpy)_2(X\text{-}bpy)]^{2+}$ complex to afford the Ru–Sp–C_{60} complex. For example, Chaignon *et al.*[84] used the 3-bromo-bpy containing complex $[Ru(bpy)_2(3\text{-}Br\text{-}bpy)]^{2+}$ and various terminal alkyne-functionalized pyrrolidino [60]fullerenes in a palladium(0)-catalyzed cross-coupling reaction. In general, the three routes outlined in Scheme 9 can similarly be applied for attaching bis(terpyridine) ruthenium complexes to C_{60}. Here, the reported complexes are exclusively connected to the bridge in the 4′-position of the central pyridine ring in the terpyridine (tpy) scaffold. The reason for this particular pattern is rationalized by the facile synthetic accessibility of the 4′-substituted tpy. These two types of ruthenium(II) complexes are often discussed in the context of photo-induced intramolecular energy- and/or electron-transfer processes in which the $[Ru(bpy)_3]^{2+}$ or $[Ru(tpy)_2]^{2+}$ complex serves as photosensitizer as well as electron donor and the C_{60} as electron acceptor.

The photophysical and electrochemical properties of $[Ru(bpy)_3]^{2+}$ and $[Ru(tpy)_2]^{2+}$ complexes have thoroughly been analysed in literature.[13,14] Such complexes exhibit a broad absorption in the visible region arising from intense metal-to-ligand charge-transfer (MLCT) transitions and are weakly emitting. The most striking photophysical difference between $[Ru(bpy)_3]^{2+}$ and $[Ru(tpy)_2]^{2+}$ can be observed in their excited-state properties: at room temperature, $[Ru(bpy)_2]^{2+}$ complexes exhibit a significantly longer triplet excited-state (^{3}MLCT) lifetime by around three orders of magnitude compared to similar $[Ru(tpy)_2]^{2+}$ complexes. This behavior also impacts on the emission quantum yields of the complexes. One reason for the reduced lifetime of $[Ru(tpy)_2]^{2+}$ is the lower lying metal-centred triplet state (^{3}MC). Hence, population of this state becomes more likely and increases the non-radiative decay back to the ground state. However, a long-lived excited state is often required to guarantee subsequent photodynamic processes in the excited state. Therefore, $[Ru(bpy)_3]^{2+}$ is basically the more promising candidate to gain efficient charge-transfer towards fullerene. Disadvantageously, these complexes suffer from the formation of Λ-/Δ-isomers upon further substitution of the bpy ligands. On the other hand, $[Ru(tpy)_2]^{2+}$ complexes will be formed free of isomers and, if the competing energy-/electron-transfer processes are fast enough, the limitation by the intrinsic low excited-state lifetime can be circumvented. In general, in any Ru–Sp–C_{60} triad there are several photodynamic processes plausible following the photo-excitation of the ruthenium center (^{3}Ru*).

$$^3Ru^*\text{–Sp–}C_{60} \rightarrow {}^+Ru\text{–Sp–}C_{60}^{\bullet-} \rightarrow Ru\text{–Sp–}C_{60} \quad (1)$$

$$^3Ru^*\text{–Sp–}C_{60} \rightarrow {}^+Ru\text{–Sp–}C_{60}^{\bullet-} \rightarrow Ru\text{–Sp–}{}^3C_{60}^* \quad (2)$$

$$^3Ru^*\text{–Sp–}C_{60} \rightarrow Ru\text{–Sp–}{}^3C_{60}^* \quad (3)$$

$$^3Ru^*\text{–Sp–}C_{60} \rightarrow Ru\text{–}{}^3Sp^*\text{–}C_{60} \rightarrow Ru\text{–Sp–}{}^3C_{60}^* \quad (4)$$

In the first case, the formation of a charge-separated state (CSS) by an electron-transfer process is proposed. The nature of this state consists of the oxidized Ru(III) center ($^+$Ru) and the reduced C_{60} radical anion ($C_{60}^{\bullet-}$). A subsequent back-electron transfer results in the reformation of the ground-state (eqn (1)). However, if the energy of the CSS (E_{CSS}) is higher than the $^3C_{60}$* energy, an exergonic recombination towards this state is possible (eqn (2)). Another possible mechanism describes the direct triplet–triplet energy transfer from the Ru(II) center towards the C_{60} (eqn (3)). Förster-type energy transfer is usually excluded because of the negligible spectral overlap of the $[Ru(bpy)_3]^{2+}$/$[Ru(tpy)_2]^{2+}$ emission with the C_{60} absorption. For conjugated bridges, often a Dexter-type energy transfer is discussed to describe the rate constants. In short, this electron-exchange process requires an orbital overlap and the rate constants exponentially decrease with increasing donor–acceptor distance. This is the case for "innocent" bridges that do not interfere with the excited states of the ruthenium or C_{60}. For π-conjugated bridges with an increasing number of conjugated units, this does often not hold true. These bridges exhibit low-lying ^{3}π–π* transitions that can also be populated from the ^{3}MLCT state; subsequent energy transfer towards the $^3C_{60}$* state concludes this step-wise, so called "hopping" mechanism (eqn (4)).

Table 1 provides an overview of the reported Ru–Sp–C_{60} assemblies with bpy or tpy as metal-binding units. Moreover, for some of the complexes time-resolved emission spectroscopy or transient-absorption (TA) spectroscopy was applied to analyze the excited-state kinetics. For a Ru–Sp–C_{60} triad, the decreased lifetime of the ^{3}MLCT state in comparison to that of the corresponding fullerene-free reference complexes is often used to quantify the electron/energy transfer from the ruthenium complex to the C_{60} unit. Zhou *et al.* reported a Ru–Sp–C_{60} system without any bridge.[77] The complex **66** exhibited a reduced relative emission intensity *vs.* $[Ru(bpy)_3]^{2+}$ in concert with a reduced emission lifetime from 565 ns to 0.31 ns for $[Ru(bpy)_3]^{2+}$ and **66**, respectively. TA spectroscopy indicated the decay of the ^{3}MLCT state within 0.27 ns along with the for-

Table 1 Overview over Ru–Sp–C_{60} assemblies with bipyridine or terpyridine as the metal-binding unit

Entry	Ru(bpy/tpy) unit[a]	C-bridge-C[b]	C_{60} functionality (F)[c]	Route[d]	τ_{MLCT}[e]	Ref.
66	$[Ru(bpy)_2$(**4-C-bpy**)$](PF_6)_2$	—		1	270 ps[f] (MeCN)	77
67	$[Ru(tpy)$(**4′-C-tpy**)$](PF_6)_2$	—		1	—	77
68	$Ru(bpy)_2$(**4-C-4′-Me-bpy**)$(PF_6)_2$	—		1	7 ps[f] (MeCN)	74 and 83
69	$[Ru(bpy)_2$(**4-C-4′-Me-bpy**)$](PF_6)_2$	—		1	0.6 ps[f] (MeCN)	74, 83 and 85
70	**70a:** $[Ru(tpy)$(**4′-C-tpy**)$](PF_6)_2$	—	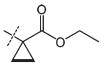	1	—	86
	70b: $[Ru(4'-(NMe_2)$-tpy)(**4′-C-tpy**)$](PF_6)_2$					
71[g]	$[Ru(bpy)_2$(**4-C-4′-Me-bpy**)$](PF_6)_2$			1	—	87
72	$[Ru(bpy)_2$(**3-C-bpy**)$](PF_6)_2$			1	—	80
73	$[Ru(tpy)$(**4′-C-tpy**)$](PF_6)_2$			1	73 ps[f] (MeCN)	88
74	$[Ru(tpy)$(**4′-C-tpy**)$](PF_6)_2$			1	93 ps[f] (MeCN)	88
75	$[RuCl_3$(**4′-C-tpy**)$]$	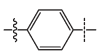		1	—	89
76[g]	$[Ru(4'-(4$-PhMe)-tpy)(**4′-C-tpy**)$](PF_6)_2$	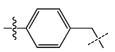		1	—	87
77	**77a:** $[Ru(bpy)_2$(**3-C-bpy**)$](PF_6)_2$	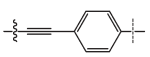		3	**77a:** 900 ps[f] (MeCN)	84
	77b: $[Ru(bpy)_2$(**4-C-bpy**)$](PF_6)_2$			3	**77b:** 700 ps[f] (MeCN)	90
78	$[Ru(tpy)$(**4′-C-tpy**)$](PF_6)_2$	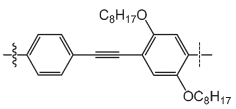		1	320 ps[f] (MeCN)	88
79	$[Ru(tpy)$(**4′-C-tpy**)$](PF_6)_2$	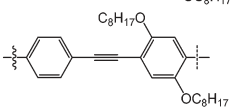		1	400 ps[f] (MeCN)	88
80	$[Ru(bpy)_2$(**3-C-bpy**)$](PF_6)_2$	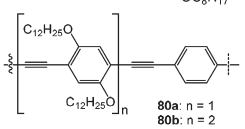		3	**80a:** 600 ps[e] (MeCN)	84
					80b: 700 ps[f] (MeCN)	
81	**81a:** $[Ru(tpy)$(**4′-C-tpy**)$](PF_6)_2$	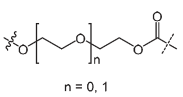	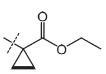	1	—	86 and 91
	81b: $[Ru(4'-(NMe_2)$-tpy)(**4′-C-tpy**)$](PF_6)_2$					
82	$[Ru(5,5''-Me_2$-tpy)(**4′-C-tpy**)$](PF_6)_2$	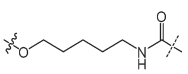	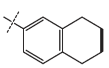	2	—	92
83	$[Ru(4'-(4-(PPV)_3$-PPE)-tpy)(**4′-C-tpy**)$]$ $(BF_4)_2$	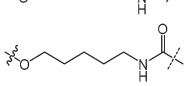	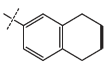	2	—	93
84	$[Ru($**4′-C-tpy**$)_2](PF_6)_2$	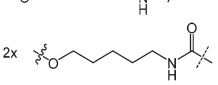	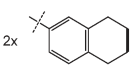	2	—	92 and 94

Table 1 *(Contd.)*

Entry	Ru(bpy/tpy) unit[a]	C-bridge-C[b]	C_{60} functionality (F)[c]	Route[d]	τ_{MLCT}[e]	Ref.
85	$[Ru(bpy)_2(\mathbf{3\text{-}C\text{-}bpy})](PF_6)_2$	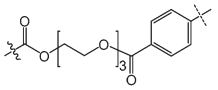	 **85a**	1	110 ns[h] (MeCN)	75 and 95
			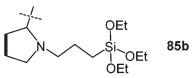 **85b**	1	—	96
86	$[Ru(bpy)_2(\mathbf{4\text{-}C\text{-}4'\text{-}Me\text{-}bpy})](PF_6)_2$	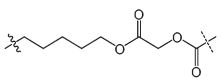	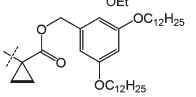	2	4.4 ns[h] (CH_2Cl_2)	82 and 97
87	$[Ru(bpy)_2(\mathbf{3\text{-}C\text{-}bpy})](PF_6)_2$	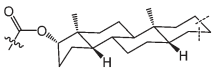		1	200 ps[f] (MeCN)	76
88	$[Ru(bpy)_2(\mathbf{3\text{-}C\text{-}bpy})](PF_6)_2$	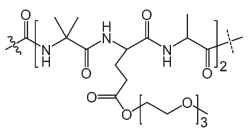		2	480 ps[f] (CH_2Cl_2) 2.9 ns[f] (CBT)	81
89	$[Ru(bpy)_2(\mathbf{4,4'\text{-}C_2\text{-}bpy})](PF_6)_2$	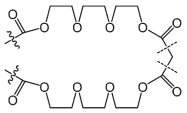		1	1.5 ns[f] (CH_2Cl_2)	79
90	$[Ru(NCS)_2$(4,4′-COOH-bpy)$(\mathbf{4\text{-}C\text{-}4'\text{-}COOH\text{-}bpy})]$	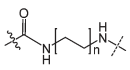 **90a**: n = 1; **90d**: n = 4 **90b**: n = 2; **90e**: n = 5 **90c**: n = 3; **90f**: n = 6		3	1.8 ns[h] (CH_2Cl_2) 2.4 ns[h] (MeCN)	98
91	$[Ru(bpy)_2(\mathbf{3\text{-}C\text{-}bpy})](PF_6)_2$	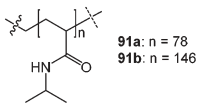 **91a**: n = 78 **91b**: n = 146		1	—	99
92	$[Ru(bpy)_2(\mathbf{4\text{-}C\text{-}4'\text{-}Me\text{-}bpy})](PF_6)_2$	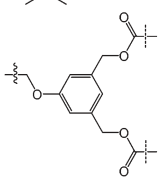	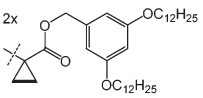	1	—	78
93	$[Ru(bpy)_2(\mathbf{3,3'\text{-}C_2\text{-}bpy})](PF_6)_2$	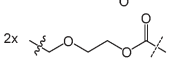	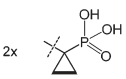	1	—	80

[a] Chemical structure of the ruthenium complex (the bold text highlights the bpy/tpy ligand that is connected to Sp–C_{60} unit; **C** denotes the position of the bpy/tpy-connection (*i.e.*, 3, 4 or 4′ position) to the bridge). [b] Schematic representation of the bridging unit with the connection between the functionalized bpy/tpy (waved line) and C_{60} (dashed line). [c] Schematic representation of the C_{60} functionality (the bold line represents a [6,6]-bond on the C_{60} surface). [d] The synthetic route used for the preparation (for details, see Scheme 9). [e] ^{3}MLCT lifetime at room temperature (the solvent used is given in parentheses). [f] Determined by TA spectroscopy. [g] The bold lines represent an open [5,6]-bond on the C_{60} surface. [h] Determined by time-resolved emission spectroscopy.

mation of the $^3C_{60}$* state. These photodynamics suggested an intramolecular energy transfer from the $[Ru(bpy)_3]^{2+}$ chromophore to the C_{60} sphere. The authors assumed that electron transfer did not occur due to the higher energy of the charge-separated state E_{CSS} (*i.e.*, 1.64 eV) compared to the $^3C_{60}$* state (*i.e.*, 1.50 eV). The analogous $[Ru(tpy)_2]^{2+}$ complex **67** was also synthesized, but not analyzed by spectroscopy. Similar bridgeless Ru–Sp–C_{60} complexes were synthesized by Modin *et al.*:[74] In complexes **68** and **69** the $[Ru(bpy)_3]^{2+}$ units are connected to the C_{60} *via* a pyrrolidine and a pyrazoline ring, respectively. In the structurally related pyrazolino[60]fullerene complex **94** (Fig. 23), the N-atom of the pyrazoline ring was coordinated together with its pyridine substituent to the ruthenium in a bidentate fashion. For all these three complexes, the E_{CSS} energy was found to be higher than the $^3C_{60}$* energy and, consequently, electron transfer could not be observed.[83] The observed energy transfer was very fast in the pyrrolidino[60]fullerene **68** (τ_{MLCT} = 7 ps) and even faster for the pyrazolino[60]fullerenes **69** and **94** (τ_{MLCT} = 0.6 ps). This very fast energy-transfer process was ascribed to the short donor–acceptor distance. It was assumed that the significant longer lifetime in **68** was due to the non-conjugated pyrrolidine-based C_{60}-function-

ality resulting in a reduced orbital overlap. Armspach *et al.* prepared $[Ru(tpy)_2]^{2+}$-methano[60]fullerene diads that are bridgeless **70a** or oligoethoxy-bridged **81a**, respectively.[86,91] These complexes were also prepared as triads **70b** and **81b**, in which the second terpyridine ligand was modified by an electron-donating NMe_2– group. It was shown that the redox potentials of the first C_{60}-based reduction and the first Ru- or NMe_2-based oxidation of the bridgeless complexes **70a** and **70b** are shifted compared to the free tpy-C_{60} ligand and C_{60}-free reference complexes, respectively. In fact, the first oxidation and reduction process in **70a** and **70b** appeared anodically and cathodically shifted by around 50 mV, respectively. These findings indicated a degree of interaction between the donor and the acceptor moiety. Both NMe_2-substituted complexes **70b** and **81b** featured proper E_{CSS} values (*i.e.*, 1.49 eV and 1.47 eV) making electron-transfer processes favorable. However, time-resolved experiments were not reported. Brunet *et al.*[80] reported on methano[60]fullerene (**72** and **93**) containing $[Ru(bpy)_2]^{2+}$ complexes. Complex **93** is a bis-functionalized C_{60} and was synthesized as a mixture of regioisomers *via* route 1. The ruthenium-based emission for **72** and **93** was quenched in solution. Compounds **72** and **93** exhibit one or two phosphonate groups, respectively, which were required as anchoring groups to incorporate them into an inorganic matrix based on zirconium. The reaction of **72** and $Zr(n\text{-}BuO)_4$ produced a hybrid material that was analyzed by EA, mass spectrometry (MS), solid-state ^{31}P and ^{13}C NMR spectroscopy as well as TGA and revealed an approximate chemical formula of $Zr(\mathbf{72})_{0.2-0.4}(n\text{-}BuO)_{3.6-3.8}$. This material was analyzed in the solid state by emission spectroscopy and exhibited also no ruthenium-based emission indicating an energy-/electron-transfer processes. Schubert and co-workers recently reported a series of rigid phenyl- and *para*-PPE-bridged $[Ru(tpy)_2]^{2+}$ complexes of pyrrolidino- (**73** and **78**) and methano[60]fullerenes (**74** and **79**), respectively (PPE: phenyleneethynylene).[88] The compounds were analyzed in the same context as the above-mentioned Ru–Sp–C_{60} systems and exhibited similar findings, *i.e.*, quenched ruthenium-based emission and only energy transfer could be observed. Thereby, a distance and linker dependency of the decay of the ^{3}MLCT state and the energy transfer was observed. The pyrrolidino[60]fullerene-based complex **73** featured an ^{3}MLCT lifetime of 73 ps, while for the methano[60]fullerene analogue **74** a lifetime of 93 ps was detected. The difference in lifetime was assumed to be owed by the different angles between the complex and C_{60} surface. Upon increasing the donor–acceptor distance in **78** (τ_{MLCT} = 320 ps) and **79** (τ_{MLCT} = 400 ps) the lifetimes were extended. A variation of the solvent (*i.e.*, utilizing dichloromethane and acetonitrile) did not result in significant lifetime changes; this behavior suggested that electron transfer – being more pronounced in polar solvents – had a negligible contribution in the series. Similarly, the $[Ru(bpy)_3]^{2+}$-functionalized pyrrolidino[60]fullerenes **77a** and **80a**, **80b** were synthesized by Chaignon *et al.*[84] The length of the bridge was varied by using oligo-PPE-type spacers of different lengths. Energy transfer was observed for all three complexes with similar ^{3}MLCT lifetimes of *ca.* 700 ps, independent from the donor–acceptor distance. This unusual behavior was rationalized by the above-mentioned hopping mechanism (eqn (4)). The complex **80b** with three PPE units exhibited a lower energetic $^3\pi$–π^* state *vs.* the ^{3}MLCT energy that would favor an exergonic population. For complexes **80a** (two PPE units) and **77a** (one PPE unit) higher energies for the $^3\pi$–π^* states were assumed, but should be thermally accessible from the ^{3}MLCT state. Allen *et al.* reported a similar complex:[90] In this compound **77b** the only difference compared to **77a** was the position of bpy functionalization. The different positions did not significantly influence the lifetime of the ^{3}MLCT state: for **77b** a lifetime of around 700 ps was observed, 200 ps shorter than in **77a**. **77b** was analysed further in butyronitrile at low temperatures down to 77 K and resulted in an increased ^{3}MLCT lifetime (τ_{MLCT} up to 2 ns). However, the lifetime at 77 K was still reduced by three orders of magnitude *vs.* the corresponding C_{60}-free reference complexes ($\tau_{MLCT} \approx 5$ μs) and, thus, independently of the temperature, the photoinduced energy transfer remains quantitative due to the low activation energy. In contrast to Chaignon's work, Allen *et al.* assumed that a contribution of the single PPE unit in **77b** should not be involved in the energy transfer, since the ^{3}MLCT lifetime exponentially increases with decreasing temperatures and a thermal population of the $^3\pi$–π^* states is excluded at low temperatures.

Maggini *et al.* reported the first Ru–Sp–C_{60} system in 1995.[75] Complex **85a** consisted of a flexible triethylene glycol unit as bridge with two ester groups as connection between the $[Ru(bpy)_3]^{2+}$ complex and the pyrrolidino[60]fullerene units. Time-resolved emission spectroscopy revealed a decreased lifetime at room temperature of 180 ns or 110 ns in the solid-state or acetonitrile solution, respectively (*vs.* 400 ns or 370 ns of the reference compound). Additionally, the solid state sample was analyzed by light-induced electron-spin resonance (LESR): two spin signals appeared after light irradiation, while in the reference substances, *i.e.*, pristine C_{60} and $[Ru(bpy)_2(3\text{-}COOH\text{-}bpy)](PF_6)_2$, both signals were absent under identical conditions. Therefore, the authors assigned one signal to the radical anion of C_{60}, which is photo-generated by an electron-transfer process. Applying this method, they could proof that a CSS was formed upon light irradiation – at least as an intermediate state. A more detailed analysis on the mechanism was carried out by Armaroli *et al.* for the related complex **86**.[82] The compound comprises a $[Ru(bpy)_3]^{2+}$ complex and a methano[60]fullerene unit, which were bridged by a pentyl acetate spacer. The authors could indirectly proof that electron-transfer process occurred as an intermediate step, and was followed by charge recombination to populate the $^3C_{60}$* state. At first, the authors referred to a publication from MacQueen *et al.*[100] describing the rate constant of a Dexter-type energy-transfer process by the Marcus parabola in the inverted region. Accordingly, the change in free energy (ΔE°) for the electron-transfer process would be closer to that maximum rate than for the energy-transfer process and should prefer electron transfer as the initial step. Their assumption was supported by steady-state and time-resolved emission

spectroscopy at room temperature and 77 K. As in the above-mentioned cases, the ruthenium-based emission was strongly quenched at room temperature, while emission at 77 K was almost fully recovered; the emission lifetime was similar to that of the reference complex $[Ru(bpy)_2(4,4'\text{-Me-bpy})](PF_6)_2$. This indicated that an energy- or electron-transfer process should be inhibited at low temperatures. Moreover, the authors referred to a publication from Hammarström *et al.*[101] where the energy-transfer rate in a heterodinuclear ruthenium(II) and osmium(II) bis(terpyridine) complex remained unchanged over a 200 to 90 K temperature interval. Hence, they assumed that electron transfer would outcompete the energy-transfer process as the initial step after the ^{3}MLCT state is once formed. However, the fast, subsequent recombination and formation of $^3C_{60}$* did not allow the presence of a long-lived CSS. Longer CSS states are observed for the complexes **87** and **88**. Maggini *et al.* reported on the $[Ru(bpy)_3]^{2+}$ complex **87** containing a pyrrolidino[60]fullerene moiety and a rigid androstane bridging unit.[76] In this system, a short ^{3}MLCT lifetime of 200 ps in acetonitrile at room temperature is observed (τ_{MLCT} = 480 ps in CH_2Cl_2). These values are comparable with those reported for $[Ru(bpy)_3]^{2+}$ systems that contained no spacer (**66**) or a conjugated spacer (**77** and **80**), respectively, and suggested a stronger intramolecular quenching if compared to the systems containing flexible linkers in which the ^{3}MLCT lifetime is in the nanosecond range. The following photodynamic processes were analysed by nanosecond-flash photolysis experiments revealing an absorption band in the NIR region – a peak maximum at 1040 nm is a characteristic signal for the radical anion of C_{60} and serves as an indicator for the formation of a CSS. The lifetime of this state was 210 ns in acetonitrile (τ_{CSS} = 100 ns in CH_2Cl_2). Surprisingly, the authors suggested different pathways for the charge recombination in different solvents: for acetonitrile, the $^3C_{60}$* state should be formed (eqn (2)), whereas in dichloromethane a repopulation of the ^{3}MLCT state was proposed. One year later, the same group reported a hexapeptide-bridged $[Ru(bpy)_3]^{2+}$ complex with a pyrrolidino[60]fullerene moiety (**88**). The secondary structure of the peptide was analyzed by 2D NMR spectroscopy (*i.e.*, NOE correlation experiments) and confirmed the expected 3_{10}-helical conformation in chloroform. The ruthenium-based emission was significantly quenched in 1-chlorobutane (CBT) and a decrease of the ^{3}MLCT lifetime from 220 ns (for the C_{60}-free reference complex) to 2.9 ns was observed. Nanosecond-flash photolysis experiments revealed a diagnostic absorption band in the NIR-region indicating electron transfer and the formation of a CSS with a lifetime longer than 100 ns; the back-electron transfer product proceeds with the formation of the $^3C_{60}$*. Noteworthy, the addition of highly protic solvents (*i.e.*, hexafluoroisopropanol) fully re-established the ruthenium-based emission and hampered any energy- and/or electron-transfer process. This behavior was attributed to the collapse of the hydrogen-bond network along with an unfolding of the peptide oligomer. Consequently, the donor–acceptor distance increased and mutual through-bond interactions became disabled. The deactivation of this process was found to be reversible and could be reactivated by evaporation of the solvent.

Pure triplet-energy transfer was described by Possamai *et al.* for the compound **89**, which consisted of a $[Ru(bpy)_3]^{2+}$ complex, a crown ether macrocycle as bridge, and a methano [60]fullerene unit.[79] The ^{3}MLCT lifetime in dichloromethane was decreased to 1.5 ns *vs.* 544 ns for the reference complex.

Aiming for a potential application in dye-sensitized solar cells (DSSCs), Lim *et al.* prepared the dyes **90a–90f**, which consists of a $[Ru(NCS)_2(4,4'\text{-COOH-bpy})(4C\text{-}4'\text{-COOH-bpy})]$ complex, the C_{60} moiety and six different, linear alkyl spacers (2 to 12 carbons in steps of two) as bridge between the active components.[98] The idea was that the C_{60} molecules would form a hydrophobic layer to prevent direct contact of the electrolyte (*i.e.*, I_3^-) with the semiconductor surface (*i.e.*, TiO_2), thereby reducing the back-electron transfer reaction. This effect was initially reported by Lagref *et al.* for ruthenium complexes bearing hydrophobic alkyl chains.[102] The Ru–Sp–C_{60} compounds were synthesized by the third route, in which the first step was the reaction of a diamino alkane derivative with C_{60} by NH-addition of one amino group to the [6,6]-double bond.[103] The second amino group was used subsequently for amidation with $[Ru(NCS)_2(4,4'\text{-COOH-bpy})_2]$ (this particular complex is commonly referred to as the N3 dye) using one of the carboxylic acid groups. The complexes were adsorbed on a TiO_2 surface *via* the remaining carboxylic acid groups, and to ensure a full surface loading, a final treatment with the pristine N3 dye was applied. DSSCs were prepared from the six different systems (assigned as **90a–90f**/N3) and compared with the system containing only N3 in the context of J_{SC}, open-circuit voltage (V_{OC}), fill-factor (FF), conversion efficiency (η) and the relative amount of adsorbed complex. For the systems **90a**/N3 (Fig. 20) and **90f**/N3 with the shortest and longest bridge, respectively, slightly decreased values were observed, that were mainly ascribed to the few percentage (<20%) of the Ru–Sp–C_{60} complexes adsorbed on the surface. However, slightly increased values were obtained for the systems **90b–90e**/N3 (Fig. 20), since around 50% of the complex is adsorbed.

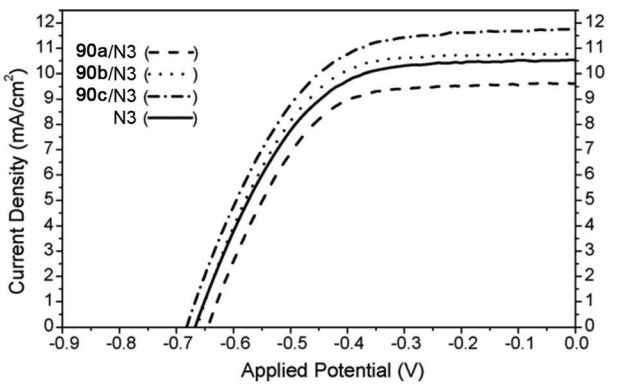

Fig. 20 (a) Representation of the *J–V* spectra of the prepared DSSCs with **90a–90c**/N3 or pure N3 as the photosensitizer. Figure adapted with permission from ref. 98, copyright 2007 Elsevier B.V.

Maximum values are detected for the system **90c**/N3 with a conversion efficiency of 4.5% *vs.* 4% for the pure N3. However, the authors assumed that the small improvement was not only ascribed to a worse adsorption. Moreover, the low-lying LUMO level of C_{60} was believed to act as an electron shuttle in the back-electron transfer reaction between TiO_2 and I_3^-.

The amphiphilic character of Ru–Sp–C_{60} systems was investigated by Guldi and co-workers at the example of complex **85b**.[96] The idea was to form Langmuir–Blodgett films, in which the hydrophilic $[Ru(bpy)_3]^{2+}$ complex and polar triethylene glycole spacer align in the aqueous phase, while the hydrophobic C_{60} moiety was expected to settle down at the water–air interface. Applying this technique allowed a controlled two-dimensional growth of **85b** on the air–water interface. Measuring surface pressure *vs.* area isotherms and Brewster angle microscopy confirmed the exclusive formation of a monolayer with a surface area of 117 $Å^2$ that is comparable to pure C_{60}. Multiple layers were prepared by repeated dipping of a quartz substrate into the mono-layered aqueous solution of **85b**. The deposition process was monitored by UV-vis absorption spectroscopy. Each repeating step increased the MLCT absorption of the film in a linear fashion and, thereby, corroborating the expected stacking of monolayers. Moreover, a thin film on a quartz plate was obtained by compression of the monolayer until collapse occurred. The morphology of these structures were analysed by atomic force microscopy (AFM) imaging and revealed threadlike fibers with a length of several 100 μm and a width of roughly 1 μm (Fig. 21a/b). A more detailed analysis indicated that the fibers consisted of aggregated clusters with an individual diameter of around 100 nm (Fig. 21c/d). It was assumed that these clusters were core–shell nanoparticles with $[Ru(bpy)_3]^{2+}$ complexes as the core and the C_{60} units as the shell.

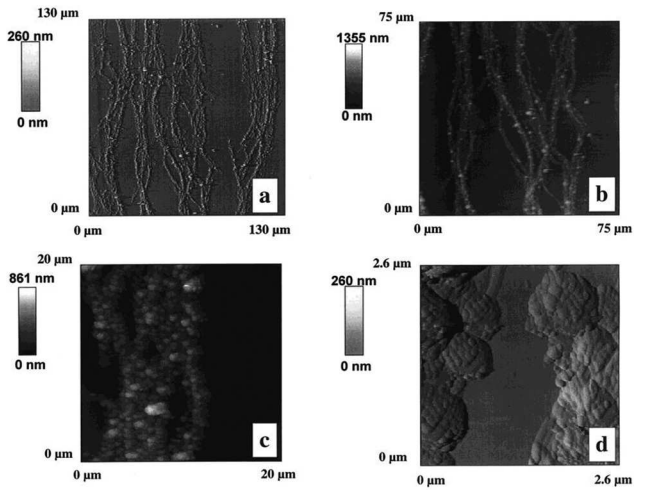

Fig. 21 AFM images of **85b** transferred from the collapsed monolayer solution to a quartz plate. Resolution: (a) 130 × 130 μm, (b) 75 × 75 μm, (c) 20 × 20 μm, and (d) 2.6 × 2.6 μm. Figure reprinted with permission from ref. 96, copyright 2000 American Chemical Society.

The amphiphilic character of Ru–Sp–C_{60} systems was also investigated by Zhou *et al.*[99] Compounds **91a** and **91b** represent metallopolymers based on a poly(*N*-isopropylacrylamide) (PNIPAAm) backbone with 78 and 146 repeating units, respectively. The chain ends were functionalized on the one side with a $[Ru(bpy)_3]^{2+}$ complex and on the other side with a C_{60} moiety. PNIPAAm was chosen as thermoresponsive and water soluble polymer to study the temperature-dependency of the electron transfer as well as the self-assembly behavior in aqueous solution. The synthesis was accomplished in three steps according to route 1. At first, polymerization of the NIPAAm monomer was achieved under reversible addition–fragmentation chain-transfer (RAFT) polymerization conditions utilizing a bpy-functionalized RAFT agent in order to obtain well-defined polymers with the bpy unit being directly introduced at the chain end. Secondly, the RAFT end group was cleaved by treatment with azobisisobutyronitrile (AIBN). Subsequently, the remaining radical sites on the polymer chain and the isobutyronitrile group were reacted with one [6,6]-bond of C_{60}. The final step of the sequence was the coordination of $[Ru(bpy)_2(MeOH)_2](PF_6)_2$ to the ligand-equipped polymer. Here, an excess of the reactive precursor complex guaranteed a full complexation of all bpy units. The metallopolymers were analyzed by emission spectroscopy in water and an intense ruthenium-based emission was observed for **91a** and **91b**. This behavior indicated that the polymeric bridge successfully prevented any interaction between the spatially separated $[Ru(bpy)_3]^{2+}$ complex and the C_{60} unit. However, the above-mentioned temperature-dependent analysis was not performed. Instead, the self-assembly behavior of polymers **91a** and **91b** in aqueous solution at different concentrations was analyzed by TEM imaging. Formation of micelles comprising the hydrophobic C_{60} units as the core and the hydrophilic $[Ru(bpy)_3]^{2+}$ complexes as the shell was expected (Fig. 22a). High concentrations (5 mg mL^{-1}) resulted in the formation of spherical vesicles with a diameter of 2 to 3 μm (Fig. 22b); dilution (1.7 mg mL^{-1}) yielded in smaller vesicles with diameters of 15 nm and 70 nm for **91a** and **91b**, respectively. At even lower concentrations (0.5 mg mL^{-1}), the uniform spherical structures vanished and only unstructured aggregates were detected. The highly concentrated solutions were analyzed further by fluorescence microscopic imaging and revealed the same particle size as already observed by TEM measurements (Fig. 22c).

So far, there are only a few complexes known where a bidentate ligand other than bpy-type has been connected to C_{60} (Fig. 23). The complex **94** consist of a 2-(4,5-dihydro-1*H*-pyrazol-3-yl)pyridine metal-binding unit and has already been discussed above. The complexes **95** and **96** bear a 4,5-diazafluorene (df) moiety as metal-binding unit, connected *via* their 9-position to a [6,6]-double bond of C_{60} and feature either two CO or PPh_3 ligands in *cis*- or *trans*-configuration, respectively. These two complexes were synthesized by the reaction of $Ru(CO)_2Cl_2$ or $Ru(PPh_3)_2Cl_2$ with the C_{60}-modified df ligand and were analyzed regarding their non-linear optical properties. Both complexes featured remarkable high quadratic hyper-

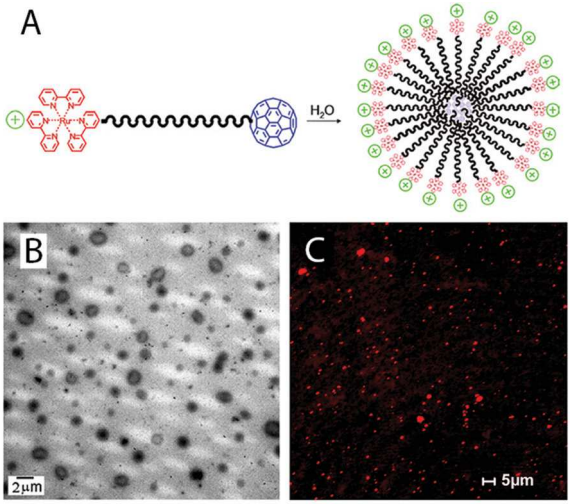

Fig. 22 (a) Schematic representation of the self-assembly process of **91a** and **91b** in water. (b) TEM image of **91b**. (c) Fluorescence microscopic image of **91b**. Figure adapted with permission from ref. 99, copyright 2008 The Royal Chemical Society.

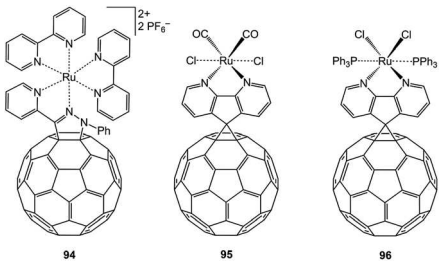

Fig. 23 Schematic representation of the complexes **94**, **95** and **96** containing other bidentate metal-binding units.

polarizability values ($\mu\beta_{1.907}$) up to −3435 esu *vs.* −1040 esu for the C_{60}-free reference complexes. This finding was mainly ascribed to the large polarizability as well as the electron-withdrawing effect of the C_{60}-substituent.

3.2. Tetradentate coordination in Ru–Sp–C_{60} systems

Ru–Sp–C_{60} systems with tetradentate metal binding units, such as porphyrins (Por) or phthalocyanines (Pc), are summarized in Fig. 24. In general, the ruthenium complexes of these tetradentate macrocyles are connected to the C_{60} by an axial coordination of a pyridine (py) unit; a CO ligand in the second axial position completes the octahedral coordination sphere. The synthesis of these systems is accomplished by the reaction of an appropriate ruthenium precursor (*i.e.*, [Ru(Por)(CO)(ROH)] or [Ru(Pc)(CO)]) with the corresponding py-functionalized C_{60}, which proceeds spontaneously even at room temperature. Interestingly, [Ru(Por)(CO)(py)] complexes exhibit an emissive $^3\pi$–π^* state with a very long lifetime of about 50 μs at room temperature[104] and, thus, such complexes are more beneficial for the formation of long-lived CSS when compared to $[Ru(bpy)_3]^{2+}$ or $[Ru(tpy)_2]^{2+}$ systems. However, the weak

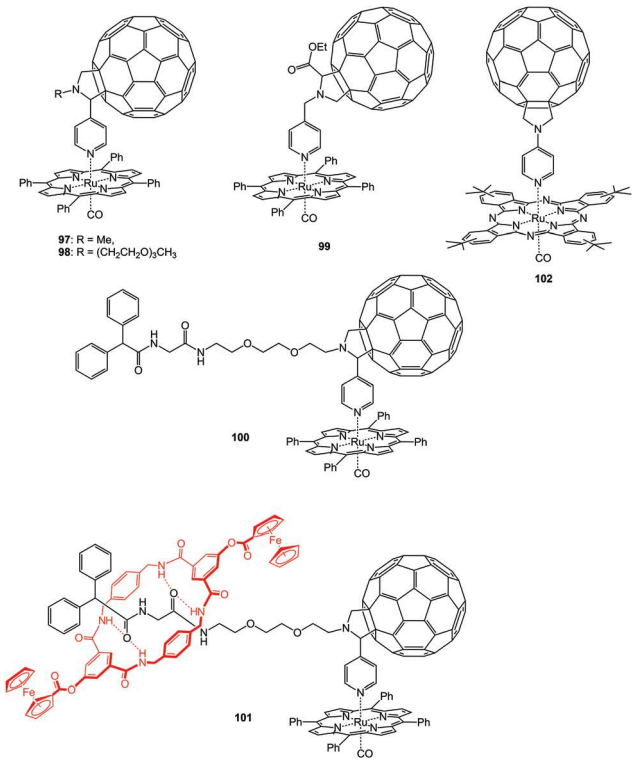

Fig. 24 Schematic representation of the complexes **97–102** containing tetradentate metal binding units.

thermal stability of these complexes resulting in ligand exchange of the monodentate py ligand in the presence of competing ligands at room temperature represents a major disadvantage of the axial coordination.[105] The similarly structured TPPor-based compounds **97**,[106] **98**,[107] and **99**[108] were reported by Da Ros and Guldi *et al.* and were analysed in solution as well as in thin films (TPPor = 5,10,15,20-tetraphenylporphyrin). The complex **97** was irradiated at 530 nm in the porphyrin Q-band and showed a solvent-dependent quenching behavior:[106] For polar solvents (*i.e.*, benzonitrile and THF) a moderate quenching was observed, whereas for nonpolar solvents (*i.e.*, toluene and dichloromethane) a stronger quenching *vs.* the emission intensity of the C_{60}-free reference complex occurred. Quenching was accompanied by a significantly lowered lifetime of the $^3\pi$–π^* state in **97** up to 90 ps in toluene and 400 ps in benzonitrile. Remarkably, pure triplet–triplet energy transfer was observed in toluene, while in benzonitrile a CSS was formed with an intriguing long lifetime of about 50 μs (τ_{CSS} < 4 ns in dichloromethane). This major effect could not only be explained by a lower E_{CSS} value in polar solvents. The authors assumed that the CSS was moreover stabilized by a reversible dissociation of the complex into $[Ru(TPPor)CO]^{\bullet+}$ and py-$C_{60}^{\bullet-}$ fragments. This assumption was constrained by a concentration-dependent lifetime analysis, which resulted in longer lifetimes at lower concentrations according to a second-order kinetic. Similar solvent and concentration dependencies were also found for the structurally related complex **99**.[108]

Complex **98** exhibits a polar triethyleneglycol substituent and was prepared in view of potential preparation of Langmuir–Blodgett films.[107] A clear monolayer formation was not possible, even when adding a co-surfactant (*i.e.*, cadmium arachidate). Although, multilayered films on quartz slides could be prepared by the Langmuir–Blodgett technique and were analysed by UV-vis absorption spectroscopy that confirmed uniform deposition. Time-resolved spectroscopy revealed that charge separation occurred with a long lifetime of 2.2 μs. Inspired by the long-lived nature of the CSS of these complexes, Mateo-Alonso *et al.* prepared a dyad (**100**) and a triad system (**101**) (Fig. 24).[109] The dyad **100** was composed of a [Ru(TPPor)(CO)] complex, a pyrrolidino[60]fullerene and a dipeptide substructure with a diphenyl stopper. This substructure was designed as template for the preparation of a rotaxane *via* hydrogen bonding according to a procedure described by Keaveney *et al.*[110] Triad **101** featured this rotaxane with an encapsulated macrocycle that contained two redox-active Fc units. Upon excitation of the [Ru(TTPor)(CO)] chromophore, a lifetime of 2.2 ns for the CSS between [Ru(TPPor)(CO)] and C_{60} was found in the dyad **100**, which is similar to that observed in **97**. Under identical conditions, an acceleration was observed for the triad **101**: here the CSS between [Ru(TPPor)(CO)] and C_{60} decays with a lifetime of 0.9 ns. Subsequently, a new CSS was established between Fc and C_{60} with a lifetime longer than 3 ns. The mechanism was rationalized as a stepwise electron transfer according to the redox gradient of the two metal complexes. Analysis in more polar solvents were not described, presumably due to the expected weakening of the hydrogen bonding along with a decrease of CSS lifetime as shown in previous studies.[111]

[Ru(Pc)(CO)] complexes are often used as alternative to Por-based complexes, because they feature lower energetic absorption bands up to 700 nm and exhibit similar $^3\pi$–π^* lifetimes.[112] Rodríguez-Morgade *et al.*[113] established the complex **102** with tetra(*tert*-butyl)phthalocyanine (T^tBPc) as metal binding unit (Fig. 24). The time-resolved analysis was performed in toluene and results in the formation of $^1\pi$–π^* state that decays with a lifetime of 4.5 ps. However, not the $^3\pi$–π^* state is formed, instead the CSS is generated with a lifetime of 170 ns, while for the similar structured complex **97** and **99** in toluene, only energy transfer was observed. The reason for the absent ISC is ascribed to similar energies of the $^3\pi$–π^* and CS state.

3.3. Ruthenocenes in Ru–Sp–C_{60} systems

Ruthenocenes [Ru(η^5-Cp)$_2$] that are covalently connected to C_{60} were analysed by Oviedo *et al.*[114,115] An overview of the synthesized complexes along with the synthetic procedures is given in Scheme 10. The structures can be distinguished according to their C_{60}-functionalization. The pyrrolidino[60]fullerene-based ruthenocenes **103–106** were prepared by the reaction of formyl ruthenocene with a functionalized α-amino acid (*i.e.*, *N*-methylglycine, 2-hexylglycine, 2-phenylglycine or 5-methoxy-tryptophan) and C_{60} by heating under microwave (MW) irradiation in an average yield of 26%. The other examples, pyrazolino[60]fullerene-based ruthenocenes **107** and **108** were obtained in a two-step procedure. At first, the phenylhydrazone derivate of formyl ruthenocene was prepared, and subsequently reacted with *N*-bromosuccinimide (NBS) to generate a hydrazonyl bromide intermediate. The addition of NEt_3 afforded *in situ* a nitrile imine, which reacted with a [6,6]-bond in a 1,3-dipolar cycloaddition reaction. The latter reaction was performed at low temperatures (40 °C) and resulted only in rather low yields (17% on average). The pyrazolino[60]fullerene unit present in complexes **107** and **108** exhibited a higher electron affinity (similar to that of pristine C_{60}) than the complexes with the pyrrolidino[60]fullerene unit. This feature is rare, but not unusual for conjugated F-C_{60}[116] and even beneficial to reach a more efficient charge transfer between the [Ru(η^5-Cp)$_2$] and C_{60} unit. Time-resolved spectroscopy on **108** in benzonitrile corroborates this statement revealing a faster formation of the CSS upon excitation of the C_{60} unit. It was assumed that the CSS was formed from the singlet excited state of C_{60} ($^1C_{60}$*). A lifetime of 100 ns was observed for the CSS in **108** and decayed to the ground state without a contribution of the energetic higher lying $^3C_{60}$* state. For complex **105**, mainly the $^3C_{60}$* state was populated and charge-separation was ascribed to occur only as a minor process.

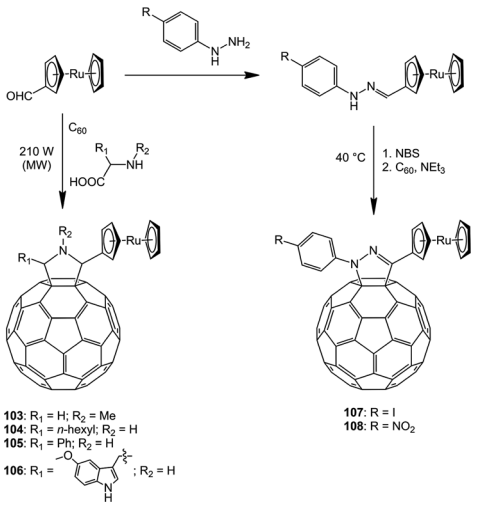

Scheme 10 Schematic representation of the synthesis of ruthenocenes **103–108** covalently connected to C_{60}.

3.4. Multiple covalently attached ruthenium complexes or fullerene cores

Beyond the range of systems of the general composition Ru–Sp–C_{60}, research is also focussed on the formation of more sophisticated structures comprising more than one ruthenium complex or C_{60} core, respectively. An overview of compounds reported in literature having a fullerene-to-ruthenium ratio of 2 : 1 is given in Fig. 25. As general structural motive, the compounds consist of a central ruthenium complex covalently connected to two adjacent fullerene cores and, thus, they can be assigned to the so-called "fullerene dumbbells".[117,118] Such structures can be prepared *via* two different approaches. First,

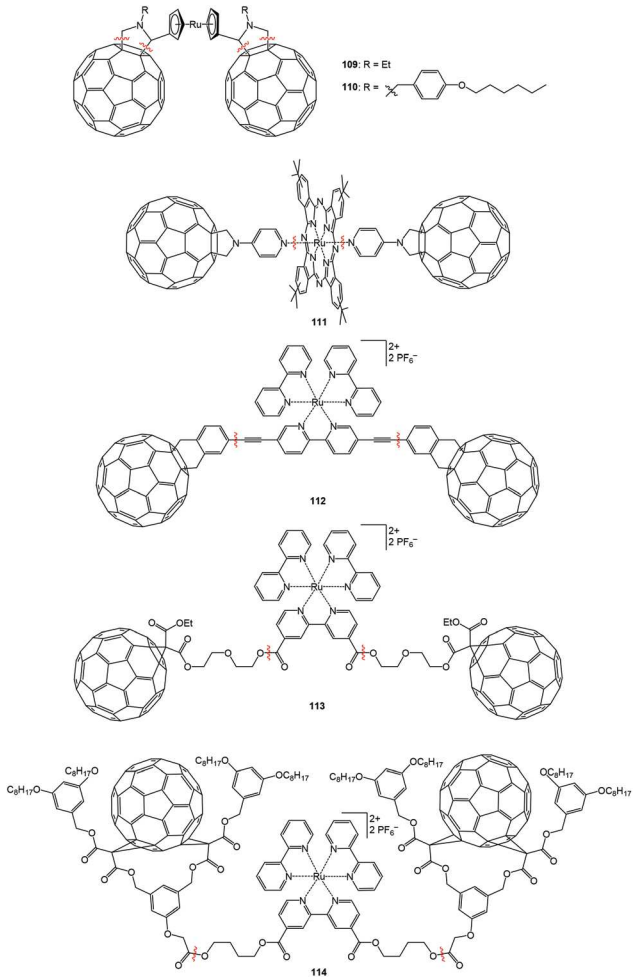

Fig. 25 Schematic representation of the fullerene dumbbells **109–114** having a ruthenium to C_{60} ratio of 1 : 2. The red waved lines mark the key-bond formation position during the dumbbell-generating process.

the reaction of two mono-functionalized C_{60} molecules with an appropriately difunctional central unit (CU) that already contains the ruthenium complex or with a ligand that can be coordinated to a ruthenium center in a subsequent step. The second approach is the reaction of a difunctional CU with pristine C_{60}; in this case, the two reactive sites of the CU must be capable for addition to C_{60}. The latter approach is more sophisticated, since polymerization or multiple-addition reaction can easily occur. The assemblies **109** and **110** were synthesized by this latter approach.[119] Here, 1,1′-diformyl ruthenocene was used as CU and was reacted on both sites with C_{60} and either *N*-ethylglycine or *N*-benzyl(hexyloxy)glycine. Worth mentioning, the formed compounds were chiral and featured two stereocenters on the pyrrolidine rings. Two diastereomers could be separated by column chromatography and each stereoisomer was obtained in *ca.* 23% yield. However, an assignment of the absolute configuration was not possible. The electrochemical analysis by performing cyclic voltammetry measurements revealed that a double amount of current (*i.e.*, two-electron reduction) was required for each of the first three C_{60}-based reduction steps compared to the irreversible ruthenocene-based oxidation (*i.e.*, one-electron oxidation) – this finding was consistent with the given 2 : 1 ratio of the redox-active moieties, C_{60} and ruthenocene. The [Ru(T^{t}BPc)(CO)]-centered complex **111** (Fig. 25) was reported together with the previously discussed mono-fullerene complex **102** (Fig. 24).[113] This complex was synthesized by the reaction of two pyridine-functionalized C_{60} molecules with the activated [Ru(T^{t}BPc)$(MeCN)_2$] precursor, in which two py units replaced the labile, axially coordinated acetonitrile molecules. Due to the absence of the strongly back-donating CO ligand, a broadening and hypsochromic shift of the Pc-based Q-band in the absorption spectrum was observed. Despite this, complex **105** behaved similar when compared to its monofullerene-based congener **96**: a $^1\pi$–π^* state lifetime and CSS lifetime of 1.7 ps and 130 ns, respectively, were determined. The $[Ru(bpy)_3]^{2+}$-based complex **112** (Fig. 25) was prepared by a Sonogashira cross-coupling reaction of the two bromo-functionalized C_{60} molecules with 3,3′-diethynyl bpy, followed by ruthenium complexation.[120] The two complexes **113** [86] and **114** [121] (Fig. 25) were both prepared by straightforward esterification reactions. For complex **113** two (diethylene glycol)-functionalized C_{60} molecules were reacted with 4,4′-bis(chlorocarbonyl)-bpy to initially prepare the metal-free ligand.[86] The complex **114** was prepared by a DCC-assisted condensation reaction (DCC = *N*,*N*′-dicyclohexylcarbodiimide) of two *cis*-2-bis-functionalized C_{60} molecules containing a carboxylic acid group with a diol-containing $[Ru(bpy)_3]^{2+}$ complex. However, applying this approach involved the removal of the dicyclohexylurea from the product, what turned out to be problematic; thus, a stepwise approach was applied (*i.e.*, first the esterification of a diol-functionalized bpy, followed by the ruthenium coordination).[121]

The reported dinuclear complexes with a ruthenium-to-C_{60} ratio of 2 : 1 are depicted in Fig. 26. For all three systems the related mononuclear complexes are also known (*vide supra*) and were used as reference systems. The $[Ru(tpy)_2]^{2+}$-based compound **115** and its mononuclear congener **74** (Table 1) were reported by Barthelmes *et al.*[88] The methano[60]fullerene functionality was chosen to gain a symmetrical bis-complex. The synthesis was performed by the cycloaddition of a diazo-derivative containing two tpy groups with C_{60}. Subsequently, the reaction with $[Ru(tpy)(MeCN)_3](PF_6)_2$ allowed to introduce the two ruthenium centers. The photophysical and electrochemical properties were similar to those reported for **74**. In fact, triplet–triplet energy transfer from the ruthenium center to the C_{60} was observed. In the cyclic voltammogram only one Ru^{2+}/Ru^{3+} redox process could be observed for the two $[Ru(tpy)_2]^{2+}$ units, thus indicating the absence of electronic interactions between the two metal centers. Moreover, this process required the double current (*i.e.*, representing a two-electron oxidation) compared to each C_{60}-based one-electron reduction, which corroborates to the given 2 : 1 ratio of ruthenium to C_{60}. Guldi *et al.* reported on the dinuclear complex **116**, with the mononuclear complex **87** as the reference.[122] The main structural difference between the two complexes is that a ditopic 2,3-di(pyridine-2-yl)quinoxaline (dpq) ligand connects the two

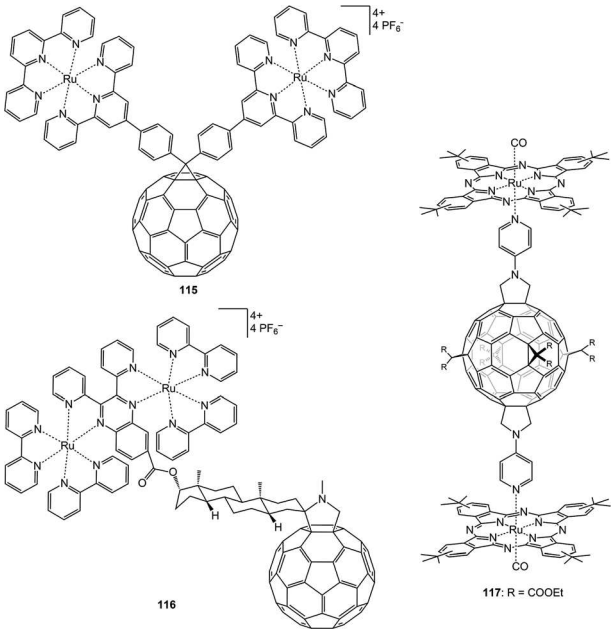

Fig. 26 Schematic representation of the dinuclear complexes **115–117** featuring a ruthenium to C_{60} ratio of 2 : 1.

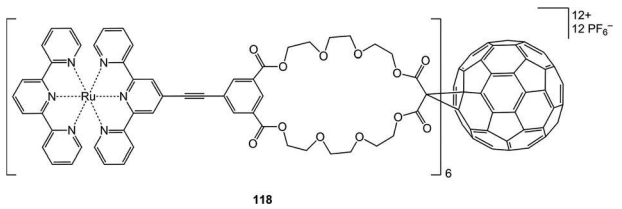

Fig. 27 Schematic representation of the hexanuclear ruthenium complex **118**.

ruthenium centers and could, thereby, mediate metal–metal interaction. Consequently, two redox processes for the Ru^{2+}/Ru^{3+} were observed in the CV measurements. Significant differences between **87** and **116** became apparent regarding their photophysical properties: while for **87**, intramolecular electron transfer was the major process, for **116** exclusively triplet–triplet energy transfer occurred in dichloromethane or acetonitrile. Both complexes were applied in the fabrication of stable photoactive films by successive layer-by-layer deposition on quartz or ITO slides. The uniform multi-layered films could generate a photocurrent that increased linearly with the number of deposited layers.[123] Another approach to obtain dinuclear complexes was shown at the example of complex **117** as reported by Rodríguez-Morgade *et al.*[113] The functionalization of C_{60} with four diethyl malonate groups in equatorial positions limited the number of further adducts. Consequently, the twofold cycloaddition of 4-formylpyridine and formaldehyde generated pyrrolidine-functionalities on both C_{60} poles. A subsequent reaction with two equivalents of [Ru(T^tBPc)(CO)] gave the desired complex in 65% yield. Electron transfer, as observed in the corresponding mononuclear species **102**, was not present in **117**. This behavior was attributed to the lowered electron-acceptability of hexafunctionalized C_{60} that resulted in a higher and, thus, not accessible CSS energy.

Recently, a hexanuclear ruthenium bis(terpyridine) complex (**118**, Fig. 27) was reported by Yan *et al.*[124] The synthesis thereof was accomplished in two steps: first, a six-fold Sonogashira-type cross-coupling reaction of a previously reported hexa(iodophenyl macrocyclic methano)[60]fullerene[125] with 4′-ethynyl-tpy was carried out. Subsequently, the ruthenium coordination with six equivalents of the reactive precursor $[Ru(tpy)(acetone)_3](BF_4)_3$ in refluxing DMF yielded 35% of the desired complex. Complex **118** featured three distinct redox processes – one reversible metal-based oxidation as well as two irreversible tpy reductions. Moreover, there was no evidence for additional metal-based oxidations or C_{60}-based reductions. This behavior indicated the absence of interactions between the pending isolated ruthenium centers. The absence of the typical C_{60}-based reduction in the applied potential window could be attributed to the electronic nature of the hexakis-addition product presumably having a significantly decreased electron-accepting ability then C_{60}.

4. Ruthenium and fullerene assemblies by non-covalent bonds

4.1. Encapsulation of fullerenes

The encapsulation of fullerenes has a high potential for their isolation and was recently reviewed by García-Simón *et al.*[9] Actually, there are so far only two systems known from literature that contain ruthenium complexes (Fig. 28). The supramolecular assembly **119** was reported by McNally *et al.* and consisted of a C_{60} molecule located in the cavity formed by two β-cyclodextrin (CD) units, each functionalized with a $[Ru(bpy)_2]^{2+}$ complex.[126] The complex is thereby covalently attached to the CD units *via* a 2-(aminomethyl) pyridine (py-MA) moiety that simultaneously acted as neutral bidentate ligand for the ruthenium coordination. The supramolecular encapsulation of C_{60} was achieved in 78% yield by the reaction with two equivalents $[Ru(bpy)_2(py\text{-}MA\text{-}CD)]^{2+}$ at 90 °C for 2.5 days. The stable complex exhibited an increased solubility in ethanol or acetonitrile compared to the virtual insolubility of pristine C_{60} in these solvents. Moreover, intramolecular energy or electron transfer occurred in this supramolecular system, as indicated by a reduced ruthenium-based emission intensity and lifetime. A fully encapsulated C_{60} molecule with six surrounding $[Ru(\eta^5\text{-}Cp)(\eta^6\text{-}Ar)]^+$ units (**120**) was reported by Wong *et al.* (Fig. 28).[127] The molecular cage comprised two cyclotriveratrylene (CTV) moieties that were bridged by six decamethylene chains (DM). The encapsulation was performed in a solid-state reaction by heating C_{60} with the DM_6-CTV_2 cage at 250 °C for 15 h. This remarkably high temperature was required to allow the C_{60} to pass into the internal cavity. Subsequently, the ruthenium coordination with three equiva-

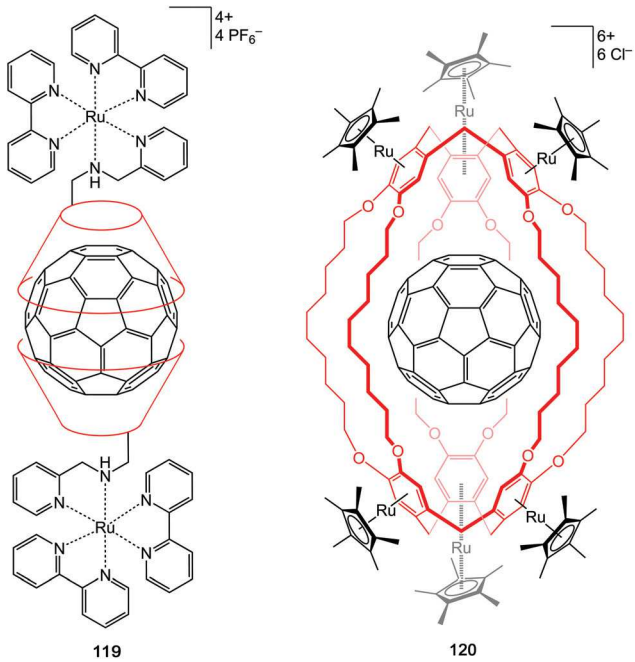

Fig. 28 Schematic representation of the ruthenium complexes **119** and **120** with encapsulated C_{60}. The red truncated cone represents a β-cyclodextrin macrocycle.

lents of the tetranuclear precursor complex $[Ru(\eta^5\text{-}Cp)(\mu_3\text{-}Cl)]_4$ yielded the hexanuclear complex **120**; the molecular structure was confirmed by X-ray single-crystal analysis. The compound featured a high stability and an increased solubility in polar solvent (*e.g.*, methanol).

4.2. Ruthenium-coated fullerenes prepared by impregnation/deposition techniques

The high potential of hybrid materials that contain zerovalent ruthenium nanoparticles embedded within an amorphous fullerene support has been shown in the fields of heterogeneous catalysis or adsorption of molecular hydrogen. Such materials have mainly been prepared by impregnation, such as incipient wetness impregnation (IWI) or deposition (*e.g.*, thermal induced deposition), and activation techniques (*e.g.*, reduction to zerovalent ruthenium by hydrogen). As mentioned briefly in the first section, Wohlers and Braun *et al.* prepared nanoparticles of zerovalent $Ru_x(CO)_y$ clusters by the reaction of $Ru_3(CO)_{12}$ with C_{60} in refluxing toluene for three days.[27] The thereby generated insoluble black product, denoted as $Ru_x(CO)_y/C_{60}$ had a composition of 20 wt% ruthenium content. The authors assumed that the ruthenium clusters were anchored onto the C_{60} surface *via* η^2-type bonds that formed branched C_{60} networks. TEM analysis indicated the formation of spherical ruthenium nanoparticles with a diameter in the range of 2 to 5 nm that were embedded in an amorphous C_{60} matrix.[27] Annealing *in vacuo* over 300 °C yielded slightly increased nanoparticle diameters, what was owed by dissociation of CO along with the formation of ruthenium metal.[128] The annealed material featured hydrogen adsorption at room temperature, which could be described by a Langmuir-type adsorption isotherm.[128] A similar behavior was reported by Saha *et al.* for ruthenium nanoparticles, obtained from the impregnation of C_{60} with ruthenium(III) acetylacetonate $[Ru(acac)_3]$ and subsequent reduction with hydrogen.[129] The catalytic activity and product selectivity of $Ru_x(CO)_y/C_{60}$ was studied and compared to other $Ru_x(CO)_y$/carbon support materials:[130] Fullerene black (FB), cathodic fullerene deposit (CFD) and graphite (G). From these, $Ru_x(CO)_y$/CFD and $Ru_x(CO)_y$/G featured a higher catalytic activity compared to $Ru_x(CO)_y/C_{60}$ in the Fischer–Tropsch hydrogenation of CO, in particular at higher temperatures, while the product selectivity (*i.e.*, methane formation) was equal at 300 °C. However, in the hydrogenation of 2-cyclohexenone, annealing of $Ru_x(CO)_y/C_{60}$ and the subsequent exposure to hydrogen could significantly increase the catalytic activity; nonetheless, the performance remained low compared to the other carbon materials. Lashdaf *et al.* prepared a catalyst for the hydrogenation of cinnamaldehyde.[131] This catalyst was prepared in a stepwise manner: at first, the impregnation C_{60} with an ethanolic solution of $[Ru(acac)_3]$ yielded a coating with ruthenium(III) centers; subsequent reduction with hydrogen formed the catalytically active zerovalent ruthenium species. During this process a Ru/C_{60} hybrid material was formed with 5 wt% of Ru loading. For Ru/C_{60} a higher product selectivity (*i.e.*, formation of cinnamyl alcohol), but a lower conversion was observed compared to ruthenium (Ru/C) and palladium on activated carbon (Pd/C). Keypour *et al.* prepared three catalysts with 1, 8 and 15 wt% ruthenium loading, respectively, for the hydrogenation of nitrobenzene to aniline.[132] The catalyst was prepared by the impregnation of a polyhydroxylated C_{60} with ruthenium(III) chloride ($RuCl_3$) in ethanol at 50 °C and subsequent ruthenium reduction with hydrogen. TEM imaging and X-ray diffraction analysis revealed the formation of nanoparticles with a diameters of 16 to 20 nm. The hydrogenation efficiency was studied by a statistical variation of the pressure, temperature, time as well as the ruthenium loading. From this data, an optimized model was calculated, predicting the best conditions for an approximately 100% hydrogenation efficiency: 22.33 atm, 150 °C, 3 h, 15 wt% loading. Bimetallic nanoparticles of ruthenium and platinum were reported by Hills *et al.*[133] The IWI of C_{60} with $PtRu_5C(CO)_{16}$ or $Pt_2Ru_4(CO)_{18}$ and subsequent reduction yielded nanoparticles in a size of 1 to 1.5 nm with a Pt/Ru ratio of 1 : 5 or 2 : 4, respectively. Another approach was reported by Bai *et al.* making use of an aqueous precursor mixture containing chloroplatinic acid (H_2PtCl_6) and $RuCl_3$, that was added dropwise to a suspension of polyaniline containing C_{60} (PANI-C_{60}) (Fig. 29a).[134] Subsequent reduction with potassium borohydride formed Pt–Ru nanoparticles with an average diameter of 2.4 nm (Fig. 29b–d). PANI-C_{60} was prepared by the oxidative polymerization of aniline in a suspension of C_{60}. The authors embedded PANI in C_{60} to introduce more designated metal binding units and to enhance the conductivity of the carbon support. The Pt–Ru/PANI-C_{60} hybrid material was studied as catalyst for the electrocatalytic methanol oxidation and

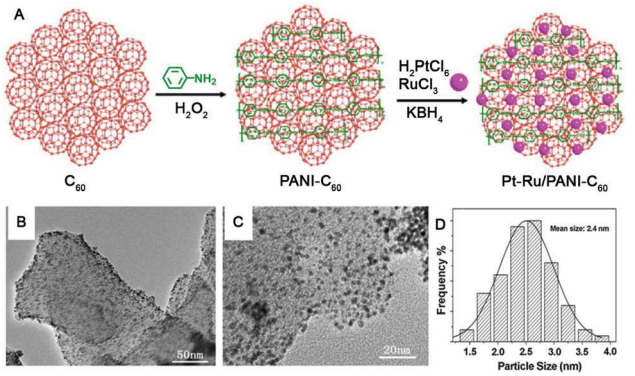

Fig. 29 (a) Schematic representation of the formation of Pt–Ru/PANI-C_{60}. (b/c) TEM images with different magnification of Pt–Ru/PANI-C_{60}. (d) Size distribution of the nanoparticles. Figure adapted with permission from ref. 134, copyright 2013 Springer.

revealed a higher catalytic activity compared to a Pt/PANI-C_{60} material that misses the ruthenium content.

4.3. Ruthenium fulleride salts

Fullerides are salts of anionically charged fullerenes with electropositive counterions and feature interesting magnetic and conductive properties.[135,136] The first ruthenium fulleride with the formula $[Ru(bpy)_3^{2+}](C_{60}^{-})_2$ was prepared by electrocrystallization.[137] The selective, one-electron reduction of C_{60} in a saturated dichloromethane solution of $[Ru(bpy)_3](PF_6)_2$ afforded black crystals on the Pt-electrode. The material was analyzed by UV-vis-NIR absorption spectroscopy and indicated characteristic absorption peak for $[Ru(bpy)_3]^{2+}$ (*i.e.*, λ_{max} = 452 nm) and C_{60}^{-} (*i.e.*, λ_{max} = 1078 nm). The known extinction coefficients of these bands were used to calculate a ratio of 1 : 2 between the components $[Ru(bpy)_3]^{2+}$ and C_{60}^{-}. A more convenient approach for the preparation of such ruthenium fullerides was reported by Hong *et al.*:[138] The controlled electrolytic two-electron reduction of $[Ru(bpy)_3^{2+}](PF_6)_2$ to $[Ru(bpy)_3]^0$ afforded a useful precursor for fulleride preparation. The subsequent reaction of $[Ru(bpy)_3]^0$ with 0.5, 1 or 2 equivalents of C_{60} in benzonitrile yielded three different ruthenium fulleride salts with the composition $[Ru(bpy)_3^{+}]_2(C_{60}^{2-})$, $[Ru(bpy)_3^{2+}](C_{60}^{2-})$ and $[Ru(bpy)_3^{2+}](C_{60}^{-})_2$, respectively. For each fulleride salt, the ratio and ion charge was confirmed by UV-vis-NIR absorption spectroscopy, X-ray single-crystal structure analysis as well as EPR measurements. At room temperature, all three salts featured electrical conductivity in the range of semiconductor-type materials. However, the individual conductivities of $[Ru(bpy)_3^{+}]_2(C_{60}^{2-})$ (*i.e.*, 9.5 S m^{-1}) and $[Ru(bpy)_3^{2+}](C_{60}^{-})_2$ (*i.e.*, 2 S m^{-1}, similar to the value reported by Foss *et al.*[137]) were 500 and 100 times higher compared to $[Ru(bpy)_3^{2+}](C_{60}^{2-})$ (*i.e.*, 0.018 S m^{-1}), respectively. The enhancement was assumed to result from an increased number of $[Ru(bpy)_3]$ or C_{60} units and shorter C_{60}–C_{60} distances that favor electron hopping.

4.4. Ruthenium-fullerene blends

A general challenge in the preparation ruthenium-fullerene blends is to identify an appropriate solvent for both, the hydrophilic ruthenium complex and the hydrophobic fullerene core. Marin *et al.* prepared printed films of a blend that consisted of a poly(methyl methacrylate) copolymer with $[Ru(bpy)_3]^{2+}$ units in the sidechain (**121**) and different amounts of PCBM (Fig. 30).[139] Both compounds were dissolved and mixed in acetophenone/*o*DCB (ratio = 5 : 95), and subsequently processed onto glass substrates applying the ink-jet printing technique. Smooth and uniform films were obtained with a thickness of 120 nm. The different amounts of PCBM in the films influenced the ruthenium-based emission: a complete quenching was observed at a 1 : 2 ratio of **121** and PCBM.

SAMs of the dinuclear ruthenium complex **122** functionalized with eight phosphonic acid moieties (Fig. 30) on ITO substrates, designed for photocurrent generation, were prepared by Terada *et al.*[140] The formed monolayer featured a void space of 1 nm between the anchored ruthenium complexes that was used for the encapsulation of fullerenes. For this purpose, **Cf-C_{60}**, a bis-adduct of C_{60} bearing two 2-(trifluoromethyl)-1,3-dioxolan-2-ol functionalities was used, due to a similar solubility in methanol as **122**. The SAMs were prepared by immersion of the ITO substrate in a methanolic solution of **122** and **Cf-C_{60}** for 24 h. A tenfold excess of **Cf-C_{60}** was necessary to achieve an effective incorporation into the ruthenium SAMs. TEM imaging and XPS analysis revealed a layer thickness of 4.3 nm and a 2.5 : 1 ratio of **Cf-C_{60}** to **122**. Photocurrent-generating devices were fabricated with ascorbic acid as sacrificial electron donor. The device yielded an anodic photocurrent with 8.8% quantum yield with 0.1 V bias. A comparison with the device containing only the ruthenium complex showed an increased photocurrent generation at 400 nm and, thus, a significant contribution of the fullerene derivate.

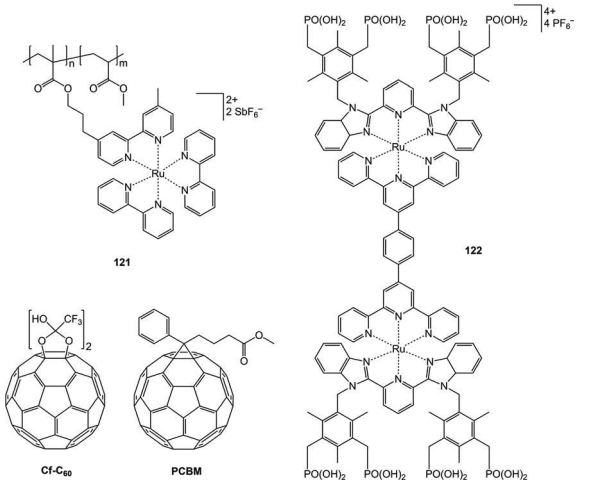

Fig. 30 Schematic representation of the structures used as ruthenium-fullerene blends **121**/PCBM and **122**/Cf-C_{60}.

5. Conclusions

The combination of ruthenium centers and fullerenes can be achieved by a variety of procedures that yield well-organized molecular architectures. As a beneficial aspect, the solubility is typically enhanced since the functionalized exohedral fullerene surface diminishes aggregation. The first described class of organometallic ruthenium complexes could be obtained by coordination of appropriate ruthenium precursor complexes to the fullerene surface. Hereby, the stability of the η^2-complexes could be enhanced by the incorporation of more ruthenium centers that form bridged complexes or ruthenium–ruthenium bonds. In general, η^5-coordinated ruthenium centers are more stable and, thus, they exhibit a fruitful chemistry and have found application as catalysts in asymmetric synthesis. A special case of η^5-coordinated ruthenium centers is represented by the bucky ruthenocenes, which are congeners of ruthenocene. These compounds reveal a high potential in several applications: organic solar cells, photocurrent-generating devices, catalysis and the transformation into C_{70} by a certain electron dose. Since ruthenocenes exhibit an irreversible ruthenium oxidation, they are not examined that extensively as the structurally related ferrocenes. In contrast, bucky ruthenocenes exhibit a quasi-reversible, metal-based one-electron oxidation that could be beneficial for further research in this field.

The second class of compounds, C_{60} with covalently linked ruthenium complexes, was prepared mainly in the context of photoactive donor–acceptor systems. The competing intramolecular energy- and/or electron-transfer processes have been studied intensively and solvent, temperature and concentration dependencies were found. A broad range of structural parameters were adjusted in these systems, *i.e.*, linker type, bridge length, fullerene functionalization and metal-binding unit. In particular, N-donor based ligands, like bpy, tpy or Por are the most commonly used metal-binding units in this context. It can be concluded that short and aromatic bridges between $[Ru(bpy)_3]^{2+}$/$[Ru(tpy)_2]^{2+}$ complexes and C_{60} result mainly in a very fast energy transfer within picoseconds, while for systems with longer non-aromatic bridges both energy- and electron-transfer processes can be observed on a nanosecond timescale. In the case of electron transfer, the thusly formed charge-separated state usually features a lifetime of several 100 ns. For [Ru(Por)(CO)]-containing systems mainly electron transfer is observed in the picosecond range. A long-lived CSS is formed and decays with a lifetime of around 50 μs, which is ascribed to dissociation of the donor and acceptor, thereby hampering the charge-recombination process. The amphiphilic character of ruthenium-fullerene architectures has been shown by their self-assembly in solution, leading to vesicles and monolayers. The latter once could, for example, be deposited on ITO substrates to fabricate photocurrent-generating devices.

The third class of materials describes ruthenium-fullerenes assemblies based on different types of non-covalent interactions. Supramolecular host–guest interactions were applied for the encapsulation of fullerenes. By this method, pristine C_{60} can be dissolved in polar solvents without chemical disruption of the π-conjugated system. Embedding of zerovalent ruthenium nanoparticles in fullerenes becomes a promising alternative in catalytic hydrogenation reactions when compared to other carbon-supported materials. Electrostatic interactions were examined in ruthenium fulleride salts that exhibit interesting semiconducting and magnetic properties.

Multiple functionalization reactions of C_{60}'s surface have been reported with high regioselectivity for the organometallic and covalently connected ruthenium complexes. By this approach well-defined 2D- and 3D-architectures have been generated, which could potentially be part of prospective research including molecular electronic devices.

Acknowledgements

Financial support by the Deutsche Forschungsgemeinschaft (DFG, grant no. SCHU1229-16/1) is kindly acknowledged.

Notes and references

1 H. W. Kroto, J. R. Heath, S. C. O'Brien, R. F. Curl and R. E. Smalley, *Nature*, 1985, **318**, 162–163.
2 C.-Z. Li, H.-L. Yip and A. K.-Y. Jen, *J. Mater. Chem.*, 2012, **22**, 4161–4177.
3 G. Accorsi and N. Armaroli, *J. Phys. Chem. C*, 2010, **114**, 1385–1403.
4 P. Mroz, G. P. Tegos, H. Gali, T. Wharton, T. Sarna and M. R. Hamblin, *Photochem. Photobiol. Sci.*, 2007, **6**, 1139–1149.
5 A. L. Balch and M. M. Olmstead, *Chem. Rev.*, 1998, **98**, 2123–2166.
6 M. D. Meijer, G. P. M. van Klink and G. van Koten, *Coord. Chem. Rev.*, 2002, **230**, 141–163.
7 L. I. Denisovich, S. M. Peregudova and Y. N. Novikov, *Russ. J. Electrochem.*, 2010, **46**, 1–17.
8 D. Soto and R. Salcedo, *Molecules*, 2012, **17**, 7151–7168.
9 C. García-Simón, M. Costas and X. Ribas, *Chem. Soc. Rev.*, 2016, **45**, 40–62.
10 M. A. Lebedeva, T. W. Chamberlain and A. N. Khlobystov, *Chem. Rev.*, 2015, **115**, 11301–11351.
11 M. R. Axet, O. Dechy-Cabaret, J. Durand, M. Gouygou and P. Serp, *Coord. Chem. Rev.*, 2016, **308**, 236–345.
12 A. L. Balch and K. Winkler, *Chem. Rev.*, 2016, **116**, 3812–3882.
13 A. Juris, V. Balzani, F. Barigelletti, S. Campagna, P. Belser and A. von Zelewsky, *Coord. Chem. Rev.*, 1988, **84**, 85–277.
14 E. A. Medlycott and G. S. Hanan, *Chem. Soc. Rev.*, 2005, **34**, 133–142.
15 Q. Zeng, F. W. Lewis, L. M. Harwood and F. Hartl, *Coord. Chem. Rev.*, 2015, **304–305**, 88–101.
16 F. L. Bowles, M. M. Olmstead and A. L. Balch, *J. Am. Chem. Soc.*, 2014, **136**, 3338–3341.

17 B. F. G. Johnson, J. Lewis and M. V. Twigg, *J. Organomet. Chem.*, 1974, **67**, C75–C76.
18 B. Giovannitti, O. Gandolfi, M. Ghedini and G. Dolcetti, *J. Organomet. Chem.*, 1977, **129**, 207–214.
19 P. J. Fagan, J. C. Calabrese and B. Malone, *Science*, 1991, **252**, 1160–1161.
20 P. J. Fagan, M. D. Ward and J. C. Calabrese, *J. Am. Chem. Soc.*, 1989, **111**, 1698–1719.
21 M. Rasinkangas, T. T. Pakkanen and T. A. Pakkanen, *J. Organomet. Chem.*, 1994, **476**, C6–C8.
22 A. N. Chernega, M. L. H. Green, J. Haggitt and A. H. H. Stephens, *J. Chem. Soc., Dalton Trans.*, 1998, 755–767.
23 I. J. Mavunkal, Y. Chi, S.-M. Peng and G.-H. Lee, *Organometallics*, 1995, **14**, 4454–4456.
24 H.-F. Hsu and J. R. Shapley, *J. Am. Chem. Soc.*, 1996, **118**, 9192–9193.
25 H.-F. Hsu, S. R. Wilson and J. R. Shapley, *Chem. Commun.*, 1997, 1125–1126.
26 H.-F. Hsu and J. R. Shapley, *J. Organomet. Chem.*, 2000, **599**, 97–105.
27 M. Wohlers, B. Herzog, T. Belz, A. Bauer, T. Braun, T. Rühle and R. Schlögl, *Synth. Met.*, 1996, **77**, 55–58.
28 K. Lee, H.-F. Hsu and J. R. Shapley, *Organometallics*, 1997, **16**, 3876–3877.
29 K. Lee and J. R. Shapley, *Organometallics*, 1998, **17**, 3020–3026.
30 L.-C. Song, G.-A. Yu, F.-H. Su and Q.-M. Hu, *Organometallics*, 2004, **23**, 4192–4198.
31 S. Li, B. Wei, P. M. N. Low, H. Kee Lee, T. S. Andy Hor, F. Xue and T. C. W. Mak, *J. Chem. Soc., Dalton Trans.*, 1997, 1289–1294.
32 R. J. Gale and R. Job, *Inorg. Chem.*, 1981, **20**, 42–45.
33 E. G. Gal'pern, N. P. Gambaryan, I. V. Stankevich and A. L. Chistyakov, *Russ. Chem. Bull.*, 1994, **43**, 547–550.
34 R. C. Haddon, *Science*, 1993, **261**, 1545–1550.
35 R. C. Haddon, *Acc. Chem. Res.*, 1988, **21**, 243–249.
36 E. Nakamura, *J. Organomet. Chem.*, 2004, **689**, 4630–4635.
37 Y. Matsuo and E. Nakamura, *Chem. Rev.*, 2008, **108**, 3016–3028.
38 M. Sawamura, H. Iikura and E. Nakamura, *J. Am. Chem. Soc.*, 1996, **118**, 12850–12851.
39 M. Sawamura, H. Iikura, T. Ohama, U. E. Hackler and E. Nakamura, *J. Organomet. Chem.*, 2000, **599**, 32–36.
40 M. Sawamura, M. Toganoh, Y. Kuninobu, S. Kato and E. Nakamura, *Chem. Lett.*, 2000, **29**, 270–271.
41 Y. Matsuo and E. Nakamura, *Organometallics*, 2003, **22**, 2554–2563.
42 Y. Matsuo, A. Muramatsu, J. Lu and E. Nakamura, *Chem. Lett.*, 2010, **39**, 342–343.
43 W.-Y. Yeh, *J. Organomet. Chem.*, 2014, **751**, 351–355.
44 Y. Matsuo, B. K. Park, Y. Mitani, Y.-W. Zhong, M. Maruyama and E. Nakamura, *Bull. Korean Chem. Soc.*, 2010, **31**, 697–699.
45 Y. Matsuo, Y. Mitani, Y.-W. Zhong and E. Nakamura, *Organometallics*, 2006, **25**, 2826–2832.
46 Y.-W. Zhong, Y. Matsuo and E. Nakamura, *Chem. – Asian J.*, 2007, **2**, 358–366.
47 Y. Matsuo, T. Uematsu and E. Nakamura, *Eur. J. Inorg. Chem.*, 2007, 2729–2733.
48 Y. Matsuo, K. Matsuo, T. Nanao, R. Marczak, S. S. Gayathri, D. M. Guldi and E. Nakamura, *Chem. – Asian J.*, 2008, **3**, 841–848.
49 G. Wilkinson, *J. Am. Chem. Soc.*, 1952, **74**, 6146–6147.
50 Y. Matsuo, Y. Kuninobu, S. Ito and E. Nakamura, *Chem. Lett.*, 2004, **33**, 68–69.
51 Y. Matsuo, T. Fujita and E. Nakamura, *Chem. – Asian J.*, 2007, **2**, 948–955.
52 D. M. Guldi and M. Prato, *Acc. Chem. Res.*, 2000, **33**, 695–703.
53 Y. Matsuo, Y. Kuninobu, S. Ito, M. Sawamura and E. Nakamura, *Dalton Trans.*, 2014, **43**, 7407–7412.
54 D. M. Guldi, G. M. A. Rahman, R. Marczak, Y. Matsuo, M. Yamanaka and E. Nakamura, *J. Am. Chem. Soc.*, 2006, **128**, 9420–9427.
55 T. Nakae, Y. Matsuo, M. Takagi, Y. Sato, K. Suenaga and E. Nakamura, *Chem. – Asian J.*, 2009, **4**, 457–465.
56 E. Nakamura, M. Koshino, T. Saito, Y. Niimi, K. Suenaga and Y. Matsuo, *J. Am. Chem. Soc.*, 2011, **133**, 14151–14153.
57 T. Niinomi, Y. Matsuo, M. Hashiguchi, Y. Sato and E. Nakamura, *J. Mater. Chem.*, 2009, **19**, 5804–5811.
58 T. Nakae, Y. Matsuo and E. Nakamura, *Org. Lett.*, 2008, **10**, 621.
59 A. Iwashita, Y. Matsuo and E. Nakamura, *Angew. Chem., Int. Ed.*, 2007, **46**, 3513–3516.
60 G. A. Olah, I. Bucsi, D. S. Ha, R. Aniszfeld, C. S. Lee and G. K. S. Prakash, *Fullerene Sci. Technol.*, 1997, **5**, 389–405.
61 G. A. Olah, I. Bucsi, C. Lambert, R. Aniszfeld, N. J. Trivedi, D. K. Sensharma and G. K. S. Prakash, *J. Am. Chem. Soc.*, 1991, **113**, 9387–9388.
62 Y. Matsuo, K. Kanaizuka, K. Matsuo, Y.-W. Zhong, T. Nakae and E. Nakamura, *J. Am. Chem. Soc.*, 2008, **130**, 5016–5017.
63 Y. Matsuo, T. Ichiki and E. Nakamura, *J. Am. Chem. Soc.*, 2011, **133**, 9932.
64 W. Yan, S. M. Seifermann, P. Pierrat and S. Bräse, *Org. Biomol. Chem.*, 2015, **13**, 25–54.
65 C.-H. Chen, A. Aghabali, C. Suarez, M. M. Olmstead, A. L. Balch and L. Echegoyen, *Chem. Commun.*, 2015, **51**, 6489–6492.
66 T. Fujita, Y. Matsuo and E. Nakamura, *Chem. Mater.*, 2012, **24**, 3972–3980.
67 Y. Matsuo, K. Tahara, K. Morita, K. Matsuo and E. Nakamura, *Angew. Chem., Int. Ed.*, 2007, **46**, 2844–2847.
68 Y. Matsuo, K. Tahara, T. Fujita and E. Nakamura, *Angew. Chem., Int. Ed.*, 2009, **48**, 6239–6241.
69 M. Sawamura, H. Iikura, A. Hirai and E. Nakamura, *J. Am. Chem. Soc.*, 1998, **120**, 8285–8286.
70 G. C. Vougioukalakis, M. M. Roubelakis and M. Orfanopoulos, *Chem. Soc. Rev.*, 2010, **39**, 817–844.
71 L. Gan, D. Yang, Q. Zhang and H. Huang, *Adv. Mater.*, 2010, **22**, 1498–1507.

72 Y. Murata, M. Murata and K. Komatsu, *Chem. – Eur. J.*, 2003, **9**, 1600–1609.
73 C.-S. Chen, Y.-F. Lin and W.-Y. Yeh, *Chem. – Eur. J.*, 2014, **20**, 936–940.
74 J. Modin, H. Johansson and H. Grennberg, *Org. Lett.*, 2005, **7**, 3977.
75 M. Maggini, A. Donò, G. Scorrano and M. Prato, *J. Chem. Soc., Chem. Commun.*, 1995, 845–846.
76 M. Maggini, D. M. Guldi, S. Mondini, G. Scorrano, F. Paolucci, P. Ceroni and S. Roffia, *Chem. – Eur. J.*, 1998, **4**, 1992–2000.
77 Z. Zhou, G. H. Sarova, S. Zhang, Z. Ou, F. T. Tat, K. M. Kadish, L. Echegoyen, D. M. Guldi, D. I. Schuster and S. R. Wilson, *Chem. – Eur. J.*, 2006, **12**, 4241–4248.
78 F. Cardinali, J.-L. Gallani, S. Schergna, M. Maggini and J.-F. Nierengarten, *Tetrahedron Lett.*, 2005, **46**, 2969–2972.
79 G. Possamai, E. Menna, M. Maggini, M. Carano, M. Marcaccio, F. Paolucci, D. M. Guldi and A. Swartz, *Photochem. Photobiol. Sci.*, 2006, **5**, 1154–1164.
80 E. Brunet, M. Alonso, M. C. Quintana, O. Juanes and J.-C. Rodríguez-Ubis, *Tetrahedron Lett.*, 2007, **48**, 3739–3743.
81 A. Polese, S. Mondini, A. Bianco, C. Toniolo, G. Scorrano, D. M. Guldi and M. Maggini, *J. Am. Chem. Soc.*, 1999, **121**, 3446–3452.
82 N. Armaroli, G. Accorsi, D. Felder and J.-F. Nierengarten, *Chem. – Eur. J.*, 2002, **8**, 2314–2323.
83 S. Karlsson, J. Modin, H.-C. Becker, L. Hammarström and H. Grennberg, *Inorg. Chem.*, 2008, **47**, 7286–7294.
84 F. Chaignon, J. Torroba, E. Blart, M. Borgström, L. Hammarström and F. Odobel, *New J. Chem.*, 2005, **29**, 1272–1284.
85 Y.-H. Kan and Q. Li, *Acta Chim. Sin.*, 2008, **66**, 2585–2591.
86 D. Armspach, E. C. Constable, F. Diederich, C. E. Housecroft and J.-F. Nierengarten, *Chem. – Eur. J.*, 1998, **4**, 723–733.
87 C. Du, Y. Li, S. Wang, Z. Shi, S. Xiao and D. Zhu, *Synth. Met.*, 2001, **124**, 287–289.
88 K. Barthelmes, J. Kübel, A. Winter, M. Wächtler, C. Friebe, B. Dietzek and U. S. Schubert, *Inorg. Chem.*, 2015, **54**, 3159–3171.
89 Z. Wu, X. Cai and Z. Yang, *J. Nanopart. Res.*, 2015, **17**, 329.
90 B. D. Allen, A. C. Benniston, A. Harriman, L. J. Mallon and C. Pariani, *Phys. Chem. Chem. Phys.*, 2006, **8**, 4112–4118.
91 D. Armspach, E. C. Constable, F. Diederich, C. E. Housecroft and J.-F. Nierengarten, *Chem. Commun.*, 1996, 2009–2010.
92 U. S. Schubert, C. H. Weidl, A. Cattani, C. Eschbaumer, G. R. Newkome, E. He, E. Harth and K. Müllen, *Polym. Prepr.*, 2000, **41**, 229–230.
93 A. El-ghayoury, A. P. H. J. Schenning, P. A. van Hal, C. H. Weidl, J. L. J. van Dongen, R. A. J. Janssen, U. S. Schubert and E. W. Meijer, *Thin Solid Films*, 2002, **403–404**, 97–101.
94 U. S. Schubert, C. Eschbaumer, P. Andres, H. Hofmeier, C. H. Weidl, E. Herdtweck, E. Dulkeith, A. Morteani, N. E. Hecker and J. Feldmann, *Synth. Met.*, 2001, **121**, 1249–1252.
95 N. S. Sariciftci, F. Wudl, A. J. Heeger, M. Maggini, G. Scorrano, M. Prato, J. Bourassa and P. C. Ford, *Chem. Phys. Lett.*, 1995, **247**, 510–514.
96 D. M. Guldi, M. Maggini, S. Mondini, F. Guérin and J. H. Fendler, *Langmuir*, 2000, **16**, 1311–1318.
97 J. N. Clifford, G. Accorsi, F. Cardinali, J.-F. Nierengarten and N. Armaroli, *C. R. Chim.*, 2006, **9**, 1005–1013.
98 M. K. Lim, S.-R. Jang, R. Vittal, J. Lee and K.-J. Kim, *J. Photochem. Photobiol., A*, 2007, **190**, 128–134.
99 G. Zhou, J. He, I. I. Harruna and K. E. Geckeler, *J. Mater. Chem.*, 2008, **18**, 5492–5501.
100 D. B. MacQueen, J. R. Eyler and K. S. Schanze, *J. Am. Chem. Soc.*, 1992, **114**, 1897–1898.
101 L. Hammarström, F. Barigelletti, L. Flamigni, N. Armaroli, A. Sour, J.-P. Collin and J.-P. Sauvage, *J. Am. Chem. Soc.*, 1996, **118**, 11972–11973.
102 J.-J. Lagref, M. K. Nazeeruddin and M. Grätzel, *Synth. Met.*, 2003, **138**, 333–339.
103 A. Hirsch, Q. Li and F. Wudl, *Angew. Chem., Int. Ed. Engl.*, 1991, **30**, 1309–1310.
104 C. D. Tait, D. Holten, M. H. Barley, D. Dolphin and B. R. James, *J. Am. Chem. Soc.*, 1985, **107**, 1930–1934.
105 S. S. Eaton, G. R. Eaton and R. H. Holm, *J. Organomet. Chem.*, 1972, **39**, 179–195.
106 T. Da Ros, M. Prato, D. M. Guldi, M. Ruzzi and L. Pasimeni, *Chem. – Eur. J.*, 2001, **7**, 816–827.
107 T. Da Ros, M. Prato, M. Carano, P. Ceroni, F. Paolucci, S. Roffia, L. Valli and D. M. Guldi, *J. Organomet. Chem.*, 2000, **599**, 62–68.
108 D. M. Guldi, T. Da Ros, P. Braiuca and M. Prato, *Photochem. Photobiol. Sci.*, 2003, **2**, 1067–1073.
109 A. Mateo-Alonso, C. Ehli, D. M. Guldi and M. Prato, *J. Am. Chem. Soc.*, 2008, **130**, 14938–14939.
110 C. M. Keaveney and D. A. Leigh, *Angew. Chem., Int. Ed.*, 2004, **43**, 1222–1224.
111 A. Mateo-Alonso, C. Ehli, G. M. A. Rahman, D. M. Guldi, G. Fioravanti, M. Marcaccio, F. Paolucci and M. Prato, *Angew. Chem., Int. Ed.*, 2007, **46**, 3521–3525.
112 Y. Rio, M. S. Rodríguez-Morgade and T. Torres, *Org. Biomol. Chem.*, 2008, **6**, 1877–1894.
113 M. S. Rodríguez-Morgade, M. E. Plonska-Brzezinska, A. J. Athans, E. Carbonell, G. de Miguel, D. M. Guldi, L. Echegoyen and T. Torres, *J. Am. Chem. Soc.*, 2009, **131**, 10484–10496.
114 J. J. Oviedo, P. de la Cruz, J. Garín, J. Orduna and F. Langa, *Tetrahedron Lett.*, 2005, **46**, 4781–4784.
115 J. J. Oviedo, M. E. El-Khouly, P. de la Cruz, L. Pérez, J. Garín, J. Orduna, Y. Araki, F. Langa and O. Ito, *New J. Chem.*, 2006, **30**, 93–101.
116 F. Langa, P. de la Cruz, E. Espíldora, A. González-Cortés, A. de la Hoz and V. López-Arza, *J. Org. Chem.*, 2000, **65**, 8675–8684.
117 J. L. Segura and N. Martín, *Chem. Soc. Rev.*, 2000, **29**, 13–25.

118 L. Sánchez, M. Á. Herranz and N. Martín, *J. Mater. Chem.*, 2005, **15**, 1409–1421.
119 D. Mancel, M. Jevric, E. S. Davies, M. Schröder and A. N. Khlobystov, *Dalton Trans.*, 2013, **42**, 5056.
120 E. A. Walsh, J. R. Deye, W. Baas, K. Sullivan, A. Lancaster and K. A. Walters, *J. Photochem. Photobiol., A*, 2013, **260**, 24–36.
121 F. Cardinali and J.-F. Nierengarten, *Tetrahedron Lett.*, 2003, **44**, 2673–2676.
122 D. M. Guldi, M. Maggini, E. Menna, G. Scorrano, P. Ceroni, M. Marcaccio, F. Paolucci and S. Roffia, *Chem. – Eur. J.*, 2001, **7**, 1597–1605.
123 C. Luo, D. M. Guldi, M. Maggini, E. Menna, S. Mondini, N. A. Kotov and M. Prato, *Angew. Chem., Int. Ed.*, 2000, **39**, 3905–3909.
124 W. Yan, C. Réthoré, S. Menning, G. Brenner-Weiβ, T. Muller, P. Pierrat and S. Bräse, *Chem. – Eur. J.*, 2016, **22**, 11522–11526.
125 P. Pierrat, S. Vanderheiden, T. Muller and S. Bräse, *Chem. Commun.*, 2009, 1748–1750.
126 A. McNally, R. J. Forster, N. R. Russell and T. E. Keyes, *Dalton Trans.*, 2006, 1729–1737.
127 T.-H. Wong, J.-C. Chang, C.-C. Lai, Y.-H. Liu, S.-M. Peng and S.-H. Chiu, *J. Org. Chem.*, 2014, **79**, 3581–3586.
128 T. Braun, M. Wohlers, T. Belz, G. Nowitzke, G. Wortmann, Y. Uchida, N. Pfänder and R. Schlögl, *Catal. Lett.*, 1997, **43**, 167–173.
129 D. Saha and S. Deng, *Langmuir*, 2011, **27**, 6780–6786.
130 T. Braun, M. Wohlers, T. Belz and R. Schlögl, *Catal. Lett.*, 1997, **43**, 175–180.
131 M. Lashdaf, A. Hase, E. Kauppinen and A. O. I. Krause, *Catal. Lett.*, 1998, **52**, 199–204.
132 H. Keypour, M. Noroozi, A. Rashidi and M. Shariati Rad, *Iran. J. Chem. Chem. Eng.*, 2015, **34**, 21–32.
133 C. W. Hills, M. S. Nashner, A. I. Frenkel, J. R. Shapley and R. G. Nuzzo, *Langmuir*, 1999, **15**, 690–700.
134 Z. Bai, M. Shi, L. Niu, Z. Li, L. Jiang and L. Yang, *J. Nanopart. Res.*, 2013, 15.
135 C. A. Reed and R. D. Bolskar, *Chem. Rev.*, 2000, **100**, 1075–1120.
136 D. V. Konarev and R. N. Lyubovskaya, *Russ. Chem. Rev.*, 2012, **81**, 336–366.
137 C. A. Foss, D. L. Feldheim, D. R. Lawson, P. K. Dorhout, C. M. Elliott, C. R. Martin and B. A. Parkinson, *J. Electrochem. Soc.*, 1993, **140**, L84–L86.
138 J. Hong, M. P. Shores and C. M. Elliott, *Inorg. Chem.*, 2010, **49**, 11378–11385.
139 V. Marin, E. Holder, M. M. Wienk, E. Tekin, D. Kozodaev and U. S. Schubert, *Macromol. Rapid Commun.*, 2005, **26**, 319–324.
140 K.-i. Terada, M. Oyama, K. Kanaizuka, M.-a. Haga and T. Ishida, *Phys. Chem. Chem. Phys.*, 2013, **15**, 16586–16593.

Publication P2

"New Ruthenium Bis(terpyridine) Methanofullerene and Pyrrolidinofullerene Complexes: Synthesis and Electrochemical and Photophysical Properties"

K. Barthelmes, J. Kübel, A. Winter, M. Wächtler,
C. Friebe, B. Dietzek, U. S. Schubert,
Inorg. Chem. **2015**, *54*, 3159-3171.

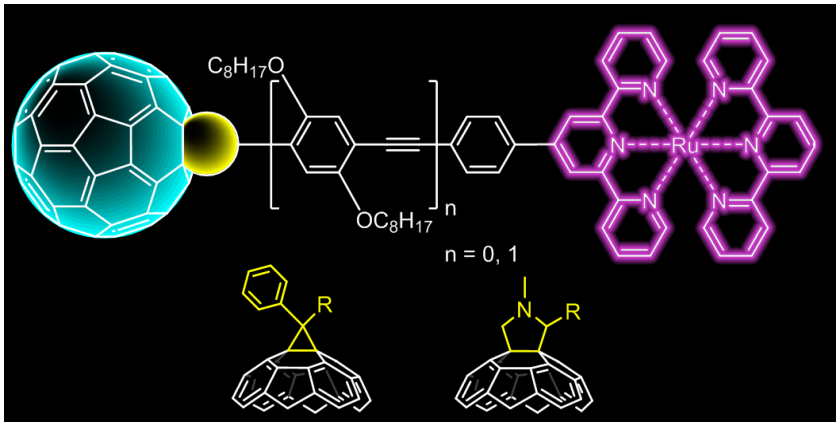

The Supplementary Information can be downloaded at the publisher's site.

Inorganic Chemistry

Article

pubs.acs.org/IC

New Ruthenium Bis(terpyridine) Methanofullerene and Pyrrolidinofullerene Complexes: Synthesis and Electrochemical and Photophysical Properties

Kevin Barthelmes,[†,‡,⊥] Joachim Kübel,[§,∥,⊥] Andreas Winter,[†,‡] Maria Wächtler,[§,∥] Christian Friebe,[†,‡] Benjamin Dietzek,*[,‡,§,∥] and Ulrich S. Schubert*[,†,‡]

[†]Laboratory of Organic and Macromolecular Chemistry (IOMC), Friedrich Schiller University Jena, Humboldtstraße 10, 07743 Jena, Germany

[‡]Jena Center for Soft Matter (JCSM), Friedrich Schiller University Jena, Philosophenweg 7, 07743 Jena, Germany

[§]Institute of Physical Chemistry (IPC) and Abbe Center of Photonics, Friedrich Schiller University Jena, Helmholtzweg 4, 07743 Jena, Germany

[∥]Leibniz Institute of Photonic Technology e.V. (IPHT), Albert-Einstein-Straße 9, 07745 Jena, Germany

Supporting Information

ABSTRACT: A series of terpyridine (tpy) methanofullerene and pyrrolidinofullerene dyads linked via *p*-phenylene or *p*-phenyleneethynylenephenylene (PEP) units is presented. The coordination to ruthenium(II) yields donor−bridge−acceptor assemblies with different lengths. Cyclic voltammetry and UV−vis and luminescence spectroscopy are applied to study the electronic interactions between the active moieties. It is shown that, upon light excitation of the ruthenium(II)-based ^{1}MLCT transition, the formed ^{3}MLCT state is readily quenched in the presence of C_{60}. The photoinduced dynamics have been studied by transient absorption spectroscopy, which reveals fast depopulation of the ^{3}MLCT (73−406 ps). As a consequence, energy transfer occurs, populating a long-lived triplet state, which could be assigned to the $^3C_{60}$* state.

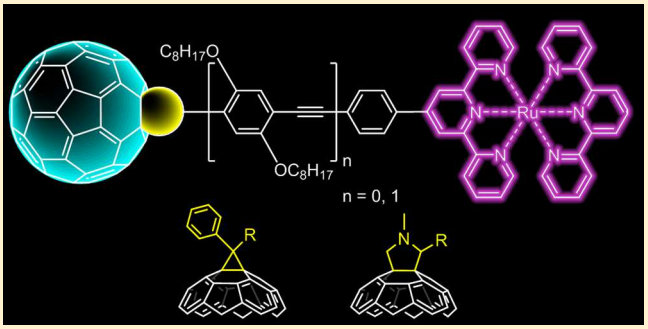

INTRODUCTION

The development of artificial devices that mimic light-triggered reactions in natural photosynthetic systems, which are based on the fundamental processes of energy and/or electron transfer, has become an attractive field in modern science and technology.[1−10] A general challenge in the molecular design of donor−bridge−acceptor systems is the generation of long-lived charge-separated (CS) states.[8,11,12] Fullerenes, in particular C_{60}, have high electron affinities, which make them favorable systems regarding their electron-accepting ability. Photoinduced electron transfer and energy transfer in (macro)-molecular assemblies containing donors, such as ferrocene,[13,14] porphyrin,[15] tetrathiafulvalene,[16,17] and others,[18,19] which are covalently linked to fullerene, were extensively studied; their electrochemical and photophysical properties are of particular interest.[20,21] Ruthenium(II) polypyridyl complexes as donors are promising materials due to their intense light absorption in the visible range and extended excited-state lifetimes.[22−24] Previous studies on Ru(II)−polypyridine−C_{60} assemblies showed that both electron and energy transfer is possible in such systems: the intermediate CS state may undergo charge recombination to the final lower lying triplet excited $^3C_{60}$* state.[25−30] Furthermore, the linker plays a crucial role in the electronic communication between the donor and acceptor parts. Several wirelike bridging units have been studied in recent years, including π-conjugated oligomers consisting of phenyleneethynylenes,[16,26] phenylenevinylenes,[31] and fluorene units[13,17] and nonconjugated oligomers consisting of glycol,[32,33] cyclohexane,[28] and peptide units.[34]

In this work, we report the investigation of new donor−acceptor systems, in which Ru(II) bis(terpyridine) complexes are connected to C_{60}. The series contains short phenyl-bridged as well as longer octyloxy-substituted phenyleneethynylenephenylene-bridged systems (Figure 1). These were chosen for their rigidity and π conjugation with low attenuation factors β,[35] which provide pathways for an efficient charge transport. Photophysical studies of these bridging units, especially in ruthenium(II) bis(terpyridine) complexes, have been thoroughly described by us previously.[36−39] This latter concept was further extended for the functionalization on C_{60} by cycloaddition reactions of 1,3-dipolar reagents with one [6,6]-double bond to form pyrrolidine or cyclopropane monoadducts. Martín and co-workers could show that cyclopropane adducts

Received: October 7, 2014
Published: March 12, 2015

DOI: 10.1021/ic502431x
Inorg. Chem. 2015, 54, 3159−3171

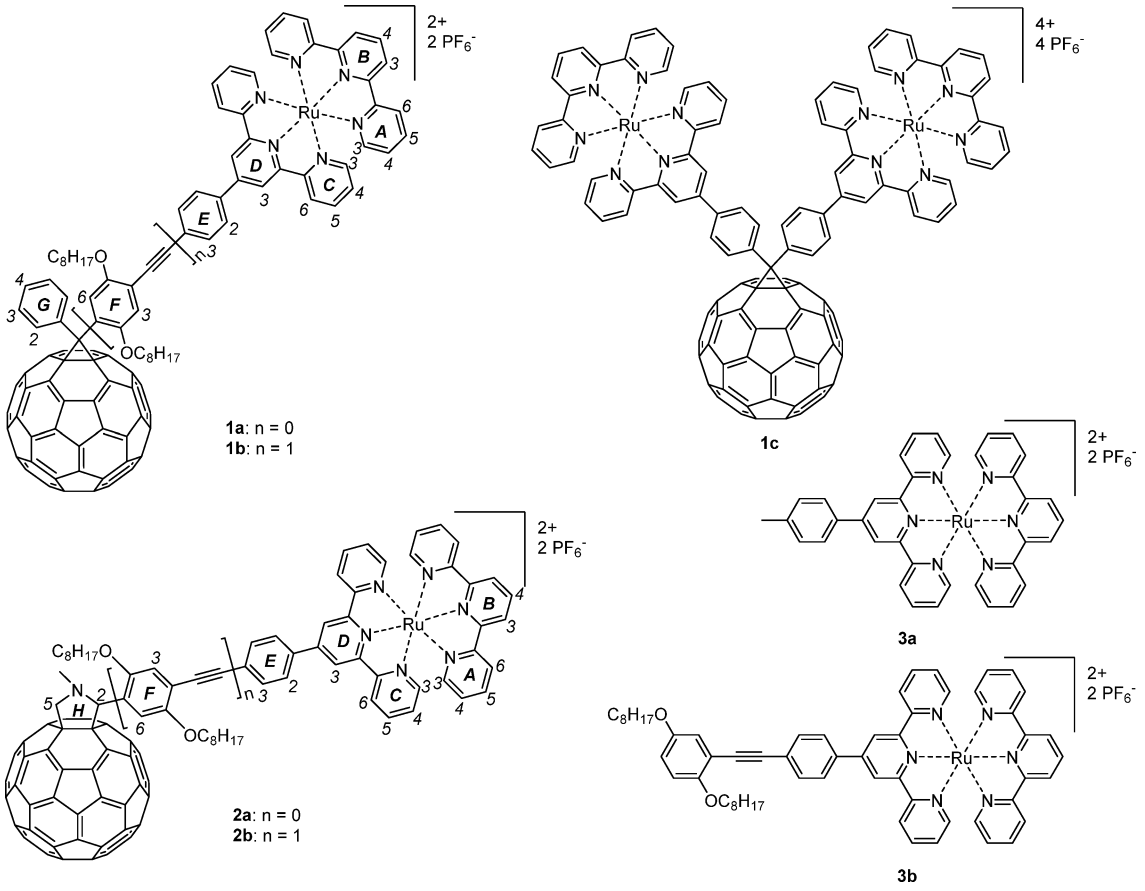

Figure 1. Schematic representations of the Ru(II)−bis(terpyridine)−C_{60} assemblies **1** and **2** as well as reference compounds **3** studied in this work, along with a numbering scheme for the complexes and precursors.

Scheme 1. Schematic Representation of the Synthetic Route[a]

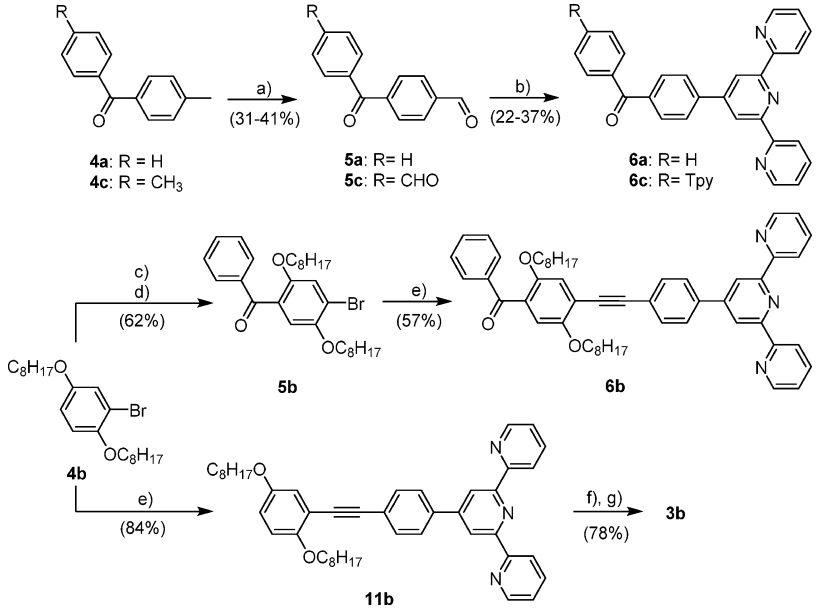

[a]Legend: (a) CrO_3, H_2SO_4, acetic anhydride, room temperature, 16 h; (b) (i) 2-acetylpyridine, NaOH, grinding, room temperature, 30 min, (ii) ammonia (aqueous), EtOH, room temperature, 48 h; (c) benzoyl chloride, $AlCl_3$, dichloromethane, room temperature, 16 h; (d) 1-bromooctane, KOH, DMSO, room temperature, 22 h; (e) 4′-(4-ethynylphenyl)-2,2′:6′,2″-terpyridine, $[Pd(PPh_3)_4]$, CuI, NEt_3, THF, 60 °C, 48−72 h; (f) $[Ru(tpy)Cl_3]$, $AgBF_4$, acetone, 70 °C, 2 h; (g) (i) DMF, 160 °C, 3 h, (ii) excess NH_4PF_6.

generally enhance the electronic communication between fluorene and C_{60} in comparison to pyrrolidine rings.[40] In addition to the mononuclear complexes **1a**,**b** and **2a**,**b**, we report the symmetrical dinuclear complex **1c**, bearing two

DOI: 10.1021/ic502431x
Inorg. Chem. 2015, 54, 3159−3171

Scheme 2. Schematic Representation of the Synthetic Route toward the Studied Ru(II) Complexes 1a−c and 2a,b[a]

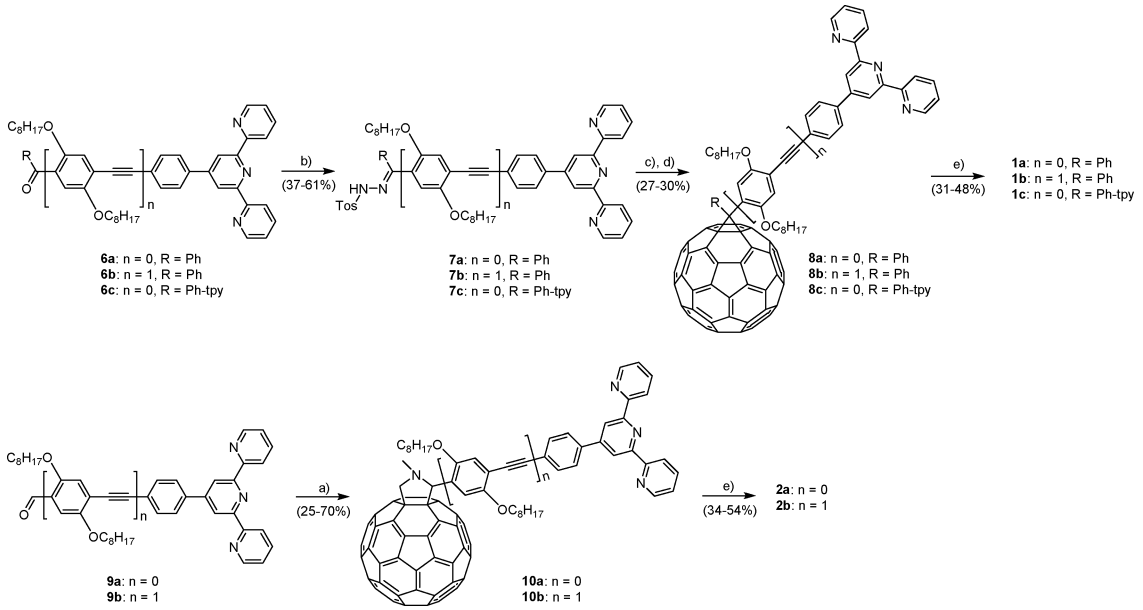

[a]Legend: (a) C_{60}, *N*-methylglycine, toluene, 120 °C, 24 h; (b) tosylhydrazine, tosylic acid, THF, 80 °C, 2−5 days; (c) $NaOCH_3$, pyridine, room temperature, 20 min; (d) C_{60}, *o*-dichlorobenzene, 180 °C, 24 h; (e) $[Ru(tpy)(MeCN)_3](PF_6)_2$, DMF, 140 °C, microwave, 30 min.

Table 1. Electrochemical Data Obtained by Cyclic Voltammetry[a]

	$E_{1/2,ox}$(Ru and/or irr P)/V	$E_{1/2,red}$(C_{60},1)/V	$E_{1/2,red}$(C_{60},2)/V	$E_{1/2,red}$(tpy,1)/V	$E_{1/2,red}$(C_{60},3 and/or tpy,2)/V
C_{60}[b]		−1.00	−1.39		−1.86
8a		−1.11	−1.49		−1.98
8b		−1.14	−1.52		−2.02
8c		−1.11	−1.48		−1.98
10a	+0.99[c]	−1.15	−1.51		−2.03
10b	+0.92[c]	−1.13	−1.53		*e*
1a	+0.91	−1.09	−1.45	−1.68	*e*
1b	+0.89	−1.12	−1.49	−1.65	*e*
1c	+0.92	−1.08	−1.46	−1.66	*e*
2a	+0.90[d]	−1.11	−1.50	−1.65	*e*
2b	+0.90[d]	−1.14	−1.50	−1.63	*e*
3a	+0.91			−1.63	−1.95
3b	+0.89			−1.59	−1.95

[a]Conditions: potentials referenced to Fc^+/Fc; scan rate 200 mV s^{-1}; glassy-carbon-disk working electrode; AgCl/Ag reference electrode; Pt-rod counter electrode; 0.1 M Bu_4NPF_6 in dichloromethane. [b]Taken from ref 68. [c]Irreversible process. The peak potential is shown. [d]Two processes. [e]Not detectable.

bis(terpyridine) ruthenium(II) centers and one C_{60} unit. The major aim of these studies is to figure out the influence of the length of the linker as well as the way the linker is connected to the C_{60} on the electrochemical and photophysical properties of the new compounds.

RESULTS AND DISCUSSION

Synthesis. The synthetic routes are depicted in Schemes 1 and 2. The benzophenone building blocks with rigid phenyl units as spacers were synthesized in a two-step reaction. Starting from para-substituted methylbenzophenones **4a,c**, the oxidation with chromium(VI) oxide yielded the desired mono- and bis-formylated[41] compounds **5a,c**, respectively. The terpyridine fragments **6a** and **6c** were prepared according to a modified Kröhnke-type procedure reported previously.[42] By grinding the starting material **5a** or **5c**, 2-acetylpyridine, and NaOH, the diketone intermediate can be prepared under these solvent-free conditions in 30 min. When the bridge length was increased, octyloxy chains were introduced to improve the solubility. For this purpose, the starting material **4b** was synthesized according to literature procedures.[43] Compound **5b** was prepared by Friedel−Crafts acylation with benzoyl chloride (during the reaction, one octyl group was cleaved off and reintroduced by alkylation). A Sonogashira cross-coupling reaction with 4′-(4-ethynylphenyl)-2,2′:6′,2″-terpyridine was applied to prepare **6b**.[44] The reference ligand **11b** was synthesized in good yield by an analogous route. The respective methanofullerenes **8a,b** as well as the symmetrical bis(terpyridine)−C_{60} compound **8c** were obtained in a three-step reaction. First, the terpyridine-functionalized benzophenones **6a−c** were reacted with tosylhydrazine and catalytic amounts of tosylic acid to yield the desired tosyl hydrazone derivatives **7a−c**. Elimination of the tosyl group with sodium methoxide by a mechanism analogous to the Bamford−Stevens

DOI: 10.1021/ic502431x
Inorg. Chem. 2015, 54, 3159−3171

reaction yielded in situ the 1,3-dipolar diazo compounds, which reacted with C_{60} to form pyrazolinofullerene derivates as intermediates.[45,46] Further thermal treatment eliminated molecular nitrogen, and the desired methanofullerenes were obtained in low to moderate yields. Recently, we reported the synthesis of the aldehyde-functionalized 2,2′:6′,2″-terpyridines **9a**,**b** used in this study.[47,48] Pyrrolidinofullerenes **10a**,**b** were synthesized by the 1,3-dipolar cycloaddition of azomethine ylides, derived from **9a**,**b**, respectively, and *N*-methylglycine to C_{60} in an optimized 1:10:4 ratio.[49] The compounds were obtained in low to good yields, respectively, mainly due to the enhanced solubility of **9b**. All fullerene ligands were purified by column chromatography using neutral alumina and *n*-hexane/toluene mixtures to remove and recover the unreacted C_{60}. $[Ru(tpy)(MeCN)_3](PF_6)_2$ was used as a precursor to obtain the corresponding heteroleptic ruthenium(II) complexes **1a**−**c** and **2a**,**b** in moderate yields. The reaction was performed under microwave irradiation for 30 min at 140 °C in DMF. Since column chromatography using silica with potassium nitrate was not applicable for these C_{60}-containing complexes, the dark red complexes were purified by treatment of a concentrated acetonitrile solution with diethyl ether vapor to force slow precipitation. So far, we have not been able to obtain single crystals suitable for X-ray structure analysis. The reference ligands 4′-(4-methylphenyl)-2,2′:6′,2″-terpyridine (ttpy) and **11b** were coordinated to ruthenium by standard complexation procedures in ethanol[50,51] or DMF.[52] All complexes exhibited a good solubility in polar solvents, such as acetonitrile, and have been characterized by NMR spectroscopy, mass spectrometry, and elemental analysis.

Electrochemical Properties. The redox behavior of the complexes **1a**−**c** and **2a**,**b**, the ligands **8a**−**c** and **10a**,**b**, and the references **3a**,**b** was studied by cyclic voltammetry. The data are summarized in Table 1, and representative spectra are depicted in Figure 2. The electrochemical measurements were performed in dichloromethane at room temperature with Bu_4NPF_6 as the conducting salt. For complexes **1a**−**c** and **2a**,**b**, the first oxidation wave at ca. 0.9 V arises from the reversible Ru(III)/Ru(II) redox couple. In addition, for the ligands **10a**,**b**, a second, irreversible oxidation, which is overlaid by the ruthenium oxidation in **2a**,**b**, was observed. This process is attributed to the electrochemical retrocycloaddition of the pyrrolidinofullerene fragment.[53] There is no significant difference for the Ru(III)/Ru(II) redox potentials within the series (and also in comparison to the reference complexes **3a**,**b**), indicating the negligible influence of the ligand sphere on the energy of the highest occupied molecular orbital. Within the accessible potential window, all fullerene-containing compounds of the series feature three reversible C_{60}-based reduction waves of similar redox potentials at around −1.1, −1.5, and −2.0 V. The half-wave potentials are shifted cathodically in comparison to pristine C_{60}. This can be attributed to the attached pyrrolidine and cyclopropane units, causing a disruption of π conjugation and a decreased electron affinity of C_{60}.[54] As reported elsewhere,[40] the values for the C_{60} reductions are slightly cathodically shifted (around 20 mV) on comparison of pyrrolidine to cyclopropane rings attached to C_{60}. Accordingly, electron delocalization is more efficient in the methanofullerene compounds. Another trend that holds true—at least for the first C_{60}-based reduction—is the cathodic shift on changing to larger bridge lengths. The third reduction wave at around −1.65 V of **1a**−**c** and **2a**,**b** is attributed to the first reduction of the terpyridine unit. The assignment is proven by comparison of the dinuclear complex **1c** to the parent mononuclear ruthenium complex **1a**. Apparently, the dinuclear complex shows similar values for the half-wave potentials but increased currents for the ruthenium- and terpyridine-related redox couples, while the C_{60}-based peak currents stay nearly constant (see Figure S3 in the Supporting Information). The second reduction of the terpyridine unit is in the same range as the third C_{60}-based reduction. According to the model complexes **3a**,**b**, the redox potential of the second terpyridine reduction is at ca. −1.95 V (see Figure S2 in the Supporting Information). In the methanofullerene ruthenium(II) complexes **1a**−**c** there is another irreversible process around −1.98 V (see Figure S4 in the Supporting Information). As is known from the literature, this process has to be assigned to the electrochemical retrocycloaddition of Bingel adducts.[55] However, this process can only be observed for the investigated complexes and is absent for the ligands **8a**−**c**.

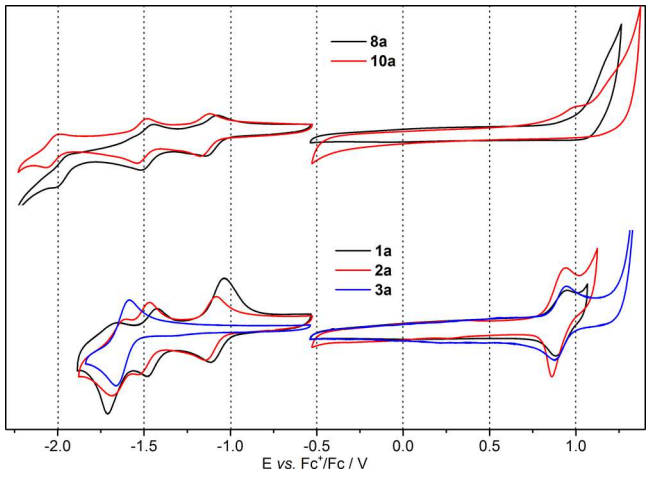

Figure 2. Cyclic voltammograms of phenyl-bridged methano- and pyrrolidinofullerene ligands and complexes in dichloromethane (with 0.1 M Bu_4NPF_6).

Photophysical Properties. The UV−vis absorption data are summarized in Table 2. A comparison of the UV−vis absorption spectra of C_{60}, **2b**, and **3b**, as shown in Figure 3, reveals that the spectrum of **2b** can be regarded as a superposition of the spectra of C_{60} and **3b**. In agreement

Table 2. UV−Vis Absorption Data[a]

	λ_{abs}/nm ($\varepsilon/10^3$ M^{-1} cm^{-1})[b]
C_{60}	405 (2.7), 329 (50.9), 258 (189.6)
8a	430 (2.6), 327 (46.0), 259 (150.0)
8b	430 (4.0), 328 (78.2), 259 (157.5)
8c	430 (3.1), 323 (61.4), 276 (sh, 172.9), 259 (195.5)
10a	430 (6.2), 317 (sh, 45.0), 271 (sh, 107.0), 256 (123.8)
10b	430 (10.3), 311 (87.4), 269 (sh, 126.5) 255 (149.0)
1a	484 (25.1), 327 (sh, 78.1), 310 (97.7), 270 (112.6)
1b	487 (31.6), 327 (sh, 83.9), 311 (107.2), 273 (105.4)
1c	484 (47.0), 326 (sh, 131.5), 310 (174.5), 273 (159.7)
2a	485 (22.8), 327 (sh, 59.3), 309 (83.7), 273 (85.8)
2b	488 (35.8), 327 (sh, 95.0), 311 (116.8), 270 (113.9)
3a	484 (23.4), 327 (sh, 43.4), 309 (77.5), 274 (49.3)
3b	487 (35.4), 326 (69.2), 310 (95.6), 274 (52.3)

[a]Measured in dichloromethane at 20 °C. [b]sh = shoulder.

DOI: 10.1021/ic502431x
Inorg. Chem. 2015, 54, 3159−3171

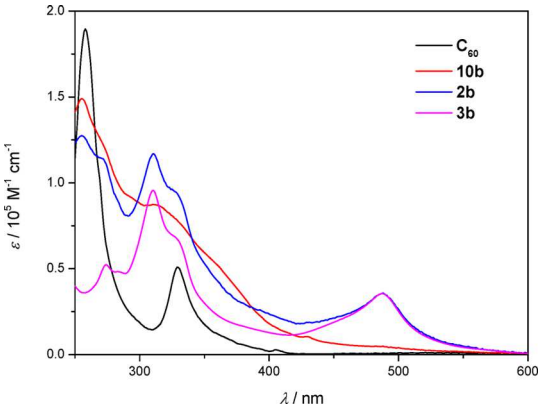

Figure 3. UV−vis absorption spectra of the long bridged pyrrolidinofullerene ligand and complexes measured in dichloromethane.

with the electrochemical measurements, there is no evidence for an electronic interaction between the Ru(II) center and the fullerene unit in the ground state. The spectral properties are similar throughout the series: while intense absorption bands between 250 and 350 nm are based on $\pi-\pi^*$ transitions within the fullerene, phenyl, and terpyridine groups, absorption bands in the region around 485 nm are related to Ru(II)-based metal-to-ligand charge-transfer (MLCT) transitions.[56] With an increased bridge length in compounds **1b** and **2b**, the additional phenylene and ethynylene groups cause a slight bathochromic shift of the $\pi-\pi^*$ transitions. An analogous behavior is observed for the MLCT transition (shift of around 3 nm), in concert with increases in the molar extinction coefficients. The fullerene ligands **8a−c** and **10a,b** possess a sharp absorption band at around 430 nm, which is bathochromically shifted in comparison to pristine C_{60} (405 nm). This transition is characteristic of closed-[6,6] fullerene monoadducts.[57,58] In the complexes, this transition is only weakly defined, because it is overlaid by the tail of the strong MLCT transition. The emission properties of **8a−c** and **10a,b** were studied in dichloromethane and compared to the reference systems ttpy and **11b**. Upon excitation of the $\pi-\pi^*$ transition (λ_{ex} = 315 or 325 nm), there is a strong quenching of the spacer- and terpyridine-based fluorescence by a factor of ca. 200 when the C_{60} unit is attached (for details, see the Supporting Information). Additionally, the fullerene-based fluorescence at ca. 700 nm is only weakly pronounced.[13] The initially weak Ru(II)-based emission at room temperature of the reference complexes (**3a**, λ_{max} = 627 nm; **3b**, λ_{max} = 645 nm) is almost fully quenched in complexes **1a−c** and **2a,b** (Figure 4). The quenching indicates an electronic interaction between the ^{3}MLCT state and the fullerene unit, as detailed below.

Photoinduced Dynamics. *Formation of the Long-Lived Excited State.* The photoinduced dynamics occurring after excitation of the ^{1}MLCT transition (λ_{exc} = 520 nm) were investigated using transient absorption (TA) spectroscopy in order to clarify the quenching mechanism. To provide consistency with the steady-state data, we will focus on the TA experiments performed in dichloromethane. Figure 5 contains transient absorption data for **2b** and for the C_{60}-free complex **3b**, as reference. The transient absorption spectra recorded for **3b** (Figure 5A) match those of typical Ru^{II} polypyridine complexes featuring ground-state bleach (GSB) in the region of the ^{1}MLCT absorption band and excited-state absorption (ESA) above 550 nm. The electronic delocalization of the ^{3}MLCT state over the extended ligand is apparent: the ESA maximum of **3a**, where ^{3}MLCT delocalization is limited to the ttpy ligand, is at ca. 560 nm in acetonitrile (see the Supporting Information). However, for **3b** the ESA maximum is located at ca. 690 nm, clearly indicating the presence of an extended π system.[59] This was also noted for related methoxyphenyl-substituted $[Ru(bpy)_3]^{2+}$ derivatives.[26] The kinetic traces (Figure 5B) illustrate that the signal decay is not completely resolved, at least within the time scale of the experiment. However, this decay likely corresponds to the decay of the ^{3}MLCT (see below).

The quantitative interpretation of the TA data is based on global multiexponential fits corresponding to a kinetic scheme involving consecutive first-order reactions (details are given in the Experimental Section). In the case of **3b**, four kinetic components are used to fit the data. The decay-associated spectra (DAS) and the corresponding characteristic time constants are given in Figure 6. The DAS (τ_4 = 1.6 ns) features a much higher amplitude than the other DAS: i.e., it plays a dominant role in the photoinduced dynamics of **3b**. The DAS (τ_4) reflects the shape of the TA spectra recorded at long delay times, indicating that τ_4 describes the decay of the

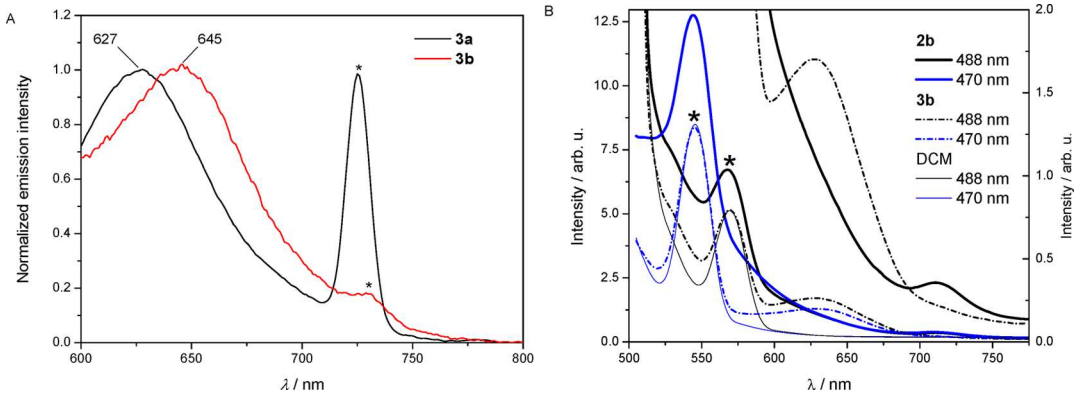

Figure 4. (A) Normalized emission spectra (λ_{ex} = 483 or 488 nm) of the reference complexes **3a,b** measured in dichloromethane at room temperature. Asterisks mark the scattered excitation light. (B) Emission spectra of isoabsorbing solutions at 487 nm of **3b** and **2b** in dichloromethane together with the signal obtained from the pure solvent. The right scale shows a magnification of the spectral region containing ^{3}MLCT phosphorescence and C_{60} fluorescence (solvent and spectra recorded at 470 nm are omitted for clarity).

DOI: 10.1021/ic502431x
Inorg. Chem. 2015, 54, 3159−3171

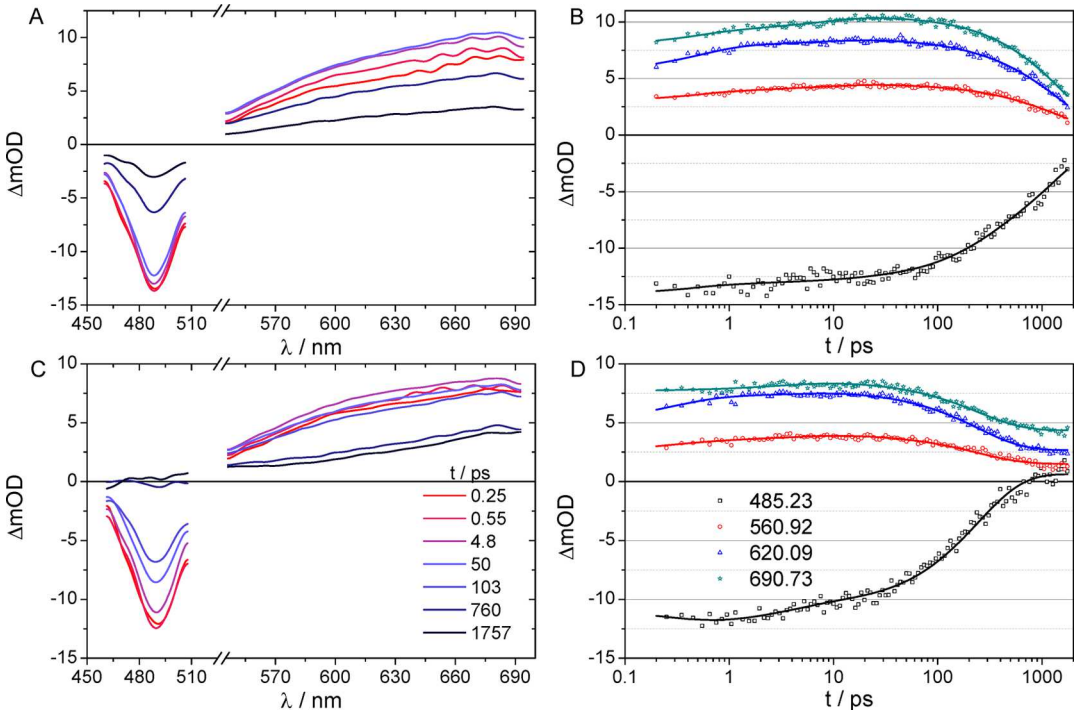

Figure 5. Transient absorption spectra (A, C) at selected delay times between 0.2 and 1.8 ns (from red to black) and selected kinetic traces (B, D) with corresponding fit curves: 488 nm (black squares), 560 nm (red circles), 620 nm (blue triangles), and 690 nm (cyan stars) for **3b** (A, B) and **2b** (C, D).

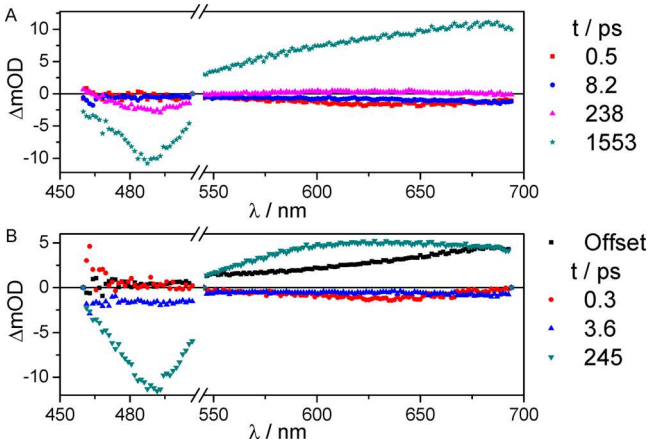

Figure 6. Global fit results in terms of decay-associated spectra for **3b** (A) and **2b** (B). The characteristic time constants are given in the legends.

^{3}MLCT and, thus, the overall decay to the ground state. This is also supported by the emission decay time of **3b** (2.3 ns in acetonitrile), determined by time-correlated single-photon counting (see the Supporting Information). This value can be compared to the 1.6 ns decay time determined in the TA experiments, as in the latter decay time there is a relatively large uncertainty due to the limited delay time range (1.8 ns) accessible in our experimental setup.

The fastest component (τ_1 = 0.5 ps) is assigned to solvent relaxation and vibrational energy dissipation[60,61] and causes an increase of the ESA between 550 and 700 nm. Generally, the picosecond components (τ_2 = 8.2 ps, τ_3 = 238 ps) can be attributed to the presence of the organic chromophore attached at the 4′-position of the tpy unit:[62] Here, the process associated with τ_2 is assigned to photoinduced planarization of the extended terpyridine ligand: i.e., excited-state torsional motion around the pyridine−phenyl bond.[63] Planarization causes an increase in the ESA in the visible part of the spectrum due to an enhanced π conjugation of the ligand. DFT calculations on **3b** suggest a strong mixing of ^{3}MLCT states with ligand-centered orbitals (see the Supporting Information) leading to delocalized states with different amounts of ^{3}MLCT and ^{3}LC character. Therefore, τ_3 (238 ps) has to be assigned to an equilibration between close-lying, mixed triplet states.[39,64]

Dyad **2b** shows transient absorption features similar to those observed for **3b** at early delay times (see Figure 5A,B). Both the spectra and the kinetic traces are similar up to 30 ps. Later, in **2b** a more pronounced decay is observed, which is not complete: i.e., the kinetic traces reach a plateau after ca. 1 ns. The transient absorption spectra at delay times >1.5 ns are positive over the entire spectral range probed in our experiment, including a rise toward 700 nm. Thus, the nanosecond dynamics of **2b** are clearly different from those of **3b**, leading to the formation of a long-lived species unique for the dyad. The global fit routine produces three kinetic components and an offset corresponding to the spectrum of the long-lived species formed. The nature of this species will be discussed in conjunction with results of nanosecond transient absorption experiments. The sub-picosecond component (τ_1 = 0.3 ps) is similar to the fastest process observed for **3b** and can be rationalized equivalently. The picosecond processes, i.e. the processes associated with τ_2 and τ_3, are accelerated in **2b** in comparison to those in **3b**. In detail, a process with τ_2 = 3.6 ps shows spectral characteristics similar to those of the equilibration process (τ_3) observed in **3b**. The time constant τ_3 = 245 ps of **2b** is identical with the value of τ_3 of **3b** (238 ps), but the corresponding DAS (τ_3) in the case of **2b** is basically identical with the DAS (τ_4) of **3b** describing the overall decay, as discussed above. Therefore, the depopulation of the ^{3}MLCT

DOI: 10.1021/ic502431x
Inorg. Chem. 2015, 54, 3159−3171

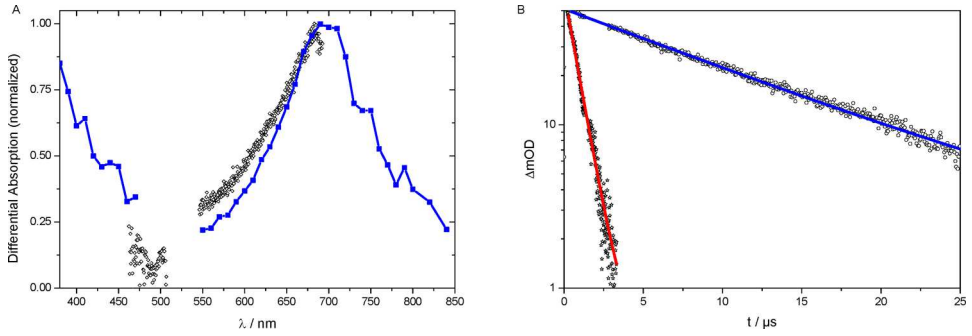

Figure 7. Nanosecond transient absorption data of **2b** in dichloromethane: (A) absorption spectra of the long-lived species constructed from integrated intervals of nanosecond transient absorption kinetics (blue solid squares) with the offset component from the femtosecond TA data (black hollow symbols) for comparison; (B) decay of the positive absorption at λ = 700 nm after photoexcitation of **2b** at 520 nm in aerated (solid stars) and deaerated (hollow spheres) solutions with respective fit curves for τ = 800 ns (red curve) and τ = 13 μs (blue curve).

(or rather a mixed ^{3}MLCT/π–π*) state occurs very quickly for **2b** with the same time constant that was assigned to excited-state equilibration in **3b**. Given the fact that the long-lived state in **2b** is due to the fullerene unit, the process that deactivates the ^{3}MLCT is the same process that populates the long-lived state (see below).

Nature of the Long-Lived Excited State. Nanosecond transient absorption experiments on **2b** (Figure 7) were conducted to detail the nature of the long-lived state: kinetic traces for the nano- to microsecond decay were recorded for selected wavelengths. From these curves, nanosecond transient absorption spectra were constructed. A broad absorption peak is found with a maximum at ca. 700 nm and steep flanks on both the high- and low-energy sides. A shoulder is observed at ca. 800 nm, and there are hints toward a rise at wavelengths shorter than 450 nm. The offset component determined from the femtosecond transient absorption data is in good agreement with the nanosecond transient absorption spectrum. Furthermore, the nanosecond spectrum coincides with the known absorption features of the $^3C_{60}$* state,[31] in particular the maximum at around 700 nm and the long-wavelength shoulder. Additional support for the assignment of the long-lived state as $^3C_{60}$* is based on oxygen-quenching experiments: Triplet states of organic molecules are prone to undergo quenching reactions with triplet oxygen, strongly reducing the excited-state lifetime.[65] From a comparison of kinetic traces of the ESA decay at 700 nm recorded in the presence and absence of oxygen (Figure 7B), it is taken that the lifetime significantly increases in the absence of oxygen, indicative of a triplet state. The lifetimes of 800 ns and 13 μs with and without oxygen, respectively, are consistent with literature reports on $^3C_{60}$*.[31]

Three possible quenching mechanisms leading to the $^3C_{60}$* state were discussed in the literature,[26] of which resonant triplet–triplet energy transfer (Förster-type) is unlikely to happen due to the weak acceptor absorption. Other possibilities are charge separation, i.e. a transport of the negative charge located on the ligand toward the fullerene after ^{1}MLCT excitation followed by a fast recombination, and Dexter-type energy transfer. The former would, however, yield a reduced C_{60} species, which would absorb in the NIR region at around 1100 nm.[31]

Solvent-polarity-dependent TA spectroscopy was performed to yield additional insight into the photoinduced processes and validate the absence of a photoinduced charge-transfer reaction. Therefore, additional TA measurements on **2b** and **3b** were performed in acetonitrile: despite the higher polarity of acetonitrile in comparison to dichloromethane, the data reveal almost identical spectral and temporal characteristics (see the Supporting Information). In particular, no significantly different time constants were found, ruling out the possibility that charge separation is contributing to the photophysics of **2b**. Similar observations are made for **2a**, i.e. the short-bridged analogue, as well as the methano-fullerene dyads **1a**,**b**, as the photoinduced dynamics probed in transient absorption experiments are rather similar for all of these compounds (see the Supporting Information). This holds true also for the dinuclear complex **1c**.

Nevertheless, the quenching kinetics are not identical for the compounds at hand. In fact, the rate constant for energy transfer measured in acetonitrile (corresponding to the process causing the ^{3}MLCT absorption characteristics to vanish) depends on both the linker type and the size of the bridge between terpyridine and fullerene moieties (see Figure 8). The

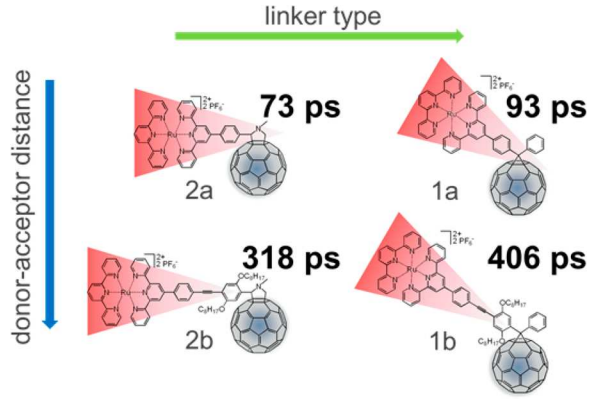

Figure 8. Schematic representation of the distance and linker dependence of the energy transfer (^{3}MLCT depopulation) rate.

fastest ^{3}MLCT deactivation (73 ps) is observed for the short-bridged pyrrolidinofullerene dyad **2a**. In **1a** the energy transfer is somewhat slower (93 ps), possibly due to the different angle of the complex fragment with respect to the fullerene surface. The larger bridge, increasing the donor–acceptor distance in the assemblies **1b** and **2b**, causes a significant prolongation of the energy transfer time.

The fact that **3b** and **2b** possess strongly delocalized ^{3}MLCT states involving orbitals of the organic chomophore indicates that orbital overlap with the fullerene unit might favor rapid Dexter-type energy transfer in the Ru(II)–C_{60} dyads. As soon as the extended ligand is planarized and electronic communi-

DOI: 10.1021/ic502431x
Inorg. Chem. 2015, 54, 3159–3171

cation between the metal center and the orbitals of the organic chromophore is enhanced, there is close spatial proximity with orbitals of the fullerene acceptor and an efficient deactivation pathway of the ^{3}MLCT is accessible.

CONCLUSION

A series of mono- and dinuclear ruthenium(II) bis(terpyridine) methanofullerene and pyrrolidinofullerene assemblies connected with phenylene and phenyleneethynylenphenylene units was synthesized. The key step of the synthetic route was the cycloaddition reaction of the terpyridine building blocks onto the fullerene unit. The complexes were compared to related reference compounds with regard to their electrochemical and photophysical properties. The methanofullerene compounds feature better electronic communication between the active units in comparison to pyrrolidinofullerenes, indicated by a small anodic shift of the C_{60}-based redox potentials. The ground-state absorption spectra are mainly a superposition of the individual moieties' characteristics, indicating weak interaction between the redox-active subunits in the ground state. However, steady-state emission spectroscopy revealed a strong interaction in the excited state: namely, by quenching of the ligand-based fluorescence and Ru(II)-based phosphorescence. Photoexcitation of the Ru(II)-based ^{1}MLCT transition results in a fast population of the lowest-lying triplet C_{60} state. A distance and linker dependence of the energy transfer rate was found. We believe that the photophysical and electrochemical properties of the presented complexes have a high potential in formation of light-induced charge-separated states for artificial photosynthetic devices, in particular when the assemblies are extended from dyads to triads by incorporation of lateral organic or organometallic donor entities. This is the topic of ongoing research.

EXPERIMENTAL SECTION

General Remarks. 2-Bromo-1,4-bis(octyloxy)benzene (**4b**),[43] 4′-(4-ethynylphenyl)-2,2′:6′,2″-terpyridine,[47] 2,5-bis(octyloxy)-4-(4-[2,2′:6′,2″]terpyridin-4′-ylphenylethynyl)benzaldehyde (**9b**),[47,48] bis-(4,4′-formyl)benzophenone (**5c**),[41] 4′-(4-formylphenyl)-2,2′:6′,2″-terpyridine (**9a**),[47] 4′-(4-methylphenyl)-2,2′:6′,2″-terpyridine (ttpy),[66] [Ru(tpy)Cl$_3$],[67] and [Ru(tpy)(MeCN)$_3$](PF$_6$)$_2$[50] were synthesized according to literature procedures. Dry toluene, THF, and dichloromethane were obtained from a Pure-Solv MD-4-EN solvent purification system (Innovative Technologies Inc.). Triethylamine was dried over KOH and distilled. All other chemicals were purchased from commercial suppliers and used as received. All reactions were performed in oven-dried flasks and were monitored by thin-layer chromatography (TLC) (silica gel on aluminum sheets with fluorescent dye F254, Merck KGaA). Microwave reactions were carried out using a Biotage Initiator Microwave synthesizer. NMR spectra were recorded on a Bruker AVANCE 250 MHz, AVANCE 300 MHz, or AVANCE 400 MHz instrument in deuterated solvents (Euriso-Top) at 25 °C. ^{1}H and ^{13}C resonances were assigned using appropriate 2D correlation spectra. Chemical shifts are reported in ppm using the solvent as internal standard. Matrix-assisted laser desorption ionization time of flight (MALDI-TOF) mass spectra were obtained using an Ultraflex III TOF/TOF mass spectrometer in reflector mode. High-resolution electrospray ionization time of flight mass spectrometry (ESI-Q-TOF MS) was performed on an ESI-(Q)-TOF-MS microTOF II (Bruker Daltonics) mass spectrometer. Melting points (mp) were determined on a Stuart SMP-3 apparatus. UV−vis absorption spectra were recorded on a PerkinElmer Lambda 750 UV/vis spectrophotometer and emission spectra on Jasco FP6500 and FP-6200 instruments, respectively. Measurements were carried out using 10^{-6} M solutions of the respective solvents (spectroscopy grade) in 1 cm quartz cuvettes at room temperature. However, some emission spectra were recorded using higher absorbances (ca. 0.2 in the maximum of the ^{1}MLCT band). Cyclic voltammetry measurements were performed on a Metrohm Autolab PGSTAT30 potentiostat with a standard three-electrode configuration using a glassy-carbon-disk working electrode, a platinum-rod auxiliary electrode, and a AgCl/Ag reference electrode; a scan rate of 200 mV s^{-1} was applied. The experiments were carried out in deaerated solvents (spectroscopy grade) containing 0.1 M Bu_4NPF_6 salt. At the end of each measurement, ferrocene was added as an internal standard.

Time-Resolved Spectroscopy. The femtosecond transient absorption measurements (λ_{exc} 520 nm) were performed on two different setups. Each setup is based on an amplified Ti:sapphire oscillator (800 nm, 1 kHz). One setup produces pulses of 35 fs at 3.5 mJ (Legend-Elite, Coherent Inc., used for measurements in acetonitrile) and the other setup 100 fs at 950 μJ (Libra, Coherent Inc., used for measurements in dichloromethane). Appropriate beam splitters split the pulses to attenuate the intensity to pump: in case of the former setup, a collinear optical-parametric amplifier (TOPAS-C, LightConversion Ltd.) with 1.35 W or, for the latter setup, a noncollinear optical-parametric amplifier (TOPASwhite, Lightconversion Ltd.) with 0.5 W. The pump pulses delayed in time with respect to the probe pulses by means of an optical delay line, and their polarization was rotated by 54.7° (magic angle) with respect to the probe beam by using a Berek compensator. For both setups white light was used as the probe, which was generated by focusing a minor fraction of the amplifier output into a sapphire plate. The probe beam is focused and recollimated using 50 cm (20 cm) spherical mirrors, while the focus of the pump beam is behind the sample in order to obtain a homogeneously excited sample volume. The pump pulse is blocked after the sample, while the probe pulse is sent to a double-stripe diode-array detection system (Pascher Instruments AB) together with the reference pulse. The pump pulse energy was typically adjusted to 1 μJ while the integrated probe intensity was a few hundred nanojoules. The sample solution (OD typically ca. 0.2 at the excitation wavelength) was kept in a 1 mm quartz cuvette. Prior to data analysis, the experimental differential absorption data was chirp corrected and afterward fitted globally.

The excited-state lifetimes were determined using a nanosecond transient absorption setup. Nanosecond pump pulses at 520 nm were delivered by a Continuum Surelite OPO Plus pumped by a Continuum Surelite Nd:YAG laser (pulse duration 5 ns; pulse to pulse repetition rate 10 Hz). A 75 W xenon arc lamp provided the probe light. Spherical concave mirrors were used to focus the probe light into the sample and to refocus the light on the entrance slit of a monochromator (Acton, Princeton Instruments). The probe light was detected by a Hamamatsu R928 photomultiplier tube mounted on a five-stage base at the monochromator exit slit, and the signal was processed by a commercially available detection system (Pascher Instruments AB). Some measurements were performed in oxygen-free solutions produced by performing several freeze−pump−thaw cycles. All measurements were performed in 1 cm fluorescence cuvettes, allowing a 90° angle between pump and probe beam.

4-Formylbenzophenone (5a). The oxidation of the terminal methyl group was performed according to a related literature procedure.[41] Concentrated sulfuric acid (6 mL, 113 mmol) was added dropwise to a stirred solution of 4-methylbenzophenone (**4a**; 3 g, 15.29 mmol) in acetic anhydride (30 mL) at 0 °C. To this was added a solution of chromium(VI) oxide (4.13 g, 41.3 mmol) in acetic anhydride (20 mL) dropwise at such a rate that the temperature did not exceed 10 °C. After all the chromium(VI) oxide was added, stirring was continued for a further 16 h at room temperature. Subsequently, the reaction mixture was added to an ice−water mixture (150 mL) and the solid was collected by filtration. Further material was extracted from the solution with diethyl ether (2 × 50 mL); the ethereal extracts were dried, and the solvent was evaporated. The combined solid products were washed with 2% aqueous sodium carbonate solution (1 × 50 mL) and then heated at reflux in ethanol/water/concentrated sulfuric acid (53 mL, 10/10/1) for 30 min. The solution was cooled to room temperature, the product was extracted with ethyl acetate (4 × 50 mL), the combined organic extracts were

DOI: 10.1021/ic502431x
Inorg. Chem. 2015, 54, 3159−3171

washed with saturated aqueous sodium hydrogen carbonate solution (2 × 50 mL) and dried with Na_2SO_4, and the solvent was evaporated to yield the crude product. Further purification was achieved by flash chromatography (silica, *n*-hexane/dichloromethane 1/3) to give a yellow solid (1 g, 4.76 mmol, 31%). Mp: 67−68 °C. ^{1}H NMR (300 MHz, $CDCl_3$, ppm): δ 10.13 (s, 1H, −C*H*O), 8.00 (d, ^3J = 8.4 Hz, 2H, H^{E3}), 7.92 (d, ^3J = 8.2 Hz, 2H, H^{E2}), 7.86−7.77 (m, 2H, H^{G2}), 7.63 (t, ^3J = 7.4 Hz, 1H, H^{G4}), 7.51 (t, ^3J = 7.5 Hz, 2H, H^{G3}). ^{13}C NMR (75 MHz, $CDCl_3$, ppm): δ 195.94, 191.75, 142.70, 138.61, 136.88, 133.26, 130.45, 130.24, 129.62, 128.67. Anal. Calcd for $C_{14}H_{10}O_2$: C, 79.98; H, 4.79. Found: C, 80.11; H, 4.87.

General Procedure for Kröhnke-Type Terpyridine Synthesis. 2-Acetylpyridine (2.2 equiv per aldehyde group), aldehyde derivate **5** (1 equiv), and sodium hydroxide (2.2 equiv per aldehyde group) were ground in a mortar until a bright yellow powder was formed (10−20 min). The solid was transferred to a flask, ethanol (10 mL) and 25% aqueous ammonia solution (5 mL) were added, and the suspension was stirred at room temperature for 48 h. The gray precipitate that formed was filtered and washed with water (15 mL) and ethanol (5 mL). The crude product was recrystallized in THF.

*4‴-[2,2′:6′,2″]Terpyridin-4′-ylbenzophenone (**6a**).* According to the general procedure for Kröhnke-type terpyridine synthesis, 2-acetylpyridine (0.38 g, 3.14 mmol), 4-formylbenzophenone (**5a**; 0.3 g, 1.427 mmol), and sodium hydroxide (0.126 g, 3.14 mmol) were reacted to yield a beige solid (217 mg, 0.525 mmol, 37%). Mp: 122 °C. ^{1}H NMR (300 MHz, $CDCl_3$, ppm): δ 8.78 (s, 2H, H^{D3}), 8.73 (d, ^3J = 4.7 Hz, 2H, H^{C6}), 8.68 (d, ^3J = 8.0 Hz, 2H, H^{C3}), 8.01 (d, ^3J = 8.4 Hz, 2H, H^{E3}), 7.94 (d, ^3J = 8.3 Hz, 2H, H^{E2}), 7.92−7.81 (m, 4H, H^{C4}, H^{G2}), 7.62 (t, ^3J = 7.4 Hz, 1H, H^{G4}), 7.52 (t, ^3J = 7.4 Hz, 2H, H^{G3}), 7.36 (ddd, ^3J = 7.3 Hz, ^3J = 4.8 Hz, ^4J = 0.9 Hz, 2H, H^{C5}). ^{13}C NMR (75 MHz, $CDCl_3$, ppm): δ 196.35, 156.27, 156.09, 149.28, 149.25, 142.58, 137.90, 137.66, 137.07, 132.71, 130.83, 130.20, 128.51, 127.41, 124.12, 121.52, 119.12. MS (MALDI-TOF, dithranol, *m*/*z*): 414.17, $C_{28}H_{20}N_3O$ ($[M + H]^+$) requires 414.16. Anal. Calcd for $C_{28}H_{19}N_3O\cdot H_2O$: C, 77.94; H, 4.91; N, 9.74. Found: C, 77.68; H, 4.81; N, 9.56. UV−vis (CH_2Cl_2): λ_{max}/nm (ε/L mol^{-1} cm^{-1}) 284 (57700).

*Bis(4‴,4⁗-[2,2′:6′,2″]terpyridin-4′-yl)benzophenone (**6c**).* According to the general procedure for Kröhnke-type terpyridine synthesis, 2-acetylpyridine (0.671 g, 5.54 mmol), bis(4,4′-formyl)-benzophenone (**5c**; 0.3 g, 1.26 mmol), and sodium hydroxide (0.222 g, 5.54 mmol) were reacted to yield a beige solid (180 mg, 0.279 mmol, 22%). Mp: >250 °C dec. ^{1}H NMR (300 MHz, $CDCl_3$, ppm): δ 8.80 (s, 4H, H^{D3}), 8.74 (d, ^3J = 4.1 Hz, 4H, H^{C6}), 8.69 (d, ^3J = 7.9 Hz, 4H, H^{C3}), 8.05 (d, ^3J = 8.3 Hz, 4H, H^{E3}), 7.99 (d, ^3J = 8.3 Hz, 4H, H^{E2}), 7.89 (td, ^3J = 7.8 Hz, ^4J = 1.3 Hz, 4H, H^{C4}), 7.37 (dd, ^3J = 6.6 Hz, ^3J = 5.2 Hz, 4H, H^{C5}). ^{13}C NMR (75 MHz, $CDCl_3$, ppm): δ 195.84, 156.33, 156.14, 149.34, 149.26, 142.79, 137.84, 137.07, 130.87, 127.54, 124.13, 121.54, 119.17. MS (MALDI-TOF, dithranol, *m*/*z*): 645.21, $C_{43}H_{29}N_6O$ ($[M + H]^+$) requires 645.24. Anal. Calcd for $C_{43}H_{28}N_6O \times 2\ H_2O$: C, 75.87; H, 4.74; N, 12.35. Found: C, 75.63; H, 4.87. N, 12.33. UV−vis (CH_2Cl_2): λ_{max}/nm (ε/L mol^{-1} cm^{-1}) 285 (68300).

*4-Bromo-2,5-bis(octyloxy)benzophenone (**5b**).* A solution of 2-bromo-1,4-bis(octyloxy)benzene (**4b**; 400 mg, 0.968 mmol) and benzoyl chloride (204 mg, 1.451 mmol) in dichloromethane (5 mL) was stirred at 0 °C under nitrogen, while a mixture of aluminum(III) trichloride (194 mg, 1.451 mmol) was slowly added. The solution was stirred overnight at room temperature before being poured onto iced 2 M HCl solution (50 mL). The dichloromethane layer was separated, and the aqueous phase was extracted with dichloromethane (3 × 30 mL). The combined organic layers were dried over Na_2SO_4, and the organic solvents were removed under reduced pressure. The solid residue was dissolved in dichloromethane (100 mL) and washed successively with 2 M sodium hydroxide solution (3 × 30 mL) and brine (50 mL) before the solution was dried and evaporated. The residue was purified by column chromatography (silica, *n*-hexane/dichloromethane 2/1) to yield a yellow viscous liquid (277 mg, 0.683 mmol, 71%). ^{1}H NMR indicated the formation of 4-bromo-5-hydroxy-2-octyloxybenzophenone by the loss of one octyloxy group during the reaction. The group was reintroduced according to the literature procedure. Therefore, KOH powder (190 mg, 3.38 mmol) was stirred in dried DMSO (6 mL) and the solution was deaerated. 4-Bromo-5-hydroxy-2-octyloxybenzophenone (274 mg, 0.676 mmol) in DMSO (1.5 mL) and 1-bromooctane (259 μL, 1.487 mmol) in DMSO (1.5 mL) were added. The mixture was stirred for 22 h at room temperature. The resulting solid was filtered off and dissolved in toluene (50 mL). The toluene solution was extracted with water (3 × 20 mL) and dried with Na_2SO_4, and the organic solvent was removed under reduced pressure. The residue was purified by column chromatography (silica, *n*-hexane/dichloromethane 1/1) to yield a low-melting white solid (312 mg, 0.603 mmol, 89%, 62% overall yield). Mp: 40 °C. ^{1}H NMR (300 MHz, CD_2Cl_2, ppm): δ 7.80−7.72 (m, 2H, H^{G2}), 7.60−7.52 (m, 1H, H^{G4}), 7.48−7.40 (m, 2H, H^{G3}), 7.22 (s, 1H, H^{F3}), 7.02 (s, 1H, H^{F6}), 4.00 (t, ^3J = 6.5 Hz, 2H, α-OCH_2), 3.80 (t, ^3J = 6.3 Hz, 2H, α-OCH_2), 1.89−1.75 (m, 2H, β-CH_2), 1.58−1.44 (m, 2H, β-CH_2), 1.44−1.05 (m, 20H, γ-η-CH_2), 1.04−0.84 (m, 6H, CH_3). ^{13}C NMR (75 MHz, CD_2Cl_2, ppm): δ 196.02, 151.70, 150.45, 138.83, 133.37, 129.92, 129.29, 128.79, 118.60, 115.96, 114.91, 70.71, 69.94, 32.45, 32.38, 29.91, 29.87, 29.81, 29.76, 29.69, 29.50, 26.59, 26.19, 23.30, 23.27, 14.52, 14.51. HRMS (ESI-TOF, *m*/*z*): 517.2300, $C_{29}H_{42}BrO_3$ ($[M + H]^+$) requires 517.2312.

General Procedure for Sonogashira Cross-Coupling Reactions. Copper(I) iodide (0.1−0.15 equiv) and $[Pd(PPh_3)_4]$ (0.1−0.15 equiv) were added to a deaerated solution of an aromatic bromine (1 equiv) in a mixture of THF (10 mL) and triethylamine (5 mL). With vigorous stirring, 4′-(4-ethynylphenyl)-2,2′:6′,2″-terpyridine (1.2 equiv) in THF (2 mL) was added. Subsequently, the reaction mixture was heated to 60 °C for 48−72 h. After the mixture was cooled to room temperature, the precipitated ammonia salt was filtered off and washed intensely with THF, and the solvent was removed under reduced pressure. Dichloromethane was added, and the solution was washed with saturated aqueous ammonium chloride/EDTA (1/1) solution and dried with Na_2SO_4. Further purification was achieved by column chromatography (neutral alumina, dichloromethane/*n*-hexane).

*2,5-Bis(octyloxy)-4-(4-[2,2′:6′,2″]terpyridin-4′-ylphenylethynyl)-benzophenone (**6b**).* According to the general procedure for Sonogashira cross-coupling reactions, copper(I) iodide (16.6 mg, 0.087 mmol), $[Pd(PPh_3)_4]$ (100 mg, 0.087 mmol), 4-bromo-2,5-bis(octyloxy)benzophenone (**5b**; 300 mg, 0.580 mmol), and 4′-(4-ethynylphenyl)-2,2′:6′,2″-terpyridine (232 mg, 0.696 mmol) were reacted for 72 h. Further purification was achieved by column chromatography (neutral alumina, dichloromethane/*n*-hexane 2/1) to yield an off-white solid (252 mg, 0.327 mmol, 57%). Mp: 110−112 °C. ^{1}H NMR (300 MHz, $CDCl_3$, ppm): δ 8.76 (s, 2H, H^{D3}), 8.74 (d, ^3J = 4.7 Hz, 2H, H^{C6}), 8.68 (d, ^3J = 7.9 Hz, 2H, H^{C3}), 7.93 (d, ^3J = 8.5 Hz, 2H, H^{E2}), 7.89 (td, ^3J = 7.7 Hz, ^4J = 1.7 Hz, 2H, H^{C4}), 7.82−7.77 (m, 2H, H^{G2}), 7.70 (d, ^3J = 8.4 Hz, 2H, H^{E3}), 7.55 (t, ^3J = 7.3 Hz, 1H, H^{G4}), 7.43 (t, ^3J = 7.5 Hz, 2H, H^{G3}), 7.36 (ddd, ^3J = 7.4 Hz, ^3J = 4.8 Hz, ^4J = 1.0 Hz, 2H, H^{C5}), 7.11 (s, 1H, H^{F3}), 7.01 (s, 1H, H^{F6}), 4.06 (t, ^3J = 6.4 Hz, 2H, OCH_2−), 3.84 (t, ^3J = 6.3 Hz, 2H, α-OCH_2), 1.93−1.80 (m, 2H, β-CH_2), 1.63−1.49 (m, 2H, β-CH_2), 1.46−0.93 (m, 20H, γ-η-CH_2), 0.93−0.81 (m, 6H, CH_3). ^{13}C NMR (75 MHz, $CDCl_3$, ppm): δ 196.32, 156.26, 156.19, 154.17, 150.81, 149.51, 149.27, 138.46, 138.41, 137.06, 132.90, 132.33, 130.00, 129.63, 128.29, 127.41, 124.23, 124.05, 121.52, 118.80, 117.27, 116.26, 113.99, 94.91, 87.21, 69.86, 69.27, 31.96, 31.88, 29.51, 29.48, 29.46, 29.29, 29.20, 29.07, 26.22, 25.75, 22.82, 22.77, 14.23, 14.23. HRMS (ESI-TOF, *m*/*z*): 792.4076, $C_{52}H_{55}N_3O_3Na$ ($[M + Na]^+$) requires 792.4136. Anal. Calcd for $C_{52}H_{55}N_3O_3$: C, 81.11; H, 7.20; N, 5.46. Found: C, 81.01; H, 7.30; N, 5.47. UV−vis (CH_2Cl_2): λ_{max}/nm (ε/L mol^{-1} cm^{-1}) 360 (31500), 303 (58000).

*4′-(4-((2,5-Bis(octyloxy)phenyl)ethynyl)phenyl)-2,2′:6′,2″-terpyridine (**11b**).* According to the general procedure for Sonogashira cross-coupling reactions, copper(I) iodide (9.5 mg, 0.050 mmol), $[Pd(PPh_3)_4]$ (0.058 g, 0.050 mmol), 2-bromo-1,4-bis(octyloxy)benzene (**4b**; 207 mg, 0.5 mmol), and 4′-(4-ethynylphenyl)-2,2′:6′,2″-terpyridine (200 mg, 0.600 mmol) were reacted for 48 h. Further purification was achieved by column chromatography (neutral alumina, dichloromethane/*n*-hexane 1/2, then 1/1) to yield a white

DOI: 10.1021/ic502431x
Inorg. Chem. 2015, 54, 3159−3171

solid (280 mg, 0.420 mmol, 84%). Mp: 65−67 °C. ^{1}H NMR (300 MHz, $CDCl_3$, ppm): δ 8.76 (s, 2H, H^{D3}), 8.73 (d, ^3J = 4.4 Hz, 2H, H^{C6}), 8.67 (d, ^3J = 8.0 Hz, 2H, H^{C3}), 7.95−7.83 (m, 4H, H^{E2}, H^{C4}), 7.67 (d, ^3J = 8.3 Hz, 2H, H^{E3}), 7.35 (ddd, ^3J = 7.5 Hz, ^3J = 4.8 Hz, ^4J = 1.2 Hz, 2H, H^{C5}), 7.06 (d, ^4J = 1.8 Hz, 1H, H^{F6}), 6.92−6.77 (m, 2H, H^{F4}, H^{F3}), 4.03 (t, ^3J = 6.4 Hz, 2H, α-OCH_2), 3.93 (t, ^3J = 6.5 Hz, 2H, α-OCH_2), 1.93−1.70 (m, 4H, β-CH_2), 1.63−1.20 (m, 20H, γ-η-CH_2), 0.98−0.78 (m, 6H, CH_3). ^{13}C NMR (75 MHz, $CDCl_3$, ppm): δ 156.3, 156.1, 154.4, 153.0, 149.6, 149.3, 138.0, 137.0, 132.2, 127.3, 124.7, 124.0, 121.5, 118.8, 118.5, 117.0, 114.3, 113.6, 93.1, 87.8, 70.0, 68.9, 32.99, 31.97, 29.6, 29.6, 29.5, 29.5, 29.4, 26.3, 26.2, 22.83, 22.81, 14.3. MS (MALDI-TOF, dithranol, m/z): 666.42, $C_{45}H_{52}N_3O_2$ ([M + H]$^+$) requires 666.41. Anal. Calcd for $C_{45}H_{51}N_3O_2$: C, 81.17; H, 7.72; N, 6.31. Found: C, 81.15; H, 8.07; N, 6.47. UV−vis (CH_2Cl_2): λ_{max}/nm (ε/L mol^{-1} cm^{-1}) 338 (27400), 292 (44300) nm.

General Procedure for Hydrazone Condensation Synthesis. A two-neck flask was loaded with benzophenone derivate **6** (1 equiv), *p*-toluenesulfonyl hydrazide (2 equiv), tosylic acid monohydrate (0.05 equiv), and THF or toluene and the mixture heated to reflux for 48 h under nitrogen. After the mixture was cooled to room temperature, the solvent was evaporated and the residue further purified by column chromatography (neutral alumina, chloroform/ethyl acetate 95/5). When applicable, deviations from this general protocol are given below.

*[2,2′:6′,2″]Terpyridin-4′-ylbenzophenone p-Tosyl Hydrazone (**7a**).* According to the general procedure for hydrazone condensation synthesis, 4‴-[2,2′:6′,2″]terpyridin-4′-yl-benzophenone (**6a**; 131 mg, 0.317 mmol), *p*-toluenesulfonyl hydrazide (118 mg, 0.634 mmol), and tosylic acid monohydrate (3 mg, 0.016 mmol) in toluene (10 mL) were reacted to yield a white solid (68 mg, 0.117 mmol, 37%). ^{1}H NMR suggests a mixture of *cis*- and *trans*-hydrazone isomers, which was used directly for the synthesis of **8a**. Mp: >240 °C dec. ^{1}H NMR (300 MHz, $CDCl_3$, ppm): δ 8.79−8.59 (m, 6H, H^{D3}, H^{C6}, H^{C3}), 7.98 (d, ^3J = 8.3 Hz, 1H, H^{E2}), 7.90 (d, ^3J = 8.2 Hz, 2H, Ar^{tosyl}-H), 7.92−7.75 (m, 4H, H^{C4}, H^{G2}), 7.59−7.46 (m, 4H, H^{E2}, H^{G3}, H^{G4}), 7.39−7.30 (m, 5H, NH, H^{C5}, Ar^{tosyl}-H), 7.29−7.24 (m, 1H, H^{E3}), 7.20−7.13 (m, 1H, H^{E3}), 2.43 (two singlets, 3H, Ar^{tosyl}-CH_3). ^{13}C NMR (75 MHz, $CDCl_3$, ppm): 156.27, 156.13, 156.07, 156.03, 153.92, 153.77, 149.41, 149.27, 149.20, 149.06, 144.42, 144.30, 140.54, 139.85, 137.14, 137.05, 136.48, 135.69, 135.59, 131.79, 131.06, 130.36, 130.09, 129.94, 129.85, 129.83, 129.17, 128.73, 128.46, 128.42, 128.26, 128.11, 128.09, 127.76, 127.24, 124.12, 124.02, 121.50, 119.01, 118.83, 21.77, 21.76. HRMS (ESI-TOF, m/z): 582.1903, $C_{35}H_{28}N_5O_2S$ ([M + H]$^+$) requires 582.1958. Anal. Calcd for $C_{35}H_{27}N_5O_2S{\cdot}H_2O$: C, 70.10; H, 4.87; N, 11.68; S, 5.35. Found: C, 69.93; H, 4.71; N, 11.32; S, 5.16.

*2,5-Bis(octyloxy)-4-(4-[2,2′:6′,2″]terpyridin-4′-yl-phenylethynyl)-benzophenone p-Tosyl Hydrazone (**7b**).* According to the general procedure for hydrazone condensation synthesis, 2,5-bis(octyloxy)-4-(4-[2,2′:6′,2″]terpyridin-4′-ylphenylethynyl)benzophenone (**6b**; 100 mg, 0.130 mmol), *p*-toluenesulfonyl hydrazide (48 mg, 0.260 mmol), and tosylic acid monohydrate (1.2 mg, 6.5 μmol) were reacted in THF (10 mL) for 11 days. The reaction was monitored by MALDI-TOF MS. After 6 days, additional *p*-toluenesulfonyl hydrazide (1 equiv) and tosylic acid monohydrate (0.1 equiv) were added. After purification by column chromatography (neutral alumina, chloroform) and recrystallization (*n*-hexane), a white solid (74 mg, 0.079 mmol, 61%) was obtained. ^{1}H NMR suggests a mixture of *cis*- and *trans*-hydrazone isomers, which was used directly for the synthesis of **8b**. Mp: 83 °C. ^{1}H NMR (300 MHz, $CDCl_3$, ppm): δ 8.81−8.65 (m, 6H, H^{D3}, H^{C6}, H^{C3}), 8.01−7.84 (m, 6H, Ar^{tosyl}-H, H^{E2}, H^{C4}), 7.77 (s, 1H, NH), 7.70 (d, ^3J = 8.4 Hz, 2H, H^{E3}), 7.57−7.47 (m, 2H, H^{G2}), 7.42−7.27 (m, 7H, H^{C5}, H^{G3}, H^{G4}, Ar^{tosyl}-H), 7.16 (s, 1H, H^{F3}), 6.51 (s, 1H, H^{F6}), 3.91 (t, ^3J = 6.4 Hz, 2H, α-OCH_2), 3.79 (t, ^3J = 6.3 Hz, 2H, α-OCH_2), 2.41 (s, 3H, Ar^{tosyl}−CH_3), 1.75−1.46 (m, 4H, β-CH_2), 1.46−0.93 (m, 20H, γ−η−CH_2), 0.95−0.78 (m, 6H, CH_3); ^{13}C NMR (75 MHz, $CDCl_3$, ppm): δ 156.26, 156.22, 154.69, 151.75, 149.48, 149.42, 149.28, 143.92, 138.56, 137.04, 136.66, 136.04, 132.35, 129.77, 129.68, 129.62, 129.18, 128.34, 128.32, 128.13, 127.53, 127.43, 127.37, 124.05, 121.64, 121.52, 118.79, 118.20, 115.91, 113.78, 94.86, 86.70, 69.85, 69.82, 32.00, 31.94, 31.84, 29.49, 29.44, 29.40, 29.26, 29.20, 28.93, 26.18, 25.65, 22.81, 22.76, 21.72, 14.23, 14.22. MS (MALDI-TOF, dithranol, m/z): 938.43, $C_{59}H_{64}N_5O_4S$ ([M + H]$^+$) requires 938.47.

*Bis(4‴,4′′′′-[2,2′:6′,2″]terpyridin-4′-yl)benzophenone p-Tosyl Hydrazone (**7c**).* According to the general procedure for hydrazone condensation synthesis, bis(4‴,4′′′′-[2,2′:6′,2″]terpyridin-4′-yl)-benzophenone (**6c**; 120 mg, 0.186 mmol), *p*-toluenesulfonyl hydrazide (69 mg, 0.372 mmol), and tosylic acid monohydrate (2 mg, 0.011 mmol) were reacted in toluene (10 mL) to yield a white solid (60 mg, 0.074 mmol, 40%). Mp >240 °C dec. ^{1}H NMR (300 MHz, $CDCl_3$, ppm): δ 8.79−8.61 (m, 12H, H^{D3}, H^{C6}, H^{C3}), 8.26−8.14 (m, 1H, NH), 8.02−7.94 (m, 4H, H^{E2}), 7.93−7.81 (m, 4H, H^{C4}), 7.77 (d, ^3J = 8.5 Hz, 2H, Ar^{tosyl}-H), 7.59 (d, ^3J = 8.4 Hz, 2H, Ar^{tosyl}-H), 7.44−7.28 (m, 8H, H^{E3}, H^{C5}), 2.45 (s, 3H, Ar^{tosyl}-CH_3). ^{13}C NMR (75 MHz, $CDCl_3$, ppm): δ 156.29, 156.13, 156.07, 153.32, 149.39, 149.30, 149.23, 149.08, 144.53, 140.68, 139.92, 137.07, 135.68, 131.60, 129.95, 129.28, 128.76, 128.35, 128.21, 127.30, 124.12, 124.03, 121.54, 121.50, 119.09, 118.87, 29.83; MS (MALDI-TOF, dithranol, m/z): 813.29, $C_{50}H_{37}N_8O_2S$ ([M + H]$^+$) requires 813.28.

General Procedure for Methanofullerene Synthesis. To a solution of the *p*-tosyl hydrazone derivate **7** (1 equiv) in anhydrous pyridine (3 mL) was added sodium methoxide (1.1 equiv) under a nitrogen atmosphere. After the mixture was stirred at room temperature for 15 min, a nitrogen-purged solution of C_{60} (3−4 equiv) in *o*-dichlorobenzene (15 mL) was added at once and the mixture was heated to 180 °C for 24 h. After it was cooled to room temperature, the reaction mixture was purified by column chromatography (neutral alumina, toluene/*n*-hexane 1/1) and precipitation in methanol.

*1-Phenyl-1-(4-[2,2′:6′,2″]terpyridin-4′-ylphenyl)methanofullerene (**8a**).* According to the general procedure for methanofullerene synthesis, [2,2′:6′,2″]terpyridin-4′-yl-benzophenone *p*-tosyl hydrazone (**7a**; 60 mg, 0.103 mmol), sodium methoxide (6 mg, 0.111 mmol), and C_{60} (276 mg, 0.383 mmol) were reacted to yield a brown solid (32 mg, 0.029 mmol, 28%). Mp: >360 °C. ^{1}H NMR (300 MHz, $CDCl_3$, ppm): δ 8.79 (s, 2H, H^{D3}), 8.73 (d, ^3J = 4.8 Hz, 2H, H^{C6}), 8.69 (d, ^3J = 7.9 Hz, 2H, H^{C3}), 8.27 (d, ^3J = 8.3 Hz, 2H, H^{E2}), 8.22−8.15 (m, 2H, H^{G2}), 8.02 (d, ^3J = 8.3 Hz, 2H, H^{E3}), 7.90 (td, ^3J = 7.8 Hz, ^4J = 1.8 Hz, 2H, H^{C4}), 7.53 (t, ^3J = 7.5 Hz, 2H, H^{G3}), 7.46−7.33 (m, 3H, H^{G4}, H^{C5}). MS (MALDI-TOF, negative mode, terthiophene, m/z): 1117.14, $C_{88}H_{19}N_3$ ([M + e]$^-$) requires 1117.16. Anal. Calcd for $C_{88}H_{19}N_3{\cdot}2.5H_2O{\cdot}3$(hexane): C, 89.55; H, 4.68; N, 2.96. Found: C, 89.57; H, 4.51; N, 3.01.

*1-Phenyl-1-(2,5-Bis(octyloxy)-4-(4-[2,2′:6′,2″]terpyridin-4′-ylphenylethynyl))methanofullerene (**8b**).* According to the general procedure for methanofullerene synthesis, 2,5-bis(octyloxy)-4-(4-[2,2′:6′,2″]terpyridin-4′-ylphenylethynyl)benzophenone *p*-tosyl hydrazone (**7b**; 57 mg, 0.061 mmol), sodium methoxide (4 mg, 0.074 mmol), and C_{60} (175 mg, 0.243 mmol) were reacted to yield a dark brown solid (24 mg, 0.016 mmol, 27%). Mp: 148 °C. ^{1}H NMR (300 MHz, $CDCl_3$, ppm): δ 8.76 (s, 2H, H^{D3}), 8.74 (d, ^3J = 4.8 Hz, 2H, H^{C6}), 8.68 (d, ^3J = 7.9 Hz, 2H, H^{C3}), 8.24 (d, ^3J = 7.1 Hz, 2H, H^{G2}), 7.96−7.82 (m, 4H, H^{E2}, H^{C4}), 7.68 (d, ^3J = 8.2 Hz, 2H, H^{E3}), 7.64 (s, 1H, H^{F6}), 7.50 (t, ^3J = 7.3 Hz, 2H, H^{G3}), 7.46−7.38 (m, 1H, H^{G4}), 7.36 (dd, ^3J = 6.8 Hz, ^3J = 5.4 Hz, 2H, H^{C5}), 7.18 (s, 1H, H^{F3}), 4.27−3.98 (m, 4H, α-OCH_2), 2.13−1.99 (m, 2H, β-CH_2), 1.93−1.78 (m, 2H, β-CH_2), 1.75−1.10 (m, 20H, γ-η-CH_2), 0.97−0.79 (m, 6H, CH_3). MS (MALDI-TOF, negative mode, terthiophene, m/z): 1473.38, $C_{112}H_{55}N_3O_2$ ([M + e]$^-$) requires 1473.43. Anal. Calcd for $C_{112}H_{55}N_3O_2{\cdot}8H_2O$: C, 83.10; H, 4.42%; N, 2.60. Found: C, 83.34; H, 4.47; N, 2.49.

*1,1-Bis(4-[2,2′:6′,2″]terpyridin-4′-ylphenyl)methanofullerene (**8c**).* According to the general procedure for methanofullerene synthesis, bis(4‴,4′′′′-[2,2′:6′,2″]terpyridin-4′-yl)benzophenone *p*-tosyl hydrazone (**7c**; 60 mg, 0.074 mmol), sodium methoxide (4 mg, 0.074 mmol), and C_{60} (227 mg, 0.315 mmol) were reacted to yield a brown solid (30 mg, 0.022 mmol, 30%). Mp: >360 °C. ^{1}H NMR (300 MHz, $CDCl_3$, ppm): δ 8.79 (s, 4H, H^{D3}), 8.73 (d, ^3J = 4.0 Hz, 4H, H^{C6}), 8.68 (d, ^3J = 8.0 Hz, 4H, H^{C3}), 8.31 (d, ^3J = 8.2 Hz, 4H, H^{E2}), 8.04 (d, ^3J = 8.2 Hz, 4H, H^{E3}), 7.88 (td, ^3J = 7.7 Hz, ^4J = 1.7 Hz, 4H, H^{C4}), 7.35 (ddd, ^3J = 7.4 Hz, ^3J = 4.8 Hz, ^4J = 0.9 Hz, 4H, H^{C5}). MS (MALDI-

DOI: 10.1021/ic502431x
Inorg. Chem. 2015, 54, 3159−3171

TOF, negative mode, terthiophene, m/z): 1348.23, $C_{103}H_{28}N_6$ ([M + e]$^-$) requires 1348.24. Anal. Calcd for $C_{103}H_{28}N_6{\cdot}4H_2O{\cdot}5$(hexane): C, 86.24; H, 5.77; N, 4.54. Found: C, 86.11; H, 5.48; N, 4.44.

*N-Methyl-2-(4-[2,2′:6′,2″]terpyridin-4′-ylphenyl)-pyrrolidinofullerene (**10a**).* A mixture of (4-formylphenyl)-2,2′:6′,2″-terpyridine (**9a**; 33 mg, 0.098 mmol), *N*-methylglycine (87 mg, 0.978 mmol), and C_{60} (282 mg, 0.391 mmol) in deaerated, anhydrous toluene (200 mL) was stirred at 120 °C for 24 h under a nitrogen atmosphere. After the mixture was cooled to room temperature, the solvent was evaporated. The crude product was purified by column chromatography (neutral alumina, toluene then chloroform), and slow vapor diffusion of diethyl ether into a concentrated solution yielded a brown solid (26.5 mg, 0.024 mmol, 25%). Mp: >360 °C. ^{1}H NMR (300 MHz, $CDCl_3$, ppm): δ 8.74 (s, 2H, H^{D3}), 8.72 (d, ^3J = 4.8 Hz, 2H, H^{C6}), 8.67 (d, ^3J = 7.9 Hz, 2H, H^{C3}), 8.00−7.93 (m, 4H, H^{E2}, H^{E3}), 7.87 (td, ^3J = 7.8 Hz, ^4J = 1.7 Hz, 2H, H^{C4}), 7.35 (ddd, ^3J = 7.5 Hz, ^3J = 4.8 Hz, ^4J = 1.1 Hz, 2H, H^{C5}), 5.02 (d, ^2J = 9.2 Hz, 1H, H^{H5}), 5.02 (s, 1H, H^{H2}), 4.30 (d, ^2J = 9.5 Hz, 1H, H^{H5}), 2.85 (s, 3H, NCH_3). MS (MALDI-TOF, negative mode, terthiophene, m/z): 1083.26, $C_{84}H_{19}N_4$ ([M − H]$^-$) requires 1083.16. Anal. Calcd for $C_{84}H_{20}N_4{\cdot}6H_2O$: C, 84.56; H, 2.70; N, 4.70. Found: C, 84.26; H, 2.44; N, 5.40.

*N-Methyl-2-(2,5-Bis(octyloxy)-4-(4-[2,2′:6′,2″]terpyridin-4′-ylphenylethynyl))pyrrolidinofullerene (**10b**).* A mixture of 2,5-bis-(octyloxy)-4-(4-[2,2′:6′,2″]-terpyridin-4′-ylphenylethynyl)-benzaldehyde (**9b**; 69 mg, 0.1 mmol), *N*-methylglycine (89 mg, 1.0 mmol), and C_{60} (144 mg, 0.2 mmol) in deaerated, anhydrous toluene (200 mL) was stirred at 120 °C for 24 h under a nitrogen atmosphere. After the mixture was cooled to room temperature, the solvent was evaporated. The crude product was purified by column chromatography (neutral alumina, *n*-hexane/toluene 3/1 then toluene) to yield a dark brown-black solid (101 mg, 0.07 mmol, 70%). Mp: 155 °C. ^{1}H NMR (400 MHz, CD_2Cl_2, ppm): δ 8.77 (s, 2H, H^{D3}), 8.71 (d, ^3J = 4.7 Hz, 2H, H^{C6}), 8.68 (d, ^3J = 7.9 Hz, 2H, H^{C3}), 7.93−7.86 (m, 4H, H^{E2}, H^{C4}), 7.67 (d, ^3J = 8.5 Hz, 2H, H^{E3}), 7.65 (s, 1H, H^{F5}), 7.37 (ddd, ^3J = 7.4 Hz, ^3J = 4.8 Hz, ^4J = 1.1 Hz, 2H, H^{C5}), 7.09 (s, 1H, H^{F2}), 5.58 (s, 1H, H^{H2}), 4.97 (d, ^2J = 9.4 Hz, 1H, H^{H5}), 4.33 (d, ^2J = 9.5 Hz, 1H, H^{H5}), 4.20 (dt, ^2J = 9.5 Hz, ^3J = 6.6 Hz, 1H, α-OCH_2), 4.10 (dt, ^2J = 9.6 Hz, ^3J = 6.4 Hz, 1H, α-OCH_2), 4.03 (dt, ^2J = 13.1 Hz, ^3J = 6.5 Hz, 1H, α-OCH_2), 3.74 (dt, ^2J = 8.6 Hz, ^3J = 6.5 Hz, 1H, α-OCH_2), 2.83 (s, 3H, NCH_3), 1.87−1.76 (m, 2H, β-CH_2), 1.73−1.49 (m, 6H, β-CH_2, γ-CH_2), 1.48−1.17 (m, 16H, δ-η-CH_2), 0.96−0.73 (m, 6H, CH_3). ^{13}C NMR (100 MHz, CD_2Cl_2, ppm): δ 157.34, 156.51, 156.39, 155.57, 154.70, 154.68, 154.36, 152.03, 149.59, 149.58, 147.66, 147.22, 147.15, 146.62, 146.60, 146.56, 146.47, 146.43, 146.41, 146.32, 146.31, 146.14, 145.99, 145.90, 145.66, 145.64, 145.60, 145.58, 145.54, 145.48, 144.97, 144.92, 144.85, 144.72, 143.40, 143.36, 143.03, 142.99, 142.91, 142.74, 142.70, 142.62, 142.57, 142.50, 142.49, 142.47, 142.34, 142.19, 142.10, 142.08, 140.50, 140.45, 139.97, 139.91, 137.24, 136.83, 136.76, 136.54, 135.09, 132.45, 128.24, 127.65, 124.72, 124.34, 121.50, 118.88, 116.49, 115.24, 113.12, 93.52, 88.23, 77.05, 76.00, 70.33, 70.17, 69.77, 69.21, 40.24, 32.35, 32.32, 30.11, 29.93, 29.90, 29.82, 29.74, 29.73, 29.67, 26.55, 26.48, 23.19, 23.14, 21.55, 14.40, 14.35. MS (MALDI-TOF, negative mode, terthiophene, m/z): 1440.42, $C_{108}H_{56}N_4O_2$ ([M + e]$^-$) requires 1440.44. Anal. Calcd for $C_{108}H_{56}N_4O_2{\cdot}0.5$(hexane): C, 89.79; H, 4.28; N, 3.77. Found: C, 89.78; H, 4.43; N, 3.83.

General Procedure for the Synthesis of Heteroleptic Ruthenium Bis(terpyridine) Complexes. A microwave vial was charged with [Ru(tpy)(MeCN)$_3$](PF$_6$)$_2$ (1 equiv per terpyridine group), terpyridine derivative (1 equiv), and DMF (3 mL). The vial was capped, purged with nitrogen for 20 min, and heated through microwave irradiation at 140 °C for 30 min. Subsequently, the solution was cooled to room temperature and the product was precipitated by addition of an aqueous ammonium hexafluorophosphate solution. The solid was collected by filtration, washed thoroughly with water and diethyl ether, and dissolved in acetonitrile. The solution was concentrated and treated with diethyl ether vapor to slowly precipitate the complex. When applicable, deviations from this general protocol are given below.

*[Ru(tpy)(**8a**)](PF$_6$)$_2$ (**1a**).* According to the general procedure for heteroleptic ruthenium bis(terpyridine) complexes, [Ru(tpy)(MeCN)$_3$](PF$_6$)$_2$ (6.4 mg, 8.5 μmol) and **8a** (9.4 mg, 8.4 μmol) were reacted to yield a dark red solid (6 mg, 3.4 μmol, 41%). ^{1}H NMR (400 MHz, CD_3CN, ppm): δ 9.02 (s, 2H, H^{D3}), 8.75 (d, ^3J = 8.2 Hz, 2H, H^{B3}), 8.69−8.57 (m, 4H, H^{E2}, H^{C3}), 8.48 (d, ^3J = 8.1 Hz, 2H, H^{A3}), 8.41 (t, ^3J = 8.1 Hz, 1H, H^{B4}), 8.35 (d, ^3J = 7.2 Hz, 4H, H^{G2}, H^{E3}), 8.00−7.80 (m, 4H, H^{C4}, H^{A4}), 7.61−7.48 (m, 2H, H^{G3}), 7.49−7.39 (m, 1H, H^{G4}), 7.38−7.30 (m, 4H, H^{A6}, H^{C6}), 7.21−7.01 (m, 4H, H^{C5}, H^{A5}). ^{13}C NMR (100 MHz, CD_3CN, ppm): δ 159.05, 159.00, 156.47, 156.28, 153.58, 153.22, 149.57, 149.52, 148.25, 146.94, 146.80, 146.20, 145.72, 145.70, 145.61, 145.36, 145.27, 144.83, 143.96, 143.89, 143.17, 143.08, 142.46, 141.83, 139.77, 139.10, 139.01, 138.84, 138.69, 137.71, 136.89, 133.19, 132.11, 130.11, 129.73, 129.38, 128.52, 128.47, 125.49, 124.76, 122.70, 80.14, 58.87. HRMS (ESI-TOF, m/z): 726.0829, $C_{103}H_{30}N_6Ru$ ([M − 2PF$_6$]$^{2+}$) requires 726.0785.

*[Ru(tpy)(**8b**)](PF$_6$)$_2$ (**1b**).* According to the general procedure for heteroleptic ruthenium bis(terpyridine) complexes, [Ru(tpy)(MeCN)$_3$](PF$_6$)$_2$ (6.4 mg, 8.5 μmol) and **8b** (9 mg, 6.1 μmol) were reacted to yield a dark red solid (4 mg, 1.9 μmol, 31%). ^{1}H NMR (300 MHz, CD_3CN, ppm): δ 8.96 (s, 2H, H^{D3}), 8.75 (d, ^3J = 8.2 Hz, 2H, H^{B3}), 8.59 (d, ^3J = 7.3 Hz, 2H, 2H, H^{C3}), 8.49 (d, ^3J = 8.3 Hz, 2H, H^{A3}), 8.41 (t, ^3J = 8.1 Hz, 1H, H^{B4}), 8.35 (d, ^3J = 5.8 Hz, 2H, H^{G2}), 8.21 (d, ^3J = 7.5 Hz, 2H, H^{E2}), 7.99−7.78 (m, 7H, H^{E3}, H^{F6}, H^{C4}, H^{A4}), 7.56−7.39 (m, 3H, H^{G3}, H^{G4}), 7.39 (d, ^3J = 5.2 Hz, 2H, H^{A6}), 7.34 (d, ^3J = 5.3 Hz, 2H, H^{C6}), 7.25 (s, 1H, H^{F3}), 7.21−7.07 (m, 4H, H^{C5}, H^{A5}), 4.29−4.10 (m, 3H, α-OCH_2), 4.08−3.92 (m, 1H, α-OCH_2), 1.85−1.59 (m, 4H, β-CH_2), 1.55−1.02 (m, 20H, γ-η-CH_2), 0.91−0.67 (m, 6H, CH_3). HRMS (ESI-TOF, m/z): 904.2109, $C_{127}H_{66}N_6O_2Ru$ ([M − 2PF$_6$]$^{2+}$) requires 904.2143.

*[Ru$_2$(tpy)$_2$(**8c**)](PF$_6$)$_4$ (**1c**).* According to the general procedure for heteroleptic ruthenium bis(terpyridine) complexes, [Ru(tpy)(MeCN)$_3$](PF$_6$)$_2$ (9.7 mg, 13 μmol) and **8c** (8.7 mg, 6.5 μmol) were reacted to yield a dark red solid (8 mg, 3.1 μmol, 48%). ^{1}H NMR (300 MHz, CD_3CN, ppm): δ 9.08 (s, 4H, H^{D3}), 8.80 (d, ^3J = 8.1 Hz, 4H, H^{E2}), 8.75 (d, ^3J = 8.2 Hz, 4H, H^{B3}), 8.67 (d, ^3J = 7.9 Hz, 4H, H^{C3}), 8.54−8.37 (m, 10H, H^{A3}, H^{E3}, H^{B4}), 8.00−7.86 (m, 8H, H^{C4}, H^{A4}), 7.42 (d, ^3J = 5.2 Hz, 4H, H^{A6}), 7.36 (d, ^3J = 5.2 Hz, 4H, H^{C6}), 7.23−7.10 (m, 8H, H^{C5}, H^{A5}). ^{13}C NMR (63 MHz, CD_3CN, ppm): δ 159.07, 156.56, 156.33, 153.58, 153.32, 149.39, 148.32, 146.92, 146.27, 146.24, 145.74, 145.68, 145.46, 144.86, 144.05, 143.98, 143.15, 143.07, 141.96, 141.91, 139.13, 139.06, 138.81, 138.09, 136.89, 133.46, 129.54, 128.54, 128.49, 125.58, 125.47, 124.76, 122.76, 79.99, 58.28. HRMS (ESI-TOF, m/z): 504.5643, $C_{133}H_{50}N_{12}Ru_2$ ([M − 4PF$_6$]$^{4+}$) requires 504.5599.

*[Ru(tpy)(**10a**)](PF$_6$)$_2$ (**2a**).* According to the general procedure for heteroleptic ruthenium bis(terpyridine) complexes, [Ru(tpy)(MeCN)$_3$](PF$_6$)$_2$ (8.9 mg, 12 μmol) and **10a** (13 mg, 12 μmol) were reacted to yield a dark red solid (7 mg, 4.1 μmol, 34%). ^{1}H NMR (300 MHz, CD_3CN, ppm): δ 9.00 (s, 2H, H^{D3}), 8.74 (d, ^3J = 8.2 Hz, 2H, H^{B3}), 8.62 (d, ^3J = 7.8 Hz, 2H, H^{C3}), 8.48 (d, ^3J = 8.1 Hz, 2H, H^{A3}), 8.40 (t, ^3J = 8.5 Hz, 1H, H^{B4}), 8.34−8.19 (m, 4H, H^{E2}, H^{E3}), 7.98−7.86 (m, 4H, H^{C4}, H^{A4}), 7.40 (d, ^3J = 5.5 Hz, 2H, H^{A6}), 7.32 (d, ^3J = 5.1 Hz, 2H, H^{C6}), 7.21−7.08 (m, 4H, H^{C5}, H^{A5}), 5.29 (s, 1H, H^{H2}), 5.14 (d, ^2J = 9.5 Hz, 1H, H^{H5}), 4.44 (d, ^2J = 9.7 Hz, 1H, H^{H5}), 2.91 (s, 3H, NCH_3). HRMS (ESI-TOF, m/z): 709.5853, $C_{99}H_{31}N_7Ru$ ([M − 2PF$_6$]$^{2+}$) requires 709.5839.

*[Ru(tpy)(**10b**)](PF$_6$)$_2$ (**2b**).* According to the general procedure for heteroleptic ruthenium bis(terpyridine) complexes, [Ru(tpy)(MeCN)$_3$](PF$_6$)$_2$ (15.6 mg, 21 μmol) and **10b** (30 mg, 21 μmol) were reacted to yield a dark red solid (23 mg, 11 μmol, 54%). ^{1}H NMR (400 MHz, CD_2Cl_2, ppm): δ 8.83 (s, 2H, H^{D3}), 8.69 (d, ^3J = 8.1 Hz, 2H, H^{B3}), 8.51 (d, ^3J = 7.8 Hz, 2H, H^{C3}), 8.48−8.36 (m, 3H, H^{B4}, H^{A3}), 8.12 (d, ^3J = 8.0 Hz, 2H, H^{E2}), 7.99−7.87 (m, 4H, H^{C4}, H^{A4}), 7.86 (d, ^3J = 7.9 Hz, 2H, H^{E3}), 7.69 (s, 1H, H^{F5}), 7.39 (d, ^3J = 5.4 Hz, 2H, H^{A6}), 7.32 (d, ^3J = 5.7 Hz, 2H, H^{C6}), 7.26−7.17 (m, 4H, H^{C5}, H^{A5}), 7.14 (s, 1H, H^{F2}), 5.61 (s, 1H, H^{H2}), 5.01 (d, ^2J = 9.6 Hz, 1H, H^{H5}), 4.37 (d, ^2J = 9.4 Hz, 1H, H^{H5}), 4.28−4.18 (m, 1H, α-OCH_2), 4.18−4.09 (m, 1H, α-OCH_2), 4.10−4.00 (m, 1H, α-OCH_2), 3.82−3.71 (m, 1H, α-OCH_2), 2.86 (s, 3H, NCH_3), 1.90−1.78 (m, 2H, β-CH_2), 1.73−1.12 (m, 22H, β-CH_2, γ-η-CH_2), 0.94−0.75 (m, 6H, CH_3). ^{13}C NMR (100 MHz, DMSO-d_6, ppm): δ 157.91, 157.74,

DOI: 10.1021/ic502431x
Inorg. Chem. 2015, 54, 3159−3171

157.04, 155.14, 155.00, 154.72, 154.25, 153.91, 153.54, 152.13, 152.07, 151.16, 146.80, 146.69, 146.62, 146.35, 145.74, 145.68, 145.65, 145.63, 145.57, 145.42, 145.25, 145.08, 144.99, 144.79, 144.71, 144.55, 144.49, 144.13, 143.98, 143.92, 143.85, 142.54, 142.16, 142.07, 141.89, 141.84, 141.75, 141.63, 141.49, 141.32, 141.21, 141.11, 139.65, 139.55, 139.43, 138.87, 138.77, 138.14, 138.04, 137.92, 135.85, 135.78, 135.56, 134.34, 133.52, 131.95, 129.63, 129.59, 127.92, 127.79, 127.70, 127.63, 124.88, 124.85, 124.84, 124.58, 124.56, 124.54, 124.02, 120.93, 120.91, 116.41, 114.44, 114.43, 114.40, 112.16, 109.46, 93.04, 88.81, 76.32, 75.05, 69.10, 69.06, 68.47, 40.43, 31.36, 31.30, 29.03, 28.95, 28.80, 28.73, 28.39, 25.49, 25.45, 22.25, 22.13, 14.05, 14.01. HRMS (ESI-TOF, *m*/*z*): 887.7307, $C_{123}H_{67}N_7O_2Ru$ ($[M - 2PF_6]^{2+}$) requires 887.7212.

[Ru(tpy)(ttpy)](PF$_6$)$_2$ ***(3a)***. According to the general procedure for heteroleptic ruthenium bis(terpyridine) complexes, [Ru(tpy)-(MeCN)$_3$](PF$_6$)$_2$ (58.5 mg, 0.078 mmol) and ttpy (25.3 mg, 0.078 mmol) were reacted in ethanol (5 mL) at 130 °C. Subsequently, the solvent was evaporated and the resulting residue was purified by column chromatography (silica, MeCN/H$_2$O/saturated aqueous KNO$_3$ solution 40/4/1). Concentration of the product fraction in vacuo and precipitation by addition of an aqueous ammonium hexafluorophosphate solution yielded a red solid (56 mg, 0.059 mmol, 76%). ^{1}H NMR (300 MHz, CD$_3$CN, ppm): δ 8.99 (s, 2H, H^{D3}), 8.76 (d, ^3J = 8.1 Hz, 2H, H^{B3}), 8.64 (d, ^3J = 8.1 Hz, 2H, H^{C3}), 8.50 (d, ^3J = 8.1 Hz, 2H, H^{A3}), 8.41 (t, ^3J = 8.1 Hz, 1H, H^{B4}), 8.11 (d, ^3J = 8.1 Hz, 2H, H^{E2}), 8.00−7.87 (m, 4H, H^{C4}, H^{A4}), 7.58 (d, ^3J = 7.9 Hz, 2H, H^{E3}), 7.43 (d, ^3J = 5.5 Hz, 2H, H^{A6}), 7.35 (d, ^3J = 5.4 Hz, 2H, H^{C6}), 7.22−7.11 (m, 4H, H^{C5}, H^{A5}), 2.54 (s, 3H, Ph−CH_3). ^{13}C NMR (75 MHz, CD$_3$CN, ppm): δ 159.20, 159.08, 156.41, 156.38, 153.54, 153.36, 149.42, 142.07, 139.05, 139.01, 136.71, 134.91, 131.30, 128.67, 128.46, 128.42, 125.48, 125.40, 124.70, 122.37, 21.43. Anal. Calcd for $C_{37}H_{28}F_{12}N_6P_2Ru$: C, 46.89; H, 2.98; N, 8.87. Found: C, 46.53; H, 3.02; N, 8.76.

*[Ru(tpy)(**11b**)](PF$_6$)$_2$* ***(3b)***. A mixture of [Ru(tpy)]Cl$_3$ (4.4 mg, 10 μmol) and silver(I) tetrafluoroborate (5.8 mg, 30 μmol) in deaerated acetone (3 mL) was heated to 70 °C for 2 h. After cooling and filtration, DMF (2 mL) was added to the filtrate and the acetone was removed in vacuo. The resulting blue solution of [Ru(tpy)(acetone)$_3$]-(BF$_4$)$_3$ was added to a solution of 4′-(4-((2,5-Bis(octyloxy)phenyl)-ethynyl)phenyl)-2,2′:6′,2″-terpyridine (**11b**; 20 mg, 14 μmol) in DMF (3 mL), and the mixture was heated to 160 °C for 3 h. Subsequently, the reaction mixture was cooled to room temperature and a solid was precipitated by addition of an aqueous ammonium hexafluorophosphate solution. After filtration, the solid was further purified by column chromatography (silica, MeCN/H$_2$O/saturated aqueous KNO$_3$ solution 40/4/1). Concentration of the product fraction in vacuo and precipitation by addition of an aqueous ammonium hexafluorophosphate solution yielded a red solid (10 mg, 7.8 μmol, 78%). ^{1}H NMR (300 MHz, CD$_3$CN, ppm): δ 9.01 (s, 2H, H^{D3}), 8.76 (d, ^3J = 8.2 Hz, 2H, H^{B3}), 8.65 (d, ^3J = 8.0 Hz, 2H, H^{C3}), 8.50 (d, ^3J = 8.0 Hz, 2H, H^{A3}), 8.42 (t, ^3J = 8.1 Hz, 1H, H^{B4}), 8.25 (d, ^3J = 8.5 Hz, 2H, H^{E2}), 8.00−7.84 (m, 6H, H^{C4}, H^{A4}, H^{E3}), 7.42 (d, ^3J = 4.9 Hz, 2H, H^{A6}), 7.36 (d, ^3J = 4.9 Hz, 2H, H^{C6}), 7.22−7.13 (m, 4H, H^{C5}, H^{A5}), 7.09 (d, ^4J = 2.4 Hz, 1H, H^{F6}), 7.02−6.90 (m, 2H, H^{F4}, H^{F3}), 4.08 (t, ^3J = 6.3 Hz, 2H, α-OCH_2), 3.97 (t, ^3J = 6.5 Hz, 2H, α-OCH_2), 1.91−1.68 (m, 4H, β-CH_2), 1.67−1.21 (m, 20H, γ-η-CH_2), 1.01−0.80 (m, 6H, CH_3). ^{13}C NMR (75 MHz, CD$_3$CN, ppm): δ 159.09, 159.05, 156.6, 156.3, 155.2, 153.9, 153.6, 153.4, 148.2, 139.12, 139.07, 137.4, 136.9, 133.4, 129.0, 128.5, 128.5, 126.5, 125.6, 125.4, 124.7, 122.4, 119.5, 118.1, 115.3, 113.7, 93.2, 89.7, 70.4, 69.6, 32.61, 32.59, 30.2, 30.14, 30.11, 30.07, 30.04, 30.02, 26.9, 26.7, 23.5, 23.4, 14.5, 14.4. HRMS (ESI-TOF, *m*/*z*): 500.1984, $C_{60}H_{62}N_6O_2Ru$ ($[M - 2PF_6]^{2+}$) requires 500.1992.

■ ASSOCIATED CONTENT

Ⓢ Supporting Information

Figures S1−S62, giving cyclic voltammograms, absorption and emission spectra, time-resolved data, DFT calculations, NMR data, and MS spectra. This material is available free of charge via the Internet at http://pubs.acs.org.

■ AUTHOR INFORMATION

Corresponding Authors

*E-mail for B.D.: benjamin.dietzek@ipht-jena.de.

*E-mail for U.S.S.: ulrich.schubert@uni-jena.de.

Author Contributions

$^{\perp}$The manuscript was written through contributions of all authors. All authors have given approval to the final version of the manuscript. These authors contributed equally.

Notes

The authors declare no competing financial interest.

■ ACKNOWLEDGMENTS

Financial support by the Deutsche Forschungsgemeinschaft (DFG, Grant Nos. SCHU1229-16/1 and DI1517-3/1) and the Fonds der Chemischen Industrie is kindly acknowledged. Moreover, this project was supported by the COST Action CM1202 Perspect-H2O. The authors also thank Sarah Crotty (MALDI MS), Nicole Fritz (ESI MS), and Sandra Köhn (elemental analysis) for their help with the respective measurements.

■ REFERENCES

(1) Artero, V.; Chavarot-Kerlidou, M.; Fontecave, M. *Angew. Chem., Int. Ed.* **2011**, *50*, 7238.

(2) Andreiadis, E. S.; Chavarot-Kerlidou, M.; Fontecave, M.; Artero, V. *Photochem. Photobiol.* **2011**, *87*, 946.

(3) Artero, V.; Fontecave, M. *Coord. Chem. Rev.* **2005**, *249*, 1518.

(4) Natali, M.; Campagna, S.; Scandola, F. *Chem. Soc. Rev.* **2014**, *43*, 4005.

(5) Sartorel, A.; Bonchio, M.; Campagna, S.; Scandola, F. *Chem. Soc. Rev.* **2013**, *42*, 2262.

(6) Carraro, M.; Sartorel, A.; Toma, F. M.; Puntoriero, F.; Scandola, F.; Campagna, S.; Prato, M.; Bonchio, M. *Top. Curr. Chem.* **2011**, *303*, 121.

(7) Barber, J.; Tran, P. D. *J. R. Soc. Interface* 2013, *10*.

(8) Gust, D.; Moore, T. A.; Moore, A. L. *Acc. Chem. Res.* **2001**, *34*, 40.

(9) Berardi, S.; Drouet, S.; Francàs, L.; Gimbert-Suriñach, C.; Guttentag, M.; Richmond, C.; Stoll, T.; Llobet, A. *Chem. Soc. Rev.* **2014**, *43*, 7501.

(10) Sun, L.; Gao, Y.; Yu, Z.; Ding, X.; Duan, L. *Faraday Discuss.* **2014**, DOI: 10.1039/c4fd00127c.

(11) Fukuzumi, S.; Ohkubo, K.; Suenobu, T. *Acc. Chem. Res.* **2014**, *47*, 1455.

(12) Wenger, O. S. *Chem. Soc. Rev.* **2011**, *40*, 3538.

(13) Schubert, C.; Wielopolski, M.; Mewes, L. H.; de Miguel Rojas, G.; van der Pol, C.; Moss, K. C.; Bryce, M. R.; Moser, J. E.; Clark, T.; Guldi, D. M. *Chem. Eur. J.* **2013**, *19*, 7575.

(14) Guldi, D. M.; Maggini, M.; Scorrano, G.; Prato, M. *J. Am. Chem. Soc.* **1997**, *119*, 974.

(15) Guldi, D. M. *Chem. Soc. Rev.* **2002**, *31*, 22.

(16) Wielopolski, M.; Atienza, C.; Clark, T.; Guldi, D. M.; Martín, N. *Chem. Eur. J.* **2008**, *14*, 6379.

(17) Wielopolski, M.; Santos, J.; Illescas, B. M.; Ortiz, A.; Insuasty, B.; Bauer, T.; Clark, T.; Guldi, D. M.; Martín, N. *Energy Environ. Sci.* **2011**, *4*, 765.

(18) Ventura, B.; Barbieri, A.; Zanelli, A.; Barigelletti, F.; Seneclauze, J. B.; Diring, S.; Ziessel, R. *Inorg. Chem.* **2009**, *48*, 6409.

(19) Liu, Y. F.; Zhao, J. Z. *Chem. Commun.* **2012**, *48*, 3751.

(20) Martín, N.; Sánchez, L.; Illescas, B.; Pérez, I. *Chem. Rev.* **1998**, *98*, 2527.

(21) Armaroli, N. *Photochem. Photobiol. Sci.* **2003**, *2*, 73.

(22) Medlycott, E. A.; Hanan, G. S. *Chem. Soc. Rev.* **2005**, *34*, 133.

(23) Medlycott, E. A.; Hanan, G. S. *Coord. Chem. Rev.* **2006**, *250*, 1763.

(24) *Photochemistry and Photophysics of Coordination Compounds I* ; Balzani, V., Campagna, S., Eds.; Springer: Berlin/Heidelberg, 2007.

DOI: 10.1021/ic502431x
Inorg. Chem. 2015, 54, 3159−3171

(25) Armaroli, N.; Accorsi, G.; Felder, D.; Nierengarten, J. F. *Chem. Eur. J.* **2002**, *8*, 2314.
(26) Chaignon, F.; Torroba, J.; Blart, E.; Borgström, M.; Hammarström, L.; Odobel, F. *New J. Chem.* **2005**, *29*, 1272.
(27) Zhou, Z. G.; Sarova, G. H.; Zhang, S.; Ou, Z. P.; Tat, F. T.; Kadish, K. M.; Echegoyen, L.; Guldi, D. M.; Schuster, D. I.; Wilson, S. R. *Chem. Eur. J.* **2006**, *12*, 4241.
(28) Maggini, M.; Guldi, D. M.; Mondini, S.; Scorrano, G.; Paolucci, F.; Ceroni, P.; Roffia, S. *Chem. Eur. J.* **1998**, *4*, 1992.
(29) Allen, B. D.; Benniston, A. C.; Harriman, A.; Mallon, L. J.; Pariani, C. *Phys. Chem. Chem. Phys.* **2006**, *8*, 4112.
(30) Karlsson, S.; Modin, J.; Becker, H. C.; Hammarström, L.; Grennberg, H. *Inorg. Chem.* **2008**, *47*, 7286.
(31) Armaroli, N.; Barigelletti, F.; Ceroni, P.; Eckert, J. F.; Nicoud, J. F.; Nierengarten, J. F. *Chem. Commun.* **2000**, 599.
(32) Sariciftci, N. S.; Wudl, F.; Heeger, A. J.; Maggini, M.; Scorrano, G.; Prato, M.; Bourassa, J.; Ford, P. C. *Chem. Phys. Lett.* **1995**, *247*, 510.
(33) Armspach, D.; Constable, E. C.; Diederich, F.; Housecroft, C. E.; Nierengarten, J. F. *Chem.—Eur. J.* **1998**, *4*, 723.
(34) Polese, A.; Mondini, S.; Bianco, A.; Toniolo, C.; Scorrano, G.; Guldi, D. M.; Maggini, M. *J. Am. Chem. Soc.* **1999**, *121*, 3446.
(35) Albinsson, B.; Mårtensson, J. *J. Photochem. Photobiol., C* **2008**, *9*, 138.
(36) Siebert, R.; Winter, A.; Dietzek, B.; Schubert, U. S.; Popp, J. *Macromol. Rapid Commun.* **2010**, *31*, 883.
(37) Siebert, R.; Winter, A.; Schubert, U. S.; Dietzek, B.; Popp, J. *J. Phys. Chem. C* **2010**, *114*, 6841.
(38) Siebert, R.; Hunger, C.; Guthmuller, J.; Schlutter, F.; Winter, A.; Schubert, U. S.; González, L.; Dietzek, B.; Popp, J. *J. Phys. Chem. C* **2011**, *115*, 12677.
(39) Siebert, R.; Winter, A.; Schubert, U. S.; Dietzek, B.; Popp, J. *Phys. Chem. Chem. Phys.* **2011**, *13*, 1606.
(40) La Rosa, A.; Gillemot, K.; Leary, E.; Evangeli, C.; González, M. T.; Filippone, S.; Rubio-Bollinger, G.; Agraït, N.; Lambert, C. J.; Martín, N. *J. Org. Chem.* **2014**, *79*, 4871.
(41) Denholm, A. A.; George, M. H.; Hailes, H. C.; Tiffin, P. J.; Widdowson, D. A. *J. Chem. Soc., Perkin Trans. 1* **1995**, 541.
(42) Cave, G. W. V.; Raston, C. L. *J. Chem. Soc., Perkin Trans. 1* **2001**, 3258.
(43) Egbe, D. A. M.; Carbonnier, B.; Ding, L. M.; Mühlbacher, D.; Birckner, E.; Pakula, T.; Karasz, F. E.; Grummt, U. W. *Macromolecules* **2004**, *37*, 7451.
(44) Schlütter, F.; Wild, A.; Winter, A.; Hager, M. D.; Baumgärtel, A.; Friebe, C.; Schubert, U. S. *Macromolecules* **2010**, *43*, 2759.
(45) Hirsch, A. *Synthesis* **1995**, 895.
(46) Yamada, M.; Akasaka, T.; Nagase, S. *Chem. Rev.* **2013**, *113*, 7209.
(47) Winter, A.; Egbe, D. A. M.; Schubert, U. S. *Org. Lett.* **2007**, *9*, 2345.
(48) Winter, A.; Friebe, C.; Hager, M. D.; Schubert, U. S. *Eur. J. Org. Chem.* **2009**, 801.
(49) Maggini, M.; Donò, A.; Scorrano, G.; Prato, M. *J. Chem. Soc., Chem. Commun.* **1995**, 845.
(50) Schulze, B.; Escudero, D.; Friebe, C.; Siebert, R.; Görls, H.; Sinn, S.; Thomas, M.; Mai, S.; Popp, J.; Dietzek, B.; González, L.; Schubert, U. S. *Chem. - Eur. J.* **2012**, *18*, 4010.
(51) Sinn, S.; Schulze, B.; Friebe, C.; Brown, D. G.; Jäger, M.; Kübel, J.; Dietzek, B.; Berlinguette, C. P.; Schubert, U. S. *Inorg. Chem.* **2014**, *53*, 1637.
(52) Barigelletti, F.; Flamigni, L.; Balzani, V.; Collin, J. P.; Sauvage, J. P.; Sour, A.; Constable, E. C.; Cargill Thompson, A. M. W. *J. Am. Chem. Soc.* **1994**, *116*, 7692.
(53) Lukoyanova, O.; Cardona, C. M.; Altable, M.; Filippone, S.; Martín Domenech, Á.; Martín, N.; Echegoyen, L. *Angew. Chem., Int. Ed.* **2006**, *45*, 7430.
(54) Hirsch, A.; Brettreich, M. *Fullerenes*; Wiley-VCH: Weinheim, Germany, 2005.
(55) Herranz, M. Á.; Diederich, F.; Echegoyen, L. *Eur. J. Org. Chem.* **2004**, 2299.
(56) Schubert, U. S.; Winter, A.; Newkome, G. R. *Terpyridine-based Materials*; Wiley-VCH: Weinheim, Germany, 2011.
(57) Thomas, K. G.; Biju, V.; Guldi, D. M.; Kamat, P. V.; George, M. V. *J. Phys. Chem. B* **1999**, *103*, 8864.
(58) Bensasson, R. V.; Bienvenüe, E.; Fabre, C.; Janot, J. M.; Land, E. J.; Leach, S.; Leboulaire, V.; Rassat, A.; Roux, S.; Seta, P. *Chem. Eur. J.* **1998**, *4*, 270.
(59) Amouyal, E.; Mouallem-Bahout, M.; Calzaferri, G. *J. Phys. Chem.* **1991**, *95*, 7641.
(60) Horng, M. L.; Gardecki, J. A.; Papazyan, A.; Maroncelli, M. *J. Phys. Chem.* **1995**, *99*, 17311.
(61) Bhasikuttan, A. C.; Suzuki, M.; Nakashima, S.; Okada, T. *J. Am. Chem. Soc.* **2002**, *124*, 8398.
(62) Maestri, M.; Armaroli, N.; Balzani, V.; Constable, E. C.; Cargill Thompson, A. M. W. *Inorg. Chem.* **1995**, *34*, 2759.
(63) Lainé, P. P.; Campagna, S.; Loiseau, F. *Coord. Chem. Rev.* **2008**, *252*, 2552.
(64) McClenaghan, N. D.; Leydet, Y.; Maubert, B.; Indelli, M. T.; Campagna, S. *Coord. Chem. Rev.* **2005**, *249*, 1336.
(65) Grewer, C.; Brauer, H.-D. *J. Phys. Chem.* **1994**, *98*, 4230.
(66) Winter, A.; van den Berg, A. M. J.; Hoogenboom, R.; Kickelbick, G.; Schubert, U. S. *Synthesis* **2006**, 2873.
(67) Sullivan, B. P.; Calvert, J. M.; Meyer, T. J. *Inorg. Chem.* **1980**, *19*, 1404.
(68) Igartúa-Nieves, E.; Ocasio-Delgado, Y.; Torres-Castillo, M. D. L. A.; Rivera-Betancourt, O.; Rivera-Pagán, J. A.; Rodriguez, D.; López, G. E.; Cortés-Figueroa, J. E. *Dalton Trans.* **2007**, 1293.

DOI: 10.1021/ic502431x
Inorg. Chem. 2015, 54, 3159−3171

Publication P3

"Dyads and Triads based on Phenothiazine, Bisterpyridine Ruthenium(II) Complexes and Fullerene"

K. Barthelmes, A. Winter, U. S. Schubert,

Eur. J. Inorg. Chem. **2016**, 5132-5142.

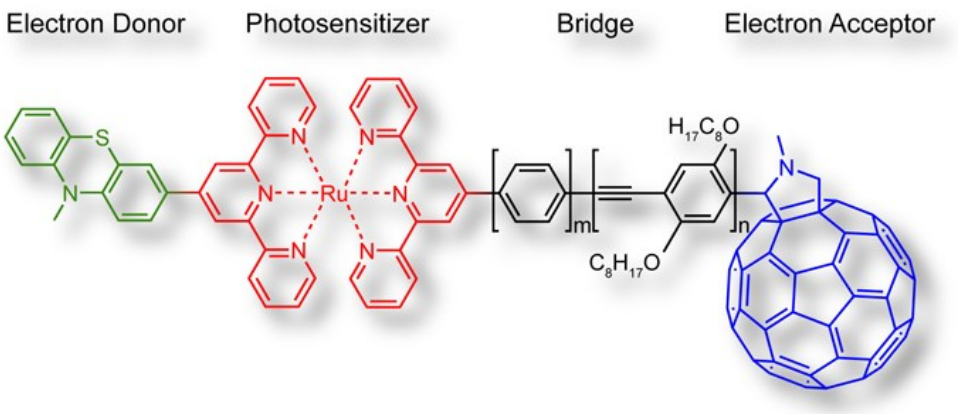

The Supplementary Information can be downloaded at the publisher's site.

ChemPubSoc Europe

DOI: 10.1002/ejic.201600793

EurJIC European Journal of Inorganic Chemistry

Full Paper

Donor–Acceptor Systems

Dyads and Triads Based on Phenothiazine, Bis(terpyridine)ruthenium(II) Complexes, and Fullerene

Kevin Barthelmes,[a,b,c] Andreas Winter,[a,b,c] and Ulrich S. Schubert*[a,b,c]

Abstract: We report the modular synthesis of donor–photosensitizer–bridge–acceptor (D–P–B–A) triads and D–P dyads for the formation of photoinduced charge-separated species. The structures are based on a phenothiazine unit (D), a bis(terpyridine) [bis(tpy)] ruthenium(II) complex (P), several phenylene(ethynylene)-type spacer units (B), and a pyrrolidino[60]fullerene entity (A). The donor–acceptor distance is between 18 and 37 Å and was varied by four different bridging units. The photophysical and electrochemical characterization revealed certain interactions between the active moieties in the ground and the excited state. In particular, a reduced ruthenium-based emission in the triads indicates the occurrence of a quenching process mediated by the fullerene entity. Strong electrostatic interactions between the ruthenium(II) complex and the pyrrolidino[60]fullerene have been observed for the shortest triad, resulting in the strongest electron-accepting pyrrolidino[60]fullerene unit in the series.

Introduction

In natural photosynthesis, sunlight is efficiently transformed into chemical energy by optimized energy- and electron-transfer reactions.[1] During these processes the light-harvesting antenna system absorbs the excitation energy and transfers it to the reaction center, where charge separation occurs. Extensive research has been focused on the construction of artificial systems to mimic this natural concept.[2] In this respect, one approach is represented by the formation of molecular triads that are composed of a photosensitizer (P), flanked by an electron donor (D), and an electron acceptor (A). In such D–P–A systems, after excitation of the photosensitizer (D–P*–A), charge migration takes place by sequential electron-transfer processes, which finally results in a charge-separated (CS) species (D^+–P–A^-). The classical Marcus theory[3] represents a useful tool for the design of D–P–A systems. In particular, long-lived CS states (CSS) can be achieved by a fast population (i.e. electron transfer) and a slow decay (i.e. charge recombination) of this state. This can be realized by a weak electronic coupling between the donor and acceptor sites, a low reorganization energy of the donor/acceptor as well as a highly exothermic free-energy change for the CS process (i.e. for normal Marcus region). The electronic coupling can be decreased by increasing the donor–acceptor distance; this is usually realized by a wire-like bridge (B) between the active moieties. The reorganization energy depends on the polarity of the solvent and the molecular rearrangement that occurs during charge distribution in the system. The free-energy change ΔG_{CS} for the CS process can be estimated from the difference in the redox potential between the electron donor and the electron acceptor and the excitation energy of the photosensitizer. Thus, high values for ΔG_{CS} can be obtained for small redox-potential differences and high excitation energies.

It has been shown that metal-based photosensitizers have great potential as light-absorbing units, such as polypyridyl-based complexes containing Ru^{II},[4] Os^{II},[4b,4e–4g,5] Ir^{III},[4a,4b,4g,6] or Pt^{II}[7] centers, or porphyrin-based complexes with Zn^{II}[2c,8] or Al^{III}[9] centers. In the case of the heavy transition-metal ions, the excitation energy usually undergoes a very fast intersystem crossing (ISC) from the singlet to the lower-lying triplet excited state; all subsequent processes (e.g. phosphorescence, non-radiative decay, energy or electron transfer) are known to start from this state.[10]

We recently reported the photodynamic processes in dyads based on a bis(tpy)ruthenium(II) complex $[Ru(tpy)_2]^{2+}$, a π-conjugated bridge, and a methano- or pyrrolidino-functionalized C_{60}.[11] $[Ru(tpy)_2]^{2+}$ was chosen as photosensitizer and electron donor because of its intense absorption at ca. 500 nm and the reversible ruthenium-based redox potential (i.e. 0.9 V vs. Fc^+/Fc; Fc = ferrocene). The rigid π-conjugated spacer units were chosen as bridges, because a precise adjustment of the donor–acceptor distance is possible, and they possess low attenuation factors β [e.g. 0.1–0.57 $Å^{-1}$ for oligo(phenyleneethynylene) spacer units][12] to promote fast and efficient charge transfer towards the electron acceptor. C_{60} was chosen as electron-accept-

[a] *Laboratory of Organic and Macromolecular Chemistry (IOMC), Friedrich Schiller University Jena, Humboldtstr. 10, 07743 Jena, Germany*
E-mail: ulrich.schubert@uni-jena.de
http://www.schubert-group.de
[b] *Jena Center for Soft Matter (JCSM), Friedrich Schiller University Jena, Philosophenweg 7, 07743 Jena, Germany*
http://www.jcsm.uni-jena.de/
[c] *Center for Energy and Environmental Chemistry Jena (CEEC Jena), Friedrich Schiller University Jena, Philosophenweg 7a, 07743 Jena, Germany*
http://www.ceec.uni-jena.de/

Supporting information for this article is available on the WWW under http://dx.doi.org/10.1002/ejic.201600793.

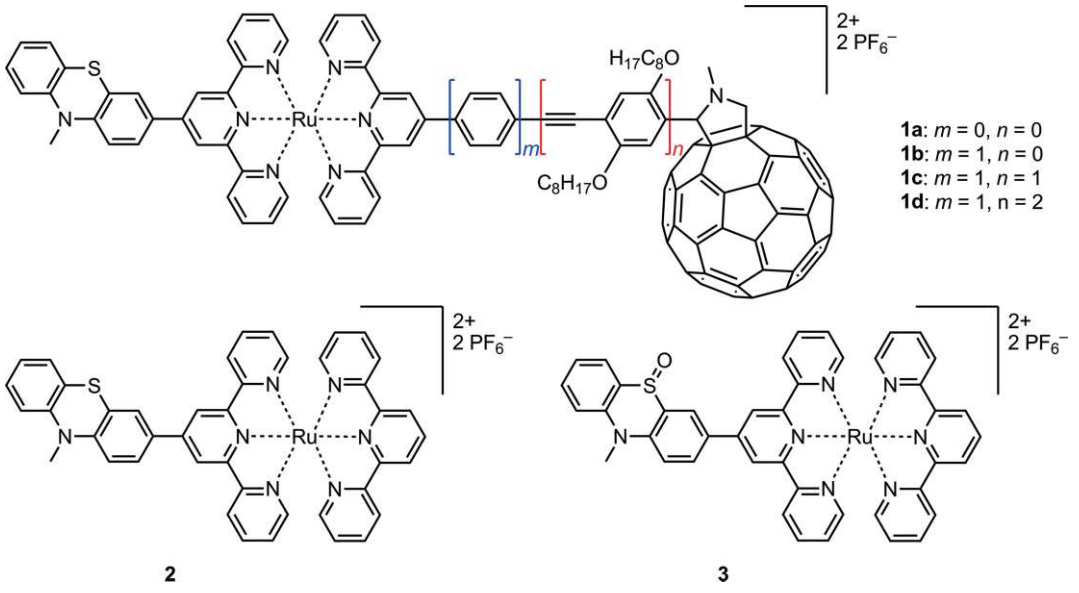

Figure 1. Schematic representation of the triads **1a**–**d** and model dyads **2** and **3**.

ing entity since it exhibits a remarkable electron-accepting ability and low reorganization energy due to its unique, spherical shape. Thereby, the excitation energy of the $[Ru(tpy)_2]^{2+}$ complex was transferred to the lowest-lying $^3C_{60}$* state on the ps timescale. A population of the CSS (i.e. $^+$Ru–B–C_{60}^-) was not observed, which can be mainly ascribed to the high energy of this state as it is reported in similar ruthenium complexes with bipyridine (bpy) as metal-binding unit.[13] On this basis, we employed the modular design of $[Ru(tpy)_2]^{2+}$ complexes to introduce an additional organic electron-donor moiety that should lower the CSS energy (i.e. $^+$D–Ru–B–C_{60}^-). By this approach, four triads **1a**–**d** were constructed, all having a phenothiazine entity as electron donor (Figure 1). Phenothiazine is commonly used as organic electron donor and its potential to form CSSs has been documented for several D–P–A architectures.[7b,9b,14] Recently, a very long-lived CSS of 0.71 ms was obtained in a phenothiazine-bridged cyclic porphyrin dimer with an encapsulated fullerene.[15] Dyad **2** is prepared as a reference complex missing both the bridge and fullerene unit (Figure 1). The related dyad **3** is also used as a reference, but it exhibits a phenothiazine sulfoxide (oxPTZ) entity with decreased electron-donation strength, and was prepared as an intermediate in the course of the alternative synthetic procedure for **2** (Figure 1).

Results and Discussion

Molecular Structure

The molecular structure of **1a**–**d** can be divided into different fragments: All four complexes comprise an $[Ru(tpy)_2]^{2+}$ complex, an *N*-methylphenothiazine (PTZ) unit, an *N*-methylpyrrolidino[60]fullerene unit, and a bridge of varying length. Triad **1a**, which basically is the complex without any bridge, consequently exhibits the shortest donor–acceptor distance of 18.3 Å. The distance was estimated from geometry-optimized structures (Figure S1–S4) by taking the sulfur atom of the PTZ and the center of C_{60} as marks. In the other compounds, the bridge consists of a phenyl spacer unit (**1b**), or one (**1c**) or two (**1d**) octyloxy-functionalized *para*-phenyleneethynylene (PPE) spacer units. The increasing bridge length results in donor–acceptor distances of 22.9, 30.1, and 37.1 Å for **1b**, **1c**, and **1d**, respectively.

Synthesis

An overview of the synthetic route towards the fullerene-containing tpy ligands is shown in Scheme 1. Recently, we reported the synthesis of the C_{60}–Sp–tpy ligands **5b** and **5c** (Sp = spacer).[11] In a repetition of the reported synthesis we could increase the yield to 60 and 81 % for **5b** and **5c**, respectively. Accordingly, the shorter C_{60}–Sp–tpy ligand **5a** and the longer ligand **5d** were synthesized. For this purpose, compounds **4a** and **4d** that contain an aldehyde group were treated with *N*-methylglycine and C_{60} in a ratio of 1:10:2.5 in toluene at 120 °C for 24 h (Scheme 1). The monoaddition products **5a** and **5d** were separated by column chromatography on neutral alumina and isolated in 32 and 62 % yield, respectively. The significant difference in the isolated yield is attributed to the poor solubility of **5a** compared to **5d**.

The synthesis of the second key building block, PTZ–tpy ligand **7**, and the ruthenium coordination thereof is summarized in Scheme 2. Compound **6** was synthesized by a Vilsmeier-type formylation of 10-methylphenothiazine according to a literature procedure.[16] In the following step a Kröhnke-type tpy synthesis was carried out according to analogous literature procedures[17] to build up the 4′-substituted tpy fragment in compound **7** with 57 % yield. Importantly, PTZ–tpy ligand **7** is more appropriate for the preparation of a ruthenium precursor com-

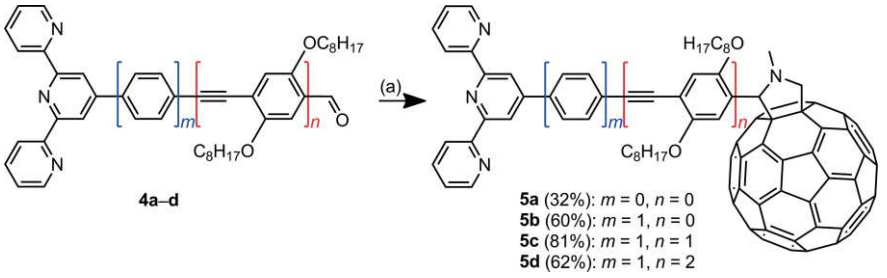

Scheme 1. Schematic representation of the synthesis of the C_{60}–Sp–tpy ligands **5a**–**d**. Conditions: (a) *N*-methylglycine, C_{60}, toluene, 120 °C, 24 h.

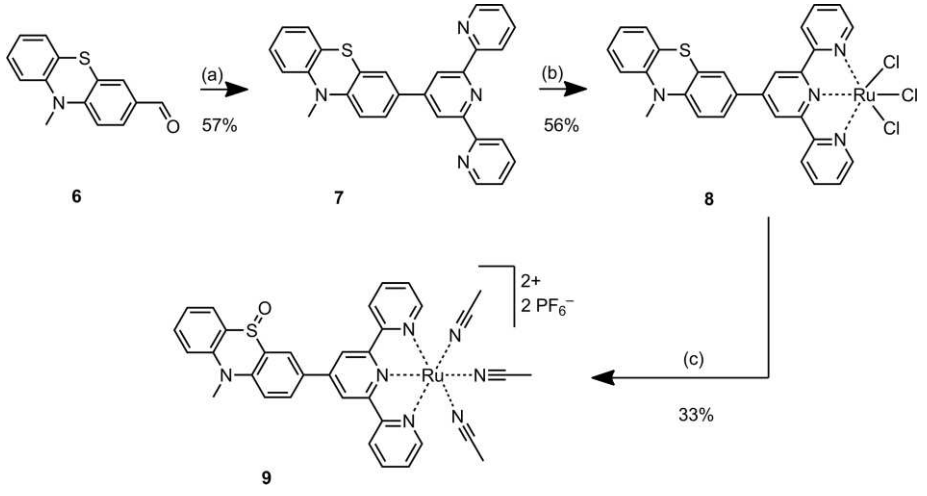

Scheme 2. Schematic representation of the synthesis of PTZ–tpy ligand **7** and its coordination to the ruthenium center. Conditions: (a) 2-acetylpyridine, KOH, aqueous NH_3, EtOH, r.t., 24 h; (b) $RuCl_3(i\text{PrSPh})_2(MeOH)$, MeCN, 90 °C, 21 h; (c) (i) $AgNO_3$, MeCN/EtOH/H_2O (6:1:1), 90 °C, 2 h; (ii) excess NH_4PF_6.

plex compared to the C_{60}–Sp–tpy ligands. The reason for this is that both preparation and purification of ruthenium precursors based on C_{60}–Sp–tpy are challenging. Additionally, four C_{60}-based Ru precursors would have to be prepared compared to a single PTZ-based Ru precursor. Therefore, PTZ–tpy ligand **7** was coordinated to a ruthenium(III) center by the reaction with an equimolar amount of $RuCl_3(i\text{PrSPh})_2(MeOH)$ in acetonitrile heated to reflux.[18] After the reaction, crude trichloridoruthenium(III) precursor **8** was obtained as precipitate and was sonicated in ethyl acetate. The remaining solid was not analyzed and used without further purification for the subsequent reaction step. In order to guarantee a facile coordination of the second C_{60}–Sp–tpy ligand, we chose to substitute the chlorido ligands by neutral acetonitrile ones according to an Ag^I-assisted procedure.[19] During this reaction, the ruthenium(III) center is reduced by the solvent, and tris(acetonitrile)ruthenium(II) precursor **9** was obtained in 33 % yield. The rather low yield can be ascribed to the moderate purity of the trichlorido precursor **8**. Subsequent analysis by ESI-MS indicated an oxidation of the sulfide to the corresponding sulfoxide (oxPTZ).

The oxidation occurred during the substitution reaction and not in the previous steps, namely the tpy synthesis or the ruthenium coordination. This assumption could be confirmed by the preparation of reference dyad **2** by three different routes (Scheme 3). All ruthenium coordination reactions with a second tpy-based ligand were performed in DMF at 130 °C for 1 h, as described previously.[11] The first route represents the coordination of PTZ–tpy ligand **7** with $[Ru(tpy)(MeCN)_3](PF_6)_2$[19] and afforded complex **2** in 70 % yield. However, this procedure is not applicable for the triad preparation, since the corresponding C_{60}–Sp–tpy ruthenium precursors are not available. For the second route, the order of coordination to the Ru center was inverted. The reaction of trichloridoruthenium(III) precursor **8** with 2,2′:6′,2″-tpy resulted in the formation of complex **2** in moderate 31 % yield, caused by the low purity of **8**. However, this reaction confirmed that the PTZ unit in precursor **8** was intact, since no oxidation product could be observed in the ESI mass spectra of **2**. Finally, the third route describes a two-step procedure towards complex **2**. Initially, the reaction of tris(acetonitrile)ruthenium(II) complex **9** with 2,2′:6′,2″-tpy yielded the desired oxPTZ-based dyad **3** (63 %), similar to Route 1. Subsequently, complex **3** could be transformed into complex **2** by quantitative sulfoxide reduction with triflic anhydride (Tf_2O, 2 equiv.) and potassium iodide (3 equiv.) in acetonitrile. The selective reduction procedure has previously been established by Bahrami et al. for aryl sulfoxides bearing several other redox-active groups.[20] In summary, the second and third route are both applicable for the targeted triad preparation. However, the

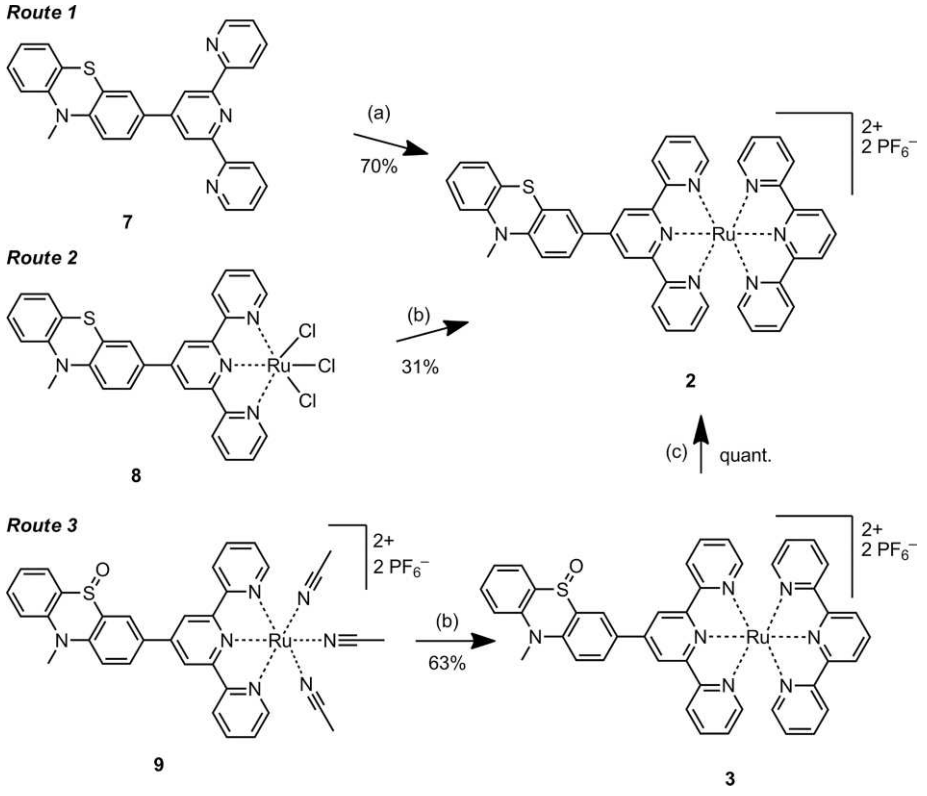

Scheme 3. Schematic representation of three different synthetic routes towards dyad **2** and synthesis of dyad **3**. Conditions: (a) $[Ru(tpy)(MeCN)_3](PF_6)_2$, DMF, 130 °C, 1 h; (b) (i) 2,2′:6′,2″-tpy, DMF, 130 °C, 1 h; (ii) excess NH_4PF_6; (c) (i) Tf_2O, KI, MeCN, r.t., 30 min; (ii) excess NH_4PF_6.

third route was chosen, since in the second route trichloridoruthenium(III) precursor **8** was obtained as crude mixture resulting in lower yields, and a final purification of the triads was expected to be difficult.

The synthetic route towards triads **1a**–**d** is shown in Scheme 4. Tris(acetonitrile)ruthenium(II) complex **9** was treated with equimolar amounts of C_{60}–Sp–tpy ligands **5a**–**d** in DMF at 130 °C for 1 h. The sulfoxide intermediates were obtained in 52–84 % yield and directly reduced by the above-mentioned procedure in quantitative yields. ESI-MS data confirmed the selective reduction of the sulfoxide moiety. The complexes are moderately soluble in acetonitrile and dichloromethane,

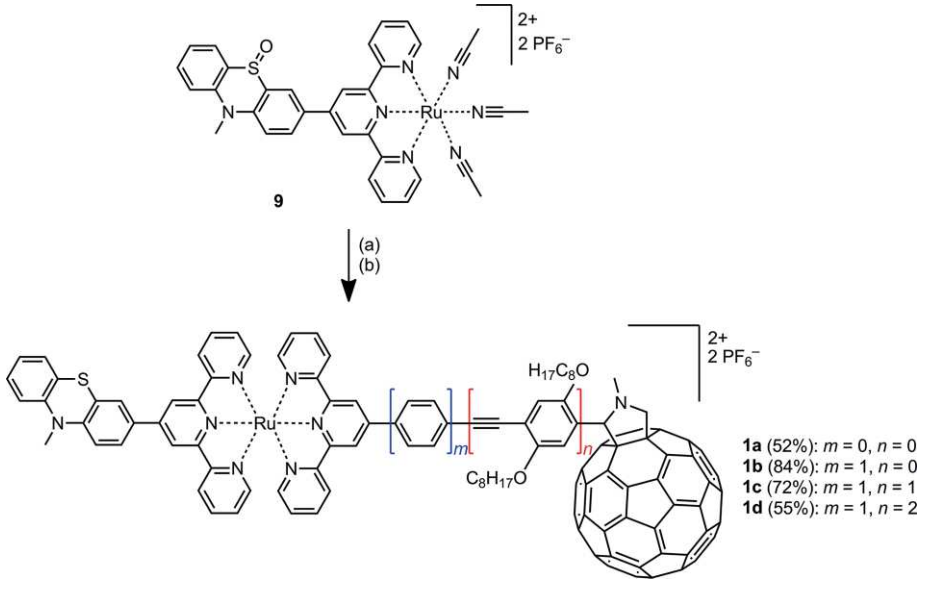

Scheme 4. Schematic representation of the synthesis of triads **1a**–**d**. Conditions: (a) **5a**–**d**, DMF, 130 °C, 1 h; (b) (i) Tf_2O, KI, MeCN, r.t., 30 min; (ii) excess NH_4PF_6.

whereby the complexes **1a** and **1b** with shorter chains are better soluble in acetonitrile, and complexes **1c**–**d** containing the octyloxy chains are better soluble in dichloromethane.

NMR Spectroscopy

^{1}H NMR spectroscopy was applied to analyze dyads **2** and **3** in acetonitrile as well as triads **1a**–**d** in [D_6]DMSO. The stacked spectra of **3**, **2**, and **1c** are shown in Figure 2, along with a numbering scheme for the oxPTZ unit (red), the central pyridine ring of the PTZ–tpy unit (green), and the pyrrolidino[60]fullerene unit (blue). The numbering in the PTZ unit is the same as in the oxPTZ unit. The assignment of the resonances was accomplished with the help of 2D NMR techniques. The oxPTZ and PTZ units gave rise to seven signals in the aromatic region and one signal in the aliphatic region [i.e. the methyl (Me) group]. When comparing sulfoxide-containing dyad **3** with the reduced form **2**, significant shifts of all oxPTZ signals could be observed. In fact, upfield shifts of ca. 0.8, 0.5, 0.4, 0.6, and 0.4 ppm were detected for the PTZ signals 2/2′, 3, 4/4′, 5/5′, and Me, respectively. This behavior may be explained by the change of the electron-withdrawing (EWG) sulfoxide group into an electron-donating (EDG) sulfide group that introduces more electron density to the aromatic rings. Apparently, the highest shift was observed for PTZ signals 2 and 2′, which are in closest proximity to the transformed group. Moreover, a slight upfield shift of 0.15 ppm was observed for the signal of the central pyridine ring of the PTZ–tpy ligand (i.e. 3′, 5′), indicating an influence of the PTZ unit on the tpy fragment. Triad **1c** features several new signals, for example the four signals at δ = 5.6, 5.1, 4.4, and 2.8 ppm belonging to positions 2, 5 (2 ×), and Me (not shown), respectively, of the *N*-methylpyrrolidino[60]fullerene unit (Figure 2). Obviously, the signals in **1c** appeared broadened, and some of the PTZ signals as well as the signal of the central pyridine ring were slightly downfield shifted. These shifts presumably resulted from the change of the solvent to [D_6]DMSO, rather than from an influence of the second C_{60}–Sp–tpy ligand.

Absorption Spectroscopy

UV/Vis absorption spectra were recorded in dichloromethane and acetonitrile. For **3**, **2**, and **1c**, the spectra measured in dichloromethane are exemplarily shown in Figure 3 (for the remaining spectra and the spectra measured in acetonitrile, see Figures S5–S7). Complex **3** exhibits the characteristic spectral features known for polypyridylruthenium(II) complexes.[21] The UV region is dominated by an intense π–π^* transition of the tpy unit with absorption maxima at 274 and 310 nm. The oxPTZ moiety contributes to the latter absorption bands and additionally shows a distinct absorption band at 379 nm in dichloromethane (Figure 3). When changing the solvent to acetonitrile, a significant increase (i.e. 1.5 times) and hypsochromic shift to 357 nm of this latter band was observed, indicating a certain degree of solvatochromism (Figure S5). In the visible region, a broad absorption band up to 600 nm was observed. Mainly the

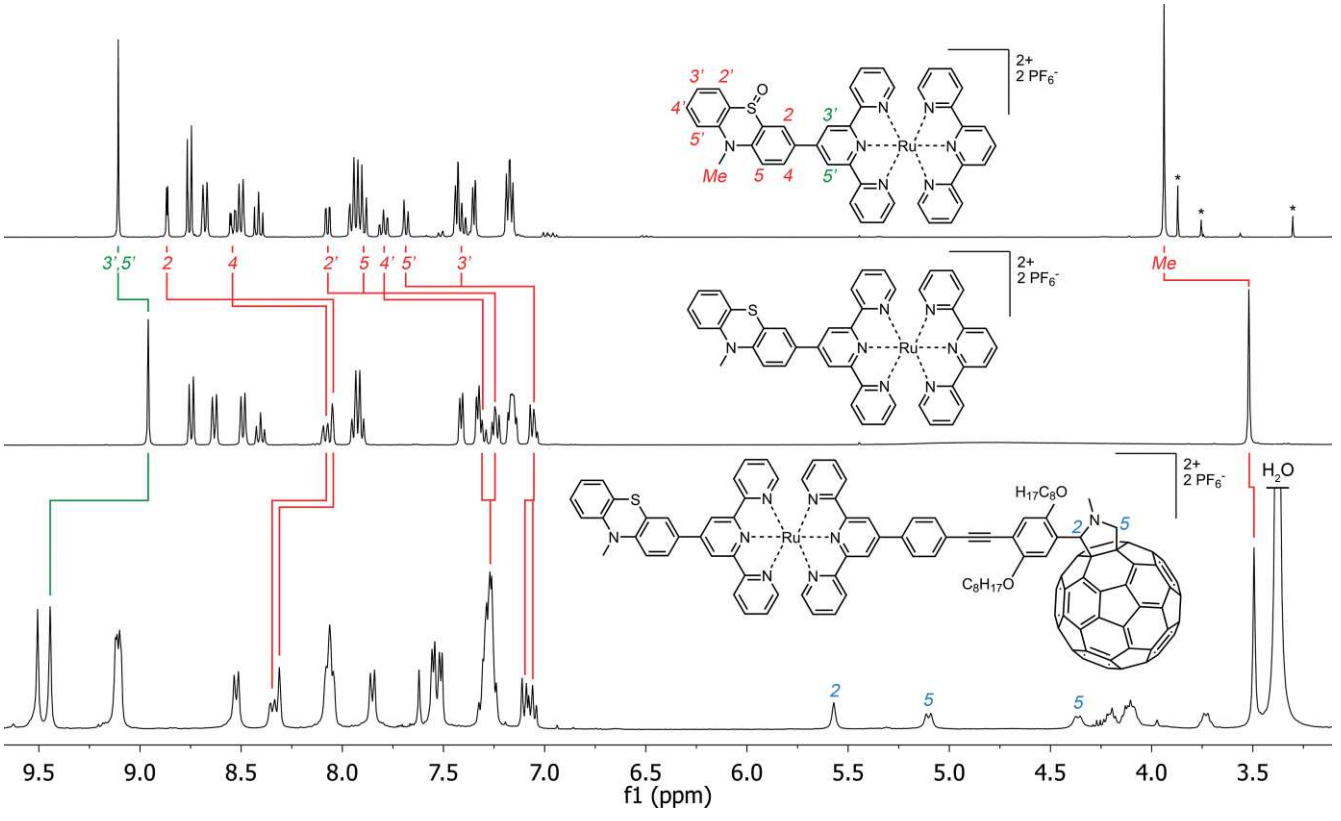

Figure 2. ^{1}H NMR spectra (400 MHz) of dyads **3** (top; in CD_3CN) and **2** (middle; in CD_3CN), and triad **1c** (bottom; in [D_6]DMSO). Impurities are marked with asterisks.

ruthenium-based metal-to-ligand charge-transfer (MLCT) transitions with a maximum at 488 nm and the extinction coefficient ε of ca. 40000 M^{-1} cm^{-1} contribute to this region (Table 1). PTZ-containing complex **2** exhibits similar spectral features as **3**, though missing the absorption peak exclusively assigned to the oxPTZ unit (Figure 3). However, weaker absorption in the UV/Vis region and a slight bathochromic shift of the MLCT transition was observed. The latter effect suggests an influence of the PTZ unit on the transitions of the $[Ru(tpy)_2]^{2+}$ complex, which is typical for functionalized complexes.[22] Triad **1c** revealed a stronger absorption in the UV region compared to those of **3** and **2**, which is caused by additional absorption of the C_{60} and the spacer unit (Figure 3). For the visible region, a sharp peak at 430 nm became apparent for **1c**, being characteristic for [6,6]-closed fullerene monoadducts.[23] Furthermore, the MLCT transition was bathochromically shifted to 505 nm compared to those of **3** and **2**, due to the π-conjugated system connected to the tpy ligand.

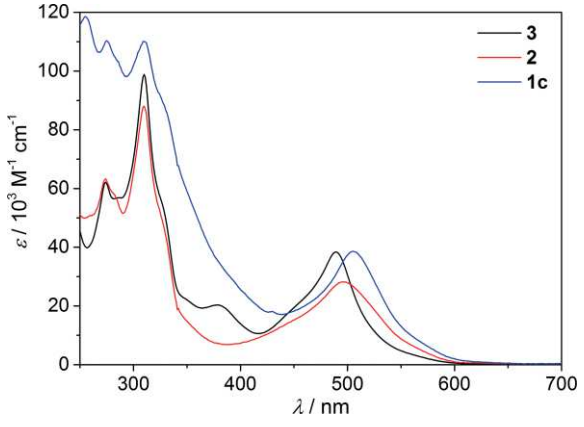

Figure 3. UV/Vis absorption spectra of dyads **3** and **2** and triad **1c** in dichloromethane.

Table 1. Photophysical properties.[a]

	λ_{abs}/nm [ε_{abs}/10^3 M^{-1} cm^{-1}][b]
1a	255 [88.5], 277 [83.8], 307 [78.6], 499 [17.3] (246 [92.9], 273 [49.1], 309 [44.7], 494 [15.3])
1b	255 [108.9], 276 [103.8], 310 [99.9], 501 [28.8] (246 [95.2], 275 [69.8], 310 [67.0], 498 [26.4])
1c	255 [118.6], 275 [110.3], 310 [110.1], 505 [38.6] (246 [110.4], 274 [72.9], 310 [74.5], 500 [32.2])
1d	255 [134.3], 276 [129.1], 306 [130.5], 375 [68.5],[c] 506 [42.7] (246 [177.8], 274 [70.4], 311 [67.6], 380 [37.8],[c] 501 [34.0])
2	274 [63.3], 310 [88.1], 496 [28.2] (273 [51.8], 308 [72.7], 491 [26.1])
3	274 [62.2], 310 [98.8], 379 [20.3], 489 [38.4] (273 [69.8], 309 [101.6], 357 [35.2], 487 [40.6])

[a] Conditions: dichloromethane solution (acetonitrile solution is used for values in parentheses). [b] Absorption band maxima are given. [c] Shoulder.

When comparing triads **1a**–**d**, an increase in the bridge length, along with an enhanced π-conjugation, resulted in a bathochromic shift of the spacer-unit-based π–π* transitions in the UV region (Figures S6 and S7). In fact, a shoulder at 375 nm was observed for **1d** with the longest bridge length. In the visible region, a bathochromic shift and increased extinction coefficients were observed for the MLCT absorption maxima in the series of **1a**–**d**. In fact, the shortest triad **1a** exhibits an absorption maximum at 499 nm ($\varepsilon \approx 20000$ M^{-1} cm^{-1}), while for **1d** a value of 506 nm ($\varepsilon \approx 40000$ M^{-1} cm^{-1}) was measured (Table 1, Figures S6 and S7).

Emission Spectroscopy

Emission spectroscopy was applied to analyze the ^{3}MLCT-based emission of the $[Ru(tpy)_2]^{2+}$ complexes. The emission spectra of dyads **3** and **2** as well as those of triads **1a**–**d** in isoabsorbing (optical density: $OD_{495\ nm}$ = 0.54) dichloromethane and acetonitrile solutions are shown in Figure 4. Upon light irradiation in the visible region (i.e. λ_{exc} = 495 nm) of **3**, a very weak emission at 641 and 646 nm was observed in dichloromethane (Figure 4a) and acetonitrile (Figure 4b), respectively, which is characteristic for functionalized $[Ru(tpy)_2]^{2+}$ complexes.[22,24] Under identical conditions, complex **2** exhibited a similarly intense, but broader emission with an untypically large bathochromic shift of the emission at 693 nm in dichloromethane (Figure 4a). It was figured out that spectrometer artifacts (i.e. the double-wavelength emission of a second emission in the UV region) were overlapping with the ^{3}MLCT emission resulting in the broadening and the bathochromic shift of the maximum. A more detailed explanation is given in the Supporting Informa-

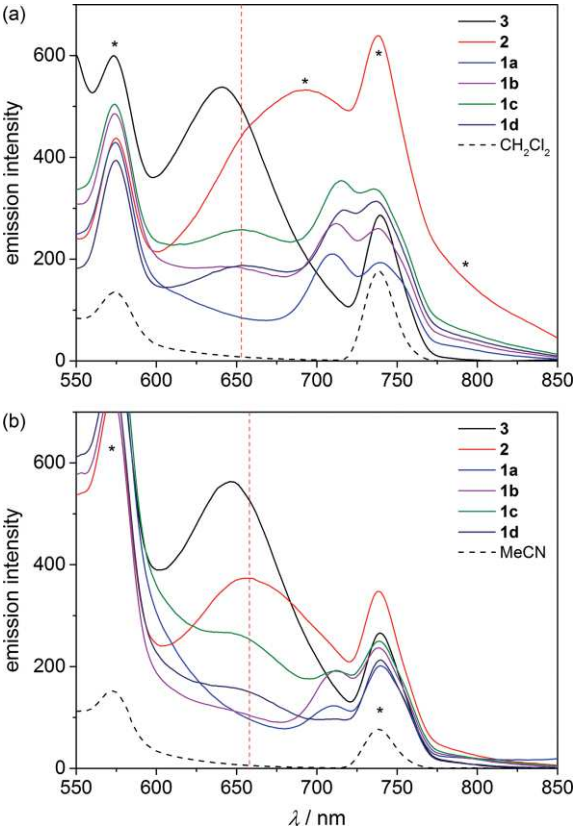

Figure 4. Emission spectra (isoabsorbing solutions at λ_{exc} = 495 nm) of dyads **3** and **2** and triads **1a**–**d** in dichloromethane (a) and acetonitrile (b) solution at r.t. The red, dashed line marks the approximate maximum of the ^{3}MLCT-based emission in **2**. Blank measurements of the solvents are marked with black, dashed lines (i.e. CH_2Cl_2 and MeCN). Spectrometer artifacts are marked with asterisks.

tion (Figures S8–S10). The correct maximum should be located at ca. 653 nm (marked as red dashed line), indicated by a small shoulder and residual emission of **1c** (Figure 4a). In acetonitrile, the corresponding emission of **2** behaved as expected, and the maximum was slightly bathochromically shifted to 658 nm (Figure 4b), since the spectrometer artifacts have only a minor contribution. Interestingly, the emission intensity of **3** was reduced in comparison to that of **2** in acetonitrile, which may indicate quenching by electron transfer from the PTZ unit to the excited $[Ru(tpy)_2]^{2+}$ moiety. Such a reductive quenching has been shown for the ^{3}MLCT emission of an $[Ru(bpy)_3]^{2+}$ complex by the addition of amines.[25] For triads **1a**–**d**, the ^{3}MLCT-based emission was generally reduced relative to that of the dyads and may be explained by the occurrence of an additional quenching process induced by the C_{60} moiety. The strongest quenching was observed for **1a** in dichloromethane and acetonitrile (Figure 4). Higher residual emissions were recorded for triads **1b** and **1d** (Figure 4). This behavior may be explained by the increasing bridge length along with a longer distance between the $[Ru(tpy)_2]^{2+}$ complex and the C_{60} moiety. Surprisingly, for the third shortest triad **1c** the residual emission intensity was highest in dichloromethane and acetonitrile (Figure 4). A possible explanation could be the participation of a low-lying $^3\pi$–π^* transition of the bridge in the quenching process, which could be a reservoir for the ^{3}MLCT emission.[4e,24,26]

In all triads **1a**, **1b**, **1c**, and **1d** a second emission was observed in dichloromethane at 709, 712, 715, 717 nm, respectively. The origin of this emission was fluorescence from the *N*-methylpyrrolidino[60]fullerene (NMP-C_{60}) unit (Figure S11) and was significantly reduced compared to pristine NMP-C_{60}.[27] Based on the extinction coefficients of NMP-C_{60}, the NMP-C_{60} unit in the triads contributed with 4–9 % to the absorption at 495 nm, and thus, a direct excitation should be possible.

Electrochemistry

Cyclic voltammetry (CV) and differential pulse voltammetry (DPV) measurements were performed in dichloromethane or acetonitrile solutions containing 0.1 M Bu_4NPF_6, and the potential was referenced against that of ferrocene. The CV curves measured in dichloromethane are exemplary shown for **3**, **2**, and **1c** in Figure 5 (for the remaining spectra and spectra in acetonitrile, see Figures S12–S14). An overview of the redox potentials of complexes **1a**–**d**, **2**, and **3** is given Table 2.

In the anodic region, dyad **3** revealed one reversible process at 0.88 V and an irreversible process at 1.09 V (only observed in the CV spectrum) (Figure 5). In acetonitrile, the first process occurred at 0.86 V, followed by the irreversible oxidation at 1.06 V (Figure S12). The first process was assigned to the Ru^{3+}/Ru^{2+} redox couple. The latter process appeared to be correlated with the presence of the oxPTZ unit, since it is absent in $[Ru(tpy)_2](PF_6)_2$.[28] In the cathodic region of **3**, two reversible tpy-based reduction processes at –1.64 V and –1.92 V are observed in a potential window up to –2.5 V. In acetonitrile, additionally, a third (–2.24 V) and fourth (–2.61 V) reduction were observed in the DPV spectrum (Figure S12). Dyad **2** exhibits in principle the same redox processes as found for **3** without any

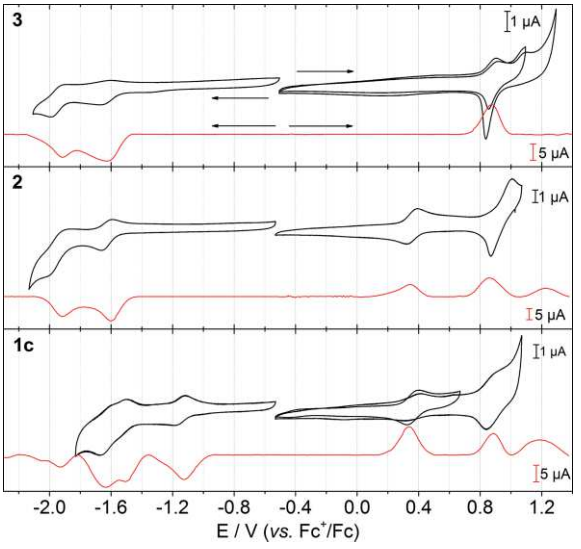

Figure 5. CV (black line, 5th cycle is shown) and DPV spectra (red line) of dyads **3** and **2** and triad **1c** in dichloromethane. The arrows show the scan direction.

Table 2. Electrochemical properties.[a]

	E_{ox} (PTZ) [V]	E_{ox} (Ru) [V]	E_{red} (C_{60},1) [V]	E_{red} (C_{60},2) [V]	E_{red} (tpy,1) [V]	E_{red} (tpy,2) [V]
1a	0.34	0.99	–1.03	–1.43	–1.67	–1.98
	(0.40)	(0.94)	(–0.80)	(–1.22)	(–1.54)	(–1.90)
1b	0.34	0.90	–1.11	–1.48	–1.64	–1.97
	(0.40)	(0.89)	(–0.86)	(–1.28)	(–1.54)	(–1.80)
1c	0.35	0.89	–1.13	–1.51	–1.65	–1.93
	(0.39)	(0.89)	(–0.94)	(–1.32)	(–1.52)	(–1.79)
1d	0.34	0.89	–1.14	–1.54	–1.67	–1.96
	(0.39)	(0.88)	(–0.90)	(–1.33)	(–1.53)	(–1.79)
2	0.35	0.87	–	–	–1.60	–1.92
	(0.39)	(0.91)			(–1.57)	(–1.81)
3	–	0.88	–	–	–1.64	–1.92
		(0.86)			(–1.57)	(–1.82)

[a] DPV potentials are given; conditions: deaerated 0.1 M solution of Bu_4NPF_6 in dichloromethane (acetonitrile solution is used for values in parentheses); scan rate: 0.2 V s^{-1}, referenced against Fc^+/Fc, r.t.

significant shifts (Figure 5), indicating only slight electronic interactions between the PTZ unit and the ruthenium center or the tpy moiety. However, an additional reversible oxidation process occurred at 0.35 and 0.39 V in dichloromethane and acetonitrile, respectively. This process was assigned to a one-electron oxidation of the PTZ unit to the radical cation.[7b] Further oxidation was observed in dichloromethane at 1.22 V in the DPV spectrum, which may be related to the irreversible process seen in acetonitrile at 1.08 V that is present in **2** and **3**.

In triad **1c**, the aforementioned redox processes as well as the additional C_{60}-based processes were present (Figure 5). The observed values for the PTZ redox couple were the same as those in **2**, indicating no electronic interaction of the spacer unit or the C_{60} with the lateral PTZ moiety. The same holds true when comparing the Ru-based oxidation potential of **1c** with that of **2** in acetonitrile and dichloromethane (Table 2). A slight cathodic shift of 50 mV was observed for the first tpy-based reduction process versus **2**. A similar behavior was also ob-

served in a related complex missing the PTZ moiety.[11] Two reversible C_{60}-based reduction processes were recorded in the cathodic region for **1c** at –1.13 and –1.51 V in dichloromethane. The signal of the second C_{60}-based reduction is overlapping with that of the first tpy-based reduction in the CV spectrum, while two clearly separated peaks occurred in the DPV spectrum. When measuring in acetonitrile, both C_{60}-based redox processes became anodically shifted by ca. 200 mV, which resulted from the stabilization of the charged species in the more polar solvent. When comparing triads **1a**–**d**, a clear trend for the first C_{60}-based reduction process was found: With increasing bridge length, the first C_{60}-based redox process shifted cathodically to –1.03, –1.11, –1.13, and –1.14 V for **1a**, **1b**, **1c**, and **1d**, respectively. Interestingly, **1a** exhibited the largest shift and, consequently, the best electron-accepting C_{60} in the series. Moreover, the shortest triad **1a** showed its individual role when compared to the other triads by deviations in the Ru^{3+}/Ru^{2+} redox potential. Apparently, a cathodic shift of ca. 100 mV of this latter process was observed for **1a** versus **1b**–**d** and **2** in dichloromethane. By changing the solvent to acetonitrile, the Ru potential in **1a** cathodically shifted by ca. 50 mV, whereby an anodic shift in **2** was observed. For **1b**–**d** no significant shift of the Ru redox potential upon changing the solvent was observed (Table 2). This behavior clearly revealed a certain degree of electronic interaction due to the rather close distance between the ruthenium center and the C_{60} cage in **1a**.

Conclusions

A new modular, synthetic procedure has been established for the synthesis of phenothiazine-containing bis(tpy)ruthenium(II) complexes $[Ru(tpy)_2]^{2+}$. According to this approach, four triads were prepared with an $[Ru(tpy)_2]^{2+}$ complex as central photosensitizer, a phenothiazine unit as the electron donor, and a pyrrolidino[60]fullerene entity as the electron acceptor. The triads differ in the length of the bridging unit, which results in donor–acceptor distances between 18 and 37 Å. The complexes were investigated regarding their photophysical and electrochemical properties and were compared with two dyads missing the fullerene entity. The phenothiazine moiety has a slight influence on the ground- and excited-state properties of the $[Ru(tpy)_2]^{2+}$ complex. For all four triads significant interactions between the $[Ru(tpy)_2]^{2+}$ complex and the fullerene entity occur in the excited state, which has been concluded from a reduced $[Ru(tpy)_2]^{2+}$-based ^{3}MLCT emission. Moreover, in the shortest triad, remarkable electrostatic interactions have been found between $[Ru(tpy)_2]^{2+}$ and the fullerene moieties, which was indicated by a more electron-rich ruthenium center and a more electron-deficient fullerene unit compared to those of the other triads. Preliminary results based on calculated charge-separated state energies (i.e. 1.38 and 1.26 eV in dichloromethane and acetonitrile, respectively, for a charge separation between the phenothiazine and the fullerene unit) favor the quenching process through a photoinduced electron-transfer mechanism, rather than a triplet–triplet energy transfer, since the energy is lower than that of the $^3C_{60}$* state (i.e. 1.5 eV). Evaluation of the photodynamic processes is the topic of ongoing research including time-resolved spectroscopy and computational investigations. Preliminary results by nanosecond transient absorption spectroscopy could identify the formation of charge-separated states in the dyad and triad systems.

Experimental Section

Materials and Instrumentation: Compounds 4′-(4-formylphenyl)-2,2′:6′,2″-tpy (**4b**),[29] **4c**,[30] **5b**,[11] **5c**,[11] 10-methyl-3-formylphenothiazine (**6**),[16] and $[Ru(tpy)(MeCN)_3](PF_6)_2$[19] were prepared according to analogous literature procedures. 4′-Formyl-2,2′:6′,2″-tpy (**4a**) was purchased from HetCat. The synthetic procedure for **4d** is shown in the Supporting Information. All other chemicals were purchased from commercial suppliers and used as received. All reactions were monitored by thin-layer chromatography (TLC) (silica gel on aluminum sheets with fluorescent dye F254, Merck KGaA). Flash column chromatography was carried out with a Biotage Isolera One system. NMR spectra were recorded with a Bruker Avance (300 or 400 MHz) instrument in deuterated solvents (Euriso-Top) at 25 °C. ESI-TOF MS was performed with a Bruker ESI-(Q)-TOF-MS microTOF II mass spectrometer. MALDI-TOF mass spectra were obtained by using a Bruker Ultraflex III TOF/TOF mass spectrometer in reflector mode. Elemental analyses were performed with a EuroVector EuroEA3000 elemental analyzer. UV/Vis absorption spectra were recorded with a PerkinElmer Lambda 750 UV/Vis spectrometer, and emission spectra were recorded with a Jasco FP6500 instrument. CV and DPV measurements were performed with a Metrohm Autolab PGSTAT30 potentiostat with a standard three-electrode configuration by using a glassy-carbon-disk working electrode, a platinum-rod auxiliary electrode, and an AgCl/Ag reference electrode; a scan rate of 0.2 V s^{-1} was applied. The experiments were carried out in deaerated solvents (HPLC grade) containing 0.1 M Bu_4NPF_6 salt. At the end of each measurement, ferrocene was added as an internal standard.

Compound 5a: A mixture of **4a** (50 mg, 0.191 mmol), *N*-methylglycine (170 mg, 1.914 mmol), and C_{60} (345 mg, 0.478 mmol) in toluene (200 mL) was stirred under nitrogen at 120 °C for 24 h. After the mixture was cooled to r.t., the solvent was evaporated. The crude product was purified by column chromatography (neutral alumina, toluene then chloroform), and the first brown band was collected. The fraction was concentrated to a volume of 10 mL and added slowly to methanol (100 mL) under continuous stirring. The suspension was stored overnight in a refrigerator, and the formed precipitate was filtered off. Compound **5a** was obtained as brown solid (61 mg, 0.060 mmol, 32 %). M.p. >360 °C. ^{1}H NMR (300 MHz, $CDCl_3$): δ = 8.92 (s, 2 H), 8.73 (d, J = 4.1 Hz, 2 H), 8.64 (d, J = 8.1 Hz, 2 H), 7.85 (t, J = 7.6 Hz, 2 H), 7.37–7.30 (m, 2 H), 5.16 (s, 1 H), 5.05 (d, J = 9.6 Hz, 1 H), 4.33 (d, J = 9.4 Hz, 1 H), 2.88 (s, 3 H) ppm. MS (MALDI-TOF, neg. mode, matrix DCTB): calcd. for $C_{78}H_{16}N_4$ $[M + e]^-$ 1008.137; found 1008.195. $C_{78}H_{16}N_4$•0.6PDMS•(C_2H_6OSi) (1052.55): calcd. C 90.30, H 1.88, N 5.32; found C 90.34, H 1.87, N 5.44.

Compound 5d: A mixture of **4d** (50 mg, 0.048 mmol), *N*-methylglycine (42 mg, 0.480 mmol), and C_{60} (86 mg, 0.119 mmol) in toluene (100 mL) was stirred under nitrogen at 120 °C for 24 h. After the mixture was cooled to r.t., the solvent was evaporated. The crude product was purified by column chromatography (neutral alumina, toluene then chloroform), and the first dark brown band was collected. Compound **5d** was obtained as a black solid (53 mg, 0.029 mmol, 62 %). M.p. 105 °C. ^{1}H NMR (300 MHz, $CDCl_3$): δ = 8.76 (s, 2 H), 8.74 (d, J = 4.5 Hz, 2 H), 8.68 (d, J = 7.9 Hz, 2 H), 7.96–7.84

(m, 4 H), 7.67 (d, J = 8.1 Hz, 2 H), 7.60 (s, 1 H), 7.40–7.32 (m, 2 H), 7.05 (s, 1 H), 7.03 (s, 1 H), 7.02 (s, 1 H), 5.55 (s, 1 H), 4.98 (d, J = 9.3 Hz, 1 H), 4.32 (d, J = 9.4 Hz, 1 H), 4.23–3.93 (m, 7 H), 3.77–3.64 (m, 1 H), 2.84 (s, 3 H), 1.94–1.74 (m, 6 H), 1.67–1.14 (m, 42 H), 0.95–0.76 (m, 12 H) ppm. MS (MALDI-TOF, neg. mode, matrix DCTB): calcd. for $C_{132}H_{92}N_4O_4$ [M + e]$^-$ 1797.715; found 1797.738. $C_{132}H_{92}N_4O_4$•2.7PDMS•(C_2H_6OSi) (1996.56): calcd. C 82.58, H 5.46, N 2.80; found C 82.33, H 5.44, N 3.09.

PTZ–tpy (7): To a solution of **6** (813 mg, 3.37 mmol) and 2-acetylpyridine (898 mg, 7.41 mmol) in EtOH (50 mL) was added KOH (416 mg, 7.41 mmol), and the mixture was stirred at r.t. for 30 min. Subsequently, aqueous NH_3 solution (25 %, 10 mL, 135 mmol) was then added, and the stirring was continued at r.t. for 24 h. The formed precipitate was collected by filtration and washed with EtOH (3 × 10 mL). The crude solid was further purified by column chromatography (neutral alumina, dichloromethane/ethyl acetate, 3:1). Compound **7** was obtained as yellowish powder (849 mg, 1.91 mmol, 57 %). M.p. 202 °C. ^{1}H NMR (400 MHz, $CDCl_3$): δ = 8.73 (d, J = 4.1 Hz, 2 H), 8.67 (s, 2 H), 8.66 (d, J = 8.1 Hz, 2 H), 7.87 (td, J = 7.7, 1.7 Hz, 2 H), 7.77–7.70 (m, 2 H), 7.38–7.32 (m, 2 H), 7.22–7.15 (m, 2 H), 6.96 (t, J = 7.5 Hz, 1 H), 6.90 (d, J = 8.2 Hz, 1 H), 6.84 (d, J = 7.9 Hz, 1 H), 3.43 (s, 3 H) ppm. ^{13}C{^{1}H} NMR (101 MHz, $CDCl_3$): δ = 156.44 (2 C), 156.04 (2 C), 149.25 (2 C), 149.06, 146.74, 145.42, 136.98 (2 C), 132.61, 127.69, 127.40, 126.63, 125.81, 124.24, 123.93 (2 C), 123.11, 122.91, 121.50 (2 C), 118.09 (2 C), 114.36 (2 C), 35.59 ppm. MS (MALDI-TOF, matrix dithranol): calcd. for $C_{28}H_{21}N_4S$ [M + H]$^+$ 445.148; found 445.153. $C_{28}H_{20}N_4S$•0.2EtOH•(C_2H_6O) (453.35): calcd. C 75.17, H 4.71, N 12.35, S 7.07; found C 74.92, H 4.58, N 11.99, S 7.41.

[Ru(PTZ–tpy)Cl$_3$] (8): Compound **7** (170 mg, 0.381 mmol) and $RuCl_3$(iPrSPh)$_2$(MeOH)[18] (207 mg, 0.381 mmol) in acetonitrile (25 mL) were heated at 90 °C for 21 h. After cooling to r.t., the precipitate was filtered off and washed with ethanol (10 mL). Subsequently, the solid was sonicated (3 min) with ethyl acetate (50 mL), filtered off, and washed with ethanol (10 mL) and diethyl ether (2 × 30 mL). Compound **8** was obtained as a brown solid (140 mg, 0.215 mmol, 56 %).

[Ru(oxPTZ–tpy)(MeCN)$_3$](PF$_6$)$_2$ (9): A suspension of **8** (50 mg, 0.077 mmol), $AgNO_3$ (39.7 mg, 0.234 mmol) in a mixture of acetonitrile, ethanol, and water (6:1:1, 4 mL) was heated to 90 °C for 2 h. The solvent was removed, and the remaining crude mixture purified by column chromatography (silica; acetonitrile/water/satd. aqueous KNO_3, 40:4:1). The orange band was collected (R_f = 0.3) and concentrated in vacuo. Excess ammonium hexafluorophosphate was added; the solution was concentrated, and water was added. The formed precipitate was collected by filtration and washed with water (5 mL). Subsequently, the solid was dried in vacuo and dissolved in a small amount of acetonitrile. The concentrated solution was treated with diethyl ether vapor overnight to force slow precipitation of the complex. Compound **9** was obtained as an orange solid (25 mg, 0.026 mmol, 33 %). ^{1}H NMR (300 MHz, CD_3CN): δ = 8.94 (d, J = 5.3 Hz, 2 H), 8.76 (s, 2 H), 8.72 (d, J = 2.0 Hz, 1 H), 8.59 (d, J = 8.1 Hz, 2 H), 8.38 (dd, J = 8.8, 1.8 Hz, 1 H), 8.21 (t, J = 8.0 Hz, 2 H), 8.04 (d, J = 6.8 Hz, 1 H), 7.83–7.72 (m, 4 H), 7.64 (d, J = 8.4 Hz, 1 H), 7.39 (t, J = 7.5 Hz, 1 H), 3.87 (s, 3 H), 2.75 (s, 3 H), 1.96 (s, 6 H) ppm. HRMS (ESI-TOF): calcd. for $C_{34}H_{29}N_7ORuS$ [M – 2 PF_6]$^{2+}$ 342.5593; found 342.5588. $C_{34}H_{29}F_{12}N_7OP_2RuS$ (974.70): calcd. C 41.90, H 3.00, N 10.06, S 3.29; found C 42.25, H 3.17, N 9.98, S 3.28.

[Ru(PTZ–tpy)(tpy)](PF$_6$)$_2$ (2)

Route 1: A microwave vial was charged with **7** (12 mg, 0.027 mmol), [Ru(tpy)(MeCN)$_3$](PF$_6$)$_2$ (20 mg, 0.027 mmol), and DMF (1.5 mL). The vial was capped, and the solution was then purged with nitrogen for 10 min. Subsequently, the mixture was heated in an oil bath at 130 °C under exclusion of light for 1 h. After cooling to r.t., diethyl ether was added, and the precipitate was collected by filtration. The crude product was purified by column chromatography (silica; acetonitrile/water/satd. aqueous KNO_3, 40:4:1). The first red fraction was collected, and ammonium hexafluorophosphate was added. The solution was concentrated in vacuo to a volume of 5 mL. Water (30 mL) was added, and the formed precipitate collected by filtration, washed with water (20 mL), and dried in vacuo. Compound **2** was obtained as a red solid (20 mg, 0.019 mmol, 70 %). ^{1}H NMR (400 MHz, CD_3CN): δ = 8.96 (s, 2 H), 8.75 (d, J = 8.1 Hz, 2 H), 8.63 (d, J = 8.1 Hz, 2 H), 8.49 (d, J = 8.1 Hz, 2 H), 8.40 (t, J = 8.1 Hz, 1 H), 8.08 (dd, J = 8.5, 2.3 Hz, 1 H), 8.05 (d, J = 2.2 Hz, 1 H), 7.98–7.87 (m, 4 H), 7.41 (d, J = 5.5 Hz, 2 H), 7.35–7.28 (m, 3 H), 7.28–7.20 (m, 2 H), 7.20–7.12 (m, 4 H), 7.09–7.02 (m, 2 H), 3.52 (s, 3 H) ppm. HRMS (ESI-TOF): calcd. for $C_{43}H_{31}N_7RuS$ [M – 2 PF_6]$^{2+}$ 389.5697; found 389.5702. $C_{43}H_{31}F_{12}N_7P_2RuS$•0.8MeCN•($C_2H_3N$) (1101.89): calcd. C 48.62, H 3.06, N 9.92, S 2.91; found C 48.58, H 3.12, N 9.90, S 2.87.

Route 2: A microwave vial was charged with **8** (10 mg, 0.015 mmol), 2,2′:6′,2″-tpy (3.58 mg, 0.015 mmol), and DMF (1 mL). The vial was capped, and the solution was then purged with nitrogen for 10 min. Subsequently, the mixture was heated in an oil bath at 130 °C under exclusion of light for 1 h. After cooling to r.t., diethyl ether was added, and the precipitate was collected by filtration. The crude product was purified by column chromatography (silica; acetonitrile/water/satd. aqueous KNO_3, 40:4:1). The first red fraction was collected and ammonium hexafluorophosphate added. The solution was concentrated in vacuo to a volume of 5 mL. Water (30 mL) was added, and the formed precipitate was collected by filtration, washed with water (20 mL), and dried in vacuo. Compound **2** was obtained as a red solid (5 mg, 0.005 mmol, 31 %). The characterization of compound **2** is shown in Route 1.

[Ru(oxPTZ–tpy)(tpy)](PF$_6$)$_2$ (3)

Route 3 (First Step): A microwave vial was charged with **9** (10 mg, 0.010 mmol), 2,2′:6′,2″-tpy (2.4 mg, 0.010 mmol), and DMF (1 mL). The vial was capped, and the solution was then purged with nitrogen for 10 min. Subsequently, the mixture was heated in an oil bath at 130 °C under exclusion of light for 1 h. After cooling to r.t., diethyl ether was added, and the precipitate was collected by filtration. The crude mixture was purified by flash column chromatography (Biotage® SNAP KP-NH cartridge, dichloromethane/acetonitrile, 2:1). The first red fraction was collected, and the solvent was evaporated in vacuo. Compound **3** was obtained as a red solid (7 mg, 0.007 mmol, 63 %). ^{1}H NMR (400 MHz, CD_3CN): δ = 9.11 (s, 2 H), 8.87 (d, J = 2.4 Hz, 1 H), 8.76 (d, J = 8.2 Hz, 2 H), 8.68 (d, J = 8.0 Hz, 2 H), 8.54 (dd, J = 8.8, 2.4 Hz, 1 H), 8.50 (d, J = 8.1 Hz, 2 H), 8.41 (t, J = 8.2 Hz, 1 H), 8.07 (dd, J = 7.7, 1.6 Hz, 1 H), 7.98–7.87 (m, 5 H), 7.80 (ddd, J = 8.7, 7.2, 1.6 Hz, 1 H), 7.68 (d, J = 8.3 Hz, 1 H), 7.45–7.38 (m, 3 H), 7.35 (dd, J = 5.6, 0.8 Hz, 2 H), 7.17 (ddt, J = 7.2, 5.5, 1.5 Hz, 4 H), 3.94 (s, 3 H) ppm. HRMS (ESI-TOF): calcd. for $C_{43}H_{31}N_7ORuS$ [M – 2 PF_6]$^{2+}$ 397.5672; found 397.5670.

Route 3 (Second Step): Compound **3** (5 mg, 0.005 mmol) was dissolved in acetonitrile (10 mL), and triflic anhydride (1.7 µL, 0.010 mmol). Potassium iodide (2.6 mg, 0.015 mmol) was added, and the mixture was stirred at r.t. for 30 min. Subsequently, excess ammonium hexafluorophosphate was added. The solution was concentrated in vacuo and water added to precipitate the complex. The formed solid was washed with water (20 mL), methanol (2 mL), toluene (20 mL), and diethyl ether (10 mL). Compound **2** was obtained as a red solid in quantitative yield. The characterization of compound **2** is shown in Route 1.

General Procedure for the Synthesis of Heteroleptic Ru^{II} Complexes [Ru(PTZ–tpy)(C_{60}–Sp–tpy)](PF_6)$_2$ (1a–d): A microwave vial (2 mL) was charged with **9** (10 mg, 0.01 mmol), C_{60}–Sp–tpy ligand (**5a**–**d**; 0.01 mmol), and DMF (1 mL). The vial was capped, and the solution deaerated with nitrogen for 10 min. Subsequently, the vial was heated in an oil bath under exclusion of light at 130 °C for 1 h. TLC (silica; acetonitrile/water/satd. aqueous KNO_3, 40:4:1) showed the consumption of ruthenium precursor **9** and a new, not eluting red spot. The solution was filtered and treated overnight with diethyl ether vapor to force slow precipitation of the complex. The complex was isolated as a sulfoxide in 50–80 % yield. Subsequently, the compound was dissolved in acetonitrile (100 mL), and triflic anhydride (3.64 µL, 0.02 mmol) and potassium iodide (5 mg, 0.03 mmol) were added. The mixture was stirred at r.t. for 30 min Subsequently, excess ammonium hexafluorophosphate was added. The solution was concentrated in vacuo, and water added to precipitate the complex. The formed solid was washed with water (20 mL), methanol (2 mL), toluene (20 mL), and diethyl ether (10 mL). Complexes **1a**–**d** were obtained as dark red solids, and the deoxygenation of the sulfoxides was performed in quantitative yields.

Compound 1a: Yield 52 %. ^{1}H NMR (400 MHz, [D$_6$]DMSO): δ = 9.59 (s, 2 H), 9.44 (s, 2 H), 9.20–8.98 (m, 2 H), 8.97–8.81 (m, 2 H), 8.32 (d, J = 8.6 Hz, 1 H), 8.29 (s, 1 H), 8.01 (t, J = 7.9 Hz, 4 H), 7.53 (d, J = 5.4 Hz, 2 H), 7.39–7.22 (m, 7 H), 7.14–7.01 (m, 4 H), 5.71 (s, 1 H), 5.32 (d, J = 9.7 Hz, 1 H), 4.63 (d, J = 9.7 Hz, 1 H), 3.49 (s, 3 H), 3.17 (s, 3 H) ppm. HRMS (ESI-TOF): calcd. for $C_{106}H_{36}N_8RuS$ [M – 2 PF_6]$^{2+}$ 777.0908; found: 777.0931.

Compound 1b: Yield 84 %. ^{1}H NMR (300 MHz, [D$_6$]DMSO): δ = 9.51 (s, J = 12.9 Hz, 2 H), 9.44 (s, 2 H), 9.11 (d, J = 8.0 Hz, 4 H), 8.55 (d, J = 7.7 Hz, 2 H), 8.35 (d, J = 8.2 Hz, 1 H), 8.31 (s, 1 H), 8.21 (d, J = 7.0 Hz, 2 H), 8.12–7.98 (m, 4 H), 7.61–7.47 (m, 4 H), 7.37–7.18 (m, 7 H), 7.16–7.00 (m, 2 H), 5.36 (s, 1 H), 5.19 (d, J = 9.5 Hz, 1 H), 4.42 (d, J = 9.6 Hz, 1 H), 3.50 (s, 3 H), 2.88 (s, 3 H) ppm. HRMS (ESI-TOF): calcd. for $C_{112}H_{40}N_8RuS$ [M – 2 PF_6]$^{2+}$ 815.1065; found 815.1070.

Compound 1c: Yield 72 %. ^{1}H NMR (400 MHz, [D$_6$]DMSO): δ = 9.51 (s, 2 H), 9.45 (s, 2 H), 9.17–9.07 (m, 4 H), 8.53 (d, J = 8.3 Hz, 2 H), 8.35 (d, J = 8.5 Hz, 1 H), 8.32 (s, 1 H), 8.14–8.02 (m, 4 H), 7.86 (d, J = 8.2 Hz, 2 H), 7.63 (s, 1 H), 7.56 (d, J = 5.4 Hz, 2 H), 7.52 (d, J = 5.5 Hz, 2 H), 7.36–7.22 (m, 8 H), 7.15–7.03 (m, 2 H), 5.58 (s, 1 H), 5.11 (d, J = 9.4 Hz, 1 H), 4.37 (d, J = 9.3 Hz, 1 H), 4.26–4.18 (m, 1 H), 4.16–4.05 (m, 2 H), 3.78–3.67 (m, 1 H), 3.50 (s, 3 H), 2.80 (s, 3 H), 1.80–1.68 (m, 2 H), 1.63–1.43 (m, 6 H), 1.41–1.12 (m, 16 H), 0.90–0.73 (m, 6 H) ppm. HRMS (ESI-TOF): calcd. for $C_{136}H_{76}N_8O_2RuS$ [M – 2 PF_6]$^{2+}$ 993.2440; found 993.2452.

Compound 1d: Yield: 55 %. ^{1}H NMR (300 MHz, [D$_6$]DMSO): δ = 9.52 (s, 2 H), 9.45 (s, 2 H), 9.18–9.04 (m, 4 H), 8.63–8.47 (m, 2 H), 8.39–8.24 (m, 2 H), 8.13–7.95 (m, 4 H), 7.92–7.79 (m, 2 H), 7.62–7.49 (m, 3 H), 7.55–7.48 (m, 2 H), 7.36–7.16 (m, 8 H), 7.15–7.00 (m, 4 H), 5.57 (s, 1 H), 5.04–4.76 (m, 1 H), 4.41–3.70 (m, 9 H), 3.50 (s, 3 H), 2.73 (s, 3 H), 2.03–0.99 (m, 48 H), 0.93–0.61 (m, 12 H) ppm. HRMS (ESI-TOF): calcd. for $C_{160}H_{112}N_8O_4RuS$ [M – 2 PF_6]$^{2+}$ 1171.8808; found 1171.8820.

Supporting Information (see footnote on the first page of this article): Synthetic procedures, geometry-optimized molecular structures, CV spectra, NMR spectra, mass spectra, absorption and emission spectra.

Acknowledgments

The authors are grateful for financial support by the Deutsche Forschungsgemeinschaft (DFG) (grants no. SCHU1229-16/1). The authors also thank Gabriele Sentis (NMR), Tina Schlotthauer (ESI MS), Sarah Crotty (MALDI MS), and Sandra Köhn (elemental analysis) for their help with the respective measurements.

Keywords: Donor–acceptor systems · Electrostatic interactions · Fullerenes · N ligands · Synthetic methods

[1] J. Barber, *Q. Rev. Biophys.* **2003**, *36*, 71–89.
[2] a) L. Sun, L. Hammarström, B. Åkermark, S. Styring, *Chem. Soc. Rev.* **2001**, *30*, 36–49; b) D. Gust, T. A. Moore, A. L. Moore, *Acc. Chem. Res.* **2001**, *34*, 40–48; c) D. M. Guldi, *Chem. Soc. Rev.* **2002**, *31*, 22–36; d) M. R. Wasielewski, *J. Org. Chem.* **2006**, *71*, 5051–5066; e) D. Gust, T. A. Moore, A. L. Moore, *Acc. Chem. Res.* **2009**, *42*, 1890–1898.
[3] a) R. A. Marcus, *J. Chem. Phys.* **1956**, *24*, 966–978; b) R. A. Marcus, N. Sutin, *Biochim. Biophys. Acta Rev. Bioenerg.* **1985**, *811*, 265–322.
[4] a) L. Flamigni, F. Barigelletti, N. Armaroli, J.-P. Collin, I. M. Dixon, J.-P. Sauvage, J. A. G. Williams, *Coord. Chem. Rev.* **1999**, *190–192*, 671–682; b) E. Baranoff, J.-P. Collin, L. Flamigni, J.-P. Sauvage, *Chem. Soc. Rev.* **2004**, *33*, 147–155; c) M. H. V. Huynh, D. M. Dattelbaum, T. J. Meyer, *Coord. Chem. Rev.* **2005**, *249*, 457–483; d) V. Balzani, G. Bergamini, F. Marchioni, P. Ceroni, *Coord. Chem. Rev.* **2006**, *250*, 1254–1266; e) P. P. Lainé, S. Campagna, F. Loiseau, *Coord. Chem. Rev.* **2008**, *252*, 2552–2571; f) E. A. Alemán, C. D. Shreiner, C. S. Rajesh, T. Smith, S. A. Garrison, D. A. Modarelli, *Dalton Trans.* **2009**, 6562–6577; g) J. Hankache, M. Niemi, H. Lemmetyinen, O. S. Wenger, *Inorg. Chem.* **2012**, *51*, 6333–6344.
[5] a) J.-P. Collin, S. Guillerez, J.-P. Sauvage, F. Barigelletti, L. De Cola, L. Flamigni, V. Balzani, *Inorg. Chem.* **1992**, *31*, 4112–4117; b) J. Fortage, F. Puntoriero, F. Tuyèras, G. Dupeyre, A. Arrigo, I. Ciofini, P. P. Lainé, S. Campagna, *Inorg. Chem.* **2012**, *51*, 5342–5352.
[6] J. H. Klein, T. L. Sunderland, C. Kaufmann, M. Holzapfel, A. Schmiedel, C. Lambert, *Phys. Chem. Chem. Phys.* **2013**, *15*, 16024–16030.
[7] a) S.-H. Lee, C. T.-L. Chan, K. M.-C. Wong, W. H. Lam, W.-M. Kwok, V. W.-W. Yam, *Dalton Trans.* **2014**, *43*, 17624–17634; b) S.-H. Lee, C. T.-L. Chan, K. M.-C. Wong, W. H. Lam, W.-M. Kwok, V. W.-W. Yam, *J. Am. Chem. Soc.* **2014**, *136*, 10041–10052.
[8] a) M. E. El-Khouly, C. A. Wijesinghe, V. N. Nesterov, M. E. Zandler, S. Fukuzumi, F. D'Souza, *Chem. Eur. J.* **2012**, *18*, 13844–13853; b) J. B. Kelber, N. A. Panjwani, D. Wu, R. Gómez-Bombarelli, B. W. Lovett, J. J. L. Morton, H. L. Anderson, *Chem. Sci.* **2015**, *6*, 6468–6481; c) M. R. Wasielewski, G. L. Gaines, M. P. O'Neil, W. A. Svec, M. P. Niemczyk, *J. Am. Chem. Soc.* **1990**, *112*, 4559–4560; d) H. Imahori, Y. Sekiguchi, Y. Kashiwagi, T. Sato, Y. Araki, O. Ito, H. Yamada, S. Fukuzumi, *Chem. Eur. J.* **2004**, *10*, 3184–3196.
[9] a) P. K. Poddutoori, G. N. Lim, A. S. D. Sandanayaka, P. A. Karr, O. Ito, F. D'Souza, M. Pilkington, A. van der Est, *Nanoscale* **2015**, *7*, 12151–12165; b) P. K. Poddutoori, A. S. D. Sandanayaka, N. Zarrabi, T. Hasobe, O. Ito, A. van der Est, *J. Phys. Chem. A* **2011**, *115*, 709–717; c) P. K. Poddutoori, A. S. D. Sandanayaka, T. Hasobe, O. Ito, A. van der Est, *J. Phys. Chem. B* **2010**, *114*, 14348–14357; d) P. K. Poddutoori, G. N. Lim, S. Vassiliev, F. D'Souza, *Phys. Chem. Chem. Phys.* **2015**, *17*, 26346–26358.
[10] S. Yoon, P. Kukura, C. M. Stuart, R. A. Mathies, *Mol. Phys.* **2006**, *104*, 1275–1282.
[11] K. Barthelmes, J. Kübel, A. Winter, M. Wächtler, C. Friebe, B. Dietzek, U. S. Schubert, *Inorg. Chem.* **2015**, *54*, 3159–3171.
[12] B. Albinsson, M. P. Eng, K. Pettersson, M. U. Winters, *Phys. Chem. Chem. Phys.* **2007**, *9*, 5847–5864.
[13] a) F. Chaignon, J. Torroba, E. Blart, M. Borgström, L. Hammarström, F. Odobel, *New J. Chem.* **2005**, *29*, 1272–1284; b) G. Possamai, E. Menna, M. Maggini, M. Carano, M. Marcaccio, F. Paolucci, D. M. Guldi, A. Swartz, *Photochem. Photobiol. Sci.* **2006**, *5*, 1154–1164
[14] a) S. Chakraborty, T. J. Wadas, H. Hester, R. Schmehl, R. Eisenberg, *Inorg. Chem.* **2005**, *44*, 6865–6878; b) N. Bucci, T. J. J. Müller, *Tetrahedron Lett.* **2006**, *47*, 8323–8327; c) C. B. KC, G. N. Lim, M. E. Zandler, F. D'Souza, *Org. Lett.* **2013**, *15*, 4612–4615; d) V. Bandi, H. B. Gobeze, V. N. Nesterov, P. A. Karr, F. D'Souza, *Phys. Chem. Chem. Phys.* **2014**, *16*, 25537–25547.
[15] T. Kamimura, K. Ohkubo, Y. Kawashima, S. Ozako, K.-i. Sakaguchi, S. Fukuzumi, F. Tani, *J. Phys. Chem. C* **2015**, *119*, 25634–25650.
[16] T. Miyazaki, M. Shibahara, J.-i. Fujishige, M. Watanabe, K. Goto, T. Shinmyozu, *J. Org. Chem.* **2014**, *79*, 11440–11453.

[17] a) J. Wang, G. S. Hanan, *Synlett* **2005**, 1251–1254; b) A. Winter, A. M. J. van den Berg, R. Hoogenboom, G. Kickelbick, U. S. Schubert, *Synthesis* **2006**, 2873–2878.
[18] M.-P. Santoni, A. K. Pal, G. S. Hanan, A. Proust, B. Hasenknopf, *Inorg. Chem. Commun.* **2011**, *14*, 399–402.
[19] B. Schulze, D. Escudero, C. Friebe, R. Siebert, H. Görls, S. Sinn, M. Thomas, S. Mai, J. Popp, B. Dietzek, L. González, U. S. Schubert, *Chem. Eur. J.* **2012**, *18*, 4010–4025.
[20] K. Bahrami, M. M. Khodaei, A. Karimi, *Synthesis* **2008**, 2543–2546.
[21] A. Juris, V. Balzani, F. Barigelletti, S. Campagna, P. Belser, A. von Zelewsky, *Coord. Chem. Rev.* **1988**, *84*, 85–277.
[22] E. A. Medlycott, G. S. Hanan, *Coord. Chem. Rev.* **2006**, *250*, 1763–1782.
[23] A. Hirsch, M. Brettreich, *Fullerenes*, Wiley-VCH, Weinheim, **2005**.
[24] E. A. Medlycott, G. S. Hanan, *Chem. Soc. Rev.* **2005**, *34*, 133–142.
[25] H. A. Garrera, J. J. Cosa, C. M. Previtali, *J. Photochem. Photobiol. A* **1989**, *47*, 143–153.
[26] R. Siebert, A. Winter, U. S. Schubert, B. Dietzek, J. Popp, *Phys. Chem. Chem. Phys.* **2011**, *13*, 1606–1617.
[27] G. Accorsi, N. Armaroli, *J. Phys. Chem. C* **2010**, *114*, 1385–1403.
[28] B. Schulze, C. Friebe, M. D. Hager, A. Winter, R. Hoogenboom, H. Görls, U. S. Schubert, *Dalton Trans.* **2009**, 787–794.
[29] A. Winter, D. A. M. Egbe, U. S. Schubert, *Org. Lett.* **2007**, *9*, 2345–2348.
[30] A. Winter, C. Friebe, M. D. Hager, U. S. Schubert, *Eur. J. Org. Chem.* **2009**, 801–809.

Received: July 21, 2016
Published Online: October 17, 2016

Publication P4

"Molecular Dyads and Triads Based on Phenothiazine and
π-extended Tetrathiafulvalene Donors,
Ruthenium(II) Bisterpyridine Complexes and Polyoxometalates"

K. Barthelmes, M. Sittig, A. Winter, U. S. Schubert,

submitted.

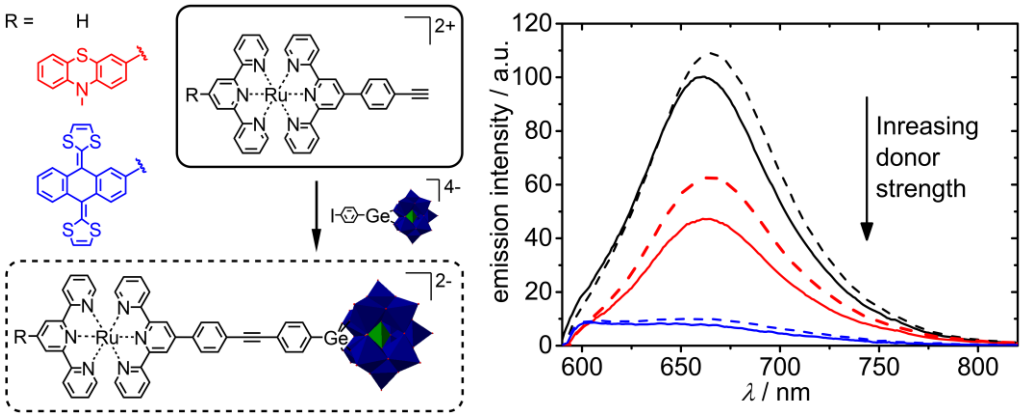

Molecular Dyads and Triads Based on Phenothiazine and π-extended Tetrathiafulvalene Donors, Ruthenium(II) Bisterpyridine Complexes and Polyoxometalates

Kevin Barthelmes,[a,b] Maria Sittig,[a] Andreas Winter,[a,b] Ulrich S. Schubert*[a,b]

Abstract: Molecular dyads were prepared by the functionalization of organic electron donor units, *i.e.*, a phenothiazine (PTZ) moiety and a π-extended tetrathiafulvalene (exTTF) moiety with Ru(II) bisterpyridine complexes. In addition, the complexes were equipped with a terminal alkyne group, which was used for the coupling with a Keggin-type polyoxometalate (POM). In this regard, molecular triads were prepared whereby the central Ru(II) complex should act as photosensitizer and the POM as electron acceptor. Certain spectral changes were observed upon attachment of the donors and the POM framework to the Ru(II) complexes. In particular, the emission of the Ru(II) complex became reduced significantly with increasing donor strength, which suggested an intramolecular electron transfer *via* reductive emission quenching. The introduction of the POM framework revealed no further quenching of the emission and is tentatively ascribed to minor influence of the electron acceptor on the excited states of the Ru(II) complex.

Introduction

The preparation of artificial photosynthetic devices represents one major scientific challenge for the direct generation of solar fuels.[1] In the last decades, the design of photoactive systems focused on one of the key steps, the photo-induced charge-separation (CS). It is generally required that after photo-excitation a long-living charge-separated state is efficiently formed. One approach to realize this is the covalent linkage within donor-photosensitizer-acceptor systems (D-P-A). In this respect, the functionalization of a redox active organometallic photosensitizer with an electron donor and acceptor with a lower oxidation and a higher reduction potential, respectively, would introduce a redox gradient whereby a photo-induced CS with two sequential electron-transfer processes is possible. Such an approach has successfully been applied for a variety of organometallic systems with attached electron donor and acceptor moieties;[2] however, to best of our knowledge, such a molecular design has not yet been established for polyoxometalates (POMs). POMs have recently attracted considerable interest for use as electron acceptor material. Many different structures of these cluster-type metal oxides were investigated, taking their elemental composition, size, charge and molecular structure into account.[3] As a main characteristic, redox-active POMs are able to store several electrons, and the reduced species have shown their potential as efficient catalyst in many electrocatalytic reactions.[4] The ability to functionalize POMs by surface attachment of organic fragments opens the field of covalently linked organic-inorganic hybrid materials that offer new features for applications in catalysis, photochemistry and medicine as well as for surface modification.[5] For POMs that were covalently connected to metal-based photosensitizers, like Ru(II)[6] and Ir(III)[7] polypyridyl complexes or metalloporphyrins with Zn(II)[8] and Ru(II) ions,[9] an intramolecular electron transfer upon light excitation and the formation of a CS state could be observed.

In this study, intense visible light absorbing ruthenium(II) bisterpyridine ($[Ru(tpy)_2]^{2+}$) complexes were used as photosensitizer despite their short excited-state lifetime compared to the related Ru(II) trisbipyridine ($[Ru(bpy)_3]^{2+}$) complexes. Nevertheless, we focused on $[Ru(tpy)_2]^{2+}$ sensitizers, because of the rapid access to functionalized tpy ligands in 4'-position by one-pot reactions[10] and their relative mild coordination to Ru(II) centers resulting in linear and isomer free D-P-A systems. We introduced a phenothiazine (PTZ) donor and a π-extended tetrathiafulvalene (exTTF) donor on anthraquinone basis, on one of the two tpy ligand in the $[Ru(tpy)_2]^{2+}$ complex. Both organic donors have already shown their potential in artificial photosynthetic devices.[11] The second tpy ligand bears a terminal alkyne unit, which is used for attaching the complex to an organo-functionalized POM. Moreover, dyads were prepared, which miss either the donor or the acceptor unit, to elucidate the influence of the active units on the excited state properties of $[Ru(tpy)_2]^{2+}$ complex.

Results and Discussion

Synthesis. The preparation of alkyne-functionalized Ru(II) bisterpyridine complexes was accomplished by a synthetic route following a method introduced by the group of Stahl.[12] Here, the Sonogashira cross-coupling reaction of 4'-(4-bromophenyl)-2,2':6',2''-terpyridine (**1**) with (triisopropylsilyl)acetylene yielded the triisopropylsilyl-protected (TIPS) alkyne-functionalized tpy **2** (Scheme 1). The protection group was necessary for the subsequent coordination reaction with Ru(III) trichloride hydrate, since it has been reported that unprotected alkynes decompose during the reaction.[13] The resulting Ru(III) trichloro precursor **3** was subsequently rendered to the Ru(II) trisacetonitrile precursor **4** *via* a Ag(I)-assisted dehalogenation method developed by Jäger *et al*.[14]

[a] Laboratory of Organic and Macromolecular Chemistry (IOMC)
Friedrich Schiller University Jena
Humboldtstr. 10, 07743 Jena, Germany
E-mail: ulrich.schubert@uni-jena.de
http://www.schubert-group.de
[b] Center for Energy and Environmental Chemistry Jena (CEEC Jena)
Friedrich Schiller University Jena
Philosophenweg 7a, 07743 Jena, Germany
Supporting information for this article is given via a link at the end of the document

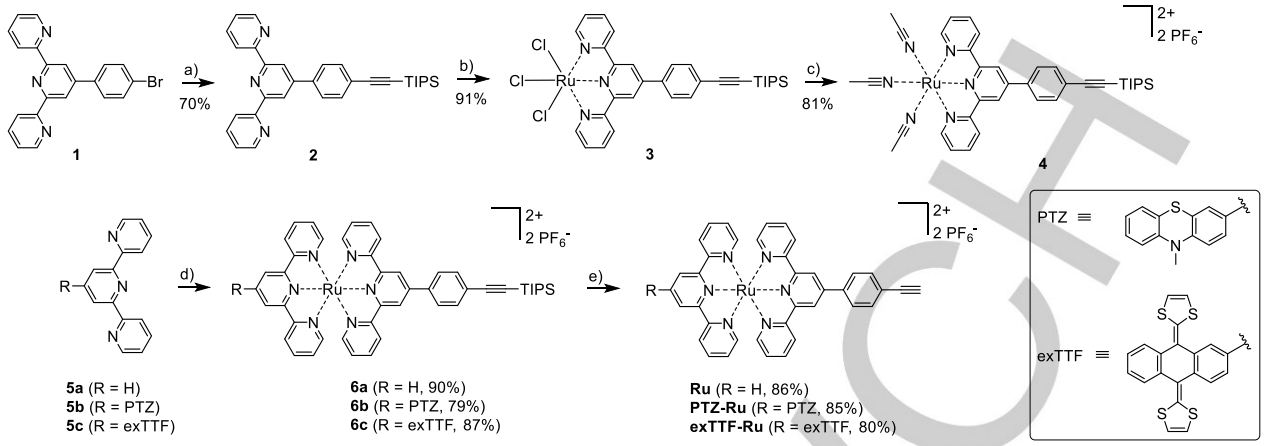

Scheme 1. Schematic representation of the synthesis of the Ru(II) complexes **Ru**, **PTZ-Ru** and **exTTF-Ru**: a) (trisopropylsilyl)acetylene, $Pd(PPh_3)_2Cl_2$, CuI, NEt_3, THF, 60 °C, 24 h; b) $RuCl_3 \times xH_2O$, EtOH, 96 °C, 4 h; c) (i) $AgNO_3$, MeCN/EtOH/H_2O, 80 °C, 4 h, (ii) excess NH_4PF_6; d) **4**, DMF, 130 °C, 1 h; e) NBu_4F/KF, CH_2Cl_2/MeOH, 40 °C, 5 days.

The labile acetonitrile ligands in **4** could easily be substituted by a second tridentate ligand.[14-15] Hereby, **4** was reacted with three different tpy ligands, *i.e.*, 2,2′:6′,2″-terpyridine (**5a**), PTZ-tpy ligand (**5b**) or the exTTF-tpy ligand (**5c**), at 130 °C in DMF and gave the heteroleptic Ru(II) complexes **6a-c** in high yields (Scheme 1). The PTZ-tpy (**5b**)[2d] and exTTF-tpy (**5c**) ligands were prepared in a one-pot Kröhnke-type synthesis starting from the corresponding aldehydes. However, in the case of **5c**, the solvent for the reaction had to be changed from EtOH to an EtOH/THF mixture, since the **exTTF-CHO** compound is hardly soluble in EtOH (Scheme 2).

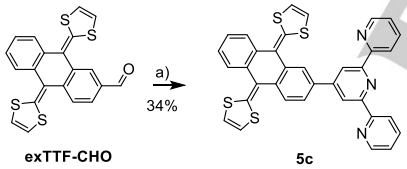

Scheme 2. Schematic representation of the syntheses of the exTTF-tpy ligand **5c**: a) (i) 2-acetylpyridine, NaOH, $NH_{3\ aq.}$, EtOH/THF, 48 h, 30 °C.

Finally, the TIPS groups in **6a-c** were cleaved of with a Bu_4NF/KF salt mixture at 40 °C in CH_2Cl_2/MeOH; the alkyne-functionalized complexes **Ru** and **PTZ-Ru** and **exTTF-Ru** were obtained in good yields (Scheme 1). Worth a note, the reaction proceeded very slow and required five days at elevated temperatures to reach a full conversion; an alternative protocol employing AgF in MeCN, followed by a protonation with perchloric acid, was also successfully applied on **6b**.[12]

The preparation of the Ru(II) complex/POM conjugates was realized by the grafting approach developed by the group of Izzet and Proust (Scheme 3).[5d] Hereby, the positively charged Ru(II) complexes (*i.e.*, **Ru**, **PTZ-Ru** or **exTTF-Ru**) were coupled in a Sonogashira cross-coupling reaction *via* their terminal alkyne groups to the negatively charged lacunary Keggin-type polyoxotungstate $[PW_{11}O_{39}\{GeC_6H_4I\}]^{4-}$ (**POM**) containing a 4-iodophenyl germane functionality in the cavity. The coupling reaction was performed under microwave irradiation and gave the dyad **Ru-POM** and the two triads **PTZ-Ru-POM** and **exTTF-Ru-POM** in high yields within 1 h. The cation was subsequently exchanged to 1-butyl-3-methyl-1*H*-imidazol-3-ium ($BMIm^+$); as reported in literature, isolation problems might occur when retaining the NBu_4^+ cations. As an alternative route also the ruthenium(III) coordination to a tpy-functionalized POM was explored.[16] However, the conditions required for this reaction were not capable for the POM system. In contrast to the starting Ru(II) complexes and the starting POM, the Ru(II) complex/POM conjugates were moderately soluble in DMF or DMSO and virtually insoluble in acetonitrile.

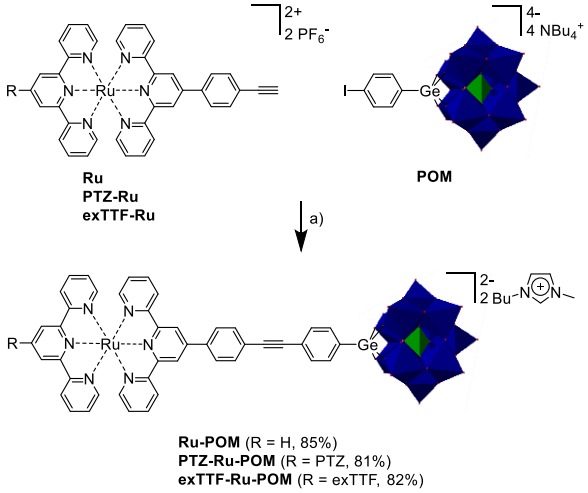

Scheme 3. Schematic representation of the syntheses of the Ru(II) complex/POM conjugates **Ru-POM**, **PTZ-Ru-POM** and **exTTF-Ru-POM**: a) (i) $Pd(PPh_3)_2Cl_2$, CuI, NEt_3, DMF, 70 °C MW irradiation, 1 h, (ii) excess BMImCl, DMSO, r.t., 1 h.

NMR Spectroscopy. The Ru(II) complex/POM conjugates were identified by their ^{1}H NMR spectra in DMSO-d_6 confirming the successful synthesis. Noteworthy, it was reported that the positively and negatively charged starting materials could also form hybrids *via* electrostatic attraction of the components, thereby preventing a coupling reaction.[6] As confirmed by 2D-NMR techniques, the spectrum of **Ru-POM** exhibits the same signals in the aromatic region, though slightly shifted and broadened as found in **Ru** (Figure 1). The successful coupling-reaction was also concluded from the disappearance of the terminal alkyne signal at around 4.5 ppm, along with a small shift for the signal of the phenyl group (assigned as *3''''*) next to triple bond from 7.88 to 7.95 ppm, resulted by the coupling-reaction. Moreover, two new doublets appeared at 7.70 and 7.58 ppm (assigned as *2* and *3*) that belong to the second phenyl group next to the POM (Figure 1). Noteworthy, the aromatic signals of the BMIm$^+$ cation appear at 7.69, 7.76 and 8.30 ppm and the integral ratio between signals of the cations and signals the organic part fits to the overall negative charge of two. A detailed signal assignment for **PTZ-Ru-POM** (Figure S2) and **exTTF-Ru-POM** (Figure S3) is given in the SI.

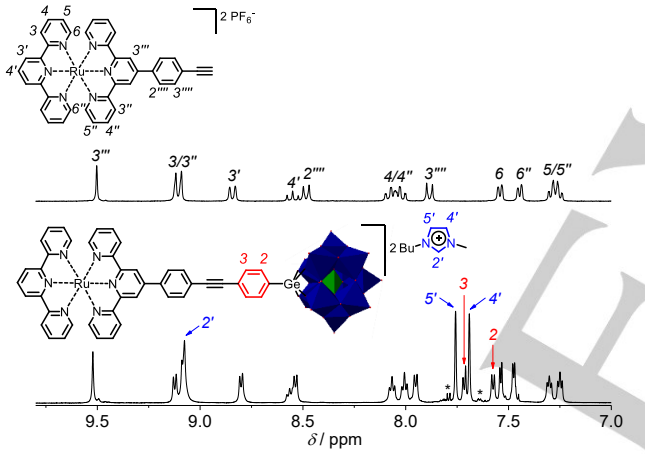

Figure 1. ^{1}H NMR spectra (aromatic region) of **Ru** (top) and **Ru-POM** (bottom) in DMSO-d_6. The asterisks mark impurities.

Electrochemistry. The electrochemical properties of the compounds were investigated by cyclic voltammetry (CV) and differential pulse voltammetry (DPV) measurements in 0.1 M Bu_4NPF_6/DMF solution using a potential window between −2 and +1 V against ferrocene as reference. The Ru(II) complex **Ru** exhibited two reversible processes in the cathodic region at −1.56 and −1.81 V (*i.e.*, DPV potentials), which were ascribed to one-electron reductions of the tpy units (Figure 2). In the anodic region, a reversible Ru(III)/Ru(II) redox couple appeared at 0.82 V. In the case of dyad **PTZ-Ru**, the same redox processes were observed with the Ru(III)/Ru(II) couple being slightly cathodically shifted to 0.78 V (Table 1, Figure 2). Additionally, a reversible redox process at 0.37 V was present, which was ascribed to the one-electron oxidation of the PTZ unit to the radical cation ($PTZ^{\bullet+}$).[2b]

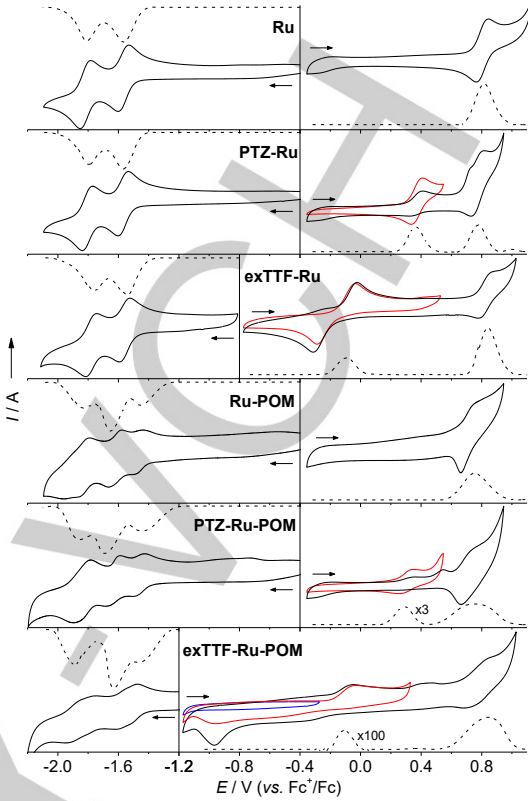

Figure 2. Cyclic (solid lines, different colors illustrate different potential ranges, scan rate = 0.2 V s^{-1}, 5th cycle is shown) and differential pulse (dashed lines) voltammograms in DMF/0.1 M Bu_4NPF_6. Left: Cathodic region. Right: Anodic region. The arrows show the scan direction.

Table 1. Electrochemical properties[a]

entry	$E_{ox,1}$ / V	$E_{ox,2}$ / V	$E_{ox,3}$ / V	$E_{red,1}$ / V	$E_{red,2}$ / V	$E_{red,3}$ / V
Ru	0.82	-	-	−1.56	−1.81	-
PTZ-Ru	0.37	0.73[b,d]	0.78	−1.57	−1.80	-
exTTF-Ru	−0.03[b] −0.30[c]	0.84	-	−1.55	−1.76	-
POM	-	-	-	−1.50	−2.00	-
Ru-POM	0.75	-	-	−1.46	−1.65	−1.84
PTZ-Ru-POM	0.29	0.55[b,d]	0.75	−1.45	−1.69	−1.86
exTTF-Ru-POM	−0.03[b] −0.57[c] −0.97[c]	0.43[b,d]	0.84	−1.46	−1.63	−1.89

Conditions: deaerated 0.1 M Bu_4NPF_6/DMF solution, referenced against Fc^+/Fc. [a] DPV potentials are given. [b] Anodic peak potentials from the CV. [c] Cathodic peak potentials from the CV. [d] Irreversible process.

An irreversible oxidation was observed at 0.73 V close to the Ru(III)/Ru(II) redox couple and might be the reason for the irreversibility of the PTZ$^{\bullet+}$/PTZ redox couple when the ruthenium center was oxidized in the same cycle (Figure 2). For the dyad **exTTF-Ru**, the Ru(III)/Ru(II) redox wave was centered at +0.84 V and similar potentials were observed for the tpy reductions (Table 1, Figure 2). Furthermore, the exTTF unit in the complex could be oxidized at −0.03 V (anodic peak potential) quasi-reversibly in one two-electron oxidation step to the dicationic exTTF^{2+} species and got re-reduced at −0.30 V (cathodic peak potential) in one two-electron reduction step (Figure 3).[17] Consequently, the exTTF unit represented the stronger donor when compared to PTZ by roughly 0.4 V. The large peak split (*i.e.*, 270 mV) of the exTTF^{2+}/exTTF redox couple is known from literature and is caused by the tremendous geometrical changes of the exTTF fragment during its oxidation/re-reduction.[17-18] It is supposed that this behavior caused the difference between the DPV potential and the half-wave potential of the CV.

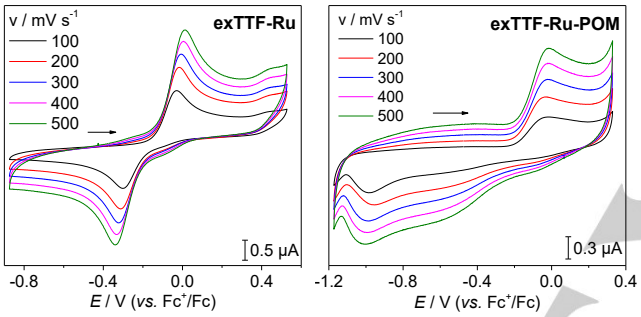

Figure 3. Cyclic (5th cycle is shown) voltammograms of **exTTF-Ru** and **exTTF-Ru-POM** in DMF/0.1 M Bu_4NPF_6 with different scan rates showing the exTTF^{2+}/exTTF redox couple with a two-electron oxidation step and the re-reduction in either a two-electron re-reduction (left) or two one-electron re-reduction steps (right). The arrow shows the scan direction.

As reported,[19] the starting **POM** exhibited no oxidation process and two reversible redox waves at −1.50 and −2.00 V arising from two one-electron reductions of the polyoxotungstate unit (Figure S4). In the dyad **Ru-POM**, the Ru(III)/Ru(II) couple was shifted to +0.75 V and, thus, the ruthenium center became easier to be oxidized – probably due to the anionic effect of the POM (Figure 2). The first reductive process in this system occured at −1.46 V and was tentatively assigned to the first one-electron reduction of the POM. The potential appeared slightly anodically shifted (*i.e.*, 40 mV) *vs.* **POM**, indicating a certain electrostatic interaction to the Ru(II) complex. The following redox processes appear at −1.65 and −1.84 V; however, a precise assignment of each process to a certain fragment in the molecule by comparing it to the reference spectra was not possible. According to the spectra of **Ru** and **POM** four reductive processes should appear in cathodic region, however, only three processes could be observed and presumably two processes were overlapping (Figure 2). An indication for this could be the increased peak current in the CV for the third reductive process at −1.84 V. The triad **PTZ-Ru-POM** exhibited similar potentials as the dyad **Ru-POM** with the PTZ$^{\bullet+}$/PTZ redox couple at +0.29 V. The process was anodically shifted *vs.* the dyad **PTZ-Ru**, and indicated that the anionic POM still had an effect on the PTZ redox potential although they were separated by the Ru(II) complex. As in **PTZ-Ru**, for **PTZ-Ru-POM** an irreversible oxidation at +0.55 V could be observed, which tentatively led to the irreversibility of the PTZ$^{\bullet+}$/PTZ redox couple (Figure 2). The triad **exTTF-Ru-POM** revealed a worse resolved cathodic region in the CV voltammogram; nevertheless, the DPV potentials were similar to the other POM-based conjugates. The anodic peak potential of the exTTF oxidation in **exTTF-Ru-POM** was identical to that of **exTTF-Ru**, however the re-reduction occurred in two one-electron steps with cathodic peak potentials at −0.57 and −0.97 V and, consequently, resulted in an even larger peak split, respectively (Figure 3). To proof that the two re-reduction steps were the result of the oxidation step, we applied a narrower potential range (*i.e.*, excluding the oxidation step), which did not show any reduction processes (Figure 2, blue line). The larger peak split, as well as the two one-electron re-reductions clearly showed the influence of the POM on the exTTF^{2+}/exTTF redox couple, in particular during the re-reductions of the exTTF^{2+} species, which was more hindered. Furthermore, we observed in-between the exTTF and ruthenium oxidation an irreversible process; however, this did not result in any irreversibility of the latter two processes. In both triads (**exTTF-Ru-POM** and **PTZ-Ru-POM**) the peak current in the DPV of the donor oxidation was low compared to the peak current of the ruthenium oxidation (Figure 2). A possible explanation for this could be an adsorption processes during the ruthenium oxidation on the electrode.

UV-vis Spectroscopy. The UV-vis absorption spectra of the compounds in DMSO are depicted in Figure 4 (spectra in DMF are shown in Figure S5).

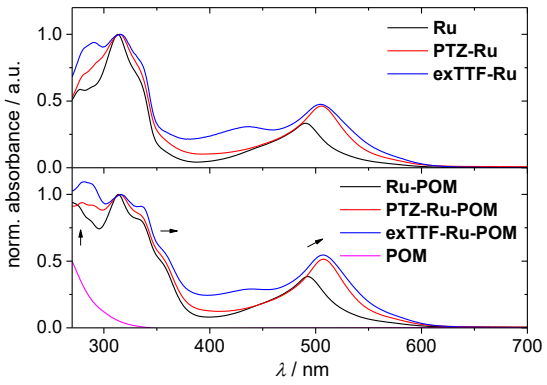

Figure 4. UV-vis absorption spectra in DMSO. The black arrows indicate the spectral changes compared to their reference Ru(II) complexes and the starting **POM**.

The Ru(II) complexes **Ru**, **PTZ-Ru** and **exTTF-Ru** showed the typical spectra known for Ru(II) polypyridyl complexes:[20] The UV region was dominated by an absorption band with a

maximum at around 314 nm and a weakly pronounced lower energetic shoulder. The absorption was ascribed mainly to π-π^* transitions of the tpy ligands and their 4'-functionalities, *i.e.*, the PTZ unit, the exTTF unit and the 4-ethynylphenyl group. The visible region of the Ru(II) complexes was dominated by absorption bands of metal-to-ligand charge-transfer (^{1}MLCT) transitions with maxima at 490 nm (ε = 22.3×10^3 M^{-1} cm^{-1}), 506 nm (ε = 33.5×10^3 M^{-1} cm^{-1}) and 505 nm (ε = 35.2×10^3 M^{-1} cm^{-1}) for **Ru**, **PTZ-Ru** and **exTTF-Ru**, respectively. The bathochromic shift and increased extinction coefficient clearly revealed the influence of the PTZ unit and the exTTF unit on the ^{1}MLCT absorption band, which was attributed to an extended electron delocalization between the tpy and the PTZ/exTTF orbitals. Moreover, the complex **exTTF-Ru** exhibited a distinct absorption band at 436 nm, which was assigned to lower energetic π-π^* transitions within the exTTF unit.[21] The spectra of the Ru(II) complex/POM conjugates **Ru-POM**, **PTZ-Ru-POM** and **exTTF-Ru-POM** were similar regarding their spectral shape to the corresponding Ru(II) complexes without the POM unit (Figure 4). An additional absorption band appeared at around 280 nm, which was presumably associated with the spectral characteristics of the aryl functionalized **POM** (Figure 4). Moreover, next to the UV absorption band at 314 nm, a second shoulder at 358 nm on the low-energetic flank could be related to π-π^* transitions in the increased π-conjugated system of the 4-phenylethynyl-4'-phenyl subunit. The effect of increased π-conjugation was also visible in a slight bathochromic shift and higher extinction coefficients of the ^{1}MLCT absorption maxima (Table 2).[22]

Table 2. Photophysical properties

entry	$\lambda_{abs,\ MLCT}$ / nm (ε / 10^3 M^{-1} cm^{-1})	$\lambda_{max,\ em}$ / nm[a]	Area of the emission band[b] / %
Ru	490 (22.3)	660	100
PTZ-Ru	506 (33.5)	662	47
exTTF-Ru	505 (35.2)	–[c]	11
Ru-POM	493 (26.8)	665	109
PTZ-Ru-POM	508 (37.7)	665	62
exTTF-Ru-POM	507 (39.8)	–[c]	14

Conditions: aerated DMSO solution, room temperature. [a] Isoabsorbing solutions with 0.3 optical density at λ_{exc} = 500 nm. [b] Area between 588 and 900 nm relative to **Ru**. [c] No defined emission maximum determinable.

The emission spectra were recorded in isoabsorbing (optical density was 0.3 at 500 nm) DMSO solutions (spectra in DMF are shown in Figure S5) of the Ru(II) complexes and the Ru(II) complex/POM conjugates. The compounds were excited with 500 nm, which is the lower energetic flank of ^{1}MLCT absorption band in **Ru** and **Ru-POM**, while it is the higher energetic flank in donor-functionalized complexes. Since $[Ru(tpy)_2]^{2+}$ complexes exhibit a reduced excited-state lifetime, they also show a weaker ^{3}MLCT emission compared to $[Ru(bpy)_3]^{2+}$ complexes. Nevertheless, a weak emission with a maximum at 660 nm was observed for the complex **Ru** (Figure 5). The complex **PTZ-Ru** showed a similar emission band at 662 nm; however, the emission intensity (*i.e.*, the area of the emission band) was reduced to ca. 50% compared to **Ru** (Figure 5). This effect was previously ascribed in related PTZ–P systems (P = Ru(II) polypyridyl photosensitizer) as a reductive emission quenching by the PTZ unit, which resulted in a charge-separated species with a formal PTZ$^+$–P$^-$ character.[2d, 11h, 23] The fact that the exTTF unit represents the stronger electron donor was in full agreement with the observed further reduced emission in **exTTF-Ru** (Figure 5). Here, the emission intensity is decreased down to ca. 10% compared to **Ru** and ca. 20% compared to **PTZ-Ru**, respectively. Also in this case reductive quenching by the exTTF moiety results in the formation of the charge-separated species with a formal exTTF$^+$–P$^-$ character and was already described in several TTF-P systems.[24]

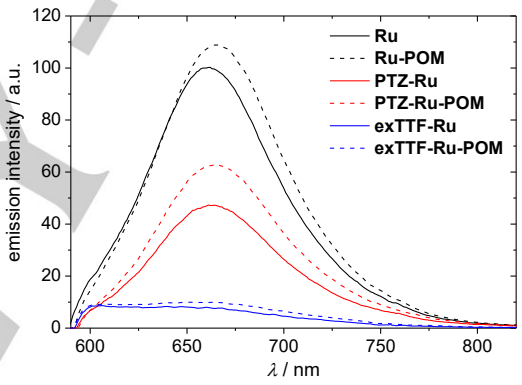

Figure 5. Room temperature emission spectra in isoabsorbing (λ_{exc} = 500 nm) DMSO solutions of the Ru(II) complexes and the Ru(II) complex/POM conjugates.

It was expected that the emission was reduced further in the Ru(II)/POM conjugates, due to an oxidative quenching by POM framework; however, we could not observe any additional quenching behavior. In contrast, higher emission intensities and slightly bathochromically shifted emission maxima were observed compared to the corresponding Ru(II) complexes (Figure 5, Table 2). In the case of the dyad **Ru-POM**, the emission was increased by around 10%, while for the triads an increase of 30% (**PTZ-Ru-POM**) and 25% (**exTTF-Ru-POM**) could be observed. The reason for the increased emission intensity is tentatively ascribed to the presence of an increased π-conjugated system, resulting in stabilization of the excited ^{3}MLCT state.[22]

A different emission behavior has been observed for similar systems developed by the group of Izzet based on two cyclometalated Ru(II) polypyridine complexes covalently connected by a silyl group to the same POM framework.[6] However, the different mode of functionalization resulted in an

overall less negatively charged POM and, thereby, in an easier to reduce POM. In that study, the ^{3}MLCT emission was quenched by around 50% (*i.e.*, based on the quantum yields) when the POM was attached. The reduced luminescence was attributed to an oxidative quenching by the POM, which resulted in a CS state between the Ru(II) complex and the POM. However, no CS state could be detected by nanosecond transient absorption spectroscopy. According to the simplified Rehm-Weller equation (1) an exergonic electron-transfer process with an estimated driving force of approximately ΔG_{CS} = −0.65 eV should populate the CS state.[25]

$$\Delta G_{CS} = E_{ox,1} - E_{red,1} - E_{00} \quad (1)$$

Here, $E_{ox,1}$ and $E_{red,1}$ represent the first oxidation and reduction potentials, and E_{00} is the energy of the excited ^{3}MLCT state, which can be estimated from the energy of the emission maximum in the Ru(II) complex/POM conjugate. Estimating the driving force for the shown systems, CS would occur by an endergonic process in **Ru-POM** (ΔG_{CS} = 0.35 eV to the Ru^+–POM^- species) and by exergonic processes in **PTZ-Ru-POM** (ΔG_{CS} = −0.12 eV to the PTZ^+–Ru–POM^- species) and **exTTF-Ru-POM** (ΔG_{CS} = −0.43 eV to the $exTTF^+$–Ru–POM^- species). If one would argue with the driving forces, a CS involving the POM should be plausible at least for **exTTF-Ru-POM**. However, based on the current steady-state measurements, we cannot evaluate the population of a long-range CS state between the donor and the POM. A possible reason could be the similar redox potentials for the tpy reduction and the POM reduction, which prevent the electron transfer from the reduced tpy (Ru^-) to the POM. Time-resolved spectroscopy measurements are required to elucidate the photodynamic processes and are part of ongoing research.

Conclusions

In summary, the reported exTTF/PTZ-functionalized Ru(II) complex/POM conjugates were readily synthesized by straightforward and versatile method for the preparation of molecular triads. The compounds were analyzed regarding their electrochemical and photophysical properties with respect to their interactions between the redox and photoactive moieties. Electrostatic interaction has been found between the POM framework and the PTZ/exTTF units although they are separated by the Ru(II) complex. The excited-state properties were investigated by emission spectroscopy and revealed a donor strength depending quenching behavior of the $[Ru(tpy)_2]^{2+}$ based emission. It is assumed that the excited ^{3}MLCT state gets depopulated by an intramolecular electron transfer, which results in a charge-separated state between the organic donors and the Ru(II) complex. The introduced POM framework did not result in further emission quenching; however, to elucidate a contribution by the POM to the excited-states of the Ru(II) complex, time-resolved spectroscopy measurements are required, which will be performed in the future.

Experimental Section

Materials and Instrumentation.

The compounds 9,10-di(1,3-dithiol-2-ylidene)-9,10-dihydroanthracene-2-carbaldehyde (**exTTF-CHO**)[26], 4'-(4-bromophenyl)-2,2':6',2"-terpyridine (**1**)[10], 3-([2,2':6',2"-terpyridin]-4'-yl)-10-methyl-10*H*-phenothiazine (**5b**)[2d] and $(Bu_4N)_4[PW_{11}O_{39}\{GeC_6H_4I\}]$ (**POM**)[19] were prepared according to literature procedures. All other chemicals were purchased from commercial suppliers and were used as received. Triethylamine was distilled over calcium hydride. The reactions were monitored by thin-layer chromatography (TLC, silica gel on aluminum sheets with fluorescent dye F254, Merck KGaA). NMR spectra were recorded with a Bruker Avance (300, 400 and 600 MHz) instrument in deuterated solvents (Euriso-Top) at 25 °C. Chemical shifts are given in ppm and referenced to the solvent signal. ESI-TOF mass spectra were recorded with a Bruker ESI-(Q)-TOF microTOF II mass spectrometer. Elemental analyses were carried out with a EuroVector EuroEA3000 elemental analyzer. UV/Vis absorption spectra were recorded with a PerkinElmer Lambda 750 UV/Vis spectrometer in 10^{-5} M solutions of DMF and DMSO. Emission spectra were recorded with a Jasco FP6500 instrument at room temperature in DMF and DMSO solutions with optical densities of 0.3 at 500 nm excitation wavelength. The emission spectra were corrected by subtraction of the solvent spectrum. CV and DPV measurements were carried out with a Metrohm Autolab PGSTAT30 potentiostat with a standard three-electrode configuration by using a glassy-carbon-disk working electrode, a platinumrod auxiliary electrode, and an AgCl/Ag reference electrode. The experiments were carried out in deaerated DMF (HPLC grade) containing 0.1 M Bu_4NPF_6 salt. At the end of each measurement, ferrocene was added as an internal standard.

Compound 2. A microwave vial was charged with CuI (2.2 mg, 0.012 mmol), $Pd(PPh_3)_2Cl_2$ (8.1 mg, 0.012 mmol), **1** (450 mg, 1.159 mmol), THF (10 mL) and NEt_3 (4 mL). The vial was capped, degassed with nitrogen for 20 min and, subsequently, (triisopropylsilyl)acetylene (0.650 mL, 2.90 mmol) was added. After 24 h stirring at 60 °C in an oil bath, the reaction mixture was cooled to room temperature and the ammonium bromide precipitate was filtered off. The solvents were removed on rotary evaporator; the remaining dark oil was dissolved in CH_2Cl_2 (60 mL) and washed with a brine solution (3 × 20 mL). The organic layer was dried over Na_2SO_4, filtered and the solvent evaporated. The remaining creamy residue was recrystallized in methanol to yield **2** (70%) as a colorless powder. ^{1}H NMR (300 MHz, $CDCl_3$) δ 8.76–8.70 (m, 4H), 8.66 (d, J = 8.0 Hz, 2H), 7.93–7.81 (m, 4H), 7.61 (d, J = 8.3 Hz, 2H), 7.35 (ddd, J = 7.5 Hz, J = 4.8 Hz, J = 1.2 Hz, 2H), 1.16 (s, 21H). ^{13}C{^{1}H} NMR (75 MHz, $CDCl_3$) δ 156.28, 156.16, 149.55, 149.27, 138.31, 137.04, 132.72, 127.23, 124.41, 124.03, 121.53, 118.78, 106.81, 92.45, 18.85, 11.49. Anal. Calcd for $C_{32}H_{35}N_3Si$+0.4 H_2O, C, 77.34; H, 7.26; N, 8.46. Found: C, 77.27; H, 6.95; N, 8.65.

Compound 3. A microwave vial was charged with $RuCl_3 \times xH_2O$ (75 mg, 0.288 mmol), **2** (141 mg, 0.288 mmol) and EtOH (20 mL). The vial was capped and degassed with nitrogen for 30 min. The suspension was heated for 4 h at 96 °C in an oil bath. After cooling to room temperature, the reaction mixture was filtered and the solid washed with ethanol (20 mL) and diethyl ether (20 mL). After drying *in vacuo*, **3** (91%) was obtained as dark brown solid. Anal. Calcd for $C_{32}H_{35}Cl_3N_3RuSi$+0.3 H_2O, C, 54.71; H, 5.11; N, 5.98. Found: C, 54.56; H, 4.94; N, 6.07.

Compound 4. A microwave vial was charged with **3** (250 mg, 0.359 mmol), $AgNO_3$ (186 mg, 1.094 mmol) and MeCN/EtOH/water (6:1:1, 13.33 mL). The vial was capped, degassed with nitrogen for 20 min, and heated to 80 °C in an oil bath for 4 h under light exclusion. The mixture

was cooled to r.t. and the fine AgCl precipitate was filtered off through a pad of celite. An excess NH_4PF_6 salt was added to the solution, which was subsequently concentrated *in vacuo*. When precipitation occurred, water was added and the formed precipitate was collected by filtration and washed with water. The fine precipitate was filtered, washed with water and redissolved with a minimum amount of acetonitrile. Vapor diffusion of diethyl ether into the concentrated acetonitrile solution yielded **4** (81%) as orange plate-like powder. ^{1}H NMR (300 MHz, CD_3CN) δ 8.94 (d, J = 4.9 Hz, 2H), 8.65 (s, 2H), 8.56 (d, J = 8.0 Hz, 2H), 8.21 (td, J = 7.9 Hz, 1.3 Hz, 2H), 8.05 (d, J = 8.4 Hz, 2H), 7.84–7.69 (m, 4H), 2.76 (s, 3H), 1.96 (s, 6H), 1.24–1.12 (m, 21H). ^{13}C{^{1}H} NMR (75 MHz, CD_3CN) δ 159.98, 159.42, 155.36, 149.68, 139.93, 137.21, 133.67, 129.00, 128.83, 128.34, 126.13, 125.07, 124.34, 121.49, 107.11, 94.41, 18.94, 12.04, 4.65, 3.93. Anal. Calcd for $C_{38}H_{44}F_{12}N_6P_2RuSi$, C, 45.46; H, 4.42; N, 8.37. Found: C, 45.24; H, 4.57; N, 8.33.

Compound 5c. To a solution of 2-acetylpyridine (196 mg, 1.62 mmol) and **exTTF-CHO** (300 mg, 0.73 mmol) in THF (15 mL) was added a solution of sodium hydroxide (65 mg, 1,62 mmol) in EtOH (15 mL). The resulting mixture was stirred for 30 min and the solution became red. Subsequently, an aqueous NH_3 solution (25%, 2.2 ml, 29.4 mmol) was added and continued stirred for 48 h at 30 °C. The THF was removed *in vacuo* and EtOH (15 mL) was added. The formed precipitate was collected by filtration and the remaining solid was recrystallized in a THF/EtOH/ethyl acetate mixture to yield **5c** (34%) as an orange powder. ^{1}H NMR (400 MHz, $CDCl_3$) δ 8.82 (s, 2H), 8.74 (d, J = 4.8 Hz, 2H), 8.67 (d, J = 8.0 Hz, 2H), 8.26 (d, J = 1.5 Hz, 1H), 7.92–7.80 (m, 4H), 7.79–7.70 (m, 2H), 7.38–7.28 (m, 4H), 6.38–6.28 (m, 4H). ^{13}C{^{1}H} NMR (100 MHz, $CDCl_3$) δ 156.48, 156.17, 149.97, 149.34, 136.96, 136.73, 136.63, 136.34, 136.20, 136.03, 135.51, 135.42, 126.26, 126.19, 125.74, 125.12, 125.05, 123.92, 123.81, 121.94, 121.90, 121.49, 118.84, 117.50, 117.46, 117.42, 117.27. Anal. Calcd for $C_{35}H_{21}N_3S_4$+1.7 H_2O, C, 65.44; H, 3.83; N, 6.54; S, 19.96. Found: C, 65.40; H, 3.36; N, 6.08; S, 19.54.[27]

Compound 6a. A microwave vial was charged with **4** (38 mg, 0.038 mmol), 2,2′:6′,2″-terpyridine (**5a**, 9 mg, 0.038 mmol) and DMF (2 mL). The vial was capped, degassed with nitrogen for 20 min and heated to 130 °C in an oil bath for 1 h. Subsequently, the reaction mixture was cooled to r.t. and dropped into diethyl ether (30 mL). The fine precipitate was collected by filtration, and washed with diethyl ether (2 × 20 mL). After drying *in vacuo*, **6a** (90%) was obtained as red powder. ^{1}H NMR (300 MHz, CD_3CN) δ 9.00 (s, 2H), 8.77 (d, J = 8.2 Hz, 2H), 8.65 (d, J = 8.1 Hz, 2H), 8.51 (d, J = 8.1 Hz, 2H), 8.43 (t, J = 8.1 Hz, 1H), 8.21 (d, J = 8.3 Hz, 2H), 8.01–7.86 (m, 4H), 7.84 (d, J = 8.3 Hz, 2H), 7.43 (d, J = 5.3 Hz, 2H), 7.37 (d, J = 5.2 Hz, 2H), 7.24–7.11 (m, 4H), 1.26–1.15 (m, 21H). ^{13}C{^{1}H} NMR (75 MHz, CD_3CN) δ 158.97, 158.93, 156.44, 156.21, 153.43, 153.30, 148.05, 138.99, 138.94, 137.77, 136.75, 133.77, 128.88, 128.40, 128.35, 125.89, 125.46, 125.33, 124.63, 122.40, 107.26, 94.25, 18.97, 12.05.

Compound 6b. A microwave vial was charged with **4** (50 mg, 0.050 mmol), **5b** (22 mg, 0.050 mmol) and DMF (2 mL). The vial was capped, degassed with nitrogen for 20 min and heated to 130 °C for 1 h in an oil bath. Subsequently, the reaction mixture was cooled to r.t. and dropped to diethyl ether (30 mL). The fine precipitate was collected by filtration, and washed with diethyl ether (2 × 20 mL). The solid was further purified by column chromatography (silica, MeCN/water/satd. aq. KNO_3 solution, 40:4:1) and the red fraction was collected. An excess of NH_4PF_6 salt was added to the solution, which was subsequently concentrated *in vacuo*. When precipitation occurred, water was added and the formed precipitate was collected by filtration and washed with water. After drying *in vacuo*, **6b** (79%) was obtained as dark red-purple powder. ^{1}H NMR (400 MHz, CD_3CN) δ 9.01 (s, 2H), 8.98 (s, 2H), 8.66 (d, J = 8.3 Hz, 4H), 8.22 (d, J = 8.4 Hz, 2H), 8.10 (dd, J = 8.5 Hz, J = 2.3 Hz, 1H), 8.06 (d, J = 2.3 Hz, 1H), 7.99–7.91 (m, 4H), 7.84 (d, J = 8.3 Hz, 2H), 7.47–7.40 (m, 4H), 7.35–7.26 (m, 1H), 7.27–7.14 (m, 6H), 7.09–7.01 (m, 2H), 3.51 (s, 3H), 1.29–1.12 (m, 21H). ^{13}C{^{1}H} NMR (100 MHz, CD_3CN) δ 159.16, 159.07, 156.52, 156.17, 153.37, 153.30, 148.70, 147.95, 147.92, 145.82, 138.94, 138.93, 137.79, 133.78, 131.34, 129.03, 128.88, 128.43, 128.31, 128.20, 127.95, 126.68, 125.90, 125.47, 125.40, 125.10, 124.13, 122.91, 122.39, 121.49, 116.07, 115.97, 107.27, 94.28, 36.17, 18.98, 12.07.

Compound 6c. Compound **6c** was prepared in analogy to **6a** and was isolated as dark red solid (87%).^{1}H NMR (300 MHz, CD_3CN) δ 9.02 (s, 4H), 8.66 (d, J = 8.1 Hz, 4H), 8.46 (d, J = 1.9 Hz, 1H), 8.22 (d, J = 8.4 Hz, 2H), 8.16 (dd, J = 8.1, 2.0 Hz, 1H), 8.03 (d, J = 8.1 Hz, 1H), 7.96 (td, J = 7.9, 1.5 Hz, 4H), 7.85 (d, J = 8.4 Hz, 2H), 7.82–7.74 (m, 2H), 7.50–7.37 (m, 6H), 7.26–7.13 (m, 4H), 6.62–6.48 (m, 4H), 1.21 (d, J = 2.1 Hz, 21H). ^{13}C{^{1}H} NMR (75 MHz, CD_3CN) δ 159.11, 159.07, 156.52, 156.44, 153.46, 153.40, 148.58, 148.14, 139.90, 139.07, 139.03, 137.94, 137.83, 137.52, 136.01, 135.98, 135.34, 133.87, 128.96, 128.50, 127.63, 127.60, 127.29, 126.66, 126.20, 126.16, 126.01, 125.62, 125.60, 125.03, 122.51, 122.35, 121.96, 121.60, 118.94, 118.93, 118.82, 118.63, 118.49, 107.33, 94.39, 19.05, 12.14.

Compound Ru. A microwave vial was charged with **6a** (32 mg, 0.029 mmol) and CH_2Cl_2 (10 mL). The vial was capped and degassed with nitrogen until 5 mL of the CH_2Cl_2 was evaporated. Subsequently, NBu_4F (75 mg, 0.29 mmol) and KF (17 mg, 0.29 mmol) dissolved MeOH (2 mL) was added to the solution. The reaction mixture was stirred for 5 days in an oil bath at 40 °C under light exclusion. TLC was performed to monitor the reaction and a slow conversion was visible. After full conversion, the solvent was evaporated by a stream of nitrogen and the solid was purified by column chromatography (silica, MeCN/water/satd. aq. KNO_3 solution, 40:4:1). The red fraction was collected, an excess of NH_4PF_6 salt added, and concentrated *in vacuo*. When precipitation occurred, water was added and the formed precipitate was collected by filtration and washed with water. After drying *in vacuo*, **Ru** (86%) was obtained as red powder. ^{1}H NMR (300 MHz, CD_3CN) δ 9.00 (s, 2H), 8.75 (d, J = 8.2 Hz, 2H), 8.64 (d, J = 8.1 Hz, 2H), 8.50 (d, J = 8.1 Hz, 2H), 8.42 (t, J = 8.1 Hz, 1H), 8.21 (d, J = 8.4 Hz, 2H), 7.99–7.84 (m, 6H), 7.41 (d, J = 5.5 Hz, 2H), 7.35 (d, J = 5.5 Hz, 2H), 7.23–7.11 (m, 4H), 3.65 (s, 1H). ^{1}H NMR (300 MHz, DMSO-d_6) δ 9.50 (s, 2H), 9.10 (d, J = 8.4 Hz, 4H), 8.84 (d, J = 8.1 Hz, 2H), 8.55 (t, J = 8.1 Hz, 1H), 8.48 (d, J = 8.4 Hz, 2H), 8.12–7.98 (m, 4H), 7.88 (d, J = 8.4 Hz, 2H), 7.54 (d, J = 5.3 Hz, 2H), 7.45 (d, J = 5.1 Hz, 2H), 7.35–7.18 (m, 4H), 4.50 (s, 1H). ^{13}C{^{1}H} NMR (75 MHz, DMSO-d_6) δ 158.06, 157.86, 155.29, 154.86, 152.33, 152.21, 146.02, 138.32, 138.25, 136.61, 136.14, 132.88, 132.82, 128.12, 127.96, 127.91, 125.01, 124.68, 124.14, 123.69, 121.30, 83.23. HRMS (ESI-TOF, solvent: MeCN) Calcd for $C_{38}H_{26}N_6Ru$ ([M − $2PF_6$]$^{2+}$): *m/z* 334.0626. Found: *m/z* 334.0635. Anal. Calcd for $C_{38}H_{26}F_{12}N_6P_2Ru$, C, 47.66; H, 2.74; N, 8.78. Found: C, 47.34; H, 3.08; N, 8.20.[27]

Compound PTZ-Ru. Compound **PTZ-Ru** was prepared in analogy to **Ru** and was isolated as dark red-purple solid (85%). ^{1}H NMR (400 MHz, CD_3CN) δ 9.01 (s, 2H), 8.98 (s, 2H), 8.65 (d, J = 8.1 Hz, 4H), 8.22 (d, J = 8.4 Hz, 2H), 8.10 (dd, J = 8.5, J = 2.3 Hz, 1H), 8.06 (d, J = 2.3 Hz, 1H), 7.98–7.92 (m, 4H), 7.88 (d, J = 8.3 Hz, 2H), 7.44 (d, J = 5.5 Hz, 2H), 7.42 (d, J = 5.5 Hz, 2H), 7.34–7.27 (m, 1H), 7.27–7.14 (m, 6H), 7.09–7.02 (m, 2H), 3.65 (s, 1H), 3.51 (s, 3H). ^{1}H NMR (300 MHz, DMSO-d_6) δ 9.50 (s, 2H), 9.45 (s, 2H), 9.11 (d, J = 8.1 Hz, 4H), 8.49 (d, J = 8.5 Hz, 2H), 8.39–8.29 (m, 2H), 8.13–8.00 (m, 4H), 7.89 (d, J = 8.4 Hz, 2H), 7.61–7.50 (m, 4H), 7.37–7.21 (m, 7H), 7.15–7.02 (m, 2H), 4.49 (s, 1H), 3.50 (s, 3H). ^{13}C{^{1}H} NMR (100 MHz, CD_3CN) δ 159.16, 159.05, 156.53, 156.17, 153.36, 153.31, 148.72, 147.96, 147.88, 145.83, 138.95, 138.93, 138.13, 134.02, 131.34, 129.03, 128.87, 128.43, 128.31, 128.20, 127.96, 126.68, 125.47, 125.40, 125.11, 124.85, 124.14, 122.91, 122.47, 121.50, 116.08, 115.98, 83.49, 81.27, 36.17. HRMS (ESI-TOF, solvent: MeCN) Calcd for

$C_{51}H_{35}N_7RuS$ ($[M - 2PF_6]^{2+}$): *m/z* 439.5854. Found: *m/z* 439.5852. Anal. Calcd for $C_{51}H_{35}F_{12}N_7P_2RuS$, C, 52.40; H, 3.02; N, 8.39; S, 2.74. Found: C, 52.02; H, 3.21; N, 8.27; S, 2.51.

Compound exTTF-Ru. Compound **exTTF-Ru** was prepared in analogy to **Ru** and was isolated as dark red solid (80%). ^{1}H NMR (400 MHz, CD_3CN) δ 9.03 (s, 2H), 9.02 (s, 2H), 8.66 (d, *J* = 8.0 Hz, 4H), 8.47 (d, *J* = 2.0 Hz, 1H), 8.23 (d, *J* = 8.4 Hz, 2H), 8.17 (dd, *J* = 8.1, 2.0 Hz, 1H), 8.05 (d, *J* = 8.1 Hz, 1H), 7.95 (td, *J* = 7.9, 1.5 Hz, 4H), 7.88 (d, *J* = 8.4 Hz, 2H), 7.84–7.76 (m, 2H), 7.48–7.39 (m, 6H), 7.22–7.15 (m, 4H), 6.60–6.51 (m, 4H), 3.66 (s, 1H). ^{1}H NMR (300 MHz, DMSO-d_6) δ 9.56 (s, 2H), 9.51 (s, 2H), 9.16 (d, *J* = 8.5 Hz, 2H), 9.12 (d, *J* = 8.4 Hz, 2H), 8.79 (d, *J* = 1.9 Hz, 1H), 8.49 (d, *J* = 8.3 Hz, 2H), 8.39 (dd, *J* = 8.3, 1.9 Hz, 1H), 8.14–8.00 (m, 5H), 7.89 (d, *J* = 8.2 Hz, 2H), 7.82–7.73 (m, 2H), 7.59 (d, *J* = 5.7 Hz, 2H), 7.55 (d, *J* = 5.7 Hz, 2H), 7.51–7.41 (m, 2H), 7.36–7.23 (m, 4H), 6.93–6.76 (m, 4H), 4.50 (s, 1H). ^{13}C{^{1}H} NMR (100 MHz, CD_3CN) δ 159.10, 159.08, 156.53, 156.44, 153.45, 153.42, 148.59, 148.09, 139.93, 139.09, 139.07, 139.02, 138.16, 137.97, 137.55, 136.02, 135.99, 135.34, 134.10, 128.95, 128.50, 127.65, 127.61, 127.30, 126.67, 126.22, 126.16, 125.61, 125.59, 125.04, 124.96, 122.59, 122.37, 121.97, 121.59, 118.97, 118.96, 118.80, 118.59, 118.47, 83.55, 81.37. HRMS (ESI-TOF, solvent: MeCN) Calcd for $C_{58}H_{36}N_6RuS_4$ ($[M - 2PF_6]^{2+}$): *m/z* 523.0458. Found: *m/z* 523.0457.

Compound Ru-POM. The Sonogashira reaction was performed according to a modified literature procedure.[6] A microwave vial (5 mL) was charged with **Ru** (20 mg, 0.021 mmol), **POM** (65 mg, 0.017 mmol), $Pd(PPh_3)_2Cl_2$ (5 mol%, 0.6 mg, 0.855 µmol), CuI (7.5 mol%, 0.24 mg, 1.26 µmol) and dry DMF (3 ml). The vial was capped and degassed with nitrogen for 20 min. Subsequently, triethylamine (0.05 ml, 0.361 mmol) was added to the solution and the mixure was heated to 70 °C by microwave irradiation for 1 h. $(n\text{-Bu})_4NBr$ (107 mg, 0.331 mmol) was added to the solution and the solution was dropped into diethyl ether (30 mL). The precipitate was collected by filtration, redissolved in DMSO (6 mL) and 1-butyl-3-methyl-1*H*-imidazol-3-ium chloride (BMImCl, 58 mg, 0.331 mmol) was added. The solution was stirred for 1 h at r.t., dropped into EtOH (30 mL) and stored overnight in the fridge. Subsequently, the fine precipitate was filtrated, washed with ethanol and washed with acetonitrile (*i.e.*, stirring 24 h at r.t.). Compound **Ru-POM** was obtained as a red powder (85%). ^{1}H NMR (400 MHz, DMSO-d_6) δ 9.52 (s, 2H), 9.12 (d, *J* = 8.4 Hz, 2H), 9.10–9.04 (m, 4H), 8.80 (d, *J* = 8.1 Hz, 2H), 8.61–8.50 (m, 3H), 8.07 (t, *J* = 7.7 Hz, 2H), 8.01 (t, *J* = 7.8 Hz, 2H), 7.95 (d, *J* = 8.0 Hz, 2H), 7.78–7.74 (m, 2H), 7.71 (d, *J* = 7.9 Hz, 2H), 7.70–7.68 (m, 2H), 7.57 (d, *J* = 7.9 Hz, 2H), 7.54 (d, *J* = 5.7 Hz, 2H), 7.47 (d, *J* = 5.4 Hz, 2H), 7.30 (t, *J* = 6.6 Hz, 2H), 7.25 (t, *J* = 6.6 Hz, 2H), 4.17 (t, *J* = 7.1 Hz, 4H), 3.85 (s, 6H), 1.84–1.70 (m, 4H), 1.32–1.19 (m, 4H), 0.90 (t, *J* = 7.3 Hz, 6H). ^{31}P{^{1}H} NMR (162 MHz, DMSO-d_6) δ −14.98. HRMS (ESI-TOF, solvent: DMSO/MeCN) Calcd for $C_{44}H_{29}GeN_6O_{39}PRuW_{11}$ ($[M - 2BMIm]^{2-}$): *m/z* 1746.6460. Found: *m/z* 1746.6564. Anal. Calcd for $C_{60}H_{59}GeN_{10}O_{39}PRuW_{11}$, C, 19.11; H, 1.58; N, 3.71. Found: C, 20.19; H, 1.51; N, 3.56.[27]

Compound PTZ-Ru-POM. Compound **PTZ-Ru-POM** was prepared in analogy to **Ru-POM** and was isolated as dark red-purple solid (81%). ^{1}H NMR (600 MHz, DMSO-d_6) δ 9.53 (s, 2H), 9.42 (s, 2H), 9.13 (d, *J* = 8.2 Hz, 2H), 9.11–9.02 (m, 4H), 8.54 (d, *J* = 7.9 Hz, 2H), 8.44–8.35 (m, 1H), 8.29 (s, 1H), 8.13–8.02 (m, 4H), 7.96 (d, *J* = 7.7 Hz, 2H), 7.79–7.74 (m, 2H), 7.73–7.67 (m, 4H), 7.60 (d, *J* = 7.5 Hz, 2H), 7.55 (d, *J* = 5.7 Hz, 4H), 7.36 (d, *J* = 8.1 Hz, 1H), 7.34–7.20 (m, 6H), 7.12–7.01 (m, 2H), 4.17 (t, *J* = 7.1 Hz, 4H), 3.86 (s, 6H), 3.49 (s, 3H), 1.76 (p, *J* = 7.3 Hz, 4H), 1.26 (h, *J* = 7.3 Hz, 4H), 0.89 (t, *J* = 7.4 Hz, 6H). ^{31}P{^{1}H} NMR (162 MHz, DMSO-d_6) δ −14.97. HRMS (ESI-TOF, solvent: DMSO/MeCN) Calcd for $C_{57}H_{38}GeN_7O_{39}PRuSW_{11}$ ($[M - 2BMIm]^{2-}$): *m/z* 1852.1784. Found: *m/z* 1852.1781. Anal. Calcd for $C_{73}H_{68}GeN_{11}O_{39}PRuSW_{11}$, C, 22.02; H, 1.72; N, 3.87; S, 0.81. Found: C, 23.46; H, 1.86; N, 3.91; S, 0.76.[27]

Compound exTTF-Ru-POM. Compound **exTTF-Ru-POM** was prepared in analogy to **Ru-POM** and was isolated as dark red solid (82%). ^{1}H NMR (600 MHz, DMSO-d_6) δ 9.54 (s, 4H), 9.14 (d, *J* = 8.2 Hz, 4H), 9.08 (s, 2H), 8.78 (s, 1H), 8.55 (d, *J* = 7.8 Hz, 2H), 8.40 (d, *J* = 8.1 Hz, 1H), 8.15–8.02 (m, 5H), 7.99 (d, *J* = 7.5 Hz, 2H), 7.82–7.72 (m, 6H), 7.71–7.68 (m, 2H), 7.66 (d, *J* = 7.5 Hz, 2H), 7.60–7.55 (m, 4H), 7.50–7.40 (m, 2H), 7.35–7.25 (m, 4H), 6.92–6.77 (m, 4H), 4.17 (t, *J* = 7.1 Hz, 4H), 3.85 (s, 6H), 1.81–1.71 (m, 4H), 1.31–1.20 (m, 4H), 0.90 (t, *J* = 7.4 Hz, 6H). ^{31}P{^{1}H} NMR (162 MHz, DMSO-d_6) δ −14.97. HRMS (ESI-TOF, solvent: DMSO/MeCN) Calcd for $C_{64}H_{39}GeN_6O_{39}PRuS_4W_{11}$ ($[M - 2BMIm]^{2-}$): *m/z* 1935.6293. Found: *m/z* 1935.6408.

Acknowledgements

The study was supported by the *Deutsche Forschungsgemeinschaft* (grant no. SCHU1229-16/1). The authors also thank Dr. Peter Bellstedt and Gabriele Sentis (NMR), Tina Schlotthauer (ESI MS), Sandra Köhn and Beate Lentvogt (elemental analysis) for their help with the respective measurements.

Keywords: donor-acceptor systems • polyoxometalates • N ligand • electron transfer • ruthenium

[1] a) M. D. Kärkäs, O. Verho, E. V. Johnston, B. Åkermark, *Chem. Rev.* **2014**, *114*, 11863–12001; b) P. D. Tran, L. H. Wong, J. Barber, J. S. C. Loo, *Energy Environ. Sci.* **2012**, *5*, 5902–5918; c) Z. Yu, F. Li, L. Sun, *Energy Environ. Sci.* **2015**, *8*, 760–775.

[2] a) C. B. KC, F. D'Souza, *Coord. Chem. Rev.* **2016**, *322*, 104–141; b) S.-H. Lee, C. T.-L. Chan, K. M.-C. Wong, W. H. Lam, W.-M. Kwok, V. W.-W. Yam, *J. Am. Chem. Soc.* **2014**, *136*, 10041–10052; c) J. B. Kelber, N. A. Panjwani, D. Wu, R. Gómez-Bombarelli, B. W. Lovett, J. J. L. Morton, H. L. Anderson, *Chem. Sci.* **2015**, *6*, 6468–6481; d) K. Barthelmes, A. Winter, U. S. Schubert, *Eur. J. Inorg. Chem.* **2016**, *2016*, 5132–5142; e) S.-H. Lee, C. T.-L. Chan, K. M.-C. Wong, W. H. Lam, W.-M. Kwok, V. W.-W. Yam, *Dalton Trans.* **2014**, *43*, 17624–17634; f) S. V. Kirner, C. Henkel, D. M. Guldi, J. D. Megiatto, D. I. Schuster, *Chem. Sci.* **2015**, *6*, 7293–7304; g) I. M. Dixon, J. P. Collin, J. P. Sauvage, F. Barigelletti, L. Flamigni, *Angew. Chem.* **2000**, *112*, 1348–1351; h) J. Hankache, O. S. Wenger, *Chem. Commun.* **2011**, *47*, 10145–10147.

[3] M. T. Pope, *Heteropoly and Isopoly Oxometalates*, Springer-Verlag, New-York, **1983**.

[4] M. Sadakane, E. Steckhan, *Chem. Rev.* **1998**, *98*, 219–238.

[5] a) A. Dolbecq, E. Dumas, C. R. Mayer, P. Mialane, *Chem. Rev.* **2010**, *110*, 6009–6048; b) A. Proust, B. Matt, R. Villanneau, G. Guillemot, P. Gouzerh, G. Izzet, *Chem. Soc. Rev.* **2012**, *41*, 7605–7622; c) M.-P. Santoni, G. S. Hanan, B. Hasenknopf, *Coord. Chem. Rev.* **2014**, *281*, 64–85; d) G. Izzet, F. Volatron, A. Proust, *Chem. Rec.* **2017**, *17* 250–266.

[6] B. Matt, C. Coudret, C. Viala, D. Jouvenot, F. Loiseau, G. Izzet, A. Proust, *Inorg. Chem.* **2011**, *50*, 7761–7768.

[7] a) B. Matt, J. Moussa, L.-M. Chamoreau, C. Afonso, A. Proust, H. Amouri, G. Izzet, *Organometallics* **2012**, *31*, 35–38; b) B. Matt, X. Xiang, A. L. Kaledin, N. Han, J. Moussa, H. Amouri, S. Alves, C. L. Hill, T. Lian, D. G. Musaev, G. Izzet, A. Proust, *Chem. Sci.* **2013**, *4*, 1737–1745; c) B. Matt, J. Fize, J. Moussa, H. Amouri, A. Pereira, V. Artero, G. Izzet, A. Proust, *Energy Environ. Sci.* **2013**, *6*, 1504–1508; d) S. Schönweiz, S.

A. Rommel, J. Kübel, M. Micheel, B. Dietzek, S. Rau, C. Streb, *Chem. Eur. J.* **2016**, *22*, 12002–12005.

[8] a) C. Allain, D. Schaming, N. Karakostas, M. Erard, J.-P. Gisselbrecht, S. Sorgues, I. Lampre, L. Ruhlmann, B. Hasenknopf, *Dalton Trans.* **2013**, *42*, 2745–2754; b) A. Harriman, K. J. Elliott, M. A. H. Alamiry, L. L. Pleux, M. Séverac, Y. Pellegrin, E. Blart, C. Fosse, C. Cannizzo, C. R. Mayer, F. Odobel, *J. Phys. Chem. C* **2009**, *113*, 5834–5842.

[9] C. Allain, S. Favette, L.-M. Chamoreau, J. Vaissermann, L. Ruhlmann, B. Hasenknopf, *Eur. J. Inorg. Chem.* **2008**, *2008*, 3433–3441.

[10] J. Wang, G. S. Hanan, *Synlett* **2005**, 1251–1254.

[11] a) S. Chakraborty, T. J. Wadas, H. Hester, R. Schmehl, R. Eisenberg, *Inorg. Chem.* **2005**, *44*, 6865–6878; b) F. G. Brunetti, J. L. López, C. Atienza, N. Martín, *J. Mater. Chem.* **2012**, *22*, 4188–4205; c) S. Castellanos, A. A. Vieira, B. M. Illescas, V. Sacchetti, C. Schubert, J. Moreno, D. M. Guldi, S. Hecht, N. Martín, *Angew. Chem. Int. Ed.* **2013**, *52*, 13985–13990; d) Y. Takano, S. Obuchi, N. Mizorogi, R. García, M. Á. Herranz, M. Rudolf, S. Wolfrum, D. M. Guldi, N. Martín, S. Nagase, T. Akasaka, *J. Am. Chem. Soc.* **2012**, *134*, 16103–16106; e) H. Kawauchi, S. Suzuki, M. Kozaki, K. Okada, D. M. S. Islam, Y. Araki, O. Ito, K.-i. Yamanaka, *J. Phys. Chem. A* **2008**, *112*, 5878–5884; f) P. K. Poddutoori, A. S. D. Sandanayaka, N. Zarrabi, T. Hasobe, O. Ito, A. van der Est, *J. Phys. Chem. A* **2011**, *115*, 709–717; g) T. Kamimura, K. Ohkubo, Y. Kawashima, S. Ozako, K.-i. Sakaguchi, S. Fukuzumi, F. Tani, *J. Phys. Chem. C* **2015**, *119*, 25634–25650; h) S. L. Larson, C. M. Elliott, D. F. Kelley, *Inorg. Chem.* **1996**, *35*, 2070–2076.

[12] J. B. Gerken, M. L. Rigsby, R. E. Ruther, R. J. Pérez-Rodríguez, I. A. Guzei, R. J. Hamers, S. S. Stahl, *Inorg. Chem.* **2013**, *52*, 2796–2798.

[13] N. Zabarska, D. Sorsche, F. W. Heinemann, S. Glump, S. Rau, *Eur. J. Inorg. Chem.* **2015**, *2015*, 4869–4877.

[14] M. Jäger, R. J. Kumar, H. Görls, J. Bergquist, O. Johansson, *Inorg. Chem.* **2009**, *48*, 3228–3238.

[15] a) B. Schulze, D. Escudero, C. Friebe, R. Siebert, H. Görls, U. Köhn, E. Altuntas, A. Baumgaertel, M. D. Hager, A. Winter, B. Dietzek, J. Popp, L. González, U. S. Schubert, *Chem. Eur. J.* **2011**, *17*, 5494–5498; b) S. Sinn, B. Schulze, C. Friebe, D. G. Brown, M. Jäger, J. Kübel, B. Dietzek, C. P. Berlinguette, U. S. Schubert, *Inorg. Chem.* **2014**, *53*, 1637–1645.

[16] M.-P. Santoni, A. K. Pal, G. S. Hanan, A. Proust, B. Hasenknopf, *Inorg. Chem.* **2011**, *50*, 6737–6745.

[17] a) M. R. Bryce, A. J. Moore, *Synth. Met.* **1988**, *27*, 557–561; b) N. Martín, I. Pérez, L. Sánchez, C. Seoane, *J. Org. Chem.* **1997**, *62*, 870–877.

[18] N. E. Gruhn, N. A. Macías-Ruvalcaba, D. H. Evans, *Langmuir* **2006**, *22*, 10683–10688.

[19] C. Rinfray, G. Izzet, J. Pinson, S. Gam Derouich , J.-J. Ganem, C. Combellas, F. Kanoufi, A. Proust, *Chem. Eur. J.* **2013**, *19*, 13838–13846.

[20] A. Juris, V. Balzani, F. Barigelletti, S. Campagna, P. Belser, A. von Zelewsky, *Coord. Chem. Rev.* **1988**, *84*, 85–277.

[21] N. Martín, L. Sánchez, C. Seoane, E. Ortí, P. M. Viruela, R. Viruela, *J. Org. Chem.* **1998**, *63*, 1268–1279.

[22] E. A. Medlycott, G. S. Hanan, *Coord. Chem. Rev.* **2006**, *250*, 1763–1782.

[23] a) G. Ajayakumar, K. Sreenath, K. R. Gopidas, *Dalton Trans.* **2009**, 1180–1186; b) D. Hanss, O. S. Wenger, *Inorg. Chem.* **2009**, *48*, 671–680.

[24] a) S. Campagna, S. Serroni, F. Puntoriero, F. Loiseau, L. D. Cola, C. J. Kleverlaan, J. Becher, A. P. Sørensen, P. Hascoat, N. Thorup, *Chem. Eur. J.* **2002**, *8*, 4461–4469; b) C. Goze, C. Leiggener, S.-X. Liu, L. Sanguinet, E. Levillain, A. Hauser, S. Decurtins, *ChemPhysChem* **2007**, *8*, 1504–1512; c) M. Abrahamsson, M. Jäger, R. J. Kumar, T. Österman, P. Persson, H.-C. Becker, O. Johansson, L. Hammarström, *J. Am. Chem. Soc.* **2008**, *130*, 15533–15542; d) N. Dupont, Y.-F. Ran, H.-P. Jia, J. Grilj, J. Ding, S.-X. Liu, S. Decurtins, A. Hauser, *Inorg. Chem.* **2011**, *50*, 3295–3303.

[25] D. Rehm, A. Weller, *Isr. J. Chem.* **1970**, *8*, 259–271.

[26] N. Martín, I. Peréz, L. Sánchez, C. Seoane, *J. Org. Chem.* **1997**, *62*, 5690–5695.

[27] Although these results are outside the range viewed as establishing analytical purity, they are provided to illustrate the best values obtained to date.

Supporting Information for:

Molecular Dyads and Triads Based on Phenothiazine and π-extended Tetrathiafulvalene Donors, Ruthenium(II) Bisterpyridine Complexes and Polyoxometalates

Kevin Barthelmes,[†,‡] Maria Sittig,[†] Andreas Winter,[†,‡] Ulrich S. Schubert*[,†,‡]

[†] Laboratory of Organic and Macromolecular Chemistry (IOMC), Friedrich Schiller University Jena, Humboldtstr. 10, 07743 Jena, Germany

[‡] Center for Energy and Environmental Chemistry Jena (CEEC Jena), Friedrich Schiller University Jena, Philosophenweg 7a, 07743 Jena, Germany

*E-mail: ulrich.schubert@uni-jena.de

Table of Contents:

1. Stacked ^{1}H NMR spectra

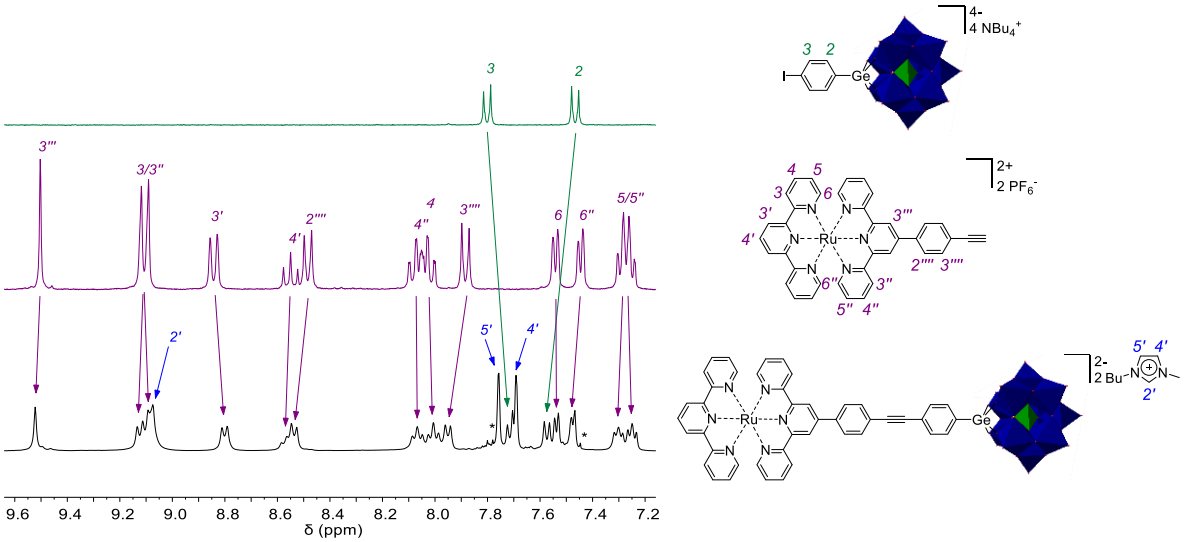

Figure S1. ^{1}H NMR (DMSO-d_6) spectra (aromatic region) and signal assignment of **POM** (top), **Ru** (middle) and **Ru-POM** (bottom). The asterisks mark impurities, tentatively assigned to unreacted **POM**.

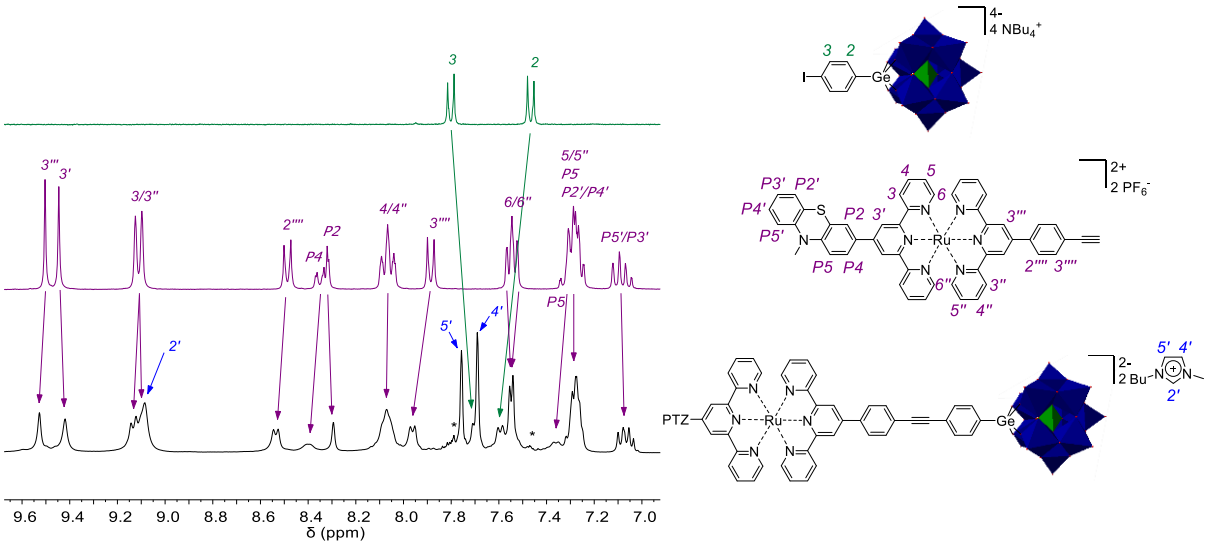

Figure S2. ^{1}H NMR (DMSO-d_6) spectra (aromatic region) and signal assignment of **POM** (top), **PTZ-Ru** (middle) and **PTZ-Ru-POM** (bottom). The asterisks mark impurities, tentatively assigned to unreacted **POM**.

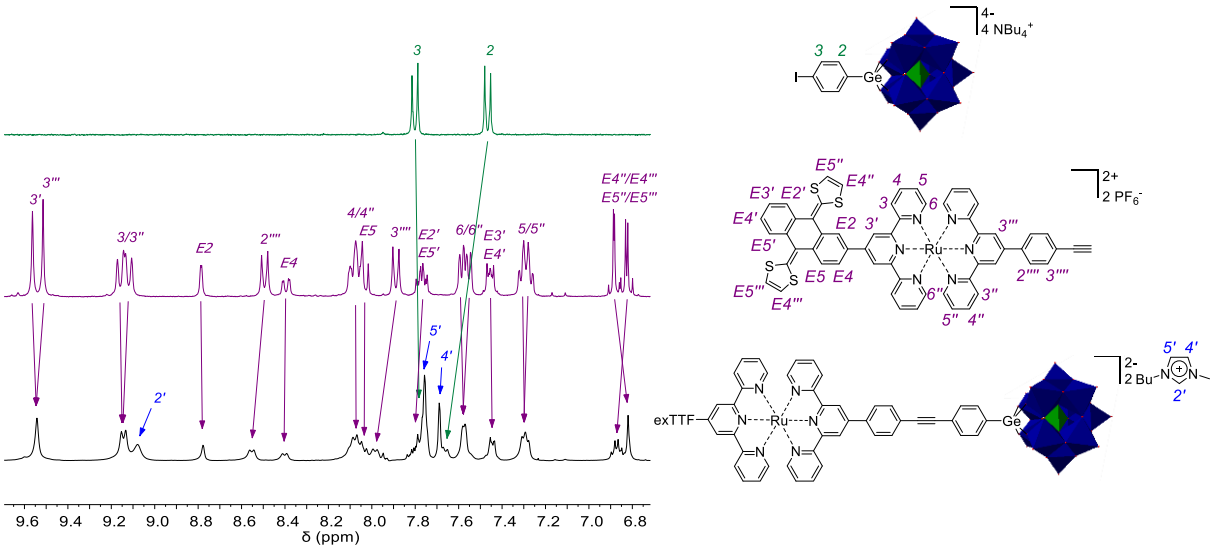

Figure S3. ^{1}H NMR (DMSO-d_6) spectra (aromatic region) and signal assignment of **POM** (top), **exTTF-Ru** (middle) and **exTTF-Ru-POM** (bottom).

2. CV and DPV

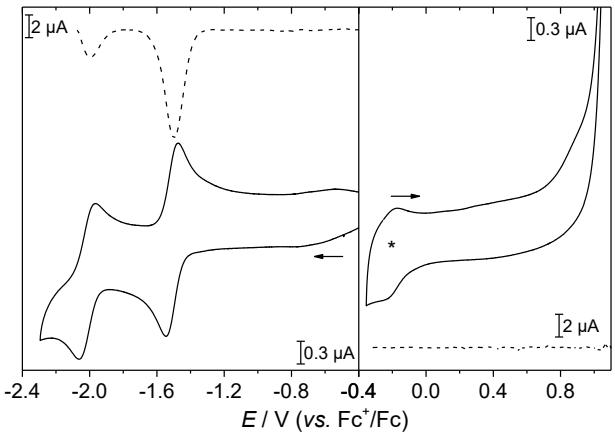

Figure S4. Cyclic (solid lines, scan rate = 0.2 V/s, 5th cycle is shown) and differential pulse (dashed lines) voltammograms of **POM** in DMF/0.1 M Bu_4NPF_6. Left: Cathodic region. Right: Anodic region. The arrows show the scan direction. The asterisk marks a redox process, which is caused by the oxidation of the DMF (*i.e.*, rise of current over 0.8 V).

3. UV-vis absorption and emission spectra in DMF

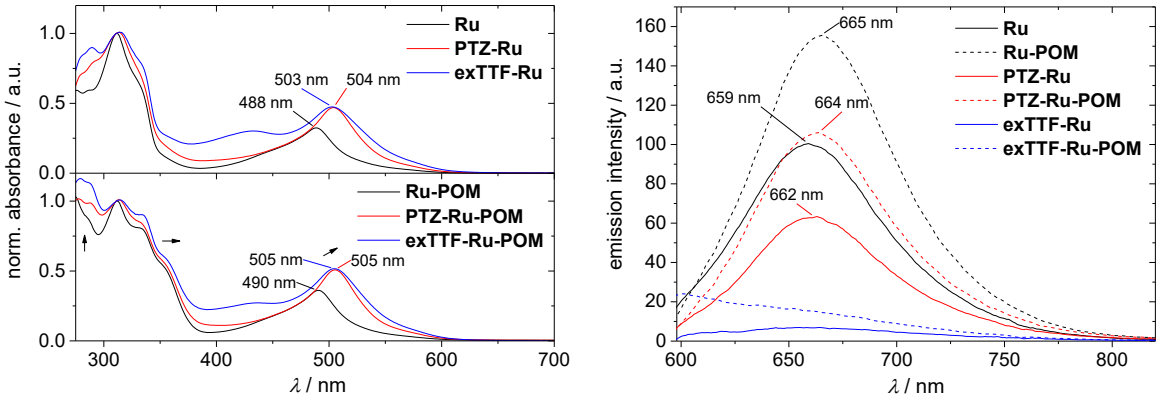

Figure S5. Room-temperature UV-vis absorption (left) and emission (right, isoabsorbing solutions with 0.3 OD at λ_{exc} = 500 nm) spectra of the Ru(II) complexes and the Ru(II) complex/POM conjugates in DMF.

4. NMR spectra

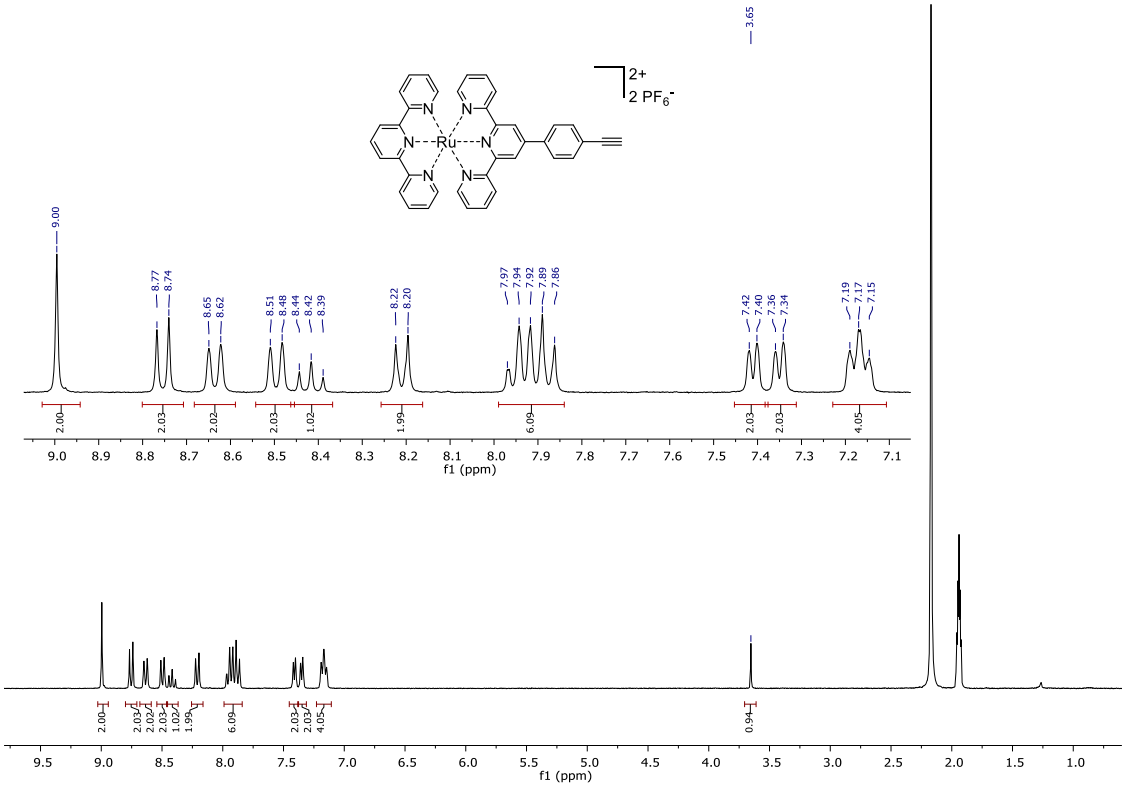

Figure S6. ^{1}H NMR (300 MHz, CD_3CN) spectrum of **Ru**.

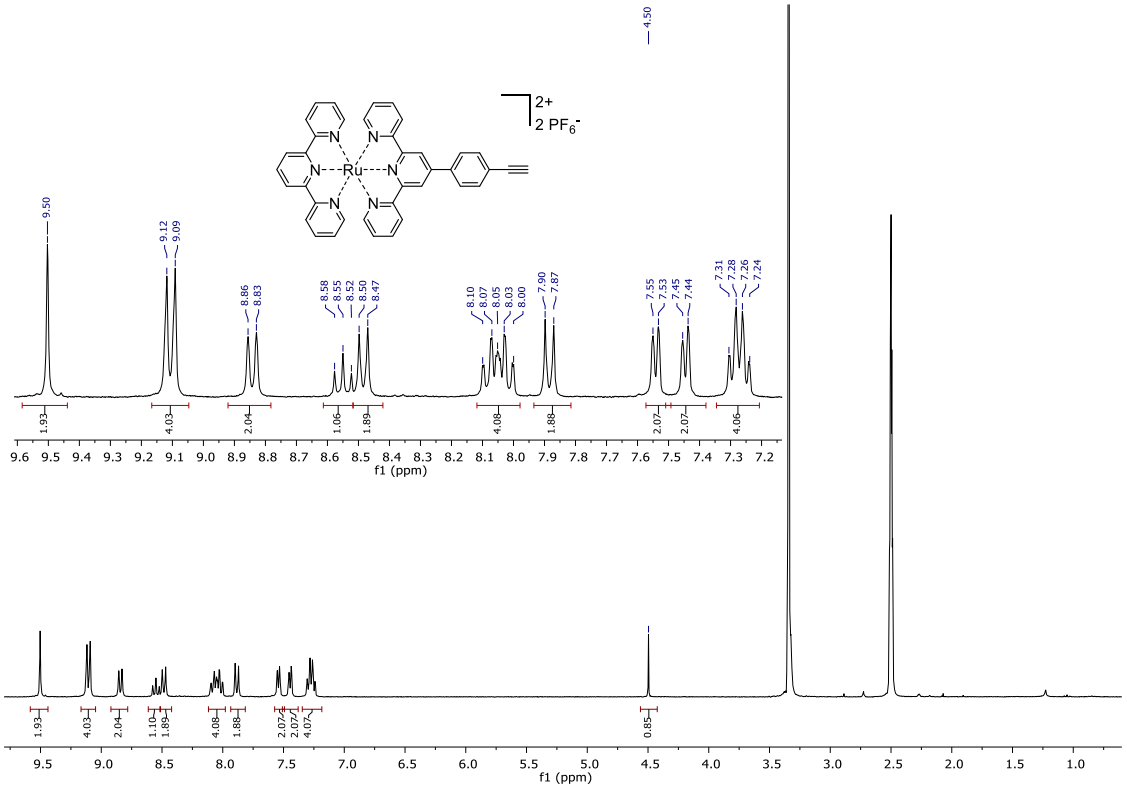

Figure S7. ^{1}H NMR (300 MHz, DMSO-d_6) spectrum of **Ru**.

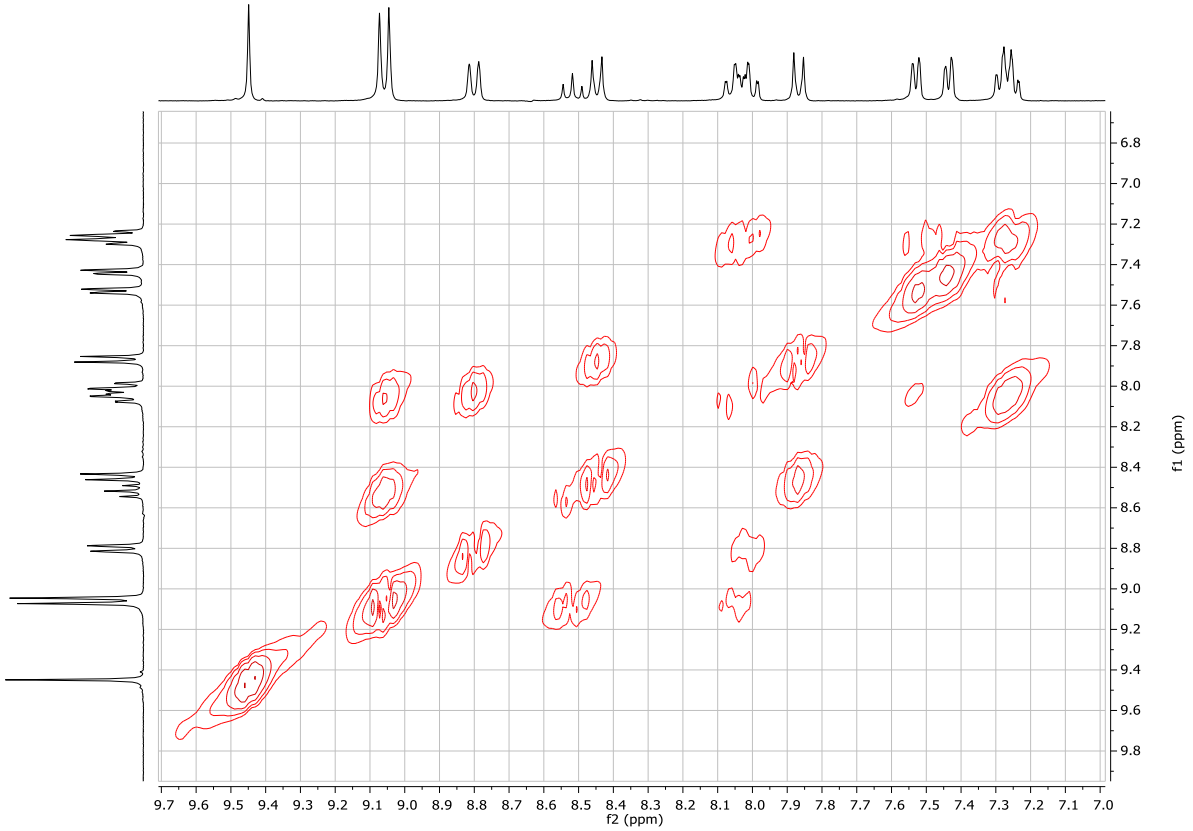

Figure S8. ^{1}H,^{1}H COSY NMR (300 MHz, DMSO-d_6, aromatic region) spectrum of **Ru**.

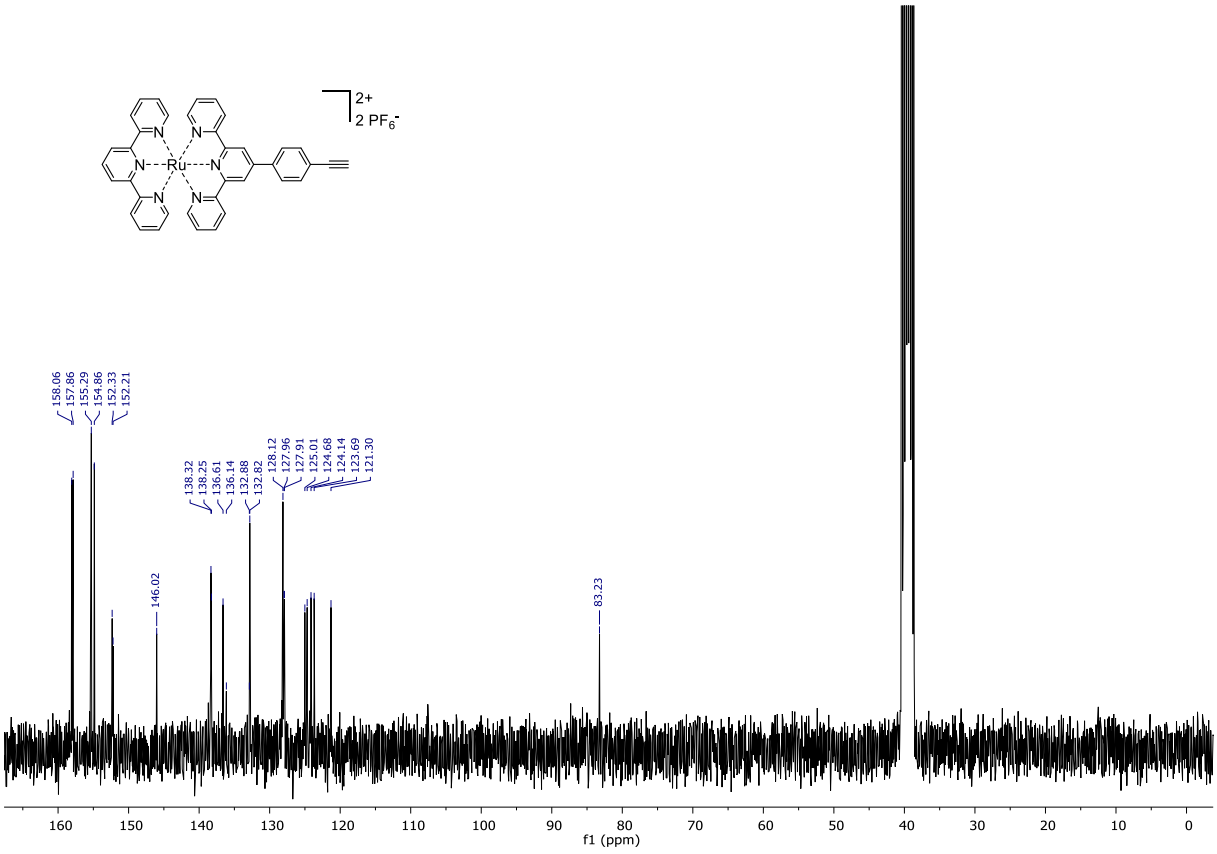

Figure S9. ^{13}C{^{1}H} NMR (75 MHz, DMSO-d_6) spectrum of **Ru**.

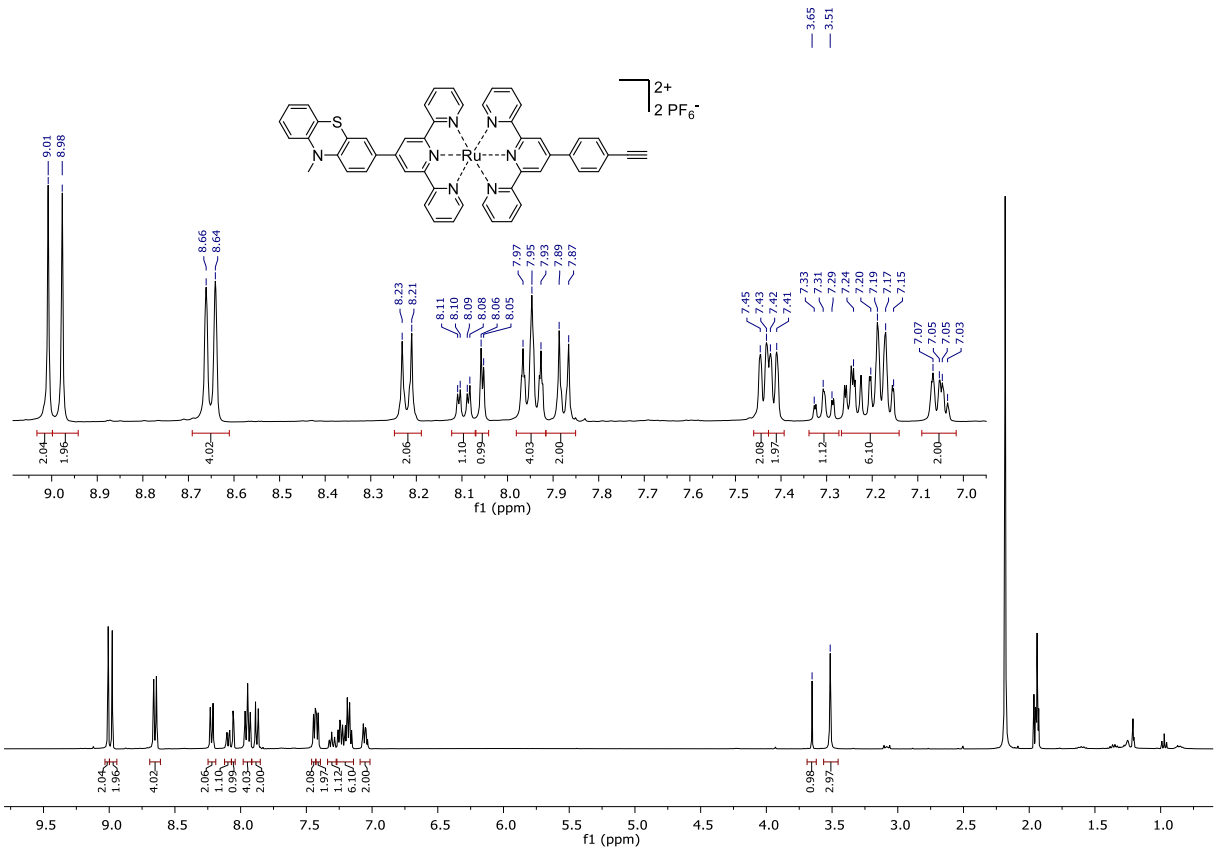

Figure S10. ^{1}H NMR (400 MHz, CD_3CN) spectrum of **PTZ-Ru**.

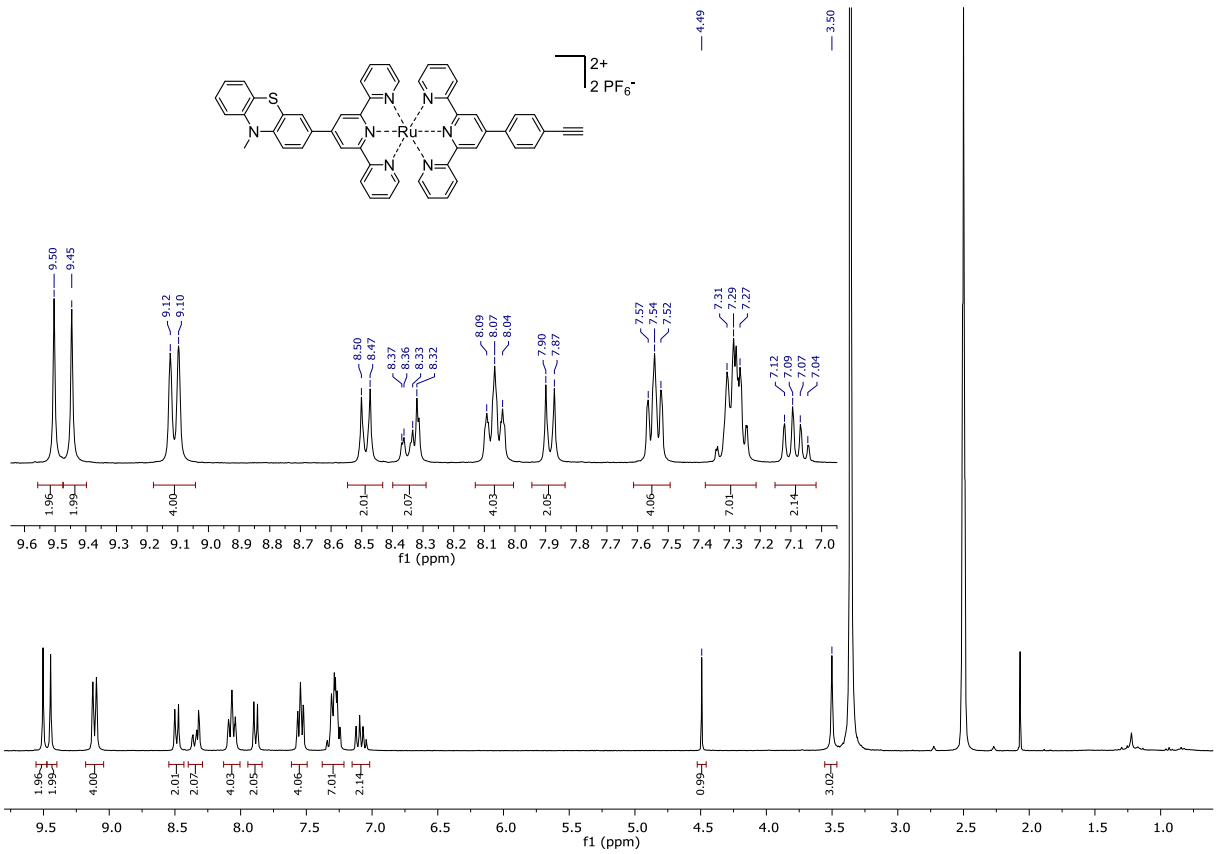

Figure S11. ^{1}H NMR (300 MHz, DMSO-d_6) spectrum of **PTZ-Ru**.

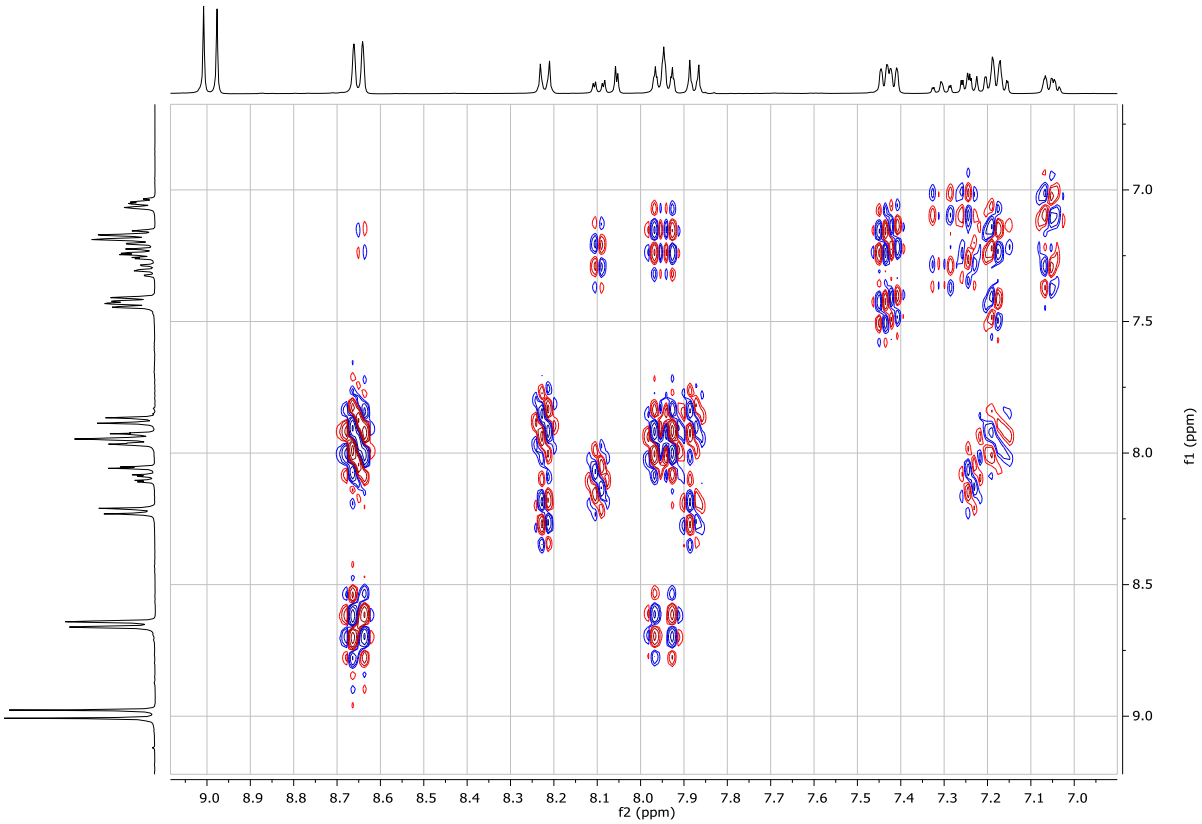

Figure S12. $^{1}H,^{1}H$ COSY NMR (400 MHz, CD_3CN, aromatic region) spectrum of **PTZ-Ru**.

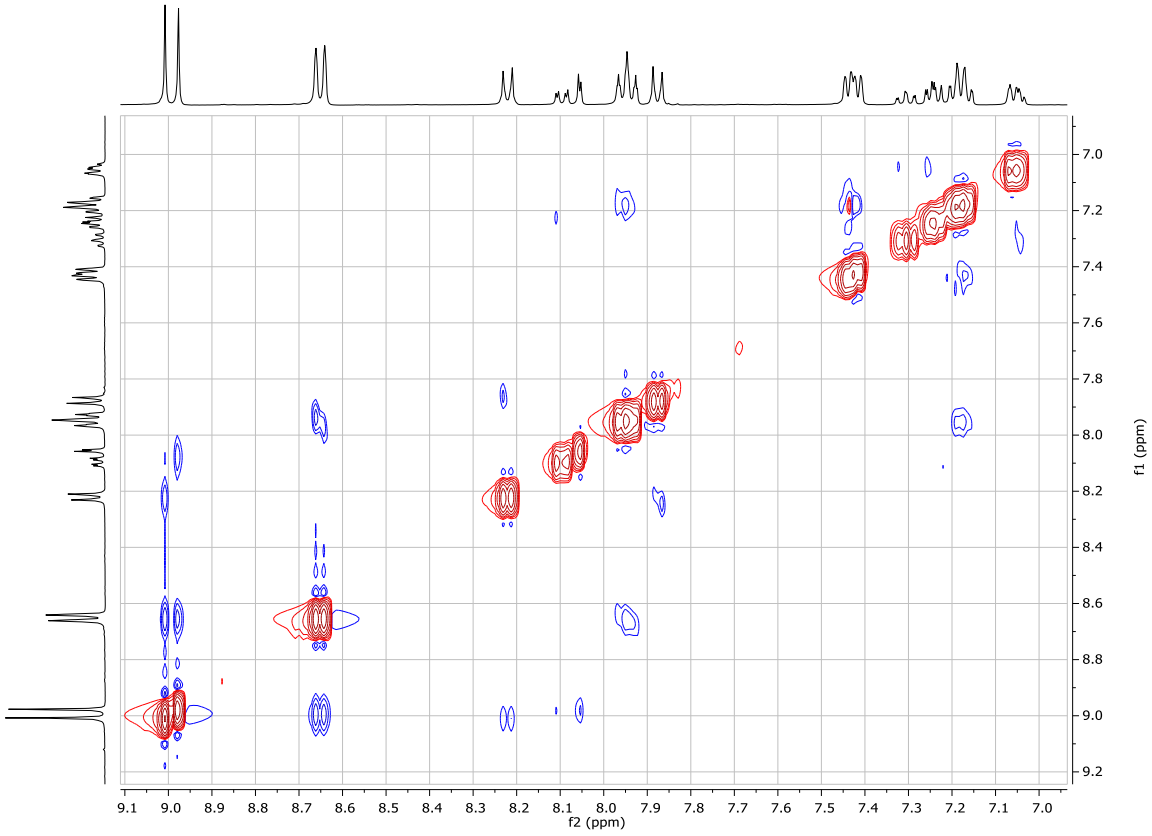

Figure S13. $^{1}H,^{1}H$ NOESY NMR (400 MHz, CD_3CN, aromatic region) spectrum of **PTZ-Ru**.

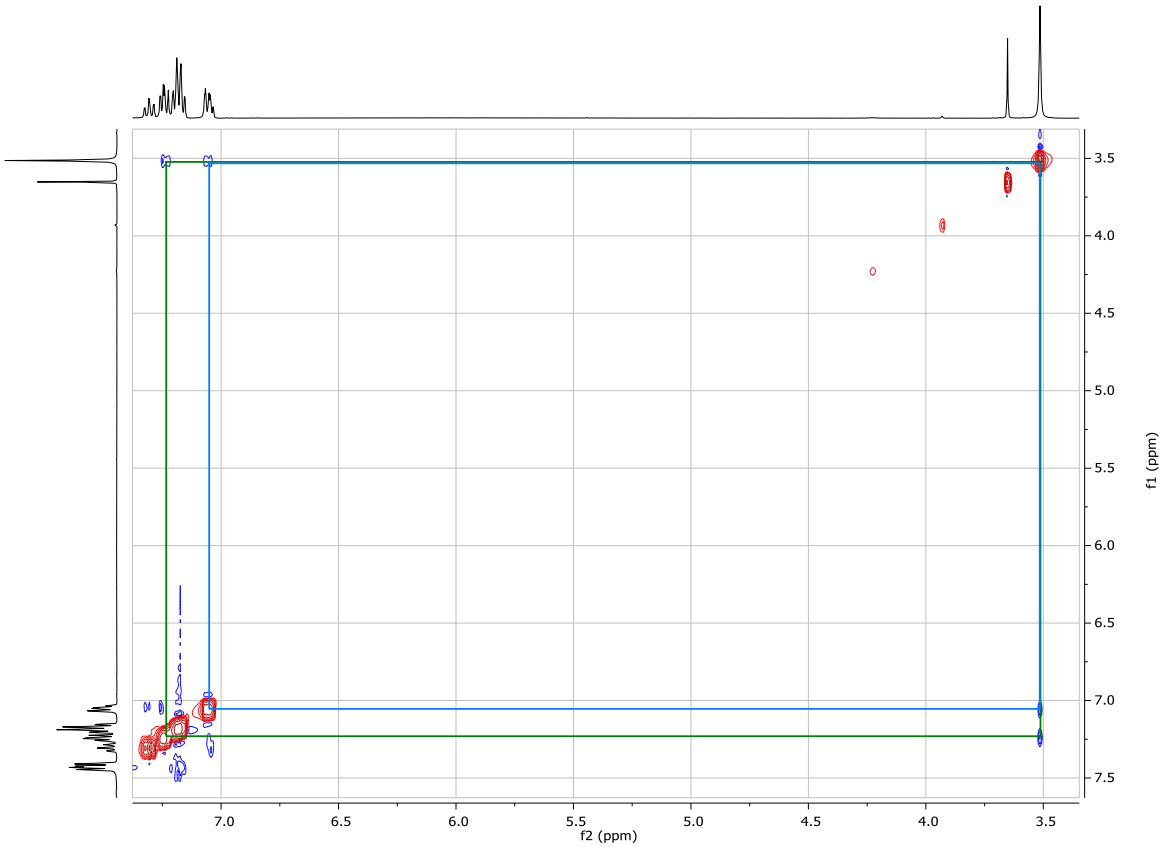

Figure S14. ^{1}H,^{1}H NOESY NMR (400 MHz, CD_3CN, aromatic & aliphatic region) spectrum of **PTZ-Ru**. The green and blue square marks cross peaks.

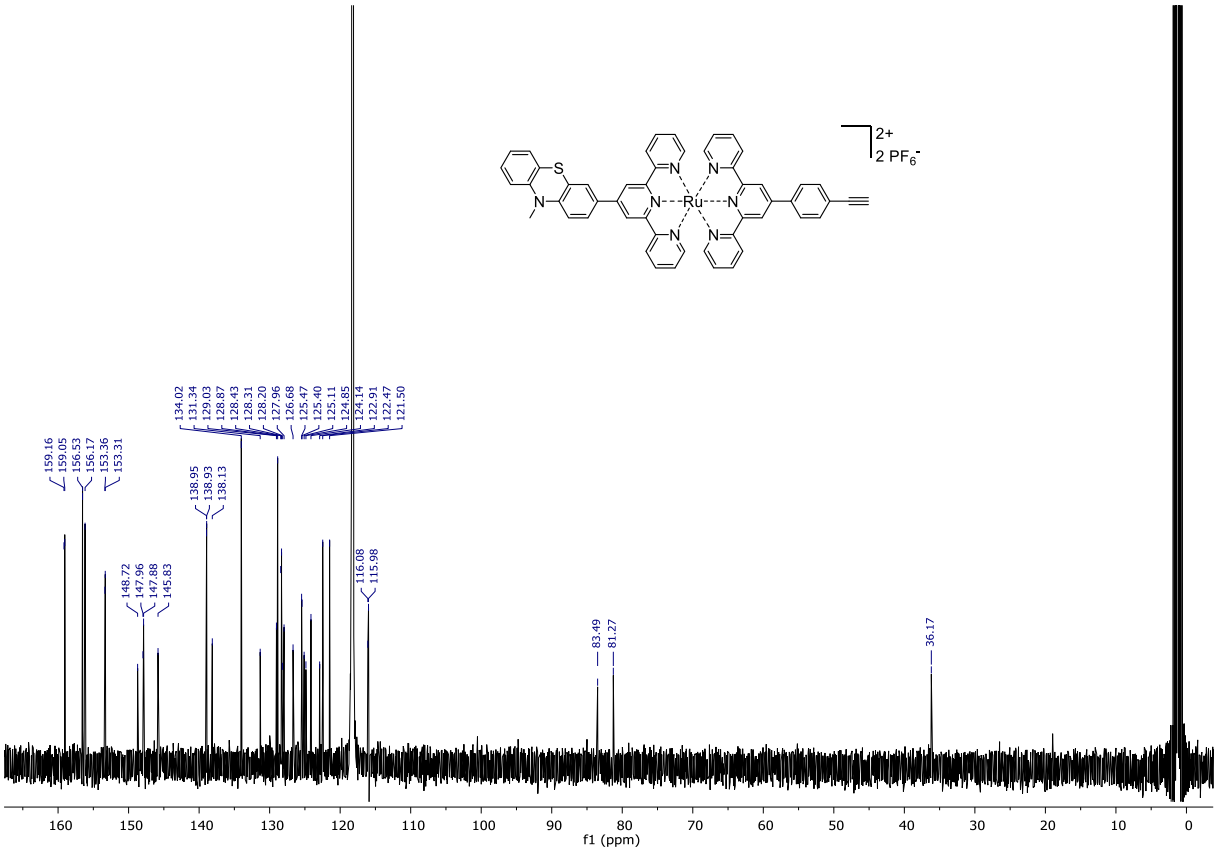

Figure S15. ^{13}C{^{1}H} NMR (100 MHz, CD_3CN) spectrum of **PTZ-Ru**.

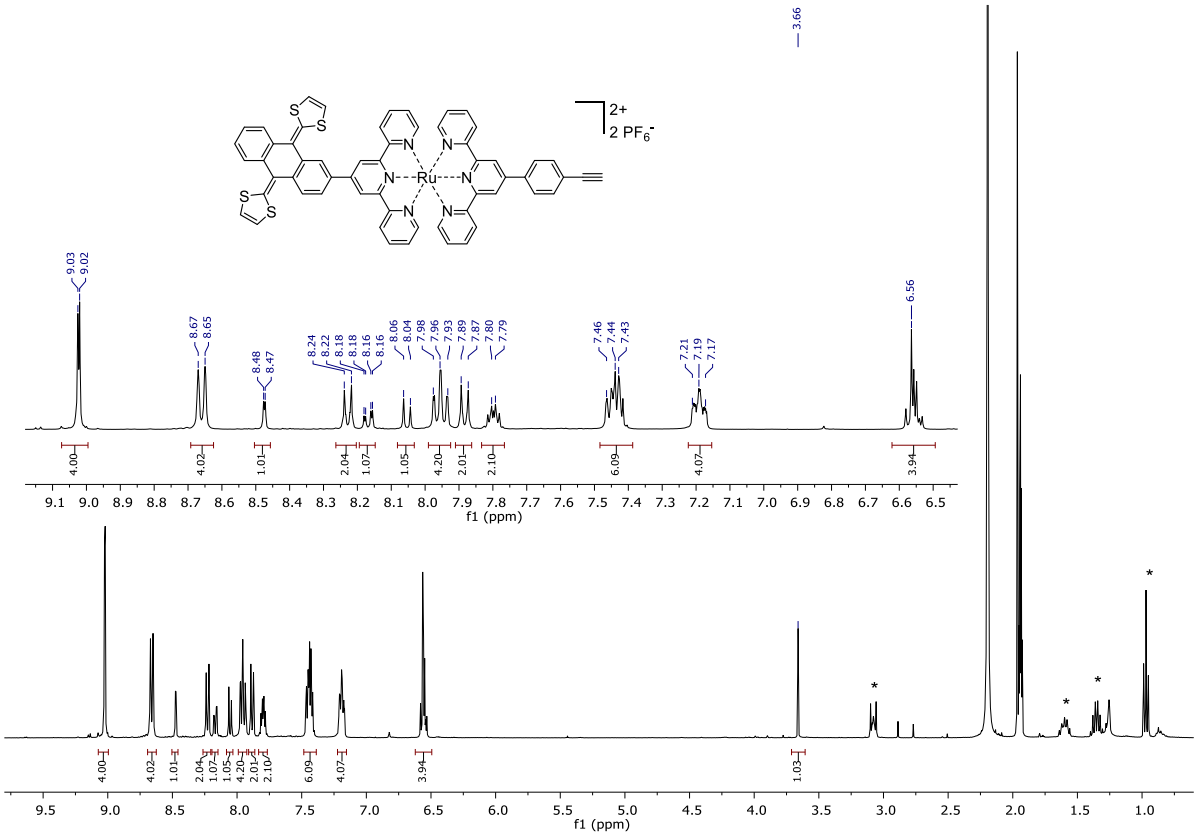

Figure S16. ^{1}H NMR (400 MHz, CD_3CN) spectrum of **exTTF-Ru**. The asterisks mark signals of residual tetrabutylammonium salt.

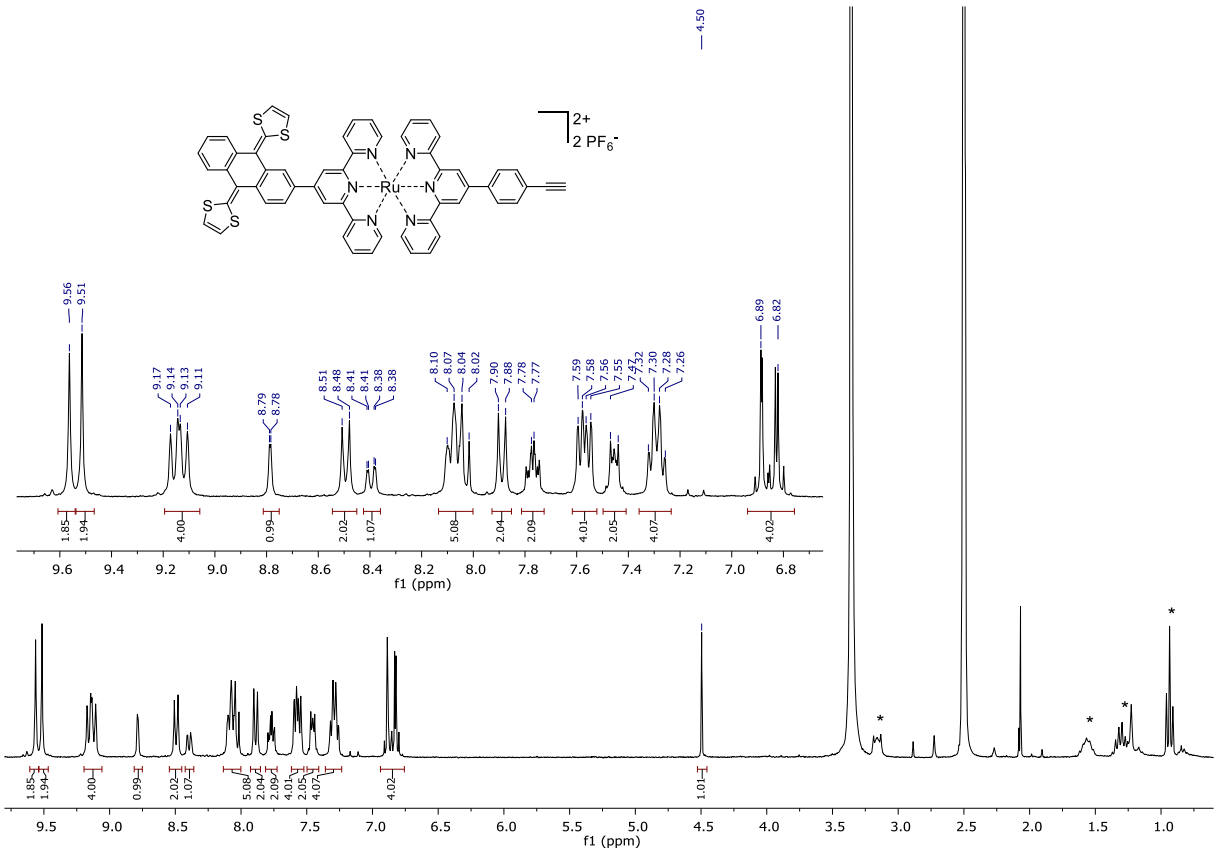

Figure S17. ^{1}H NMR (300 MHz, DMSO-d_6) spectrum of **exTTF-Ru**. The asterisks mark signals of residual tetrabutylammonium salt.

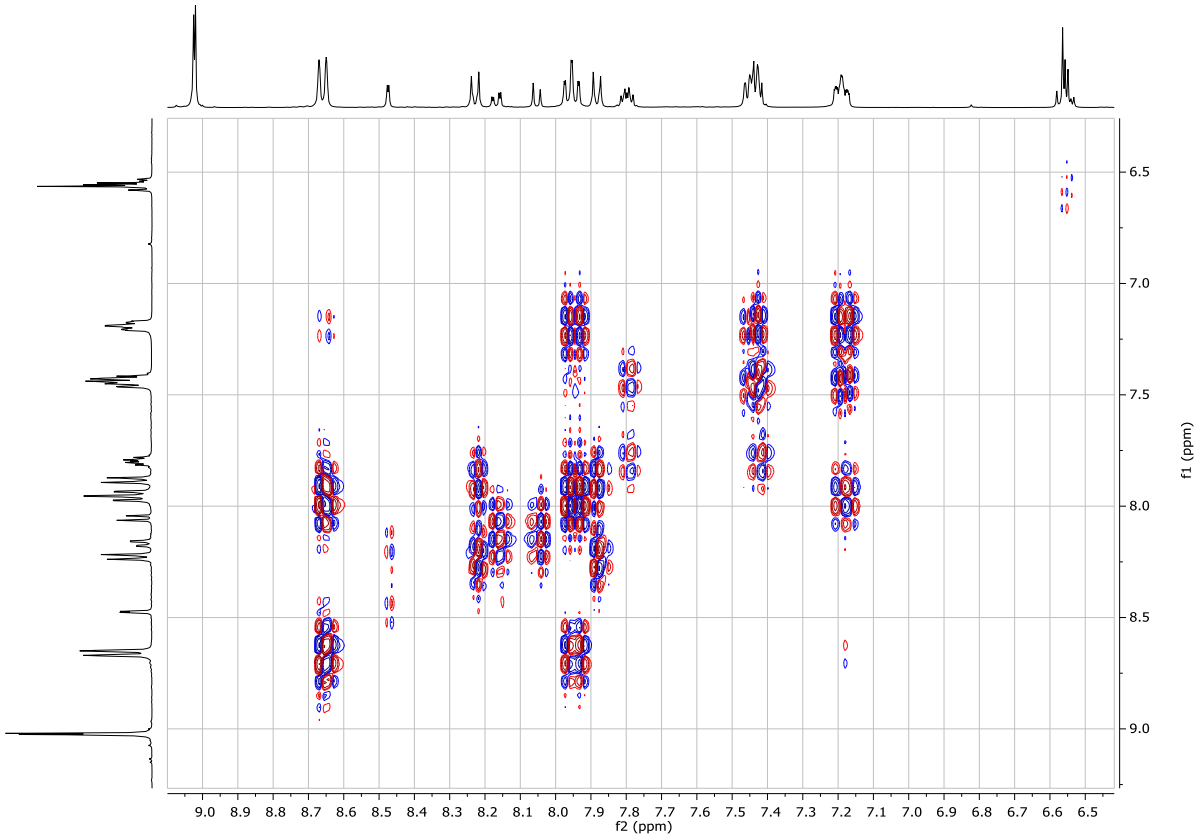

Figure S18. $^{1}H,^{1}H$ COSY NMR (400 MHz, CD_3CN, aromatic region) spectrum of **exTTF-Ru**.

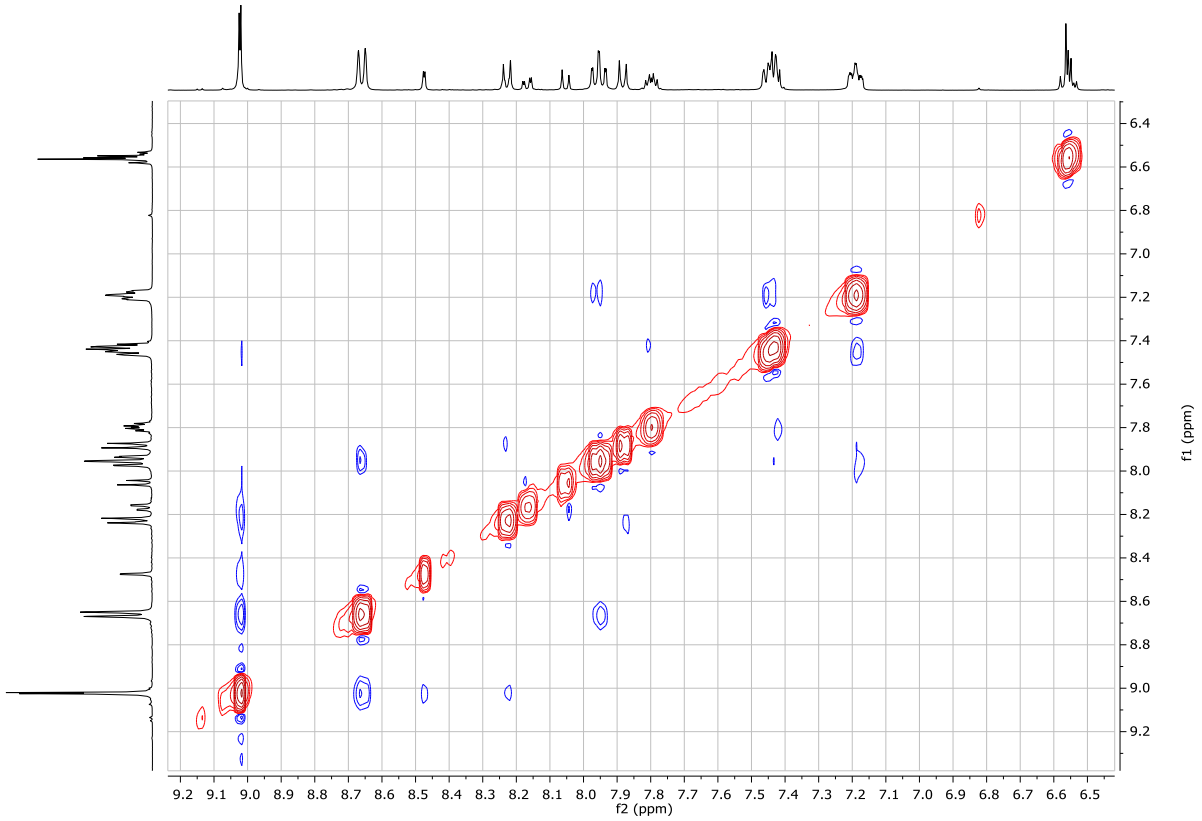

Figure S19. $^{1}H,^{1}H$ NOESY NMR (400 MHz, CD_3CN, aromatic region) spectrum of **exTTF-Ru**.

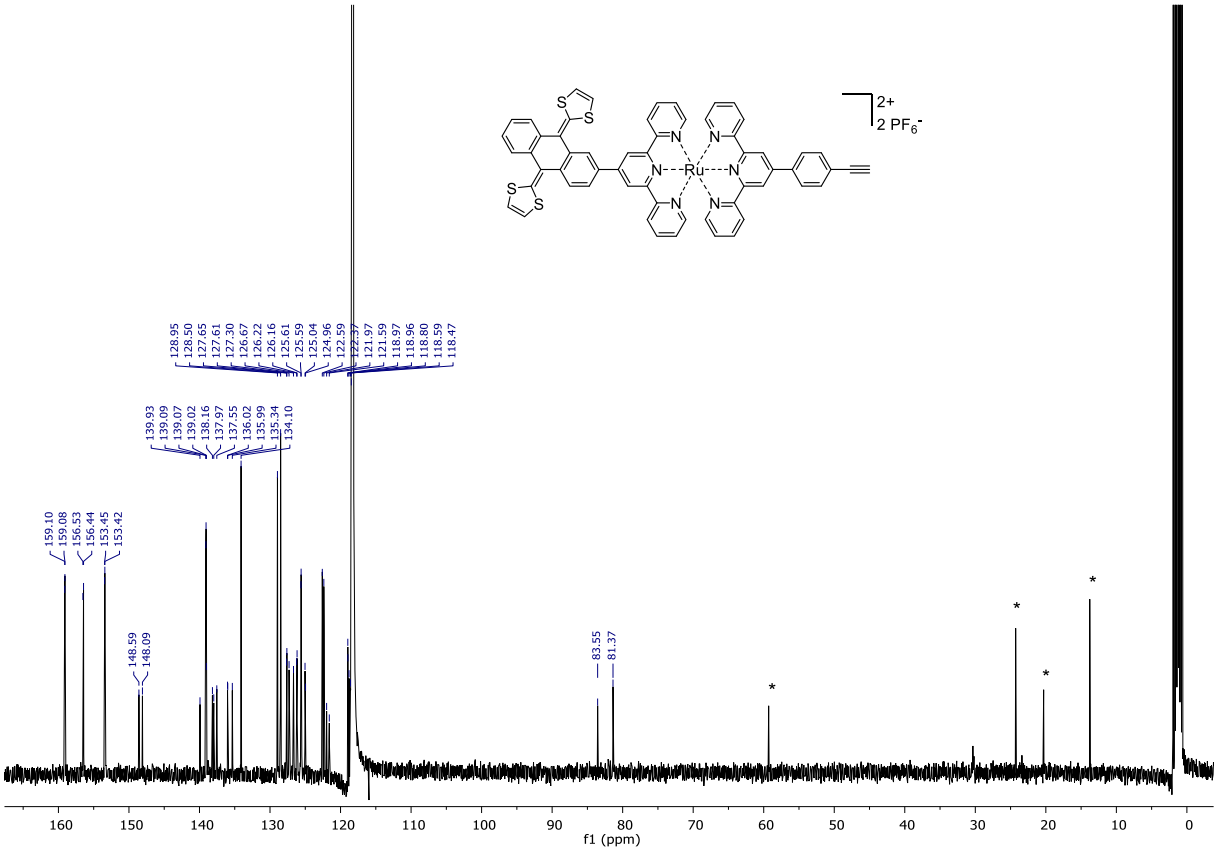

Figure S20. $^{13}C\{^{1}H\}$ NMR (100 MHz, CD_3CN) spectrum of **exTTF-Ru**. The asterisks mark signals of residual tetrabutylammonium salt.

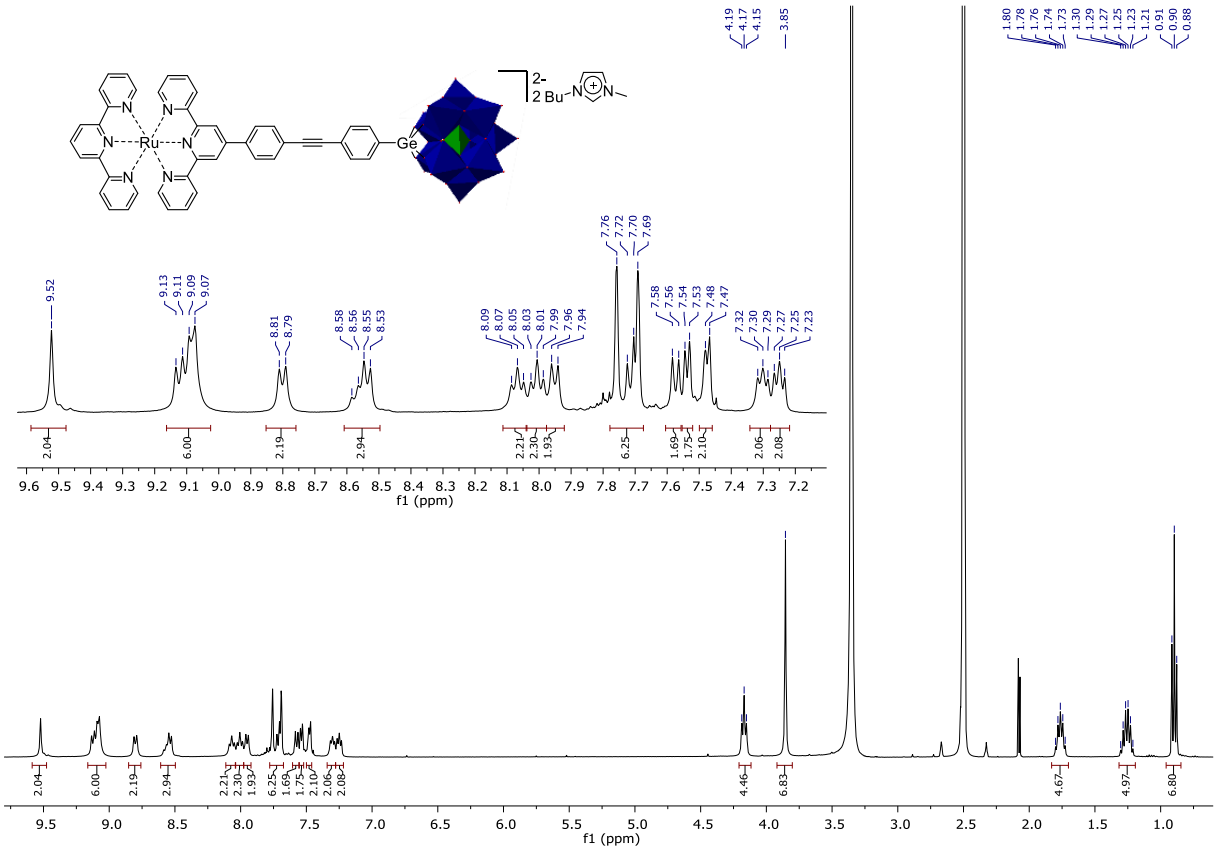

Figure S21. ^{1}H NMR (400 MHz, DMSO-d_6) spectrum of **Ru-POM**.

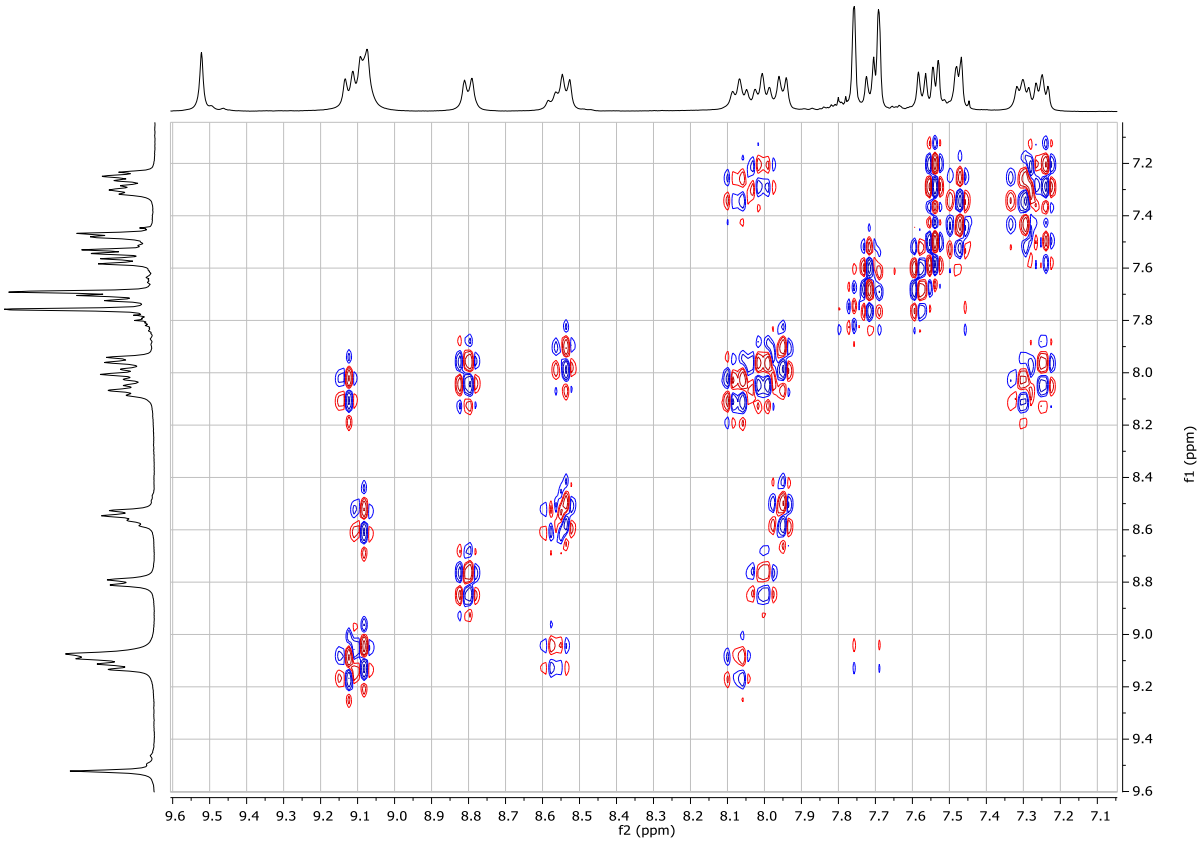

Figure S22. ^{1}H,^{1}H COSY NMR (400 MHz, DMSO-d_6, aromatic region) spectrum of **Ru-POM**.

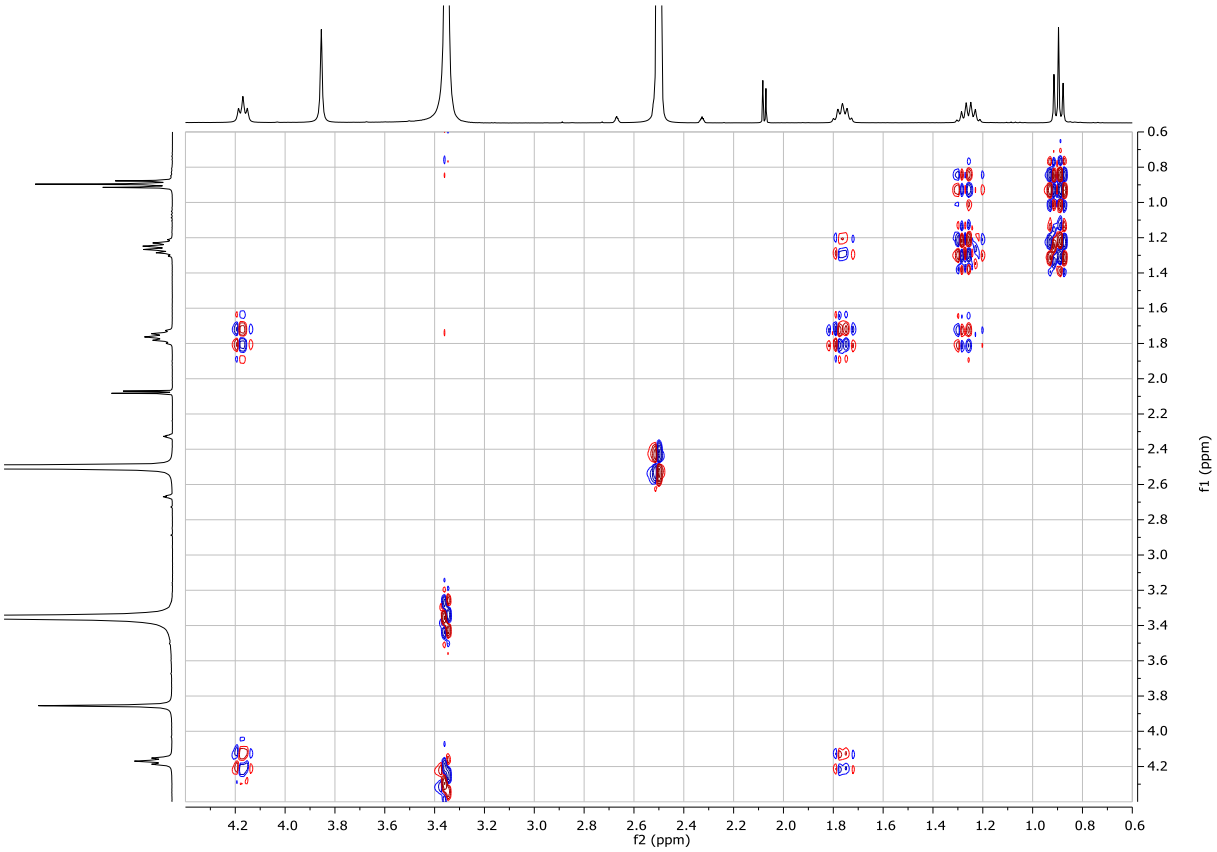

Figure S23. ^{1}H,^{1}H COSY NMR (400 MHz, DMSO-d_6, aliphatic region) spectrum of **Ru-POM**.

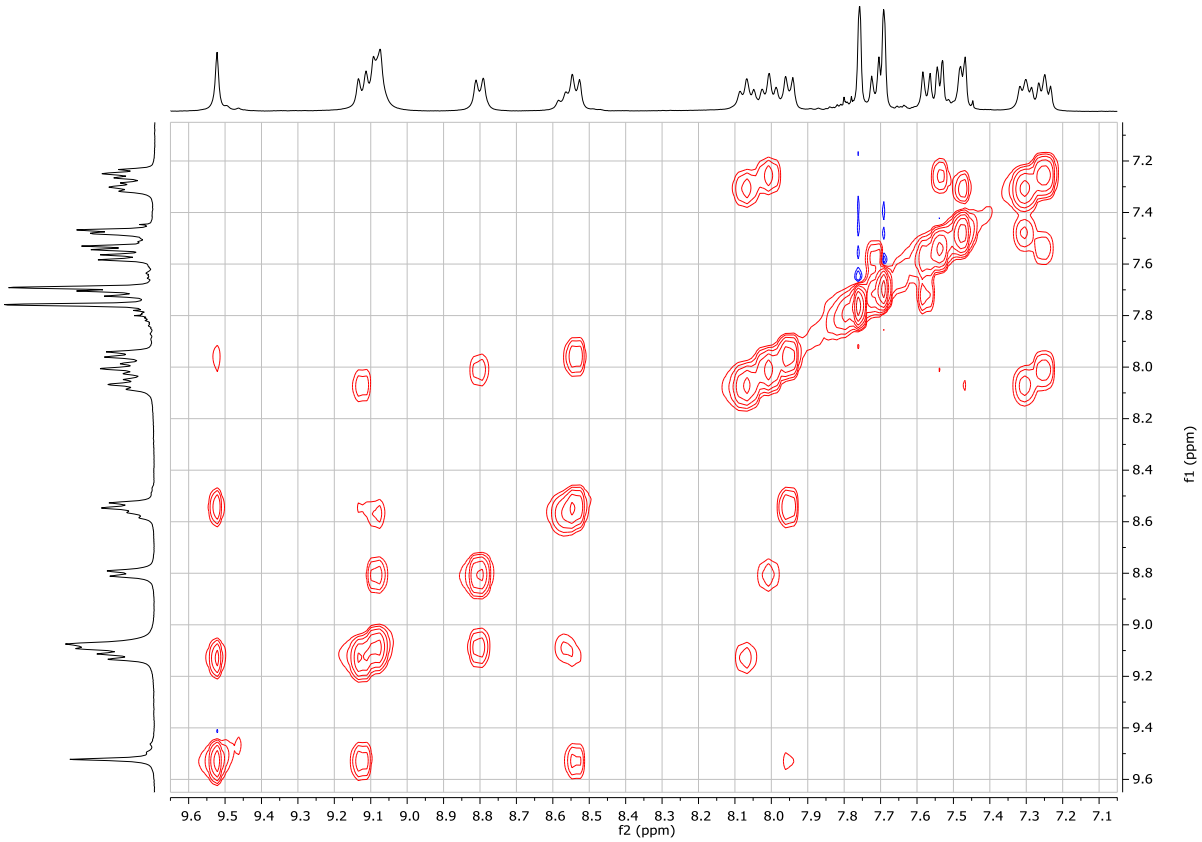

Figure S24. ^{1}H,^{1}H NOESY NMR (400 MHz, DMSO-d_6, aromatic region) spectrum of **Ru-POM**.

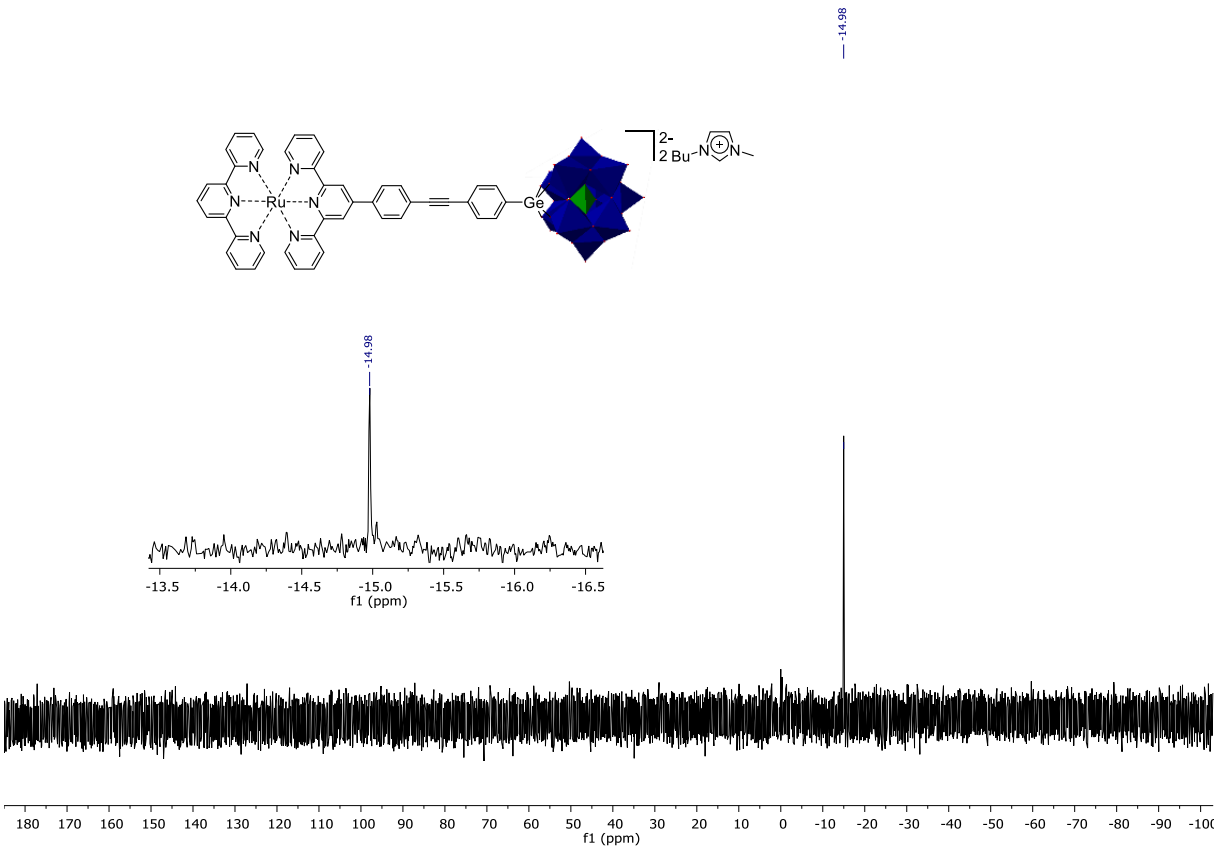

Figure S25. ^{31}P{^{1}H} NMR (162 MHz, DMSO-d_6) spectrum of **Ru-POM**.

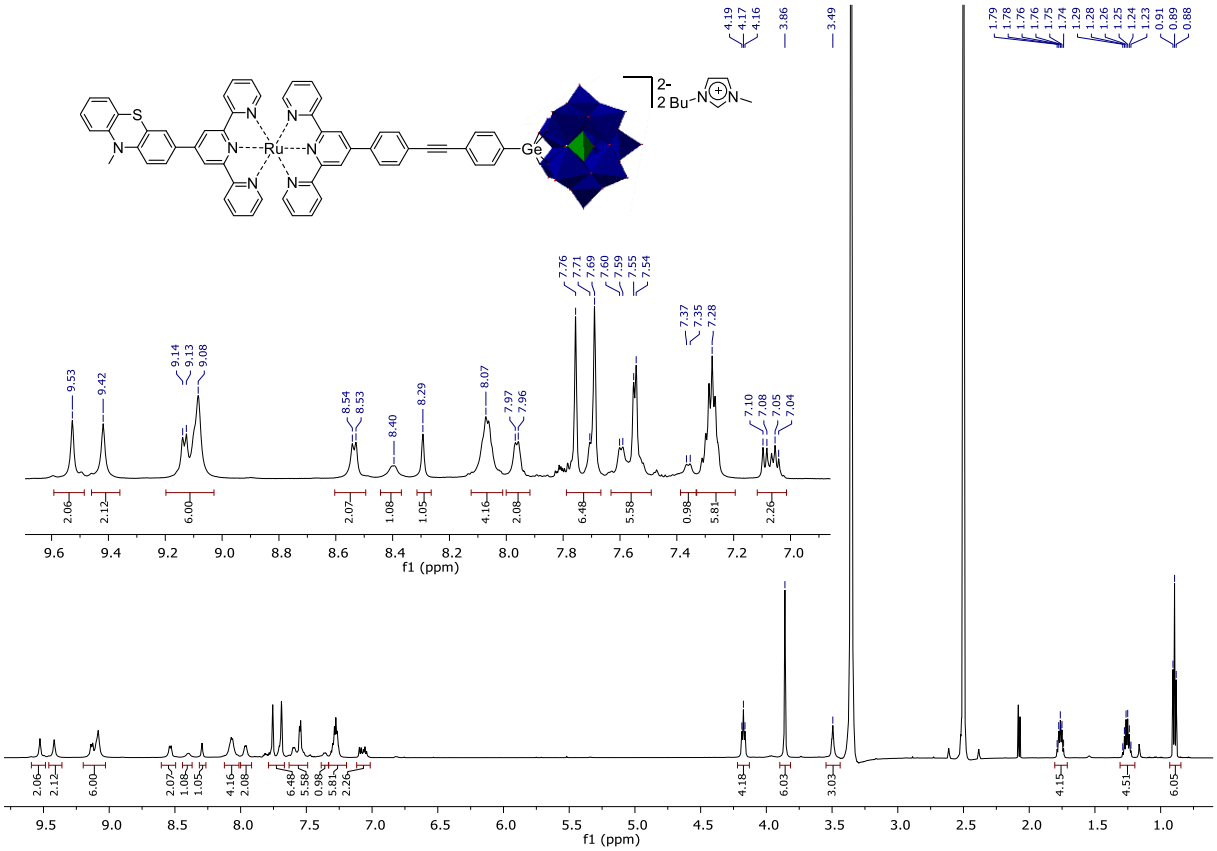

Figure S26. ^{1}H NMR (600 MHz, DMSO-d_6) spectrum of **PTZ-Ru-POM**.

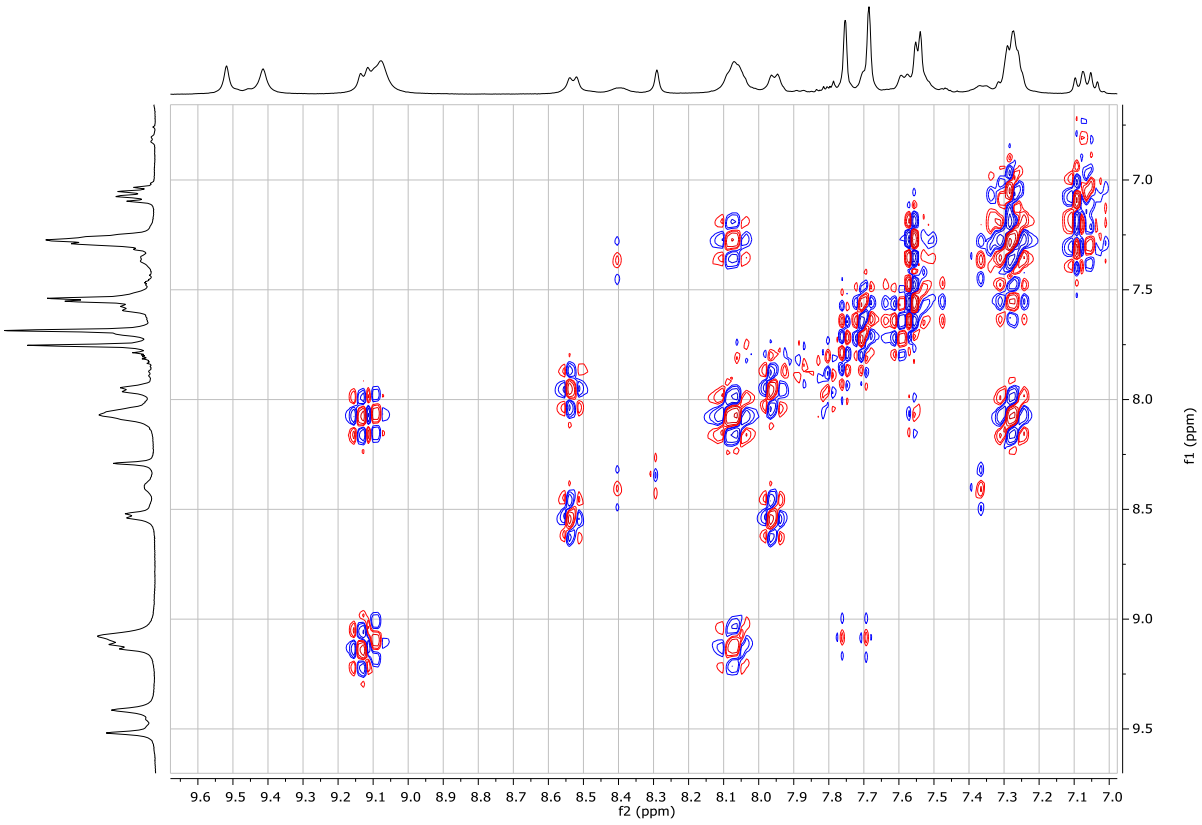

Figure S27. ^{1}H,^{1}H COSY NMR (400 MHz, DMSO-d_6, aromatic region) spectrum of **PTZ-Ru-POM**.

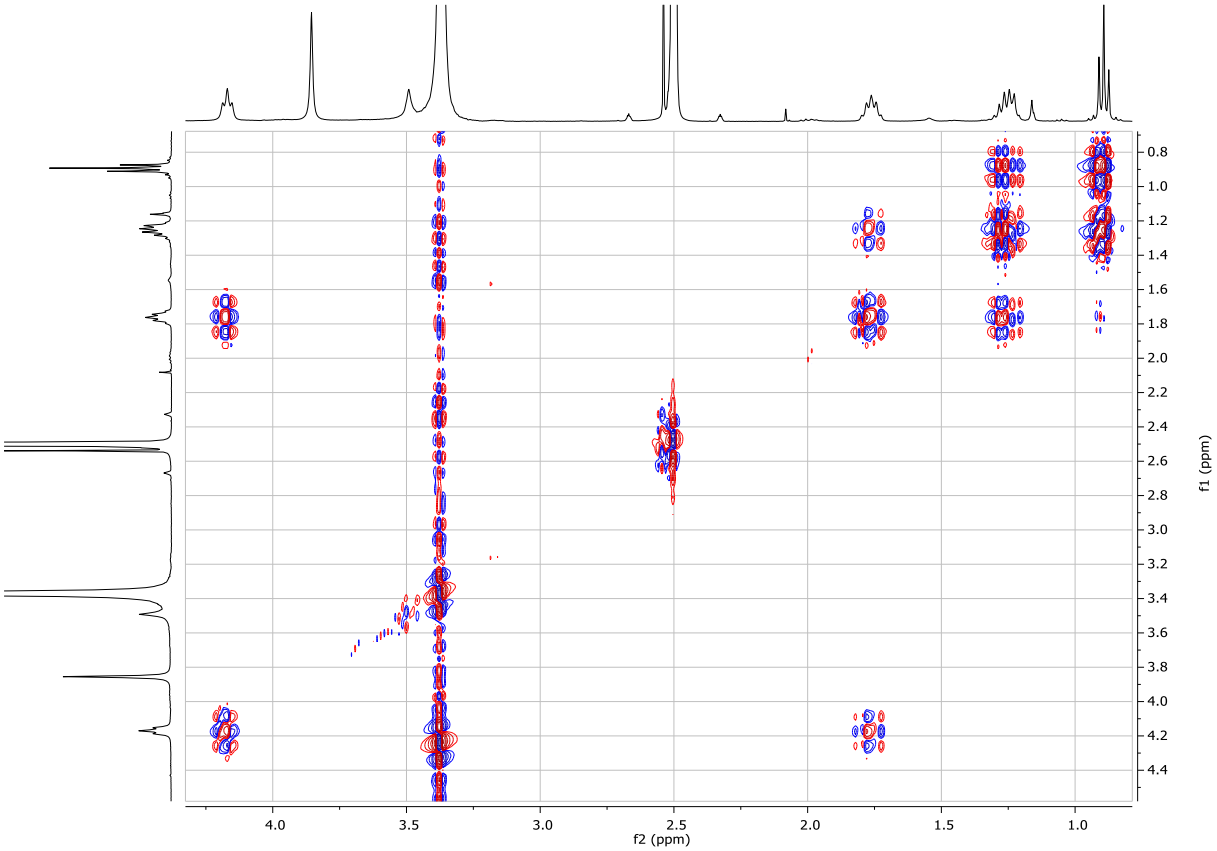

Figure S28. ^{1}H,^{1}H COSY NMR (400 MHz, DMSO-d_6, aliphatic region) spectrum of **PTZ-Ru-POM**.

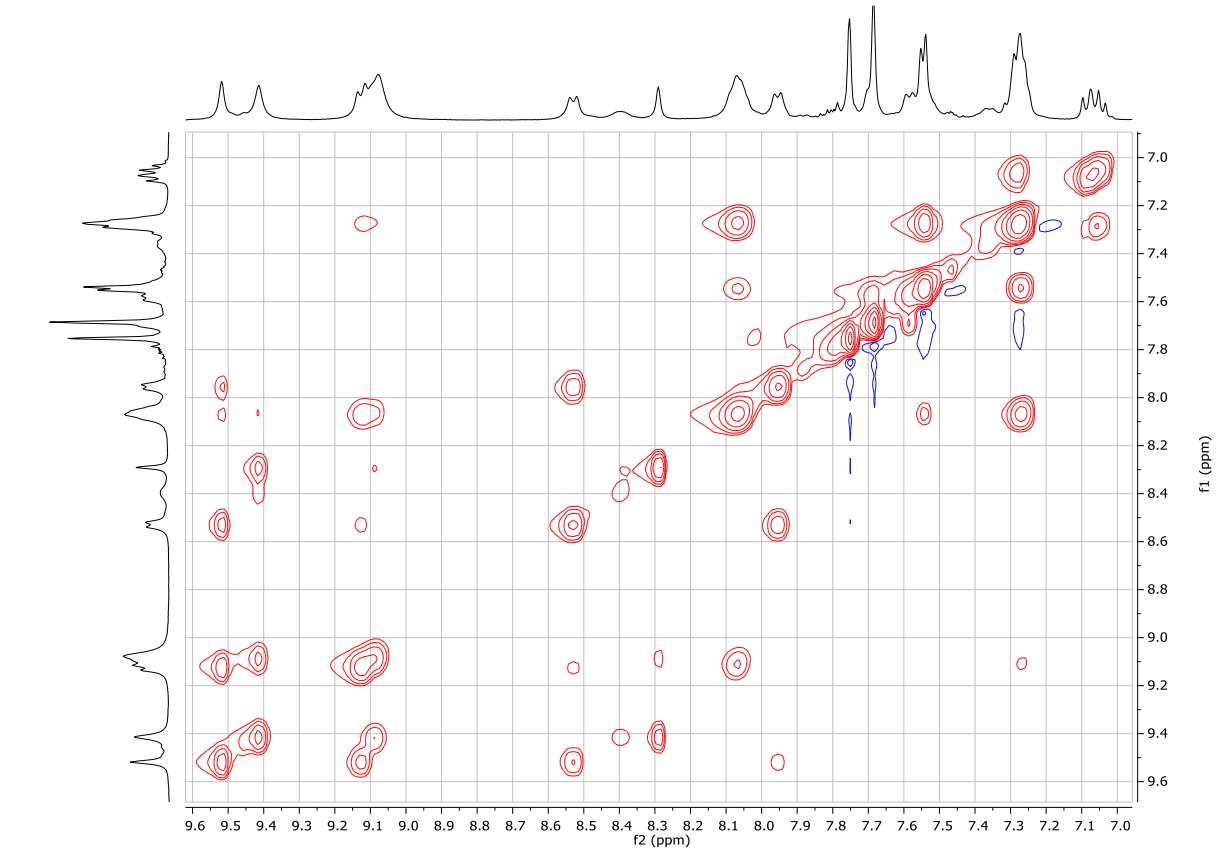

Figure S29. ^{1}H,^{1}H NOESY NMR (400 MHz, DMSO-d_6, aromatic region) spectrum of **PTZ-Ru-POM**.

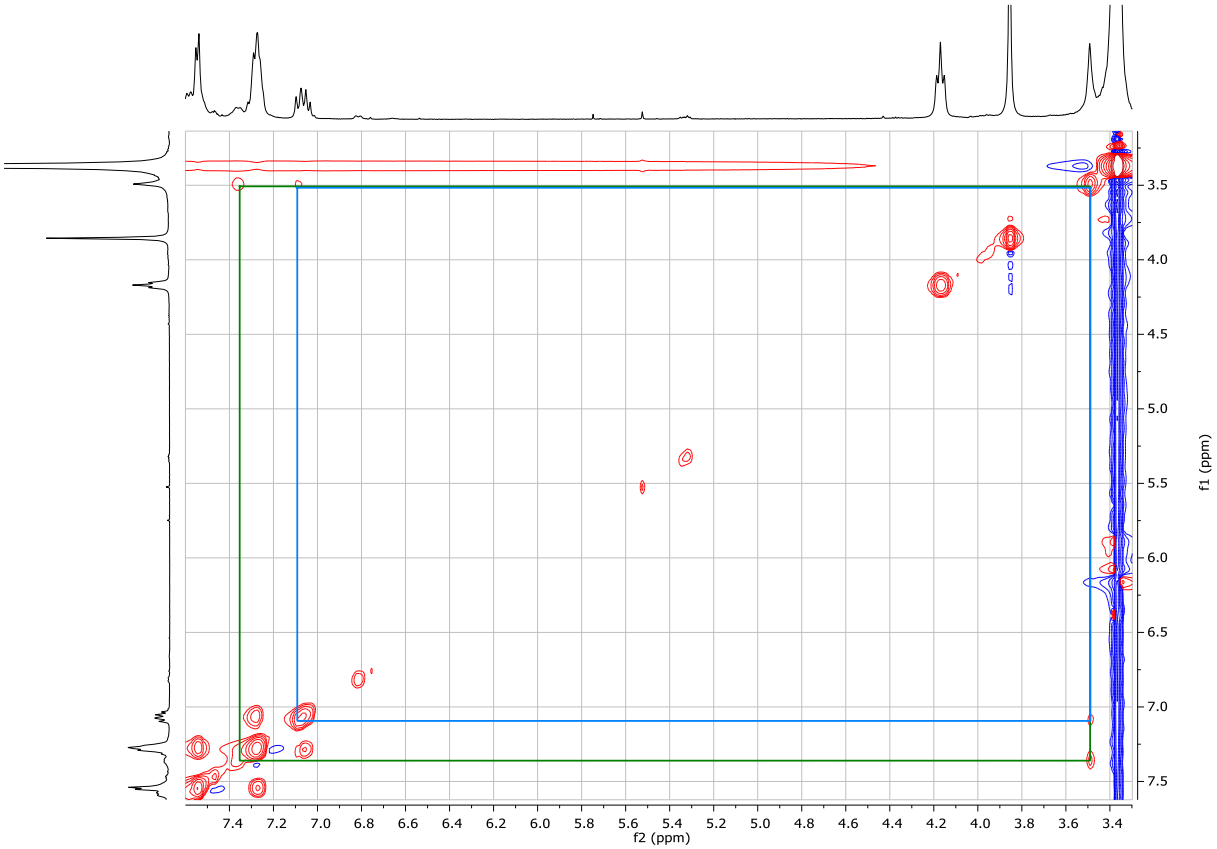

Figure S30. ^{1}H,^{1}H NOESY NMR (400 MHz, DMSO-d_6, aromatic & aliphatic region) spectrum of **PTZ-Ru-POM**. The green and blue square marks cross peaks.

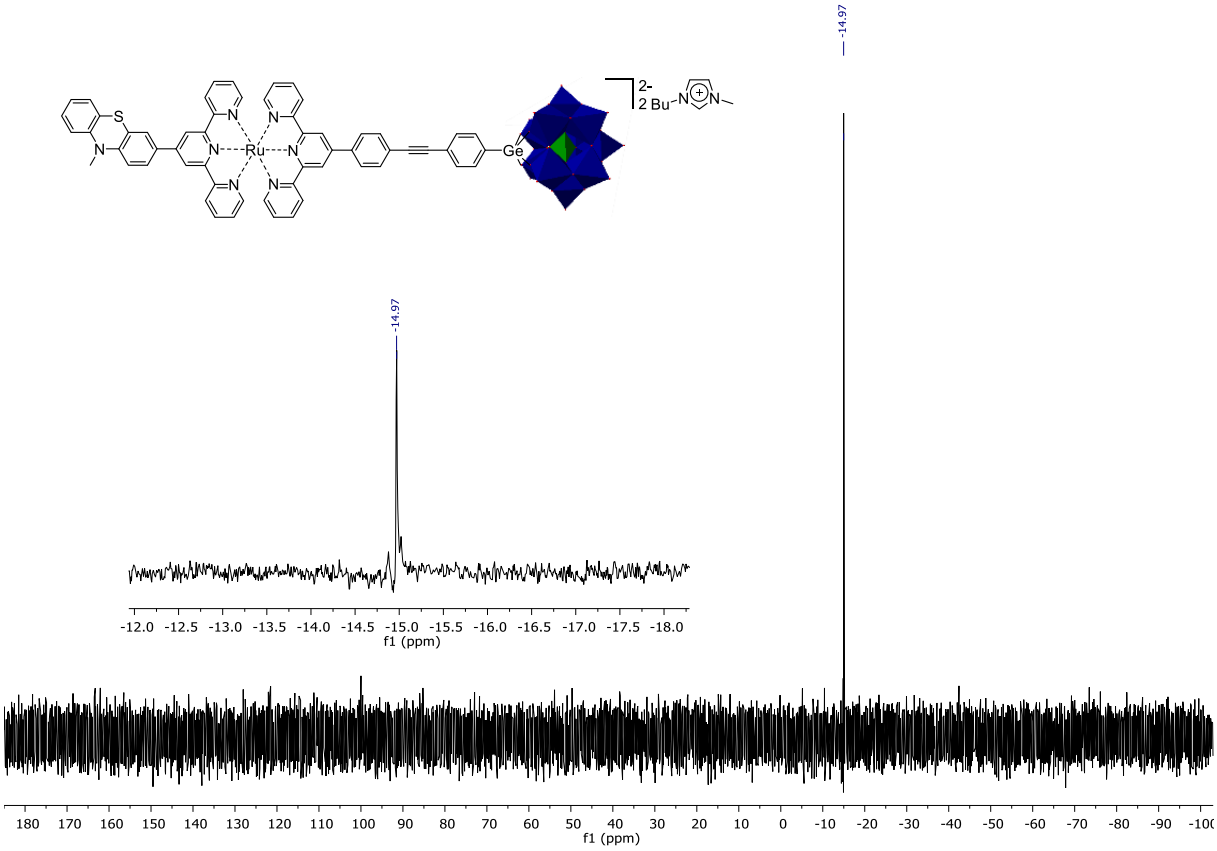

Figure S31. ^{31}P{^{1}H} NMR (162 MHz, DMSO-d_6) spectrum of **PTZ-Ru-POM**.

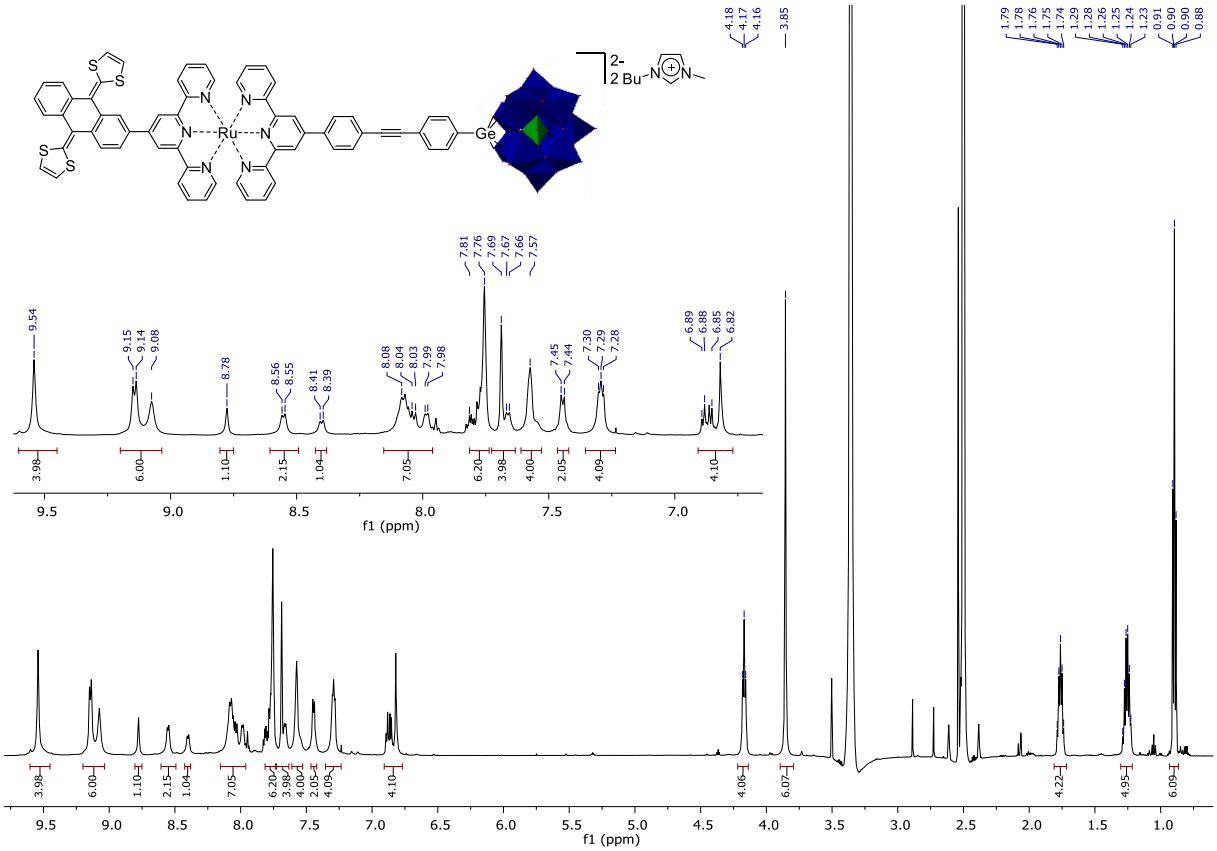

Figure S32. ^{1}H NMR (600 MHz, DMSO-d_6) spectrum of **exTTF-Ru-POM**.

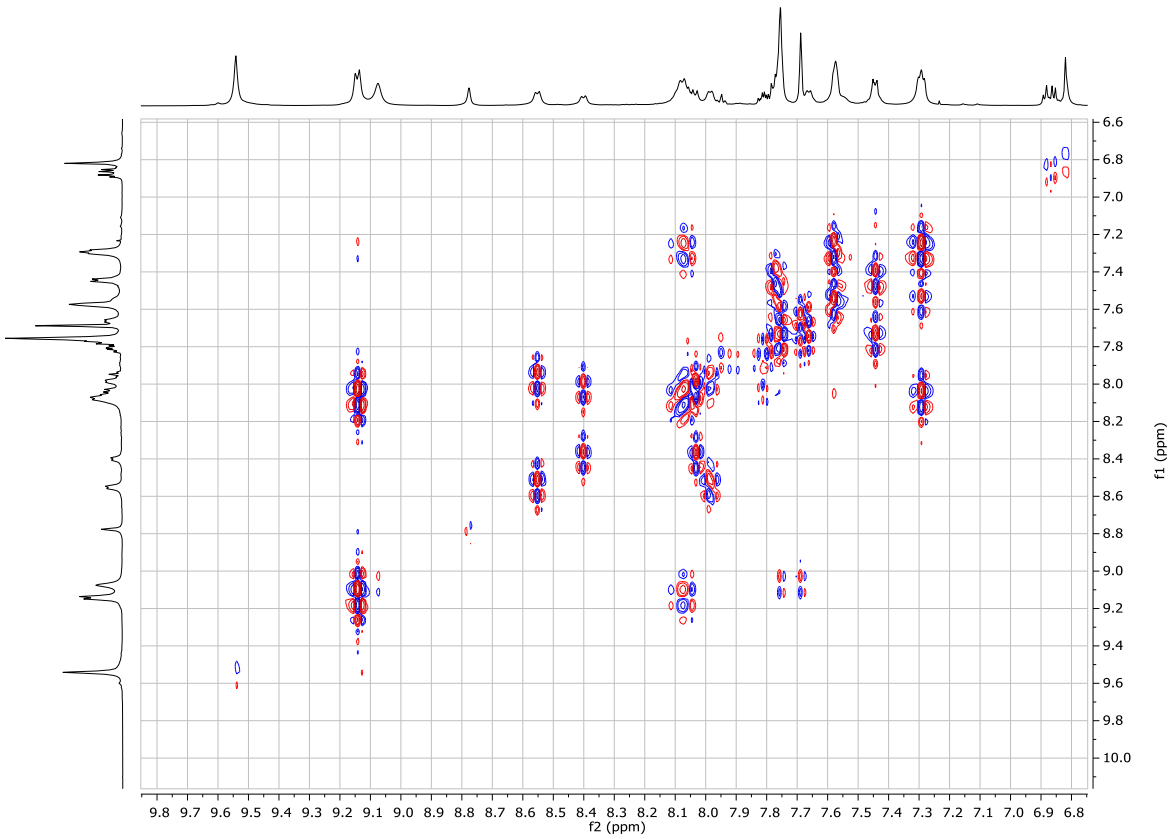

Figure S33. ^{1}H,^{1}H COSY NMR (600 MHz, DMSO-d_6, aromatic region) spectrum of **exTTF-Ru-POM**.

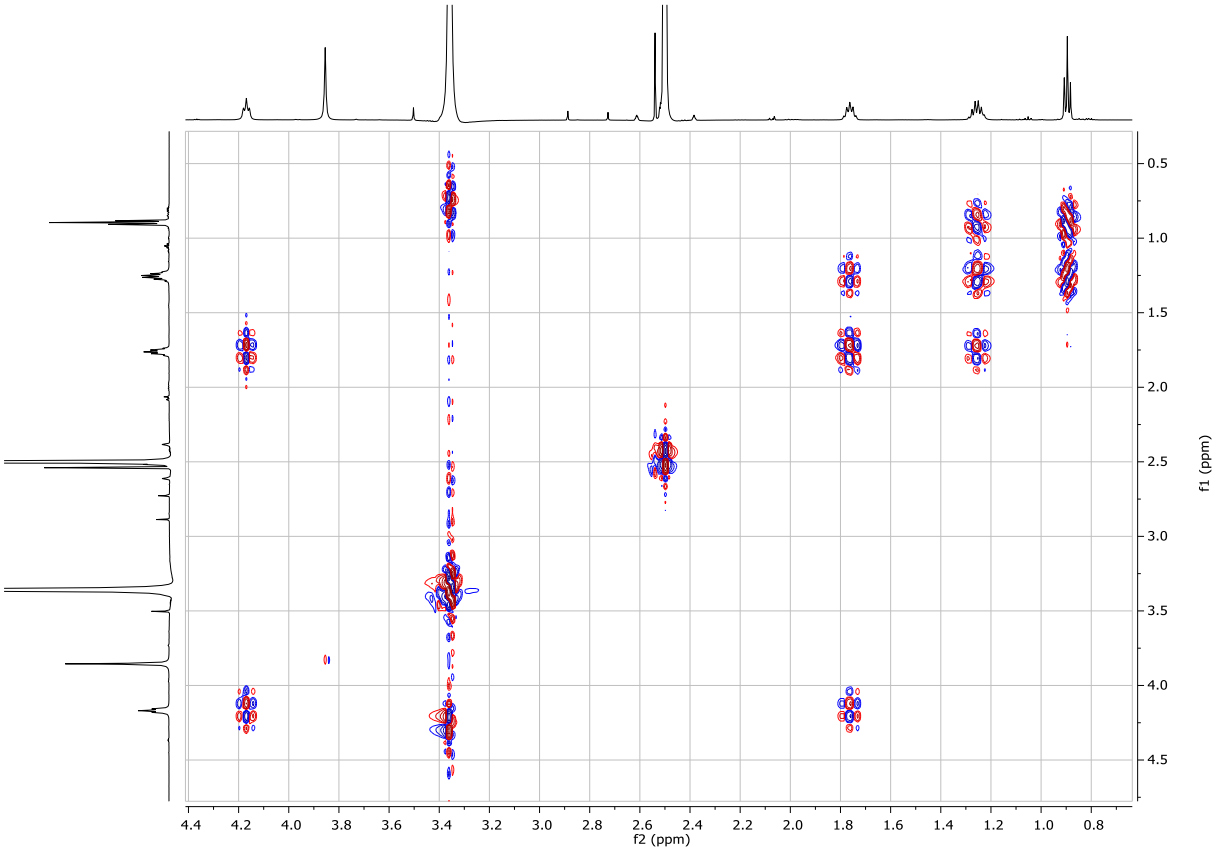

Figure S34. ^{1}H,^{1}H COSY NMR (600 MHz, DMSO-d_6, aliphatic region) spectrum of **exTTF-Ru-POM**.

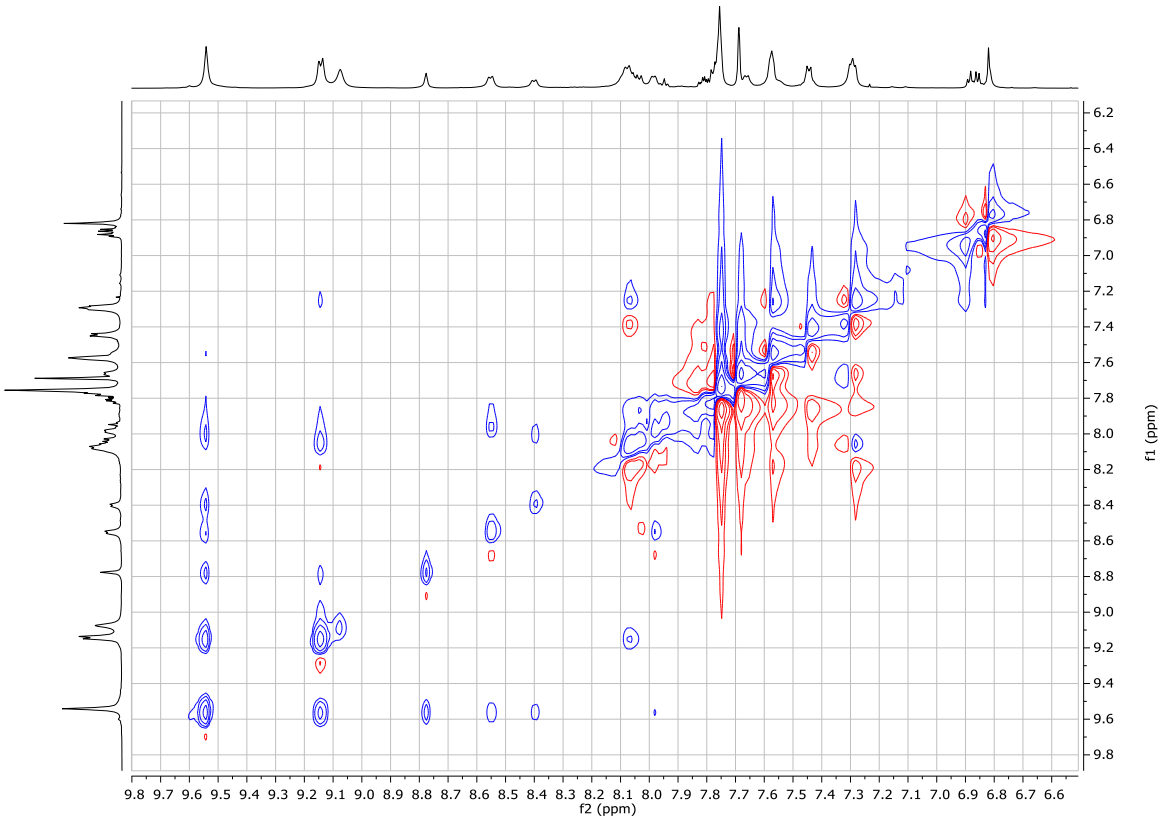

Figure S35. ^{1}H,^{1}H NOESY NMR (600 MHz, DMSO-d_6, aromatic region) spectrum of **exTTF-Ru-POM**.

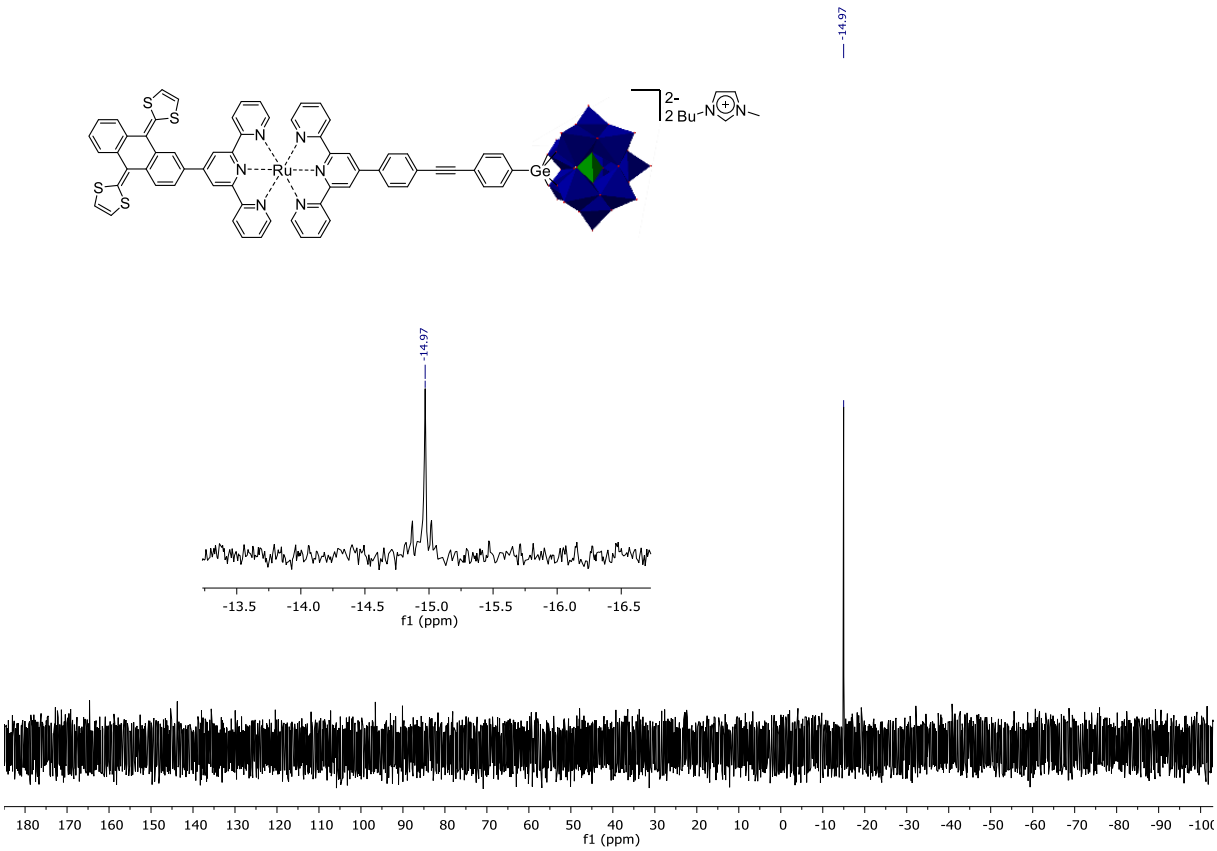

Figure S36. $^{31}P\{^{1}H\}$ NMR (162 MHz, DMSO-d_6) spectrum of **exTTF-Ru-POM**.

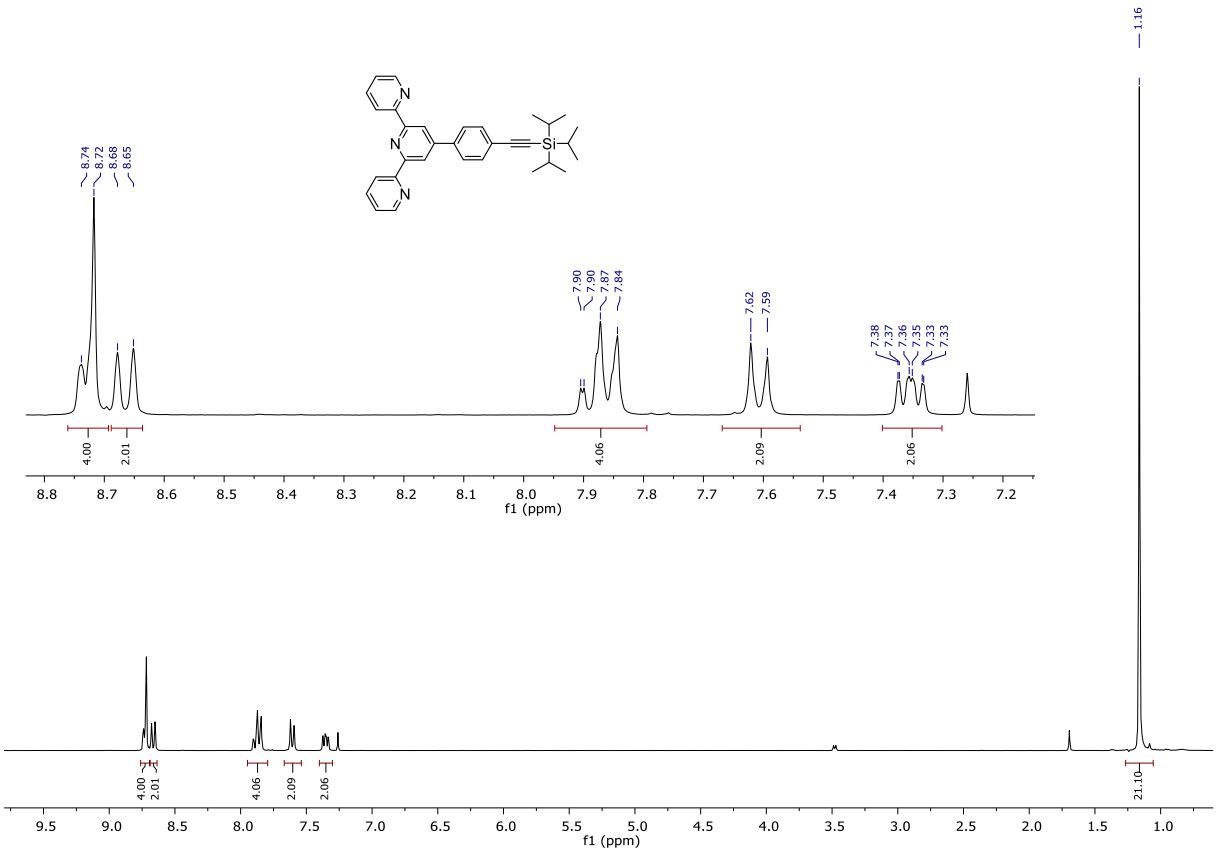

Figure S37. ^{1}H NMR (300 MHz, $CDCl_3$) spectrum of **2**.

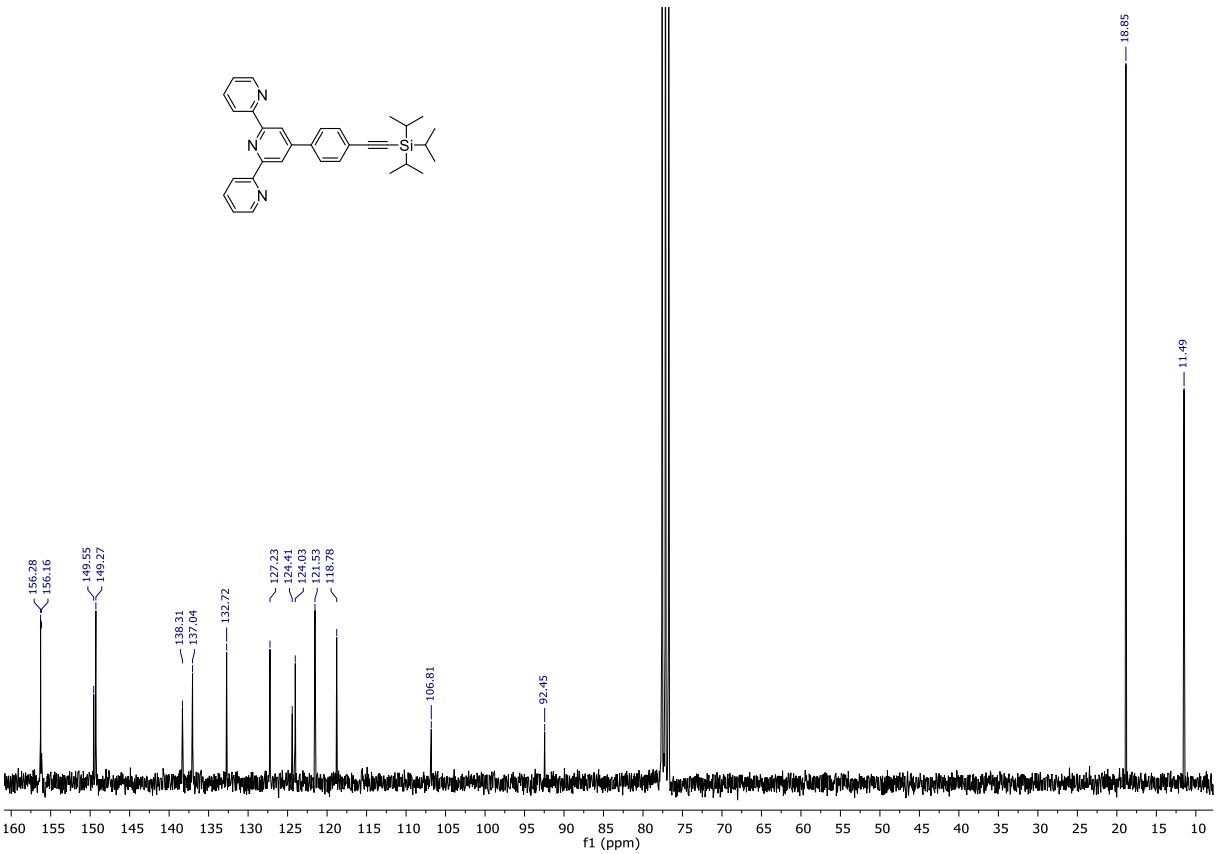

Figure S38. $^{13}C\{^{1}H\}$ NMR (75 MHz, $CDCl_3$) spectrum of **2**.

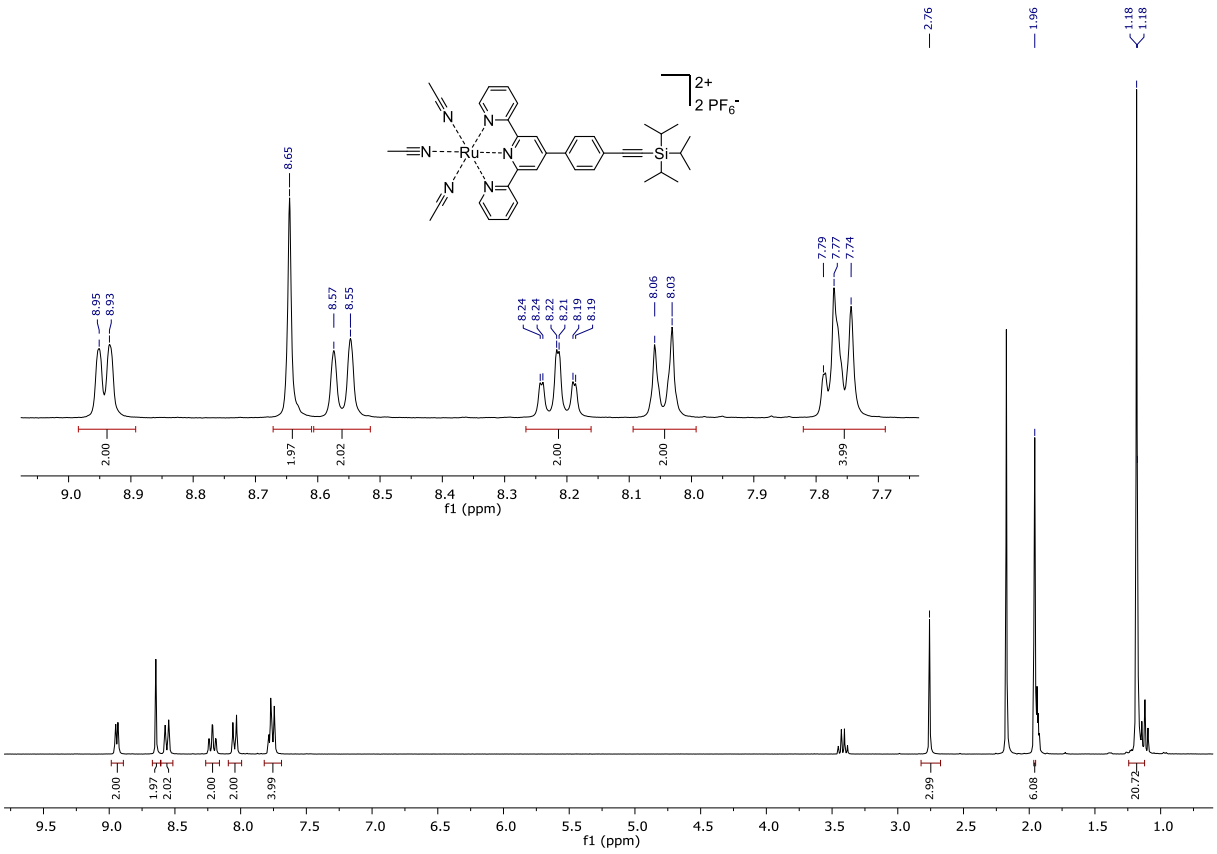

Figure S39. ^{1}H NMR (300 MHz, CD_3CN) spectrum of **4**.

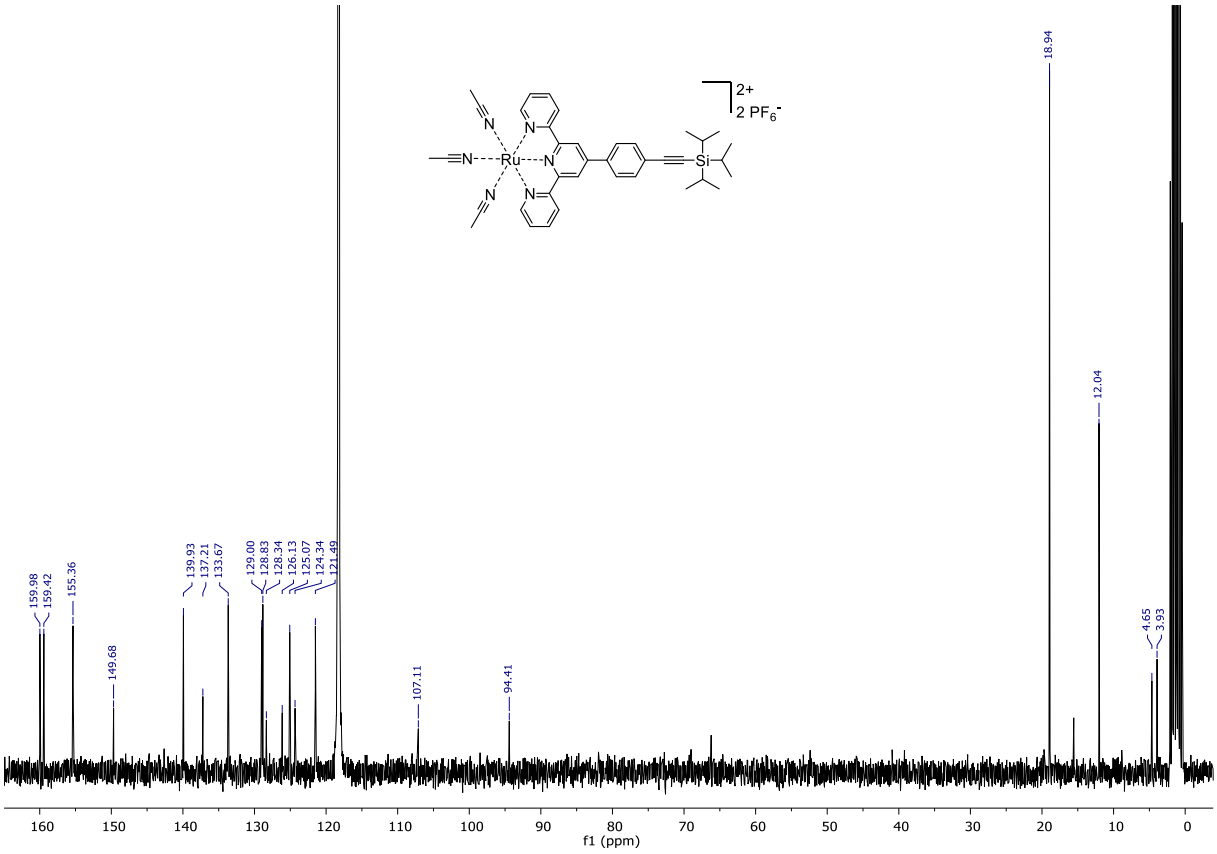

Figure S40. $^{13}C\{^{1}H\}$ NMR (75 MHz, CD_3CN) spectrum of **4**.

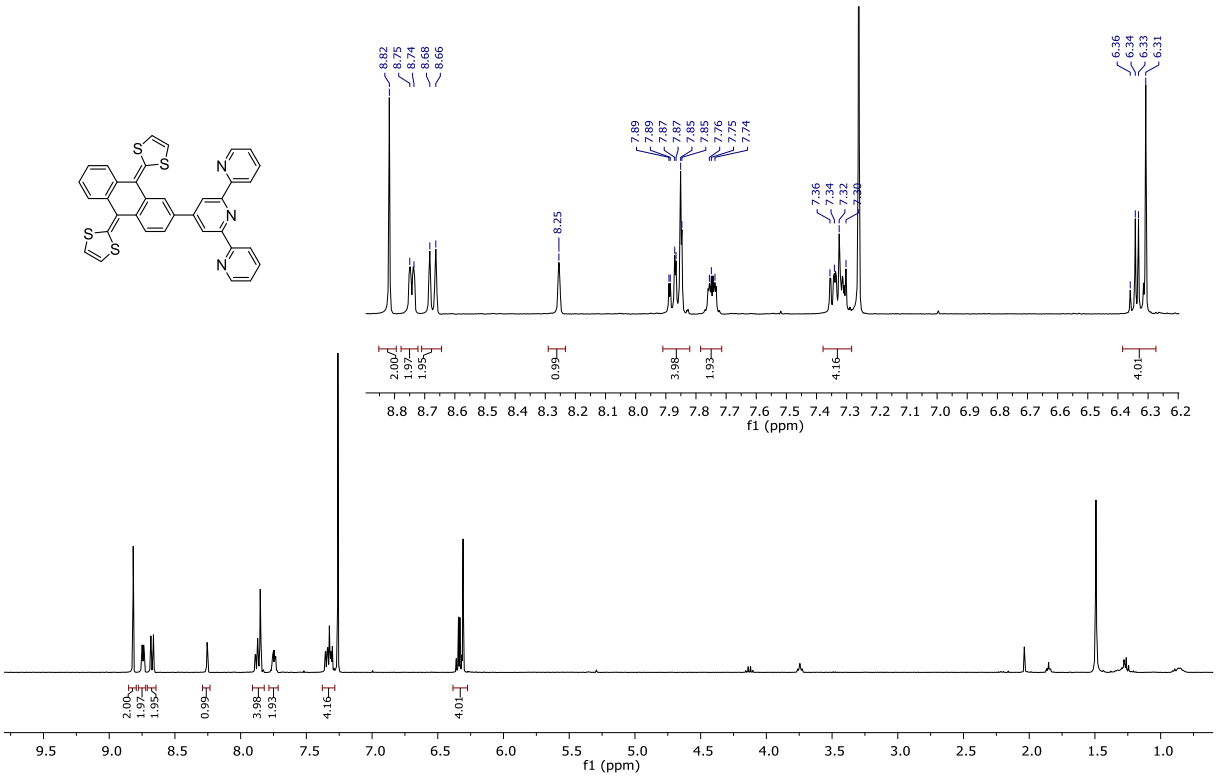

Figure S41. ^{1}H NMR (400 MHz, $CDCl_3$) spectrum of **5c**.

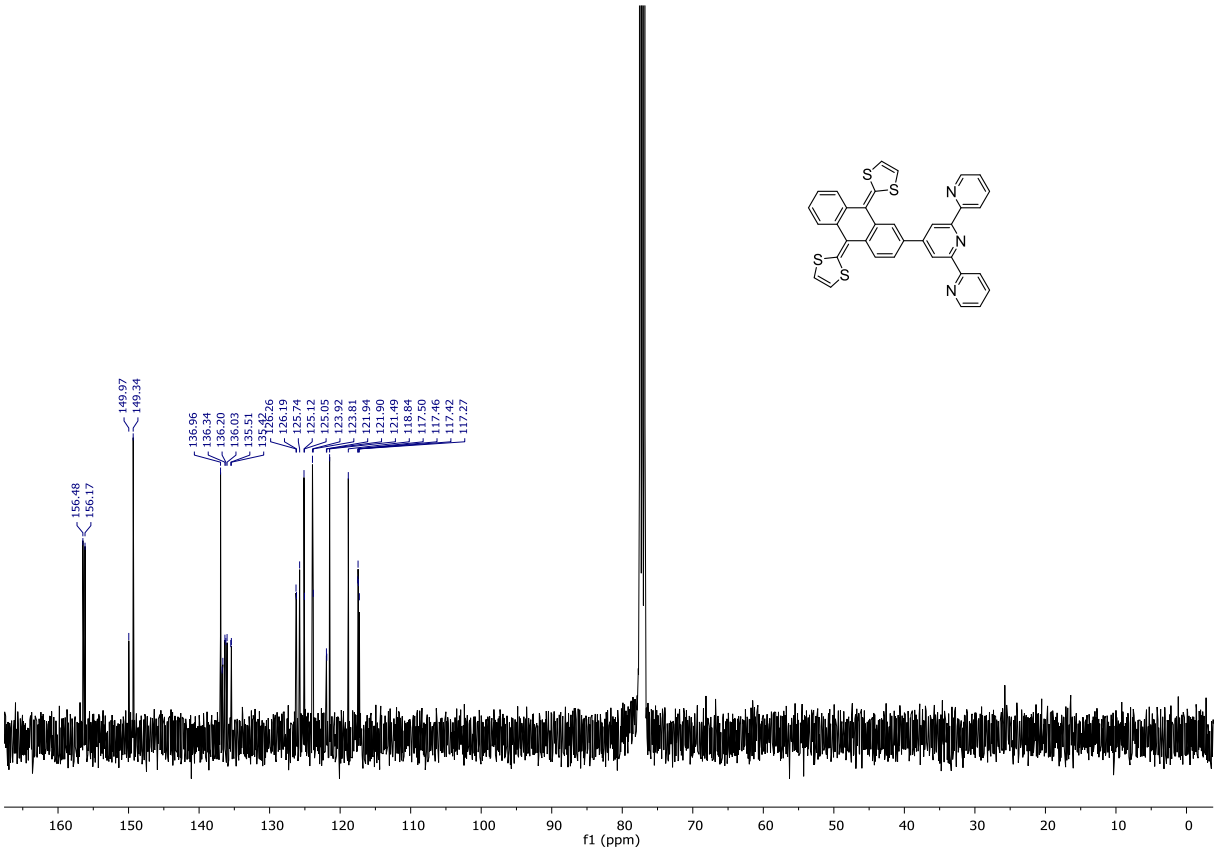

Figure S42. $^{13}C\{^{1}H\}$ NMR (100 MHz, $CDCl_3$) spectrum of **5c**.

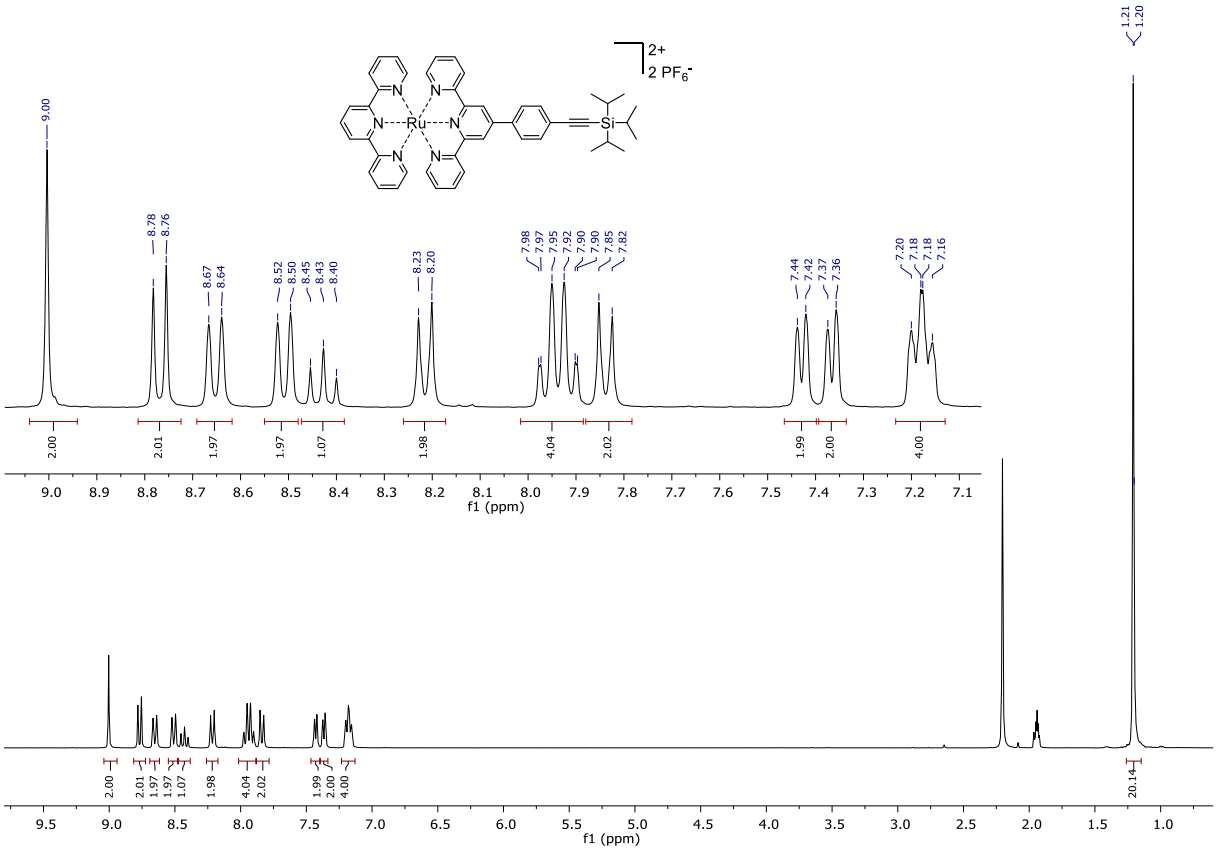

Figure S43. ^{1}H NMR (300 MHz, CD_3CN) spectrum of **6a**.

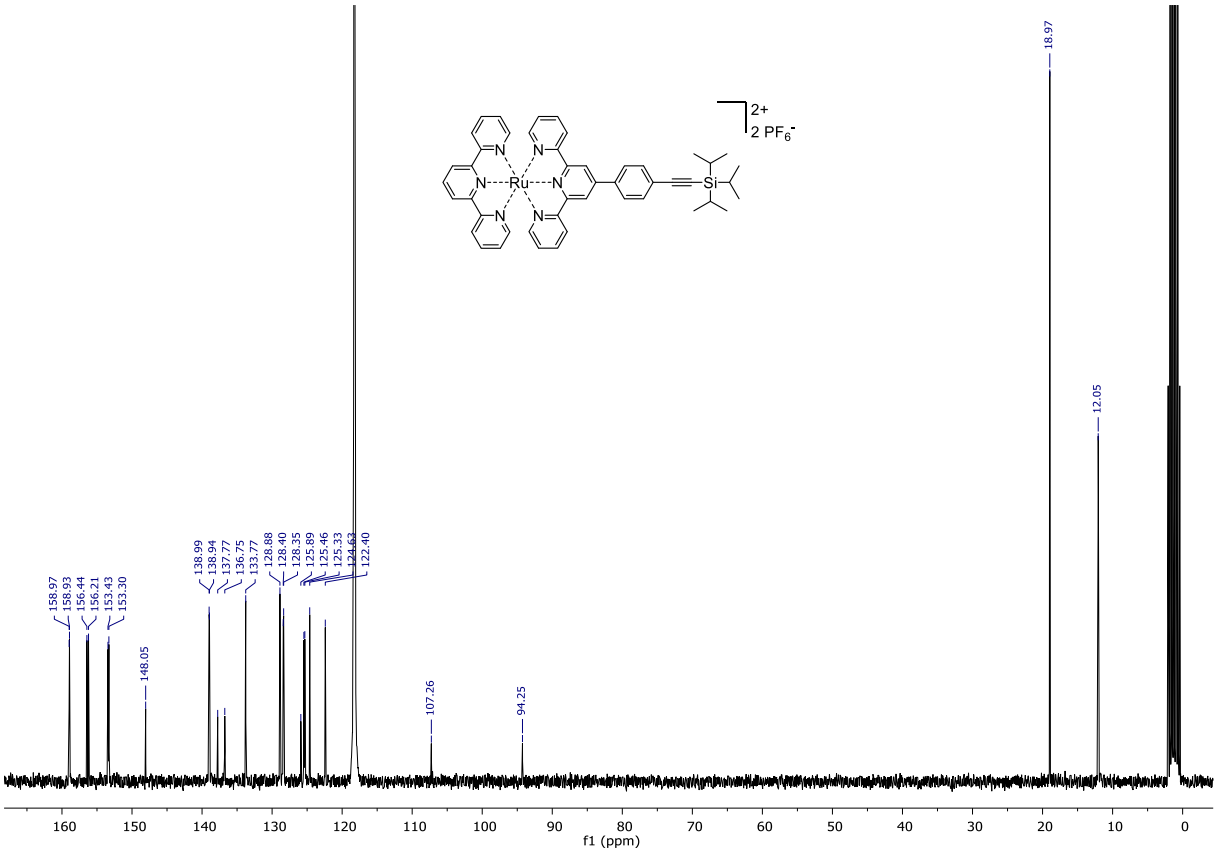

Figure S44. $^{13}C\{^{1}H\}$ NMR (75 MHz, CD_3CN) spectrum of **6a**.

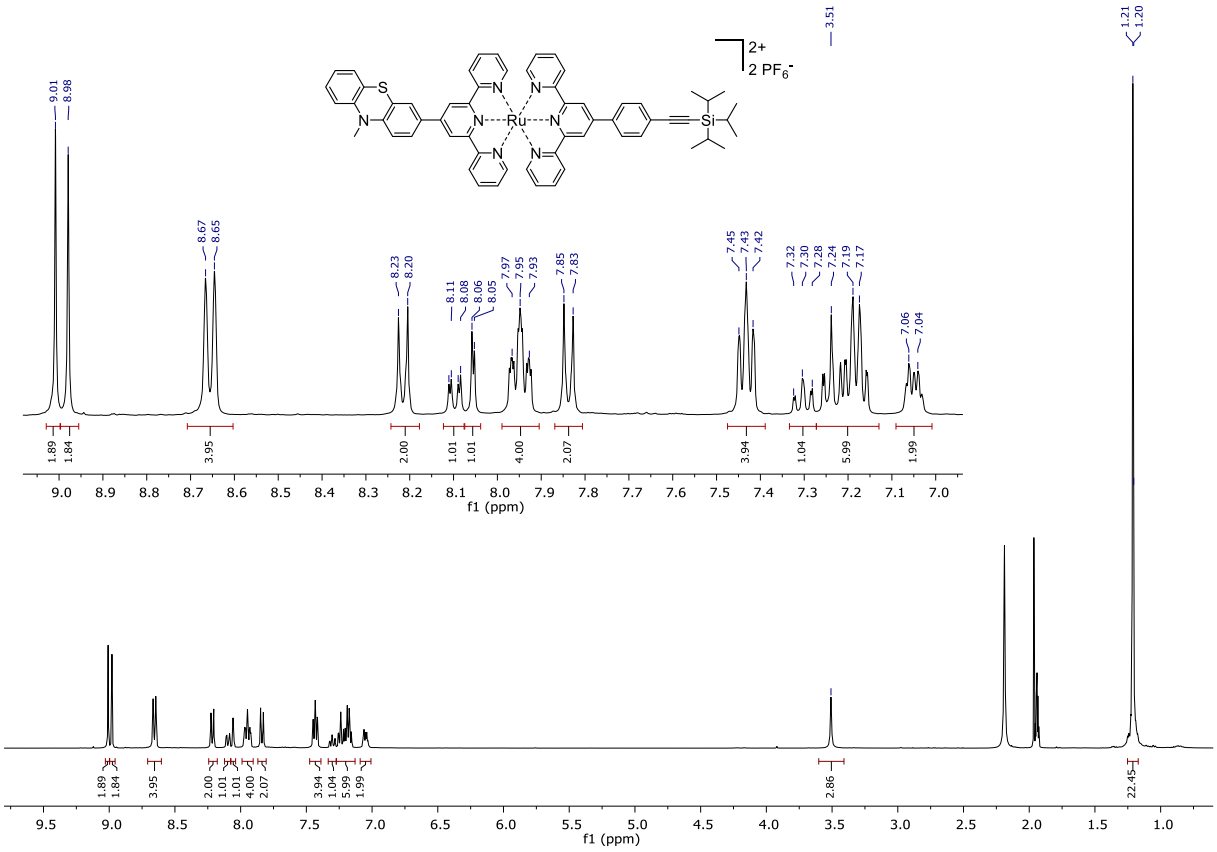

Figure S45. ^{1}H NMR (400 MHz, CD_3CN) spectrum of **6b**.

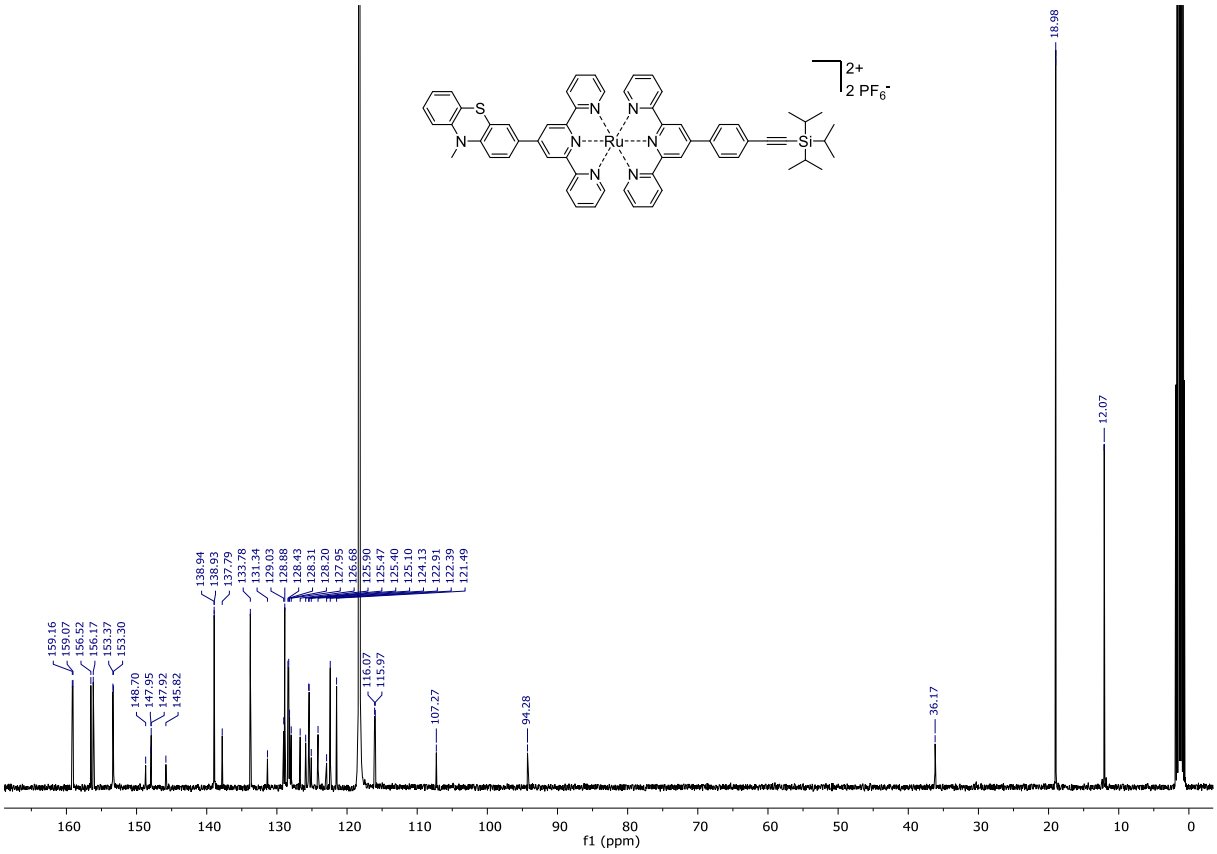

Figure S46. $^{13}C\{^{1}H\}$ NMR (100 MHz, CD_3CN) spectrum of **6b**.

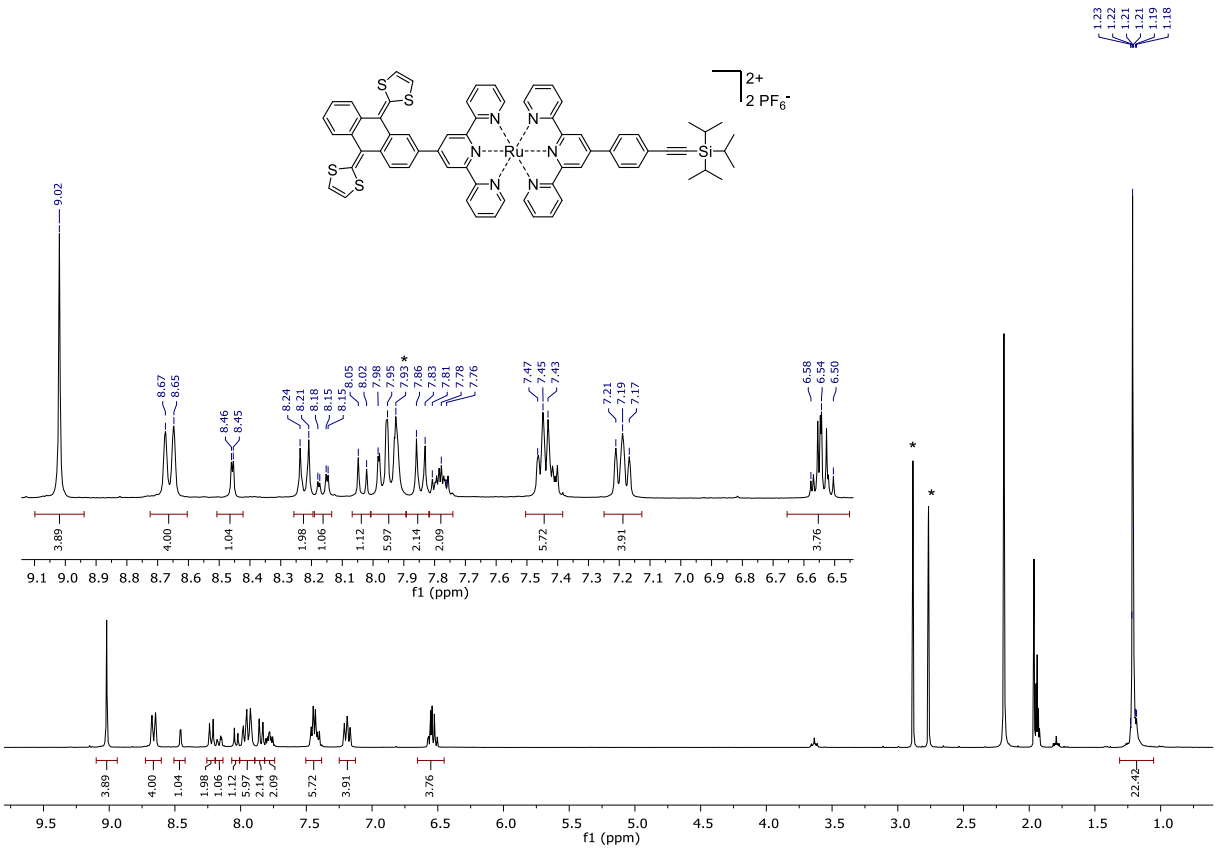

Figure S47. ^{1}H NMR (300 MHz, CD_3CN) spectrum of **6c**. The asterisks mark signals of residual DMF.

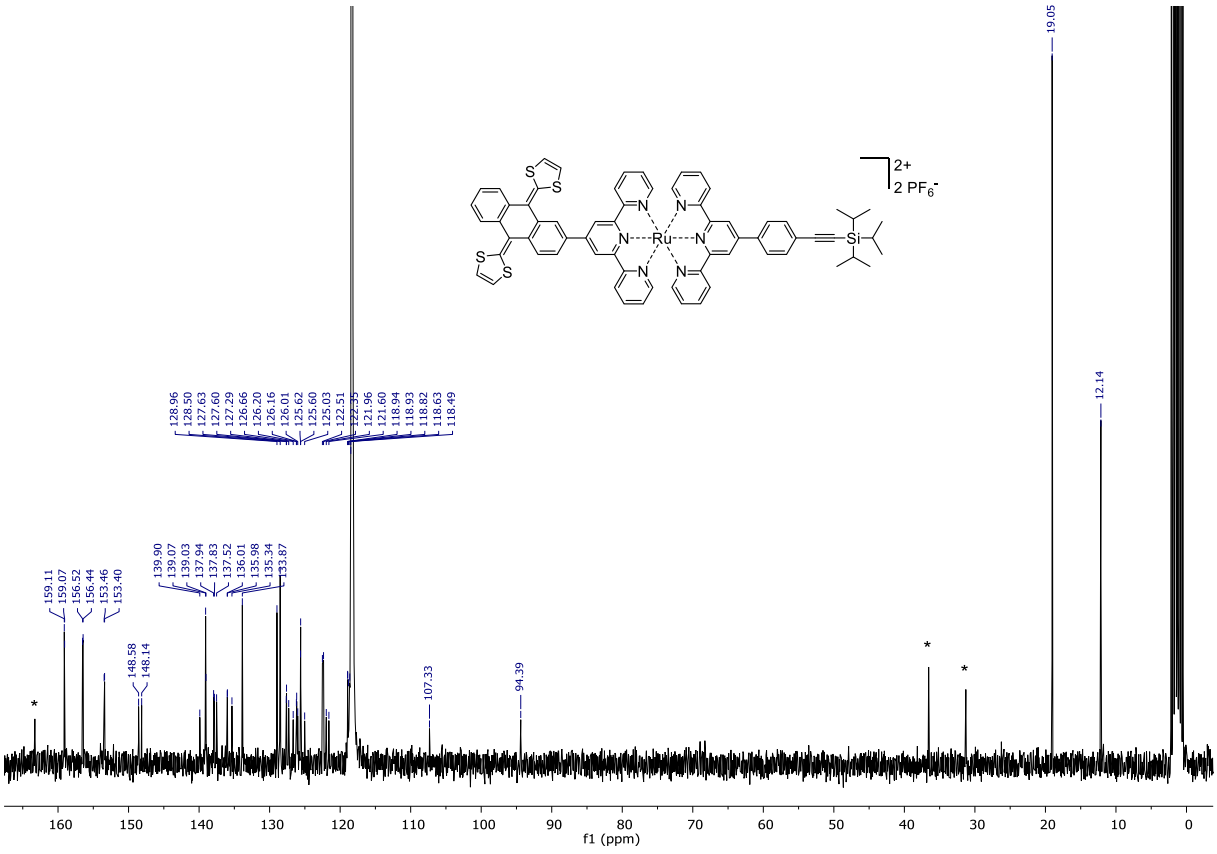

Figure S48. $^{13}C\{^{1}H\}$ NMR (75 MHz, CD_3CN) spectrum of **6c**. The asterisks mark signals of residual DMF.

5. Mass spectra

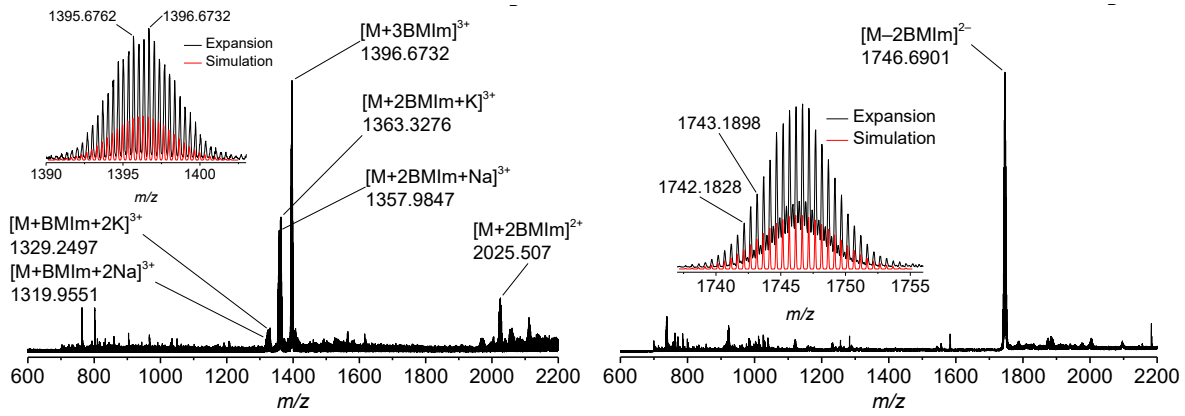

Figure S49. ESI-TOF mass spectra (solvent: DMSO/MeCN) of **Ru-POM** in positive (left) and negative mode (right). The insets show the expanded and simulated spectrum of the species $[M + 3BMIm]^{3+}$ (left) and $[M - 2BMIm]^{2-}$ (right).

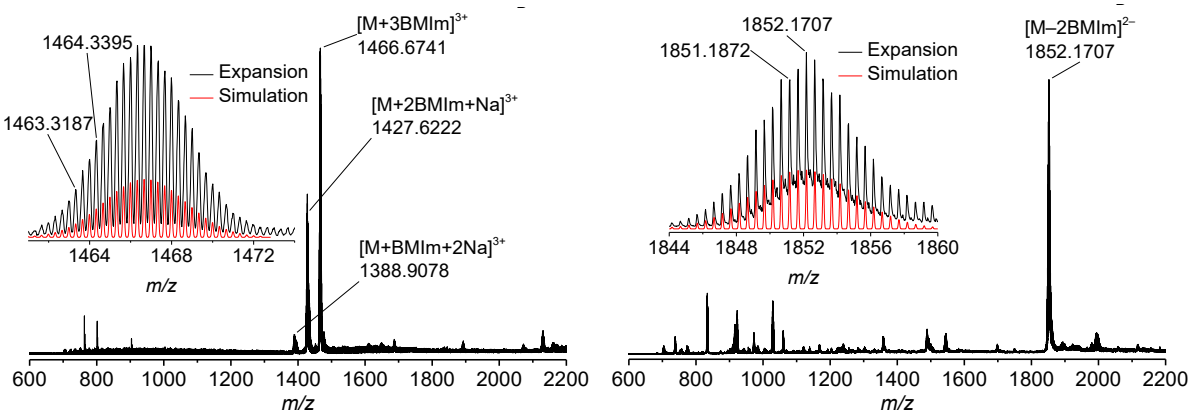

Figure S50. ESI-TOF mass spectra (solvent: DMSO/MeCN) of **PTZ-Ru-POM** in positive (left) and negative mode (right). The insets show the expanded and simulated spectrum of the species $[M + 3BMIm]^{3+}$ (left) and $[M - 2BMIm]^{2-}$ (right).

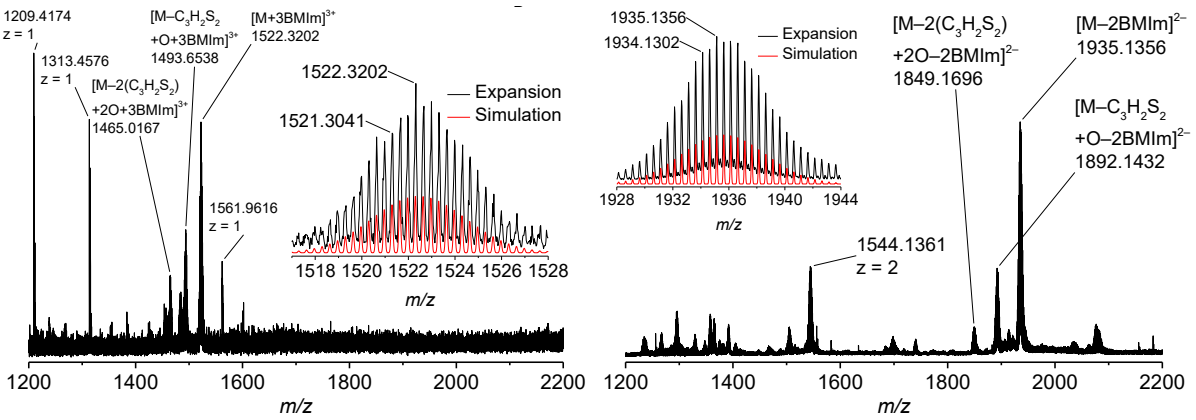

Figure S51. ESI-TOF mass spectra (solvent: DMSO/MeCN) of **exTTF-Ru-POM** in positive (left) and negative mode (right). The insets show the expanded and simulated spectrum of the species $[M + 3BMIm]^{3+}$ (left) and $[M - 2BMIm]^{2-}$ (right).

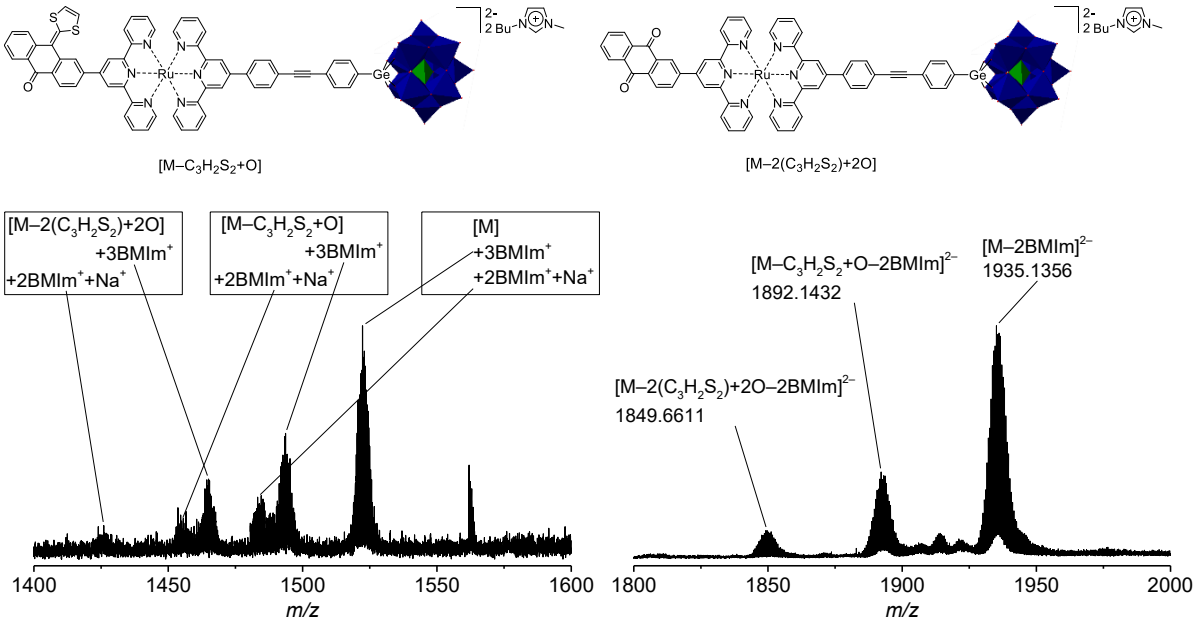

Figure S52. Fragmentation products (top) and expansion of the ESI-TOF mass spectra of **exTTF-Ru-POM** in positive (left) and negative mode (right).

Publication P5

"Efficient Energy Transfer and Metal Coupling in Cyanide-Bridged Heterodinuclear Complexes Based on (Bipyridine)(terpyridine)ruthenium(II) and (Phenylpyridine)iridium(III) Complexes"

K. Barthelmes, M. Jäger, J. Kübel, C. Friebe, A. Winter,
M. Wächtler, B. Dietzek, U. S. Schubert,

Inorg. Chem. **2016**, *55*, 5152-5167.

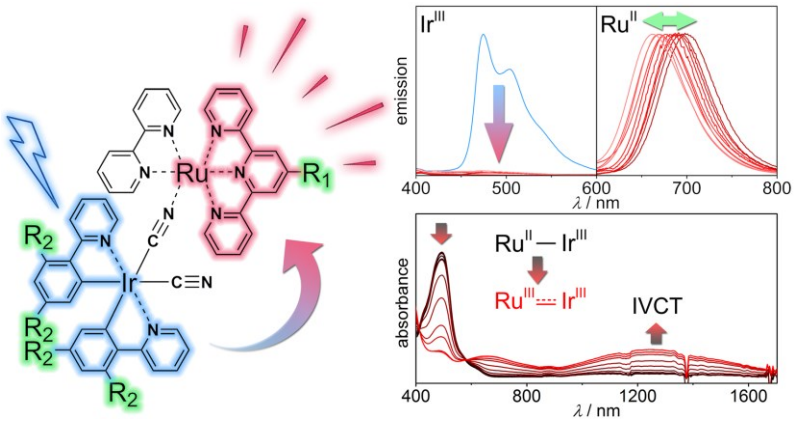

The Supplementary Information can be downloaded at the publisher's site.

Inorganic Chemistry

Article

pubs.acs.org/IC

Efficient Energy Transfer and Metal Coupling in Cyanide-Bridged Heterodinuclear Complexes Based on (Bipyridine)(terpyridine)ruthenium(II) and (Phenylpyridine)iridium(III) Complexes

Kevin Barthelmes,[†,‡] Michael Jäger,[†,‡] Joachim Kübel,[§,⊥] Christian Friebe,[†,‡] Andreas Winter,[†,‡] Maria Wächtler,[§] Benjamin Dietzek,[§,⊥,‡] and Ulrich S. Schubert*[,†,‡]

[†]Laboratory of Organic and Macromolecular Chemistry, Friedrich Schiller University Jena, Humboldtstraße 10, 07743 Jena, Germany

[‡]Center for Energy and Environmental Chemistry, Friedrich Schiller University Jena, Philosophenweg 7a, 07743 Jena, Germany

[§]Leibniz Institute of Photonic Technology, Albert-Einstein-Straße 9, 07745 Jena, Germany

[⊥]Institute of Physical Chemistry and Abbe Center of Photonics, Friedrich Schiller University Jena, Helmholtzweg 4, 07743 Jena, Germany

Supporting Information

ABSTRACT: We report a series of cyanide-bridged, heterodinuclear iridium(III)−ruthenium(II) complexes with the generalized formula $[Ir((R_2)_2\text{-ppy})_2(CN)(\mu\text{-}CN)Ru(bpy)(tpy\text{-}R_1)]PF_6$ (ppy = 2-phenylpyridine, bpy = 2,2′-bipyridine, and tpy = 2,2′:6′,2″-terpyridine). The structural, spectroscopic, and electrochemical properties were analyzed in the context of variation of the electron-withdrawing (e.g., −F, −Br, −CHO) and -donating (e.g., −Me) and extended π-conjugated groups at several positions. In total, ten dinuclear complexes and the appropriate model complexes have been prepared. The iridium(III)-based emission is almost fully quenched in these complexes, and only the ruthenium(II)-based emission is observed, which indicates an efficient energy transfer toward the Ru center. Upon oxidation of the Ru center, the fluorinated complexes **2** exhibit a broad intervalence charge-transfer transition in the near-infrared region. The complexes are assigned to a weakly coupled class II system according to the Robin−Day classification. The electronic structure was evaluated by density functional theory (DFT) and time-dependent DFT calculations to corroborate the experimental data.

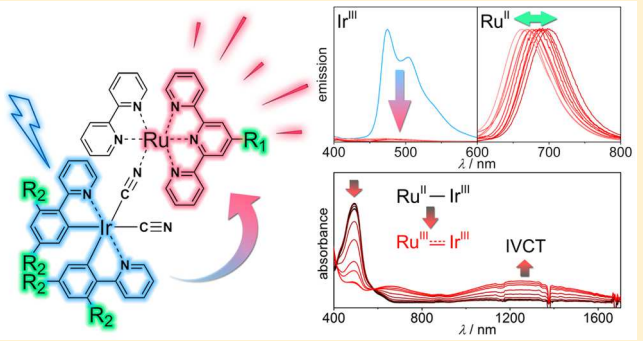

INTRODUCTION

During the last decades, polypyridyl complexes of d^6 transition metals have been intensively studied regarding their potential in light-driven devices.[1] The presence of relatively long excited-state lifetimes and sufficiently high quantum yields is the basis for further photoinduced processes that play an important role in the development of light-harvesting antennae or artificial photosynthetic systems. Polypyridyl transition-metal complexes, e.g., of ruthenium(II)[2] and iridium(III),[3] are well-known for their readily tunable photophysical and electrochemical properties. In a covalently bridged multinuclear assembly, the metal's individual properties can be combined. Thereby, the geometry, length, and nature of the bridging ligand are crucial parameters for controlling electronic communication and, thus, the energy- and/or electron-transfer processes between the components.[4] Recently, efficient energy transfer between polypyridyliridium(III) and -ruthenium(II) complexes, i.e., bridged by either *p*-diphenylene,[5] 7,7-diphenylnorbornane,[6] 3,5-bis(2-pyridyl)-1,2,4-triazole,[7] or 2,3,5,6-tetrakis(2-pyridyl)pyrazine[8] units, was shown. In these heterometallic complexes, the iridium(III)-based emission is strongly quenched by the Ru^{II} center. In contrast, triphenylene units in a meta arrangement lead to weak coupling between the metals and result in two independent metal-based emissions at room temperature.[9] Dual emission is also observed for an ion pair based on anionic $[Ir(ppy)_2(CN)_2]^-$ complexes (ppy = 2-phenylpyridine) and a cationic $[Ru(bpy)_3]^{2+}$ complex (bpy = 2,2′-bipyridine) in a 2:1 stoichiometric mixture.[10] These ion pairs were studied as light-emitting devices and electroluminescent materials.[11]

In the last three decades, research on the very short ambidentate cyanide ligand focused on its use as a bridging unit because it is able to simultaneously bind two metal ions and to promote strong electronic as well as magnetic coupling between them.[12] For example, multinuclear homometallic

Received: December 17, 2015
Published: May 23, 2016

DOI: 10.1021/acs.inorgchem.5b02919
Inorg. Chem. 2016, 55, 5152−5167

A

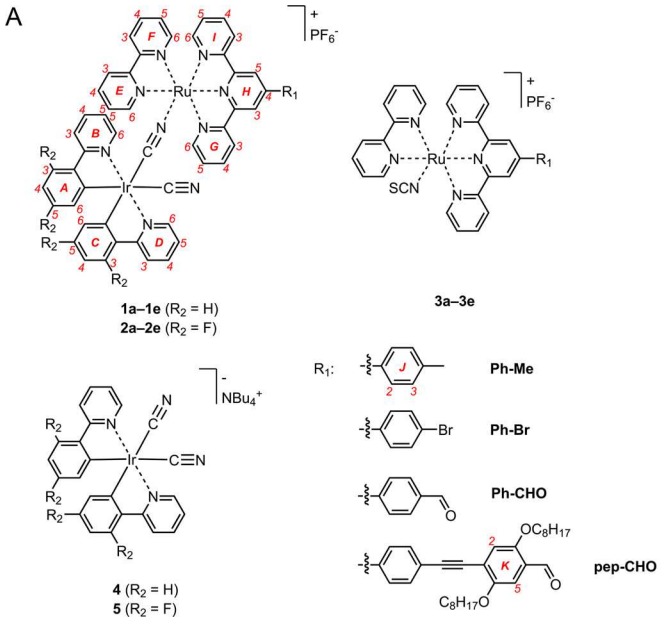

B

compound	R_1	R_2
1a	H	H
1b	Ph-Me	H
1c	Ph-Br	H
1d	Ph-CHO	H
1e	pep-CHO	H
2a	H	F
2b	Ph-Me	F
2c	Ph-Br	F
2d	Ph-CHO	F
2e	pep-CHO	F
3a	H	-
3b	Ph-Me	-
3c	Ph-Br	-
3d	Ph-CHO	-
3e	pep-CHO	-
4	-	H
5	-	F

Figure 1. Schematic representation of the cyanide-bridged iridium(III)−ruthenium(II) complexes **1a**−**1e** and **2a**−**2e** and their model complexes **3a**−**3e**, **4**, and **5** (panel A), along with a numbering scheme for the complexes (the numbering is analogous for **3**−**5**). Panel B lists an overview of the complexes.

ruthenium(II/III) complexes in their mixed-valence (MV) form exhibit a broad intervalence charge-transfer (IVCT) absorption in the near-infrared (NIR) region, which reflects the electronic interactions between both metal centers.[13] Furthermore, related heterometallic ruthenium(II/III) complexes containing $Os^{II/III}$,[12d,13a] $Rh^{I/III}$,[12e,14] Fe^{II},[15] Cr^{III},[12e,15c] or Ln^{III} [16] centers were discussed in the same context of metal coupling. On the other hand, there are a limited number of cyanide-bridged iridium(III) complexes containing Ln^{III},[17] Re^{I},[17] or Ir^{III} [18] centers. However, to the best of our knowledge, a dinuclear system based on cyanide-bridged Ir^{III} and Ru^{II} centers has not yet been established.

Herein, we present the synthesis of such close-coupled heterodinuclear iridium(III)−ruthenium(II) complexes and analyzed the electrochemical and spectroscopic properties with respect to their electronic coupling as well as their capability for light-harvesting antennae. The assemblies consist of $[Ru(bpy)(tpy\text{-}R_1)]^{2+}$ and $[Ir((R_2)_2\text{-}ppy)_2(CN)]$ moieties (tpy = 2,2′:6′,2″-terpyridine) linked by a cyanide group. To gain detailed information about the influence of the ancillary tpy and ppy ligands on the photophysical and electrochemical properties, a systematic variation of the substituents—electron-withdrawing (e.g., −F, −Br, −CHO) and -donating (e.g., −Me) groups—as well as extension of the ligand via π-conjugated groups has been performed. Related mononuclear model complexes based on $[Ru(bpy)(tpy\text{-}R_1)(SCN)]PF_6$ and anionic $Bu_4N[Ir((R_2)_2\text{-}ppy)_2(CN)_2]$ complexes[19] were used as reference to analyze the photophysical and electrochemical properties of the individual metal centers. The cyanide fragment in the ruthenium model complexes was chosen as the isothiocyanato ligand because the S atom can mimic the electron-withdrawing effect of the Ir^{III} center. On the other hand, the iridium model complexes were chosen because the cyanide group can be protonated to simulate a Coloumbic contribution by the Ru^{II} center.

RESULTS AND DISCUSSION

Synthesis. An overview of the synthesized complexes is shown in Figure 1. The dinuclear iridium(III)−ruthenium(II) complexes are denoted with **1** for pristine ppy ligands (R_2 = H) and **2** for fluorinated ppy ligands (R_2 = F). The functionalization pattern on the tpy ligand in **1** and **2** is additionally labeled by **a**−**e**, i.e., **a** for pristine tpy, **b**, **c**, and **d** for phenyl-substituted tpy's, and **e** for tpy functionalized with an extended π-conjugated group. The same labeling scheme is used for the isothiocyanatoruthenium(II) complexes $[Ru(bpy)(tpy\text{-}R_1)(SCN)]PF_6$ (**3a**−**3e**). The iridium(III) model complexes $Bu_4N[Ir((R_2)_2\text{-}ppy)_2(CN)_2]$ are denoted as **4** for pristine ppy ligands (R_2 = H) and **5** for fluorinated ppy ligands (R_2 = F). They were prepared according to literature procedures.[19]

An overview of the synthetic route is shown in Scheme 1. The chloro complexes **6a**−**6e** (Scheme 1) of the general formula $[Ru(bpy)(tpy\text{-}R_1)(Cl)]^+$ represent the key molecule

Scheme 1. Schematic Representation of the Synthetic Route[a]

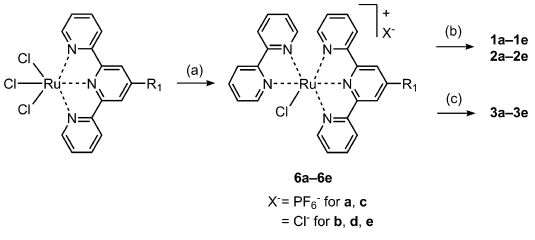

[a](a) (i) 2,2′-Bipyridine, LiCl, *N*-ethylmorpholine, methanol/water, 3 h, 75 °C, for **a** and **c**; (ii) excess NH_4PF_6. (b) (i) **4** or **5**, methanol/water, 120 °C, microwave, 30 min; (ii) excess NH_4PF_6, for **d** and **e**; (iii) 1 M HCl, DMSO, rt, 3 h; (iv) excess NH_4PF_6. (c) (i) KSCN, methanol/water, 120 °C, microwave, 30 min; (ii) excess NH_4PF_6; (iii) DMSO, 80 °C, 3 h, for **d** and **e**; (iv) 1 M HCl, DMSO, rt, 3 h; (v) excess NH_4PF_6.

DOI: 10.1021/acs.inorgchem.5b02919
Inorg. Chem. 2016, 55, 5152−5167

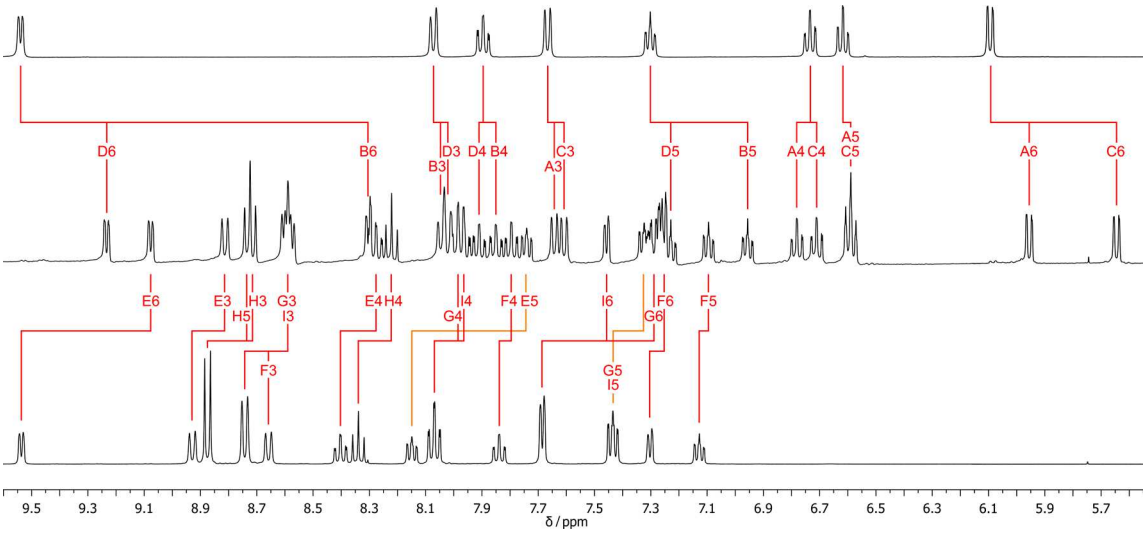

Figure 2. ^{1}H NMR spectra (DMSO-d_6, 400 MHz) of the model complexes **4** (top) and **3a** (bottom) and the dinuclear complex **1a** (middle). See Figure 1 for the numbering.

for the synthesis of heterodinuclear complexes **1** and **2**. These polypyridylruthenium(II) compounds were prepared as their chloride salts by heating the respective ruthenium(III) precursors Ru(tpy-R_1)Cl_3 with stoichiometric amounts of bpy in a methanol/water mixture.[20] Compounds **6a** and **6c** had to be purified by column chromatography and were isolated as hexafluorophosphate salts. Compounds **6d** and **6e** were isolated as an acetal/aldehyde mixture and used without deprotection for subsequent reactions. Finally, **1** and **2** were prepared by the reaction of **6** with an excess of **4** and **5**, respectively. The synthesis was performed in a methanol/water mixture at 120 °C under microwave irradiation for 30 min. The reddish complexes were obtained in moderate-to-good yields after column chromatography. The solubility in organic solvents (e.g., acetonitrile, dichloromethane) was increased for complexes **2**, which contain fluoro groups, compared to the parent compounds **1**. The ruthenium(II) model complexes **3** were prepared in an analogous manner, using an excess of potassium thiocyanate. Because of the ambident nature of the thiocyanate anion, a small fraction of complexes with S-coordinated thiocyanate was observed; isomerization toward the thermodynamically more stable N-coordinated thiocyanate in >97% purity could be achieved by heating the mixture in DMSO for 3 h at 80 °C (for kinetic studies on compound **3e**, see Figures S2–S4).[21] Compounds **1d**, **1e**, **2d**, **2e**, **3d**, and **3e**, which contained aldehyde/acetal mixtures after the reaction, were treated with aqueous HCl (1 M) in DMSO, as a final purification step, in order to cleave all acetal entities.

NMR Spectroscopy. The heterodinuclear complexes were thoroughly studied by ^{1}H, ^{13}C, and ^{19}F NMR spectroscopy in DMSO-d_6 (for **1**) and CD_3CN (for **2**). The assignment of the resonances was accomplished with the help of the model compounds and 2D NMR techniques. The ^{1}H NMR spectra of **4**, **1a**, and **3a** are exemplarily shown in Figure 2. The iridium compound **4** shows eight well-resolved signals in the aromatic region arising from the two equal ppy ligands. The ruthenium compound **3a** possesses eight bpy-related (denoted as E and F) and six tpy-related signals. Because of the decreased symmetry in the dinuclear complex **1a**, the signals of the two ppy units (denoted as A–D) as well as the tpy signals (denoted as G–I) become unequal and are, consequently, split up in the respective spectrum. Significant shifts are observed for those signals that are in proximity to the newly formed μ-CN group. Namely, atoms B6 and E6 are more shielded, and the signals are thus shifted upfield. ^{13}C NMR analysis showed that the chemical shift for the carbon in the CN group is at 131 ppm in the iridium model complex **4**. The chemical shift for the ^{13}C signal of the SCN group in **3a** is at 134 ppm. The carbon in the bridging CN group features less electron density and is more deshielded than the terminal CN group. Consequently, the chemical shifts for the CN groups in the heterodinuclear complex are at 143 ppm for the bridging CN and at 130 ppm for the terminal CN. The ^{19}F NMR spectrum of **2** shows four well-resolved resonances in the range between −110 and −112 ppm, which are assigned to the four unequal fluorine substituents on the two ppy units. Moreover, a doublet at −73 ppm is assigned to the PF_6^- counterion, and the integral ratio of 4:6 for the signals of the aromatic fluorine substituents and the counterion matches the monocationic nature of the assembly.

Electrochemistry. Cyclic voltammetry (CV) for all compounds was performed in dichloromethane using a potential window between −2.5 and +1.5 V against ferrocene as the reference. The model compound **4** shows an irreversible process in the anodic region at 0.53 V (peak potential) assigned to an Ir^{IV}/Ir^{III} oxidation.[22] For the fluorinated compound **5**, this process is anodically shifted by 0.3 V because of the electron-withdrawing substituents. The ruthenium model complexes **3** show a reversible signal in the anodic region with a half-wave potential of around 0.5 V, assigned to a Ru^{III}/Ru^{II} couple.[15c] Here, functionalization on the tpy moiety has a negligible influence. For the complex **3e**, a second reversible process at 1.09 V is observed. This process is assigned to oxidation of the bis(octyloxy)phenylene groups in the extended π-conjugated substituent. In the cathodic region, two redox processes at around −1.7 and −2.2 V are present, ascribed to tpy and bpy reduction. For the complexes containing an aldehyde function, a further reversible redox process is observed at around −2.0 V.

In the case of the nonfluorinated dinuclear complexes **1**, the first oxidation is observed at around 0.68 V (Figure 3). Because of its irreversible nature, this process is assigned to the Ir^{IV}/Ir^{III} oxidation. The process is shifted anodically by 0.15 V versus **4**

DOI: 10.1021/acs.inorgchem.5b02919
Inorg. Chem. 2016, 55, 5152–5167

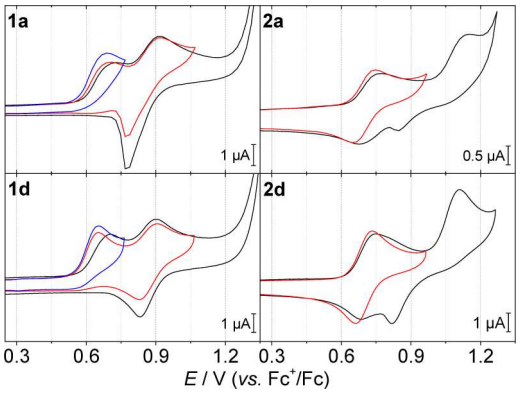

Figure 3. Cyclic voltammograms of selected dinuclear complexes in dichloromethane/0.1 M Bu_4NPF_6 at a 0.2 V/s scan rate (the fifth cycle is shown; different colors illustrate different potential ranges).

because of the electron-withdrawing effect of the Ru center to the iridium oxidation. The second process at around 0.83 V (half-wave potential) is assigned to a Ru^{III}/Ru^{II} redox couple. In contrast, the order of metal center oxidation is inverted for the fluorinated compounds **2** because the fluorine substituents have a strong influence on the iridium oxidation potential, as was already seen for the model compounds. Here, the first process at around 0.7 V is related to the reversible Ru^{III}/Ru^{II} redox couple and is shifted anodically by 0.2 V versus **3** because of the influence of the iridium metal. The second process at around 1.13 V is the irreversible Ir^{IV}/Ir^{III} oxidation. The functionalization pattern on the tpy fragment in **1** and **2** results in minor shifts of the Ru^{III}/Ru^{II} redox couple, as for the above-mentioned complexes **3**. The potential splitting (ΔE_{PS}) between the anodic Ir^{IV}/Ir^{III} and Ru^{III}/Ru^{II} peak potentials is, on average, 0.22 and 0.37 V for **1** and **2**, respectively (Table 1). Moreover, the ΔE_{PS} value for the fluorinated compounds **2** is increased when using acetonitrile as the solvent. This implies that electronic coupling between the metal centers becomes more pronounced in more polar solvents and is analyzed in more detail by spectroelectrochemistry (SEC; vide infra).

UV−Vis Spectroscopy. The absorption spectra of the dinuclear complex **1d** and the corresponding model complexes **3d** and **4** are exemplarily shown in Figure 4. The iridium model

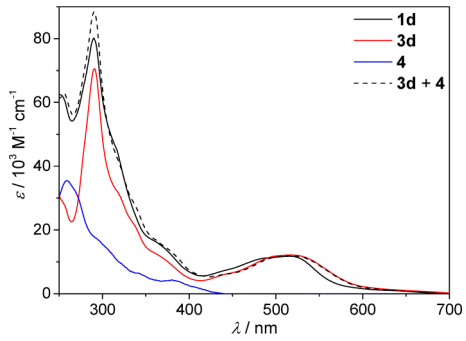

Figure 4. Room-temperature UV−vis absorption spectra of **1d**, **3d**, and **4** and superposition of **3d** and **4** in dichloromethane.

complex **4** exhibits a distinct absorption band in the UV region (λ_{max} = 259 nm), which mainly arises from ligand-centered (LC) transitions of the ppy moiety. Weaker absorption bands up to 400 nm correspond to iridium-based metal−ligand-to-ligand charge-transfer (MLLCT) transitions, with the longest-wavelength absorption maximum at 380 nm. For the fluorinated compound **5**, the longest-wavelength absorption maximum is shifted hypsochromically to 365 nm. A protonation experiment was performed on **4** and **5** to mimic the Coloumbic contribution by a Ru^{II} center (Figures S5 and S6). Upon protonation of the cyano group, a hypsochromic shift of the longest-wavelength absorption maximum is observed. A similar behavior has been shown recently for compound **4** versus related isocyanoboratoiridium(III) complexes.[23]

Complex **3d** features the characteristic absorption bands known from polypyridylruthenium(II) complexes.[24] In the UV

Table 1. Electrochemical Properties[a]

compound	$E_{pa}(Ir^{IV}/Ir^{III})^{irr}$/V[b]	$E_{pa}(Ru^{III}/Ru^{II})$/V[b]	$E_{1/2}(Ru^{III}/Ru^{II})$/V[c]	ΔE_{PS}/V[d]	$E_{1/2}(ox_3)$/V[c]	$E_{1/2}(red_1)$/V[c]	$E_{1/2}(red_2)$/V[c]	$E_{1/2}(red_3)$/V[c]
1a	0.70 (1.02)	0.92 (1.24)	0.85 (1.17)	0.22 (0.22)		−1.79		−2.18
1b	0.68	0.89	0.82	0.21		−1.77		−2.17
1c	0.68	0.90	0.83	0.22		−1.72		−2.15
1d	0.65	0.91	0.85	0.26		−1.64	−1.95	−2.20
1e	0.69	0.90	0.83	0.21	1.07	−1.70	−1.98	−2.17
2a	1.14 (1.31)	0.77 (0.71)	0.72 (0.67)	0.37 (0.60)		−1.77		−2.15
2b	1.12 (1.30)	0.73 (0.70)	0.69 (0.64)	0.39 (0.60)		−1.75		−2.15
2c	1.14 (1.24)	0.76 (0.71)	0.71 (0.67)	0.38 (0.53)		−1.71		−2.16
2d	1.11 (1.31)	0.75 (0.72)	0.70 (0.68)	0.36 (0.59)		−1.60	−1.95	−2.17
2e	1.12 (1.18)	0.75 (0.71)	0.72 (0.67)	0.37 (0.47)	1.09	−1.67	−1.98	−2.14
3a		0.56	0.51			−1.77		−2.12
3b		0.55	0.50			−1.75		−2.12
3c		0.54	0.50			−1.72		−2.12
3d		0.54	0.49			−1.63	−1.94	−2.15
3e		0.54	0.51		1.09	−1.69	−1.99	−2.16
4	0.53							
5	0.83							

[a]Conditions: differential pulse voltammetry (DPV) and CV potentials are given, and a deaerated dichloromethane solution is used as the solvent (a deaerated acetonitrile solution is used as the solvent for values in parentheses), 0.1 M Bu_4NPF_6, scan rate = 0.2 V/s, referenced against Fc^+/Fc^0; irr = irreversible process. [b]The anodic peak potential from the cyclic voltammogram is shown. [c]The half-wave potentials were determined with DPV. [d]Potential splitting between $E_{pa}(Ir^{IV}/Ir^{III})$ and $E_{pa}(Ru^{III}/Ru^{II})$.

DOI: 10.1021/acs.inorgchem.5b02919
Inorg. Chem. 2016, 55, 5152−5167

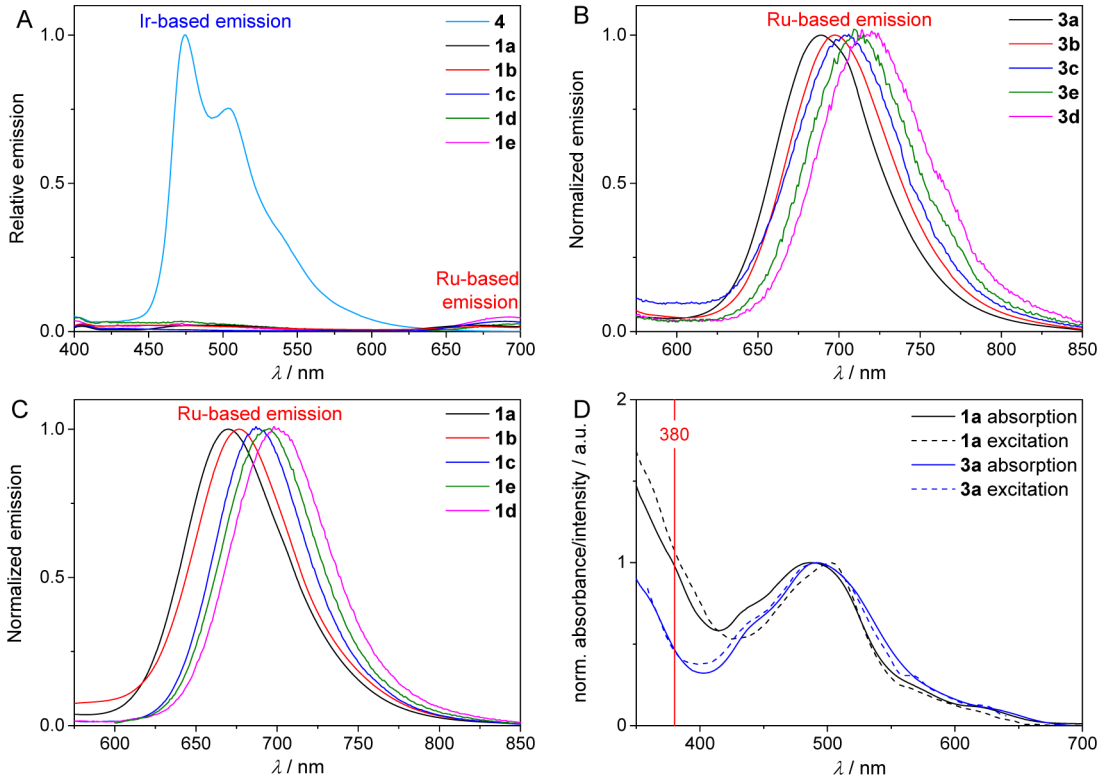

Figure 5. Room-temperature emission spectra of **4** (panel A, λ_{exc} = 380 nm), the ruthenium(II) model complexes **3** (panel B, λ_{exc} = 500 nm), and the dinuclear complexes **1** (panel A, λ_{exc} = 380 nm; panel C, λ_{exc} = 500 nm). Panel D shows the normalized absorption and excitation spectra of **1a** (λ_{det} = 670 nm) and **3a** (λ_{det} = 689 nm). The red line indicates the longest-wavelength absorption maximum of **4**. All spectra were recorded in dichloromethane.

region, a sharp absorption band (λ_{max} = 291 nm) arises from LC transitions of the bpy and the functionalized tpy moieties. The visible region exhibits broad absorption bands up to 600 nm (λ_{max} = 516 nm), which are assigned to ruthenium-based metal-to-ligand charge-transfer (MLCT) transitions. When the individual absorption spectra of complexes **3a**−**3e** are compared with each other, a shift of the long-wavelength absorption maximum is observed. In fact, for the non-functionalized complex **3a**, the maximum is located at 492 nm. Upon functionalization on the tpy fragment, a bathochromic shift of the absorption maximum at the longest wavelength is observed in the following order: **3b**/**3c**, **3d**, and **3e**.

The absorption spectrum of dinuclear complex **1d** correspond, in principle, to the spectra of the respective model complexes, i.e., intensive absorption in the UV region and broad absorption in the visible region. Deviations are found for the broad absorption band between 400 and 700 nm, i.e., the maximum in **3d** is slightly bathochromically shifted versus **1d**. This spectral region is governed by the ruthenium(II)-based MLCT transitions because the iridium model complex shows no contribution. On the other hand, a superposition of the spectra of the model complex (**3d** + **4**) matches very well with that of **1d**, in particular for the UV region, while a superposition of the protonated species of **4** and **3d** resulted in a hypsochromic shift and a worse match. This indicates that the dinuclear spectra are a result of compensation of the deviations found in the model complexes, i.e., a hypsochromic shift by the protonated iridium(III) model complex and a bathochromic shift by the isothiocyanatoruthenium(II) model complex. In the analogous series of fluorinated complexes **2**, the longest-wavelength absorption maximum is hypsochromically shifted compared to the nonfluorinated species **1**. This obvious influence of fluorination on the visible-region absorption maximum indicates a contribution of the Ir^{III} d orbitals to the Ru^{II} MLCT-dominated transitions and is discussed in more detail in the computational section (vide infra).

Emission Spectroscopy. The emission spectra of the dinuclear and reference complexes, as measured in dichloromethane, are depicted in Figure 5 and summarized in Table 2. The excitation wavelengths were chosen according to the longest-wavelength MLCT absorption maxima of **4** (λ_{exc} = 380 nm) and the ruthenium(II) model complexes **3** (λ_{exc} = 500 nm). The iridium(III) model complex **4** exhibits a vibronically structured emission band with a maximum at 474 nm and shoulders at 503 and 540 nm, which indicates the emission from ^{3}LC states (Figure 5, panel A).[25] In comparison, the fluorinated complex **5** (λ_{exc} = 360 nm) shows a similar emission structure, although hypsochromically shifted by 20 nm. The ruthenium model complexes **3** exhibit a ^{3}MLCT-based emission at around 704 nm, and the tpy substituent likewise has a distinct influence on the energy of the emission (Figure 5, panel B). In fact, the complex **3a**, with the nonfunctionalized tpy moiety, exhibits the shortest emission wavelength within their series. Complexes with functionalized tpy units show an increasing bathochromic shift in the following order: Ph-Me (**3b**), Ph-Br (**3c**), pep-CHO (**3e**), and Ph-CHO (**3d**). This is known for ruthenium(II) complexes and stems from delocalization of the electron density over the increasing conjugated system.[4b] When the dinuclear complexes **1** are excited at 380 nm (λ_{exc} = 360 nm for **2**), virtually no iridium-based emission is observed (see Figure 5, panel A, Figure S10

DOI: 10.1021/acs.inorgchem.5b02919
Inorg. Chem. 2016, 55, 5152−5167

Table 2. Photophysical Properties[a]

	absorption			emission	
compound	λ_{abs}/nm[b] ($\varepsilon/10^3$ M^{-1} cm^{-1})	$\varepsilon_{365\ nm}$[c]/ 10^3 M^{-1} cm^{-1}	$\varepsilon_{380\ nm}$[d]/ 10^3 M^{-1} cm^{-1}	$\lambda_{max,\ em}$/nm	lifetime/ ns
1a	488 (8.8)		8.6	670[e]	n.d.
1b	496 (10.8)		8.6	677[e]	n.d.
1c	509 (15.6)		12.5	688[e]	n.d.
1d	515 (11.8)		12.0	700[e]	71,[e,g] 39[f,g]
1e	518 (16.7)		35.3	694[e]	45,[e,g] 39[f,g]
2a	487 (8.2)	8.6		663[e]	n.d.
2b	501 (12.5)	11.6		669[e]	n.d.
2c	503 (9.3)	8.8		677[e]	n.d.
2d	508 (14.6)	16.7		691[e]	53,[e,g] 60[f,g]
2e	511 (18.0)	33.7		684[e]	55,[e,g] 33[f,g] (347)[f,h]
3a	492 (11.1)	7.9	5.2	689[e]	n.d.
3b	503 (10.1)	7.7	4.9	698[e]	n.d.
3c	501 (12.8)	9.6	6.0	705[e]	n.d.
3d	516 (12.1)	12.0	8.9	718[e]	50[e,g]
3e	516 (16.5)	31.6	32.4	711[e]	32[e,g]
4	380 (4.3)			474, 503 (sh), 540 (sh)[f]	90[f,g] (93)[f,h]
5	365 (7.1)			453, 480 (sh), 515 (sh)[f]	183[f,g] (163)[f,h]

[a]Conditions: an aerated dichloromethane solution, room temperature. [b]Longest-wavelength absorption maxima. [c]Extinction coefficients at 365 nm given for fluorinated complexes. [d]Extinction coefficients at 380 nm given for nonfluorinated complexes. [e]Ruthenium-based emission. [f]Iridium-based emission. [g]Measured in an aerated acetonitrile solution. [h]Measured in an aerated dichloromethane solution.

for **2**, and Table 2). However, for some of the dinuclear complexes, a weak residual emission is visible, which is ascribed as inefficient quenching, and is discussed in more detail in the time-resolved spectroscopy section (vide infra). To mimic a Coloumbic contribution by a Ru^{II} center on the model compounds **4** and **5**, the above-mentioned protonation experiment was applied to investigate the influence on their emission spectra. No quenching of the iridium-based emission was observed upon protonation of the cyano ligand with a hexafluorophosphoric acid solution, although there were hypsochromically shifted emission maxima for the protonated species of **4** ($\lambda_{max,em}$ = 453 nm) and **5** ($\lambda_{max,em}$ = 441 nm). A similar, but weaker hypsochromic shift is observed for related isocyanoboratoiridium(III) complexes.[23] In contrast, the residual iridium-based emission in **1** and **2** is only slightly hypsochromically shifted compared to those of **4** and **5**, respectively (Figures S11 and S12). This indicates that an additional contribution by the Ru^{II} center leads to a compensation and, thus, to the less pronounced hypsochromic shift.

Direct excitation of **1** and **2** at 500 nm leads to the occurrence of a ruthenium-based emission (Figure 5, panel C) similar to the ruthenium model complexes **3**. The emission of **1** is generally shifted hypsochromically (on average, $\lambda_{max,em}$ = 686 nm) versus **3**, while the trend on the emission energy upon tpy functionalization is the same. It is also worth noting that the fluoro substitution (**2**) on the ppy moiety leads to a hypsochromic shift (on average, $\lambda_{max,em}$ = 677 nm) versus **1** (Figure S10), confirming the effect of the peripheral substitution of the iridium(III) fragment (R_2) on the Ru-tpy-based emission.

A rough estimate based on the extinction coefficients at 365 and 380 nm of the model and dinuclear complexes shows that there is significant absorption of the ruthenium model complexes present over the whole range of iridium-based absorption (Table 2). Hence, selective excitation of the Ir^{III} center is not possible for these complexes. Therefore, considering the emission spectra alone, it is not possible to conclude about the presence of intramolecular energy transfer between the Ir^{III} and Ru^{II} centers. However, the fact that the iridium-based absorption bands contribute to the ruthenium-based emission can serve as an indication for the presence of energy transfer. To investigate this matter, the origin of the ruthenium-based emission was analyzed by the corresponding excitation spectra and compared to the respective absorption profiles. The excitation spectra match very well in the visible region of the absorption spectra (exemplarily shown for **1a** in Figure 5, panel D, and Figures S17–S21). More importantly, the excitation spectra of the dinuclear complexes below 400 nm also fit to the absorption profiles and clearly show the additive contribution of the iridium fragment to the ruthenium-based emission. This finding is corroborated in a similar analysis for the ruthenium model complexes **3**, which show significantly

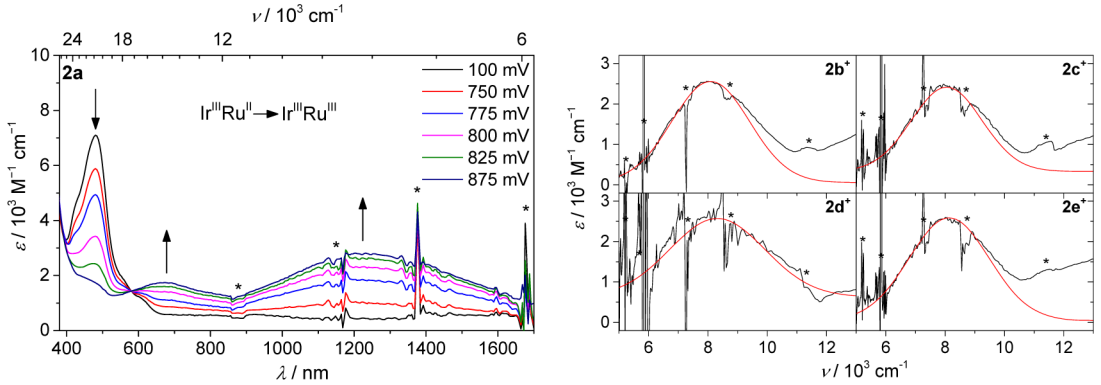

Figure 6. Left: Vis–NIR SEC spectra of **2a**, during the first ruthenium-based oxidation. Right: NIR absorptions showing the IVCT transitions (black curve) and Gaussian fittings (red curve) of **2b**–**2e**$^+$. Solvent and spectrometer artifacts are marked with asterisks. All spectra are recorded in a 0.1 M Bu_4NPF_6 solution of acetonitrile.

DOI: 10.1021/acs.inorgchem.5b02919
Inorg. Chem. 2016, 55, 5152–5167

less intensity in the UV region (exemplarily shown for **3a** in Figure 5, panel D, and Figures S17–S21).

SEC and IVCT Analysis. The dinuclear complexes **1a** and **2a** (Figure S22) were analyzed by UV–vis–NIR SEC in acetonitrile (for **2b**–**2e**, see Figures S23–S25). For this purpose, stepwise oxidations were performed, and the related spectral changes were recorded. The first iridium-based oxidation process of **1a** shows a hypsochromic shift of the MLCT band (Figure S22, left). The oxidation product is tentatively denoted as $Ir^{IV}Ru^{II}$ species. However, it should be noted that the irreversible process destroys or changes the chemical structure of the complex. This could also be the reason for the absent absorption in the NIR region, typically observed for an electronically coupled system in the MV state (vide infra). The second, ruthenium-based oxidation (formally labeled as $[Ir^{IV}Ru^{III}]$) leads to a depletion of the MLCT band, associated with a weak absorption at around 700 nm, assigned to LMCT transitions of the ruthenium(III) species.[26] Surprisingly, the re-reduction (labeled as $[Ir^{III}Ru^{II}]_{rered}$) of the double-oxidized species reproduces qualitatively the initial spectrum with only minor spectral changes. As discussed before, the reaction order for **2a** is inversed, rendering the first oxidation process reversible, with a formal $Ir^{III}Ru^{III}$ character of the formed $\mathbf{2a}^+$ species. As a result, the long-wavelength MLCT band is fully depleted and associated with a weak absorption at around 700 nm (Figure 6, left) assigned to the LMCT transition because it is also present in double-oxidized species ($Ir^{IV}Ru^{III}$; Figure S22, right). Surprisingly, subsequent computational studies suggest an IVCT character (vide infra). Furthermore, a very broad band in the NIR region with a flat maximum at 1220 nm (E_{IT} = 8200 cm^{-1}) arises. This band is ascribed to a $Ru^{III} \leftarrow Ir^{III}$ IVCT transition because it is absent in the initial ($Ir^{III}Ru^{II}$) and the double-oxidized species ($Ir^{IV}Ru^{III}$), as well as in the fully re-reduced species ($[Ir^{III}Ru^{II}]_{rered}$) (Figure S22, right). The re-reduction, furthermore, shows qualitatively the reappearance of the MLCT transition, which is hypsochromically shifted and less intense, with respect to the initial state, caused by the irreversibility of the iridium oxidation. Compounds $\mathbf{2b}^+$–$\mathbf{2e}^+$ exhibit IVCT transition energies similar to those observed for $\mathbf{2a}^+$ (Figure 6, right, and Table 3). Additionally, an IVCT absorption band for $\mathbf{2d}^+$ in dichloromethane is not observed (Figure S23, right), which could be ascribed to a less intense IVCT absorption in nonpolar solvents, as seen in other compounds.[13a] The generalized Mulliken–Hush expression was applied to calculate the electronic coupling matrix element (H_{ab}), where ε_{IT} is the extinction coefficient, $\Delta\tilde{\nu}_{1/2}$ is the bandwidth, and r_{ab} is the metal-to-metal distance (Table 3).[27] The distance between the metal centers is provided by the density functional theory (DFT)-optimized structure (vide infra) and was calculated as r_{ab} = 5.3 Å. Similar metal-to-metal distances were found by X-ray crystal structure analysis in related cyanide-bridged complexes.[13a,15c] Consequently, H_{ab} values of approximately 1000 cm^{-1} for $\mathbf{2a}^+$–$\mathbf{2e}^+$ were obtained. Additionally, the interaction parameter α^2, which gives an estimate for the degree of electronic coupling between the metal ions, was calculated (Table 3). The average value for α^2 is 1.5% in the series of $\mathbf{2a}^+$–$\mathbf{2e}^+$. These values and the solvent dependency are typical for weakly coupled Robin–Day class II systems.[28] For related cyanide-bridged bimetallic ruthenium(II) complexes with the simplified formula *trans*-$[(NC)Ru(R\text{-}py)_4(\mu\text{-}CN)Ru(py)_4Cl]PF_6$ (py = pyridine),[13b] similar E_{IT} values but higher values for H_{ab} and α^2 are reported (Table 3).

Time-Resolved Spectroscopy. The quenching of the iridium-based emission in the dinuclear complexes is apparent from the steady-state emission data presented above. Along with a reduced emission quantum yield, quenching, in general, is governed by a decrease of the donor emission lifetime. As a consequence, the respective measurements were carried out in aerated acetonitrile for the selected dinuclear complexes **1d**, **1e**, **2d**, and **2e** and their respective monometallic model compounds, i.e., **3d**, **3e**, **4**, and **5** (Table 2). The lifetime of the iridium-based emission is reduced in the dinuclear complexes compared to the respective model complexes: For the nonfluorinated complexes **1d** and **1e** versus **4**, lifetimes of 39 versus 90 ns were determined, respectively, and for the fluorinated complexes **2d** and **2e** versus **5**, lifetimes of 60 and 33 versus 183 ns were obtained, respectively. Similar lifetimes of 93 and 163 ns for **4** and **5**, respectively, were obtained in aerated dichloromethane and differ from previously reported lifetimes.[22b] In contrast, the lifetime of the residual iridium-based emission in **2e** becomes 10 times longer (347 ns) when the solvent is changed from acetonitrile to dichloromethane. It should be noted that the apparent solvent dependence and the lifetime differences in the dinuclear complexes compared to the model complexes contradict an assignment of the residual iridium-based emission to impurities of **4** or **5**. The fact that emission from energetically significantly higher-lying iridium-based states (^{3}MLLCT/^{3}LC) is strong enough to be measured is remarkable but is a known feature for a number of related iridium(III) complexes.[29]

Thermal deactivation of the iridium-based ^{3}LC state is energetically favorable in light of the lower-lying ruthenium-based MLCT states, but time-resolved emission spectroscopy with ca. 120 ps time resolution enables no clear indication of emission quenching via this pathway (Figures S26 and S27). This motivated us to look closer into the early events occurring after photoexcitation using transient absorption (TA) spectroscopy. Unfortunately, no isolated excitation of an iridium-based transition is possible because of the omnipresent overlap with various π–π^* transitions of the ruthenium(II) fragment. Therefore, all TA experiments were carried out using 200 fs pump pulses centered at 355 nm. Selected TA spectra of isoabsorbing solutions with optical densities of ca. 0.6 for **1d**, **1e**, **2d**, and **2e** and ca. 0.3 for **3d** and **3e** at the excitation wavelengths are shown in Figure 7.

Table 3. IVCT Transition Energy and Electronic Coupling Parameter for Oxidized Complexes $\mathbf{2a}^+$–$\mathbf{2e}^+$ in Acetonitrile

compound	E_{IT}/ cm^{-1}	ε_{IT}/ M^{-1} cm^{-1}	$\Delta\tilde{\nu}_{1/2}$/ cm^{-1}	H_{ab}/ cm^{-1}	α^2
$\mathbf{2a}^+$	8200	2300	3420	990[b]	0.014[c]
$\mathbf{2b}^+$	8100	2500	3180	990[b]	0.015[c]
$\mathbf{2c}^+$	8050	2400	2810	910[b]	0.013[c]
$\mathbf{2d}^+$	8320	2600	3780	1110[b]	0.018[c]
$\mathbf{2e}^+$	8140	2500	3180	990[b]	0.015[c]
trans-$[(NC)Ru(py)_4(\mu\text{-}CN)Ru(py)_4Cl]PF_6$[a]	8400	6000	3400	1700	0.039
trans-$[(NC)Ru(MeOpy)_4(\mu\text{-}CN)Ru(py)_4Cl]PF_6$[a]	7200	8500	3100	1800	0.066

[a]Taken from ref 13b. [b]Calculated as $H_{ab} = 0.0206\frac{(\Delta\tilde{\nu}_{1/2}\varepsilon_{IT}E_{IT})^{1/2}}{r_{ab}}$. [c]Calculated as $\alpha^2 = 0.00042\frac{\Delta\tilde{\nu}_{1/2}\varepsilon_{IT}}{E_{IT}r_{ab}^2}$.

DOI: 10.1021/acs.inorgchem.5b02919
Inorg. Chem. 2016, 55, 5152–5167

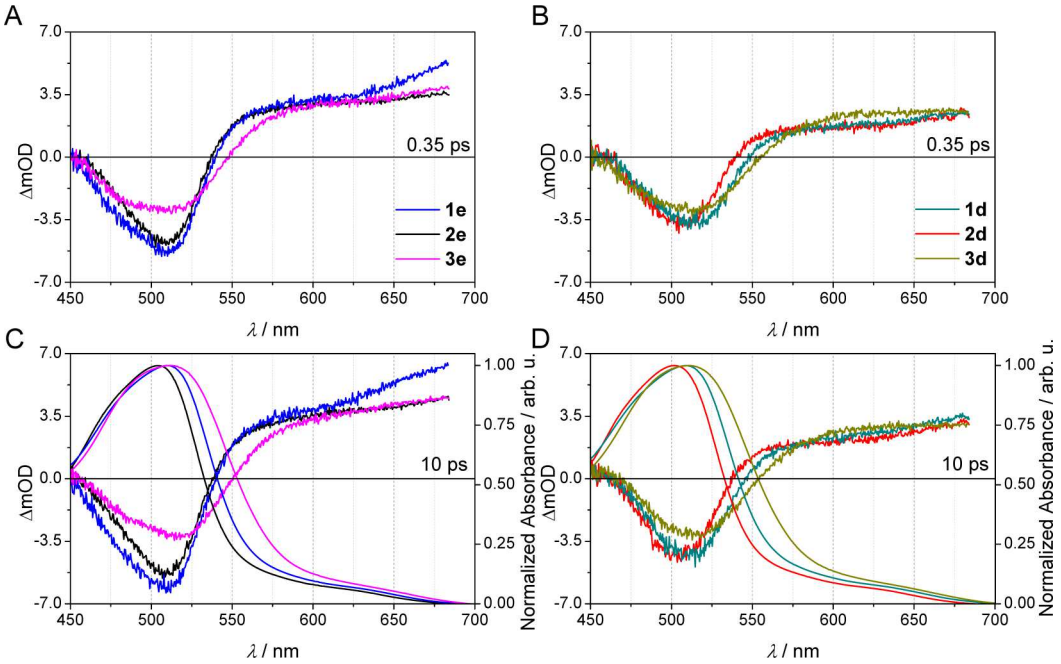

Figure 7. TA data (λ_{exc} = 355 nm) for selected molecular species measured in acetonitrile. Raw TA spectra at 0.35 ps (10 ps) delay time are plotted in panels A (C) and B (D). The data in panels A and C belong to **1e**, **2e**, and **3e**, while the data in panels B and D belong to **1d**, **2d**, and **3d**. The ground-state absorption spectra (normalized to the MLCT band maximum) of the respective compounds are shown in panels C and D for comparison (right scale).

Already at early delay times (0.35 ps; Figure 7, panels A and B), the TA spectra contain the typical characteristics of ruthenium-based ^{3}MLCT states regardless of the actual compound: Ground-state bleach below 535−550 nm and excited-state absorption (ESA) at longer wavelengths are observed. Those observations are consistent with the SEC data, which show that oxidation from Ru^{II} to Ru^{III} causes the MLCT band to vanish, which is typical for such types of transition-metal complexes.[30] Within the first 10 ps, i.e., a typical time scale for cooling and solvent relaxation, the spectra undergo only very minor changes. This indicates that no significant changes regarding the nature of the excited state or the molecular structure are occurring on this time scale. The positions of the respective minimum and the zero-crossing depend on the actual compound investigated and are consistent with the spectral positions of their individual ground-state absorption bands (Figure 7). The absolute signal intensities do not seem to be determined by the absorbance at the excitation wavelength for the respective samples only, i.e., specific molecular features for each compound may play a role. It should be emphasized that the very similar TA spectra, particularly for the compounds with smaller tpy ligands (**1d**−**3d**; Figure 7, panels B and D), reflect very similar excited states, considering that the differences, e.g., regarding the zero-crossing, correspond to the differences also found in the ground-state absorption. These observations suggest that the electronic structure of the ground state is more strongly influenced by the presence of the Ir center than it is the case for the excited state (at least the one probed in the TA measurements). The slightly different ESA signatures, e.g., the rise of the positive band above 630 nm observed for **2e** (Figure 7, panels A and C), which is not as pronounced in the nonfluorinated analogue or the model complex, may be attributed to a somewhat different extent of mixing between the ^{3}MLCT state and the orbitals of the extended ligand including the alkoxyphenyl unit, which is known to shift the ESA band toward 690 nm.[31]

When the observations from emission spectroscopy are related with the TA data, it is intriguing to note that while iridium-based ^{3}LC emission is observed, no iridium-specific signatures are observed in the TA data. On the one hand, the oscillator strength (based on their extinction coefficients; see Figure 4 and Table 2) of iridium-based ^{1}MLLCT transitions is much lower than that for the ruthenium-based ^{1}MLCT transitions. This trend might be the same in the excited state (also for triplet−triplet transitions), i.e., the iridium-based population will lead to lower TA signals compared to the ruthenium-based population. On the other hand, in emission spectroscopy, even small populations of iridium-based ^{3}LC states can be identified: Because of the absence of low-lying ^{3}MC states, emitters based on iridium typically possess significantly higher quantum yields than the ruthenium analogues, for which deactivation via ^{3}MC states provides an efficient decay channel from ^{3}MLCT states.[32] There are numerous examples for iridium(III) complexes described in the literature with quantum yields in the order of 90%.[19,33] The presented analysis suggests that there is a fast (within 0.35 ps), yet incomplete, deactivation of iridium-based states toward ruthenium-based ^{3}MLCT states in all compounds investigated here.

Computational Investigation. Selected representative model and dinuclear complexes (**1a**−**3a**, **1d**−**3d**, **1e**−**3e**, **4**, and **5**) were investigated by DFT and its time-dependent formalism (TD-DFT). In order to shorten the computational efforts, the flexible octyl chains (**1e**−**3e**) were replaced by methyl groups. For each complex, the geometry was first optimized for its singlet ground state (S_0), which served as the basis for the TD-DFT calculation as well as for a later optimization of the triplet (T_1) and formally oxidized (D^+) states. In all cases, the true minimum nature of the optimized

DOI: 10.1021/acs.inorgchem.5b02919
Inorg. Chem. 2016, 55, 5152−5167

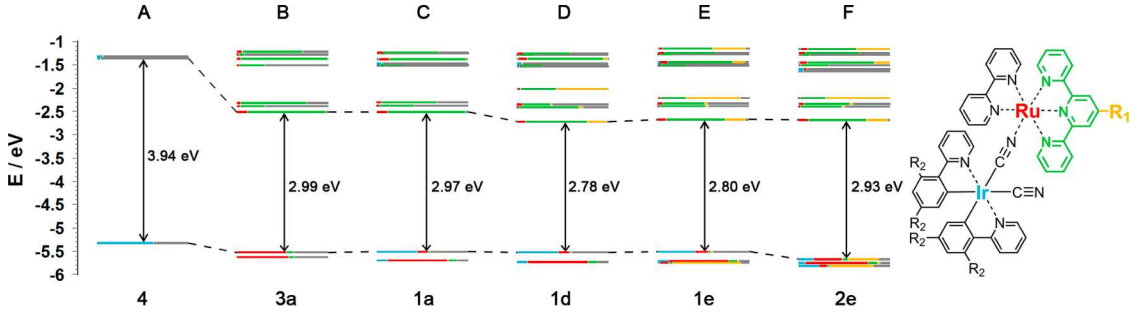

Figure 8. Energy diagram of the frontier MOs for selected complexes, including a color code for the spatial localization (legend: iridium, blue; ruthenium, red; tpy, green; tpy substituent, orange; rest of the compound, gray).

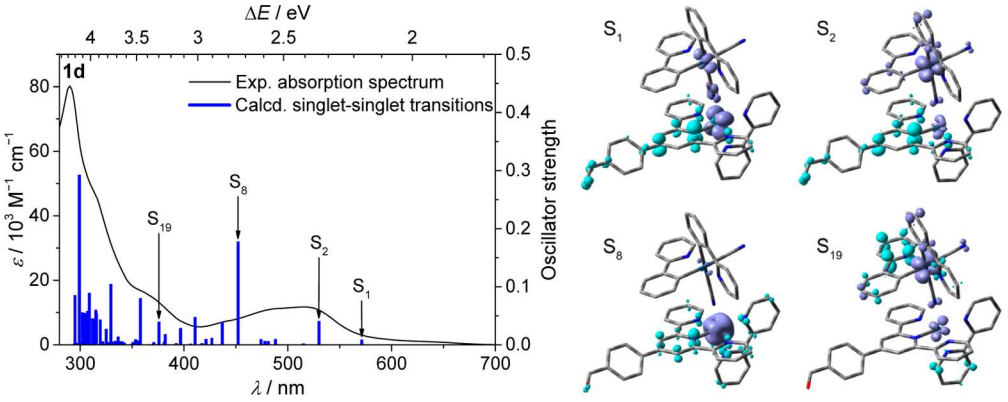

Figure 9. Experimental absorption spectra and calculated singlet−singlet transition energies with selected EDDM plots (plum-blue = depletion of electron density; cyan = accumulation of electron density; isovalue = 0.004) of **1d**. H atoms are omitted for clarity.

geometries was confirmed by vibrational analysis. The obtained ground-state geometries of the model complexes match the crystallographic data, i.e., the quasi-octahedral geometry of the Ir^{III} (**4**)[22b] and Ru^{II} (**3a**)[15c] centers. In the case of dinuclear complexes, the intervening cyanide bridge adapts a quasi-linear arrangement with a net Ru−Ir distance of approximately 5.3 Å (Figure S29). Hence, the ligands of the Ir and Ru centers, namely, the ppy and tpy moieties, are nearly coplanar with a large spatial interannular separation (>5 Å) and inferior contribution of π stacking. In addition, the effect of rotation around the Ru−Ir axis is expected to lead to minor changes in the electronic structure, in analogy to a recent report for related Ru−C≡N−Ru complexes.[34]

The electronic structures of representative complexes were analyzed in terms of molecular orbitals (MOs). Figure 8 displays the energy diagram of the frontier MOs, complemented by a color code to describe the spatial localization of the respective MO. First, two selected iridium (**4**; Figure 8, panel A) and ruthenium (**3a**; Figure 8, panel B) model complexes were analyzed. They represent the dominating contribution of the metal centers to the highest occupied molecular orbitals (HOMOs), while the lowest occupied molecular orbitals (LUMOs) are LC. The HOMO energies suggest that **4** (−5.3 eV) is more easily oxidized than **3a** (−5.5 eV), while the LUMO energies differ significantly between **4** (−1.4 eV) and **3a** (−2.5 eV), caused by the electron-rich ppy ligands versus electron-poor bpy and tpy units. In the case of **3a**, the LUMO is primarily localized on the tpy fragment. The results of **4** agree very well with reported data,[22b] while no computational data are available for complex **3a**. The corresponding dinuclear complex **1a** (Figure 8, panel C) reveals the generally preserved properties of its constituents, i.e., the HOMO is dominated by the Ir^{III} center, and the LUMO is tpy-localized. The lower HOMO energy of **1a** versus **4** is attributed to the electron-withdrawing effect of the ruthenium(II) fragment mediated by the cyanide bridge, while the LUMO stays tpy-localized and its energy level is not affected. These assignments are corroborated by the electrochemical data, i.e., the observed anodic shift of the oxidation and the maintained reduction potential. Next, the effect of delocalization by the tpy substituent is explored for representative complexes **1a** (R_1 = H; Figure 8, panel C), **1d** (R_1 = Ph−CHO; Figure 8, panel D), and **1e** (R_1 = pep-CHO; Figure 8, panel E). In all three cases, the HOMOs remain Ir^{III}-centered at the same energy, while the LUMO of the aryl-decorated complexes (**1d** and **1e**) exhibit an additional contribution of R_1, which further leads to a stabilization by approximately 150 meV. Finally, the influence of fluorination is exemplified for **1e** (Figure 8, panel E) versus **2e** (Figure 8, panel F). In line with the previous assignments, the character and energy levels of the LUMOs are retained, while the fluoro groups stabilize the ppy-based orbitals and lead to lower energies of the Ir^{III} d orbitals. As a consequence, the HOMOs are now dominated by Ru^{II} d orbitals, in excellent agreement with the assignments derived from the electrochemical data. The corresponding optical gap can be easily estimated from the color-coded HOMOs and LUMOs, i.e., a proper localization upon taking interacting fragments into account. For example, the optical gap of complex **1e** (panel E) is governed by LUMO and HOMO−1 because the donating Ir^{III}-localized HOMO has a very small spatial overlap with the tpy-localized LUMO. A consistent behavior was found for the remaining studied complexes (see the Supporting Information), which supports the generalized conclusions.

DOI: 10.1021/acs.inorgchem.5b02919
Inorg. Chem. 2016, 55, 5152−5167

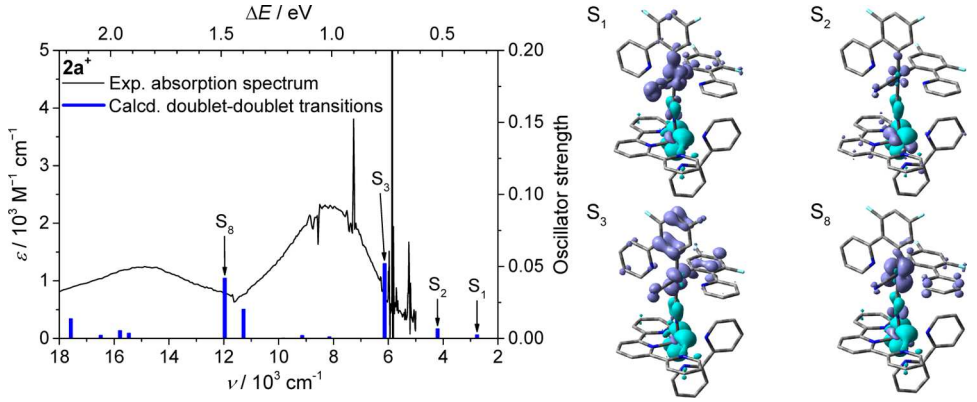

Figure 10. Experimental absorption spectra and calculated doublet−doublet transition energies with selected EDDM plots (plum-blue = depletion of electron density; cyan = accumulation of electron density; isovalue = 0.002) of $\mathbf{2a}^+$. H atoms are omitted for clarity.

TD-DFT calculations were performed to detail the absorption properties of selected complexes (Figures S30−S40). The calculated singlet−singlet transitions (S_n) fit qualitatively very well with the experimental absorption spectrum, as exemplified for the dinuclear complex **1d** (Figure 9). Characteristic electronic transitions are visualized by their electron density difference maps (EDDMs), which share similarities with natural transition orbitals but compact all contributing MO pairs into a single plot of redistributed electron density. The longest-wavelength transition (S_1) reveals the depletion of the electron density at the Ru−N≡C−Ir fragment and the increase of the electron density at the tpy fragment and the aldehyde group. The donating fragment is dominated by a Ru^{II} d orbital, which is coupled through aligned p orbitals of the cyanide bridge with the corresponding Ir^{III} d orbital. The low oscillator strength of S_1 is reflected by the improper alignment (symmetry) of the accepting fragment, i.e., the central pyridine's N p orbital. Consequently, the S_2 transition is more intense because of the proper orbital symmetry between Ru^{II} d and N p orbitals and is best described as MLCT with tpy(π^*) ← Ru(d) character, with admixed Ir d and cyanide p donor contributions. All further transitions >400 nm are of similar MLCT character. The calculated transition S_8 consists of more than one contributing Ru^{II} d orbital and an extended delocalization across the bpy and tpy fragments, which can explain the high oscillator strength and energetic stabilization (red shift vs experimental data) due to the known deficiencies of the B3LYP functional to describe delocalized and/or charge-transfer states.[35] The S_{19} transition of **1d** is the first transition with a sizable ppy(π^*) ← Ir(d) contribution, in excellent agreement with the model complex (Figures S30 and S31) and the experimental absorption data. The remaining complexes exhibit qualitatively similar transitions in the visible region and show the effect of delocalization by the tpy substituent (R_1), i.e., a similar absorption profile for **1e** (R_1 = pep-CHO) but a hypsochromic shift for **1a** (R_1 = H). In addition, a blue-shifted absorption upon fluorination of the ppy-Ir fragment (**1d** vs **2d**) was found. The excellent agreement with the experimental data demonstrates that TD-DFT calculations satisfyingly reproduce the experimental absorption spectra, thus assisting the future design of complexes with enhanced charge transfer:[35] For example, the darkness of S_1 can be traced to the improper orbital symmetry of the Ru^{II} d and N p orbitals, whose spatial orientation is dictated by the interaction with cyanide−Ir^{III} orbitals and the extended π system of R_1, respectively. Hence, this symmetry constraint would be overcome if the R_1 substituent was placed onto a peripheral pyridine instead (cf. S_1 in Figure 9). In order to further test the influence of selected functionals qualitatively, the two popular functionals PBE0[36] and MPWB1K from the Minnesota suite of functionals[37] were chosen for TD-DFT calculations on **2d**. When the B3LYP-optimized nuclear geometry is employed, the calculated set of vertical transitions for PBE0 and MPWB1K agrees well with the B3LYP-derived transitions. In the case of MPWB1K, a sizable blue shift of the entire spectrum was noticed, as was also reported for range-separated functionals. The EDDM plots (see Figure S36) confirm the similar nature of the corresponding transitions among the tested functionals. As stated above, the EDDM representation simplifies an elaborate analysis based on MOs and thereby assists the qualitative comparison between different computational methods. In summary, no profound difference between the functionals was found with regard to the MLCT nature of the low-energy transitions.

The triplet- and single-oxidized doublet states of selected complexes were optimized to exemplify the emission and electrochemical properties (Figures S41−S44). In all studied cases, the spin-density plots of the triplet state reveal the localization on the ruthenium(II) and tpy fragments without a significant iridium(III) contribution and corroborate the previous assignment as the emissive ^{3}MLCT excited state. In contrast, the single-oxidized states exhibit distinct differences upon fluorination, i.e., the nonfluorinated complexes are best described by a diphenyliridium-based oxidation, while the fluorinated congeners reveal the dominant spin localization on the ruthenium fragment (Figures S41−S43). In both cases, the corresponding d orbitals are aligned to promote coupling over the cyanide bridge. The vertical doublet−doublet transitions were calculated for $\mathbf{2a}^+$, $\mathbf{2d}^+$, and $\mathbf{2e}^+$ on the basis of TD-DFT calculations employing the B3LYP functional. Pieslinger et al. recently analyzed a series of Ru−C≡N−Ru MV complexes using the same functional,[13f] and our results qualitatively follow the drawn conclusions. In the following analysis, compound $\mathbf{2a}^+$ was chosen for reasons similar to those in Pieslinger's work. Figure 10 displays the calculated transitions with characteristic EDDM plots for visualization. The transition energies are shifted to lower wavenumbers by approximately 2000 cm^{-1} with correct oscillator strengths. The nature of most of the low-energy transitions (<12000 cm^{-1}) is best described as IVCT transitions. In all cases, admixing of interconfigurational (IC) contributions is observed, which is particularly expressed for S_2. The LMCT transitions are hypsochromically shifted with

DOI: 10.1021/acs.inorgchem.5b02919
Inorg. Chem. 2016, 55, 5152−5167

respect to the Ru−C≡N−Ru MV complexes,[13f] which is tentatively attributed to the higher electron deficiency of our iridium(III) fragment. It is worth noting that complexes $\mathbf{2d}^+$ and $\mathbf{2e}^+$ bearing π-conjugated substituents also exhibit IVCT character of the low-energy transitions (Figure S45). However, the large deviation of the calculated transition energies and corresponding oscillator strengths with respect to the experimentally observed values indicate the weakness of the employed computational methodology as discussed before for the ground-state transitions. A further assessment of the functionals is beyond the scope of this work. More importantly, the assignment of the low-energy transitions consistently reveals the IVCT nature with some admixing of IC contributions.

CONCLUSION

The reported dinuclear complexes, a combination of cyanide-bridged $(ppy)_2Ir^{III}$ and $(bpy)(tpy)Ru^{II}$ building blocks, were readily synthesized and subsequently analyzed regarding their photophysical and electrochemical properties. The series, featuring different substituents, reveals a strong influence upon fluorination of the ppy unit, while functionalization on the tpy fragment resulted only in minor changes. A different spectral behavior is observed for complexes **1a−1e** and **2a−2e** in their MV form upon first oxidation. The fluorinated $\mathbf{2a}^+$−$\mathbf{2e}^+$ exhibit broad $Ru^{III} \leftarrow Ir^{III}$ IVCT bands in the NIR region that indicate slight electronic interaction between the two metal centers (weakly coupled class II system). For the non-fluorinated analogues **1a−1e**, the first irreversible iridium oxidation changes or destroys the complex structures and could explain the absence of an IVCT band. However, an efficiently quenched iridium emission and an observable ruthenium emission are present for all heterodinuclear complexes. DFT and TD-DFT calculations support that the short cyanide bridge mediates electronic contribution from the Ir center to the Ru moiety. Time-resolved spectroscopy indicates that a fast energy transfer (<350 fs after photoexcitation) from the excited states of iridium toward lower-lying ruthenium ^{3}MLCT states takes place. For future works, the reported heterometallic complexes are considered as effective donor (i.e., the Ir center) and acceptor (i.e., the Ru center) systems that can be further extended over the bromine or aldehyde functionality by either chromophores or other acceptor units to generate assemblies that offer directional, cascade-like energy transfer.

EXPERIMENTAL SECTION

Materials and Instrumentation. Compounds **4**[22b] and **5**,[22b] the ligands tpy-Ph-Me,[38] tpy-Ph-Br,[38] tpy-Ph-CHO,[39] and tpy-pep-CHO,[39] and the ruthenium(III) precursor complexes $Ru(tpy\text{-}R_1)Cl_3$[40] were prepared according to analogous literature procedures. All other chemicals were purchased from commercial suppliers and used as received. All reactions were monitored by thin-layer chromatography (silica gel on aluminum sheets with fluorescent dye F254, Merck KGaA). Microwave-assisted reactions were carried out using a Biotage Initiator Microwave synthesizer. NMR spectra were recorded on a Bruker AVANCE (250, 300, 400, or 600 MHz) instrument in deuterated solvents (Euriso-Top) at 25 °C. ^{1}H and ^{13}C NMR resonances were assigned using appropriate 2D correlation spectra. Chemical shifts are reported in ppm using the solvent as the internal standard. ^{19}F NMR spectra were referenced to −73.3 ppm for the resonance of the hexafluorophosphate anion. High-resolution electrospray ionization time-of-flight mass spectrometry (ESI-TOF HRMS) was performed on a Bruker Daltonics ESI-(Q)-TOF MS microTOF II mass spectrometer. UV−vis absorption spectra were recorded on a PerkinElmer Lambda 750 UV−vis−NIR spectrophotometer and emission spectra on a Jasco FP6500 instrument. Measurements were carried out using 10^{-5}−10^{-6} M solutions of the respective solvents (spectroscopy grade) in 1 cm quartz cuvettes at room temperature. CV measurements were performed on a Metrohm Autolab PGSTAT30 potentiostat with a standard three-electrode configuration using a glassy-carbon-disk working electrode, a platinum-rod auxiliary electrode, and a AgCl/Ag reference electrode; a scan rate of 0.2 V/s was applied. The experiments were carried out in deaerated CH_3CN or CH_2Cl_2 (spectroscopy grade) containing 0.1 M Bu_4NPF_6 salt. At the end of each measurement, ferrocene was added as an internal standard. Spectroelectrochemical experiments were carried out in a quartz cuvette (1 mm optical path length) containing 0.1 M Bu_4NPF_6 in a CH_3CN or CH_2Cl_2 solution, a platinum-grid working electrode, a platinum-wire auxiliary electrode, and a $AgNO_3$/Ag/CH_3CN reference electrode. The potential was controlled using a Metrohm Autolab PGSTAT30 potentiostat. The redox process was monitored by UV−vis−NIR spectroscopy using a PerkinElmer Lambda 750 UV−vis−NIR spectrophotometer and considered complete when there was no further spectral change.

Time-Resolved Spectroscopy. Spectrally resolved emission decay curves were determined employing a Hamamatsu HPDTA streak camera. Emission is excited by pulses centered at 355−370 nm created by frequency-doubling the output of a Ti:sapphire laser (Tsunami, Newport Spectra-Physics GmbH). The repetition rate of the fundamental is reduced to 400 kHz by a pulse selector (model 3980, Newport Spectra-Physics GmbH). Emission is collected from a 1 cm cuvette in a 90° angle and spectrally dispersed on the detector using a CHROMEX spectrograph. Measurements with and without a polarizer (set to magic angle) in the detection path were performed, but no contributions from rotational diffusion were observed on the time scales probed.

The time-resolved TA measurements were performed on a setup described earlier.[41] The setup is based on an amplified Ti:sapphire oscillator (800 nm, 1 kHz; Libra, Coherent Inc.). The pump beam (355 nm) is created in a noncollinear optical−parametric amplifier (TOPASwhite, Lightconverison Ltd.) and overlapped on the sample position with the white-light probe (created in a sapphire plate) in a close-to-collinear geometry. The mutual polarization of the linearly polarized beam was set to magic angle using a Berek compensator in the pump path. The pulse duration of the pump pulses at the sample position was determined as 200 fs via difference-frequency generation at the sample position. The pulse energy of the pump pulses was ca. 150 nJ, and the optical density of the sample at the pump wavelength was 0.6 in a 1 mm cuvette.

Computational Methods. The theoretical calculations are based on DFT or TD-DFT. All calculations were performed with the *Gaussian09* program package (version A.02).[42] The hybrid functional B3LYP[43] was selected in combination with the 6-31G* basis set for all atoms except Ru and Ir, which were described by an effective core potential and the associated orbitals (mwb). For all calculations, the solvent environment was modeled for acetonitrile using the implemented polarization continuum model.[44] The geometries of the singlet ground state (S_0) were optimized and serve as the starting point for the optimization of the corresponding triplet states (T_1) and singly oxidized doublet states (D^+). In cases of difficult self-consistent-field convergence, additional quadratic (qc) or extra quadratic (xqc) functions were used. The true nature of all minima structures was confirmed by vibrational analysis, showing no imaginary frequencies. TD-DFT calculations were performed on the same level of theory. *Chemissian3.3* was used for Mulliken population analysis and visualization of the MO composition. The EDDMs were obtained by *GaussSum2.2*.[45] The graphical visualizations were generated by *GaussView5.0.8*,[46] i.e., the isovalues were drawn at 0.002 or 0.004 (EDDM), 0.04 (Kohn−Sham MOs), or 0.004 (spin-density calculations).

Synthesis. *General Procedure for the Synthesis of Monochloro-Containing (bpy)(tpy)Ru^{II} Complexes* ***6****; [Ru(bpy)(tpy-R$_1$)Cl]Cl/PF$_6$.*[20a] $Ru(tpy\text{-}R_1)Cl_3$ and 2,2′-bipyridine were combined with LiCl and *N*-ethylmorpholine (3 drops) in a methanol/water mixture (5:1

DOI: 10.1021/acs.inorgchem.5b02919
Inorg. Chem. 2016, 55, 5152−5167

ratio). The mixture was then heated at reflux for 3 h. The solvent was removed and the residue redissolved in dichloromethane and washed with water. Subsequently, the solvent was dried over Na_2SO_4 and removed. The remaining solid was washed with diethyl ether and dried in vacuo. The complexes were isolated as chloride or hexafluorophosphate salt. When applicable, deviations from this general protocol are given below.

*[Ru(bpy)(tpy)Cl]PF_6 (**6a**).* According to the general procedure, Ru(tpy-R_1)Cl_3 (R_1 = H; 309.2 mg, 0.7 mmol), 2,2′-bipyridine (109.3 mg, 0.7 mmol), and LiCl (297 mg, 7 mmol) were reacted in 24 mL of methanol/water. Further purification by column chromatography (silica, 40:4:1 acetonitrile/water/saturated aqueous KNO_3 solution), followed by precipitation in an aqueous NH_4PF_6 solution, was carried out. A dark-purple solid was obtained (107 mg, 0.159 mmol, 23%).

^{1}H NMR (250 MHz, CD_3OD): δ 10.20 (dd, ^4J = 0.9 Hz, ^3J = 5.7 Hz, 1H, H^{E6}), 8.76 (d, ^3J = 8.3 Hz, 1H, H^{E3}), 8.65 (d, ^3J = 8.1 Hz, 2H, H^{H3}), 8.53 (d, ^3J = 8.1 Hz, 2H, H^{G3}), 8.48 (d, ^3J = 8.4 Hz, 1H, H^{F3}), 8.31 (td, ^4J = 1.4 Hz, ^3J = 7.8 Hz, 1H, H^{E4}), 8.16 (t, ^3J = 8.1 Hz, 1H, H^{H4}), 8.05−7.88 (m, 3H, H^{E5}, H^{G4}), 7.79−7.66 (m, 3H, H^{F4}, H^{G6}), 7.40−7.28 (m, 3H, H^{F6}, H^{G5}), 7.04 (ddd, ^4J = 1.2 Hz, ^3J = 5.9 Hz, ^3J = 7.2 Hz, 1H, H^{F5}).

*[Ru(bpy)(tpy-Ph-Me)Cl]Cl (**6b**).* According to the general procedure, Ru(tpy-R_1)Cl_3 (R_1 = Ph-Me; 100 mg, 0.188 mmol), 2,2′-bipyridine (29.4 mg, 0.188 mmol), and LiCl (80 mg, 1.88 mmol) were reacted in 12 mL of methanol/water to obtain a dark-purple solid (65 mg, 0.100 mmol, 53%).

^{1}H NMR (400 MHz, CD_3OD): δ 10.27 (dd, ^4J = 1.5 Hz, ^3J = 5.8 Hz, 1H, H^{E6}), 8.83 (s, 2H, H^{H3}), 8.78 (dt, ^4J = 1.0 Hz, ^3J = 8.3 Hz, 1H, H^{E3}), 8.60 (d, ^3J = 8.1 Hz, 2H, H^{G3}), 8.48 (d, ^3J = 8.1 Hz, 1H, H^{F3}), 8.33 (td, ^4J = 1.6 Hz, ^3J = 7.9 Hz, 1H, H^{E4}), 8.08−7.98 (m, 3H, H^{E5}, H^{J2}), 7.85 (td, ^4J = 1.5 Hz, ^3J = 7.9 Hz, 2H, H^{G4}), 7.75−7.66 (m, 3H, H^{F4}, H^{G6}), 7.41 (d, ^3J = 8.0 Hz, 2H, H^{J3}), 7.37 (dd, ^4J = 1.2 Hz, ^3J = 5.8 Hz, 1H, H^{F6}), 7.30 (ddd, ^4J = 1.2 Hz, ^3J = 5.5 Hz, ^3J = 7.3 Hz, 2H, H^{G5}), 7.02 (ddd, ^4J = 1.4 Hz, ^3J = 5.8 Hz, ^3J = 7.4 Hz, 1H, H^{F5}), 2.49 (s, 3H, CH_3). ^{13}C{^{1}H} NMR (63 MHz, CD_3OD): δ 160.4, 160.3, 159.4, 157.8, 153.7, 153.3, 152.9, 148.2, 141.7, 138.2, 137.9, 136.8, 135.0, 131.2, 128.8, 128.4, 128.0, 127.5, 125.4, 124.8, 124.6, 121.4, 21.4.

*[Ru(bpy)(tpy-Ph-Br)Cl]PF_6 (**6c**).* The synthesis was performed according to a literature procedure.[20b]

In a two-necked flask, 2,2′-bipyridine (44.6 mg, 0.285 mmol) was added to a solution of LiCl (66.5 mg, 1.570 mmol) dissolved in ethanol (18 mL) and water (6 mL) and deaerated with nitrogen for 15 min. Triethylamine (0.1 mL) and Ru(tpy-R_1)Cl_3 (R_1 = Ph-Br; 170 mg, 0.285 mmol) was added to the solution, and the mixture was heated to reflux for 4 h. After cooling to room temperature, the solution was evaporated and the remaining solid purified by column chromatography (silica, 40:4:1 acetonitrile/water/saturated aqueous KNO_3 solution). The purple fraction was collected, and an excess of NH_4PF_6 was added; the mixture was concentrated in vacuo, and water was added. The fine precipitate was collected by filtration, washed with water, and rinsed with dichloromethane (around 200 mL) until the filtrate was only slightly purple. The solvent was evaporated and the residue dried in vacuo to obtain a dark-purple solid (134 mg, 0.162 mmol, 57% yield).

^{1}H NMR (300 MHz, CD_3CN): δ 10.24 (dd, ^4J = 1.6 Hz, ^3J = 5.7 Hz, 1H, H^{E6}), 8.70 (s, 2H, H^{H3}), 8.60 (dt, ^4J = 0.9 Hz, ^3J = 8.1 Hz, 1H, H^{E3}), 8.48 (dt, ^4J = 1.0 Hz, ^3J = 8.1 Hz, 2H, H^{G3}), 8.33−8.23 (m, 2H, H^{F3}, H^{E4}), 8.05−7.95 (m, 3H, H^{J2}, H^{E5}), 7.90−7.77 (m, 4H, H^{G4}, H^{J3}), 7.72−7.62 (m, 3H, H^{G6}, H^{F4}), 7.35−7.22 (m, 3H, H^{F6}, H^{G5}), 6.93 (ddd, ^4J = 1.3 Hz, ^3J = 5.8 Hz, ^3J = 7.3 Hz, 1H, H^{F5}).

*[Ru(bpy)(tpy-Ph-CHO)Cl]Cl (**6d**).* According to the general procedure, Ru(tpy-R_1)Cl_3 (R_1 = Ph-CHO; 100 mg, 0.184 mmol), 2,2′-bipyridine (28.7 mg, 0.184 mmol), and LiCl (78 mg, 1.84 mmol) were reacted in 12 mL of methanol/water to obtain a dark-purple solid as an acetal/aldehyde mixture (108 mg, 0.149 mmol, 81%). ^{1}H NMR signals of the acetal are given.

^{1}H NMR (300 MHz, CD_3OD): δ 10.23 (d, ^3J = 5.7 Hz, 1H, H^{E6}), 8.95 (s, 2H, H^{H3}), 8.78 (d, ^3J = 8.2 Hz, 1H, H^{E3}), 8.69 (d, ^3J = 7.9 Hz, 2H, H^{G3}), 8.50 (d, ^3J = 7.7 Hz, 1H, H^{F3}), 8.35−8.28 (m, 1H, H^{E4}), 8.18 (d, ^3J = 8.0 Hz, 2H, H^{J2}), 8.07−7.99 (m, 1H, H^{E5}), 7.98−7.88 (m, 2H, H^{G4}), 7.80−7.67 (m, 5H, H^{F4}, H^{J3}, H^{G6}), 7.45 (d, ^3J = 5.8 Hz, 1H, H^{F6}), 7.40−7.29 (m, 2H, H^{G5}), 7.04 (t, ^3J = 6.6 Hz, 1H, H^{F5}), 5.49 (s, 1H, $CH(OCH_3)_2$), 3.42 (s, 6H, $CH(OCH_3)_2$).

*[Ru(bpy)(tpy-pep-CHO)Cl]Cl (**6e**).* According to the general procedure, Ru(tpy-R_1)Cl_3 (R_1 = pep-CHO; 125 mg, 0.139 mmol), 2,2′-bipyridine (21.7 mg, 0.139 mmol), and LiCl (59 mg, 1.39 mmol) were reacted in 19 mL of methanol/water to obtain a dark-purple solid as an acetal/aldehyde mixture (130 mg, 0.122 mmol, 88%). ^{1}H NMR signals of the acetal are given.

^{1}H NMR (300 MHz, CD_3OD): δ 10.23 (d, ^3J = 5.6 Hz, 1H, H^{E6}), 8.99 (s, 2H, H^{H3}), 8.79 (d, ^3J = 8.2 Hz, 1H, H^{E3}), 8.70 (d, ^3J = 8.0 Hz, 2H, H^{G3}), 8.50 (d, ^3J = 8.2 Hz, 1H, H^{F3}), 8.33 (t, ^3J = 7.9 Hz, 1H, H^{E4}), 8.24 (d, ^3J = 8.2 Hz, 2H, H^{J2}), 8.02 (t, ^3J = 6.7 Hz, 1H, H^{E5}), 7.93 (t, ^3J = 7.8 Hz, 2H, H^{G4}), 7.81−7.73 (m, 3H, H^{J3}, H^{F4}), 7.71 (d, ^3J = 5.4 Hz, 2H, H^{G6}), 7.44 (d, ^3J = 5.7 Hz, 1H, H^{F6}), 7.34 (t, ^3J = 6.6 Hz, 2H, H^{G5}), 7.15 (s, 1H, H^{K2}), 7.13 (s, 1H, H^{K5}), 7.05 (t, ^3J = 6.6 Hz, 1H, H^{F5}), 5.62 (s, 1H, $CH(OCH_3)_2$), 4.09 (t, ^3J = 6.2 Hz, 2H, α-OCH_2), 4.03 (t, ^3J = 6.3 Hz, 2H, α-OCH_2), 3.41 (s, 6H, $CH(OCH_3)_2$), 1.94−1.75 (m, 4H, β-CH_2), 1.70−1.50 (m, 4H, γ-CH_2), 1.50−1.23 (m, 16H, δ-η-CH_2), 0.99−0.81 (m, 6H, CH_3).

*General Procedure for Thiocyanate-Containing (bpy)(tpy)Ru^{II} Complexes **3**; [Ru(bpy)(tpy-R_1)SCN]PF_6.* A microwave vial (5 mL) was charged with [Ru(bpy)(tpy-R_1)Cl]Cl/PF_6 (**6a**−**6e**; 0.028 mmol) and KSCN (26.8 mg, 0.28 mmol) in 2.2 mL of methanol/water (10:1). The vial was capped, and the mixture was deaerated with nitrogen for 15 min. The purple solution was heated under microwave irradiation for 30 min at 120 °C. Acetonitrile (5 mL) and NH_4PF_6 (225 mg, 1.378 mmol, 50 equiv) were added, and the solution was stirred for 5 min. Subsequently, water (50 mL) was added, and the formed precipitate was filtered, washed with water, and rinsed with acetonitrile. The solvent was removed and the residue redissolved in DMSO (3 mL) and heated for 3 h at 80 °C. After cooling to room temperature, NH_4PF_6 (excess) and water (50 mL) were added. The dark-red complex was collected by filtration.

*For the complexes containing an aldehyde group (**6d** and **6e**), an additional, final step was performed.* The complex was dissolved in DMSO (3 mL), and a 1 M HCl solution (1 mL) was added. The solution was stirred for 3 h at room temperature. Subsequently, NH_4PF_6 (excess) and water (50 mL) were added to the stirred solution, and the solid was collected by filtration.

*[Ru(bpy)(tpy)SCN]PF_6 (**3a**).* Yield: 39%. ^{1}H NMR (400 MHz, DMSO-d_6): δ 9.54 (dd, ^4J = 1.4 Hz, ^3J = 5.6 Hz, 1H, H^{E6}), 8.93 (dt, ^4J = 1.1 Hz, ^3J = 8.3 Hz, 1H, H^{E3}), 8.88 (d, ^3J = 8.1 Hz, 2H, H^{H3}), 8.74 (dt, ^4J = 1.1 Hz, ^3J = 8.0 Hz, 2H, H^{G3}), 8.66 (d, ^3J = 8.1 Hz, 1H, H^{F3}), 8.40 (td, ^4J = 1.6 Hz, ^3J = 7.9 Hz, 1H, H^{E4}), 8.34 (t, ^3J = 8.1 Hz, 1H, H^{H4}), 8.15 (ddd, ^4J = 1.3 Hz, ^3J = 5.6 Hz, ^3J = 7.4 Hz, 1H, H^{E5}), 8.07 (td, ^4J = 1.5 Hz, ^3J = 7.8 Hz, 2H, H^{G4}), 7.84 (td, ^4J = 1.5 Hz, ^3J = 7.8 Hz, 1H, H^{F4}), 7.69 (dd, ^4J = 1.4 Hz, ^3J = 5.6 Hz, 2H, H^{G6}), 7.43 (ddd, ^4J = 1.3 Hz, ^3J = 5.5 Hz, ^3J = 7.1 Hz, 2H, H^{G5}), 7.30 (dd, ^4J = 1.3 Hz, ^3J = 5.7 Hz, 1H, H^{F6}), 7.13 (ddd, ^4J = 1.3 Hz, ^3J = 5.7 Hz, ^3J = 7.3 Hz, 1H, H^{F5}). ^{13}C{^{1}H} NMR (100 MHz, DMSO-d_6): δ 158.0 (2C, C^{G2}), 157.6 (C^{F2}), 157.1 (2C, C^{H2}), 155.4 (C^{E2}), 152.2 (2C, C^{G6}), 151.4 (C^{E6}), 151.1 (C^{F6}), 137.9 (2C, C^{G4}), 137.2 (C^{E4}), 136.5 (C^{F4}), 135.3 (C^{H4}), 133.6 (SCN), 128.0 (2C, C^{G5}), 127.7 (C^{E5}), 126.7 (C^{F5}), 124.2 (2C, C^{G3}), 124.2 (C^{E3}), 123.6 (C^{F3}), 123.3 (2C, C^{H3}). HRMS (ESI-TOF). Calcd for $C_{26}H_{19}N_6RuS$ ([M − PF_6]$^+$): m/z 549.0429. Found: m/z 549.0435. IR (KBr): $\tilde{\nu}_{CN}$ 2104 cm^{-1}.

*[Ru(bpy)(tpy-Ph-Me)SCN]PF_6 (**3b**).* Yield: 87%. ^{1}H NMR (300 MHz, DMSO-d_6): δ 9.56 (dd, ^4J = 1.3 Hz, ^3J = 5.6 Hz, 1H, H^{E6}), 9.21 (s, 2H, H^{H3}), 8.98 (d, ^3J = 8.1 Hz, 2H, H^{G3}), 8.94 (d, ^3J = 8.8 Hz, 1H, H^{E3}), 8.66 (d, ^3J = 8.2 Hz, 1H, H^{F3}), 8.41 (t, ^3J = 7.8 Hz, 1H, H^{E4}), 8.27 (d, ^3J = 7.9 Hz, 2H, H^{J2}), 8.16 (t, ^3J = 6.7 Hz, 1H, H^{E5}), 8.09 (td, ^4J = 1.5 Hz, ^3J = 7.8 Hz, 2H, H^{G4}), 7.84 (t, ^3J = 7.7 Hz, 1H, H^{F4}), 7.69 (dd, ^4J = 1.4 Hz, ^3J = 5.6 Hz, 2H, H^{G6}), 7.52 (d, ^3J = 7.9 Hz, 2H, H^{J3}), 7.49−7.37 (m, 3H, H^{G5}, H^{F6}), 7.13 (t, ^3J = 6.6 Hz, 1H, H^{F5}), 2.48 (s, 3H, CH_3). ^{13}C{^{1}H} NMR (63 MHz, DMSO-d_6): δ 158.2 (2C, C^{G2}), 157.7 (C^{F2}), 157.2 (2C, C^{H2}), 155.4 (C^{E2}), 152.2 (2C, C^{G6}), 151.4 (C^{E6}), 151.2 (C^{F6}), 146.5 (C^{J4}), 140.2 (C^{J1}), 137.8 (2C, C^{G4}), 137.1 (C^{E4}), 136.4 (C^{H4}), 133.8 (SCN), 133.2 (C^{F4}), 129.9 (2C, C^{J3}), 127.9

DOI: 10.1021/acs.inorgchem.5b02919
Inorg. Chem. 2016, 55, 5152−5167

(2C, C^{G5}), 127.7 (C^{E5}), 127.6 (2C, C^{J2}), 126.7 (C^{F5}), 124.5 (2C, C^{G3}), 124.18 (C^{E3}), 123.6 (C^{F3}), 120.2 (2C, C^{H3}), 21.0 (CH_3). HRMS (ESI-TOF). Calcd for $C_{33}H_{25}N_6RuS$ ($[M - PF_6]^+$): m/z 639.0896. Found: m/z 639.0905. IR (KBr): $\tilde{\nu}_{CN}$ 2098 cm^{-1}.

[Ru(bpy)(tpy-Ph-Br)SCN]PF$_6$ ***(3c)***. Yield: 51%. ^{1}H NMR (400 MHz, DMSO-d_6): δ 9.56 (dd, ^4J = 1.5 Hz, ^3J = 5.7 Hz, 1H, H^{E6}), 9.24 (s, 2H, H^{H3}), 8.97 (dt, ^4J = 1.0 Hz, ^3J = 8.3 Hz, 2H, H^{G3}), 8.94 (dt, ^4J = 1.0 Hz, ^3J = 8.4 Hz, 1H, H^{E3}), 8.66 (dt, ^4J = 1.1 Hz, ^3J = 8.3 Hz, 1H, H^{F3}), 8.41 (td, ^4J = 1.5 Hz, ^3J = 7.9 Hz, 1H, H^{E4}), 8.32 (d, ^3J = 8.7 Hz, 2H, H^{J2}), 8.16 (ddd, ^4J = 1.3 Hz, ^3J = 5.6 Hz, ^3J = 7.3 Hz, 1H, H^{E5}), 8.11 (td, ^4J = 1.6 Hz, ^3J = 7.9 Hz, 2H, H^{G4}), 7.93 (d, ^3J = 8.6 Hz, 2H, H^{J3}), 7.84 (td, ^4J = 1.5 Hz, ^3J = 7.9 Hz, 1H, H^{F4}), 7.70 (dd, ^4J = 1.4 Hz, ^3J = 5.5 Hz, 2H, H^{G6}), 7.45 (ddd, ^4J = 1.3 Hz, ^3J = 5.5 Hz, ^3J = 7.2 Hz, 2H, H^{G5}), 7.39 (dd, ^4J = 1.4 Hz, ^3J = 5.7 Hz, 1H, H^{F6}), 7.12 (ddd, ^4J = 1.3 Hz, ^3J = 5.7 Hz, ^3J = 7.2 Hz, 1H, H^{F5}). $^{13}C\{^1H\}$ NMR (100 MHz, DMSO-d_6): δ 158.1 (2C, C^{G2}), 157.6 (C^{F2}), 157.4 (2C, C^{H2}), 155.4 (C^{E2}), 152.2 (2C, C^{G6}), 151.4 (C^{E6}), 151.2 (C^{F6}), 145.2 (C^{J1}), 137.9 (2C, C^{G4}), 137.2 (C^{E4}), 136.5 (C^{H4}), 135.4 (C^{J4}), 133.8 (SCN), 132.2 (2C, C^{J3}), 129.8 (2C, C^{J2}), 128.1 (2C, C^{G5}), 127.7 (C^{E5}), 126.7 (C^{F5}), 124.6 (2C, C^{G3}), 124.2 (C^{E3}), 124.0 (C^{J4}), 123.6 (C^{F3}), 120.5 (2C, C^{H3}). HRMS (ESI-TOF). Calcd for $C_{32}H_{22}BrN_6RuS$ ($[M - PF_6]^+$): m/z 702.9826. Found: m/z 702.9853. IR (KBr): $\tilde{\nu}_{CN}$ 2098 cm^{-1}.

[Ru(bpy)(tpy-Ph-CHO)SCN]PF$_6$ ***(3d)***. Yield: 77%. ^{1}H NMR (400 MHz, DMSO-d_6): δ 10.19 (s, 1H, CHO), 9.57 (dd, ^4J = 1.4 Hz, ^3J = 5.7 Hz, 1H, H^{E6}), 9.30 (s, 2H, H^{H3}), 8.99 (d, ^3J = 8.1 Hz, 2H, H^{G3}), 8.95 (d, ^3J = 8.2 Hz, 1H, H^{E3}), 8.67 (d, ^3J = 8.2 Hz, 1H, H^{F3}), 8.57 (d, ^3J = 8.1 Hz, 2H, H^{J2}), 8.42 (td, ^4J = 1.6 Hz, ^3J = 7.9 Hz, 1H, H^{E4}), 8.23 (d, ^3J = 8.3 Hz, 2H, H^{J3}), 8.17 (ddd, ^4J = 1.3 Hz, ^3J = 5.6 Hz, ^3J = 7.3 Hz, 1H, H^{E5}), 8.11 (td, ^4J = 1.5 Hz, ^3J = 7.8 Hz, 2H, H^{G4}), 7.85 (td, ^4J = 1.5 Hz, ^3J = 7.9 Hz, 1H, H^{F4}), 7.72 (dd, ^4J = 1.4 Hz, ^3J = 5.5 Hz, 2H, H^{G6}), 7.47 (ddd, ^4J = 1.3 Hz, ^3J = 5.5 Hz, ^3J = 7.2 Hz, 2H, H^{G5}), 7.40 (dd, ^4J = 1.3 Hz, ^3J = 5.8 Hz, 1H, H^{F6}), 7.13 (ddd, ^4J = 1.3 Hz, ^3J = 5.7 Hz, ^3J = 7.3 Hz, 1H, H^{F5}). $^{13}C\{^1H\}$ NMR (100 MHz, DMSO-d_6): δ 192.9 (CHO), 158.1 (2C, C^{G2}), 157.6 (C^{F2}), 157.6 (2C, C^{H2}), 155.4 (C^{E2}), 152.3 (2C, C^{G6}), 151.4 (C^{E6}), 151.2 (C^{F6}), 144.9 (C^{J4}), 141.7 (C^{J1}), 137.9 (2C, C^{G4}), 137.4 (C^{E4}), 136.9 (C^{H4}), 136.6 (C^{F4}), 133.9 (SCN), 130.3 (2C, C^{J3}), 128.5 (2C, C^{J2}), 128.2 (2C, C^{G5}), 127.8 (C^{E5}), 126.8 (C^{F5}), 124.6 (2C, C^{G3}), 124.3 (C^{E3}), 123.7 (C^{F3}), 121.0 (2C, C^{H3}). HRMS (ESI-TOF). Calcd for $C_{33}H_{23}N_6ORuS$ ($[M - PF_6]^+$): m/z 653.0674. Found: m/z 653.0697. IR (KBr): $\tilde{\nu}_{CN}$ 2102 cm^{-1}.

[Ru(bpy)(tpy-pep-CHO)SCN]PF$_6$ ***(3e)***. Yield: 68%. ^{1}H NMR (400 MHz, DMSO-d_6): δ 10.36 (s, 1H, CHO), 9.57 (d, ^3J = 5.3 Hz, 1H, H^{E6}), 9.27 (s, 2H, H^{H3}), 8.99 (d, ^3J = 8.0 Hz, 2H, H^{G3}), 8.94 (d, ^3J = 8.2 Hz, 1H, H^{E3}), 8.67 (d, ^3J = 8.3 Hz, 1H, H^{F3}), 8.47 (d, ^3J = 8.5 Hz, 2H, H^{J2}), 8.41 (td, ^4J = 1.5 Hz, ^3J = 7.9 Hz, 1H, H^{E4}), 8.16 (ddd, ^4J = 1.2 Hz, ^3J = 5.7 Hz, ^3J = 7.4 Hz, 1H, H^{E5}), 8.11 (td, ^4J = 1.5 Hz, ^3J = 7.8 Hz, 2H, H^{G4}), 7.88−7.81 (m, 3H, H^{J3}), 7.71 (dd, ^4J = 1.5 Hz, ^3J = 5.6 Hz, 2H, H^{G6}), 7.46 (ddd, ^4J = 1.3 Hz, ^3J = 5.6 Hz, ^3J = 7.4 Hz, 2H, H^{G5}), 7.44 (s, 1H, H^{K2}), 7.39 (dd, ^4J = 1.3 Hz, ^3J = 5.7 Hz, 1H, H^{F6}), 7.28 (s, 1H, H^{K5}), 7.13 (ddd, ^4J = 1.3 Hz, ^3J = 5.7 Hz, ^3J = 7.3 Hz, 1H, H^{F5}), 4.15 (t, ^3J = 6.4 Hz, 2H, α-OCH_2), 4.10 (t, ^3J = 6.2 Hz, 2H, α-OCH_2), 1.87−1.72 (m, 4H, β-CH_2), 1.54 (quint, ^3J = 7.1 Hz, 2H, γ-CH_2), 1.49−1.16 (m, 18H, γ-η-CH_2), 0.86 (t, ^3J = 6.7 Hz, 3H, CH_3), 0.81 (t, ^3J = 6.8 Hz, 3H, CH_3). ^{13}C-$\{^1H\}$ NMR (100 MHz, DMSO-d_6): δ 188.4 (CHO), 158.2 (2C, C^{G2}), 157.7 (C^{F2}), 157.5 (2C, C^{H2}), 155.4 (C^{E2}), 155.1 (C^{K6}), 153.3 (C^{K3}), 152.2 (2C, C^{G6}), 151.4 (C^{E6}), 151.1 (C^{F6}), 145.1 (C^{H4}), 137.9 (2C, C^{G4}), 137.3 (C^{E4}), 136.6 (C^{J1}), 136.5 (C^{F4}), 133.9 (SCN), 132.1 (2C, C^{J3}), 128.1 (4C, C^{J2}, C^{G5}), 127.7 (C^{E5}), 126.7 (C^{F5}), 124.8 (C^{K4}), 124.6 (2C, C^{G3}), 124.2 (C^{E3}), 123.8 (C^{J4}), 123.7 (C^{F3}), 120.5 (2C, C^{H3}), 119.2 (C^{K1}), 118.2 (C^{K2}), 109.8 (C^{K5}), 96.4 (C^{alkyne}), 87.9 (C^{alkyne}), 69.2 (α-OCH_2), 68.8 (α-OCH_2), 31.29 (β-CH_2), 31.26 (β-CH_2), 28.82 (γ-CH_2), 28.73 (2C, γ-CH_2, δ-CH_2), 28.70 (δ-CH_2), 28.65 (ε-CH_2), 28.59 (ε-CH_2), 25.6 (ζ-CH_2), 25.5 (ζ-CH_2), 22.16 (η-CH_2), 22.15 (η-CH_2), 14.01 (CH_3), 14.00 (CH_3). HRMS (ESI-TOF). Calcd for $C_{57}H_{59}N_6O_3RuS$ ($[M - PF_6]^+$): m/z 1009.3363. Found: m/z 1009.3413. IR (KBr): $\tilde{\nu}_{CN}$ 2094 cm^{-1}.

General Procedure for Dinuclear Cyanide-Bridged Iridium(III)−Ruthenium(II) Complexes ***1*** *and* ***2****; [Ir((R$_2$)$_2$-ppy)$_2$(CN)(μ-CN)Ru(bpy)(R$_1$-tpy)]PF$_6$.* A microwave vial (5 mL) was charged with [Ru(bpy)(tpy-R_1)Cl]Cl/PF_6 (**6a−6e**; 0.039 mmol) and Bu_4N[Ir-((R$_2$)$_2$-ppy)$_2$(CN)$_2$] (**4** and **5**; 0.059 mmol) in 2.2 mL of methanol/water (10:1). The vial was capped, and the mixture was deaerated with nitrogen for 15 min. The purple solution was heated under microwave irradiation for 30 min at 120 °C. The solvent was evaporated, and the residue was purified by column chromatography (silica, 40:4:1 acetonitrile/water/saturated aqueous KNO_3 solution). The red fraction was collected, and an excess of NH_4PF_6 was added; the mixture was concentrated in vacuo, and water was added. The fine precipitate was collected by filtration and further purified by preparative size-exclusion chromatography (Bio-Beads S-X3 Beads, dichloromethane) to obtain a dark-red complex.

For the complexes containing an aldehyde group, an additional, final step was performed. The complex was dissolved in DMSO (3 mL), and a 1 M HCl solution (1 mL) was added. The solution was stirred for 3 h at room temperature. Subsequently, NH_4PF_6 (excess) and water (50 mL) were added to the stirred solution, and the solid was collected by filtration.

[Ir(ppy)$_2$(CN)(μ-CN)Ru(bpy)(tpy)]PF$_6$ ***(1a)***. Yield: 66%. ^{1}H NMR (400 MHz, DMSO-d_6): δ 9.23 (dd, ^4J = 1.2 Hz, ^3J = 5.9 Hz, 1H, H^{D6}), 9.08 (dd, ^4J = 1.1 Hz, ^3J = 5.7 Hz, 1H, H^{E6}), 8.81 (d, ^3J = 8.0 Hz, 1H, H^{E3}), 8.72 (t, ^3J = 7.8 Hz, 2H, H^{H5}, H^{H3}), 8.64−8.55 (m, 3H, H^{G3}, H^{I3}, H^{F3}), 8.33−8.25 (m, 2H, H^{B6}, H^{E4}), 8.22 (t, ^3J = 8.1 Hz, 1H, H^{H4}), 8.09−7.94 (m, 4H, H^{B3}, H^{D3}, H^{G4}, H^{I4}), 7.91 (td, ^4J = 1.6 Hz, ^3J = 7.9 Hz, ^3J = 8.3 Hz, 1H, H^{D4}), 7.85 (td, ^4J = 1.6 Hz, ^3J = 8.0 Hz, ^3J = 8.4 Hz, 1H, H^{B4}), 7.80 (td, ^4J = 1.5 Hz, ^3J = 7.8 Hz, 1H, H^{F4}), 7.74 (ddd, ^4J = 1.2 Hz, ^3J = 5.6 Hz, ^3J = 7.1 Hz, 1H, H^{E5}), 7.64 (dd, ^4J = 1.2 Hz, ^3J = 7.9 Hz, 1H, H^{A3}), 7.61 (dd, ^4J = 1.2 Hz, ^3J = 7.9 Hz, 1H, H^{C3}), 7.46 (dd, ^4J = 1.1 Hz, ^3J = 5.5 Hz, 1H, H^{G6}), 7.36−7.20 (m, 5H, H^{G5}, H^{I5}, H^{I6}, H^{F6}, H^{D5}), 7.09 (ddd, ^4J = 1.3 Hz, ^3J = 5.7 Hz, ^3J = 7.3 Hz, 1H, H^{F5}), 6.96 (ddd, ^4J = 1.5 Hz, ^3J = 5.8 Hz, ^3J = 7.3 Hz, 1H, H^{B5}), 6.78 (td, ^4J = 1.3 Hz, ^3J = 7.4 Hz, 1H, H^{A4}), 6.71 (td, ^4J = 1.3 Hz, ^3J = 7.5 Hz, 1H, H^{C4}), 6.63−6.55 (m, 2H, H^{A5}, H^{C5}), 5.96 (dd, ^4J = 1.2 Hz, ^3J = 7.6 Hz, 1H, H^{A6}), 5.65 (dd, ^4J = 1.2 Hz, ^3J = 7.4 Hz, 1H, H^{C6}). $^{13}C\{^1H\}$ NMR (150 MHz, DMSO-d_6): δ 167.7 (C^{B2}), 167.5 (C^{D2}), 161.24 (C^{C1}), 161.16 (C^{A1}), 157.7 (C^{G2}), 157.6 (C^{I2}), 157.3 (C^{F2}), 156.70 (C^{H2}), 156.67 (C^{H6}), 155.4 (C^{E2}), 153.0 (C^{D6}), 151.8 (C^{G6}), 151.6 (C^{I6}), 151.5 (C^{B6}), 150.93 (C^{E6}), 150.85 (C^{F6}), 144.1 (C^{C2}), 143.9 (C^{A2}), 142.9 (μ-CN), 137.7 (C^{G4}), 137.6 (C^{I4}), 136.9 (C^{D4}), 136.8 (C^{E4}), 136.6 (C^{B4}), 136.5 (C^{F4}), 135.2 (C^{H4}), 130.4 (C^{A6}), 130.2 (C^{C6}), 129.7 (CN), 129.0 (C^{C5}), 128.6 (C^{A5}), 127.89 (C^{G5}), 127.85 (C^{I5}), 127.0 (C^{E5}), 126.6 (C^{F5}), 124.08 (C^{G3}), 124.05 (C^{I3}), 123.92 (C^{E3}), 123.90 (C^{A3}), 123.86 (C^{C3}), 123.5 (C^{F3}), 123.1 (C^{H3}), 123.0 (C^{H5}), 122.9 (C^{D5}), 122.4 (C^{B5}), 120.7 (C^{A4}), 120.6 (C^{C4}), 119.4 (C^{B3}), 119.2 (C^{D3}). HRMS (ESI-TOF). Calcd for $C_{49}H_{35}IrN_9Ru$ ($[M - PF_6]^+$): m/z 1044.1640. Found: m/z 1044.1688. IR (KBr): $\tilde{\nu}_{CN}$ 2101, 2116 cm^{-1}.

[Ir(F$_2$-ppy)$_2$(CN)(μ-CN)Ru(bpy)(tpy)]PF$_6$ ***(2a)***. Yield: 35%. ^{1}H NMR (600 MHz, CD_3CN): δ 9.46 (ddd, ^5J = 0.8 Hz, ^4J = 1.5 Hz, ^3J = 5.5 Hz, 1H, H^{E6}), 9.32 (ddd, ^5J = 0.8 Hz, ^4J = 1.7 Hz, ^3J = 5.8 Hz, 1H, H^{D6}), 8.59 (ddd, ^5J = 0.8 Hz, ^4J = 1.7 Hz, ^3J = 5.8 Hz, 1H, H^{B6}), 8.55 (dt, ^4J = 1.1 Hz, ^3J = 8.2 Hz, 1H, H^{E3}), 8.32 (dd, ^5J = 0.8 Hz, ^3J = 8.1 Hz, 1H, H^{H3}), 8.30−8.26 (m, 2H, H^{H5}, H^{F3}), 8.25−8.21 (m, 2H, H^{E4}, H^{G3}), 8.18−8.14 (m, 2H, H^{B3}, H^{I3}), 8.11−8.05 (m, 2H, H^{D3}, H^{H4}), 7.94−7.80 (m, 5H, H^{D4}, H^{G4}, H^{B4}, H^{E5}, H^{I4}), 7.70 (ddd, ^4J = 1.5 Hz, ^3J = 7.5 Hz, ^3J = 8.2 Hz, 1H, H^{F4}), 7.56 (ddd, ^5J = 0.8 Hz, ^4J = 1.5 Hz, ^3J = 5.5 Hz, 1H, H^{G6}), 7.39 (ddd, ^5J = 0.7 Hz, ^4J = 1.6 Hz, ^3J = 5.5 Hz, 1H, H^{I6}), 7.27−7.22 (m, 2H, H^{G5}, H^{F6}), 7.19 (ddd, ^4J = 1.5 Hz, ^3J = 5.8 Hz, ^3J = 7.4 Hz, 1H, H^{D5}), 7.15 (ddd, ^4J = 1.3 Hz, ^3J = 5.5 Hz, ^3J = 7.5 Hz, 1H, H^{I5}), 7.01 (ddd, ^4J = 1.5 Hz, ^3J = 5.8 Hz, ^3J = 7.4 Hz, 1H, H^{B5}), 6.96 (ddd, ^4J = 1.3 Hz, ^3J = 5.8 Hz, ^3J = 7.3 Hz, 1H, H^{F5}), 6.42 (ddd, ^4J = 2.4 Hz, $^3J_{HF}$ = 9.3 Hz, $^3J_{HF}$ = 12.9 Hz, 1H, H^{C4}), 6.37 (ddd, ^4J = 2.4 Hz, $^3J_{HF}$ = 9.3 Hz, $^3J_{HF}$ = 13.0 Hz, 1H, H^{A4}), 5.53 (dd, ^4J = 2.4 Hz, $^3J_{HF}$ = 8.4 Hz, 1H, H^{A6}), 5.13 (dd, ^4J = 2.4 Hz, $^3J_{HF}$ = 8.2 Hz, 1H, H^{C6}). $^{19}F\{^1H\}$ NMR (188 MHz, CD_3CN): δ −73.30 (d, $^1J_{FP}$ = 706.4 Hz, 6F), −110.43 (d, ^4J = 8.7 Hz, 1F), −111.05 (d, ^4J = 8.9 Hz, 1F), −111.34 (d, ^4J = 8.6 Hz, 1F), −111.93 (d, ^4J = 8.5 Hz, 1F). HRMS (ESI-TOF). Calcd for $C_{49}H_{31}F_4IrN_9Ru$ ($[M - PF_6]^+$): m/z 1116.1226. Found: m/z 1116.1311. IR (KBr): $\tilde{\nu}_{CN}$ 2112, 2121 cm^{-1}.

DOI: 10.1021/acs.inorgchem.5b02919
Inorg. Chem. 2016, 55, 5152−5167

*[Ir(ppy)$_2$(CN)(μ-CN)Ru(bpy)(tpy-Ph-Me)]PF$_6$ (**1b**).* Yield: 81%. ^{1}H NMR (600 MHz, DMSO-d_6): δ 9.24 (d, ^3J = 5.7 Hz, 1H, H^{D6}), 9.18 (d, ^3J = 5.4 Hz, 1H, H^{E6}), 9.04 (s, 1H, H^{H5}), 9.02 (s, 1H, H^{H3}), 8.86−8.79 (m, 3H, H^{G3}, H^{E3}, H^{I3}), 8.58 (d, ^3J = 8.5 Hz, 1H, H^{F3}), 8.37 (d, ^3J = 5.5 Hz, 1H, H^{B6}), 8.29 (td, ^4J = 1.4 Hz, ^3J = 8.1 Hz, 1H, H^{E4}), 8.24 (d, ^3J = 7.9 Hz, 2H, H^{J2}), 8.03−7.93 (m, 4H, H^{B3}, H^{G4}, H^{D3}, H^{I4}), 7.86−7.76 (m, 4H, H^{D4}, H^{B4}, H^{F4}, H^{E5}), 7.59 (d, ^3J = 7.7 Hz, 1H, H^{A3}), 7.55 (d, ^3J = 7.7 Hz, 1H, H^{C3}), 7.50 (d, ^3J = 8.0 Hz, 2H, H^{J3}), 7.48 (d, ^3J = 5.0 Hz, 1H, H^{G6}), 7.35−7.27 (m, 4H, H^{G5}, H^{F6}, H^{I6}, H^{I5}), 7.17 (td, ^4J = 1.5 Hz, ^3J = 5.8 Hz, ^3J = 7.4 Hz, 1H, H^{D5}), 7.10 (td, ^4J = 1.2 Hz, ^3J = 5.9 Hz, ^3J = 7.3 Hz, 1H, H^{F5}), 6.94 (td, ^4J = 1.4 Hz, ^3J = 5.7 Hz, ^3J = 7.3 Hz, 1H, H^{B5}), 6.72−6.66 (m, 2H, H^{A4}, H^{C4}), 6.57 (td, ^4J = 1.2 Hz, ^3J = 7.4 Hz, 1H, H^{A5}), 6.51 (td, ^4J = 1.2 Hz, ^3J = 7.3 Hz, 1H, H^{C5}), 5.93 (d, ^3J = 7.3 Hz, 1H, H^{A6}), 5.64 (d, ^3J = 7.3 Hz, 1H, H^{C6}), 2.49 (s, 3H, CH_3). ^{13}C{^{1}H} NMR (150 MHz, DMSO-d_6): δ 167.7 (C^{B2}), 167.5 (C^{D2}), 161.21 (C^{C1}), 161.17 (C^{A1}), 158.0 (C^{G2}), 157.9 (C^{I2}), 157.4 (C^{F2}), 156.91 (C^{H2}), 156.88 (C^{H6}), 155.5 (C^{E2}), 153.0 (C^{D6}), 151.8 (C^{G6}), 151.7 (C^{I6}), 151.5 (C^{B6}), 150.96 (C^{E6}), 150.95 (C^{F6}), 146.2 (C^{H4}), 144.1 (C^{C2}), 143.9 (C^{A2}), 143.0 (μ-CN), 140.2 (C^{J4}), 137.63 (C^{G4}), 137.56 (C^{I4}), 136.9 (C^{D4}), 136.8 (C^{E4}), 136.6 (C^{B4}), 136.5 (C^{F4}), 133.0 (C^{J1}), 130.4 (C^{A6}), 130.2 (C^{C6}), 129.9 (2C, C^{J3}), 129.8 (CN), 128.9 (C^{C5}), 128.6 (C^{A5}), 127.9 (C^{G5}), 127.8 (C^{I5}), 127.5 (2C, C^{J2}), 127.1 (C^{E5}), 126.6 (C^{F5}), 124.4 (C^{G3}), 124.3 (C^{I3}), 124.1 (C^{E3}), 123.9 (C^{A3}), 123.8 (C^{C3}), 123.5 (C^{F3}), 122.9 (C^{D5}), 122.4 (C^{B5}), 120.7 (C^{C4}), 120.6 (C^{A4}), 120.0 (C^{H3}), 119.8 (C^{H5}), 119.4 (C^{B3}), 119.1 (C^{D3}), 21.0 (CH_3). HRMS (ESI-TOF). Calcd for $C_{56}H_{41}IrN_9Ru$ ([M − PF_6]$^+$): m/z 1134.2171. Found: m/z 1134.2158. IR (KBr): $\tilde{\nu}_{CN}$ 2102 cm^{-1}.

*[Ir(F$_2$-ppy)$_2$(CN)(μ-CN)Ru(bpy)(tpy-Ph-Me)]PF$_6$ (**2b**).* Yield: 83%. ^{1}H NMR (600 MHz, CD_3CN): δ 9.62 (d, ^3J = 5.4 Hz, 1H, H^{E6}), 9.37 (d, ^3J = 5.5 Hz, 1H, H^{D6}), 8.66 (d, ^3J = 5.5 Hz, 1H, H^{B6}), 8.55 (d, ^3J = 8.2 Hz, 1H, H^{E3}), 8.52 (s, 1H, H^{H5}), 8.46 (s, 1H, H^{H3}), 8.36 (d, ^3J = 8.1 Hz, 1H, H^{G3}), 8.29−8.20 (m, 3H, H^{I3}, H^{F3}, H^{E4}), 8.07 (d, ^3J = 8.6 Hz, 1H, H^{B3}), 7.96−7.90 (m, 3H, H^{J2}, H^{D3}), 7.87 (t, ^3J = 6.5 Hz, 1H, H^{E5}), 7.83 (t, ^3J = 7.7 Hz, 1H, H^{G4}), 7.78−7.69 (m, 3H, H^{B4}, H^{D4}, H^{I4}), 7.67 (t, ^3J = 7.8 Hz, 1H, H^{F4}), 7.59 (d, ^3J = 5.5 Hz, 1H, H^{G6}), 7.45−7.41 (m, 3H, H^{J3}, H^{I6}), 7.24−7.19 (m, 2H, H^{G5}, H^{F6}), 7.13−7.06 (m, 2H, H^{I5}, H^{D5}), 6.99−6.92 (m, 2H, H^{B5}, H^{F5}), 6.29 (ddd, ^4J = 2.4 Hz, $^3J_{HF}$ = 9.2 Hz, $^3J_{HF}$ = 12.2 Hz, 1H, H^{A4}), 6.23 (ddd, ^4J = 2.4 Hz, $^3J_{HF}$ = 9.1 Hz, $^3J_{HF}$ = 12.1 Hz, 1H, H^{C4}), 5.47 (dd, ^4J = 2.4 Hz, $^3J_{HF}$ = 8.4 Hz, 1H, H^{A6}), 5.18 (dd, ^4J = 2.4 Hz, $^3J_{HF}$ = 8.2 Hz, 1H, H^{C6}), 2.49 (s, 3H, CH_3). ^{19}F{^{1}H} NMR (188 MHz, CD_3CN): δ −73.30 (d, $^1J_{FP}$ = 706.8 Hz, 6F), −110.25 (d, ^4J = 9.5 Hz, 1F), −110.94 (d, ^4J = 9.7 Hz, 1F), −111.34 (d, ^4J = 9.6 Hz, 1F), −111.80 (d, ^4J = 9.7 Hz, 1F). HRMS (ESI-TOF). Calcd for $C_{56}H_{37}F_4IrN_9Ru$ ([M − PF_6]$^+$): m/z 1206.1738. Found: m/z 1206.1781. IR (KBr): $\tilde{\nu}_{CN}$ 2111, 2124 cm^{-1}.

*[Ir(ppy)$_2$(CN)(μ-CN)Ru(bpy)(tpy-Ph-Br)]PF$_6$ (**1c**).* Yield: 64%. ^{1}H NMR (400 MHz, DMSO-d_6): δ 9.23 (d, ^3J = 4.9 Hz, 1H, H^{D6}), 9.19 (d, ^3J = 5.3 Hz, 1H, H^{E6}), 9.07 (s, 1H, H^{H5}), 9.05 (s, 1H, H^{H3}), 8.84 (d, ^3J = 7.6 Hz, 1H, H^{E3}), 8.82 (d, ^3J = 7.2 Hz, 2H, H^{G3}, H^{I3}), 8.59 (d, ^3J = 8.2 Hz, 1H, H^{F3}), 8.36 (d, ^3J = 4.9 Hz, 1H, H^{B6}), 8.34−8.24 (m, 3H, H^{E4}, H^{J2}), 8.01 (d, ^3J = 8.1 Hz, 2H, H^{G4}, H^{I4}), 7.97 (d, ^3J = 8.2 Hz, 2H, H^{D3}, H^{B3}), 7.89 (d, ^3J = 7.7 Hz, 2H, H^{J3}), 7.87−7.76 (m, 4H, H^{B4}, H^{D4}, H^{E5}, H^{F4}), 7.59 (d, ^3J = 7.8 Hz, 1H, H^{A3}), 7.56 (d, ^3J = 7.8 Hz, 1H, H^{C3}), 7.49 (d, ^3J = 5.0 Hz, 1H, H^{G6}), 7.39−7.26 (m, 4H, H^{G5}, H^{I5}, H^{I6}, H^{F6}), 7.17 (t, ^3J = 6.6 Hz, 1H, H^{D5}), 7.10 (t, ^3J = 7.1 Hz, 1H, H^{F5}), 6.95 (t, ^3J = 6.6 Hz, 1H, H^{B5}), 6.69 (t, ^3J = 7.4 Hz, 2H, H^{A4}, H^{C4}), 6.57 (t, ^3J = 7.4 Hz, 1H, H^{A5}), 6.52 (t, ^3J = 7.3 Hz, 1H, H^{C5}), 5.92 (d, ^3J = 7.5 Hz, 1H, H^{A6}), 5.64 (d, ^3J = 6.6 Hz, 1H, H^{C6}). ^{13}C{^{1}H} NMR (150 MHz, DMSO-d_6): δ 167.7 (C^{B2}), 167.4 (C^{D2}), 161.13 (C^{C1}), 161.06 (C^{A1}), 157.8 (C^{G2}), 157.7 (C^{I2}), 157.3 (C^{F2}), 157.1 (C^{H2}), 157.0 (C^{H6}), 155.4 (C^{E2}), 153.0 (C^{D6}), 151.8 (C^{G6}), 151.7 (C^{I6}), 151.4 (C^{B6}), 150.9 (2C, C^{E6}, C^{F6}), 144.7 (C^{H4}), 144.1 (C^{C2}), 143.9 (C^{A2}), 143.2 (μ-CN), 137.6 (C^{G4}), 137.6 (C^{I4}), 136.9 (C^{E4}), 136.8 (C^{D4}), 136.60 (C^{B4}), 136.55 (C^{F4}), 135.0 (C^{J1}), 132.2 (2C, C^{J3}), 130.3 (C^{A6}), 130.2 (C^{C6}), 129.7 (CN), 129.6 (2C, C^{J2}), 128.8 (C^{C5}), 128.6 (C^{A5}), 127.94 (C^{G5}), 127.90 (C^{I5}), 127.1 (C^{E5}), 126.6 (C^{F5}), 124.4 (C^{I3}), 124.3 (C^{G3}), 124.1 (C^{E3}), 123.93 (C^{J4}), 123.85 (C^{A3}), 123.8 (C^{C3}), 123.5 (C^{F3}), 122.9 (C^{D5}), 122.4 (C^{B5}), 120.7 (C^{C4}), 120.6 (C^{A4}), 120.1 (C^{H3}), 119.9 (C^{H5}), 119.4 (C^{B3}), 119.1 (C^{D3}). HRMS (ESI-TOF). Calcd for $C_{55}H_{38}BrIrN_9Ru$ ([M − PF_6]$^+$): m/z 1198.1125. Found: m/z 1198.1106. IR (KBr): $\tilde{\nu}_{CN}$ 2106, 2117 cm^{-1}.

*[Ir(F$_2$-ppy)$_2$(CN)(μ-CN)Ru(bpy)(tpy-Ph-Br)]PF$_6$ (**2c**).* Yield: 76%. ^{1}H NMR (600 MHz, CD_3CN): δ 9.61 (d, ^3J = 5.5 Hz, 1H, H^{E6}), 9.35 (d, ^3J = 5.6 Hz, 1H, H^{D6}), 8.65 (d, ^3J = 5.6 Hz, 1H, H^{B6}), 8.56 (d, ^3J = 8.2 Hz, 1H, H^{E3}), 8.54 (s, 1H, H^{H5}), 8.48 (s, 1H, H^{H3}), 8.37 (d, ^3J = 8.0 Hz, 1H, H^{G3}), 8.28 (d, ^3J = 8.2 Hz, 2H, H^{F3}, H^{I3}), 8.25 (t, ^3J = 7.9 Hz, 1H, H^{E4}), 8.05 (d, ^3J = 8.6 Hz, 1H, H^{B3}), 7.97 (d, ^3J = 8.3 Hz, 2H, H^{J2}), 7.94 (d, ^3J = 8.7 Hz, 1H, H^{D3}), 7.88 (t, ^3J = 6.6 Hz, 1H, H^{E5}), 7.85 (t, ^3J = 8.0 Hz, 1H, H^{G4}), 7.78 (d, ^3J = 8.2 Hz, 2H, H^{J3}), 7.75 (t, ^3J = 7.9 Hz, 3H, H^{I4}, H^{D4}, H^{B4}), 7.68 (t, ^3J = 7.5 Hz, 1H, H^{F4}), 7.60 (d, ^3J = 5.3 Hz, 1H, H^{G6}), 7.44 (d, ^3J = 5.4 Hz, 1H, H^{I6}), 7.23 (t, ^3J = 6.6 Hz, 1H, H^{G5}), 7.19 (d, ^3J = 5.7 Hz, 1H, H^{F6}), 7.14 (t, ^3J = 6.5 Hz, 1H, H^{I5}), 7.09 (t, ^3J = 6.6 Hz, 1H, H^{D5}), 6.98−6.92 (m, 2H, H^{B5}, H^{F5}), 6.32−6.19 (m, 2H, H^{A4}, H^{C4}), 5.46 (dd, ^4J = 2.4 Hz, $^3J_{HF}$ = 8.4 Hz, 1H, H^{A6}), 5.16 (dd, ^4J = 2.3 Hz, $^3J_{HF}$ = 8.2 Hz, 1H, H^{C6}). ^{19}F{^{1}H} NMR (188 MHz, CD_3CN): δ −73.30 (d, $^1J_{FP}$ = 706.8 Hz, 6F), −110.24 (d, ^4J = 9.5 Hz, 1F), −110.88 (d, ^4J = 9.7 Hz, 1F), −111.30 (d, ^4J = 9.6 Hz, 1F), −111.74 (d, ^4J = 9.7 Hz, 1F). HRMS (ESI-TOF). Calcd for $C_{55}H_{34}BrF_4IrN_9Ru$ ([M − PF_6]$^+$): m/z 1270.0686. Found: m/z 1270.0729. IR (KBr): $\tilde{\nu}_{CN}$ 2111 cm^{-1}.

*[Ir(ppy)$_2$(CN)(μ-CN)Ru(bpy)(tpy-Ph-CHO)]PF$_6$ (**1d**).* Yield: 82%. ^{1}H NMR (600 MHz, DMSO-d_6): δ 10.18 (s, 1H, CHO), 9.26 (d, ^3J = 5.2 Hz, 1H, H^{E6}), 9.24 (d, ^3J = 5.1 Hz, 1H, H^{D6}), 9.09 (s, 1H, H^{H5}), 9.07 (s, 1H, H^{H3}), 8.84 (d, ^3J = 8.4 Hz, 1H, H^{E3}), 8.81 (d, ^3J = 8.4 Hz, 1H, H^{G3}), 8.80 (d, ^3J = 8.6 Hz, 1H, H^{I3}), 8.59 (d, ^3J = 8.3 Hz, 1H, H^{F3}), 8.50 (d, ^3J = 8.0 Hz, 2H, H^{J2}), 8.39 (d, ^3J = 5.4 Hz, 1H, H^{B6}), 8.31 (dd, ^3J = 8.2 Hz, ^4J = 1.3 Hz, 1H, H^{E4}), 8.18 (d, ^3J = 8.1 Hz, 2H, H^{J3}), 8.03−7.90 (m, 4H, H^{B3}, H^{G4}, H^{D3}, H^{I4}), 7.86−7.77 (m, 4H, H^{D4}, H^{F4}, H^{B4}, H^{E5}), 7.58 (d, ^3J = 7.8 Hz, 1H, H^{A3}), 7.53 (d, ^3J = 7.7 Hz, 1H, H^{C3}), 7.51 (d, ^3J = 5.2 Hz, 1H, H^{G6}), 7.37−7.27 (m, 4H, H^{G5}, H^{F6}, H^{I5}, H^{I6}), 7.14 (t, ^3J = 6.4 Hz, 1H, H^{D5}), 7.10 (t, ^3J = 6.6 Hz, 1H, H^{F5}), 6.96 (t, ^3J = 6.6 Hz, 1H, H^{B5}), 6.70−6.63 (m, 2H, H^{A4}, H^{C4}), 6.56 (t, ^3J = 7.4 Hz, 1H, H^{A5}), 6.51 (t, ^3J = 7.2 Hz, 1H, H^{C5}), 5.91 (d, ^3J = 7.5 Hz, 1H, H^{A6}), 5.66 (d, ^3J = 7.3 Hz, 1H, H^{C6}). ^{13}C{^{1}H} NMR (150 MHz, DMSO-d_6): δ 192.8 (CHO), 167.7 (C^{B2}), 167.5 (C^{D2}), 161.1 (C^{C1}), 161.0 (C^{A1}), 157.8 (C^{G2}), 157.7 (C^{I2}), 157.3 (C^{F2}), 157.23 (C^{H2}), 157.20 (C^{H6}), 155.3 (C^{E2}), 153.0 (C^{D6}), 151.9 (C^{G6}), 151.7 (C^{I6}), 151.5 (C^{B6}), 151.0 (2C, C^{E6}, C^{F6}), 144.4 (C^{H4}), 144.1 (C^{C2}), 143.9 (C^{A2}), 143.3 (μ-CN), 141.3 (C^{J1}), 137.7 (C^{G4}), 137.6 (C^{I4}), 137.0 (C^{E4}), 136.9 (C^{D4}), 136.8 (C^{J4}), 136.7 (2C, C^{B4}, C^{F4}), 130.3 (C^{A6}), 130.24 (C^{C6}), 130.22 (2C, C^{J3}), 129.8 (CN), 128.9 (C^{C5}), 128.7 (C^{A5}), 128.3 (2C, C^{J2}), 128.03 (C^{G5}), 127.99 (C^{I5}), 127.2 (C^{E5}), 126.7 (C^{F5}), 124.5 (C^{I3}), 124.4 (C^{G3}), 124.1 (C^{E3}), 123.9 (C^{A3}), 123.8 (C^{C3}), 123.6 (C^{F3}), 122.9 (C^{D5}), 122.5 (C^{B5}), 120.8 (C^{C4}), 120.7 (C^{A4}), 120.6 (C^{H3}), 120.5 (C^{H5}), 119.5 (C^{B3}), 119.2 (C^{D3}). HRMS (ESI-TOF). Calcd for $C_{56}H_{39}IrN_9ORu$ ([M − PF_6]$^+$): m/z 1148.1917. Found: m/z 1148.1950. IR (KBr): $\tilde{\nu}_{CN}$ 2099, 2115 cm^{-1}.

*[Ir(F$_2$-ppy)$_2$(CN)(μ-CN)Ru(bpy)(tpy-Ph-CHO)]PF$_6$ (**2d**).* Yield: 69%. ^{1}H NMR (600 MHz, CD_3CN): δ 10.18 (s, 1H, CHO), 9.55 (d, ^3J = 5.3 Hz, 1H, H^{E6}), 9.34 (d, ^3J = 5.5 Hz, 1H, H^{D6}), 8.67−8.63 (m, 2H, H^{B6}, H^{H3}), 8.61 (s, 1H, H^{H5}), 8.57 (d, ^3J = 8.2 Hz, 1H, H^{E3}), 8.42 (d, ^3J = 8.0 Hz, 1H, H^{G3}), 8.35 (d, ^3J = 8.0 Hz, 1H, H^{I3}), 8.31−8.23 (m, 4H, H^{F3}, H^{J2}, H^{E4}), 8.18 (d, ^3J = 7.9 Hz, 2H, H^{J3}), 8.11 (d, ^3J = 8.4 Hz, 1H, H^{B3}), 7.98 (d, ^3J = 8.8 Hz, 1H, H^{D3}), 7.93−7.85 (m, 2H, H^{G4}, H^{E5}), 7.83 (t, ^3J = 7.7 Hz, 1H, H^{I4}), 7.79 (t, ^3J = 7.9 Hz, 2H, H^{B4}, H^{D4}), 7.70 (td, ^4J = 1.5 Hz, ^3J = 8.4 Hz, 1H, H^{F4}), 7.60 (d, ^3J = 4.9 Hz, 1H, H^{G6}), 7.44 (d, ^3J = 4.9 Hz, 1H, H^{I6}), 7.26 (t, ^3J = 6.4 Hz, 1H, H^{G5}), 7.23 (d, ^3J = 5.5 Hz, 1H, H^{F6}), 7.17 (t, ^3J = 6.5 Hz, 1H, H^{I5}), 7.13 (t, ^3J = 6.5 Hz, 1H, H^{D5}), 7.01−6.93 (m, 2H, H^{B5}, H^{F5}), 6.32 (ddd, ^4J = 2.3 Hz, $^3J_{HF}$ = 9.4 Hz, $^3J_{HF}$ = 12.2 Hz, 1H, H^{A4}), 6.28 (ddd, ^4J = 2.4 Hz, $^3J_{HF}$ = 9.2 Hz, $^3J_{HF}$ = 12.1 Hz, 1H, H^{C4}), 5.48 (dd, ^4J = 2.4 Hz, $^3J_{HF}$ = 8.4 Hz, 1H, H^{A6}), 5.16 (dd, ^4J = 2.4 Hz, $^3J_{HF}$ = 8.2 Hz, 1H, H^{C6}). ^{19}F{^{1}H} NMR (188 MHz, CD_3CN): δ −73.30 (d, $^1J_{FP}$ = 706.5 Hz, 6F), −110.24 (d, ^4J = 9.6 Hz, 1F), −110.96 (d, ^4J = 9.7 Hz, 1F), −111.28 (d, ^4J = 9.4 Hz, 1F), −111.83 (d, ^4J = 9.7 Hz, 1F). HRMS (ESI-TOF). Calcd for $C_{56}H_{35}F_4IrN_9ORu$ ([M − PF_6]$^+$): m/z 1220.1530. Found: m/z 1220.1574. IR (KBr): $\tilde{\nu}_{CN}$ 2108, 2125 cm^{-1}.

DOI: 10.1021/acs.inorgchem.5b02919
Inorg. Chem. 2016, 55, 5152−5167

*[Ir(ppy)$_2$(CN)(μ-CN)Ru(bpy)(tpy-pep-CHO)]PF$_6$ (**1e**).* Yield: 60%. ^{1}H NMR (600 MHz, DMSO-d_6): δ 10.37 (s, 1H, C*H*O), 9.24 (d, ^3J = 5.6 Hz, 1H, H^{D6}), 9.21 (d, ^3J = 5.9 Hz, 1H, H^{E6}), 9.13 (s, 1H, H^{H3}), 9.12 (s, 1H, H^{H5}), 8.92−8.80 (m, 3H, H^{G3}, H^{I3}, H^{E3}), 8.60 (d, ^3J = 8.2 Hz, 1H, H^{F3}), 8.47 (d, ^3J = 7.9 Hz, 2H, H^{J2}), 8.37 (d, ^3J = 5.4 Hz, 1H, H^{B6}), 8.30 (td, ^4J = 1.5 Hz, ^3J = 7.9 Hz, 1H, H^{E4}), 8.08−7.97 (m, 3H, H^{G4}, H^{I4}, H^{B3}), 7.96 (d, ^3J = 8.0 Hz, 1H, H^{D3}), 7.86 (d, ^3J = 7.9 Hz, 2H, H^{J3}), 7.84−7.78 (m, 4H, H^{D4}, H^{E5}, H^{B4}, H^{F4}), 7.58 (d, ^3J = 8.3 Hz, 1H, H^{A3}), 7.56 (d, ^3J = 7.9 Hz, 1H, H^{C3}), 7.51 (d, ^3J = 5.4 Hz, 1H, H^{G6}), 7.45 (s, 1H, H^{K2}), 7.37−7.30 (m, 4H, H^{G5}, H^{I5}, H^{I6}, H^{F6}), 7.30 (s, 1H, H^{K5}), 7.17 (t, ^3J = 6.5 Hz, 1H, H^{D5}), 7.10 (t, ^3J = 6.7 Hz, 1H, H^{F5}), 6.94 (ddd, ^4J = 1.4 Hz, ^3J = 5.6 Hz, ^3J = 7.2 Hz, 1H, H^{B5}), 6.72−6.65 (m, 2H, H^{C4}, H^{A4}), 6.57 (t, ^3J = 7.4 Hz, 1H, H^{A5}), 6.53 (t, ^3J = 7.2 Hz, 1H, H^{C5}), 5.94 (d, ^3J = 7.5 Hz, 1H, H^{A6}), 5.66 (d, ^3J = 7.3 Hz, 1H, H^{C6}), 4.16 (t, ^3J = 6.4 Hz, 2H, α-OCH_2), 4.11 (t, ^3J = 6.3 Hz, 2H, α-OCH_2), 1.87−1.74 (m, 4H, β-CH_2), 1.55 (quint, ^3J = 6.5 Hz, 2H, γ-CH_2), 1.46 (quint, ^3J = 7.6 Hz, 2H, γ-CH_2), 1.42−1.19 (m, 16H, δ-η-CH_2), 0.86 (t, ^3J = 6.8 Hz, 3H, CH_3), 0.80 (t, ^3J = 7.0 Hz, 3H, CH_3). ^{13}C{^{1}H} NMR (150 MHz, DMSO-d_6): δ 188.4 (CHO), 167.7 (C^{B2}), 167.4 (C^{D2}), 161.11 (C^{C1}), 161.10 (C^{A1}), 157.9 (C^{G2}), 157.8 (C^{I2}), 157.3 (C^{F2}), 157.10 (C^{H2}), 157.07 (C^{H6}), 155.3 (C^{E2}), 155.0 (C^{K3}), 153.2 (C^{K6}), 153.0 (C^{D6}), 151.8 (C^{G6}), 151.6 (C^{I6}), 151.5 (C^{B6}), 150.92 (C^{E6}), 150.89 (C^{F6}), 144.7 (C^{H4}), 144.0 (C^{C2}), 143.9 (C^{A2}), 143.0 (μ-CN), 137.7 (C^{G4}), 137.6 (C^{I4}), 136.9 (C^{E4}), 136.8 (C^{D4}), 136.5 (2C, C^{B4}, C^{F4}), 136.4 (C^{J1}), 132.1 (2C, C^{J3}), 130.3 (C^{A6}), 130.2 (C^{C6}), 129.6 (CN), 128.8 (C^{C5}), 128.6 (C^{A5}), 128.0 (3C, C^{J2}, C^{G5}), 127.9 (C^{I5}), 127.1 (C^{E5}), 126.6 (C^{F5}), 124.8 (C^{K4}), 124.5 (C^{I3}), 124.3 (C^{G3}), 124.1 (C^{E3}), 123.83 (C^{C3}), 123.77 (2C, C^{J4}, C^{A3}), 123.5 (C^{F3}), 122.8 (C^{D5}), 122.3 (C^{B5}), 120.7 (C^{C4}), 120.5 (C^{A4}), 120.2 (C^{H5}), 120.0 (C^{H3}), 119.4 (C^{B3}), 119.2 (C^{K1}), 119.1 (C^{D3}), 118.2 (C^{K2}), 109.8 (C^{K5}), 96.4 (C^{alkyne}), 87.8 (C^{alkyne}), 69.1 (α-OCH_2), 68.8 (α-OCH_2), 31.3 (β-CH_2), 31.2 (β-CH_2), 28.77 (γ-CH_2), 28.71 (γ-CH_2), 28.70 (δ-CH_2), 28.67 (δ-CH_2), 28.63 (ε-CH_2), 28.57 (ε-CH_2), 25.53 (ζ-CH_2), 25.49 (ζ-CH_2), 22.1 (2C, η-CH_2), 13.97 (CH_3), 13.96 (CH_3). HRMS (ESI-TOF). Calcd for $C_{80}H_{75}IrN_9O_3Ru$ ([M − PF_6]$^+$): *m*/*z* 1504.4621. Found: *m*/*z* 1504.4666. IR (KBr): $\tilde{\nu}_{CN}$ 2100, 2116 cm^{-1}.

*[Ir(F$_2$-ppy)$_2$(CN)(μ-CN)Ru(bpy)(tpy-pep-CHO)]PF$_6$ (**2e**).* Yield: 50%. ^{1}H NMR (600 MHz, CD_3CN): δ 10.43 (s, 1H, C*H*O), 9.63 (d, ^3J = 5.3 Hz, 1H, H^{E6}), 9.36 (d, ^3J = 5.5 Hz, 1H, H^{D6}), 8.65 (d, ^3J = 5.7 Hz, 1H, H^{B6}), 8.59 (s, 1H, H^{H3}), 8.56−8.51 (m, 2H, H^{E3}, H^{H5}), 8.41 (d, ^3J = 8.1 Hz, 1H, H^{G3}), 8.30 (d, ^3J = 8.1 Hz, 1H, H^{I3}), 8.27 (d, ^3J = 8.2 Hz, 1H, H^{F3}), 8.22 (td, ^4J = 1.4 Hz, ^3J = 7.9 Hz, 1H, H^{E4}), 8.14 (d, ^3J = 7.8 Hz, 2H, H^{J2}), 8.05 (d, ^3J = 8.5 Hz, 1H, H^{B3}), 7.94 (d, ^3J = 8.2 Hz, 1H, H^{D3}), 7.91−7.85 (m, 2H, H^{E5}, H^{G4}), 7.79 (d, ^3J = 8.1 Hz, 2H, H^{J3}), 7.78−7.70 (m, 3H, H^{I4}, H^{D4}, H^{B4}), 7.69 (td, ^4J = 1.2 Hz, ^3J = 7.7 Hz, 1H, H^{F4}), 7.62 (d, ^3J = 5.2 Hz, 1H, H^{G6}), 7.44 (d, ^3J = 5.2 Hz, 1H, H^{I6}), 7.33 (s, 1H, H^{K5}), 7.29−7.24 (m, 2H, H^{K2}, H^{G5}), 7.22 (d, ^3J = 5.6 Hz, 1H, H^{F6}), 7.15 (t, ^3J = 6.5 Hz, 1H, H^{I5}), 7.10 (t, ^3J = 6.5 Hz, 1H, H^{D5}), 6.99−6.91 (m, 2H, H^{F5}, H^{B5}), 6.29 (ddd, ^4J = 2.4 Hz, $^3J_{HF}$ = 9.3 Hz, $^3J_{HF}$ = 12.1 Hz, 1H, H^{A4}), 6.25 (ddd, ^4J = 2.4 Hz, $^3J_{HF}$ = 9.1 Hz, $^3J_{HF}$ = 12.0 Hz, 1H, H^{C4}), 5.48 (dd, ^4J = 2.3 Hz, $^3J_{HF}$ = 8.5 Hz, 1H, H^{A6}), 5.18 (dd, ^4J = 2.4 Hz, $^3J_{HF}$ = 8.2 Hz, 1H, H^{C6}), 4.13−4.04 (m, 4H, α-OCH_2), 1.85−1.76 (m, 4H, β-CH_2), 1.54 (quint, ^3J = 7.5 Hz, 2H, γ-CH_2), 1.48 (quint, ^3J = 7.3 Hz, 2H, γ-CH_2), 1.42−1.20 (m, 16H, δ-η-CH_2), 0.88 (t, ^3J = 6.9 Hz, 3H, CH_3), 0.82 (t, ^3J = 6.9 Hz, 3H, CH_3). ^{19}F{^{1}H} NMR (188 MHz, CD_3CN): δ −73.30 (d, $^1J_{FP}$ = 706.7 Hz), −110.19 (d, ^4J = 9.3 Hz), −110.87 (d, ^4J = 9.4 Hz), −111.28 (d, ^4J = 9.4 Hz), −111.71 (d, ^4J = 9.4 Hz). HRMS (ESI-TOF). Calcd for $C_{80}H_{71}F_4IrN_9O_3Ru$ ([M − PF_6]$^+$): *m*/*z* 1576.4230. Found: *m*/*z* 1576.4289. IR (KBr): $\tilde{\nu}_{CN}$ 2109, 2125 cm^{-1}.

■ ASSOCIATED CONTENT

Supporting Information

The Supporting Information is available free of charge on the ACS Publications website at DOI: 10.1021/acs.inorgchem.5b02919.

NMR spectra, CV, SEC spectra, kinetic studies on the thiocyanate isomerism, absorption, excitation, and emission spectra, and additional experimental and computational details (PDF)

■ AUTHOR INFORMATION

Corresponding Author

*E-mail: ulrich.schubert@uni-jena.de.

Notes

The authors declare no competing financial interest.

■ ACKNOWLEDGMENTS

The authors are grateful for financial support by the Deutsche Forschungsgemeinschaft (Grants SCHU1229-16/1 and DI1517-3/1). The authors also thank Dr. Wolfgang Günther (NMR), Gabriele Sentis (NMR and IR), Tina Schlotthauer (ESI MS), and Nicole Fritz (ESI MS) for their help with the respective measurements.

■ REFERENCES

(1) (a) Balzani, V.; Bergamini, G.; Marchioni, F.; Ceroni, P. *Coord. Chem. Rev.* **2006**, *250*, 1254−1266. (b) Frischmann, P. D.; Mahata, K.; Würthner, F. *Chem. Soc. Rev.* **2013**, *42*, 1847−1870. (c) Balzani, V.; Juris, A.; Venturi, M.; Campagna, S.; Serroni, S. *Chem. Rev.* **1996**, *96*, 759−833. (d) Puntoriero, F.; Sartorel, A.; Orlandi, M.; La Ganga, G.; Serroni, S.; Bonchio, M.; Scandola, F.; Campagna, S. *Coord. Chem. Rev.* **2011**, *255*, 2594−2601. (e) Zanoni, K. P. S.; Coppo, R. L.; Amaral, R. C.; Murakami Iha, N. Y. *Dalton Trans.* **2015**, *44*, 14559.

(2) (a) Tschierlei, S.; Karnahl, M.; Presselt, M.; Dietzek, B.; Guthmuller, J.; González, L.; Schmitt, M.; Rau, S.; Popp, J. *Angew. Chem., Int. Ed.* **2010**, *49*, 3981−3984. (b) Pfeffer, M. G.; Kowacs, T.; Wächtler, M.; Guthmuller, J.; Dietzek, B.; Vos, J. G.; Rau, S. *Angew. Chem., Int. Ed.* **2015**, *54*, 6627−6631. (c) Pfeffer, M. G.; Schäfer, B.; Smolentsev, G.; Uhlig, J.; Nazarenko, E.; Guthmuller, J.; Kuhnt, C.; Wächtler, M.; Dietzek, B.; Sundström, V.; Rau, S. *Angew. Chem., Int. Ed.* **2015**, *54*, 5044−5048.

(3) Kübel, J.; Winter, A.; Schubert, U. S.; Dietzek, B. *J. Phys. Chem. A* **2014**, *118*, 12137−12148.

(4) (a) De Cola, L.; Belser, P. *Coord. Chem. Rev.* **1998**, *177*, 301−346. (b) Medlycott, E. A.; Hanan, G. S. *Coord. Chem. Rev.* **2006**, *250*, 1763−1782.

(5) Sabatini, C.; Barbieri, A.; Barigelletti, F.; Arm, K. J.; Williams, J. A. G. *Photochem. Photobiol. Sci.* **2007**, *6*, 397−405.

(6) Osio Barcina, J. O.; Herrero-García, N.; Cucinotta, F.; De Cola, L.; Contreras-Carballada, P.; Williams, R. M.; Guerrero-Martínez, A. *Chem. - Eur. J.* **2010**, *16*, 6033−6040.

(7) Van Diemen, J. H.; Hage, R.; Haasnoot, J. G.; Lempers, H. E. B.; Reedijk, J.; Vos, J. G.; De Cola, L.; Barigelletti, F.; Balzani, V. *Inorg. Chem.* **1992**, *31*, 3518−3522.

(8) Vogler, L. M.; Scott, B.; Brewer, K. J. *Inorg. Chem.* **1993**, *32*, 898−903.

(9) Cavazzini, M.; Pastorelli, P.; Quici, S.; Loiseau, F.; Campagna, S. *Chem. Commun.* **2005**, 5266−5268.

(10) Sandroni, M.; Zysman-Colman, E. *Dalton Trans.* **2014**, *43*, 3676−3680.

(11) Swanick, K. N.; Sandroni, M.; Ding, Z. F.; Zysman-Colman, E. *Chem. - Eur. J.* **2015**, *21*, 7435−7440.

(12) (a) Vahrenkamp, H.; Geiß, A.; Richardson, G. N. *J. Chem. Soc., Dalton Trans.* **1997**, 3643−3652. (b) Tanase, S.; Reedijk, J. *Coord. Chem. Rev.* **2006**, *250*, 2501−2510. (c) Baraldo, L. M.; Forlano, P.; Parise, A. R.; Slep, L. D.; Olabe, J. A. *Coord. Chem. Rev.* **2001**, *219*, 881−921. (d) Macatangay, A. V.; Endicott, J. F. *Inorg. Chem.* **2000**, *39*, 437−446. (e) Watzky, M. A.; Macatangay, A. V.; Van Camp, R. A.; Mazzetto, S. E.; Song, X. Q.; Endicott, J. F.; Buranda, T. *J. Phys. Chem. A* **1997**, *101*, 8441−8459. (f) Ward, M. D. *Dalton Trans.* **2010**, *39*, 8851−8867.

(13) (a) Cadranel, A.; Aramburu Troselj, B. M.; Yamazaki, S.; Albores, P.; Kleiman, V. D.; Baraldo, L. M. *Dalton Trans.* **2013**, *42*,

DOI: 10.1021/acs.inorgchem.5b02919
Inorg. Chem. 2016, 55, 5152−5167

16723−16732. (b) Pieslinger, G. E.; Albores, P.; Slep, L. D.; Coe, B. J.; Timpson, C. J.; Baraldo, L. M. *Inorg. Chem.* **2013**, *52*, 2906−2917. (c) Cutin, E. H.; Katz, N. E. *Polyhedron* **1993**, *12*, 955−960. (d) Scandola, F.; Argazzi, R.; Bignozzi, C. A.; Chiorboli, C.; Indelli, M. T.; Rampi, M. A. *Coord. Chem. Rev.* **1993**, *125*, 283−292. (e) Pieslinger, G. E.; Albores, P.; Slep, L. D.; Baraldo, L. M. *Angew. Chem., Int. Ed.* **2014**, *53*, 1293−1296. (f) Pieslinger, G. E.; Aramburu-Troselj, B. M.; Cadranel, A.; Baraldo, L. M. *Inorg. Chem.* **2014**, *53*, 8221−8229.

(14) Varshavsky, Y. S.; Cherkasova, T. G.; Galding, M. R.; Khrustalev, V. N.; Podkorytov, I. S.; Gindin, V. A.; Smirnov, S. N.; Nikol'skii, A. B. *J. Organomet. Chem.* **2009**, *694*, 2917−2922.

(15) (a) Dowling, N.; Henry, P. M.; Lewis, N. A.; Taube, H. *Inorg. Chem.* **1981**, *20*, 2345−2348. (b) Ma, X.; Lin, C. S.; Hu, S. M.; Tan, C. H.; Wen, Y. H.; Sheng, T. L.; Wu, X. T. *Chem. - Eur. J.* **2014**, *20*, 7025−7036. (c) Cadranel, A.; Albores, P.; Yamazaki, S.; Kleiman, V. D.; Baraldo, L. M. *Dalton Trans.* **2012**, *41*, 5343−5350.

(16) Baca, S. G.; Adams, H.; Sykes, D.; Faulkner, S.; Ward, M. D. *Dalton Trans.* **2007**, 2419−2430.

(17) Ali, N. M.; MacLeod, V. L.; Jennison, P.; Sazanovich, I. V.; Hunter, C. A.; Weinstein, J. A.; Ward, M. D. *Dalton Trans.* **2012**, *41*, 2408−2419.

(18) Baranoff, E.; Orselli, E.; Allouche, L.; Di Censo, D.; Scopelliti, R.; Gratzel, M.; Nazeeruddin, M. K. *Chem. Commun.* **2011**, *47*, 2799−2801.

(19) Nazeeruddin, M. K.; Humphry-Baker, R.; Berner, D.; Rivier, S.; Zuppiroli, L.; Graetzel, M. *J. Am. Chem. Soc.* **2003**, *125*, 8790−8797.

(20) (a) Wasylenko, D. J.; Ganesamoorthy, C.; Koivisto, B. D.; Henderson, M. A.; Berlinguette, C. P. *Inorg. Chem.* **2010**, *49*, 2202−2209. (b) Gerken, J. B.; Rigsby, M. L.; Ruther, R. E.; Pérez-Rodriguez, R. J.; Guzei, I. A.; Hamers, R. J.; Stahl, S. S. *Inorg. Chem.* **2013**, *52*, 2796−2798.

(21) (a) Brewster, T. P.; Ding, W. D.; Schley, N. D.; Hazari, N.; Batista, V. S.; Crabtree, R. H. *Inorg. Chem.* **2011**, *50*, 11938−11946. (b) Hue, R.; Mann, K. R.; Gladfelter, W. L. *J. Coord. Chem.* **2014**, *67*, 17−28.

(22) (a) Li, J.; Djurovich, P. I.; Alleyne, B. D.; Yousufuddin, M.; Ho, N. N.; Thomas, J. C.; Peters, J. C.; Bau, R.; Thompson, M. E. *Inorg. Chem.* **2005**, *44*, 1713−1727. (b) Di Censo, D.; Fantacci, S.; De Angelis, F.; Klein, C.; Evans, N.; Kalyanasundaram, K.; Bolink, H. J.; Grätzel, M.; Nazeeruddin, M. K. *Inorg. Chem.* **2008**, *47*, 980−989.

(23) Chan, K.-C.; Chu, W.-K.; Yiu, S.-M.; Ko, C.-C. *Dalton Trans.* **2015**, *44*, 15135−15144.

(24) Juris, A.; Balzani, V.; Barigelletti, F.; Campagna, S.; Belser, P.; Vonzelewsky, A. *Coord. Chem. Rev.* **1988**, *84*, 85−277.

(25) Chi, Y.; Chou, P. T. *Chem. Soc. Rev.* **2010**, *39*, 638−655.

(26) Hewitt, J. T.; Vallett, P. J.; Damrauer, N. H. *J. Phys. Chem. A* **2012**, *116*, 11536−11547.

(27) (a) Mulliken, R. S. *J. Am. Chem. Soc.* **1952**, *74*, 811−824. (b) Hush, N. S. *Prog. Inorg. Chem.* **1967**, *8*, 391−444. (c) Hush, N. S. *Electrochim. Acta* **1968**, *13*, 1005−1023. (d) Brunschwig, B. S.; Creutz, C.; Sutin, N. *Chem. Soc. Rev.* **2002**, *31*, 168−184. (e) D'Alessandro, D. M.; Keene, F. R. *Chem. Soc. Rev.* **2006**, *35*, 424−440.

(28) Robin, M. B.; Day, P. *Adv. Inorg. Chem. Radiochem.* **1968**, *10*, 247−422.

(29) (a) Rommel, S. A.; Sorsche, D.; Rockstroh, N.; Heinemann, F. W.; Kübel, J.; Wächtler, M.; Dietzek, B.; Rau, S. *Eur. J. Inorg. Chem.* **2015**, *2015*, 3730−3739. (b) Happ, B.; Kübel, J.; Pfeffer, M. G.; Winter, A.; Hager, M. D.; Dietzek, B.; Rau, S.; Schubert, U. S. *Macromol. Rapid Commun.* **2015**, *36*, 671−677. (c) King, K. A.; Watts, R. J. *J. Am. Chem. Soc.* **1987**, *109*, 1589−1590.

(30) (a) Brown, A. M.; McCusker, C. E.; McCusker, J. K. *Dalton Trans.* **2014**, *43*, 17635−17646. (b) Zhang, Y.; Kupfer, S.; Zedler, L.; Schindler, J.; Bocklitz, T.; Guthmuller, J.; Rau, S.; Dietzek, B. *Phys. Chem. Chem. Phys.* **2015**, *17*, 29637−29646.

(31) (a) Chaignon, F.; Torroba, J.; Blart, E.; Borgström, M.; Hammarström, L.; Odobel, F. *New J. Chem.* **2005**, *29*, 1272−1284. (b) Barthelmes, K.; Kübel, J.; Winter, A.; Wächtler, M.; Friebe, C.; Dietzek, B.; Schubert, U. S. *Inorg. Chem.* **2015**, *54*, 3159−3171.

(32) Meyer, T. J. *Pure Appl. Chem.* **1986**, *58*, 1193−1206.

(33) Puntoriero, F.; Nastasi, F.; Galletta, M.; Campagna, S. Photophysics and Photochemistry of Non-Carbonyl-Containing Coordination and Organometallic Compounds. In *Comprehensive Inorganic Chemistry II*, 2nd ed.; Poeppelmeier, J. R., Ed.; Elsevier: Amsterdam, The Netherlands, 2013; pp 255−337.

(34) Tsai, C.-N.; Allard, M. M.; Lord, R. L.; Luo, D.-W.; Chen, Y.-J.; Schlegel, H. B.; Endicott, J. F. *Inorg. Chem.* **2011**, *50*, 11965−11977.

(35) Jaeger, M.; Freitag, L.; González, L. *Coord. Chem. Rev.* **2015**, *304*−*305*, 146−165.

(36) Adamo, C.; Barone, V. *J. Chem. Phys.* **1999**, *110*, 6158−6170.

(37) Zhao, Y.; Truhlar, D. G. *J. Phys. Chem. A* **2004**, *108*, 6908−6918.

(38) Wang, J.; Hanan, G. S. *Synlett* **2005**, 1251−1254.

(39) Winter, A.; Egbe, D. A. M.; Schubert, U. S. *Org. Lett.* **2007**, *9*, 2345−2348.

(40) Sullivan, B. P.; Calvert, J. M.; Meyer, T. J. *Inorg. Chem.* **1980**, *19*, 1404−1407.

(41) Kübel, J.; Schroot, R.; Wächtler, M.; Schubert, U. S.; Dietzek, B.; Jäger, M. *J. Phys. Chem. C* **2015**, *119*, 4742−4751.

(42) Frisch, M. J.; Trucks, G. W.; Schlegel, H. B.; Scuseria, G. E.; Robb, M. A.; Cheeseman, J. R.; Scalmani, G.; Barone, V.; Mennucci, B.; Petersson, G. A.; Nakatsuji, H.; Caricato, M.; Li, X.; Hratchian, H. P.; Izmaylov, A. F.; Bloino, J.; Zheng, G.; Sonnenberg, J. L.; Hada, M.; Ehara, M.; Toyota, K.; Fukuda, R.; Hasegawa, J.; Ishida, M.; Nakajima, T.; Honda, Y.; Kitao, O.; Nakai, H.; Vreven, T.; Montgomery, J. A., Jr.; Peralta, J. E.; Ogliaro, F.; Bearpark, M.; Heyd, J. J.; Brothers, E.; Kudin, K. N.; Staroverov, V. N.; Kobayashi, R.; Normand, J.; Raghavachari, K.; Rendell, A.; Burant, J. C.; Iyengar, S. S.; Tomasi, J.; Cossi, M.; Rega, N.; Millam, N. J.; Klene, M.; Knox, J. E.; Cross, J. B.; Bakken, V.; Adamo, C.; Jaramillo, J.; Gomperts, R.; Stratmann, R. E.; Yazyev, O.; Austin, A. J.; Cammi, R.; Pomelli, C.; Ochterski, J. W.; Martin, R. L.; Morokuma, K.; Zakrzewski, V. G.; Voth, G. A.; Salvador, P.; Dannenberg, J. J.; Dapprich, S.; Daniels, A. D.; Farkas, Ö.; Foresman, J. B.; Ortiz, J. V.; Cioslowski, J.; Fox, D. J. *Gaussian 09*, revision A.02; Gaussian, Inc.: Wallingford, CT, 2010.

(43) (a) Becke, A. D. *J. Chem. Phys.* **1993**, *98*, 5648−5652. (b) Lee, C. T.; Yang, W. T.; Parr, R. G. *Phys. Rev. B: Condens. Matter Mater. Phys.* **1988**, *37*, 785−789.

(44) (a) Cancès, E.; Mennucci, B.; Tomasi, J. *J. Chem. Phys.* **1997**, *107*, 3032−3041. (b) Tomasi, J.; Mennucci, B.; Cammi, R. *Chem. Rev.* **2005**, *105*, 2999−3093.

(45) (a) O'Boyle, N. M.; Tenderholt, A. L.; Langner, K. M. *J. Comput. Chem.* **2008**, *29*, 839−845. (b) O'Boyle, N. M.; Vos, J. G. *GaussSum*, version 2.2.5; Dublin City University: Dublin, 2009.

(46) Dennington, R.; Keith, T.; Millam, J. *GaussView*, version 5.0.8; Semichem Inc.: Shawnee Mission, KS, 2009.

NOTE ADDED AFTER ASAP PUBLICATION

This paper was published ASAP on May 23, 2016. The Supporting Information was updated. The revised paper was reposted on May 26, 2016.

DOI: 10.1021/acs.inorgchem.5b02919
Inorg. Chem. 2016, 55, 5152−5167